Aspects of the geology of massive sulfide deposits from the Balcooma district, northern Queensland and Rosebery, Tasmania: Implications for ore genesis

by

David Lowell Huston, B.Sc., M.Sc.

in the Faculty of Science, Department of Geology

A thesis submitted in partial fulfillment of the requirements for the degree of Doctor of Philosophy

University of Tasmania

December 1988

This thesis contains no material that has been accepted for the award of any other higher degree or graduate diploma in any tertiary institution and, to the best of the author's knowledge and belief, no material that has been written or published by another person except where reference is given.

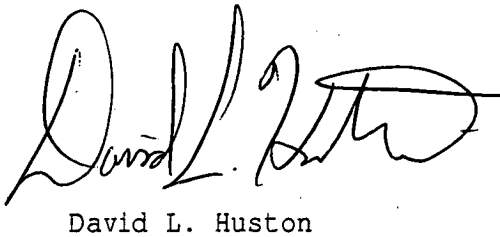

David L. Huston
December 1988

Abstract

Balcooma massive sulfide district

The Balcooma and Dry River South volcanogenic massive sulfide deposits occur in the Cambro-Ordovician Balcooma metamorphic belt in northern Queensland. Structural and stratigraphic studies indicate: (1) the Balcooma deposit originally contained three stratigraphically separate sulfide bodies in a pelitic lens that have been folded and faulted to produce the present five bodies; (2) faulting has been more significant than folding at the Dry River South deposit; and (3) the two prospects occur at approximately the same stratigraphic level where significant volcaniclastic input ceased.

Alteration studies indicate that chloritic alteration at Balcooma has involved silica, iron, magnesium, copper, zinc and sulfur addition, and sodium, calcium, potassium, strontium and rubidium loss. An outer zone of quartz-muscovite-pyrite alteration involved silica, base metals and sulfur addition, and sodium, calcium, and strontium loss at Balcooma. Alteration at Dry River South involved similar changes to the Balcooma quartz-muscovite-pyrite alteration. Halos of weak sodium loss exist around both deposits.

Metal zonation studies indicate that gold is associated with copper at both deposits. Mineragraphic studies confirm this association at Balcooma. Silver occurs as a trace metal in galena in lead-rich mineralization from both prospects, but in Balcooma copper-rich mineralization it occurs in chalcopyrite.

Precious metals at Rosebery

Metal zonation studies at Rosebery indicate that gold is strongly associated with zinc at the top of the massive sulfide mound, and silver is associated with lead. Electrum is usually associated with pyrite although in baritic zones it occurs with other minerals. Tetrahedrite hosts most silver.

Geological and geochemical controls on metal deposition

Observation and geochemical modelling indicate that constant 100Zn/(Zn+Pb) ratios result from the saturation of mineralizing fluids in zinc and lead. This ratio is useful in distinguishing massive sulfide mineralization from other types of mineralization.

Gold in volcanogenic massive sulfide deposits has two associations: (1) with zinc at the top of the mound (e.g. Rosebery), and (2) with copper at the base of the mound (e.g. Balcooma and Dry River South). The former association is caused by thio-transport of gold in high pH (>4.5), low temperature (<275°C) fluids and deposition by oxidation and dilution at the seawater interface. The latter association is caused by chloro-transport of gold in low pH (<4.5), high temperature (>275°C) fluids and deposition by pH increase and/or temperature decrease. High gold grades are favored at extreme pH conditions.

Silver in massive sulfide deposits has three occurrences: (1) in chalcopyrite in copper-rich mineralization (e.g. Balcooma), (2) in galena in zinc-lead-rich mineralization (e.g. Dry River South and Balcooma), and (3) in tetrahedrite in zinc-lead-rich mineralization (e.g. Rosebery). The fluid temperature and the Bi/Sb ratio of the mineralizing fluid controls these associations.

Electrum from deposits of the copper-gold association has a generally high and narrow range in fineness (700 to 900), whereas electrum from the zinc-gold association has a lower and wider range (300 to 800). These differences can be modelled by assuming gold chlorocomplexes in the copper-gold association and gold-thiocomplexing in the zinc-gold association.

Acknowledgements

During his doctoral studies the author has benefited from interaction with the staff of the University of Tasmania, the geologic staffs of the Electrolytic Zinc Company of Australasia and the Carpentaria Exploration Company, and the staff of the Tasmanian Department of Mines. First and foremost, Ross Large of the University of Tasmania provided many of the initial ideas that were investigated during the authors studies as well as inspiration and excellent advice on various aspects of the project. Ron Berry helped the author to understand the complexities of the structure of the Balcooma and Dry River South prospects, and Bruce Gemmell assisted in the understanding of controls on silver mineralogy in these deposits. Members of the University of Tasmania's Ore Deposit Research Team, which includes Sharon Adrichem, Garry Davidson, Ian Gordon, Steve Hunns, Khin Zaw, Mark Rattenbury, Peter McGoldrick, Peter Ruxton Joe Stolz and Richard Wedekind, provided much critical advice on the author's studies. The rest of the staff and students from the Department of Geology, University of Tasmania are thanked for their support and assistance with various aspects of the project. The author also thanks the University of Tasmania for financial support through a University of Tasmania Postgraduate Research Award.

Bob Hall of Carpentaria Exploration Company and Peter Legge of Electrolytic Zinc provided support for the investigations undertaken by the author. The author recognizes the important early contributions of Ken Harvey, Mike Mulroney and John Nenke to the understanding of the Balcooma prospect and the important contributions of Terry Taylor, John Fabray and Bruce Stainforth to the understanding of the Dry River South prospect. The latter three are especially thanked for keeping the author sane during the long field seasons in Balcooma camp. The author thanks Geoff Iliff, Terry Lees, John Howarth, Lorraine Walshe, Linda Martin-Frazier, Jim Farquhar, Rod Sainty, Ian McDonald and Gerald Purvis for their discussion and help during studies at the Rosebery deposit.

Geoff Green of the Tasmanian Department of Mines was very helpful when the author was puzzled about the significance of numbers that came magically from the mass spectrometer. The author thanks

Mike Power Sr. and Mike Power Jr. for their introduction and help on the maze of isotope lines, and Phil Robinson for his instructions and help with analytical chemistry and patience when the author had difficulties with the XRF. June Pongratz helped immensely by drafting many of the diagrams in the thesis. Simon Stevens is thanked for cutting and polishing the many thin sections used in this study.

Finally, the author wishes to thank his wife Siau Hwi for all her support and sacrifice to finish this thesis. Hopefully the inordinate lengths of time spent in the Geology Department during studies will now be spent with her.

Table of contents

List of figures

List of tables

List of Plates

Introduction

The research presented in this thesis has been divided into three parts which address three separate aspects of the author's research. The first part reports the author's studies on the geology of deposits in the newly discovered Balcooma massive sulfide district which is located in northern Queensland which were undertaken from May 1985 to December 1988. The original intent of this research was to describe in detail the geology of the highly deformed Balcooma prospect. During these studies the adjacent Dry River South prospect was discovered and the author extended his studies to this deposit.

The second part addresses the author's research on the distribution of gold and silver in the north-end of the Rosebery deposit which was undertaken between October 1984 and May 1985. Much of this work has been published in Huston and Large (1988). The Rosebery research was conducted while waiting for the Balcooma project to commence.

Parts one and two are intended to be largely descriptive although some interpretation is offered regarding the geological environment of formation and the style of deformation of the ores. In part three studies of the behaviour of lead, zinc, gold and silver have been undertaken to produce thermodynamic models that have a wider application to volcanogenic massive sulfide deposits in general. This modelling was undertaken throughout the course of the author's doctoral studies. The modelling in Chapters one and two in Part three was undertaken in conjunction with the author's supervisor, Dr. Ross Large, and has been published as Huston and Large (1987a, 1987b and 1989). These two chapters were written as to exclude as much of Dr. Large's contribution as possible although this was not always possible and the input of Dr. Large is recognized by a reference to the relevant published paper. Additional material relating to the author's research since the papers in question were submitted has been added to the material previously published.

Part I

The geology of the Balcooma massive sulfide district

Chapter 1
Introduction and regional geology

Introduction

The Balcooma metamorphic belt is a northeast trending Lower Paleozoic sequence of strongly deformed metasediments and metavolcanics located some 40 km northwest of Greenvale in northeastern Queensland (Fig. 1). The potential for base metal mineralization in the belt was initially realized with the discovery of a gossan near the junction of Clayhole Creek and Dry River by Geopeko geologists in 1976. Mining lease 805 (Surveyor 1) of 128 hectares was granted on June 1 of that year to Geopeko.

Exploration interest in the area waned until August 1978 when Carpentaria Exploration Company applied for, and was granted, Authority to Prospect 2036M (Balcooma) upon recognition that the region had potential for volcanogenic massive sulfide mineralization. The recognition of color anomalies on aerial photographs in combination with anomalous stream sediment, rock chip and soil geochemistry led to the sighting of the first drill hole at Balcooma under a lead gossan in late 1978. This hole resulted in two intersections of copper-rich massive sulfide of 7 m at 2.6% Cu and 26 m at 2.3% Cu, respectively (Harvey, 1979 and 1984a) Later holes indicated the presence of zinc-lead-rich massive sulfide mineralization to the west.

Subsequent to the discovery of the Balcooma deposit, interest in the area intensified, and persistent exploration on the down plunge extensions of the Surveyor 1 gossan resulted in the discovery of zinc-lead-rich massive sulfide in 1983 by the Conjubuoy Joint Venture (Noranda Pacific, 1985). Since that time, the application of Sirotem transient electromagnetics resulted in the discovery of the Dry River South massive sulfide lens to the south of the Surveyor lease in 1985 (Shalley, 1987). Subsequent drilling by the Conjubuoy Joint Venture has indicated that the Dry River South mineralization extends north onto the Surveyor 1 lease and forms a separate zone of mineralization from the Surveyor 1 deposit (McKinnon, 1988). The three deposits lie along a 4 km long, north-northeast trend around the contact between metasediments and metavolcanics (Fig. 1). Table 1 summarizes the

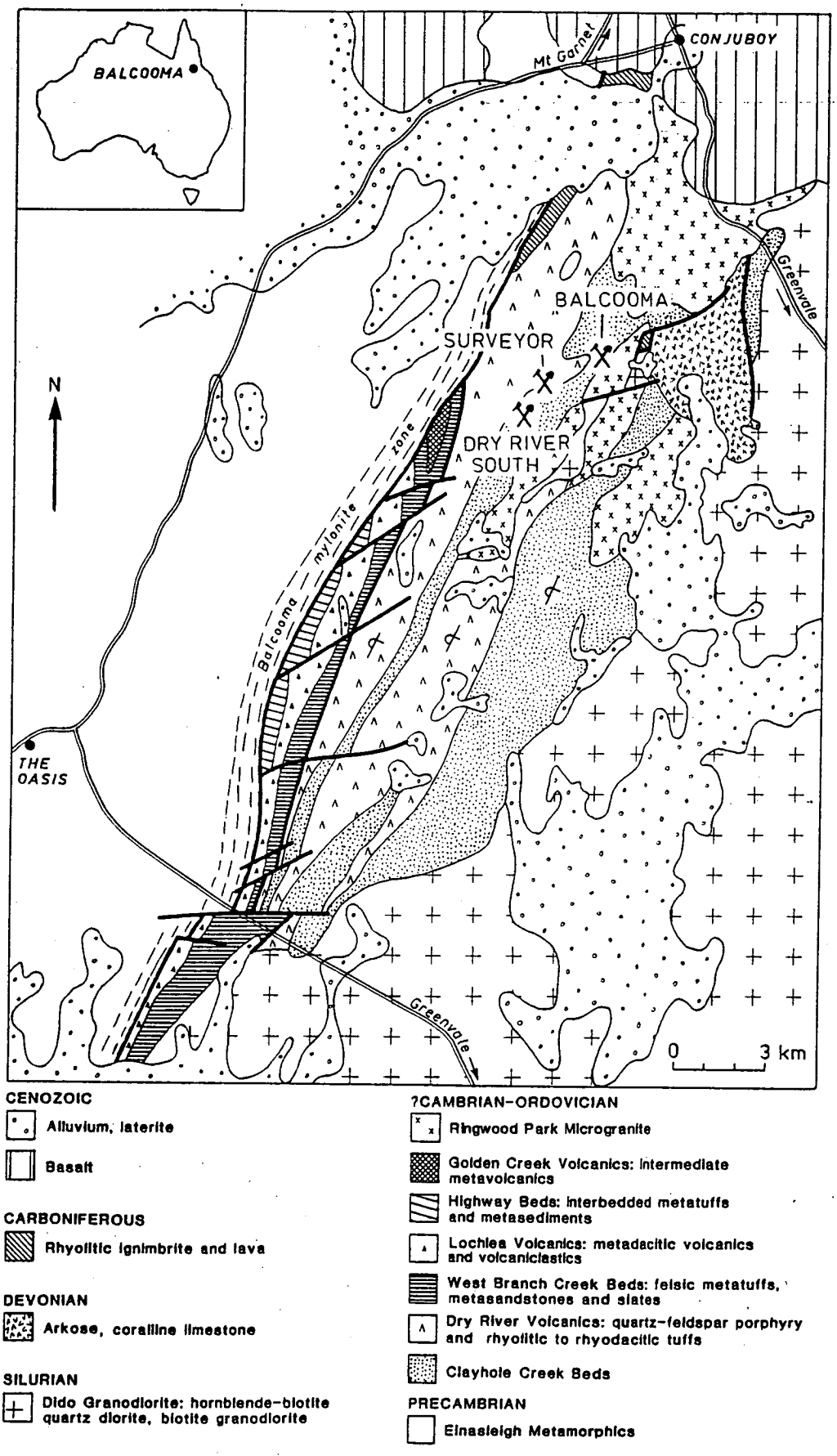

Figure 1. Geology of the Balcooma metamorphic belt (after Withnall, 1982, 1987).

Table 1. Published grade and tonnage data for volcanogenic massive sulfide deposits in the Balcooma Metamorphics.

Deposit	Tonnage (m.t.)	Cu (%)	Pb (%)	Zn (%)	Ag (g/t)	Au (g/t)	References
Balcooma							
Cu shoots	3.5	3.0	--	--	--	--	Harvey (1984a)
Zn-Pb shoots	--	--	--	--	--	--	
Surveyor	0.48	0.8	7.3	19.7	146	1.0	McKinnon (1988)
Dry River South							
A to P 2036M	1.3	1.0	3.6	9.9	98	0.7	Huston and Taylor (in press)
ML805	0.23	1.6	2.0	6.9	89	0.8	McKinnon (1988)
Dry River South (total)	1.5	1.1	3.4	9.4	97	0.7	

published grades and tonnages for the deposits. The Balcooma copper-rich mineralization also contains roughly 20-30 g/t Ag and 0.3-0.4 g/t Au but negligible lead and zinc. A zone of several hundred thousand tonnes of zinc-lead-rich massive sulfide also occurs to the west of copper-rich mineralization at Balcooma, but published grade and tonnage data for this zone is not available. The estimates for the Dry River South massive sulfide lens do not include recent drilling on the southern edge of the prospect.

In addition to these three major deposits, several minor occurrences have been noted, the most significant of which is the West Boyds Creek stratiform barite occurrence which is located in the southwestern part of the Balcooma metamorphic belt (Fig. 1; Mulroney, 1983). A total of 30 kg of gold was recovered from placer and shallow hard rock operations on steeply dipping, north trending quartz veins (Harvey, 1979) in the west-central part of the belt near the contact between metasediments and metavolcanics (Fig. 1).

Regional geology

The interpretation of the rocks containing the Balcooma massive sulfide district has been subject to much controversy. The units that were to become the Balcooma metamorphic belt were initially described by White (1962, 1965) and assigned a late Paleozoic age by Branch (1966). However, Rubenach (1978) interpreted them as mylonitized granite. As late as 1980, these rocks were considered to have a middle Proterozoic age (Withnall et al., 1980).

K. Harvey of Carpentaria Exploration Company initially proposed that the Balcooma Metamorphics were a mixed sequence of metasediments and metavolcanics of Lower Paleozoic age based on lithological similarities to the Mt. Windsor Volcanics some 200 km to the south. This interpretation has since been supported by other workers (Withnall, 1982; and Henderson, 1986), and by lead isotope studies on the Balcooma deposit (Gulson and Vaasjoki, 1987).

The Balcooma metamorphics are bounded on the east by the Balcooma Mylonite Zone and the Proterozoic Einesleigh Metamorphics (Fig. 1; Withnall, 1982; and Harvey, 1984b). To the east the belt is bounded by the Silurian Dido Granodiorite, and in the very north the belt is covered by Cenozoic basalt (Withnall, 1982).

Stratigraphy

Due to the intensity of deformation and the lack of complete outcrop in the region, the detailed statigraphy of the Balcooma Metamorphics has not been resolved. Withnall (1982) has estimated a thickness of some 4000 m for the entire package. Harvey (1984b) has proposed a working statigraphic column (Table 2) and his terminology is adopted here with some changes to the inferred stratagraphic relationships.

According to Harvey (1984b), the basal unit of the Balcooma Metamorphics is the Clayhole Creek Beds. This unit consists of interbedded quartz-albite and quartz-muscovite-biotite-staurolite schists which are interpreted as a sequence of metamorphosed graywackes, siltstones and shales. The Balcooma deposit lies within this sequence along the eastern side of a major anticline.

Harvey (1984b) inferred that the Clayhole Creek Beds are overlain by a sequence of rhyolitic to rhyodacitic volcanics that he terms the Dry River Volcanics. This unit consists largely of quartz-feldspar porphyry, coarse felsic fragmentals and fine tuffs with minor interbedded sediments (Withnall, 1982; and Harvey, 1984b). Harvey (1984b) interpreted the presence of columnar jointing in quartz-feldspar porphyry some 10 km south of the Balcooma prospect. The Dry River Volcanics form two belts on the western and eastern sides of the central area of Clayhole Creek Beds. The Dry River South and Surveyor deposits occur near the contact between these two units.

The statigraphic relationship between the Clayhole Creek Beds and the Dry River Volcanics is not clear cut. Both the Dry River South and the Surveyor prospects have a footwall composed predominately of metamorphosed rhyolitic to rhyodacitic fragmentals and lavas (Chapter 3 and Noranda Pacific, 1985). Moreover, the immediate footwall to the Balcooma prospect contains some 10% felsic fragmentals (Chapter 2). As sediments of the Clayhole Creek Beds occur in the immediate hanging wall to the Balcooma and Dry River South prospects (Chapters 2 and 3), a more complicated relationship between the Clayhole Creek Beds and the Dry River Volcanics is envisaged. The presence of felsic metavolcaniclastic rocks stratigraphically below the Clayhole Creek Beds can be explained in two ways: (1) a unit of felsic volcanics lies below the Clayhole Creek Beds, or (2) the Dry River Volcanics and the Clayhole Creek

Table 2. Stratigraphic column as interpreted by Harvey (1984b).

Unit	Thickness (m)	Lithology	Premetamorphic lithology
Golden Creek Volcanics	800+	Actinolite-albite schist and quartz-mica schist.	Intermediate to mafic tuffs, flows and breccias with minor intercalated sediments.
Highway Beds	600-800	Quartz-mica schist and quartz-mica-albite schist.	Sediments, felsic tuffs and minor mafic volcanics.
Lochlea Volcanics	500-800	Metarhyolite, Metadacite and minor metasediments.	Rhyolitic to dacitic flows and tuffs with minor sediments.
Dry River Volcanics	1500+	Quartz-mica-albite schist and quartz-feldspar porphyry.	Rhyolites, rhyodacites, dacites and associated volcaniclastic rocks.
Clayhole Creek Beds	1500+	Quartz-mica schist, quartz-mica-staurolite schist and quartz-mica-albite schist.	Graywackes, siltstones, shales and acid tuffs.

Beds have an interfingering relationship and are at least in part time equivalents. The latter option is preferred as the felsic volcanics in footwall to Surveyor are continuous with the Dry River Volcanics that Harvey (1984b) interpreted to overly the Clayhole Creek Beds (Figs. 1 and 2). Henderson (1986) proposed an interfingering relationship between the Trooper Creek Formation and an inferred volcanic arc in the Mt. Windsor Subprovince. In an analogous way, the Dry River Volcanics may be the volcanic island arc and the Clayhole Creek Beds may be equivalent to the Trooper Creek Formation.

Harvey (1984b) interpreted that the West Branch Creek Beds, which contain the West Boyds Creek mineralization and the Balcooma goldfield, occur stratigraphically above the Dry River Volcanics to the west. These rocks contain a mixture of felsic tuffs, sandstones, siltstones and slates. Overlying this unit to the west is a massive dacite (the Lochlea Volcanics) that differs from the Dry River Volcanics by lacking quartz phenocrysts, containing plagioclase phenocrysts only locally, and containing lenticular clasts and wisps reminiscent of fiamme (Withnall, 1982; and Harvey, 1984b). The uppermost and westernmost unit in the Balcooma Metamorphics is the Highway Beds. This unit consists of interbedded metatuffs and metasediments (Harvey, 1984b). Finally, a small package of intermediate volcanics, the Golden Creek Volcanics, occurs between the Dry River Volcanics and the Lochlea Volcanics in the west-central portion of the belt (Harvey, 1984b; and Withnall, 1982). Harvey (1984b) interpreted this rock unit as an infaulted block so its statigraphic position is unclear.

B. Stainforth (pers. com., 1987) has interpreted the contact between the Dry River Volcanics and the West Branch Creek Beds as a thrust fault; this lends uncertainty to the stratigraphic relationship between the Clayhole Creek Beds/Dry River Volcanics package to the West Boyds Creek/Lochlea Volcanics/Highway Beds package.

A marked unconformity exists between the Cambro-Ordovician (?) Balcooma Metamorphics and the overlying units. A Devonian package of coarse conglomerate, sandstone and coralline limestone (the Broken River Formation) occurs in the northern part of the belt along the Balcooma Mylonite Zone. A small patch of coralline limestone also occurs in the eastern part of the belt (Fig. 1; Harvey, 1984b; and

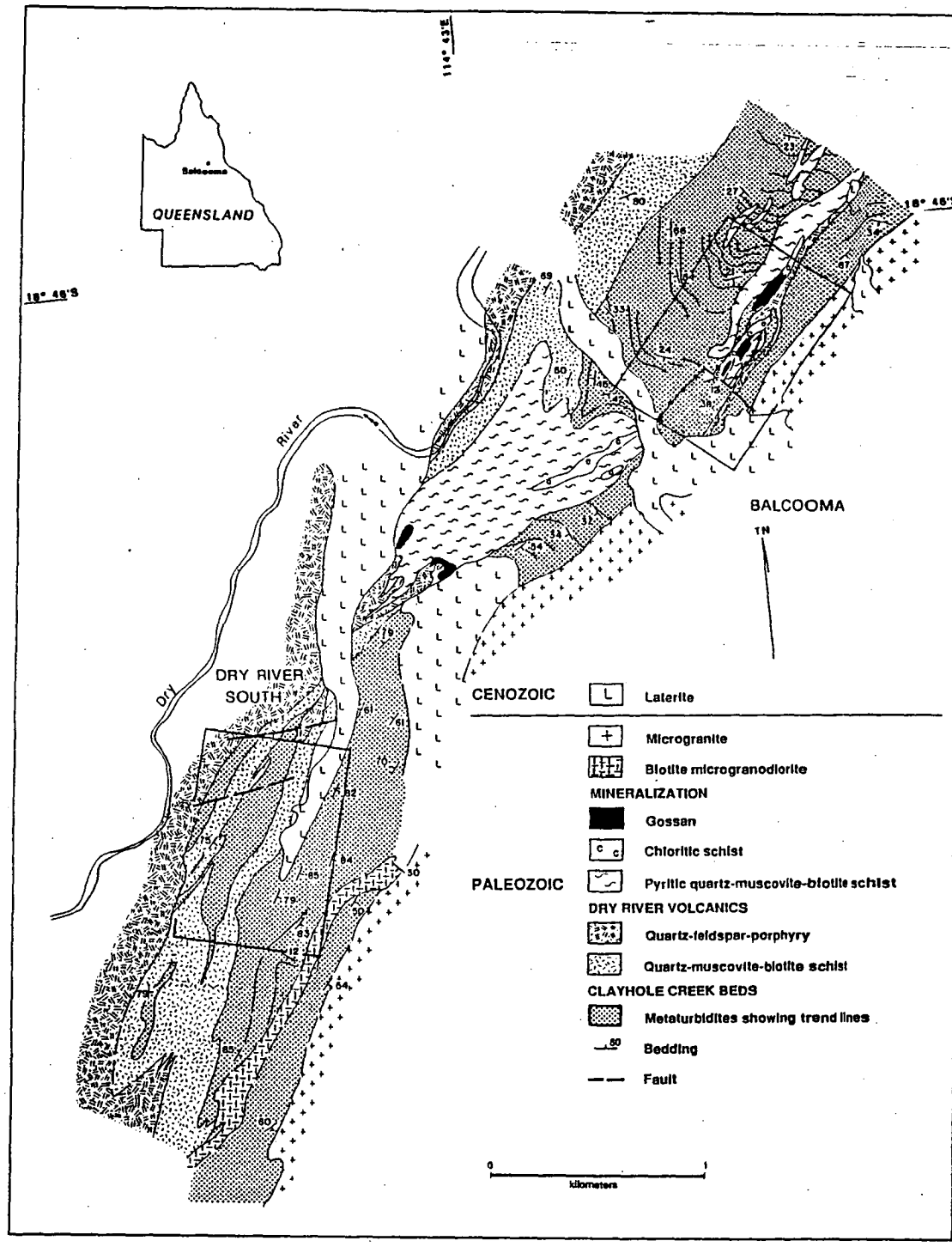

Figure 2. Geology of the Balcooma metamorphic belt around known massive sulfide deposits (after Huston and Taylor, in press). Mapping by T. Taylor.

Withnall, 1982). As this unit is not cleaved, cleavage forming deformation must have ceased prior to the Devonian.

A small package of Carboniferous continental felsic volcanics of the Bundock Creek Formation occurs to the northeast of the Balcooma Metamorphics. The northern end of the belt is covered by Cenozoic basalt (Withnall, 1982; Fig. 1) Alluvium and laterite occurs throughout the region.

Structure

The Balcooma Metamorphic belt has undergone at least five phases of deformation (Table 3). Three of these have involved folding, one has involved faulting; and one has involved a combination of folding and mylonitization.

Previous workers (Withnall, 1982; Harvey, 1984b; and Noranda Pacific, 1985) have recognized two major cleavages throughout the Balcooma Metamorphics. The dominant foliation (S_2 in this study) is present in most rock types. This foliation has a general strike to the north-northeast and a variable dip. Van der Hor (1984) observed that this foliation usually parallels bedding and infers that the associated F_2 folds are isoclinal in nature. This folding event may also have been accompanied by thrusting.

An earlier cleavage (S_1) has been recognized to the west of the Balcooma prospect (Chapter 2). This cleavage has not been recognized elsewhere, which indicates that it has been weakly developed or almost entirely destroyed by later pervasive cleavage (S_2).

The pervasive S_2 cleavage is commonly crenulated by a cleavage (S_3) with a north-northeast strike and a near vertical dip (Withnall, 1982; and Harvey, 1984b). The only recognized D_3 fold occurs to the west of the Balcooma prospect (Fig. 2; see also Chapter 2), has an open character, and has an amplitude of several hundred meters. The first three folding events were coaxial with fold axes plunging shallowly to the south-southwest.

A fourth cleavage (S_4) has been recognized as a crenulation overprinting S_2 and S_3 in micaceous lithologies from both Balcooma and Dry River South (Chapters 2 and 4). This cleavage strikes roughly east-west at Balcooma and northwest at Dry River South. The

Table 3. Structural elements of the Balcooma Metamorphics.

Event	Associated fabrics	Fold styles	Comments
D_1	S_1	Unknown, but axes plunge shallowly to the south-southwest.	Weakly developed or destroyed by later events. Coaxial with D_2 and D_3.
D_2	S_2	Isoclinal folds with axes plunging shallowly to the south-southwest.	Dominant foliation. Coaxial with D_1 and D_3. May be associated with thrust faulting.
D_3	S_3	Open, upright folds with axes plunging to the south-southwest. Possibly associated with the Balcooma Mylonite Zone.	Dominant crenulation cleavage. Coaxial with D_1 and D_2. S_3 is parallel to the fabric in the Balcooma Mylonite Zone.
D_4	S_4	Unknown, but axes plunge moderately to steeply to the south.	Developed only in very mica-rich lithologies.
D_5	--	--	Northeast trending faults with southwest blocks up.

fold axes plunge steeply to the south. As the orientation of S_3 has not undergone a large spread, the deformation that produced S_4 must not have affected the rocks around the prospects strongly.

The Balcooma Metamorphics are bounded to the west by the regionally important Balcooma Mylonite Zone. The mylonite zone is several hundred meters wide and has a north-northeast trend and a near vertical dip. As the adjacent Devonian Broken River Formation has a dip of 30° to the west, Harvey (1984b) inferred that the original mylonite zone dipped 60° to the west. Van der Hor (1984) inferred that the Balcooma Mylonite Zone formed prior to S_3 (his S_4) although he recognizes that it may have formed coevally as the orientation of the mylonitic fabric is similar to S_3.

All structures recognized have been cut by a series of northeasterly trending reverse faults (Figs. 1 and 2). Based on relationships in the prospects, the southeastern blocks have been thrown up. Displacement of the Balcooma Mylonite Zone (Fig. 1) indicates an apparent right-lateral movement on these faults. Late, brittle shearing that postdates S_3 is also present in both prospects.

Intrusions

The Balcooma Metamorphics have been intruded by two different granitoids: the Cambro-Ordovician Ringwood Park Granite and Silurian Dido Granodiorite. The Dido Granodiorite consists of hornblende-biotite tonalite, quartz diorite, diorite and minor gabbro with a minimum age of between 385 m.y. amd 415 m.y. based on Rb-Sr and K-Ar mineral ages (Withnall, 1982). This intrusion forms the eastern boundary to the Balcooma Metamorphics, and it may crosscut the Balcooma Mylonite Zone.

The Ringwood Park Granite intrudes the Dry River Volcanics and Clayhole Creek Beds largely in the east-central section of the Balcooma Metamorphics. At its contacts the granite is a fine grained microgranite with a local granophyric texture. Withnall (1982) inferred that this granite is a subvolcanic intrusion associated with the Dry River Volcanics.

Quartz-feldspar porphyry sills commonly intrude the Clayhole Creek Beds and may form much of the Dry River Volcanics. These are probably shallow level equivalents to the Ringwood Park Granite.

A series of post-S_3, steeply dipping dolerites occur in the western part of the belt. These have been noted at the Dry River South prospect and around the Balcooma goldfield.

Chapter 2
The structure and statigraphy of the Balcooma prospect

Introduction

The interpretation of the structural and stratigraphic relationships of the Balcooma deposit in northern Queensland have been somewhat enigmatic since its discovery in 1978. Although the structure around the immediate copper ore shoots was well described by Carpentaria Exploration Company geologists (Mulroney, 1983; and Harvey, 1984b), the lack of adequate marker beds and the interfingering relationships between litholigical units have prevented the development of a coherent structural/stratigraphic model to relate mineralization intersected in the copper shoots to zinc-lead mineralization that was intersected in drill holes to the west and crops out as a gossan to the east.

An initial objective of research at the Balcooma prospect was to produce a structural/statigraphic model for the Balcooma prospect as a whole. This chapter presents such a model and is predicated on the following: (1) the possibility that mineralization at Balcooma may occur at multiple stratigraphic horizons, (2) reinterpretation of highly quartzose rocks, which were originally interpreted as siliceous exhalite (hereafter termed "exhalite"), as metamorphosed result of quartz-sericite alteration based on similarities to the footwall alteration zone at Dry River South and the occurrence of oxidized pyrite stringers, (3) recognition that the three earliest generations of folds are coaxial, and (4) the presence of two domains of distinctly different structural styles in the prospect area.

Stratigraphy

As evidenced by the presence of staurolite, andalusite and cordierite, the rocks surrounding the Balcooma prospect have undergone amphibolite facies metamorphism. Enough relict textures exist to make inferences on the pre-metamorphic lithologies.

The descriptons herein are derived from the author's own field mapping, K. Harvey's M.Sc. thesis (1984b) and internal C.E.C. reports (Mulroney, 1983).

Enclosing metasediments

The metasediments immediately surrounding the Balcooma prospect, which Harvey (1984b) termed the "Clayhole Creek beds", may be divided into three units. The basal unit is a quartz-albite-biotite schist which is overlain by a quartz-muscovite-biotite schist. Along the contact between these two units, and interfingering with them, lies a unit consisting dominantly of staurolite-bearing schists. The entire sequence contains several volcaniclastic lenses of varying thickness. These volcaniclastic units may relate to the Dry River Volcanics which are located to the west of the prospect.

Quartz-albite-biotite schist (lower metagraywacke). The basal unit in the immediate prospect area is a fine grained quartz-albite-biotite schist (the lower metagraywacke) which occurs in 0.1 to 1 m beds with 5 to 10 cm interbeds of very fine grained muscovite-quartz-biotite schist that rarely contain staurolite porphyroblasts (Fig. 3a). The unit occupies the core of an upright, open D_3 anticline to the west of the prospect hill although small patches may be found throughout the prospect area (Fig. 4 and Plate 1). In outcrop it has a flaggy appearance and weathers to a yellowish brown color. Despite the intensity of deformation, primary textures may occasionally be recognized. Load casts and ripple marks (Fig. 3b) have been recognized to the west of the prospect. In core the lower metagraywacke appears as a moderate to dark gray, massive, fine grained quartzofeldspathic schist; it is usually found at the bottom of deep drill holes.

This unit is interpreted as a fine grained feldspathic sandstone or graywacke with minor interbedded siltstones and shales. It is very similar in appearance and mineralogy to the metagraywacke at the Dry River South prospect.

Quartz-muscovite-biotite schist (upper metagraywacke). A fine grained quartz-muscovite-biotite schist in 0.1 to 1 m beds interbedded with lesser staurolite bearing schists (see below) locally overlies the lower metagraywacke (Figs. 4 and 5). In addition to the interbeds, this unit may contain rare (<2%) staurolite, andalusite or cordierite porphyroblasts.

The upper metagraywacke is located largely to the east of the prospect hill and is truncated to the east by the microgranite (Fig. 4).

Figure 3. Photographs showing relic, primary sedimentary textures, Balcooma prospect: (a) bedding in the lower metagraywacke (9179 mN 2085 mE, Balcooma grid); (b) ripple marks in the lower metagraywacke (9271 mN 1862 mE, Balcooma grid); (c) bedding in the spotted schist (9151 mN 2096 mE, Balcooma grid); (d) "reverse grading" in spotted schist (DDH-52, 191.1 m; facing is to the left in the photo) (e) Coarse volcaniclastic (DDH-52, 264.9 m); and (f) graded bedding in volcaniclastic units (DDH-23, 209.8 m to 225.5 m; facing is to the top and left, and the grading is over 0.5 to 2 m).

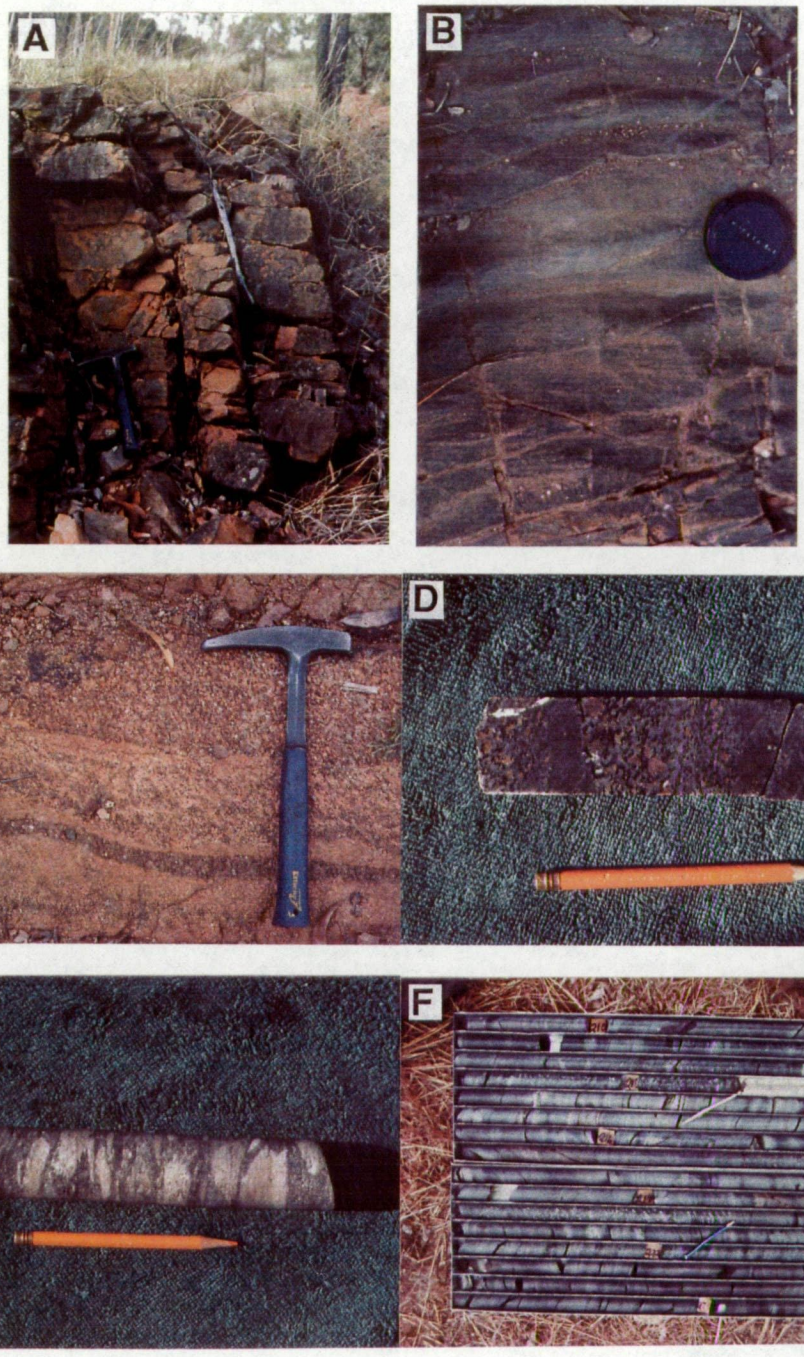
A
B
C
D
E
F

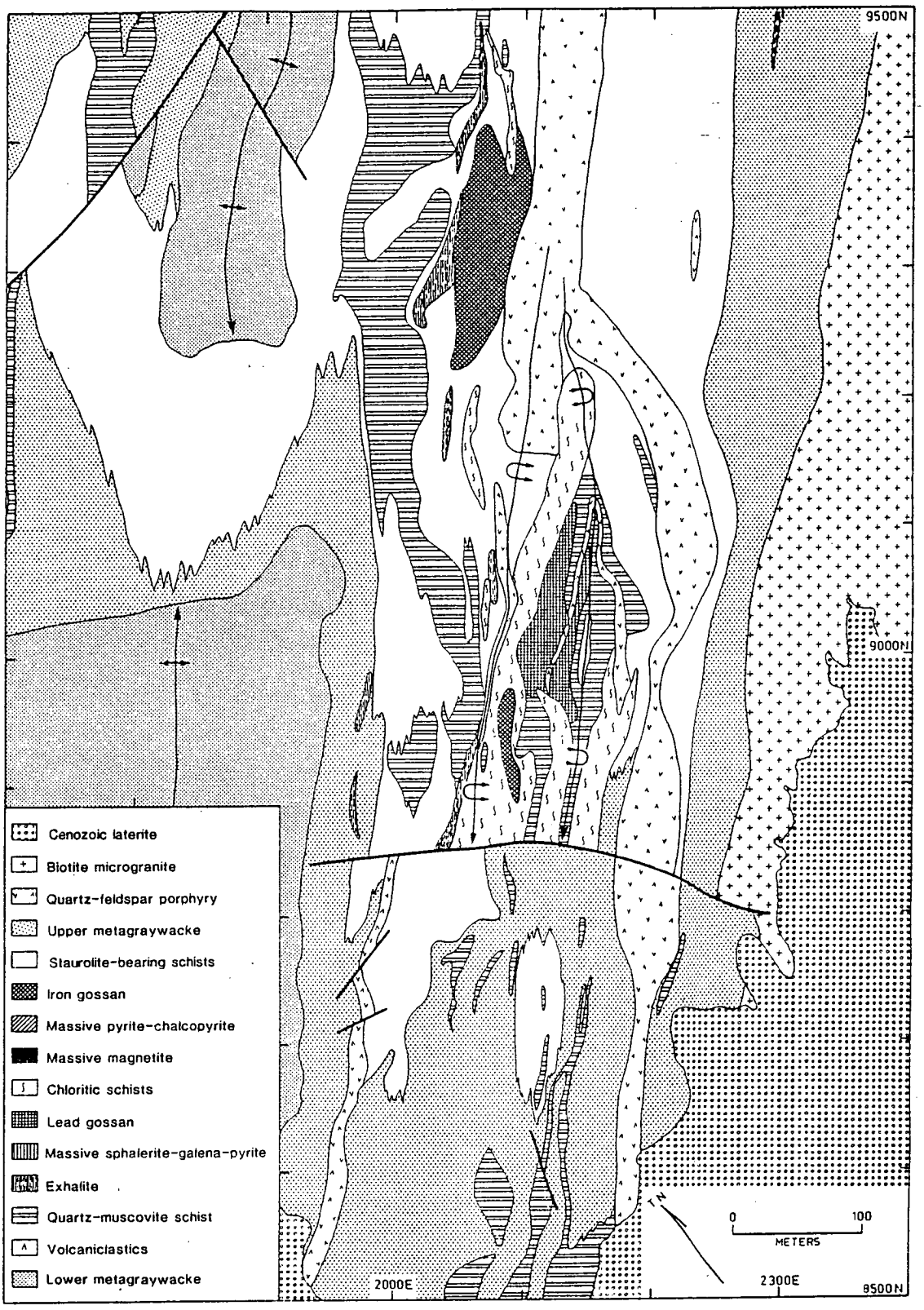

Figure 4. Surface geology of the Balcooma prospect. Compiled from mapping by D.L. Huston and Carpentaria Exploration Company geologists.

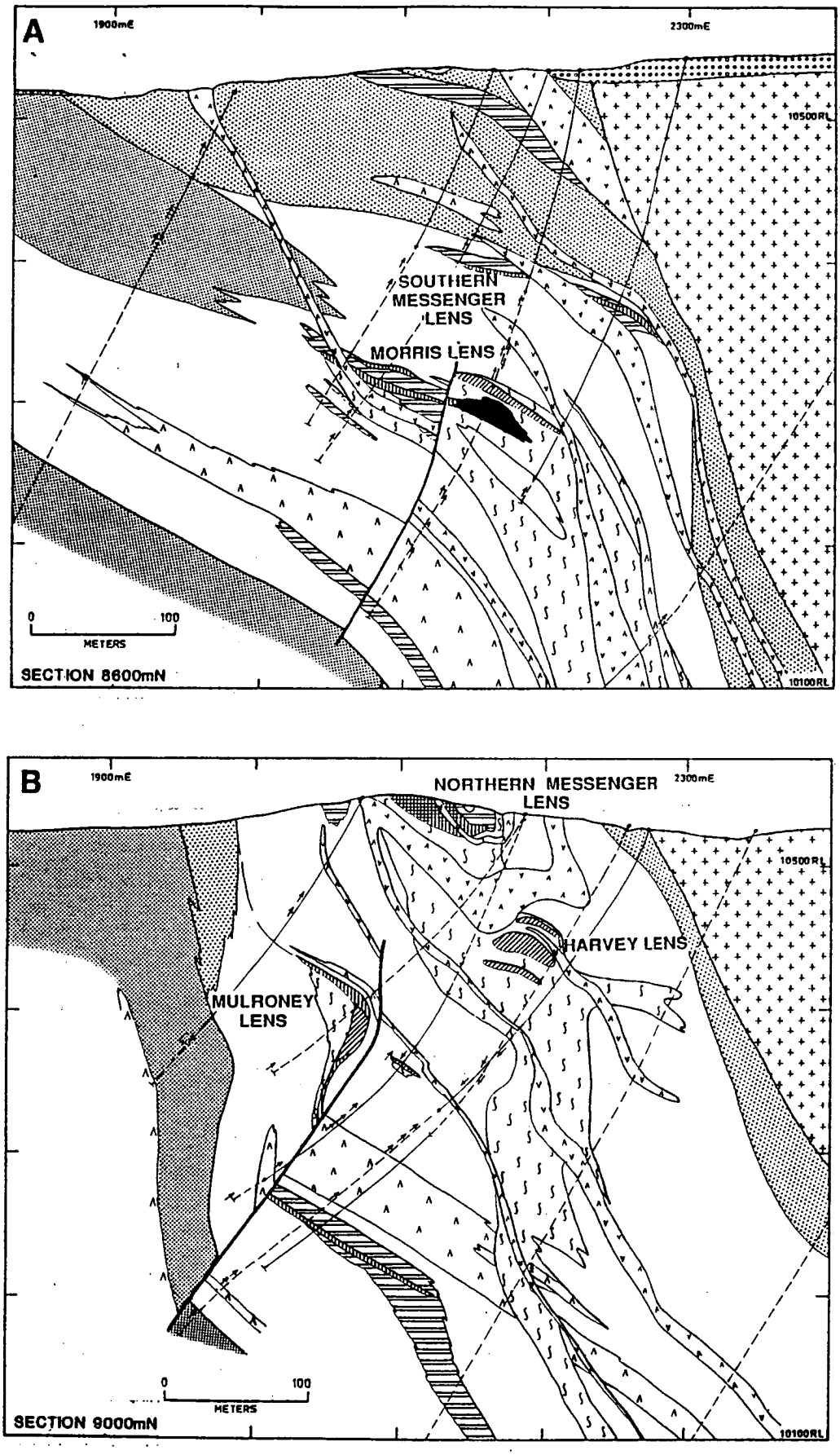

Figure 5. Geologic cross sections at (a) 8600 mN and (b) 9000 mN, Balcooma prospect.

In outcrop the upper metagraywacke may be difficult to distinguish from the lower metagraywacke. The latter is distinguished by the presence of strongly crenulated muscovite-quartz-biotite schist interbeds, and its yellowish color and flaggy appearance in outcrop. The former is characterized by the lack of albite, the presence of additional muscovite, and the presence of rare staurolite, andalusite and/or cordierite porphyroblasts.

The upper metagraywacke appears to be a weakly altered variant of the lower metagraywacke lithology based on whole rock composition (Chapter 4). The inferred alteration zone occurs in the hanging wall to mineralization, and recognition of the upper metagraywacke rock type may be useful in exploration.

Staurolite-bearing schists. A sequence of pelitic schists forms a major lens at the contact betwen the underlying lower metagraywacke and the overlying upper metagraywacke. It occurs along the prospect hill and hosts the majority of the mineralization (Figs. 4 and 5). Small lenses and beds of staurolite-bearing schist also occur within the upper metagraywacke, particularly near the granite contact at 2300 mE 9200 mN.

Two distinctly different staurolite-bearing schists may be found in the prospect area: (1) a fine to medium grained quartz-muscovite schist with 10-20% medium grained biotite and 20-40% medium to coarse grained staurolite porphyroblasts (includes minor medium grained quartz-muscovite-biotite schist; the spotted schist), and (2) a very fine to fine grained quartz-biotite-muscovite schist with 2-20% medium to coarse grained staurolite porphyroblasts (the snowball schist). Both lithologies contain locally significant amounts of andalusite and cordierite and minor amounts of garnet.

The major difference between these two units is cleavage development and the habit of biotite. In the snowball schist, biotite occurs with lesser muscovite in a strongly foliated groundmass that wraps around staurolite porphyroblasts. Conversely, biotite in the spotted schist occurs as unoriented porphyroblasts that are wrapped by a discontinuous cleavage developed by muscovite. Some of these biotite porphyroblasts have cores of chlorite that may have be pseudomorphs after garnet.

Within the lens of staurolite-bearing schists, bedding and facing may be determined based on grading in the amount of staurolite (c.f. Shrock, 1948). The spotted schist frequently contains beds between 1 and 30 cm thick (Fig. 3c), and the staurolite content

commonly increases towards one side of these beds. As staurolite content reflects the original pelitic content, the staurolite-rich, coarser grained side of the bed indicates the facing direction (Fig. 3d). This "reverse grading" (Shrock, 1948) and normal grading in volcaniclastic units (see below) provides nearly all the facing information in core and outcrop. The use of "reverse grading" in strongly metamorphosed pelitic schists has been used to determine facing at Broken Hill, the Canadian Shield and the Dalradian of Scotland (Shrock, 1948; and Glen and Laing, 1975). Facing information from "reverse grading" is less common in the Balcooma snowball schist.

The base of the major staurolite-bearing lens often contains interfingering beds of the lower metagraywacke, and it is often difficult to pick the contact between these two units in core due to this interfingering. The basal rock type of the staurolite-bearing lens is often the snowball schist.

The staurolite-bearing lens may be up to 250 m thick although it thins rapidly up dip (the extent down dip is unknown as all holes penetrate the unit; Fig. 5). As there may be significant structural thickening in this unit (see below), this thickness may not reflect true stratigraphic thickness. The unit shows an interfingering relationship with both the upper and lower units. It probably represents a major silty to shaly lens possibly associated with a localized change in volcanism (Chapter 8).

Volcaniclastic rocks. The sequence that hosts the Balcooma prospect contains several volcaniclastic lenses of variable thickness and extent. The lenses often contain several beds of coarse grained felsic fragmentals (the fragments contain feldspar phenocrysts and have a rhyodacitic composition; Fig. 3e) which often grade into a very fine to fine grained, well foliated quartz-feldspar-biotite-muscovite schist that makes up the majority of the lenses. Graded bedding in volcaniclastic units (Fig. 3f) serves as the second most useful indicator of facing in core. Given the relationship to the coarse grained fragmentals, the fine grained schists are interpreted as metamorphosed fine grained volcaniclastic rocks.

On the surface volcaniclastic beds only crop out to the north of the deposit in the core of the western D_3 anticline. In rare outcrop, the lenses may be distinguished by a reddidsh and/or fragmental appearance. In drill hole the rock type is distinguished

by the presence of fragmental beds, the presence of minor disseminated pyrite, a strongly developed schistosity and a mottled appearance. The appearance in drill core is quite distinct from the metagraywacke.

Volcaniclastic lenses occur in all three statigraphic units described above but tend to occur more often in the lower metagraywacke and lower part of the staurolite-bearing schists. Usually the volcaniclastic beds are relatively thin (< 10 m) and non-continuous in section, but one major volcaniclastic lens, which is up to 70 m in thickness, was observed in in core from 8500 mN to 9050 mN (Fig. 5) where it interfingers with the staurolite-bearing schists. The volcaniclastic lenses are useful local marker beds, and are particularly useful in locating mineralized horizons (see below).

The Balcooma volcaniclastic lenses are thought to be clastic flows derived from the Dry River Volcanics which crop out some 700 m to the west of the Balcooma prospect. As a consequence, some interfingering between the Dry River Volcanics and Clayhole Creek Beds is suggested.

Summary. Three metasedimentary units are present in the Balcooma prospect area. The basal unit is a quartz-albite-biotite schist (the lower metagraywacke) which is interpreted as a feldspathic metagraywacke and sits in the core of the western anticline. Stratigraphically above this unit lies a quartz-muscovite-biotite schist with minor interbedded staurolite-bearing schist (the upper metagraywacke). This unit is interpreted as weak hanging wall alteration of the lower metagraywacke rock type associated with mineralization. At the contact between the metagraywackes lies an interfingering lens of staurolite-bearing schists that hosts mineralization. Several volcaniclastic lenses of variable thickness and extent occur through the sequence. These lenses may have been derived from a volcanic pile situated to the west and south and suggest that the Clayhole Creek Beds may have an interfingering relationship to the Dry River Volcanics.

Intrusions

The prospect area has been intruded by early quartz-feldspar porphyry sills and a later granite. As these units often are foliated, they are interpreted to have been intruded before or during metamorphism, possibly just after sedimentation.

Quartz-feldspar porphyry

The metasediments in the Balcooma area have been intruded by several quartz-feldspar porphyry sills up to 50 m in thickness. Although these sills almost parallel bedding, they can be observed to cut stratigraphy throughout the prospect area.

One of the sills outlines a D_2 synform-antiform pair which crops out around 9250 mN 2150 mE (Fig. 4 and Plate 1). The fold plunges to the south at about 20° (Fig. 5b) until 8850 mN where it is truncated by a crosscutting E-W fault. Elsewhere in the prospect area, these sills have not been strongly folded.

Petrographically the quartz-feldspar porphyries contain up to 10% 1-10 mm rounded quartz eyes and up to 7% 1-5 mm subhedral albite phenocrysts in a very fine to fine grained biotite-quartzofeldspathic groundmass. Locally the groundmass is foliated.

Microgranite

A very fine to fine grained biotite-microgranite truncates the Balcooma package to the east (Figs. 4 and 5). The contact is interpreted to be intrusive based on sharp contacts between the granite and metasediments in DDH-6, DDH-8, DDH-18 and DDH-T860. The microgranite coarsens to a coarse grained, foliated granite to the east (Mulroney, 1982).

Structure

Deformation around the Balcooma prospect area is dominated by folding. Four cleavages, which indicate four separate folding events, have been recognized. The morphology of the rock units and mineralization is controlled by the two strongest folding events. Although faults acted as structural boundaries, faulting is generally of lesser importance.

The Balcooma prospect area may be divided into two areas with distinct structural styles. The first area is bounded to the south by a cross fault at 8850 mN and to the east by the microgranite (Fig. 4). To the west the structural style changes at about 2000 mE. This area is characterized by steeply dipping and locally overturned bedding and contains a D_2 antiform-synform pair (Fig. 5b).

The second area, which includes the rest of the prospect area, is characterized by shallow to moderate dipping, upright bedding (Figs. 4 and 5a; and Plate 1). This area is on the eastern limb of a regional, open D_3 anticline.

The prospect area has a north-northeast (grid north) trending structural grain, and all folds (excluding D_4 folds) plunge 20°-25° to the south-southwest (grid south).

Faults

On the surface, two relatively major faults may be recognized by the truncation or transposition of units on the surface. The first fault (8850 mN cross fault) acts a structural boundary between the two structural domains described earlier. The southern block has moved down and to the east along this fault (Mulroney, 1982).

The second fault that is recognized at the surface occurs in the northwest and trends east-northeast (grid north-northeast) with a right-lateral movement. This fault was recognized because of a linear stream and an offset of 100 m to the northeast of a band of pyritic quartz-muscovite-biotite schist in the northwestern-most part of Figure 4.

Offsets of the lower zinc-lead horizon and several volcaniclastic units recognized in section (Fig. 5b) indicate that a north-south trending reverse fault with a throw of 100 m exists between 8920 mN and 9060 mN at 2000 mE to 2100 mE (Mulroney, 1982). As this fault has gouge and brecciation that clearly postdates the two strongest cleavages, this fault is interpreted to be post-metamorphic. Other minor faults may be located in the prospect area, but offsets are small.

A major north-northwest trending fault is interpreted to truncate mineralization at the south end of the prospect underneath a thick band of laterite (Mulroney, 1983; Fig. 2). Kink banding that kinks both S_2 and S_3 was observed at 8663 mN 1840 mE and may be related to this faulting (Fig. 6a). The kink band axes plunge 2° to 100 ° which is broadly consistent with the inferred orientation of the fault. Thom (1984) interpreted the existance of a major group of northwest trending faults in the northern part of the Balcooma metamorphic belt.

Figure 6. Photographs showing structural features and alteration textures at the Balcooma prospect: (a) Kink banding in fine grained mica schist (8663 mN 1840 mE, Balcooma grid); (b) garnet porphyroblast (ga) with oriented inclusions (S_1) wrapped by the dominate S_2 cleavage (section 3-103.9); (c) mesoscopic D_2 fold in core (DDH-N860, 101.4 m); (d) S_3 crenulating S_2 (8555 mN 2084 mE, Balcooma grid); (e) chloritic alteration overprinting volcaniclastic (DDH-54, 376.8 m); and (f) chlorite-biotite schist cutting massive pyrite (DDH-45, 137.2 m).

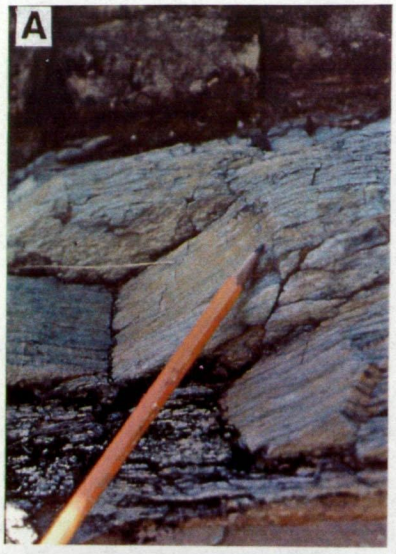
A


B
qs
S
S_2
400 µm

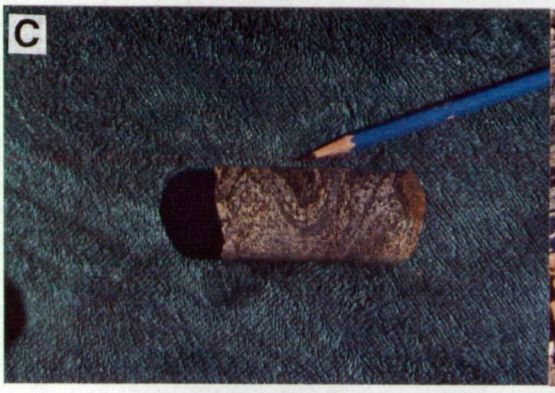
C


D

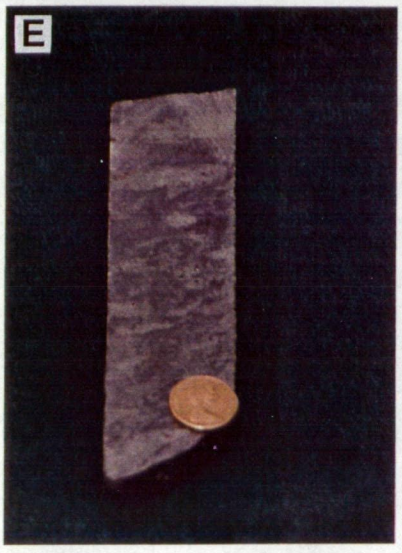
E

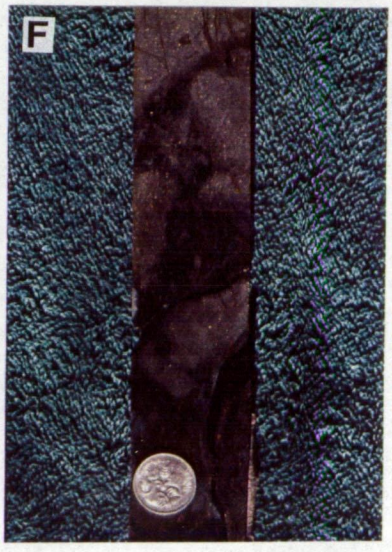
F

Folds

In addition to bedding, four distinct cleavages have been recognized around the Balcooma prospect; this indicates that at least four folding events have occurred in the area. Of these cleavages, two (S_2 and S_3) are strongly developed and may be found through the prospect area. The other two cleavages (S_1 and S_4) are locallized and/or weakly developed. Poles to S_0, S_1 and S_2 all plot along the same great circle (Fig. 7) which indicates that the first three deformation events were coaxial with fold axes plunging at 20°-25° to the south-southwest (grid south).

First deformation event. Evidence for the first deformation event comes from the presence of a cleavage in the northwestern part of prospect area (Plate 1) that predates than the dominant S_2 cleavage. This cleavage, S_1, is restricted to staurolite-bearing schists or interbeds within metagraywacke. Outside of the northwestern part of the prospect area the cleavage has been destroyed by the later S_2 cleavage. The initial overprinting and later destruction of S_1 by S_2 may be seen at 9267 mN- 1751 mE where S_1 is overprinted by S_2 (and S_3) at the base of the outcrop and then destroyed at the top.

Although F_1 folds have not been recognized in the field or in core, microstructural evidence for this deformation exists in thin section where early formed porphyroblasts (e.g. garnet) occasionally contain oriented inclusion trails of quartz. In Figure 6b an early formed garnet porphyroblast is wrapped by the dominant S_2 foliation. The garnet porphyroblast contains oriented quartz inclusions which are the remnant of the S_1 foliation that the garnet overgrew.

Second deformation event. The second deformation event was probably the most intense as evidenced by the pervasive occurrence of S_2. This cleavage is present in nearly all outcrop and core. Mulroney (1982) noted that S_2 (his S_1) usually parallels bedding which is consistent with isoclinal or near isoclinal folding during D_2.

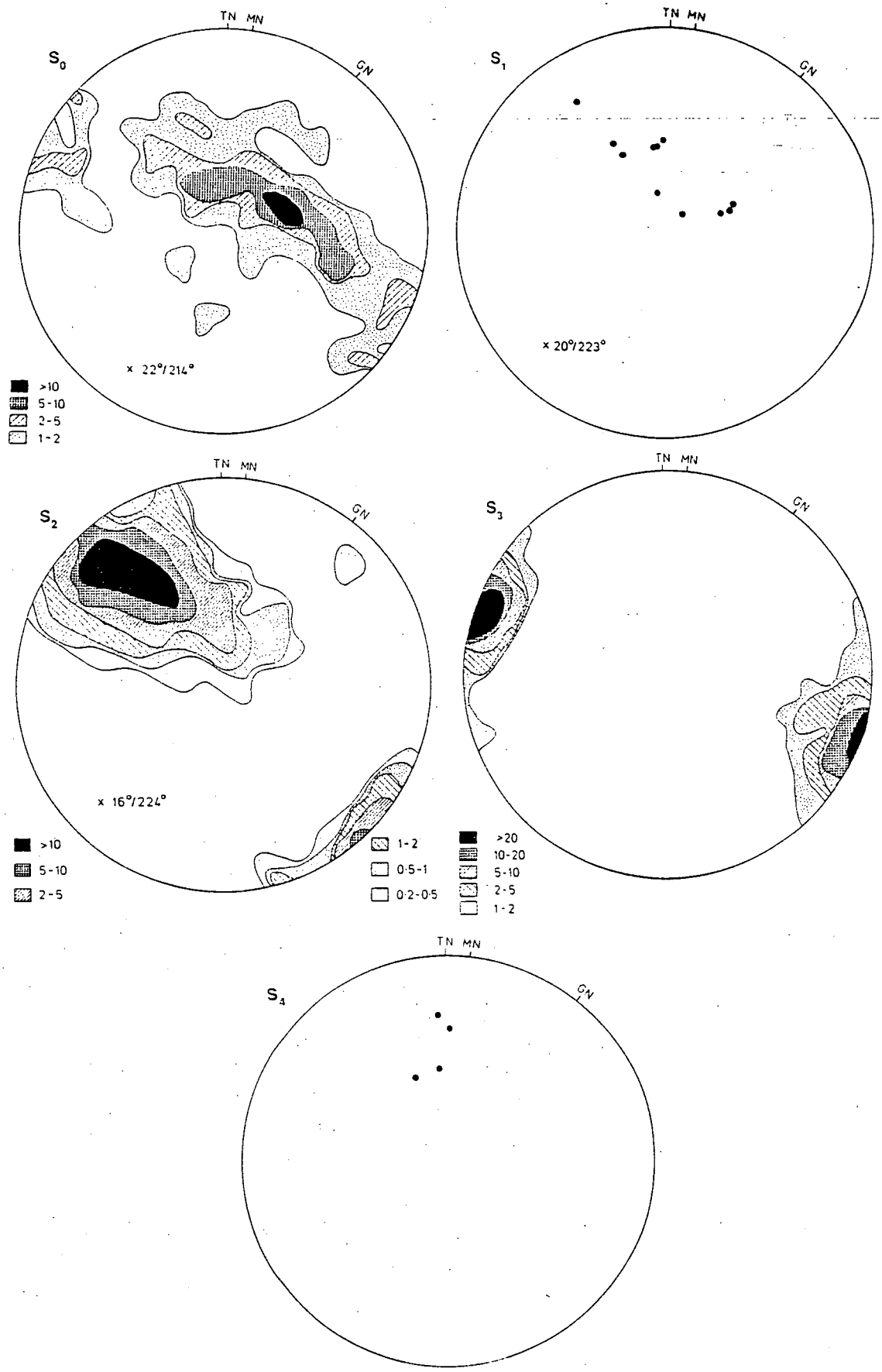

Figure 7. Pi diagrams showing the variations in S_0, S_1, S_2, S_3 and S_4 around the Balcooma prospect.

The orientation of S_2 (and other cleavages) depends to a large degree on lithology. In pelitic interbeds, S_2 tends to parallel bedding, but in psammitic units the cleavage may be refracted by up to 60°. This indicates that most of the strain associated with D_2 folding has been taken up by the pelitic interbeds in the metagraywackes.

Folds generated during D_2 vary in scale from mesoscopic (Fig. 6c) to macroscopic with the antiform-synform pair that dominates the northern structural domain being the largest, and most important, fold of this generation in the prospect area (Fig. 5b). The fold pair, as defined by the quartz-feldspar porphyry sill, is tight to isoclinal in form. The fold pair has a wavelength and amplitude of 120 m and 160 m, respectively (Fig. 5b) and the axes plunges 20°-25° to the south-southwest (grid south).

A possible control on folding in the prospect area is the relative competency of the rock units. The overturned D_2 fold pair is defined by a quartz-feldspar porphyry sill which is intruded into chlorite-rich schists. The contrast in competency of these two rock types may have controlled the formation of major D_2 folds. The same contrast in competency does not seem to be developed elsewhere in the prospect area, especially in the metagraywackes that enclose the Balcooma host rocks. The lack of competency contdrast at Dry River South (feldspathic metagraywackes, quartz-feldspar porphyry and pyritic quartz-muscovite-biotite schists) may have prevented the formation of major folds at that prospect.

The 8850 mN cross fault acts as a structural boundary separating two areas with different structural styles (see above). This fault also cuts out (<u>does not offset</u>) the D_2 antiform-synform pair. As this D_2 fold pair does not continue on the other side of the fault (Fig. 5a), the 8850 mN fault must have been a tear fault active during D_2 deformation.

<u>Third deformation event</u>. The third generation of cleavage has a consistent orientation which strikes roughly north-northeast (grid north-northwest) and has a subvertical dip (Fig. 7). It is the second most prominent cleavage, is observable in about 20% of outrop irrespecive of location, and nearly always crenulates S_2 (Fig. 8d).

The consistency in the orientation of this cleavage allows the determination of the generation of both earlier and later cleavages observed in the same outcrop.

Folds associated with S_3 tend to be upright and open. They vary in scale from mesoscopic to the major D_3 anticline to the west of the Balcooma prospect (Figs. 2 and 4). The folding of both bedding and S_2 cleavages across this anticline (Mulroney, 1982) indicates that it must be a product of D_3 deformation. This anticline is the major structural feature of the district; the Balcooma prospect lies on its eastern limb, and the Surveyor prospect occurs in the hinge 2 km to the southwest of Balcooma (Fig. 2). Although the major western anticline plunges to the south-southwest, local plunge reversals occur (Mulroney, 1982) as at 9100 mN 1900 mE (Fig. 4). These plunge reversals are related to gentle cross-folding associated with D_4.

Fourth deformation event. Four occurrences of a cleavage that crenulates S_3 are plotted in Figure 7. Although there is a fair scatter to the four poles, the general orientation of S_4 has an easterly strike (grid northeast) and a dip to the south of 30° to 60°.

Folding associated with D_4 is recognized through the plunge reversals in the D_3 anticline and an interference pattern caused by cross-folding of this anticline (see the contact between the lower metagraywacke and the upper graywacke/staurlitic schists in Fig. 4). D_4 folds have an easterly trend (grid northeast) and have not affected the distribution of mineralization significantly. A possible mesoscopic F_4 fold has been observed at 9317 mN 2291 mE and its axis has a plunge of 75° to 040°. This orientation is broadly consistent with the orientations of F_4 axes as determined from $L_{4_{INT}}$ intersections at Dry River South (Chapter 4).

Mineralization

The Balcooma deposit contains five distinct bodies of massive sulfide (Table 4). Figure 8 illustrates the surface projections of the lenses whereas Figure 9 illustrates their position on a long

Table 4. Characteristics of massive sulfide lenses, Balcooma prospect.

Lens	Stratigraphic position
Southern Messenger lens	Occurs 10-20 m stratigraphically below the contact between the upper metagraywacke and the staurolite schist lens.
Harvey lens	Occurs in the center of the staurolite schist lens.
Morris lens	Similar to the Harvey lens.
Northern Messenger lens	Similar to the Harvey lens.
Mulroney lens	Occurs near the base of the staurolite schist lens some 10-30 m stratigraphically below a thick volcaniclastic wedge.

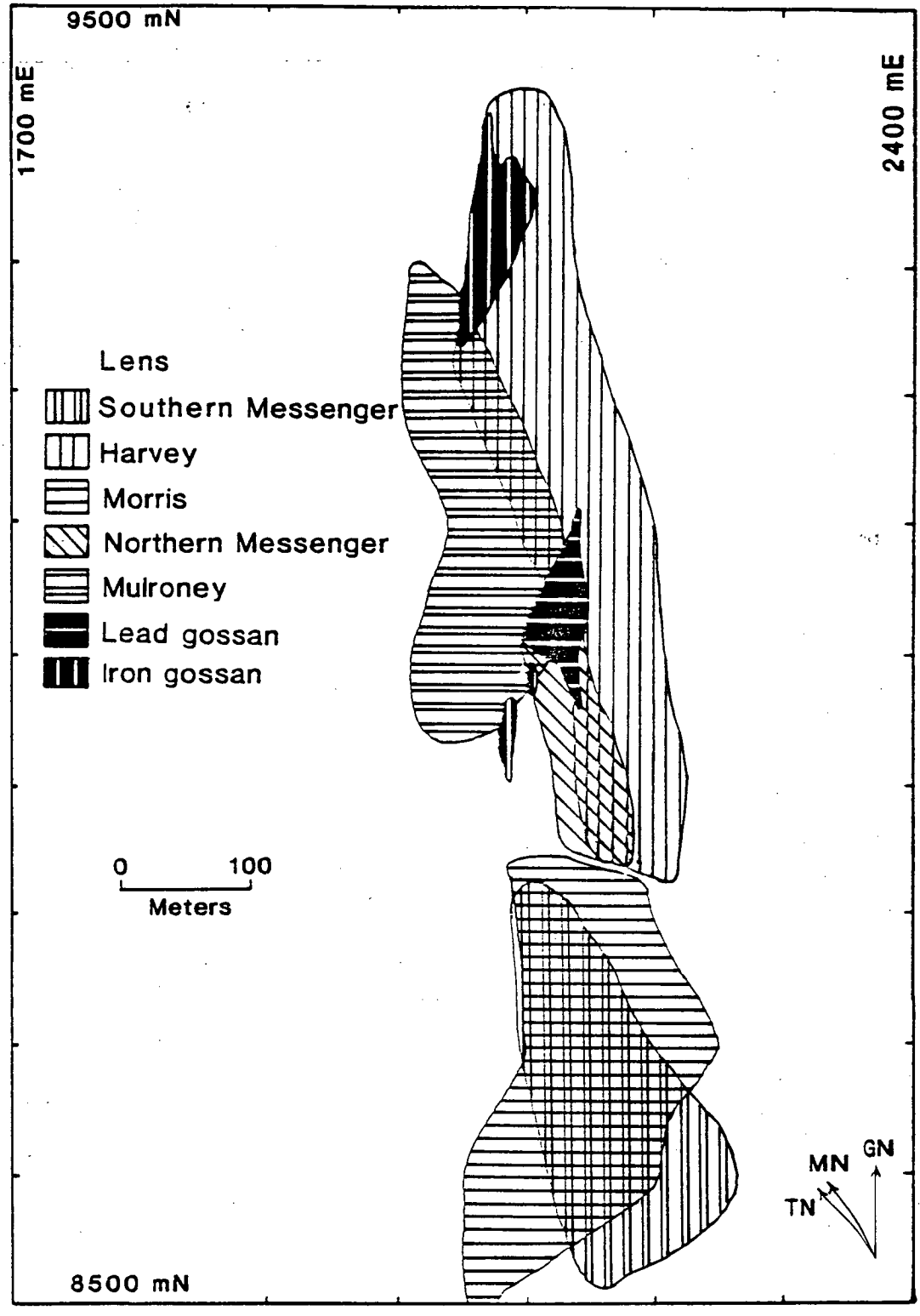

Figure 8. Surface projections of massive sulfide lenses at Balcooma.

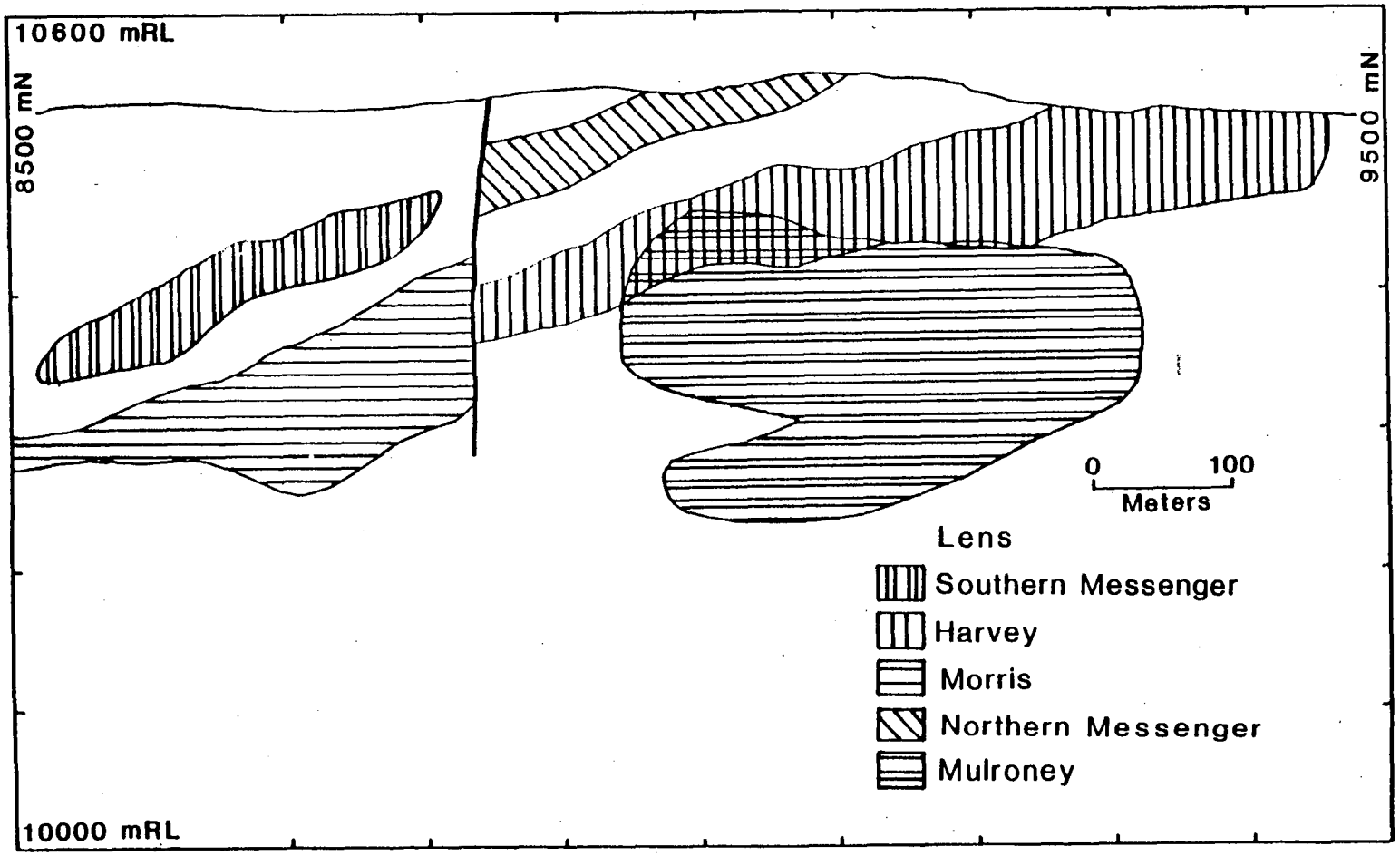

Figure 9. Projections of massive sulfide lenses onto a long section at 2200 mE, Balcooma prospect.

section projected to 2200 mN. Three general types of massive mineralization are present at in the prospect: (1) massive pyrite-chalcopyrite, (2) massive magnetite, and (3) massive pyrite-sphalerite-galena. At the surface, the first two types of massive mineralization form a gossan dominated by iron oxides whereas the last type of mineralization forms a gossan dominated by anglesite, cerrusite and iron oxides. Each body of massive mineralization contains both types of massive sulfide, and massive magnetite, albeit in varying proportions.

The Harvey and Morris sulfide lenses

The proven geologic reserves of the Balcooma prospect include 3.5 milion tonnes of mineralization grading 3.0% copper with minor silver and gold. The copper-rich mineralization occurs in two shoots known informally as the "Harvey" and "Morris" shoots (Figs. 8 and 9). The Harvey shoot, which includes the majority of the geologic ore reserves, crops out as an iron gossan centered on 9350 mN 2075 mE (Fig. 4) and plunges to the south at 20° until about 8850 mN where it is offset by an east-west cross fault (Figs. 8 and 9). The copper-rich mineralization is offset by this fault and continues at a similar plunge to 8500 mN as the Morris shoot (Harvey, 1984b).

North of 8850 mN, the Harvey shoot occupies the core of the D_2 antiform (Fig. 5b,) but south of 8850 mN, the Morris shoot consists of tabular sheets which gently dip to the east at 20° to 40° (Fig. 5a). In the Harvey shoot, a quartz-feldspar porphyry sill cuts the mineralization.

As the Harvey shoot occupies the core of the D_2 antiform to the north of the 8850 mN cross fault (Fig. 5), remobilization of the sulfides to form the southerly plunging ore shoots probably occurred during, but was not limited to, D_2. As D_1 and D_3 are coaxial with D_2, remobilization also may have occurred during these events.

The copper mineralization in the Harvey and Morris lenses is made up dominantly of pyrite with lesser magnetite, chalcopyrite and pyrrhotite. The Morris shoot becomes progressively richer in magnetite to the south (Harvey, 1984). It also contains zinc-lead-rich mineralization to the south (Fig. 5a).

The projection of the Harvey shoot crops out as an elongate north-south trending iron gossan which extends from 9225 mN to 9450 mN (Figs. 4 and 6). Hematite is the dominant mineral in the gossan although limonite also occurs. Although oxidized copper minerals are rare on the surface, malachite, azurite, tennorite, native copper (Harvey, 1984) and chrysocolla have been noted in drill core. The oxide and supergene zones extends more than 60 m below the surface.

The Mulroney lens

Most massive pyrite-sphalerite-galena in the Balcooma prospect is located to the west of the copper-rich Harvey shoot (Fig. 8). This tabular lens, which has been informally termed the "Mulroney lens," extends north from 8950 mN to 9300 mN and dips moderately to steeply to the east (Figs. 5b, 8 and 9). This lens occurs a few meters below the thick volcaniclastic lens near the base of the Balcooma schists. The Mulroney lens contains a small patch of copper-rich massive sulfide, which may represent the feeder zone, centered along 9000 mN (Fig. 5b). A steeply dipping reverse fault, which occurs between 2000 mE and 2100 mE, has offset this horizon 100 m (west block up) between 8920 mN and 9060 mN (Mulroney, 1982). The surface expression of this mineralization is limited to several small outcrops of exhalative gahnite quartzite at 1975 mE between 8850 mN and 9000 mN (Fig. 4 and Plate 1).

The northern Messenger lens

A second lens of zinc-lead-rich massive sulfide crops out as a lead-rich gossan in the core of the D_2 synform (Fig. 5b). The gossan crops out between 8900 mN and 9100 mN along 2100 mE (Figs. 4 and 8). Mineralogically it contains both anglesite and cerussite (Harvey, 1984b) along with hematite, limonite and jarosite (?). This lens is cut out to the south by the 8850 mN cross fault.

The southern Messenger lens

A fifth lens of zinc-lead-rich massive sulfide occurs 5-10 m below the contact between the upper metagraywacke and the Balcooma host rocks and has been named the "southern Messenger lens" (Fig.

5a). The tabular sheet extends between 8500 mN and 8800mN and dips gently to the east (Figs. 5a and 8). This lens appears to pinch out to the north rather than being truncated by the 8850 mN cross fault (Fig. 8), and as such appears to be a separate lens to the northern Messenger lens. Copper-rich massive sulfide was intersected in the center of the lens in holes DDH-P866(1) and DDH-P875; this appears to be the feeder zone to this lens.

Alteration

The rocks surrounding the Balcooma prospect have been intensely altered near the mineralization. Two general types of intense alteration have been recognized: (1) chloritic alteration which is associated with copper-rich mineralization and occurs on the ridge of the prospect hill (Fig. 4), and (2) quartz-muscovite alteration which is associated with zinc-lead-rich mineralization and occurs largely along the western side of the prospect (Fig. 4).

Chloritic alteration

At the surface, the choritic schists usually are purplish or maroon in color and often contain significant iron oxides. They crop out at the crest of the prospect hill and may be associated with part of the iron gossan described earlier (Fig. 4).

In core, two types of chloritic schists may be recognized: (1) quartz-chlorite±magnetite±staurolite±garnet±biotite schist ("moderate chloritic alteration"), and (2) chlorite±biotite±garnet±sulfide schist ("strong chloritic alteration"). Occasionally both types of chloritic schists may contain stringers of sulfide.

Along the contact between the spotted schist and the zone of moderate chloritic alteration, the staurolite and biotite porphyroblasts from the spotted schist have been chloritized and sericitized, and the muscovite originally present in the groundmass has been destroyed. During this process, the staurolite porphyroblasts lose their sharp boundaries, and these boundaries become feathery. This zone of incipient chloritization of the spotted schist ("weak chloritic alteration") varies from less than one meter to over ten meters in width.

Quartz-chlorite schist (moderate chloritic alteration) dominates the alteration pipe below the copper-rich massive sulfide shoots,

and, hence, is interpreted as the metamorphosed primary alteration zone. At depth, this schist occurs in a pipe that transects the stratigraphic position of the Mulroney lens and the volcaniclastic lens sitting above this position (Fig. 5b). The alteration has overprinted the volcaniclastic lens to produce a fragmental rock type with silcified clasts surrounded by a strongly chloritized groundmass (Fig. 6e).

Chlorite schist (strong chloritic alteration) occurs as veins and pods that cut all other rock types in the Balcooma host rocks, including massive sulfide (Fig. 6f). Moreover, strong chloritic alteration usually occurs as veins in moderate chloritic alteration. This rock type is interpreted as either veins of chlorite schist formed during original hydrothermal alteration or as retrograde chloritic zones formed during metamorphism.

Quartz-rich alteration and exhalite

Three types of quartz-rich rocks are present in the Balcooma prospect area: (1) fine grained, locally pyritic or sulfidic (or hematitic), quartz-muscovite-(biotite) schists or muscovite-quartzites, (2) very fine to fine grained, pyritic (or hematitic) quartzite, and (3) very fine to fine grained gahnitic quartzite.

The first type (pyritic quartz-muscovite-biotite schist) occurs in several grid north-south trending bands through the prospect area. On the surface, most of it crops out in a band up to 100 m wide centred on the 2000 mE from 8900 mN to 9500 mN (Fig. 4). Other significant bands crop out on the western limb of the D_3 syncline and in the core of the D_2 synform in association with the lead gossan of the northern Messenger shoot. Several thin bands crop out the south the the 8850 mN cross fault in the upper metagraywacke (Fig. 4).

Due to its similarity to the footwall alteration at the Dry River South prospect (Chapter 4), pyritic quartz-muscovite-biotite schist is considered to be largely footwall alteration (Harvey (1984b) interpreted this schist as exhalite). This conclusion is strengthened by the presence of crosscutting hematitic (after pyrite) stringers and chloritic patches at 9300 mN 2000 mE and the fact that this rock type may be seen to grade into the enclosing metasediments around 9400 mN 2050 mE.

The exposures on the western limb of the western D_3 anticline represent the extensions across the anticline of alteration associated with mineralization at the Balcooma prospect proper. The exposures around the northern Messenger shoot probably are footwall alteration or exhalite associated with that pod. The bands observed to the south of 8850 mN in the upper metagraywacke (Figs. 4 and 5a, and Plate 1) are probably additional weakly mineralized horizons.

An unusual characteristic of the interpreted footwall alteration both and Balcooma and Dry River South is its stratiform nature. This might have been an original characteristic of the quartz-sericite-pyrite alteration, but transposition during deformation may have enhanced this shape to form pseudo-stratiform lenses of pyritic quartz-muscovite-biotite schist.

Very fine to fine grained pyritic (hematitic) quartzites may be found at the surface with gahnitic quartzite in a 10-20 m wide stratiform band that crops out intermittently just to the east of the prominent band of pyritic quartz-muscovite-biotite schists discussed before (Fig. 4 and Plate 1). This band of quartzite is interpreted as an exhalite associated with a quartz-sericite-pyrite alteration zone. Harvey (1984b) interpreted this exhalite to be associated with the copper-rich Harvey lens. The very fine to fine grained pyritic quartzite and some gahnitic quartzite probably represent original exhalites. Patches of exhalative (hematitic) quartzite may also be found in the upper metagraywacke south of the 8850 mN fault.

As gahnitic quartzite was found well into the footwall of the Dry River South Prospect, the interpretation that all gahnitic quartzite is exhalite (Harvey, 1984b) is probably incorrect. Some of the gahnitic quartzite at Balcooma is of undoubted exhalative origin, but much at the surface and in drill core is probably original footwall alteration. In either case, the presence of gahnitic quartzite is a very useful exploration indicator.

Geologic discussion

Due to the complexity of the structure and statigraphy in the Balcooma prospect, much confusion has existed regarding the relationship between the five lenses of massive sulfide. Harvey (1984b) invoked very tight to isoclinal folding to deform an initially simple picture of one or more lenses on a single

stratigraphic horizon into the present morphology. The alternative interpretation invokes the presence of multiple lenses along different stratigraphic horizons to have been folded into the present configuration.

Any interpretation of the morphology of the Balcooma prospect will have inherent shortcomings, but the best interpretation must account the following observations: (1) facing evidence as deduced from both graded bedding in volcaniclastic units and "reverse grading" in pelitic schists, (2) the change in structural style across the 8850 mN cross fault, (3) the presence of a antiform-synform pair to the north of this fault as defined by a quartz-feldspar porphyry sill, (4) the association of some sulfide lenses with particular units or contacts (e.g. the association of the Mulroney lens with the thick volcaniclastic wedge and the association of the southern Messenger lens with the contact between the Balcooma pelitic schists and the upper metagraywacke), and (5) the morphology of the chlorite alteration pipe and quartz-muscovite alteration zones relative to the massive sulfide bodies. These five well established features are summarized in Figure 10.

Option one--a single mineralized horizon

Harvey (1984b) interpreted the copper-rich massive sulfide lenses at Balcooma (i.e. the Harvey and Morris lenses) to have been originally deposited just below the seafloor and the lead-zinc-rich massive sulfide lens (i.e. the Mulroney, and Messenger lenses) deposited simultaneously on the sea floor. He invokes strong deformation and folding to dismember the original lens and produce the present configuration. This interpretation effectively minimizes stratigraphic complexity by assuming maximum structural complexity. Harvey's (1984b) interpretation is represented schematically in Figure 11a.

Although this interpretation cannot be entirely discarded due to the complexity of the Balcooma structural history, it is considered unlikely for several reasons: (1) the preponderance of facing evidence indicates that the Mulroney lens lies statigraphically underneath the Harvey lens; (2) the Mulroney lens sits several meters below a thick volcaniclastic wedge, but this wedge is not observed in the vicinity of the Harvey or Morris lenses; and (3) the chloritic alteration pipe associated with the Harvey lens cuts the

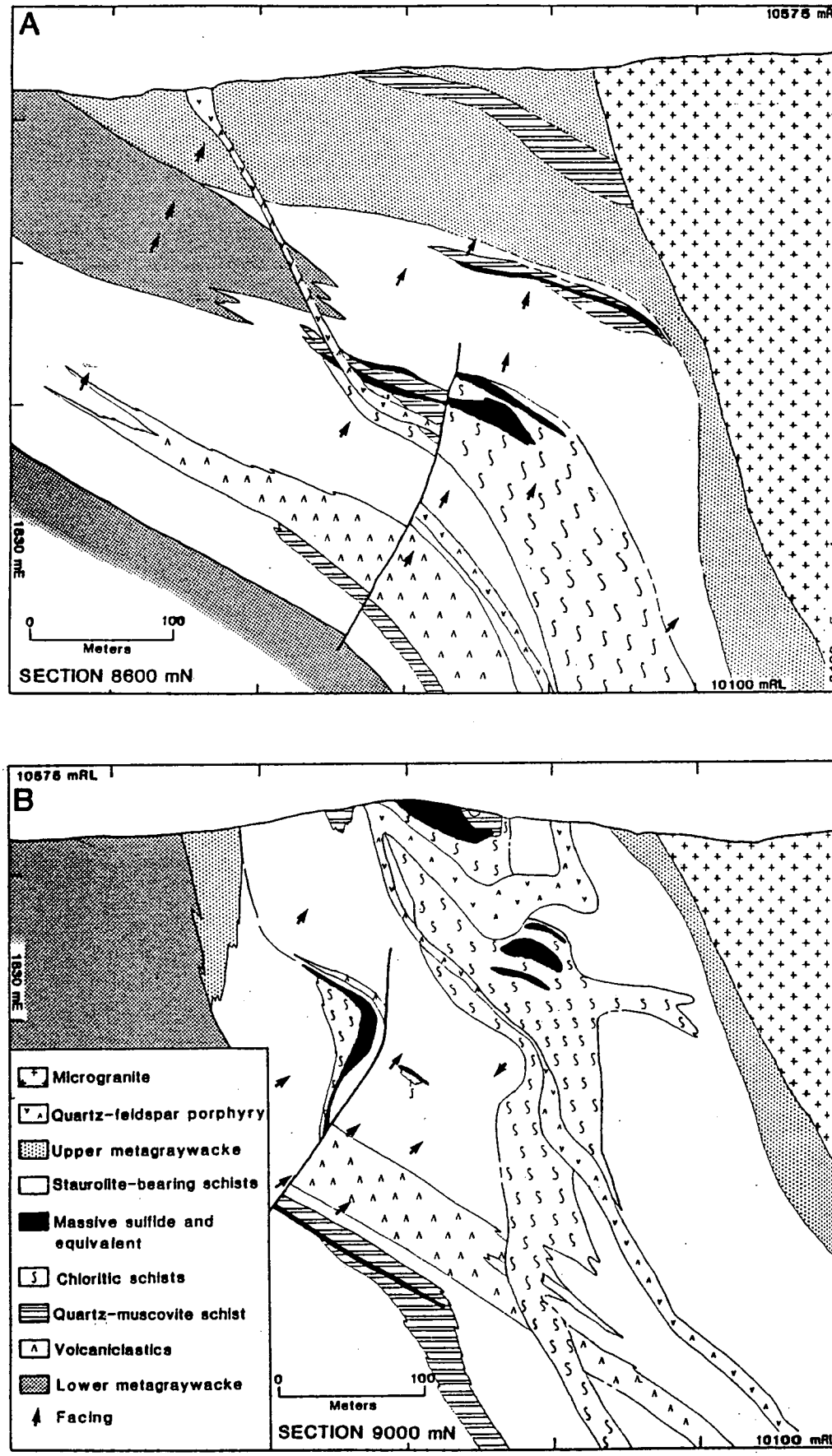

Figure 10. Simplified cross sections at (a) 8600 mN and (b) 9000 mN showing structural and stratigraphic relationships at the Balcooma prospect.

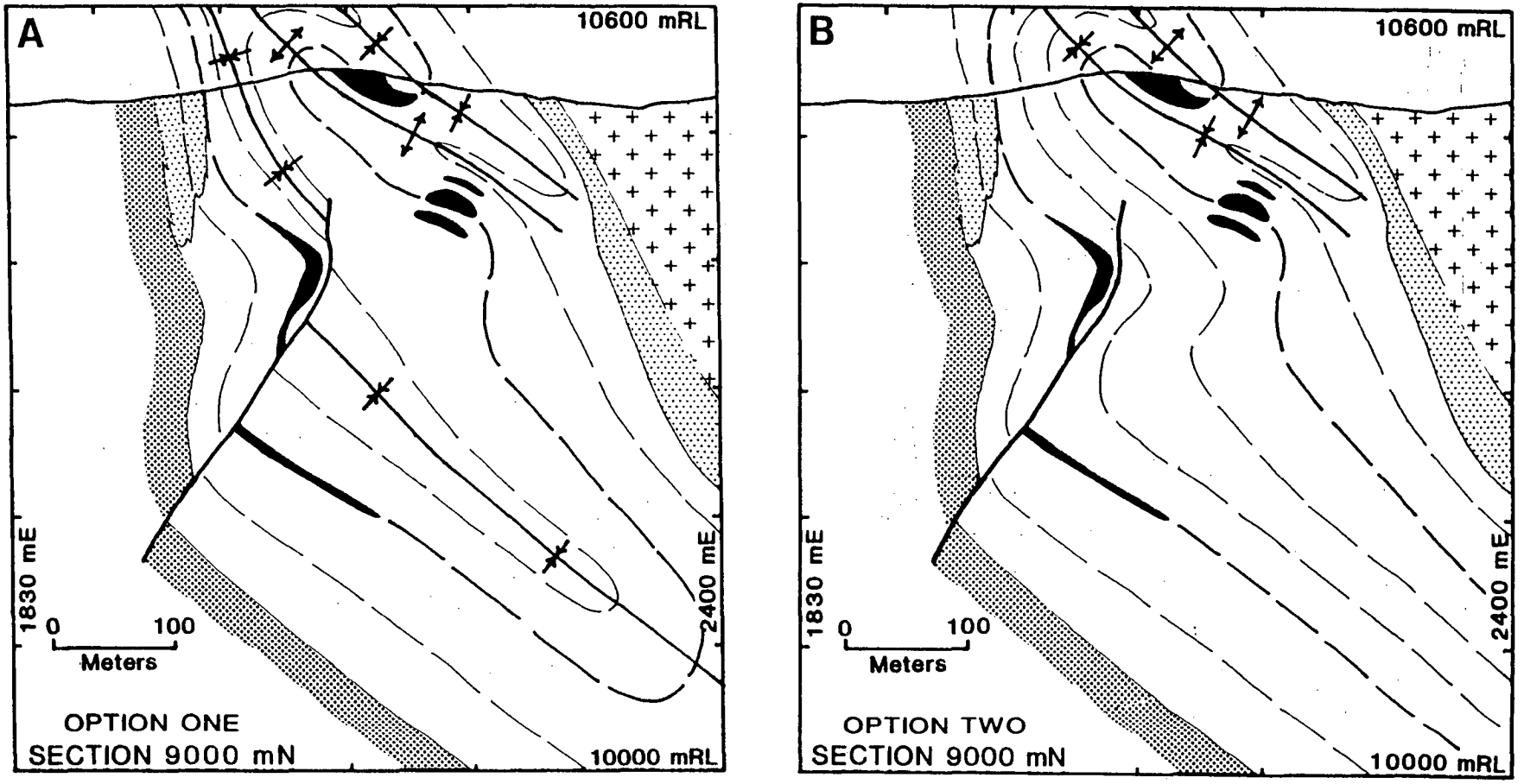

Figure 11. Alternative interpretations of the relationships between massive sulfide lenses along section 9000 mN, Balcooma prospect: (a) single mineralized horizon, and (b) multiple mineralized horizons.

volcaniclastic wedge and the stratigraphic extension of the Mulroney lens. The presence of a fault between the Harvey and Mulroney positions may have juxtaposed the two stratigraphically equivalent lenses to give the appearance of stacked lenses. However, such a fault has not been recognized in the extensive amount of drilling between the two lenses, and such a fault cannot explain the morphology of the chloritic alteration pipe associated with the Harvey and Morris lenses.

Option two--mineralization along multiple horizons

As the available facing evidence indicates that the Mulroney lens lies on a different horizon to the Harvey and Morris lenses, massive sulfide mineralization must have occurred at multiple horizons at Balcooma (Fig. 11b). Based on facing evidence, the lead-zinc-rich Mulroney lens must sit about 100 to 200 meters stratigraphically below the copper-rich Harvey shoot (Fig. 10). This breaks the general rule that in volcanogenic massive sulfide districts, copper-rich mineralization occupies a lower stratigraphic position than lead-zinc-rich mineralization. However, as both the Mulroney and Harvey lenses contain copper-rich mineralization, this difficulty is more one of the degree of copper enrichment. At the Mattabi deposit in Canada, both stacked lenses contain a central, transgressive, copper-rich massive sulfide zone (Franklin et al., 1977), which indicates that in other stacked deposits, the statigraphically upper lens may contain significant copper-rich mineralization. Furthermore, the relationship between the Mulroney lens and the chloritic stringer pipe associated with the Harvey shoot indicates that the deposits were formed from two separate systems; that is, intense alteration associated with the Harvey shoot did not overprint the Mulroney lens.

Evidence presented herein indicates that the Mulroney lens occurs stratigraphically underneath the Harvey lens, but the stratigraphic position of the northern Messenger lens is less clear. The use of the quartz-feldspar porphyry sill as a psuedo-marker bed indicates that the northern Messenger shoot lies just below or at the same stratigraphic horizon as the Harvey shoot. Unfolding of the quartz-prophyry sill indicates that the northern Messenger lens occurred about 100 meters to the west of the Harvey lens prior to deformation. The majority of the chloritic schist and pyritic

quartz-muscovite-biotite schist, as well as the inferred exhalite, at the surface is interpreted to be altered rocks and exhalite associated with the Harvey and northern Messenger lenses.

Correlation of massive sulfide lenses across the 8850 mN cross fault

The correlation of massive sulfide lenses across the 8850 mN cross fault depends largely on the structural morphology to the south of this fault. The most obvious interpretation is to extend the folds from north to south across this fault. Under this interpretation, the southern Messenger lens and the Morris lens could occur at the same stratigraphic level.

However, facing evidence indicates quite conclusively that the sequence is **uniformly upright** and east dipping throughout this region with no evidence for the large scale folding present to the north of the 8850 mN cross fault (Figs. 5a and 10a). A total of 78 facing directions were determined in the 22 holes to the south of 8850 mN logged by the author. Of these 74 indicated upright bedding and only 4 indicated overturned bedding. This indicates that the folding in the sequence is relatively small scale, and large folds present to the north of 8850 mN do not extend to the south of the cross fault. This interpretation is supported by the morphology of the quartz-feldspar sills. The intersections of these shallowly crosscutting intrusions could not be constructed to form a antiform-synform pair similar to the one present to the north of the 8850 mN cross fault.

Morphologies in which folds are terminated (not offset) by cross faults would appear to be quite unusual; however, this morphology has been noted in the Jura thrust belt of central Europe where folds with wavelengths of the order of a kilometer have been terminated by coeval "tear" faults (c.f. Fig. 7.19b of Hobbs et al., 1976; and Laubscher, 1972). Hence, the 8850 mN cross fault is more properly a tear fault that developed during D_2 and terminates the D_2 antiform-synform pair to its north. The strain that produced the D_2 antiform-synform pair to the north was taken up by the tear fault so the intensity of deformation to the south of this fault is much less.

Given this structural framework, correlations across the 8850 mN cross fault are possible. The Morris lens correlates with the Harvey and northern Messenger lenses. Gahnitic quartz-muscovite-biotite schist with disseminated sphalerite and galena that was intersected

just below the thick volcaniclastic wedge in drill hole DDH-Q860 (Fig. 5a) most likely correlates to the Mulroney lens. The southern Messenger lens, which may pinch out south of the 8850 mN cross fault, has no correlatable lens to the north of the fault. It is interpreted to occur stratigraphically some 100 meters above the Morris lens.

Stratigraphic and structural synopsis

At least three stratigraphic horizons at the Balcooma prospect contain massive sulfide mineralization. From stratigraphic bottom to top the horizons are: (1) the Mulroney lens, (2) the Harvey, northern Messenger and Morris lenses, and (3) the southern Messenger lens (Fig. 12). A fourth horizon without massive sulfide mineralization occurs higher up the stratigraphy in the upper metagraywacke (Fig. 5a). The stratigraphic positions of the Mulroney lens and the Harvey lens are both represented at the surface by very fine to fine grained sulfidic (hematitic) and gahnitic quartzites.

Although the Balcooma prospect appears to be quite complex, careful analysis of facing and structural data indicates a fairly simple picture of a antiform-synform pair that has been terminated to the south by a syn-deformational tear fault. To the south of this fault the prospect is characterized by a uniformly upwardly facing sequence with no major folding. Facing evidence observed in this study allow only this interpretation. Such a morphology has been observed in the Jura Mountains of central Europe (Laubscher, 1972).

Consideration of facing evidence also indicates that the D_2 antiform-synform pair is more precisely termed a downward facing reclined syncline-anticline pair as the core of the antiform contains younger rocks than the limbs and the opposite applies to the synform. As the Harvey and northern Messenger lenses have a plunge of 20° to the south-southwest which is consistent with F_1, F_2 and F_3 fold axes, mobilization of sulfide to form a shoot with this plunge may have occurred at any time between D_1 and D_3. The major remobilization probably occurred during D_2 as the Harvey and the northern Messenger lenses occupy the cores of D_2 folds.

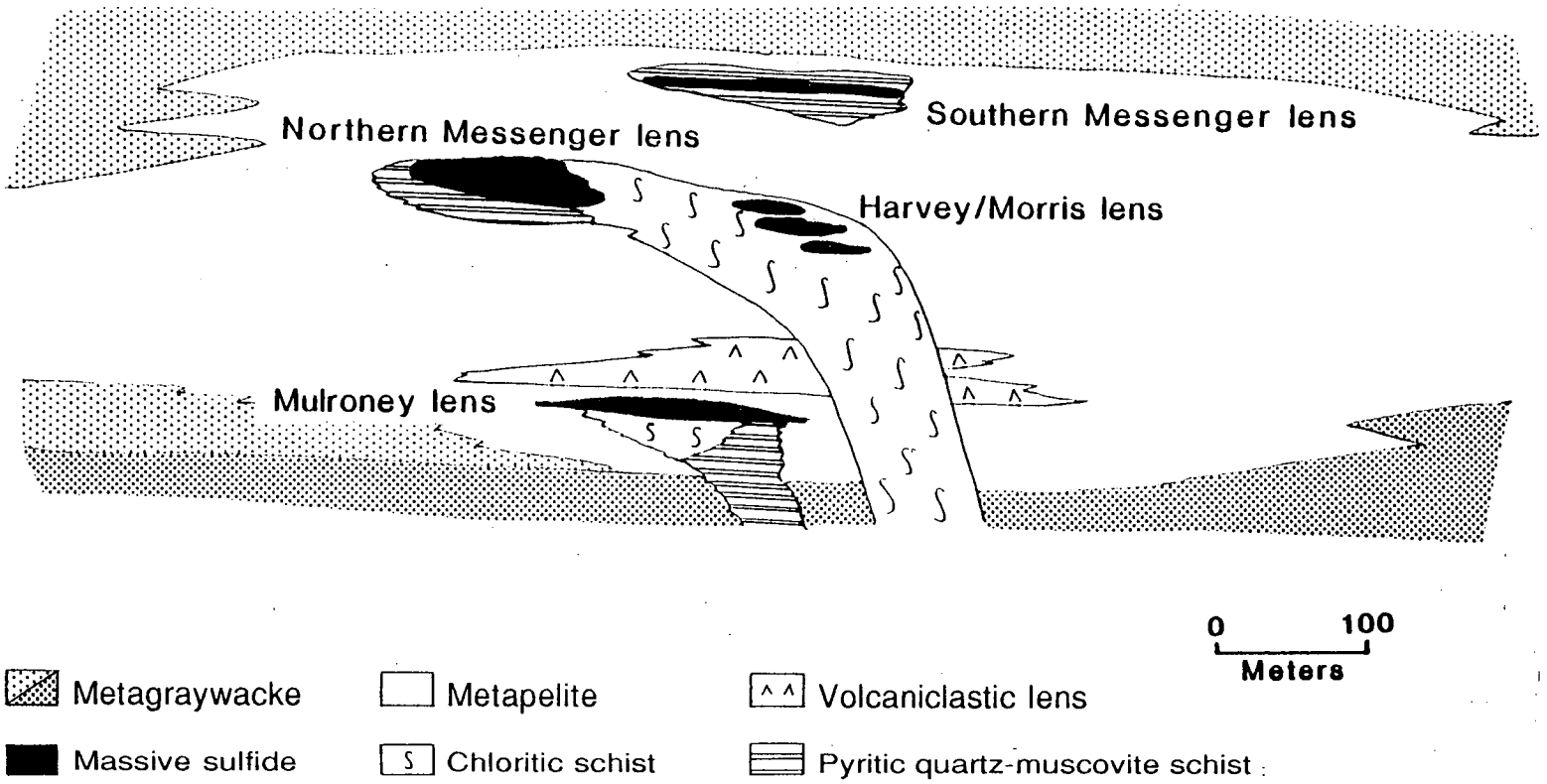

Figure 12. Schematic, unfolded east-west section illustrating the interpreted stratigraphic positions of massive sulfide lenses at Balcooma.

Geologic history of the Balcooma prospect

The Balcooma prospect has a complicated geologic history with certain aspects of structural deformation important in only part of the prospect area. Sections 8600 mN (Fig. 13) and 9000 mN (Fig. 14) are used to illustrate the inferred geologic history, as follows:

(1) Sedimentation in the Balcooma prospect area began with deposition of a feldspathic graywacke with minor interbedded volcaniclastic rocks (Figs. 13a and 14a).

(2) Deposition of the feldspathic graywacke waned and a shale lens formed. During shale deposition, three separate episodes of hydrotheraml exhalation led to massive sulfide mineralization at three different stratigraphic positions. Volcanism continued but decreased to the west as indicated by the presence of minor volcaniclastic lenses in the Balcooma host rocks (Figs. 13a and 14a).

(3) Clastic sedimentation occurred again with the deposition of additional graywacke. Weak hydrothermal alteration continued and this graywacke became weakly altered (Figs. 13a and 14a).

(4) Intrusion of quartz-feldspar porphyry sills, which are similar to the western volcanics, occurred followed by the intrusion of the microgranite (Figs. 13a and 14a).

(5) Deformation and metamorphism began during or after the granite intrusion. The effects of D_1 are largely unknown. Major folding occurred during D_2 with the formation of the recumbent antiformal syncline-synformal anticline pair north of the 8850 mN cross-fault (Fig. 14c). This fault formed as a tear during this deformation. The prospect area south of 8850 mN was not significantly affected by folding during D_2 (Fig. 13c). The Harvey lens was remobilized into the core of the D_2 overturned antiformal syncline at this time (Fig. 14c).

(6) Coaxial deformation continued with the open, upright folds of D_3. The western anticline formed during this episode (Figs 13d and 14d). The axes to D_1, D_2 and D_3 folds all plunged 20°-25° to the south-southwest.

(A) After sedimentation and mineralization

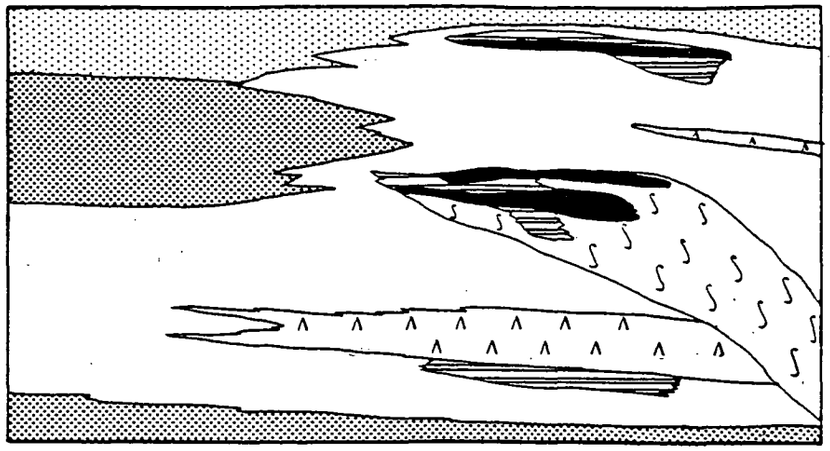

(B) After quartz–feldspar porphyry intrusion

(C) After D_2

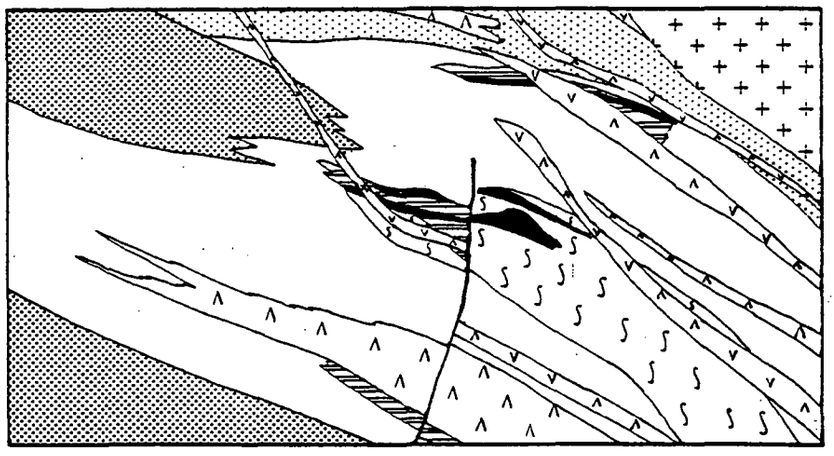

(D) After D_3

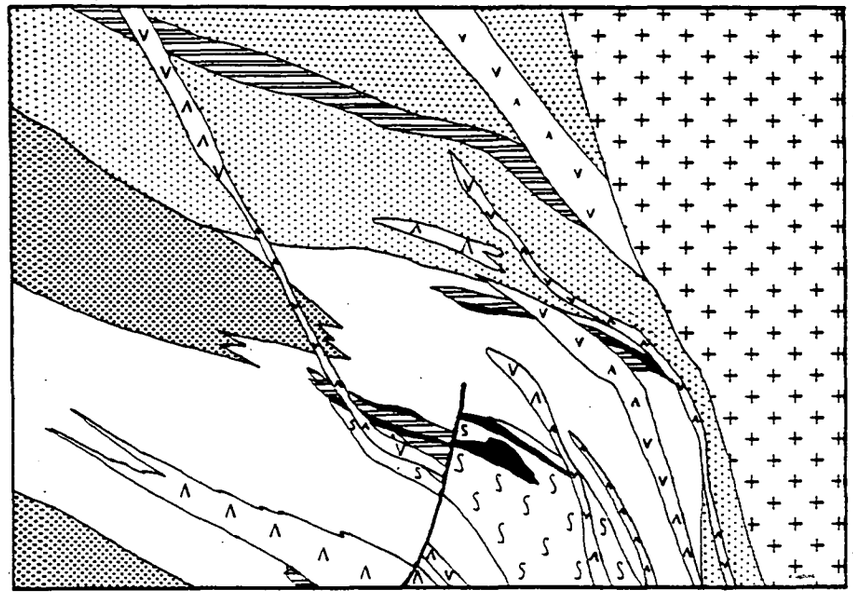

(E) After weathering

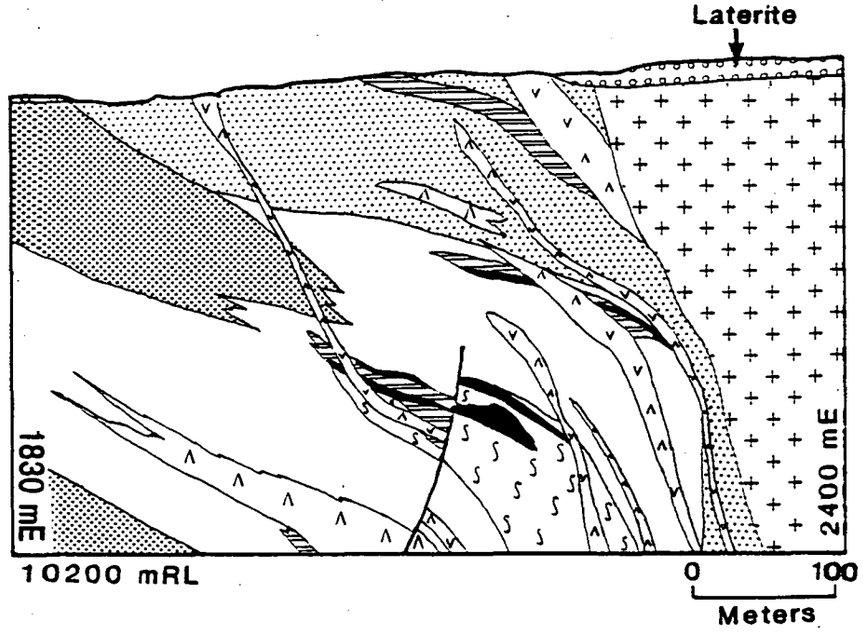

Figure 13. Geologic development of section 8600 mN, Balcooma prospect.

(A) After sedimentation and mineralization

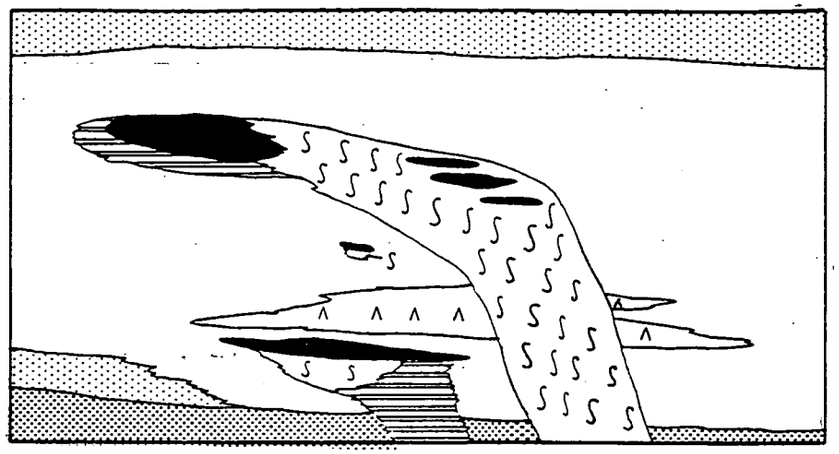

(B) After quartz-feldspar porphyry intrusion

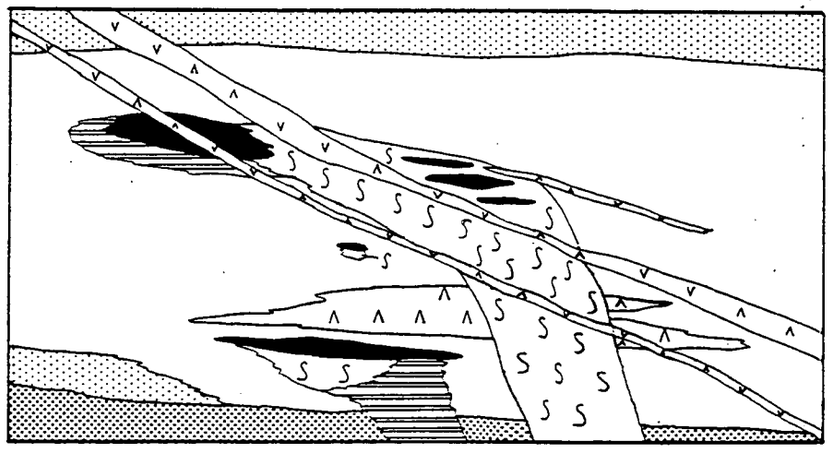

(C) After D_2

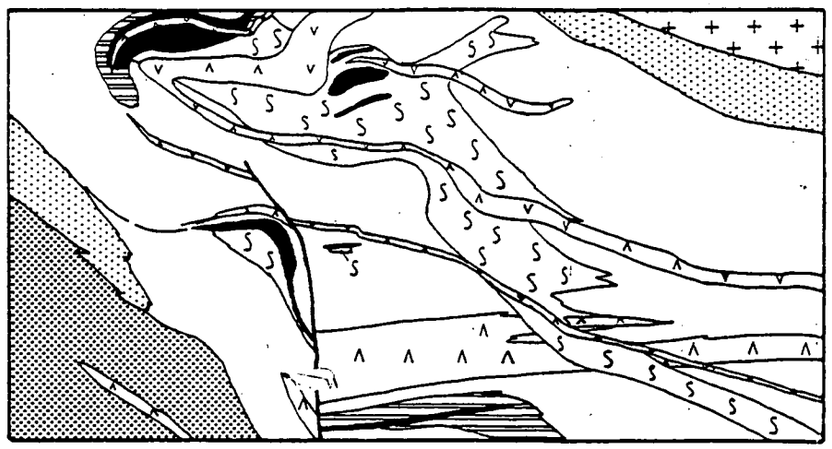

(D) After D_3

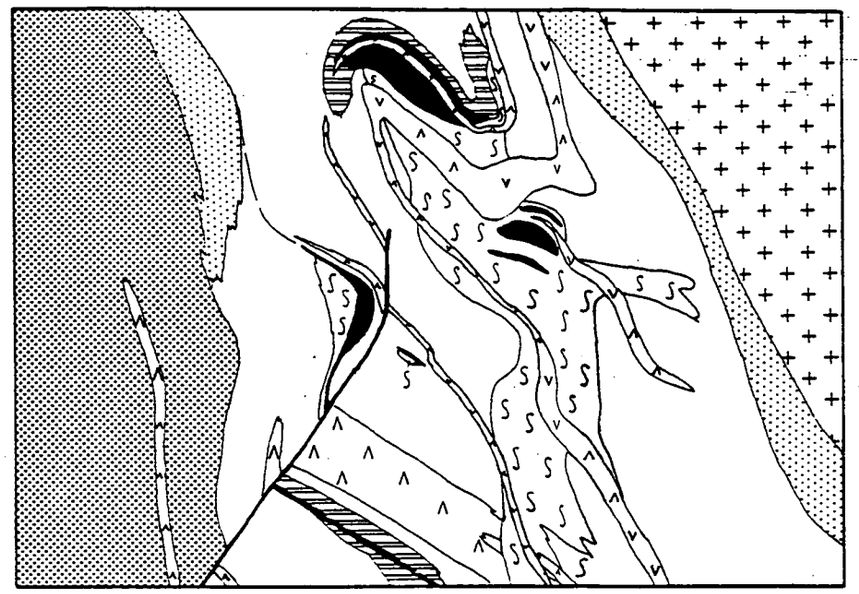

(E) After weathering

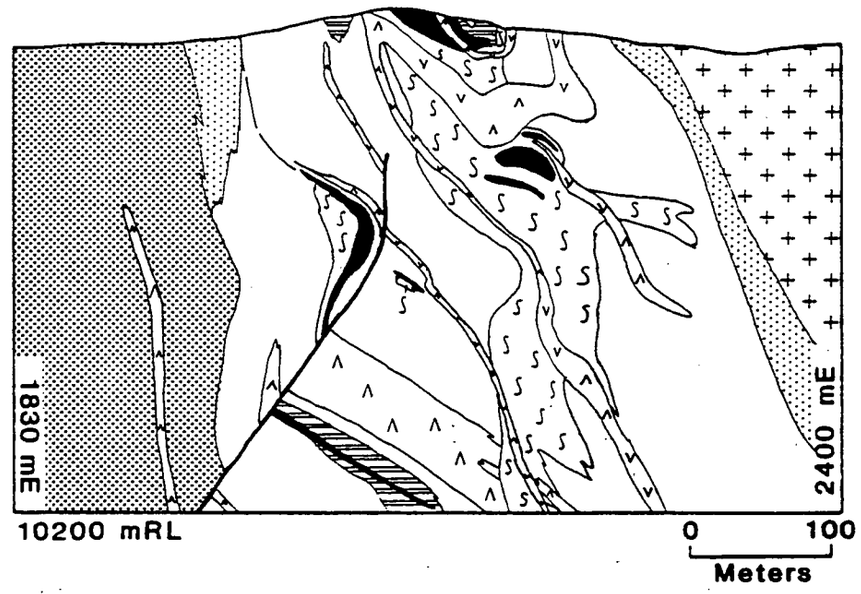

Figure 14. Geologic development of section 9000 mN, Balcooma prospect.

(7) The final deformation, D_4, gently cross-folded all previous folds; it did not affect the distribution of mineralization.

(8) Several phases of uplift and erosion occurred. The last occurred during Cenozoic time and produced widespread laterites, the lead and iron gossans and minor supergene mineralization (Figs. 13e and 14e).

Owing to a lack of unambiguous age data, the above geologic history largely ignores the ages of the events described. However indirect evidence may be used to date some of the major events. Harvey (1984b) inferred a Cambro-Ordovician age for the Balcooma metamorphic belt based on lithologic similarities to the Mt. Windsor volcanics. The Dido Granodiorite was intruded during the Silurian or early Devonian, and major folding ceased by the Middle Devonian as evidenced by the presence of uncleaved and unfolded limestones of that age 2 km to the southwest of the prospect. Carboniferous volcanics and Cenozoic basalts may also be found in the region surrounding the Balcooma prospect (Harvey, 1984).

Chapter 3
The structure and stratigraphy of the Dry River South prospect

Introduction

The Dry River South prospect occurs as a thin (1-10 m), laterally extensive (over 1 km long and up to 200 m wide) sheet of massive sulfide at the contact between footwall pyritic quartz-muscovite-biotite schist and hanging wall metagraywackes. Although much simpler than the Balcooma prospect, the structure of the Dry River South volcanogenic massive sulfide deposit has several unresolved problems, the most important being the inconsistency between surface bedding attitudes and the shallow dipping mineralized horizon. This chapter discusses this inconsistency and proposes several working hypotheses.

Surface mapping by T. Taylor has noted that bedding in the hanging wall metagraywackes is sub-vertical and strikes north-northeast, and sub-vertical dips are present near the top of many drill holes. This contrasts sharply with the shallow dip of the massive sulfide body. This body has an orientation of 047°/23° SE in the northwestern part of the prospect and rolls over to 035°/53° SE in the southeast (all orientations are relative to true north). This marked contrast in orientations (particularly the dips) indicates that there may be a structural discontinuity between the massive sulfide body and the surface.

Description of Units

This section describes the lithological units of the Dry River South prospect and offers interpretations for their origin based on studies by the author and previous work by T. Taylor (in Fabray et al., 1986; and Hall et al., 1987).

Metagraywackes

A sequence of metagraywackes with minor interbedded metapelites occupies the structural hanging wall of the massive sulfide lens

(Figs. 15 and 16) and consists dominantly of gray, fine grained quartz-biotite-albite schists with varying, but low amounts of staurolite and andalusite porphyroblasts. This unit is interpreted to be a metagraywacke and is interbedded with lesser (0-20%) metapelite. Two different types of metapelites are present: (1) brownish gray muscovite-biotite-quartz phyllite with up to 5% staurolite and andalusite porphyroblasts, and (2) gray, with black speckles and brown spots, fine to medium grained quartz-muscovite-biotite schist with up to 10% staurolite porphyroblasts. The phyllite often has a strongly developed crenulation cleavage. As the quartz-muscovite-biotite-staurolite schist has a similar composition to the phyllite (Appendix 2; compare QH26572 and QH26573) and these two units may grade into each other (particularly in Balcooma core), these two metapelites are considered to be metamorphic variants of the same parent rock.

T. Taylor (in Hall et al., 1987) also noted that a magnetite quartzite occurs on the surface intermittently along the Dry River South grid for 3 km. He interprets this as a ferruginous metachert.

Quartz-muscovite-biotite schist

Mapping and percussion chip logging by T. Taylor (Hall et al., 1987) indicated the presence of two synform-like lobes of fine grained quartz-muscovite schist with 1-10% 1-3 mm biotite porphyroblasts that extend and thicken to the south of the Dry River South prospect (Figs. 2 and 15). Considerable uncertainty exists over the nature of the protolith to this unit. Alternatives include felsic volcaniclastic rocks, lavas or intrusions.

Albite porphyry, which contains 1-2 mm albite phenocrysts in a microcrystalline albite-quartz-muscovite-biotite groundmass, occurs with the quartz-muscovite-biotite schist (Hall et al., 1987). This unit is interpreted as either a volcaniclastic unit, lava or sill.

Finally, numerous bands or dikes of quartz-amphibole-chlorite-magnetite-chlinozoisite schist occur through the upper part of the hanging wall rocks to the massive sulfide. These are largely associated with the quartz-muscovite-biotite schist and are interpreted as mafic dikes. On the surface they occur as ironstones extending along the Dry River South grid (Hall et al., 1987). These

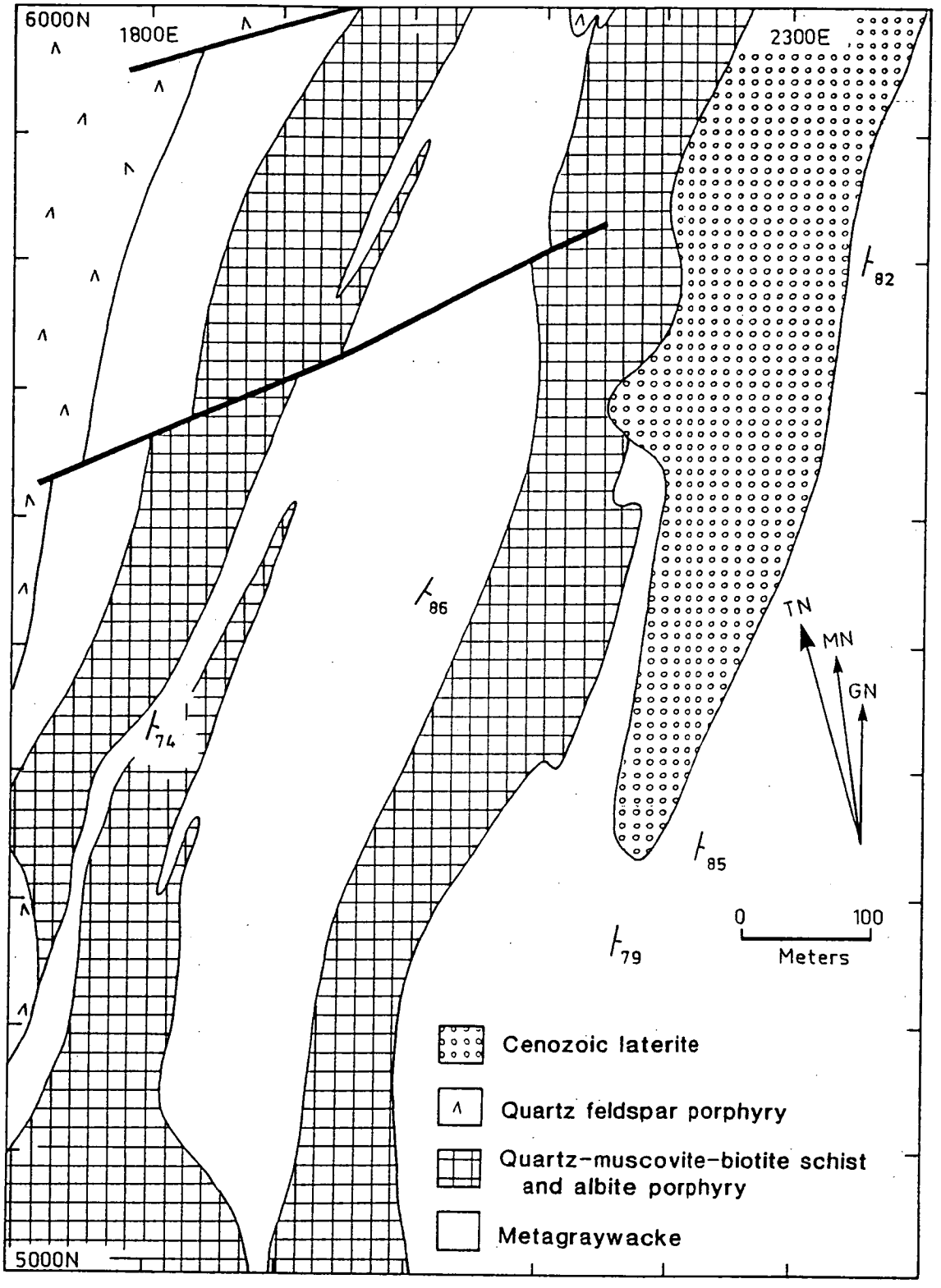

Figure 15. Surface geology of the Dry River South prospect. After mapping by T. Taylor.

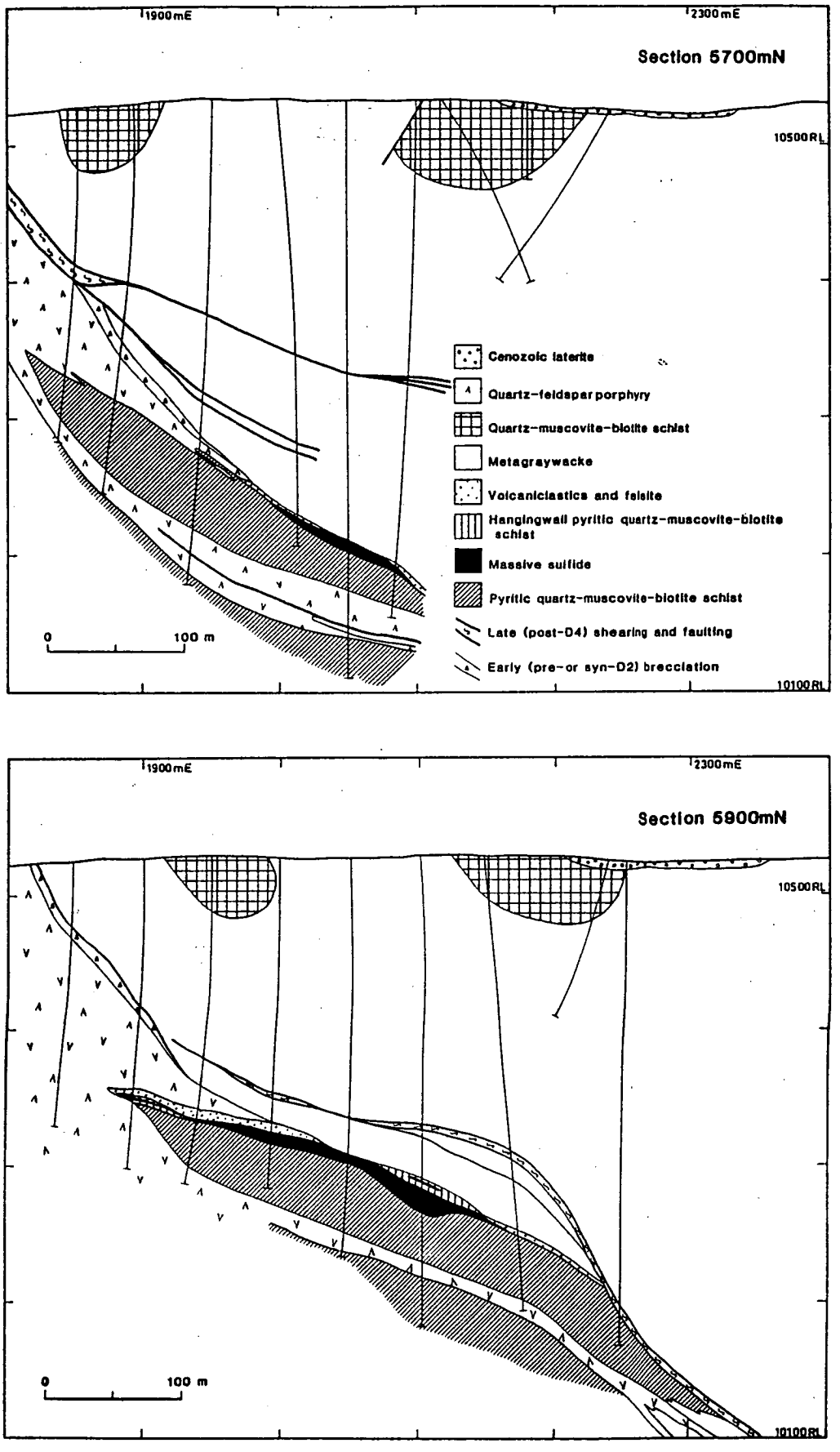

Figure 16. Uninterpretive geology for sections (a) 5700 mN and (b) 5900 mN, Dry River South prospect.

ironstones are geochemically anomalous in copper, zinc and lead, and provided the original interest in the area.

Quartz-feldspar porphyry

Two major lobes of quartz-feldspar porphyry extend into the prospect area from the west (Fig. 16). One lobe occurs some 1 to 5 m above the massive sulfide horizon (the upper porphyry), while the other lobe occurs some 10 to 50 m stratigraphically below the massive sulfide horizon. A third lobe, which T. Taylor interpreted to connect to the upper porphyry lobe (in Hall et al., 1987) occurs along the eastern part of the prospect some 1 to 5 m below the massive sulfide horizon.

The quartz-feldspar porphyry consists of 1-5% quartz eyes (2-10 mm in idameter) and 0-3% feldspar phenocrysts (2-4 mm in diameter) in an aphanitic to fine grained, gray to pink biotite-quartzofeldspathic groundmass.

Some controversy has existed over the origin of this unit. Although the lower porphyry is considered to be intrusive based on crosscutting relationships and lack or alteration, the origin of the upper porphyry has not been resolved. The stratiform nature and the presence of a breccia at the top of the upper porphyry was initially used by the author as evidence that it was a lava or crystal tuff. T. Taylor (in Hall et al., 1987) has suggested an intrusive origin based on a tentative (see above) crosscutting relationship to the massive sulfide horizon. More recent work by the author has indicated that the breccia on top of the upper porhyry is indeed tectonic and this unit has other crosscutting relationships. Based on this evidence, the upper porphyry is considered to be intrusive.

However, the eastern prophyry, which does not demonstrably connect to the upper porphyry, is often pyritized and sericitized (e.g. DRS32, 271.4 m to 272.0 m; and DRS46, 407.7 m to 408.9 m). This indicates that this lobe was either intruded before or during alteration, or was a submarine tuff or lava.

The massive sulfide horizon

Massive sulfide mineralization at Dry River South may be divided into two different types: (1) pyrite-chalcopyrite-chlorite, and (2)

pyrite-sphalerite-galena. Minor massive magnetite occurs as a facies equivalent to massive sulfide on the western side of the prospect.

The massive sulfide horizon is capped in the west, and to a lesser extent in the east, by a thin (< 2 m) veneer of felsic rocks, which include fine grained quartz-feldspar-biotite schist, fine grained quartz-biotite-muscovite-feldspar schist and a felsic fragmental with lapilli sized fragments (Figs. 16 and 17a). Although the presence of the intrusive upper porphyry adds some uncertainty, these rocks are interpreted as the last phase of volcaniclastic deposition before the onset of graywacke sedimentation.

Footwall alteration zone

The immediate footwall to the mineralized horizon contains a pyritic, fine grained quartz-muscovite schist which contains up to 3% 1-4 mm biotite, scattered 2-10 mm staurolite and rare 2-7 mm andalusite porphyroblasts. The pyrite occurs dominantly in 1-400 mm semi-massive stringers and to a lesser extent as disseminations. Along the western side of the prospect the footwall schists contain patchy zones of sphalerite-galena stringer which often have associated gahnite.

The presence of pretectonic fragmental textures in DRS-39 from the footwall alteration zone (Fig. 17c) indicates that the original footwall lithology at Dry River South was in part felsic volcaniclastic rocks. Additional observation and chemical analyses (Chapter 4) of the alteration zone confirmed the initial interpretation that this zone was originally a series of rhyodacitic to dacitic volcaniclastic rocks and/or lavas. The footwall schists often display an "augen" texture, with very siliceous, 5-30 mm diameter, augen in a fine grained quartz-muscovite schist matrix (Fig. 17d). By analogy to the Rosebery deposit (Brathwaite, 1969), this "augen" texture is interpreted to be an altered and metamorphosed volcaniclastic texture. Both Balcooma and Dry River South occur near the horizon where felsic volcanics disappear from the stratigraphic sequence. This has direct implications for exploration.

T. Taylor (in Hall et al., 1987) reported chlorite-pyrite-magnetite zones in the footwall alteration zone. These probably

Figure 17. Photographs showing primary or altered textures at Dry River South: (a) conformable contact between stratigraphically lower massive sulfide and a volcaniclastic unit with felsic clasts in a pyritic quartz-muscovite-biotite schist matrix (the cleavage is pervasive through the sample indicating a pre-tectonic origin; DRS46W, 235.3m to 235.6 m); (b) pyritic quartz-muscovite-biotite schist (typical footwall alteration (DRS15, 225.5 m to 225.7 m); (c) altered volcaniclastic with felsic clasts in a pyritic quartz-muscovite-biotite schist matrix (DRS39, 170.7 m to 170.8 m); (d) pyritic quartz-muscovite-biotite schist with silicified "augen" clasts (DRS15, 210.1 m); and (e) dolerite dike truncating S_2 cleavage in pelitic schist (DRS52, 384.6 m).

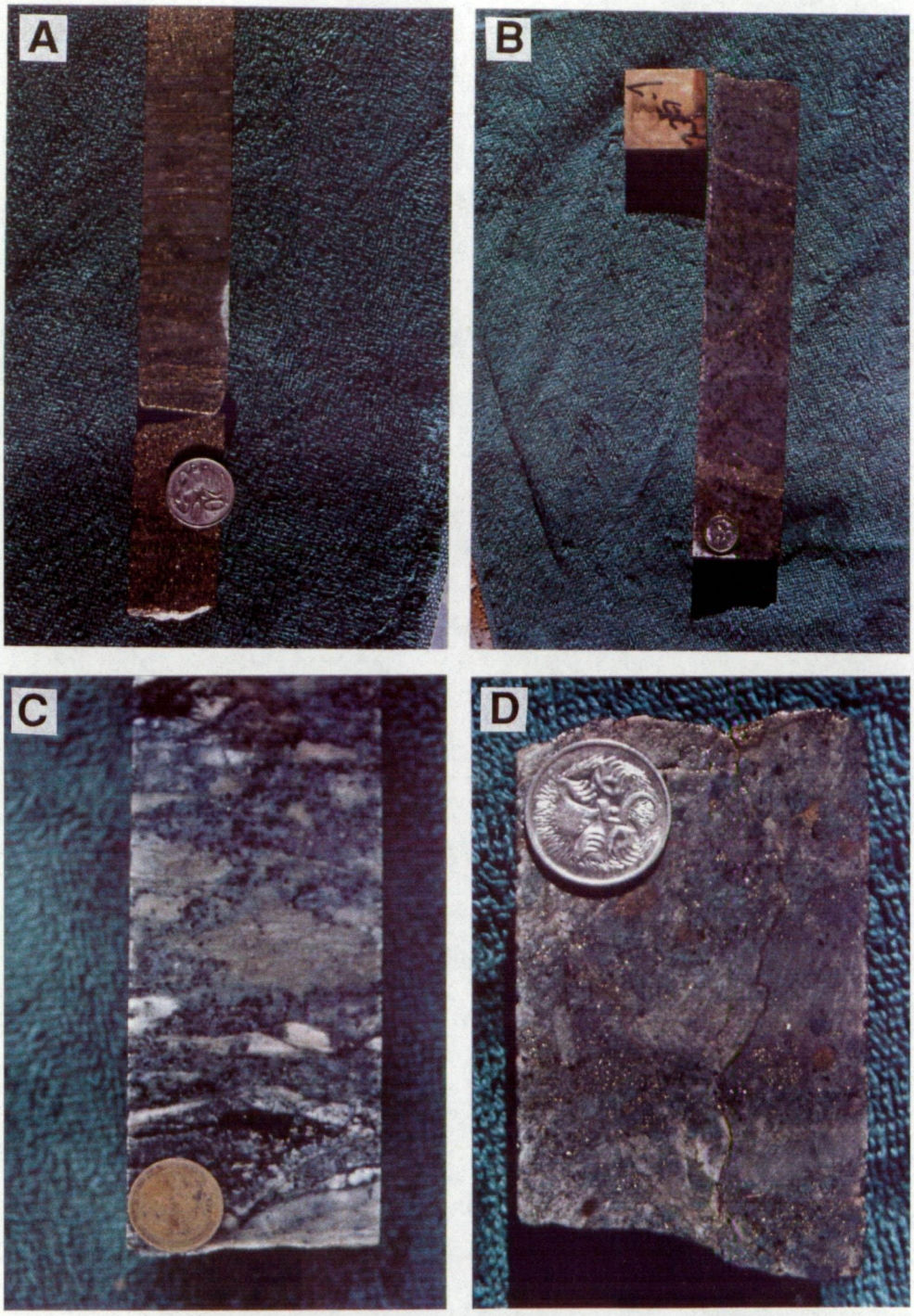
A
B
C
D
E

represent original zones of chloritic alteration and tend to occur on the eastern edge of the prospect.

Felsite

Towards the base of DRS-38, DRS-54 and DRS-55 an orange, fine grained biotite felsite has been intersected. Owing to lack of data, the origin of this unit is not certain. T. Taylor (pers. comm., 1987) has suggested that it may correlate with the albite porphyry seen at the top of many holes and at surface, but the physical separation of the two units and the differing rock associations make this correlation tenuous. This felsite may also be a border phase of the microgranite that crops out to the east, but this correlation is also tenuous.

Dolerite

A sub-vertical dolerite dike has been observed in DRS-52 where it is intersected several times throughout the hole. This unit has also been noted in the chips from the precollars of several other holes. At the surface, the dolerite may crop out sporadically as north trending mafic dikes and ironstones associated with the quartz-muscovite-biotite schist. As the unit crosscuts the metamorphic foliations in DRS-52 (Fig. 17e), it is interpreted to postdate major deformation.

Structure

Deformation at Dry River South has involved both significant folding and faulting. Three generations of cleavages have been recognized at Dry River South, and these cleavages correspond to S_2 through S_4 at Balcooma (Chapter 2). To allow direct comparisons to Balcooma structural elements the Balcooma structural classification is retained at Dry River South. Additionally, evidence for three generations of faulting exist in core. The earliest generation seems to be associated with S_2, whereas the the other two generations appear to be reactivations of this structure. The relationship of

faulting observed in core to the regional northeast set of late cross faults (Chapter 1; Figs. 2 and 15) has not been resolved.

Folding

Pi diagrams of S_0, S_2, S_3 and S_4 are presented in Figure 18. S_1, which is noted in the northwestern parts of the Balcooma prospect (Chapter 2), was not observed at Dry River South. As at Balcooma (Chapter 2), S_2 and S_3 are the major cleavages present at the deposit.

At the surface bedding is generally steeply dipping to the east and strikes to the northeast. This contrasts to Balcooma where the poles to S_0 have a great circle distribution with a pole at 22°/214°, which is the orientation of the F_2, and F_3 fold axes at Balcooma (Chapter 2).

S_2 dips moderately to steeply to the east and strikes to the northeast. However, a small amount of spread in the poles to S_2 define a great circle with a pole at 20°/223° which is interpreted as the orientation of F_3 fold axes. This is consistent with the interpretation of the S_2 orientations at Balcooma (Chapter 2), and with the majority of the measured intersections between S_3 and S_2 ($L_{3_{INT}}$) at Dry River South which also indicate the orientation of F_3 fold axes.

Although S_3 generally has a north-northeast strike and a subvertical dip, a small amount of spread in the orientations suggests a great circle with a pole that is roughly parallel to a single measurement of the intersection of S_3 and S_4 ($L_{4_{INT}}$) which plunges at 63°/217° (Fig. 19a). These data indicate that F_4 fold axes plunge steeply to the south although with some uncertainty due to difficultites in measuring $L_{4_{INT}}$.

Two observations of S_4 were made at Dry River South. Both examples were observed around 5250 mN 2100 mE (Fig. 15). The

Figure 18. Pi diagrams showing the orientations of S_0, S_2, S_3, S_4, $L_{3_{INT}}$, and $L_{4_{INT}}$ at the surface, Dry River South prospect. Data collected by D. Huston and T. Taylor.

Figure 19. Photographs showing structures and structural fabrics at the Dry River South prospect: (a) S_2, S_3 and S_4 in cleavage intersections (sample collected at 5220 mN 2120 mE, Dry River grid); (b) F_3 fold in semi-massive sulfide (DRS19, 209.0 m); (c) Tectonic breccia with 2-20 mm quartzose clasts in a fine grained muscovite-biotite-quartz schist matrix (DRS44, 167.3 m); and (d) oriented fold within D_2 (?) breccia zone which indicates thrusting with the upper block moving west (DRS44, 165.2 m).

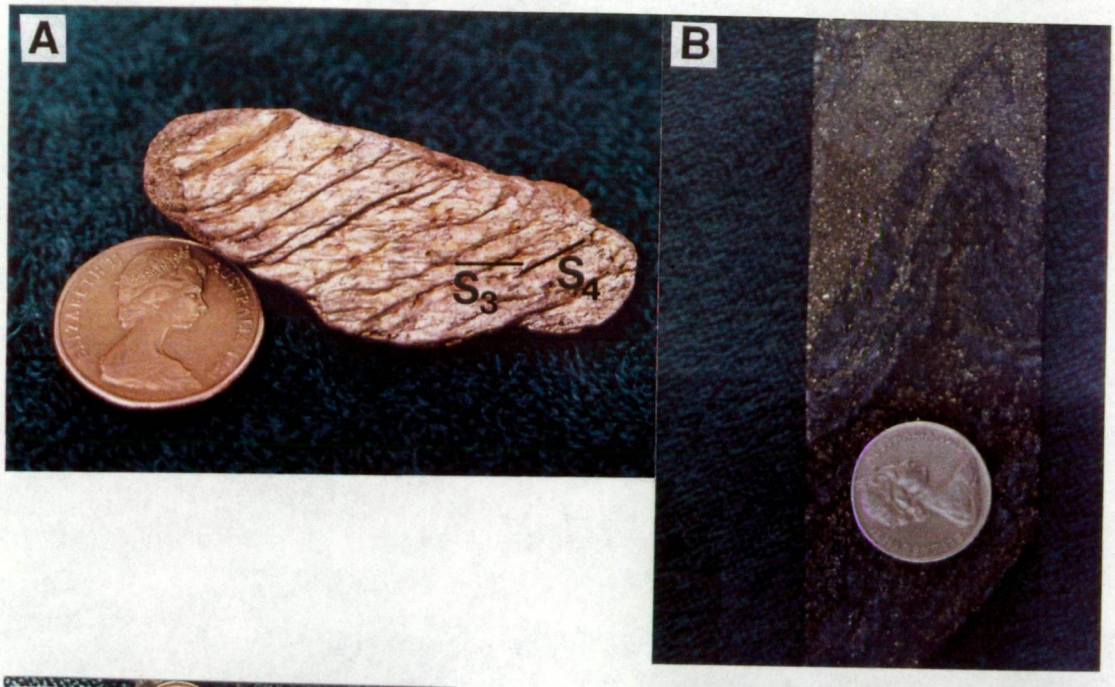
A
S3
S4
B
C
D
W
E
S2

measurements of S_4 and $L_{4_{INT}}$ indicate that the axial planes to F_4 folds at Dry River South strike to the northwest and dip moderately to the southwest.

These results indicate that the stress regimes that produced F_4 folds differed significantly from the stress regime that produced the coaxial F_2 and F_3 folds. The latter group of coaxial folds may have been formed by small changes in a compressional stress regime with the principal maximum stress axis alligned west-northwest/east-southeast. Such a stress regime could also produce thrust faults.

F_4 folds formed in a stress regime with the principal maximum stress aligned northeast/southwest and the principal intermediate stress direction plunging moderately to steeply to the south.

Mesoscopic folds are rarely observed at surface or in core at Dry River South. Evidence for folding must be inferred from changes in the orientation in structural fabrics at the surface and in section.

The best evidence for large scale folding in the prospect area is the synformal shape of the quartz-muscovite-biotite schist lenses at the surface (Fig. 16). Although disagreement exists on their origin (see below), a stratiform occurrence of this unit (i.e. a tuff or sill) requires the presence of tight north-northeast trending F_2 folds with a wavelength of some 250 m at the surface. F_2 folding is assumed as the axial planes to the inferred folds dip moderately to steeply to the east and this is consistent with observations of S_2. However, if this unit was a discordant intrusion (T. Taylor, pers. comm., 1987), folding is not required.

Although no definitive evidence of large scale F_3 folding exists at the surface, small scale F_3 folds may be observed in core (Fig. 19b) and at the surface. A mesoscopic F_3 synform-antiform pair with a wavelength of 0.5 m has been observed at 5325 mN 2225 mE (Fig. 15). This occurrence is also the only known occurrence at either Balcooma or Dry River South where D_3 has totally destroyed S_2 as S_2 has been overprinted by S_3 as to be unrecognizable.

Faulting

Structural deformation at Dry River South also included faulting of at least two (and possibly three) separate ages. Early brecciation (Fig. 19c) occurred along much of the upper contact between the upper porphyry and the metagraywackes (Fig. 16). This deformation produced a strongly developed schistosity parallel to the east dipping contact that is subparallel to S_2. This schistosity wraps around the breccia blocks which suggests that breccia formation and foliation development occurred at approximately the same time. If the foliation in the zone of strong brecciation is assumed to parallel the breccia zone and dips to the east, folds within the brecciated zone may be oriented and this orientation indicates a reverse shear during faulting (Fig. 19d). Due to these relationships, the faulting is interpreted to have occurred during D_2 and has a thrust sense of motion. The presence of this style of deformation was not observed in the metagraywackes although later puggy faults are common in this region.

Faulting of this style and age may also explain many of the geologic anomalies around the massive sulfide horizon (see below). Much of the shearing and juxtaposition of footwall pyritic quartz-muscovite biotite schist above the massive sulfide may be due to this style of faulting.

This fault zone at the upper contact between the upper porphyry and metagraywacke has been reactivated twice. Evidence for the first reactivation exists as subhorizontal stepped lineations. The lineations indicate a brittle style of deformation.

The second reactivation occurs as strongly developed, late pug zones, brecciation, quartz veining and shearing. The contact between the upper porphyry and the metagraywacke in DRS-28 (Fig. 16b) consists of a 10 m wide zone of intense shearing, quartz veining, brecciation and pug development. These zones occur also in the metagraywacke where they vary between several meters in width to less than 20 mm. Although faulting of this style may be traced across several sections (Fig. 16), it is not always observed in some sections. This may be due to variable development of gouge during late faulting or core loss.

Alternative structural models

As most data for S_0, S_2 and S_3 cluster around an orientation that dips steeply east and strike northeastly, the structure at the surface of the Dry River South prospect must either: (1) form a steep easterly dipping monocline, or (2) consist of the limbs of one or more tight to isoclinal folds with axial surfaces that dip steeply easterly.

Analysis of the structural data from the Dry River South prospect indicates that it has a deformation history similar to the Balcooma prospect. The first two major folding events (D_2 and D_3; evidence for D_1 was not observed at Dry River South) are coaxial with similar axial orientations to Balcooma, but axes to the the final folding event (D_4) have a slightly different orientation at Dry River South relative to Balcooma. Of more economic interest, however, the Dry River South prospect differs from Balcooma in that the mineralization at Dry River South has not been strongly folded.

Figure 16 illustrates the simplified, uninterpreted geology of sections 5700 mN and 5900 mN. Figure 20 illustrates the downhole variation in core to bedding angles for both sections (the data for section 5700 mN is oriented, but the data for section 5900 mN is unoriented; steep bedding has a low core to bedding angle, while shallow bedding has a high core to bedding angle). These figures illustrate the major structural inconsistency of the Dry River South prospect: steeply dipping surficial beds that strike northeast as opposed to a gently dipping mineralized horizon that dips to the southeast and strikes to the northeast. Four different hypotheses have been suggested to explain this inconsistency: (1) a monocline which steepens up dip from mineralization, (2) a shallowly dipping early fault at or just above the massive sulfide and below the upper porphyry, (3) a shallow, easterly dipping late fault located some 30 to 100 m above the mineralized horizon, and (4) concentric folding that dies out just above the massive sulfide horizon. Any model must consider the probable competency of the quartz-feldspar porphyry sills and footwall alteration zone that occur around the massive sulfide horizon. Figures 21 through 24 illustrate each option for section 5900 mN, and Table 5 summarizes the merits and faults for each option.

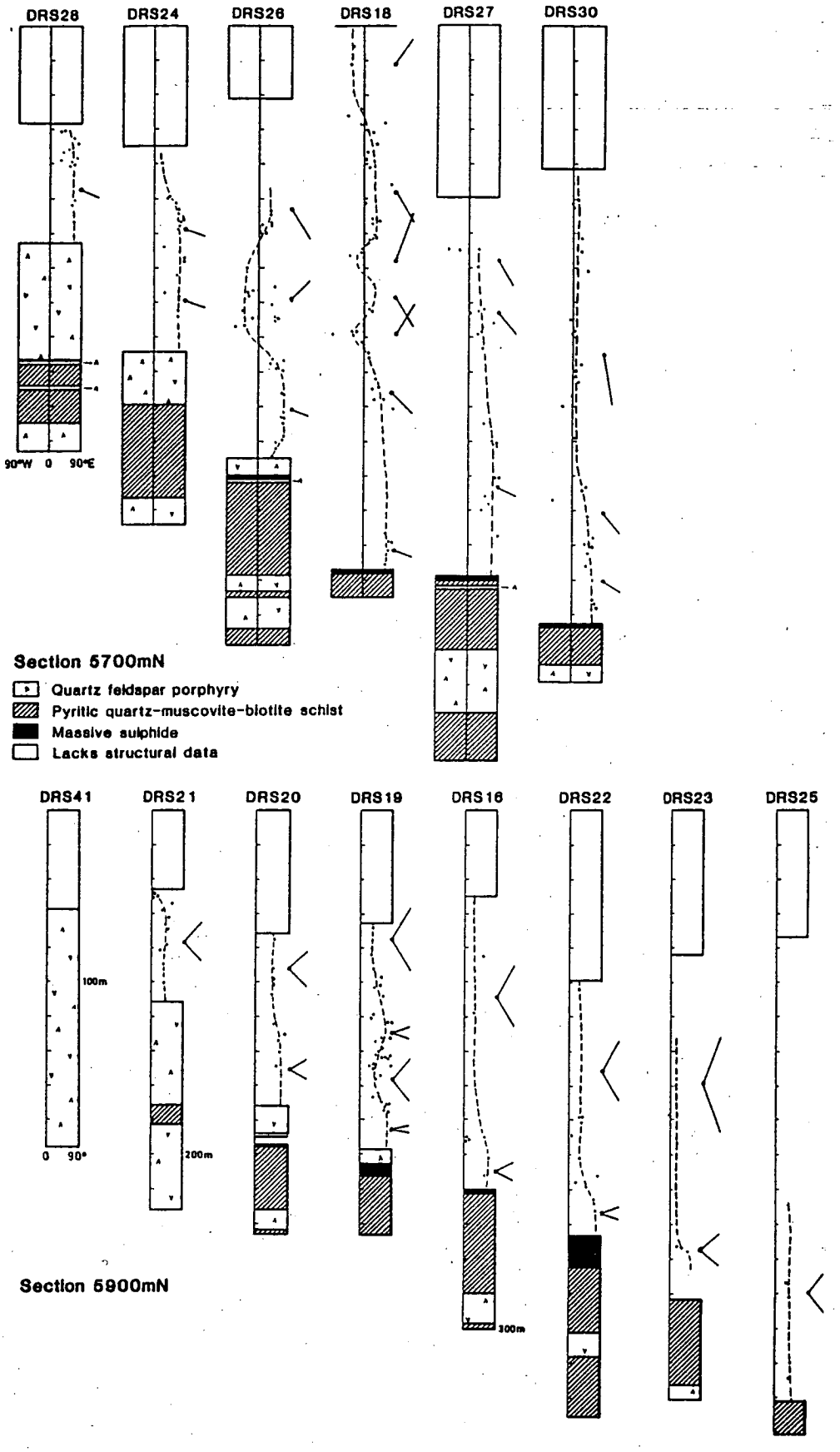

Figure 20. Down hole variation in core to bedding angles for sections (a) 5700 mN and (b) 5900 mN, Dry River South prospect. Bedding in section 5700 mN is oriented assuming that S_2 dips moderately to steeply to the east.

Table 5. Merits and problems of four structural interpretations, Dry River South prospect.

Option	Merits	Problems
One (monocline)	Simplicity; does not require the invocation of either strong folding or faulting.	Does not explain the downhole variation in core to bedding angles of dip reversals in bedding. Does not explain the shearing at the top or within the massive sulfide lens or the early brecciation at the contact between the upper porphyry and the metagraywacke. Does not explain the geometry of the quartz-muscovite-biotite schist at the surface.
Two (early fault between the massive sulfide and the upper porphyry)	Explains the differences in bedding attitudes between the massive sulfide and the surface. Explains the lack of bedding continuity above the massive sulfide. Explains the presence of shearing immediately above the massive sulfide in some holes.	The shearing above the massive sulfide is not present in all holes, and it is too steep for a shallowly dipping structure. A fault in this position is inconsistent with the inferred geometry that the upper porphyry cuts the massive sulfide. The massive body of porphyry to the west of the prospect shows no evidence of significant faulting at the inferred position. Evidence from core to bedding angles indicates that bedding remains shallow and east dipping for tens of meters above the massive sulfide horizon.
Three (late faulting 30-100 m above the massive sulfide horizon)	Thick (up to 10 m) zones of major late shearing and brecciation have been noted 30-100 m above the massive sulfide on sections 5500 mN, 5700 mN and 5900 mN. This explains the differences in bedding attitudes between the surface and the massive sulfide, and the continuation of shallowly east-dipping bedding tens of meters into the hanging wall of the massive sulfide lens.	These zones of shearing and brecciation are not continuous over the prospect; they are either weakly developed or missing on sections 5600 mN, 5800 mN and 6000 mN. It does not explain the poor or patchy continuity of bedding between the massive sulfide lens and the inferred fault.
Four (symmetric folding in the hanging wall that dies out before the massive sulfide horizon)	Explains the geometry of the quartz-muscovite-biotite schists simply as synforms. Is consistent with the downhole variation in bedding present in sections 5700 mN and 5900 mN.	Reconstructions requires a significant structural thickening of the hanging wall beds on the western side of the prospect. It does not explain the poor or patchy continuity in bedding immediately above the massive sulfide lens.

Option one

Option one (Fig. 21) invokes a steeply dipping moncline with mesoscopic parasitic folds that steepens both up dip and down dip from the mineralized horizon. The subvertical orientation of S_0 at the surface is due to steepening up dip. This option has the benefit of simplicity; it requires no faulting or complex folding. However, it cannot explain the poor continuity of the bedding above the massive sulfide horizon, the synformal morphology of the quartz-muscovite-biotite schists at surface, or the apparent dip reversals present in DRS-18 and DRS-24 (Fig. 20a).

Option two

Option two (Fig. 22) involves an early fault at or just above the massive sulfide horizon but underneath the upper porphyry. T. Taylor (in Fabray et al., 1986) initially proposed this option based on: (1) steep dips in the hanging wall rocks, (2) the lack of apparent stratigraphic correlation immediately above the mineralized horizon, and (3) the presence of strongly sheared and/or brecciated zones just above the massive sulfide horizon in a few holes. An alternative is to pass the inferred fault along the tectonic breccia that caps the upper porphyry. Objections to locating a fault between the mineralized horizon and the upper porphyry include: (1) most holes show little or no evidence of shearing, brecciation or quartz veining immediately above or at the mineralized horizon, (2) shearing immediately above the massive sulfide horizon, when present, usually has a moderate to steep orientation which is inconsistent with a shallow dipping fault, and (3) the upper porphyry, which is placed above the fault, shows no evidence of the folding which is inferred above this fault. If the fault is located above the upper porphyry, all objections are removed, but the morphology of quartz-muscovite-biotite schist at the surface is not explained.

Option three

The third option (Fig. 23) involves a major shallow easterly dipping late (i.e. post S_4) fault with major movement approximately

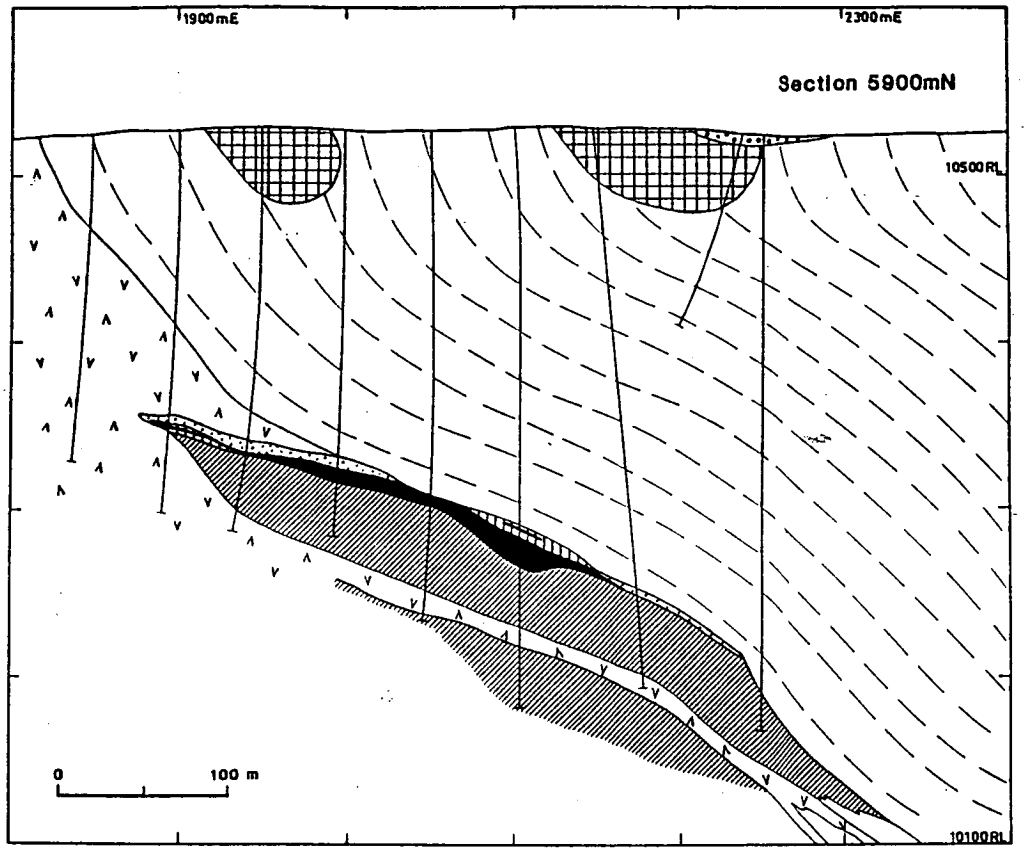

Figure 21. Structural option one illustrated on section 5900 mN (legend in Fig. 16).

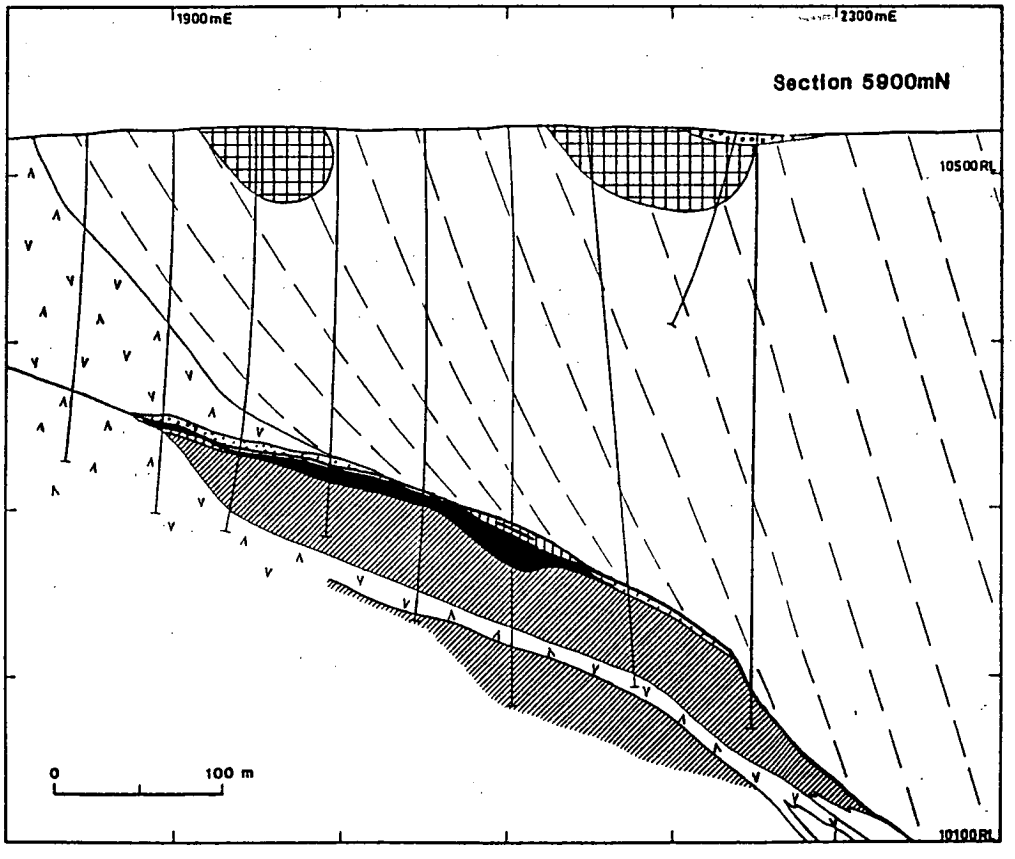

Figure 22. Structural option two illustrated on section 5900 mN (legend in Fig. 16).

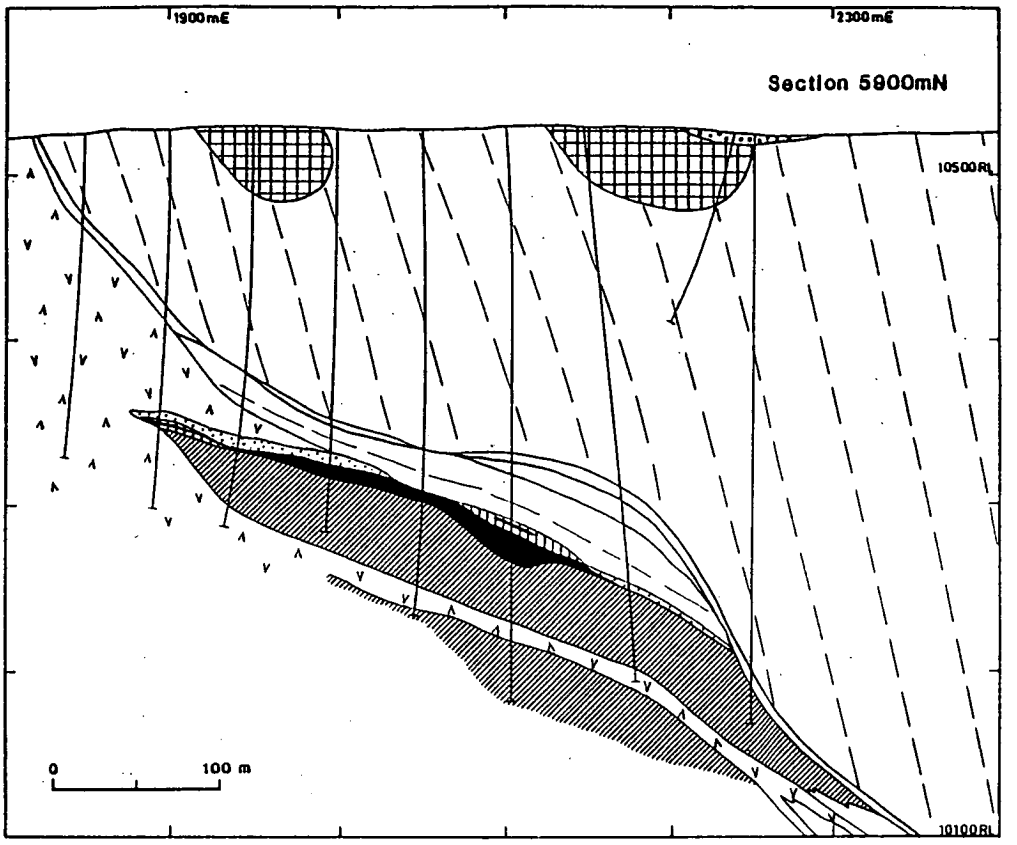

Figure 23. Structural option three illustrated on section 5900 mN (legend in Fig. 16).

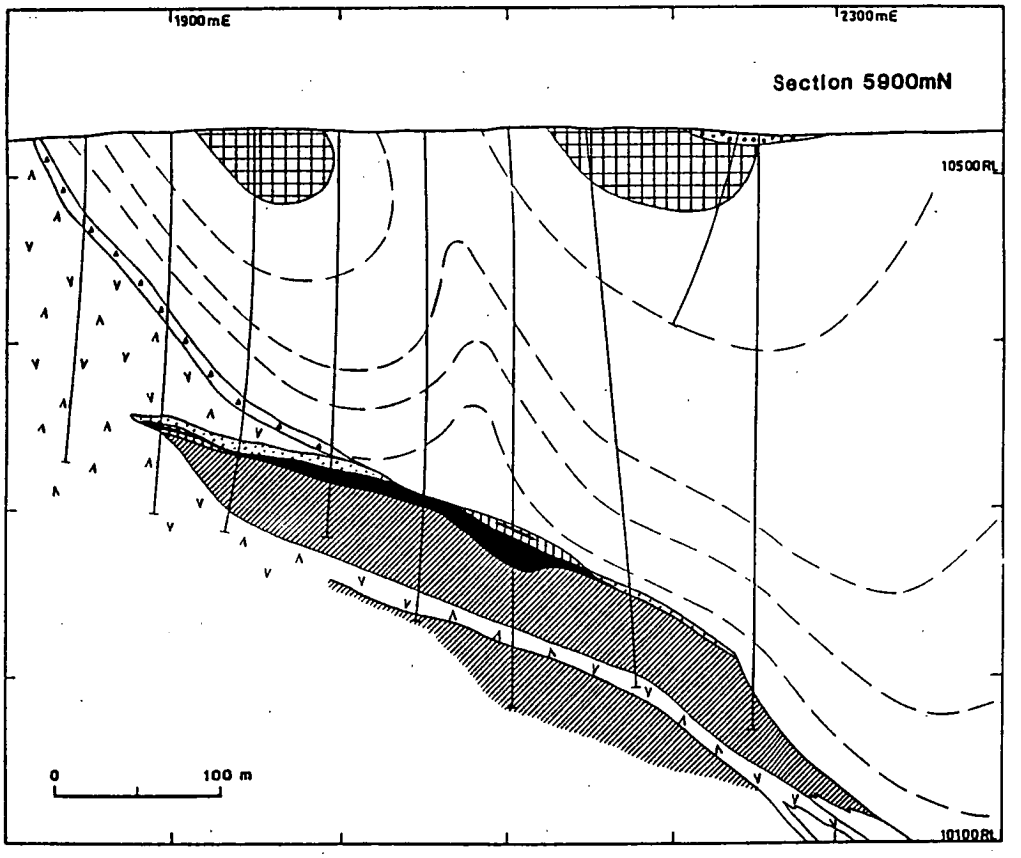

Figure 24. Structural option four illustrated on section 5900 mN (legend in Fig. 16).

30 to 100 m above the massive sulfide horizon. Zones of strong, late shearing, brecciation and pug may be found at the inferred position along sections 5700 mN and 5900 mN (Fig. 16), but the shearing and brecciation is only weakly developed along section 5800 mN and is lacking along section 6000 mN. Major late movement along this fault is unlikely due to the lack of late shearing and/or brecciation along section 6000 mN.

Option four

Option four (Fig. 24), which is slightly more complicated than the other options, involves symmetrical folding of the hanging wall metagraywackes and quartz-muscovite-biotite schists in combination with faulting along the top of the upper porphyry. The symmetrical folding is inferred to die out before it reaches the massive sulfide horizon. Faulting along the upper porphyry contact would take up the shear developed during deformation. This option has the benefit of consistency with the regional structural development. B. Stainforth (pers. com., 1987) has interpreted a major thrust on the western contact of the felsic volcanics to the west of the prospect, which is consistent with the structural style envisaged by Thom (1984). It also explains the synformal morphology of the quartz-muscovite-biotite schist if it is stratiform.

Discussion

None of the options presented can be completely discarded, but options 1 through 3 cannot explain the morphology of the quartz-muscovite-biotite schist. Of the four presented, option one is most unlikely as it does not explain the morphology of the quartz-muscovite-biotite schist or the down hole variation in core to bedding angles in DRS-19 and the holes along section 5700 mN.

Option two, which invokes a shallowly dipping fault between the upper quartz-feldspar porphyry and the massive sulfide horizon is considered unlikely because: (1) only fragmented evidence of faulting exists at this position; (2) when evidence of faulting is present, the shearing, brecciation and foliation indicate a steep dip (>45°) which is inconsistent with a shallowly dipping structure; (3) one interpretation of the upper porphyry indicates that it crosscuts

the massive sulfide horizon, and this rules out a major fault between the two units; (4) two drill holes (DRS-42 and DRS-43) which passed through quartz-feldspar porphyry to the west of the mineralization showed no evidence of significant faulting at the inferred position; and (5) core to bedding angle evidence (Fig. 20) indicates that bedding remains shallow and subparallel to the mineralized horizon for several tens of meters above this horizon in all holes.

More convincing evidence for major early faulting may be found along the upper contact of the upper lobe of quartz-feldspar porphyry. Early faulting (syn-D_2(?)) must have occurred at this contact, but this faulting cannot be traced clearly into the hanging wall metagraywacke sequence to the east of the upper porphyry lobe. Possibly the fault has been rehealed or reactivated.

Evidence for late (post-D_4) shearing and brecciation between 30 m and 100 m above the massive sulfide horizon is present on sections 5500 mN, 5700 mN and 5900 mN, but on sections 5600 mN, 5800 mN and 6000 mN evidence is only weak or missing. This late faulting may be a reactivation in the hanging wall metagraywackes of the earlier structure noted at the contact between the upper porphyry and the metagraywackes. In DRS-28 (section 5700 mN), this late shearing and brecciation occupies the position at the contact between the upper porphyry and the metagraywacke usually occupied by early brecciation and foliation (Fig. 18a).

Option four, which invokes symmetrical folding around the quartz-muscovite-biotite schist, best explains the morphology of the the rocks above the upper quartz-feldspar porphyry. It is consistent with the down hole variation of core to bedding angles in sections 5700 mN and 5900 mN (compare Figs. 20 and 24). In DRS-18 and DRS-24 on section 5700 mN, the bedding dips west just below the inferred axial plane to the hypothesized fold. Elsewhere the bedding dips to the east, and near the surface the bedding has a steep dip. This morphology is modelled well by symmetrical folds which have axial planes that dip east, parallel to the dominant foliation. Although section 5900 mN lacks orientation data, the general trend of data is consistent with this interpretation; DRS-19 shows a rise in the core to bedding angles that occurs around the hinge zone of an inferred cylindrical synform. Near the mineralized horizon the dips shallow but still dip east which indicates either that the inferred

cylindrical folds die out, have been faulted out, or some combination of these two processes.

A combination of options 2 and 4 explains the morphology of the Dry River South prospect best (Fig. 25). Symmetric folds (two synforms and an antiform) with steeply dipping limbs at the surface are faulted out above the mineralized horizon. This group of folds is floored by an early fault that was localized at the contact between the metagraywackes and the upper quartz-feldspar porphyry lobe. The fault continued out into the hanging wall metagraywackes where it has been reactivated after D_4 to produce the late shearing and brecciation present 30 m to 100 m above the massive sulfide body. Subordinate and parasitic faults associated with this major fault explain the shearing an juxtaposition of footwall alteration above massive sulfide locally along the massive sulfide horizon.

The greatest objection to this model is the lack of continuity in bedding in the metagraywacke sequence between the massive sulfide horizon and the surface. Locally, beds of metapelite can be traced between holes for up to 300 m, but in general correlation does not persist between more than two drill holes. This lack of correlation has been used as evidence for the existence of a fault just above the massive sulfide horizon (Fabray et al., 1986). However, the lack of correlation may be caused by several other factors, including: (1) sedimentary lensing, (2) deposition on an irregular topography, (3) channelling, (4) structural thickening and thinning, and (5) minor faulting associated with the major inferred early fault. Given the known complexities of the structure and the possible complexities in the sedimentology of the basin in which the Balcooma, Surveyor and Dry River South deposits formed, bedding continuity over more than a few hundred meters is not expected.

Thickening of the Dry River South Massive Sulfide Lens

The Dry River South prospect contains two south-southwest trending lobes of thickened massive sulfide (Fig. 26). As mineralization at Balcooma and Surveyor is localized along fold axes that plunge 20°/220°, Dry River South mineralization may have been remobilized in the same manner. Another explanation for the thickened lobes is the presence of a linear feeder zone or zones underneath the lobes that has caused the thickening.

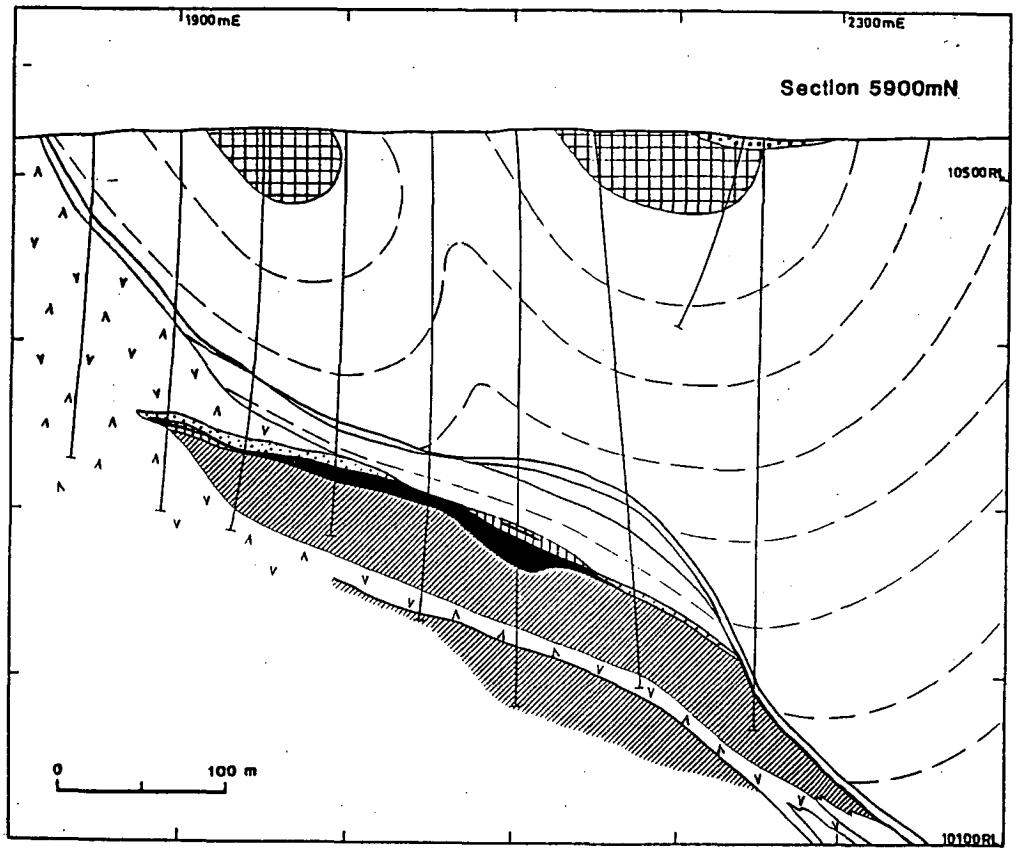

Figure 25. Preferred structural interpretation illustrated on section 5900 mN (legend in Fig. 16).

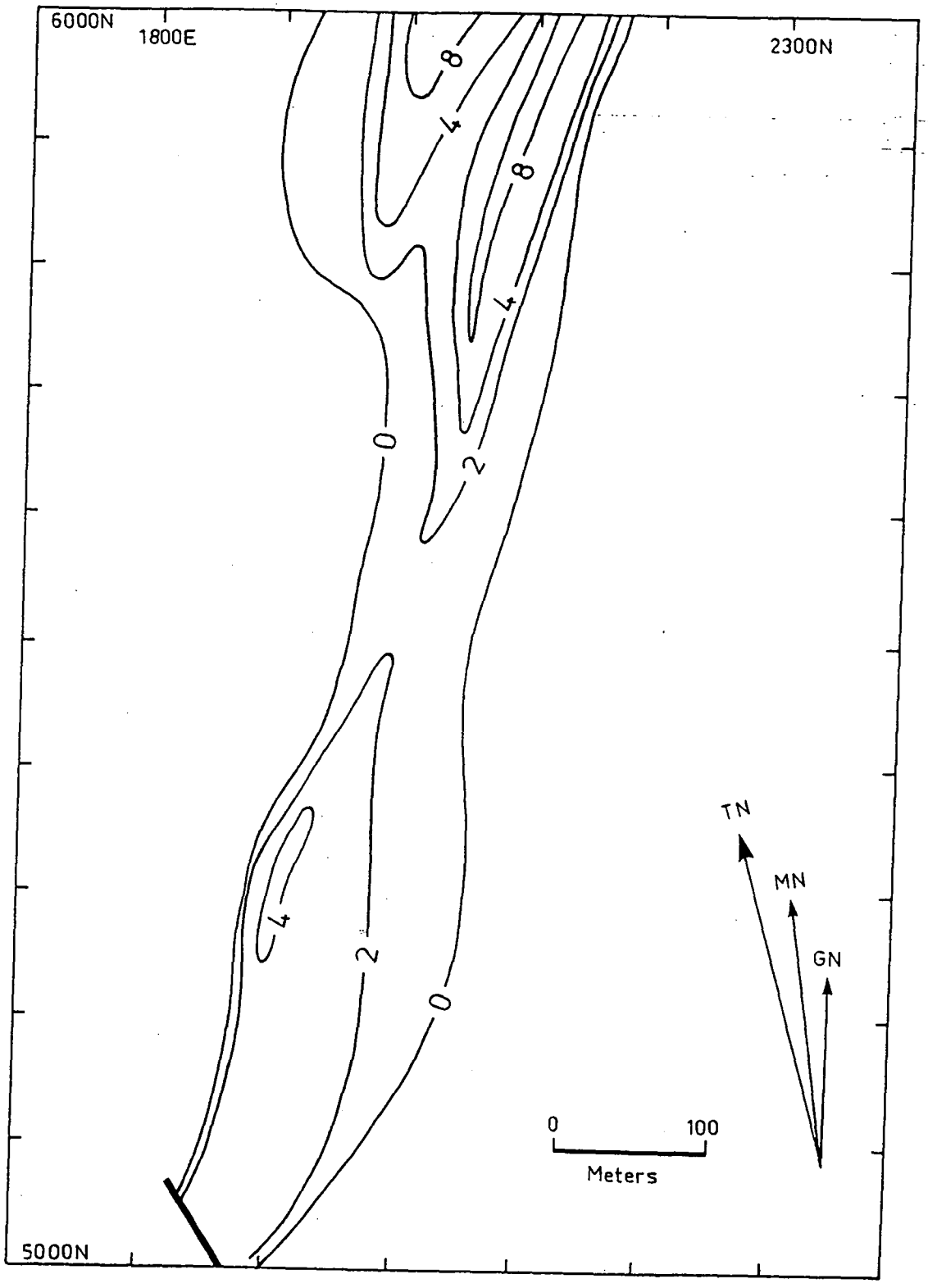

Figure 26. Plan showing the true thickness of the Dry River South massive sulfide lens (contours in meters).

In the northwestern part of the massive sulfide lens, the lobes plunge 10°/225°, but where the mineralized horizon steepens in the southeast, the plunge rotates to 24°/192°. Both plunge directions are close to, but slightly different from, the regional fold orientation. These data neither support nor preclude an interpretation of structural thickening.

The interpretation of structural thickening is partially supported by repetition of Pb-Zn to Cu zoning in several, but not all, of the drill holes along the thickened lobes (i.e. DRS-27, DRS-32 and DRS-44). Most holes that are located off the thickened zones do not show this repetition of metal zoning. Both recumbent, tight to isoclinal folding (Fig. 27a) and thrust faulting (Fig. 27b) may produce repetition in base metal zoning.

Evidence from Balcooma (Chapter 2) indicates that the D_2 deformation event is characterized by reclined to recumbent, tight folds, yet the D_3 folding event is characterized by open, upright folds. As T. Taylor (pers. com., 1987) has interpreted a recumbent, isoclinal fold in the massive sulfide along section 5900 mN (i.e. DRS-22), the most likely generation of folding that produced the thickening assuming this interpretation would be F_2.

Thrust faulting within the massive sulfide lens may also produce the repetition of metal zoning and the thickening of the massive sulfide. This interpretation is partly supported at a microscopic scale where strong foliation and even weak brecciation is noted, particularly in pyrite-rich samples (Chapter 7). These textures are more common at Dry River South than Balcooma.

Alternatively, the thickening may be primary and caused by a linear zone of coalesced stringers and focussed hydrothermal fluids (Fig. 27c). T. Taylor (in Hall et al., 1987) has noted that the eastern edge of the deposit is copper-rich relative to zinc. This zone has a trend that is parellel to, but slightly east of the eastern thickened zone, which indicates that a feeder zone may have been present in the area. Additionally, DRS-22, which is one of the thickest intersections shows a single Pb-Zn to Cu to pyrite zonation with a large amount of chloritic footwall schist.

The limited data available precludes a conclusive interpretation, but structural thickening is preferred as the plunge is subparallel to the regional pluge and either thrusting or local

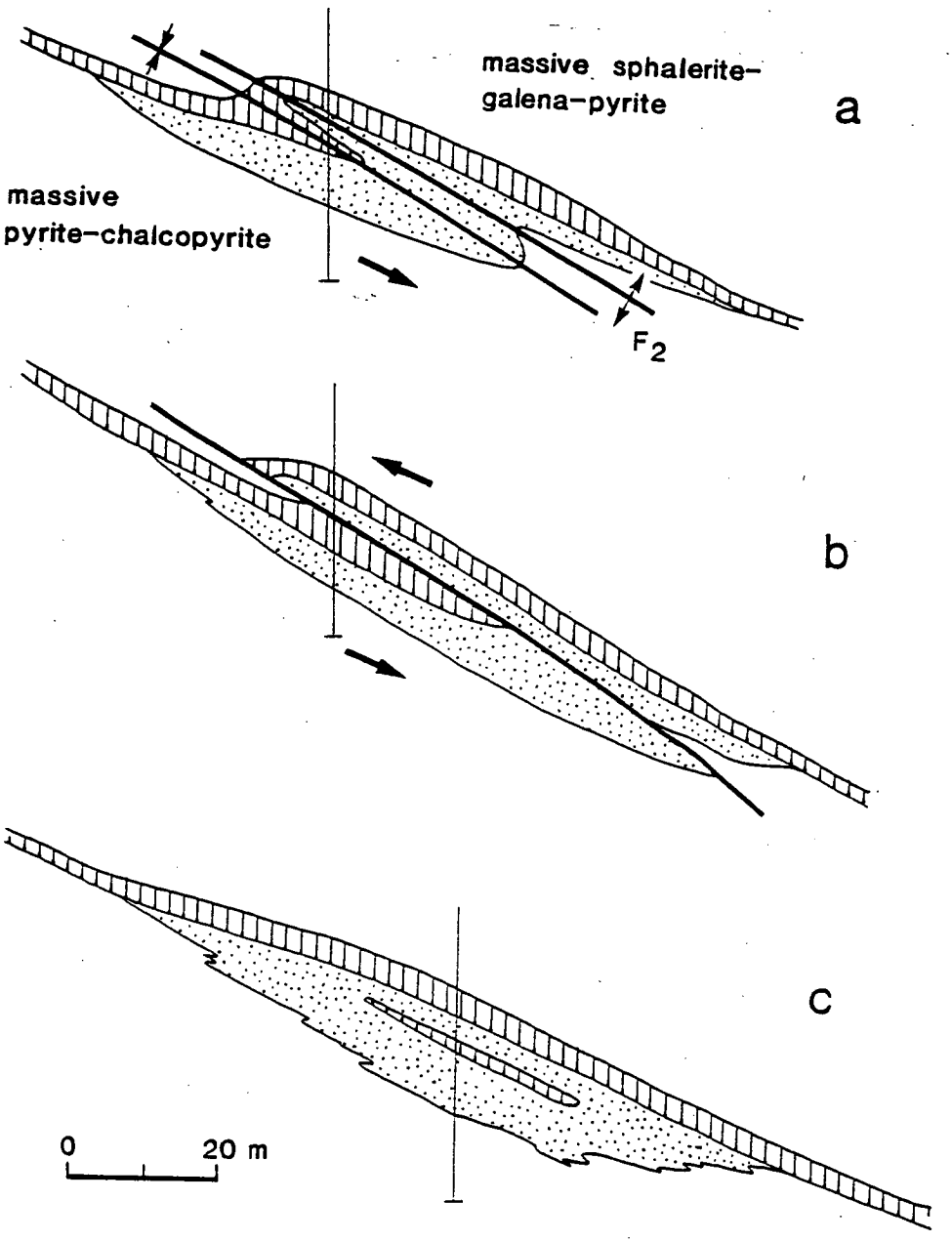

Figure 27. Alternative explanations for thickening of massive sulfide: (a) recumbent folding, (b) thrust faulting, and (c) primary linear hydrothermal discharge vents.

recumbent folding could explain the repetition of metal zoning in several holes along these thickened lobes very well. Thrusting is most consistent with preferred structural model presented above.

Exploration Implications

The presence of a major east dipping thrust fault either just above or some 30-100 m above the massive sulfide downgrades the exploration potential of the metagraywackes to the east of Dry River South as the prospective horizon would have been thrust above and to the west of the prospect and eroded.

Conclusions

Symmetric folding of the hanging wall metagraywackes combined with an early (syn-D_2(?)) fault above the upper quartz-feldspar porphyry best explains the morphology and apparent inconsistency of bedding attitudes between the surface and the mineralized horizon. Symmetric folding explains the synformal morphology of the quartz-muscovite-biotite schist; other options considered could not explain it. The best evidence for faulting between the massive sulfide and the surface occurs along the upper contact of the upper porphyry where a well developed syn-D_2(?) brecciated and sheared zone is present. The development of this early fault may have coincided with the symmetric folding of the hanging wall metagraywackes. The early fault may have been reactivated later to produce the strong late brecciation and shearing present 30 m to 100 m above the massive sulfide horizon. The lack of bedding continuity in the hanging wall metagraywackes can be explained by stratigraphic lensing, folding or faulting. No consistent evidence for faulting between the upper porphyry and the massive sulfide horizon exists.

Although lack of data prevents a definitive conclusion, the preferred explanation for the thickening of the Dry River South massive sulfide lens is either thrusting or recumbent, isoclinal F_2 folding. A less attractive alternative is primary thickening caused by a linear zone of focussed hydrothermal flow.

Chapter 4
The composition of the wall rocks and alteration zones at the Balcooma and Dry River South prospects

Introduction

The intense alteration and recrystallization associated with mineralization and subsequent metamorphism has removed or deformed most primary textures in the rocks surrounding the Balcooma and Dry River South prospects. As an aid in determining primary lithologies, 51 samples from Balcooma and 46 samples from Dry River South were analyzed by the author under the guidance of P. Robinson for major element oxides and selected trace elements using a combination of x-ray fluorescence spectrophotometry, atomic absorption spectrophotometry and titration (Norrish and Hutton, 1969; Norrish and Chappell, 1977; and Appendix 1). The samples were collected from unweathered core and varied in weight between 100 and 2000 grams. Nine commercial whole rock analyses (Analabs, Townsville for Carpentaria Exploration Company) from Dry River South have been added to the data base which is tabulated in Appendix 2. These analytical data are useful in: (1) determining the primary lithologies of altered and metamorphosed rock units, (2) characterizing the affect of alteration on element mobility during alteration, (3) provenance studies on metasediments, and (4) evaluating major and trace element abundances as an exploration guide.

Origin and provenance of visually unaltered rocks

Figures 28 and 29 illustrate the geochemical charcteristics of selected rock types from the Balcooma and Dry River South prospects, respectively. As metamorphism may have mobilized most major and trace elements, the ratio Zr/TiO_2, which should be constant under all but the most severe conditions of alteration and metamorphism (Floyd and Winchester, 1978), was selected as a reference axis for all scattergrams in Figures 28 and 29.

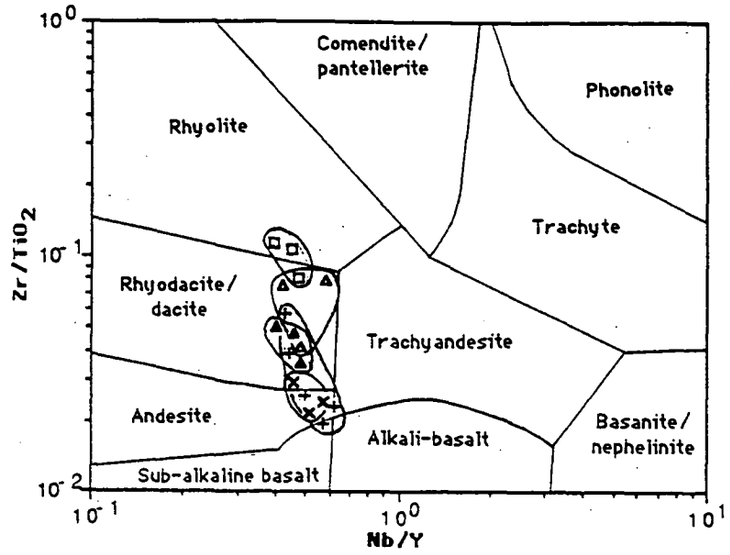

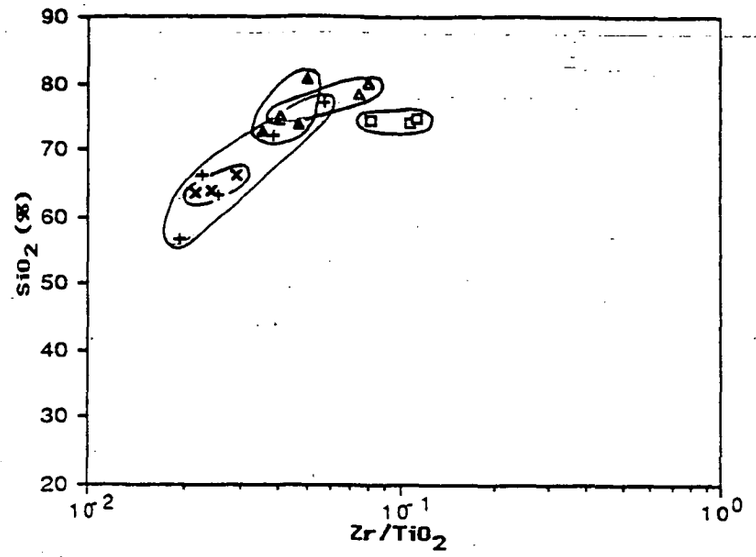

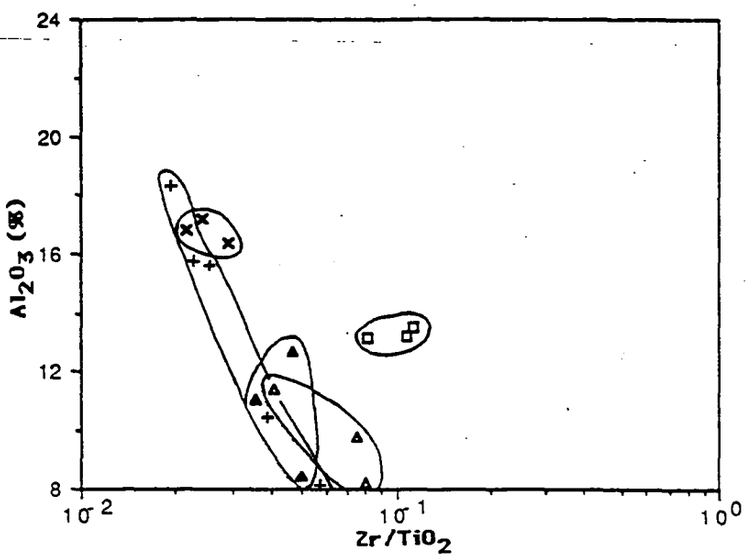

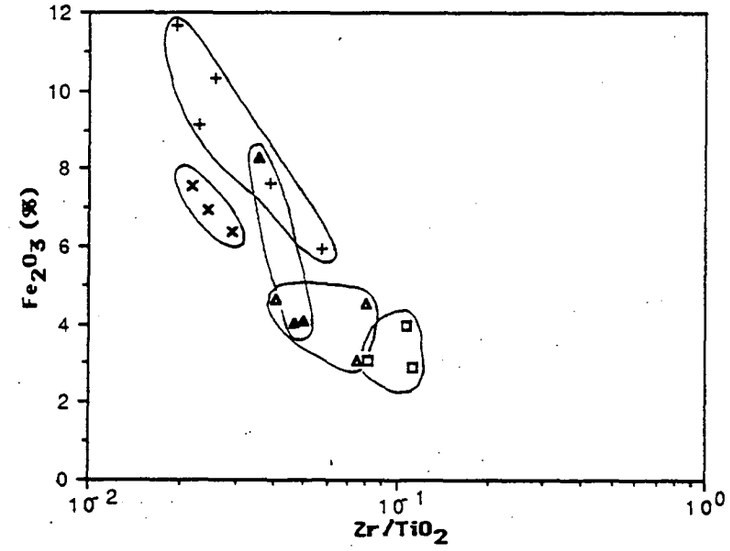

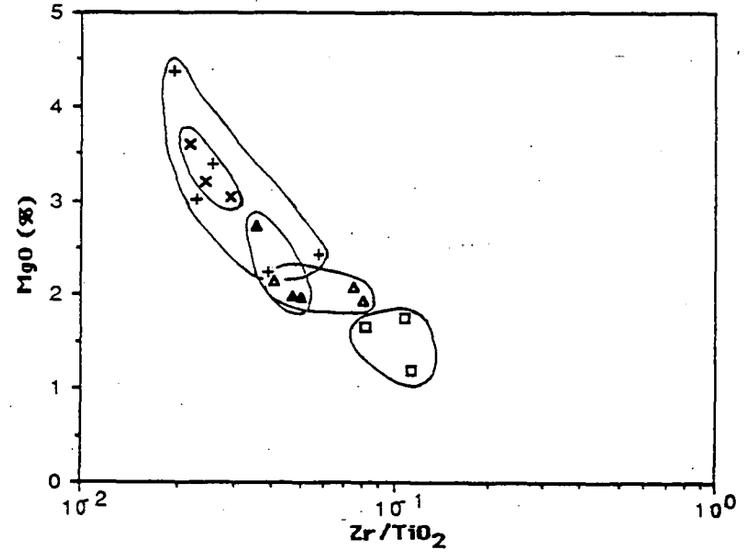

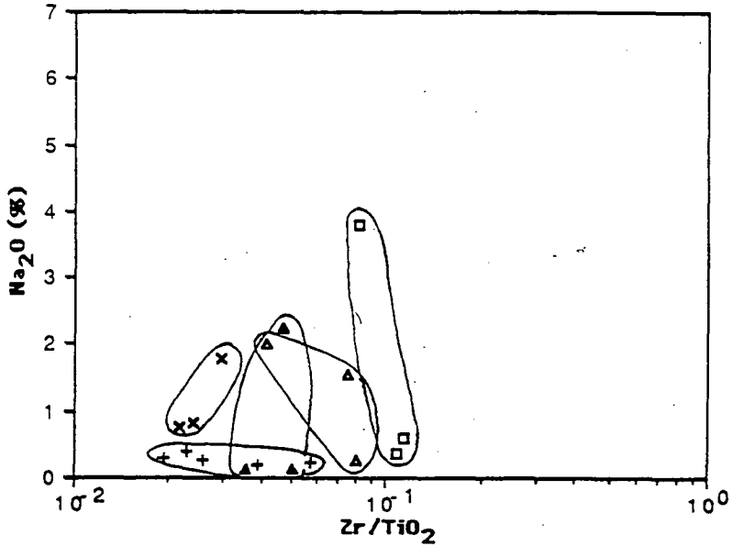

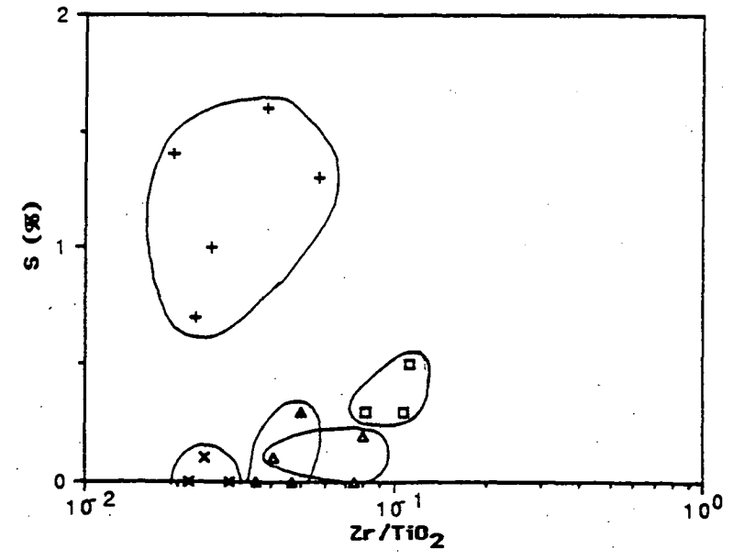

▲ Upper metagraywacke
+ Spotted schist
× Snowball schist
□ Felsic volcaniclastics
△ Lower metagraywacke

Figure 28. Selected scattergrams showing variations in trace and major elements from visibly unaltered rocks from the Balcooma prospect.

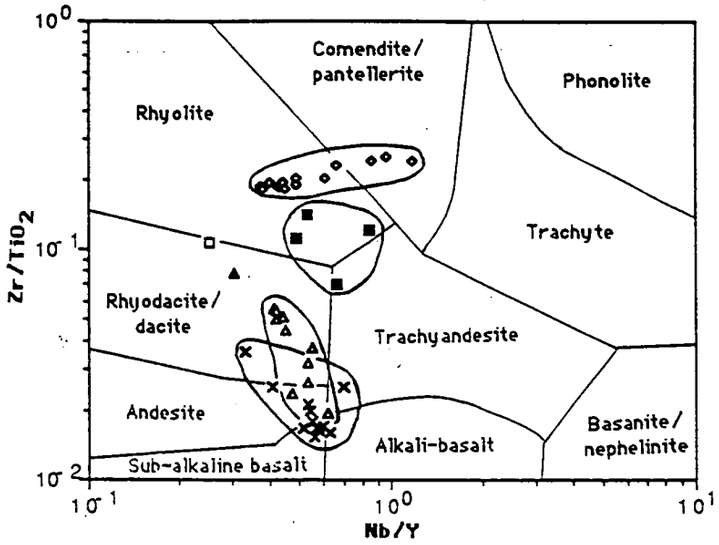

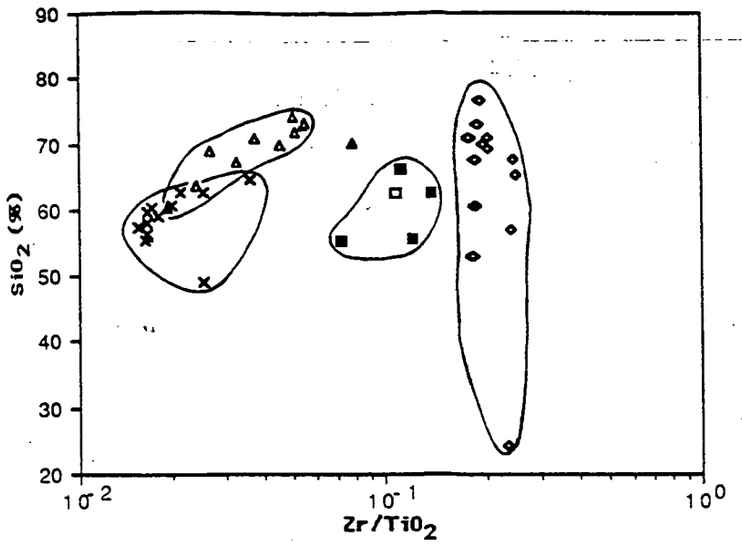

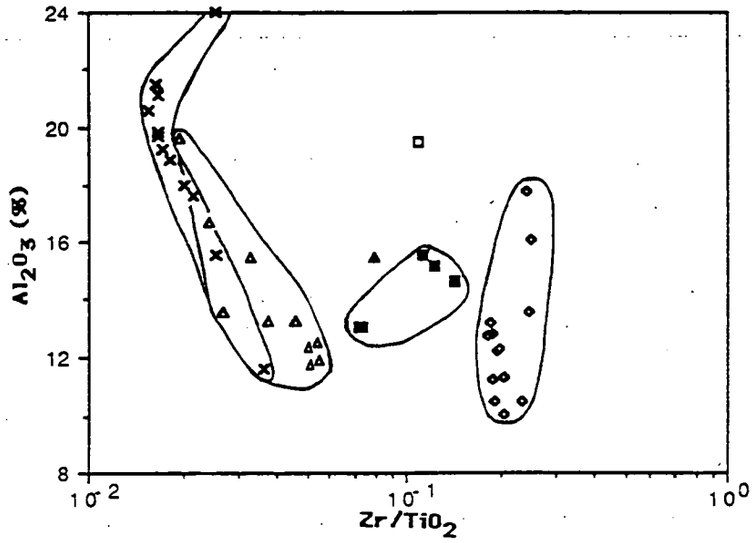

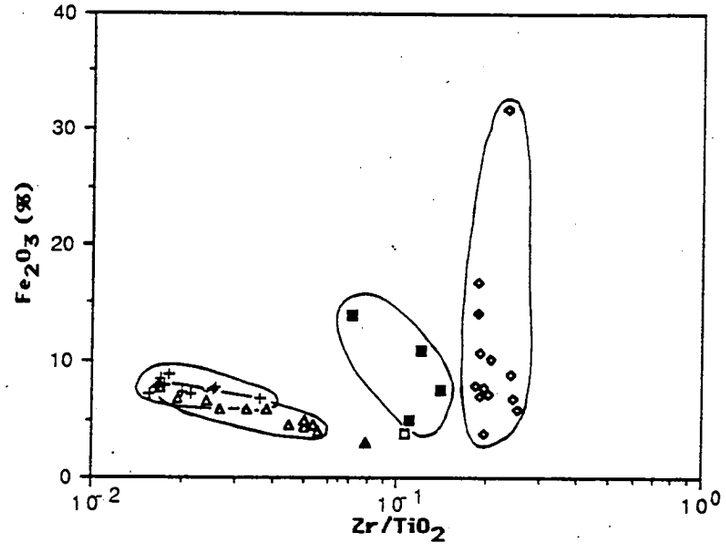

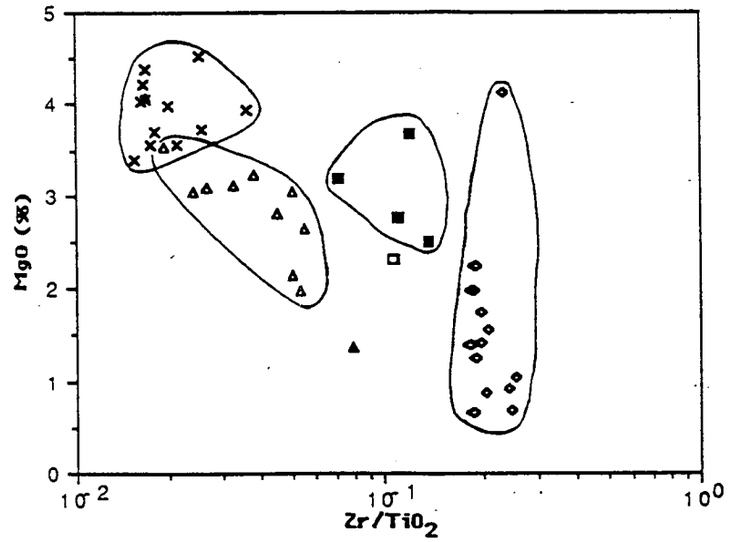

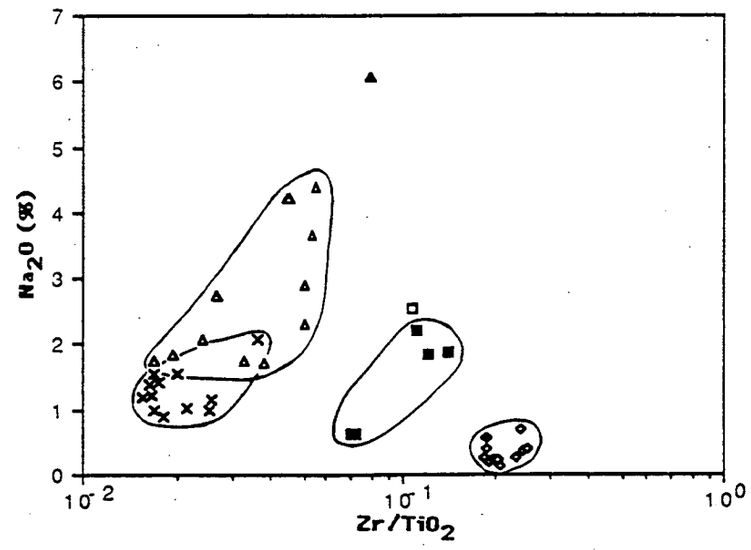

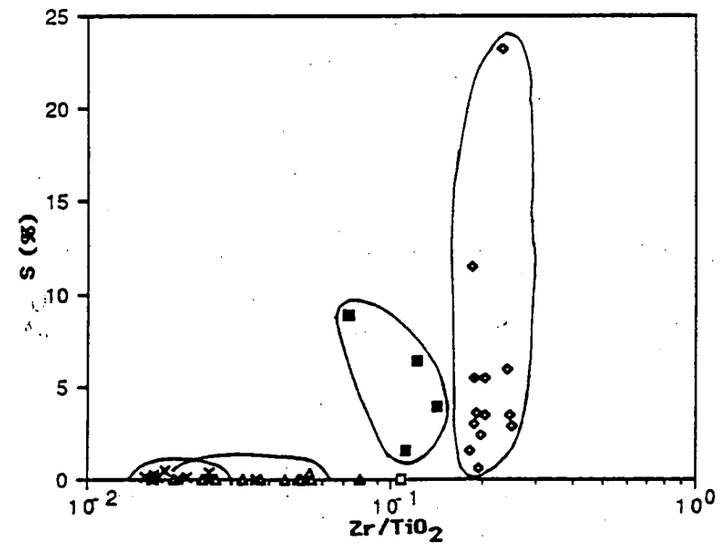

△ Metagraywacke
× Metapelite
▲ Intrusive (?) felsite
□ Felsic volcaniclastics
■ Altered felsic volcaniclastics
◆ Hanging wall pyritic quartz-muscovite-biotite schist
◇ Footwall pyritic quartz-muscovite-biotite schist

Figure 29. Selected scattergrams showing variations in trace and major elements from the Dry River South prospect.

Nb and Y

Winchester and Floyd (1977), and Floyd and Winchester (1978) have successfully used a plot of Nb/Y versus Zr/TiO_2 to distinguish primary fine grained igneous rock types of the calc-alkaline and alkaline suites from both strongly altered and strongly metamorphosed rocks. Figures 28a and 29a use similar plots to show the primary composition of selected rock types from Balcooma and Dry River South. As this diagram was initially developed for use in discriminating volcanic rock types, the most powerful use is in determining the original composition of the Balcooma volcaniclastic rocks, and the Dry River South volcaniclastic rocks, felsites and footwall pyritic quartz-muscovite-biotite schist. The diagram is also useful in empiracally discriminating metasedimentary rocks.

Analyses of metapelites and metagraywackes from both prospects plot along similar coherent trends of slightly decreasing Nb/Y with increasing Zr/TiO_2. Most metapelite analyses (excluding the spotted schist) plot at the bottom of the trend with Zr/TiO_2 ratios of less than 0.03, whereas the metagraywacke analyses plot towards the top of the trend with Zr/TiO_2 ratios between 0.02 and 0.08. The spotted schist is anomalous in that it plots along almost the entire length of the Balcooma metasediment trend.

Volcaniclastic rocks from both Balcooma and Dry River South plot above the metasediment trend along the boundary between rhyodacites and rhyolites under the classification of Winchester and Floyd (1977).

SiO_2 and Al_2O_3

Analyses of metasediments display coherent, but opposing, trends with SiO_2 and Al_2O_3. SiO_2 increases with Zr/TiO_2, but Al_2O_3 decreases with Zr/TiO_2. The metagraywackes tend to be SiO_2-rich and Al_2O_3-poor, and the metapelites have the opposite character. Volcaniclastic rocks plot off both trends and are richer in Al_2O_3 and poorer in SiO_2 than the corresponding metasediments.

Fe_2O_3 and MgO

Fe_2O_3 and MgO show similar trends and decrease with increasing Zr/TiO_2. In general the metagraywackes have lower Fe_2O_3 and MgO than metapelites. Although the fields of the spotted and snowball schists overlap in the MgO versus Zr/TiO_2 plot, analyses of the spotted schist plot on a trend to the right and above analyses of the snowball schist on the Fe_2O_3 versus Zr/TiO_2 plot. This indicates that the snowball schist has a similar Mg content to the spotted schist but the spotted schist is slightly enriched in Fe.

Na_2O

Of all the oxides plotted, Na_2O has the greatest variation and character. At Balcooma, neither the metagraywackes nor the metapelites show a consistent enrichment in Na_2O. The spotted schist is depleted in Na_2O relative to the snowball schist. The former consistently contains less than 0.5% Na_2O whereas the latter contains more than 0.7% in all cases.

Moreover, the metagraywackes may split into two groups based on their Na_2O content. Two of three samples from the upper metagraywacke and one sample from the lower metagraywacke contain less than 0.3% Na_2O. Other samples of metagraywacke contain more than 1.5% Na_2O. The generally low content of the upper metagraywacke is consistent with the lack of albite and enrichment of muscovite which characterize this unit in the field.

Conversely, the metasediments from the Dry River South prospect behave in a relatively coherent manner. Like SiO_2, Na_2O increases with an increasing Zr/TiO_2 ratio. Metapelites have characteristically low Na_2O contents (< 1.6% in all but on case), whereas metagraywackes have a higher Na_2O content (> 1.7%).

The coarse volcaniclastic rocks at Balcooma and Dry River South have high Na_2O contents (> 2.5%), whereas the fine grained volcaniclastic rocks from Balcooma have low Na_2O contents (< 0.6%).

Sulfur

The spotted schist shows a marked enrichment in sulfur relative to all other visually unaltered rock types at Balcooma and Dry River South. Samples of this rock contain between 0.6 and 1.7% sulfur whereas all other visually unaltered rock types contain less than 0.5% sulfur. The pyrite content of the spotted schist may be several percent which explains the enrichment of sulfur.

Of the other rock types, only volcaniclastic rocks have a consistent enrichment in sulfur, and this reflects the presence of minor disseminated pyrite. Two of the three Balcooma metagraywackes that are depleted in Na_2O also have elevated sulfur contents, but none the other Balcooma samples contain more than 0.1% sulfur.

At Dry River South, all visually unaltered samples except two contain not more than 0.1% sulfur. One sulfur rich sample came from a metapelite (DRS25-83.2) near the surface and is unexplained. The other sulfur-rich sample (DRS22-192.7), a metagraywacke, is strongly sheared and contains minor amounts of disseminated pyrite, pyrrhotite, chalcopyrite and sphalerite. Staurolites from this sample also have slightly anomalous Zn contents (Chapter 6).

Geologic discussion

These data indicate that the various rock types from the Balcooma and Dry River South prospects have quite distinct geochemical characteristics. Metasediments from both prospects plot along coherent, well defined trends when the ratio Zr/TiO_2 is plotted against Nb/Y, SiO_2, Al_2O_3, Fe_2O_3 and MgO. Metapelites are enriched in Al_2O_3, Fe_2O_3 and MgO but depleted in SiO_2 relative to metagraywackes. Dry River South metapelites are also depleted in Na_2O.

Bhatia (1985) noted that in immature sediments, fine grained shales and siltstones have similar compositions to interbedded metagraywackes, whereas in more mature sediments, graywackes are

enriched in SiO_2 and Na_2O, whereas pelitic rocks are enriched in Al_2O_3 and Fe_2O_3. As these relative enrichments are present in Balcooma and Dry River South metagraywacke sequences, the sediments must have undergone some degree of maturation and may have been transported for a significant distance.

As the geochemical characteristics of the metasediments differ markedly from those of the volcaniclastic rocks and felsic intrusions (see below) present around the two deposits, the metasediments probably were not derived from the felsic volcanic rocks around and to the west of the deposits. A more likely, but speculative source, may be dacitic volcanics and minor sediments that lie to the west of the aforementioned felsic pile. B. Stainforth (pers. com., 1987) has demonstrated that the contact between these two volcanic piles is faulted.

Of the metasediments analyzed, the spotted schist is anomalous in that it is consistently enriched in sulfur, slightly enriched in Fe_2O_3, and consistently depleted in Na_2O relative to the snowball schist at Balcooma and metapelites from Dry River South (Fig. 30). As these changes are commonly produced during hydrothermal alteration and large amounts of spotted schist occur only adjacent to the Balcooma prospect, the best interpretation of the spotted schist is that it is a metamorphosed zone of weak hydrothermal alteration. The intensity of alteration is slight as primary bedding and grading is metamorphically preserved as "inverse grading" in the spotted schist. Fine grained volcaniclastic rocks appear to be also weakly altered in a similar manner.

Moreover, three samples of metagraywacke from Balcooma (two of three from the upper metagraywacke and one of three from the lower metagraywacke) are also depleted in Na_2O, and two of these are enriched in sulfur (Fig. 30). The lack of feldspar and increased muscovite content of the upper metagraywacke are consistent with these chemical results. An interpretation of these data is that much of the upper metagraywacke and some of the lower metagraywacke have undergone weak alteration during mineralization. This interpretation also explains the limited distribution of the upper metagraywacke to stratigraphically above the Balcooma prospect.

Recognition of these two anomalous rock types during field mapping in the area may have application to exploration in the

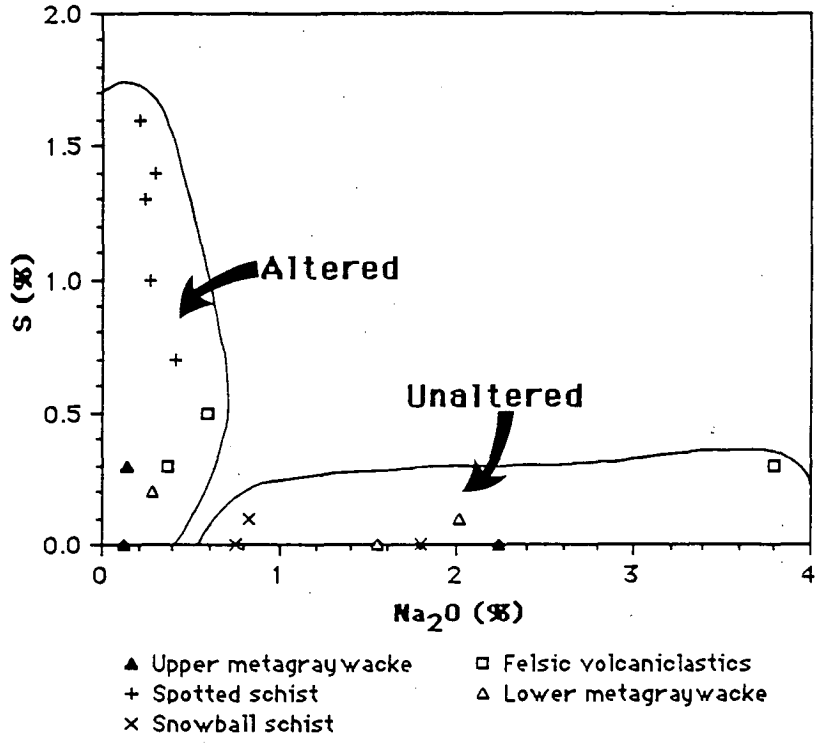

Figure 30. Na_2O versus sulfur plot of selected rock types from Balcooma indicating weakly hydrothermally altered samples.

Balcooma metamorphics. As the spotted schist seems to indicate proximity to mineralization, additional attention should be paid to areas in which spotted schist occurs. Areas containing feldspar-poor or muscovite-rich metagraywacke merit additional attention as they may overly mineralization.

Provenance of the metasediments

Bhatia (1983) used selected volatile free major oxides and major oxide ratios (TiO_2, Al_2O_3/SiO_2, Fe_2O_3 + MgO, K_2O/Na_2O and $Al_2O_3/(CaO + Na_2O)$) to classify the provenances of sandstones into one of four tectonic environments: (1) oceanic island arcs (e.g. Marianas and Aleutians), (2) continental island arcs (e.g. Sea of Japan and Lau Basin), (3) active continental margins (e.g. Andes), and (4) passive continental margins (e.g. Atlantic margins). Due to the intensity of metamorphism on rocks from the Balcooma metavolcanics, the volatile free compositions of metagraywackes were only plotted on diagrams relating TiO_2 and Al_2O_3/SiO_2 to Fe_2O_3 + MgO (Fig. 31). These oxides and ratios were selected due to their relative immobility during metamorphism and/or their coherence on previous diagrams (Figs. 28 and 29). Ratios involving K_2O, Na_2O and CaO were not used due to their mobility during metamorphism.

Data from Balcooma and Dry River South best fits a continental island arc provenance. This is best illustrated on the TiO_2 versus Fe_2O_3 + MgO plot where more than half of the data and the average composition plots within the continental island arc field. The data that plot outside the continental island arc field in and around the oceanic arc field have a composition closer to that of a metapelite.

The data does not plot within the characteristic fields on the Al_2O_3/SiO_2 versus Fe_2O_3 + MgO diagram, but plots below the continental arc and active continental margin fields. These data indicate that these rocks have more SiO_2 and/or less Al_2O_3 than "typical" rocks from these sources. As the Al_2O_3/SiO_2 ratio indicates the quartz enrichment in the rocks (Bhatia, 1983), the lower Al_2O_3/SiO_2 ratio for metagraywackes from the Balcooma and Dry River South prospects may reflect a greater maturity than the suites

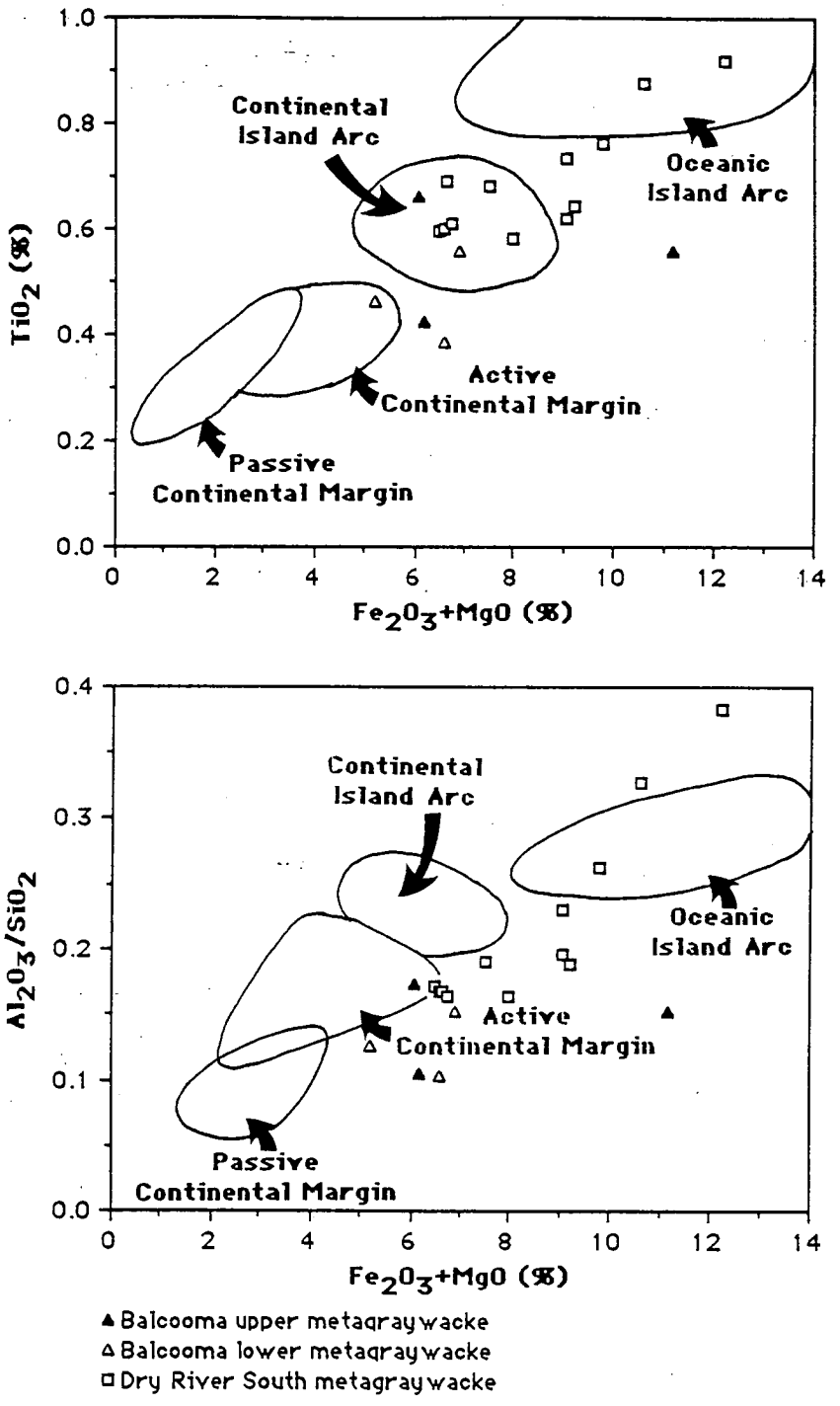

Figure 31. Diagrams illustrating the probable provenance of metagraywackes from the Balcooma Metamorphics. Fields from Bhatia (1983).

used by Bhatia (1983) to define the fields. This conclusion is supported by differences in the composition of the metagraywackes relative to the metapelites (see above).

The interpretation that the metasediments within the Balcooma metamorphics were derived from a continental island arc is consistent with the tectonic setting of the Mt. Windsor Volcanics to which the Balcooma metamorphics have been correlated (Henderson, 1986).

Composition of intrusive rocks

Four types of intrusive rocks have been recognized around the Balcooma and Dry River South prospects although the intrusive felsite at Dry River South may be a variant of the microgranite located to the east of both prospects. These rocks fall along a coherent differentiation trend of decreasing Zr/TiO_2 with slightly increasing Nb/Y (Fig. 32). The trend crosses the boundary between the rhyolite and the rhyodacite/dacite fields of Winchester and Floyd (1977); the microgranite and quartz-feldspar porphyry plot largely within the rhyodacite/dacite field whereas the two felsites plot in the rhyolite field. Due to a lack of data, these distinctions are not clear, and the felsic intrusions should be considered as a group with compositons varying between rhyolites and rhyodacites.

One sample of quartz-feldspar porphyry located just below the eastern part of the Dry River South massive sulfide lens has been extremely altered with the introduction of muscovite and pyrite (see above and below). While this sample has a similar Zr/TiO_2 ratio to the unaltered quartz-feldspar porphyry, its Nb/Y ratio has been significantly decreased, which indicates that Nb and/or Y has been mobile during alteration. Moveover, the fact that this sample has been altered and is located just below the massive sulfide lens indicates that either: (1) the eastern quartz-feldspar porphyry was intruded during mineralization and alteration, or (2) the eastern quartz-feldspar porphyry is a submarine flow or crystal tuff that was deposited just before mineralization.

The immobile element composition of the volcaniclastic rocks from both prospects is very similar to that of the intrusions. These data and stratigraphic data are consistent with the interpretation that the volcaniclastic rocks and intrusions from around the

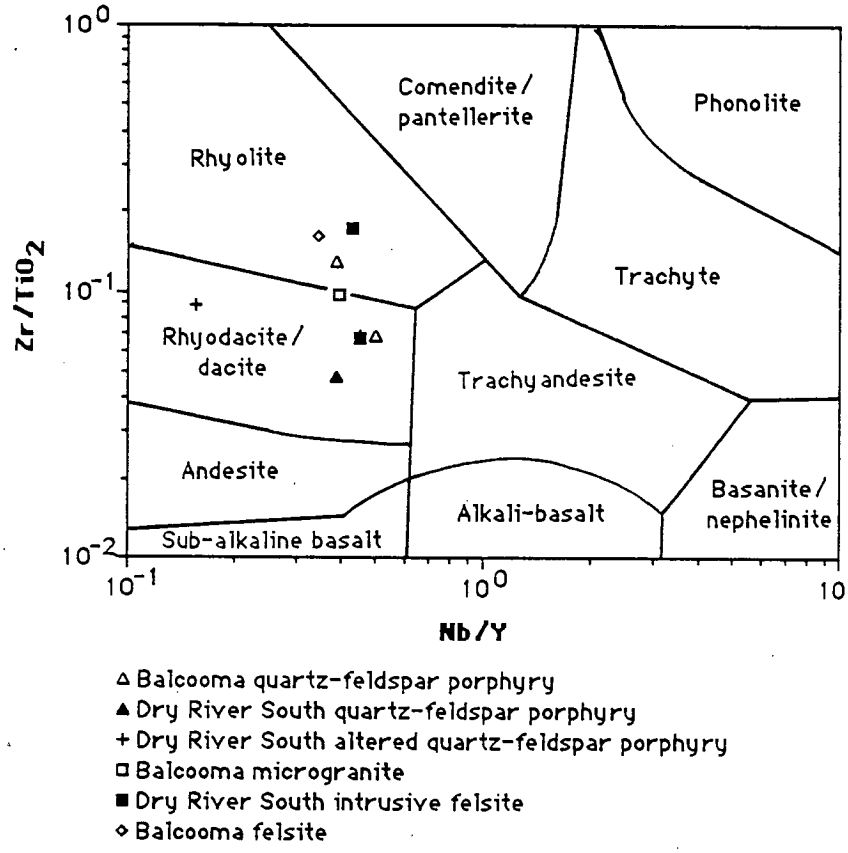

Figure 32. Nb/Y versus Zr/TiO_2 diagram showing the composition of intrusive rocks from Balcooma and Dry River South. Fields from Winchester and Floyd (1978).

prospects are part of or related to the felsic volcanic pile located to the west of the prospects.

Alteration geochemistry

The composition of alteration zones, like that of the mineralization, differs markedly between the two prospects. At Balcooma the alteration is dominated by the presence of chloritic schist that forms a pipe that extends below the copper horizon. Conversely, at Dry River South, the alteration zone is composed largely of pyritic quartz-muscovite-biotite schist that forms a wide zone stratigrahically below the massive sulfide lens that extends beyond the lateral limits of the mineralization.

Treatment of data

Gresens (1967) initially considered composition-volume relations in metasomatic alteration to determine equations useful in determining gains and losses from chemical analyses and specific gravity data. Grant (1986) and Osterberg et al. (1987) have used Gresens' (1967) equations and modified them to provide a graphical method of determining gains and losses during alteration: the isocon diagram.

Grant (1986) plots scaled chemical analyses from altered against unaltered rocks as an indication of changes in composition. Immobile elements plot along a straight line that has a slope which depends on addition (or subtraction) of net mass without gain or loss of the immobile elements used (the isocon).

The following analysis uses a slight modification of the isocon technique of Grant (1986) to increase the ease of interpretation. In this modification, the scaling parameter for a particular element is set equal to an integer divided by the chemical analysis for that element from the "unaltered equivalent" reference (i.e. scaling parameter = $n_i/[\text{unaltered rock}]_i$). The elements of interest were ordered in a manner such that immobile elements are evenly dispersed, and each element was assigned a particular integer (n_i) in ascending order (e.g. Cu was assigned 1, Pb was assigned 2, Zn was assigned 3, etc.). This integer was used in determining the scaling parameter as described above, and the resulting scaled values were plotted against

the corresponding integer (which is the scaled concentration of the "unaltered equivalent"). For ease of interpretation, the integers on the x-axis were replaced by the corresponding element symbol on the resulting isocon diagram. Use of this technique has several distinct advantages over the arbitrary scaling factors used by Grant (1986): (1) the scaled values are dimensionless, (2) the resulting diagrams may be more easily interpreted as the elements are ordered and identified in a systematic manner, (3) immobile elements may be evenly dispersed along the x-axis in order to generate a more easily estimated isocon, (4) the diagram is less cluttered as individual points do not have to be labelled, and (5) the calculation of estimates for gains and losses is simplified.

Once an isocon is determined by inspection of the distibution of immobile elements (most or all of the elements Al, Ti, P, Zr, Nb and Y should lie on the same line) or by making certain assumptions (i.e. constant mass, constant volume or constant aluminum), it can be used to estimate (1) the net gain or loss of mass from a large influx or removal of a major oxide (e.g. silica flooding), and (2) gains and losses for the elements of interest. The first parameter may be estimated using the slope of the isocon. If there has been no net gain or loss of mass during alteration, the slope of the isocon (m) will be one. If there has been a net change in mass, this can be estimated from the equation:

$$\Delta M^A\ (\%) = (M^O/m) - 100 \qquad (1)$$

where ΔM^A is the net change in mass during alteration, and M^O is the mass of the protolith (taken as 100 g as the units are percent).

Relative gains and losses for particular elements may also be estimated from the isocon. Elements that gained mass during alteration will plot above the isocon whereas elements that have lost mass will be plot below the line. Equation (2) may be used to calculate relative gains and or losses for each element.

$$\Delta C_i^A\ (\%) = 100\{[C_i^A/(mC_i^O)] - 1\} \qquad (2)$$

where ΔC_i^A is the gain or loss of element (i) in percent during alteration, C_i^A is the scaled concentration of element (i) in the altered sample, and C_i^O is the scaled concentration of element (i) in the "unaltered equivalent." Because of the choice of scaling factors, C_i^O equals n_i, therefore equation (2) reduces to equation (3).

$$\Delta C_i^A \ (\%) = 100\{[C_i^A/(mn_i)] - 1\} \qquad (3)$$

Absolute gains or losses may be calculated according to the equation:

$$\Delta C_i^A \ (g/100g) = [\Delta C_i^A \ (\%)/100][C_i^O \ (g/100g)/n_i] \qquad (4)$$

The calculated gains and/or losses are then plotted as histograms for ease of illustration. The above description of the isocon techniques adopted during this study is a modification of the techniques originally proposed by Grant (1986), and the reader is referred to that paper for additional explanation.

The interpretation of the isocon diagram has several limitations: (1) changes in concentrations are callibrated against an "unaltered equivalent" which may or may not be the protolith to the altered rock, and (2) the "unaltered equivalent" rock type will have internal variations in chemical composition independant of alteration. The former limitation may be minimized by careful selection of the "unaltered equivalent" using detailed field mapping, petrographic studies and the character of immobile elements. The latter limitation is more difficult to overcome. If enough samples of the "unaltered equivalent" are available, the mean value and standard deviation can be estimated and used to characterize this limitation. The mean values should be taken as the reference "unaltered equivalent" and the standard deviation may be used to estimate internal variations within the "unaltered equivalent." Due to this internal variation, small apparent gains or losses calculated from the isocon should not be interpreted as the result of alteration.

Balcooma

As the host rocks to mineralization at Balcooma are largely metapelites, the snowball schist was taken as the "unaltered equivalent" to the altered rocks. To minimize the effect of internal variations in the composition of the protoliths to alteration, altered samples with a similar Zr/TiO_2 ratio to the snowball schist were used in this analysis. This was possible in all cases except weak chloritic alteration where the Zr/TiO_2 ratio was higher than the snowball schist. Three analyses of the snowball schist were averaged to give the composition of the "unaltered equivalent."

Figures 33 through 37 illustrate isocon and relative gain/loss diagrams for three samples each of the spotted schist, weak chloritic alteration, moderate chloritic alteration, strong chloritic alteration and pyritic quartz-muscovite-biotite schist relative to the "unaltered equivalent." Part A of each figure (excluding Fig. 35) indicates elements that have been enriched "off-scale" on the isocon diagram in part B. In part B the dashed line indicates the visually best fit isocon, and the shaded area surrounding it is an estimate of the associated error. Part C (part B in Fig. 35) illustrates the relative gains and losses for each element. The dotted lines indicate the uncertainty limits from part B; elements falling between these lines have not undergone a significant gain or loss. The values in part C were calculated using average scaled values of the three altered samples and equation (3). For elements where one analysis differed significantly from the other two analyses, the two samples with similar analyses were averages.

Spotted schist. Results from isocon analysis (Fig. 33) confirm the previous observations that this unit is enriched in iron and sulfur, and depleted in sodium. Additionally, the unit also has a strong enrichment in copper, a weak enrichment in zinc, and a depletion in strontium and calcium. A depletion of lead may also be present. As the slope of the isocon approximates one, there has not been large scale additions or subtractions of mass. Alteration appears to be restricted to addition of pyrite and/or magnetite and destruction of plagioclase.

Weak chloritic alteration. The isocon diagram (Fig. 34) indicates that weak chloritic alteration has undergone addition of iron, manganese, magnesium and silica relative to the snowball

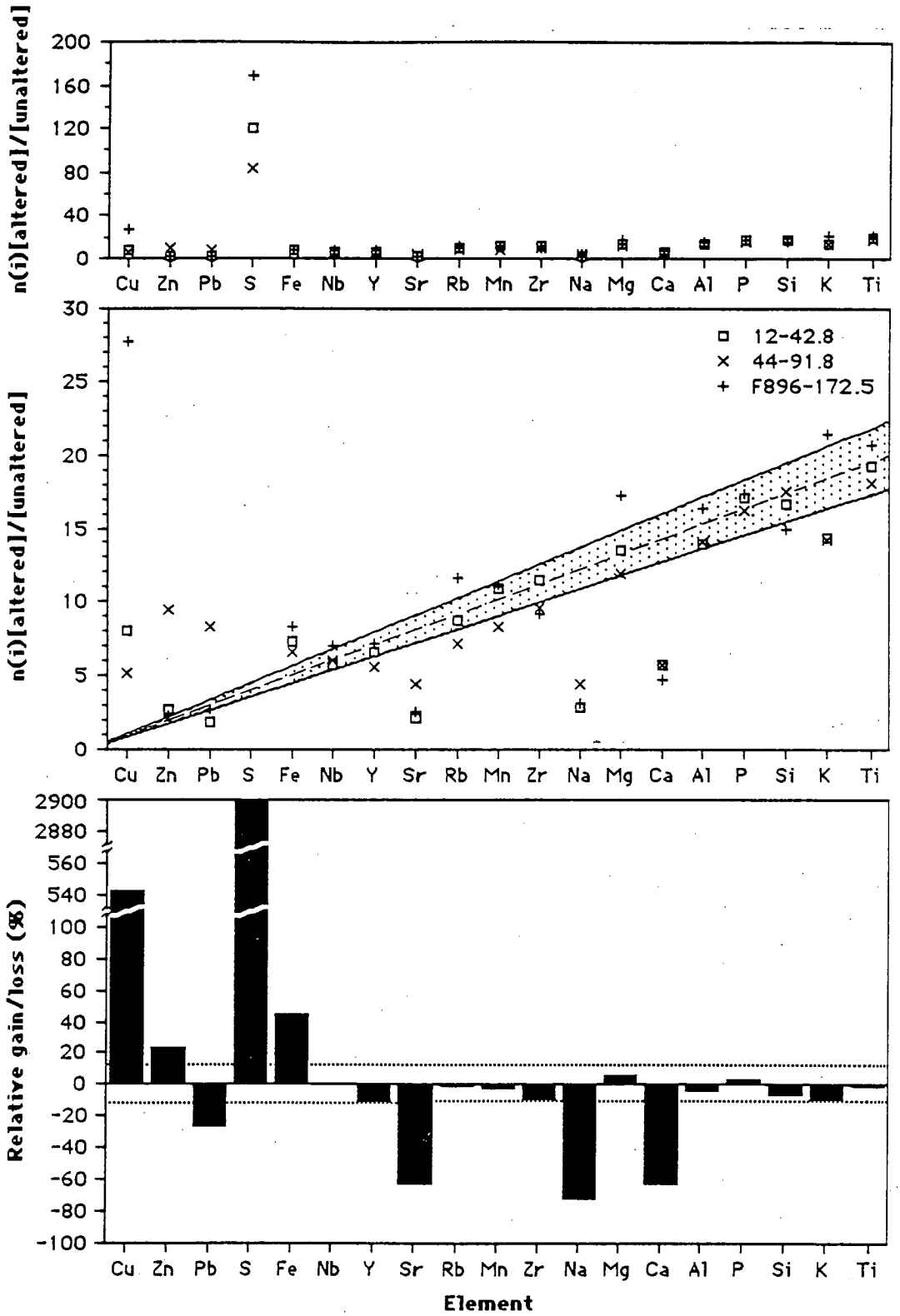

Figure 33. Isocon diagrams illustrating gains and losses for spotted schist at Balcooma. Explanation in text.

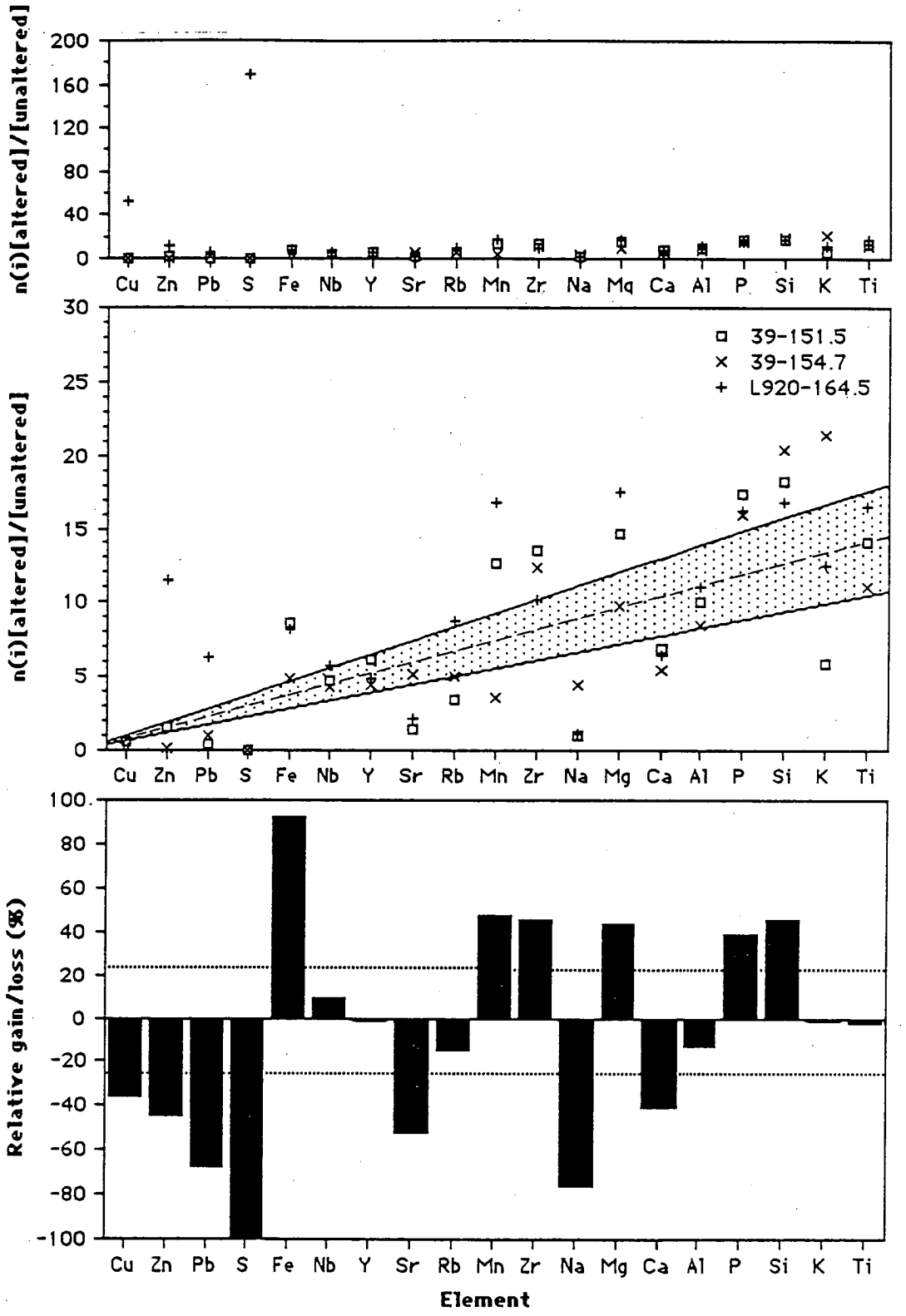

Figure 34. Isocon diagrams illustrating gains and losses for weak chloritic alteration at Balcooma. Explanation in text.

schist, and marked depletion in lead, strontium, sodium and calcium. Although there have been apparent depletions in copper, zinc and sulfur, the values are quite variable in the seven samples analyzed (Appendix 2), which indicates that some regions have undergone addition and others have undergone depletion of these elements during the processes that formed the weak chloritic alteration zone. The apparent enrichment of zirconium is probably due to the previously described variation in the Zr/TiO_2 ratio and is an artefact of the analysis. The decrease in the slope of the isocon reflects the major addition of silica during weak chloritic alteration.

Moderate chloritic alteration. The zone of moderate chloritic alteration probably best represents the extent of the original chloritic alteration zone, and, as such, best reflects the original composition of this alteration. Figure 35 indicates addition of copper, zinc, sulfur, iron, manganese, magnesium and silica, but depletion of lead, strontium, rubidium, sodium, calcium and potassium. The addition of copper, zinc, sulfur and iron may be related to the deposition of sulfide minerals. The addition of iron and magnesium is consistent with the presence of chlorite, while the loss of potassium and rubidium reflects the destruction of muscovite and, to a lesser extent, biotite. Destruction of plagioclase explains the losses in sodium, calcium and strontium. The major addition of silica and the decrease in the slope of the isocon indicate that this alteration involved major silica flooding. The addition of manganese is unexplained.

Strong chloritic alteration. The development of strong chloritic alteration (Fig. 36) involves major losses of silica coupled with major additions of iron and magnesium which probably accompanied chlorite addition and quartz removal. Sodium, calcium, strontium, rubidium and potassium have been lost through destruction of plagioclase and mica. The addition of copper, iron and sulfur reflects the addition of sulfide minerals, but again lead has been lost. The additional manganese may occur in garnet.

Strong chloritic alteration occurs as veins and pods of chlorite schist which cut both massive sulfide and other types of chloritic alteration. Its origin is unclear and may be due to either late stage hydrothermal activity or metamorphic reactions.

Pyritic quartz-muscovite-biotite schist. Pyritic quartz-muscovite-biotite schist has undergone slight addition of silica, and

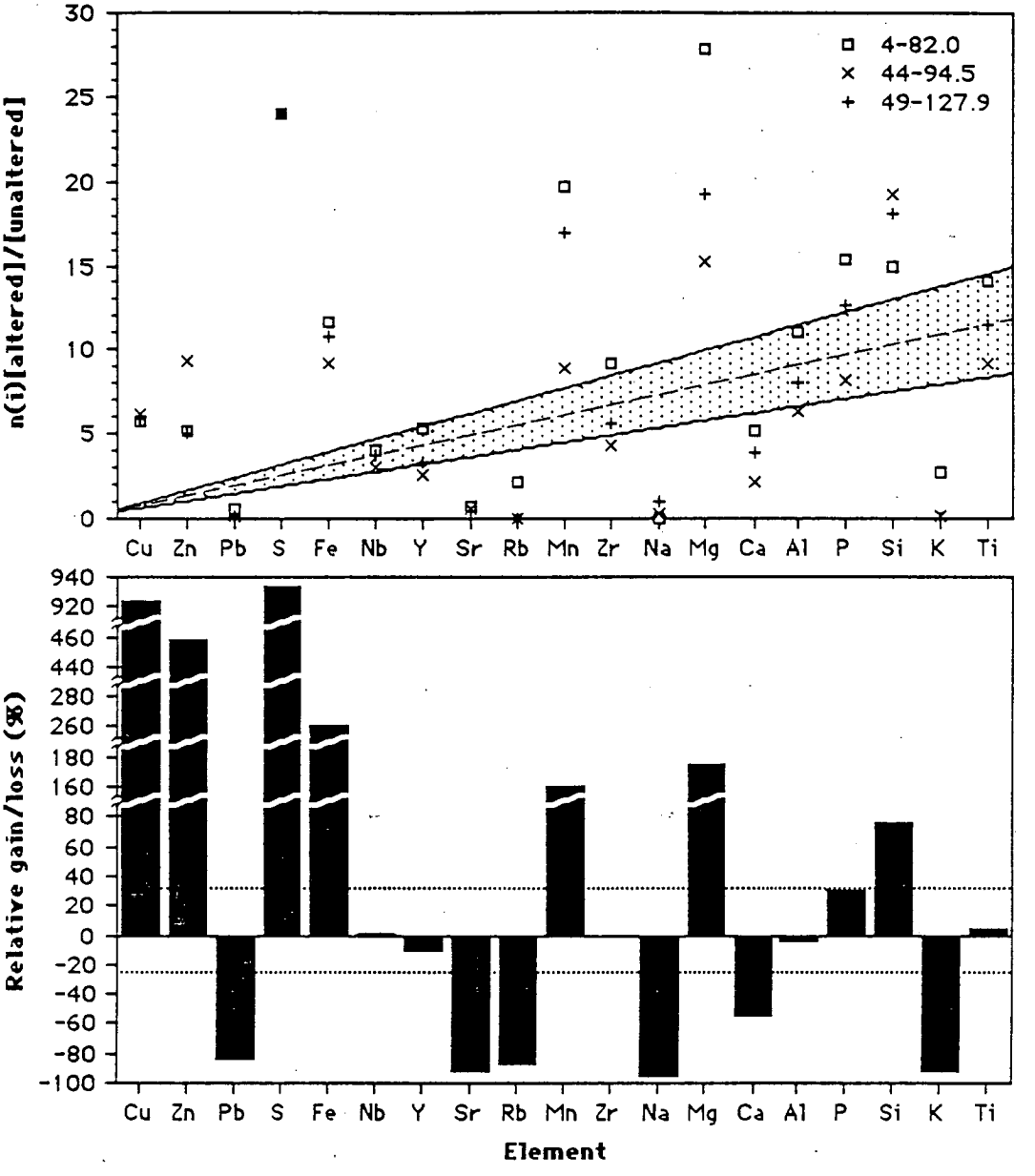

Figure 35. Isocon diagrams illustrating gains and losses for moderate chloritic alteration at Balcooma. Explanation in text.

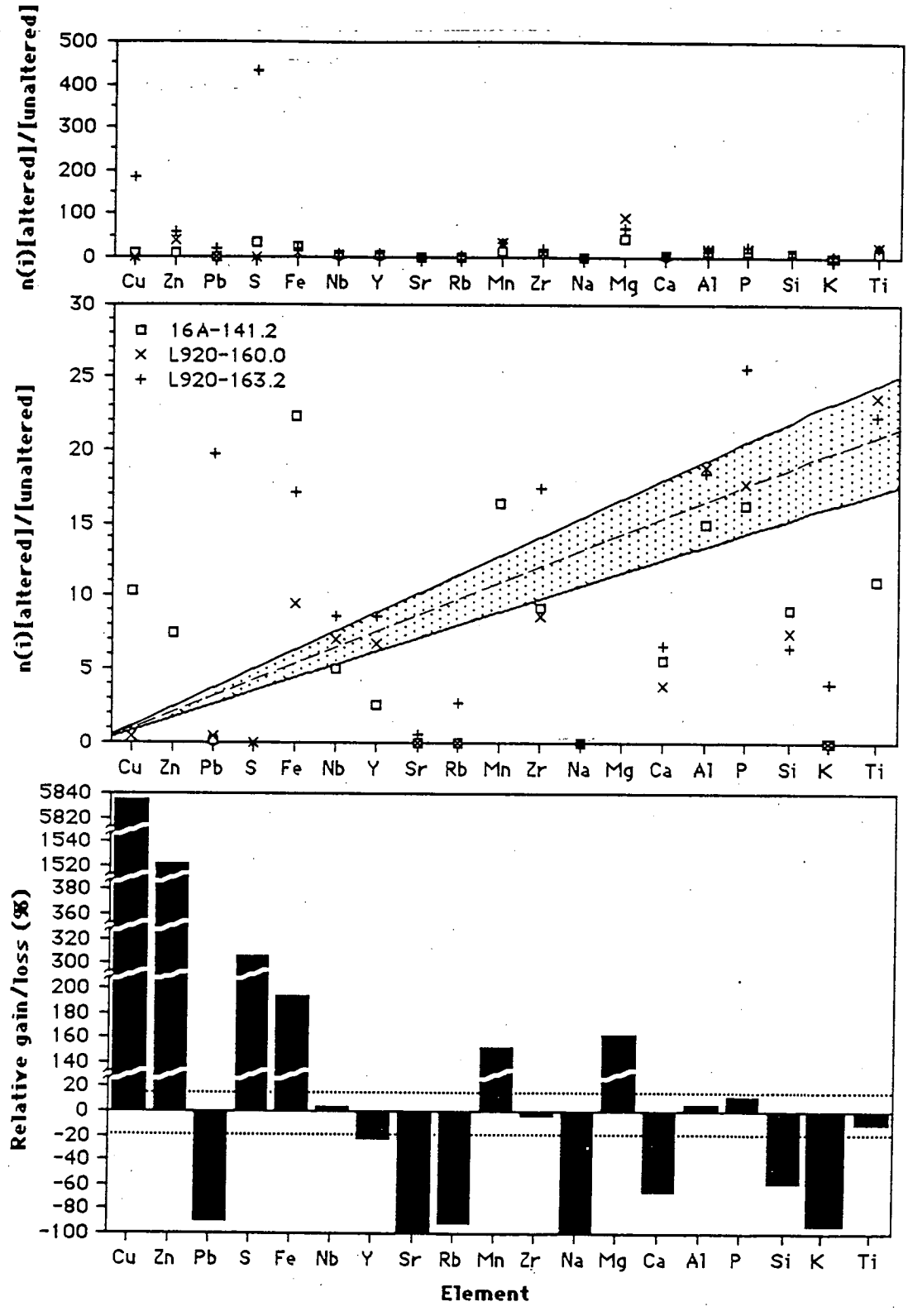

Figure 36. Isocon diagrams illustrating gains and losses for strong chloritic alteration at Balcooma. Explanation in text.

major relative gains in copper, lead and sulfur (Fig. 37). Other samples (Appendix 2) have also undergone significant enrichment in zinc. In contrast to chloritic alteration, this unit has not been enriched in either iron or magnesium. Elements that show losses include strontium and sodium. In some samples rubidium, manganese, magnesium and calcium have undergone losses. This rock type, which is considered to be metamorphosed quartz-sericite-pyrite alteration, differs from the dominant chloritic alteration at Balcooma, but is similar to the alteration style at Dry River South.

Development of alteration at Balcooma. Based on the above discussion, at least three general types of alteration developed during the formation of the Balcooma prospect: (1) quartz-chlorite-sulfide alteration accompanying copper-rich mineralization, (2) quartz-sericite-pyrite alteration accompanying zinc-lead-rich alteration, and (3) pervasive weak pyrite addition and feldspar destruction in a halo around the more intense alteration zones.

Figure 38 illustrates the absolute gains and losses (in g/100 g) of major oxides and sulfur from alteration zones. Of the oxides considered, only Fe_2O_3, MgO and SiO_2 have undergone gains or losses of greater than 5 g/100 g. While Na_2O, K_2O and CaO may have had major losses in relative terms, the absolute losses are minor. Only major gains or losses of Fe_2O_3, MgO or SiO_2 affect the net gain/loss of mass in the rocks during alteration.

Alteration began with the near total destruction of feldspar and the addition of minor pyrite and/or chalcopyrite to form a weak, but extensive, halo in the host pelitic rocks (the precursor of the spotted schist). During this period, iron may also have been added as a silicate mineral as more iron than sulfur has been added.

As the intensity of alteration increased, the precursor to the pyritic quartz-muscovite-biotite schist developed. During this alteration, additional pyrite was added along with sphalerite and galena, but MgO was apparently removed, possibly by the destruction of ferromagnesian minerals. The most important aspect of this alteration was the introduction of considerable SiO_2 (~20 g/100 g) through silicification.

As alteration intensity increased to produce the precursor to the quartz-chlorite schist, significant additional copper, Fe_2O_3, MgO and SiO_2 (~50g/100g) were added, whereas K_2O was removed. At the

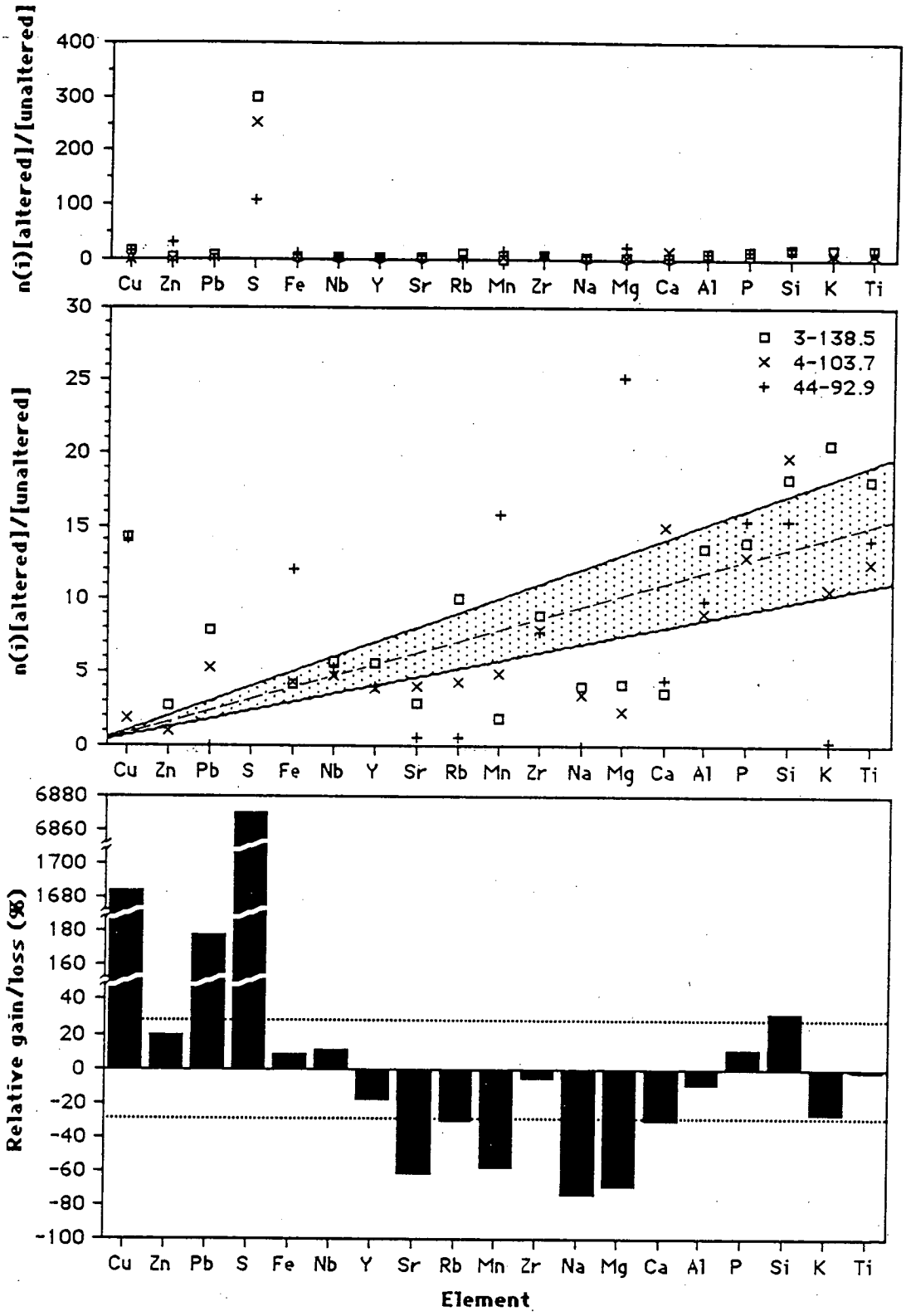

Figure 37. Isocon diagrams illustrating gains and losses for pyritic quartz-muscovite-biotite schist at Balcooma. Explanation in text.

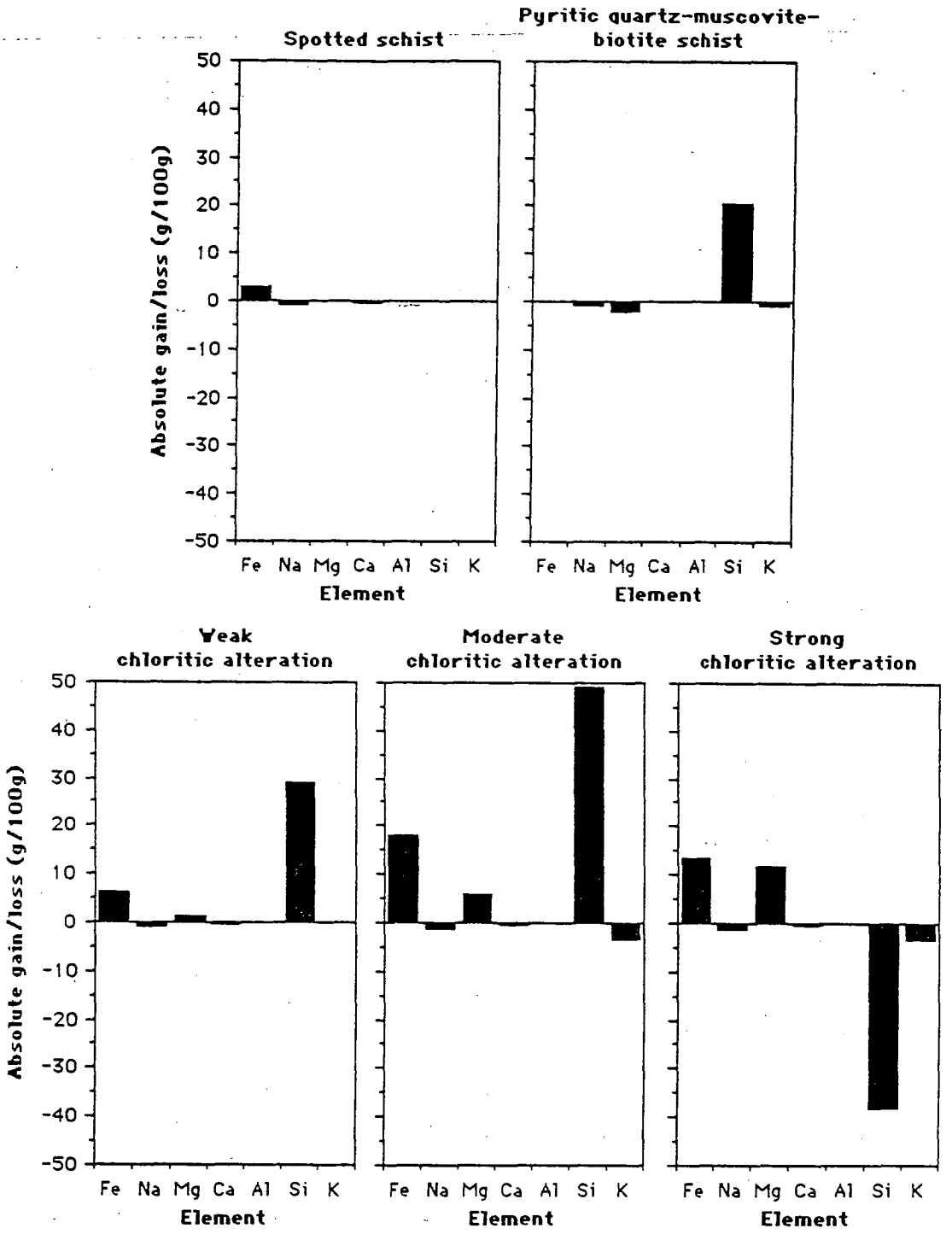

Figure 38. Absolute gains and losses for major element oxides from alteration at Balcooma. Explanation in text.

contact of the quartz-chlrite schist with the spotted schist, development of an envelope of weak chloritic alteration involved changes in the same elements but at a lower intensity. These data indicate that chloritic alteration at Balcooma involved the addition of more pyrite, chalcopyrite and quartz, and the initial addition of chlorite and destruction of micas. As lead was also removed, the hydrothermal fluids that formed chloritic alteration must have been undersaturated in lead. This is consistent with the kuroko model (Eldridge et al., 1983) where the introduction of hot, copper-bearing fluids removed sphalerite and galena from the base of kuroko deposits.

The most intense alteration (strong chloritic alteration) involved a large loss in silica (~40 g/100g) and a significant enrichment of magnesium. Other element changes were similar to moderate chloritic alteration. This reflects the removal of quartz and the addition of chlorite in this alteration type.

Alteration at Balcooma has involved dramatic changes in mass, particularly in terms of silica. Although changes in density may accoadate small change in mass, the large changes in silica (up to 50 g/100g) requires volume changes. As much of this alteration is accompanied by stringer and stockwork sulfides, the changes in volume may have been accomadated by brecciation associted with hydrothermal discharge up the alteration pipe.

Dry River South

Alteration at Dry River South differs markedly from alteration at Balcooma in both mineralogy and chemical composition. Whereas alteration at Balcooma is dominated by quartz-chlorite schist with the attendant enrichment in SiO_2, Fe_2O_3 and MgO, alteration at Dry River South is dominated by pyritic quartz-muscovite-biotite schist. Although chloritic alteration exists under some of the copper-rich intersections at Dry River South, it is of minor importance.

Footwall pyritic quartz-muscovite-biotite schist. The footwall to the Dry River South prospect consists almost entirely of pyritic quartz-muscovite-biotite schist, which is interpreted as metamorphosed quartz-sericite-pyrite alteration. Due to the intensity of alteration and deformation, primary textures are rarely present. Rare, relic, pre-tectonic fragmented textures indicate the

presence of volcaniclastic rocks. Figure 29 illustrates the variation in the geochemistry of the footwall alteration zone.

Samples from DRS-39, which show clear volcaniclastic textures, have markedly different compositions from other samples from the alteration zone. Samples from DRS-39 have trace element characteristics that are similar to the lapilli fragmental from Balcooma and the fragmental that drapes over the top of the Dry River South massive sulfide. The protolith to this unit is interpreted to be a rhyolitic or rhyodacitic lapilli tuff.

Isocon analysis (Fig. 39) of three altered samples of this inferred altered volcaniclastic unit (using the Balcooma lapilli volcaniclastic as the "unaltered equivalent") indicate that relatively weak alteration along the western edge of the Dry River South prospect introduced large but variable quantities of copper, lead, zinc and sulfur accompanied by introduction of lesser relative amounts of Fe_2O_3, rubidium, MnO and K_2O. Conversely, strontium, Na_2O, CaO and SiO_2 have been lost. The introduction of base metals, Fe_2O_3 and sulfur is due to sulfide introduction whereas the addition of rubidium, K_2O and MgO may be explained by sericitization and weak chloritization (which now occurs as metamorphic biotite). Plagioclases have been partially, but not totally, altered as Na_2O and CaO have undergone significant, but not total losses. Sericitization of feldspar and chlorite alteration at least partially explains the loss in SiO_2. As the slope of the isocon is approximately one, this alteration has not produced a significant change in rock mass.

Figure 40 illustrates the results of alteration on a flow (?) of quartz-feldspar porphyry located just below the massive sulfide horizon. As with the samples from DRS39, significant quantities of zinc, lead, Fe_2O_3, rubidium, MgO and K_2O have been added whereas strontium, Na_2O and CaO have been lost. Changes in mineralogy similar to those in DRS-39 best explain the changes in composition although the destruction of plagioclase appears to be more complete.

The trace element characteristics of the footwall alteration zone at Dry River South (Fig. 29a) indicate that the majority of the alteration zone precursor had a composition quite dissimilar to both the volcaniclastic unit and hanging wall metasediments. The data

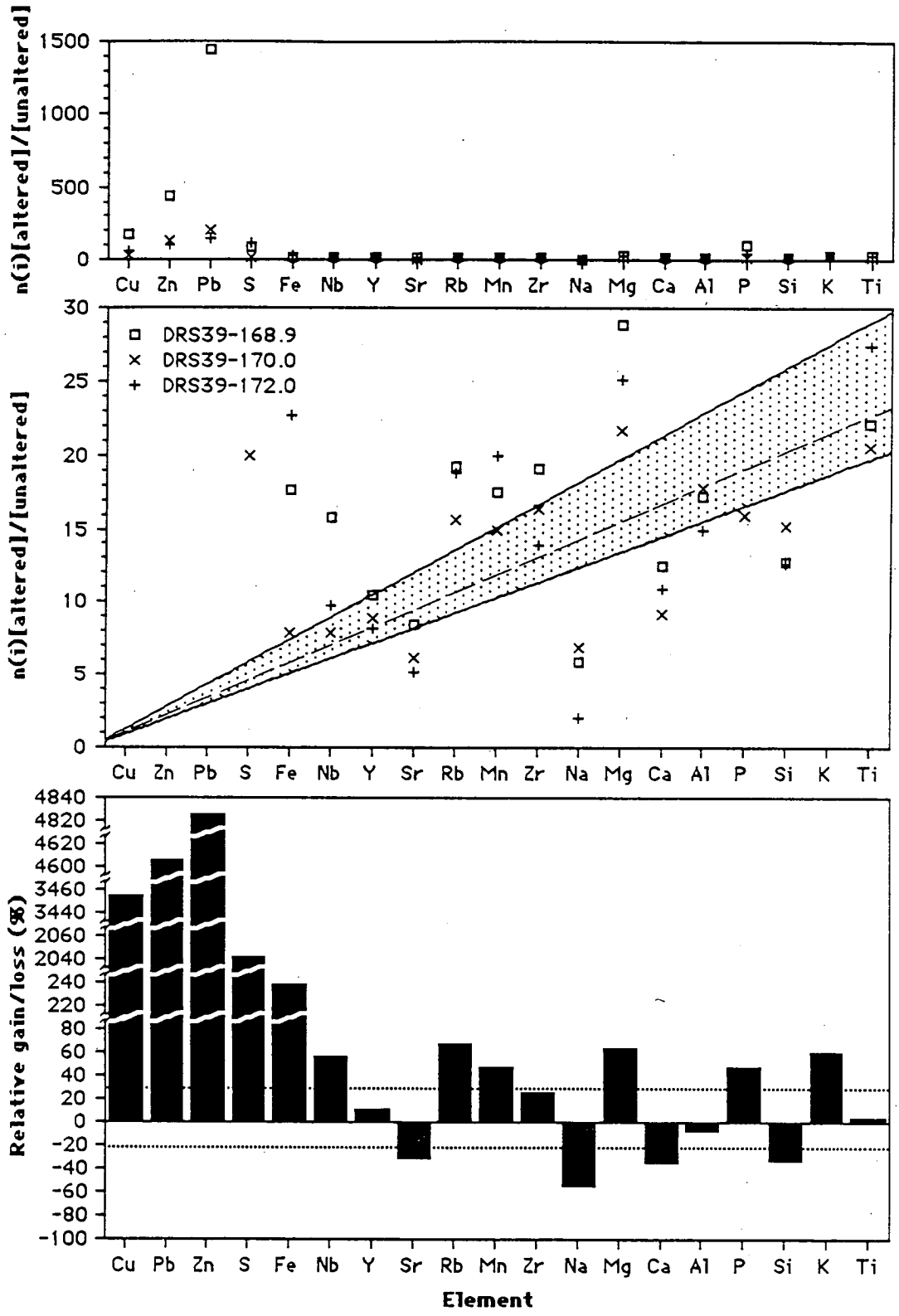

Figure 39. Isocon diagrams illustrating gains and losses for altered felsic fragmentals at Dry River South. Explanation in text.

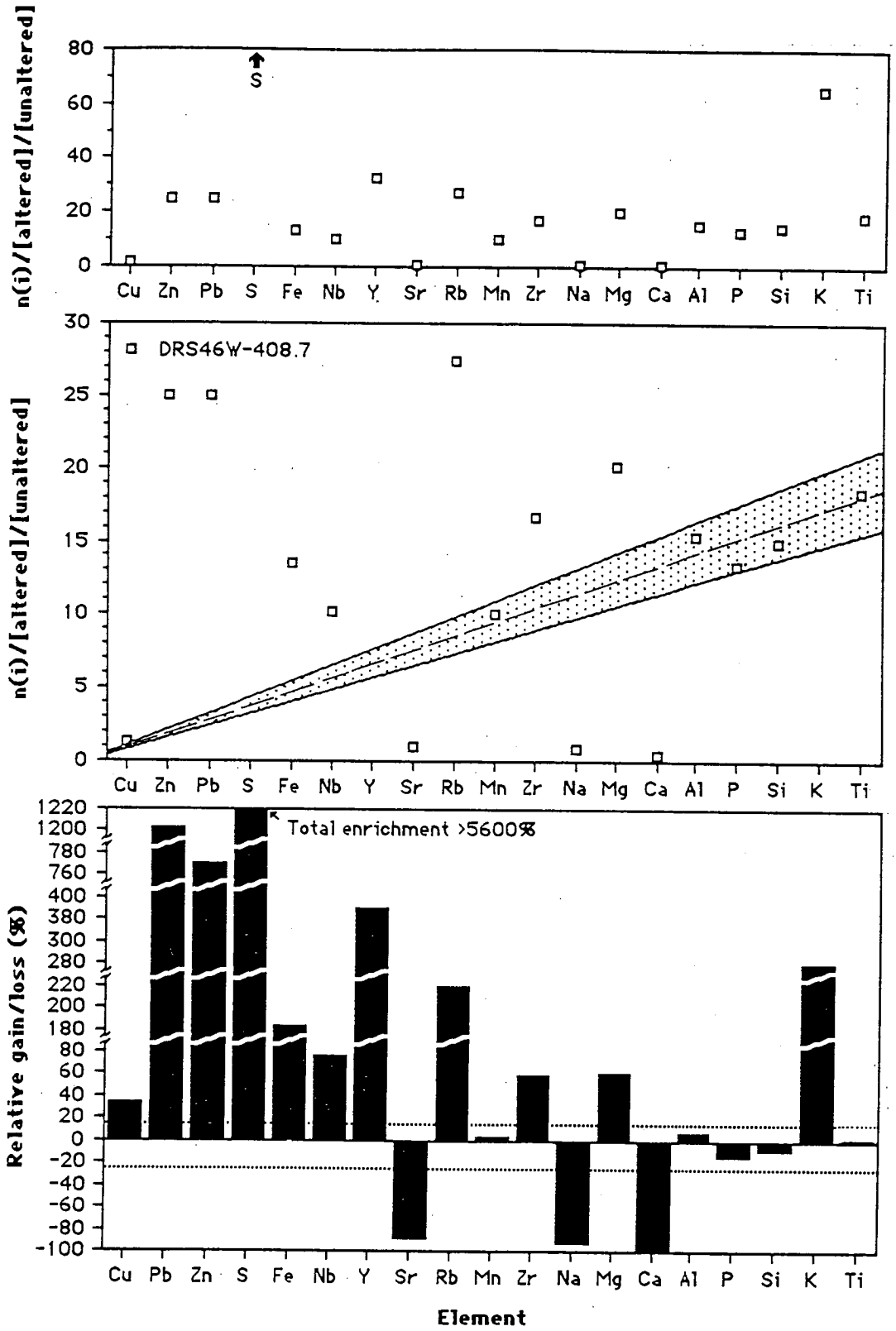

Figure 40. Isocon diagrams illustrating gains and losses for altered quartz-feldspar porphyry at Dry River South. Explanation in text.

indicate that the protolith had a rhyolitic composition. As relic fragmental textures are also present in this zone (Fig. 17c), the protolith to the major part of the Dry River South alteration zone is interpreted as a sequence of rhyolitic lavas and volcaniclastic rocks.

Due to the lack of an "unaltered equivalent", isocon analysis of this alteration was not possible. However, the variation in the Nb/Y ratio in the pyritic quartz-muscovite-biotite schist (Fig. 29a) may reflect alteration. When plotted against Pb, Na_2O, and K_2O (Fig. 41), the ratio has moderately coherent trends. Both lead and K_2O increase with increasing Nb/Y ratios, which suggests that the least altered samples have the lowest Nb/Y ratios. However, the Na_2O content tends to decrease with increasing Nb/Y ratios, which is inconsistent with an increasing alteration intensity. As the Na_2O contents of the rocks are generally low (<0.5%), this inconsistency can be dismissed and an increasing Nb/Y ratio probably indicates increasing alteration intensity.

One sample of hanging wall pyritic quartz-muscovite-biotite schist was analyzed and has also been plotted in Figures 29 and 41. In all scattergrams this sample plots along the trends defined by the footwall pyritic-quartz-muscovite-biotite schist. This confirms the interpretations of T. Taylor (pers. com., 1987) that when this rock type occurs it has been emplaced through shallow angle faulting above the massive sulfide horizon.

Hanging wall alteration. Figure 42 illustrates the downhole variation of Na_2O, Sr, MgO and Fe_2O_3 against lithology and depth in DRS22. Each element has a subtle change in concentration in the hanging wall at a depth of roughly 200 m. Below this level, and down to the massive sulfide lens, samples of metagraywacke have slightly lower concentrations of Na_2O and Sr but slightly higher concentrations of MgO and Fe_2O_3. Date et al. (1983) has documented the extension of sericite-chlorite alteration into the hanging wall above the Fukazawa deposit, and they have noted that this alteration type was characterized by depletion of Na_2O in the footwall. The results at Dry River South, therefore, could be interpreted as the effect of hanging wall alteration associated with massive sulfide formation.

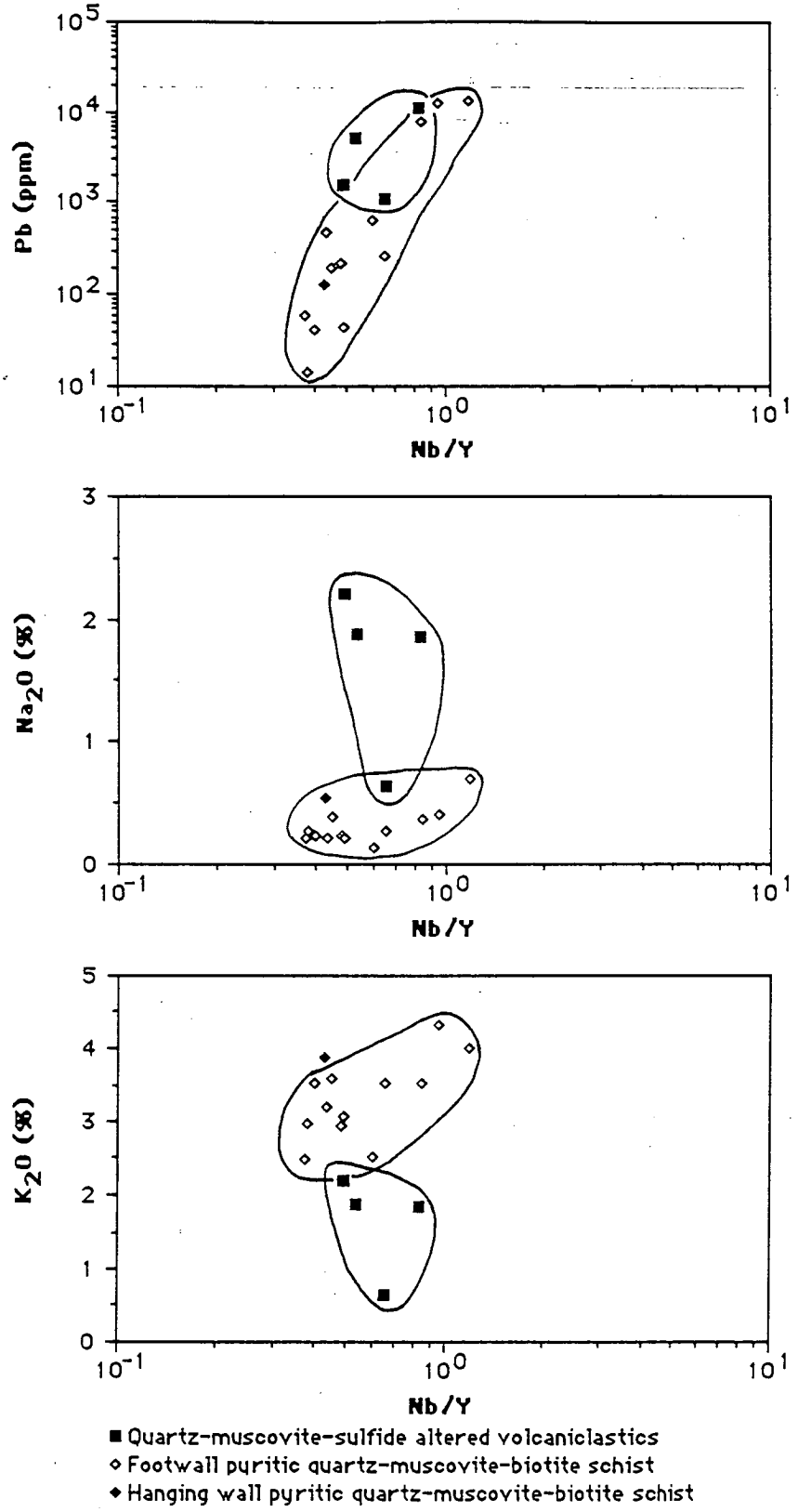

Figure 41. Scattergrams showing the variations in Pb, Na_2O and K_2O from altered rocks at the Dry River South prospect.

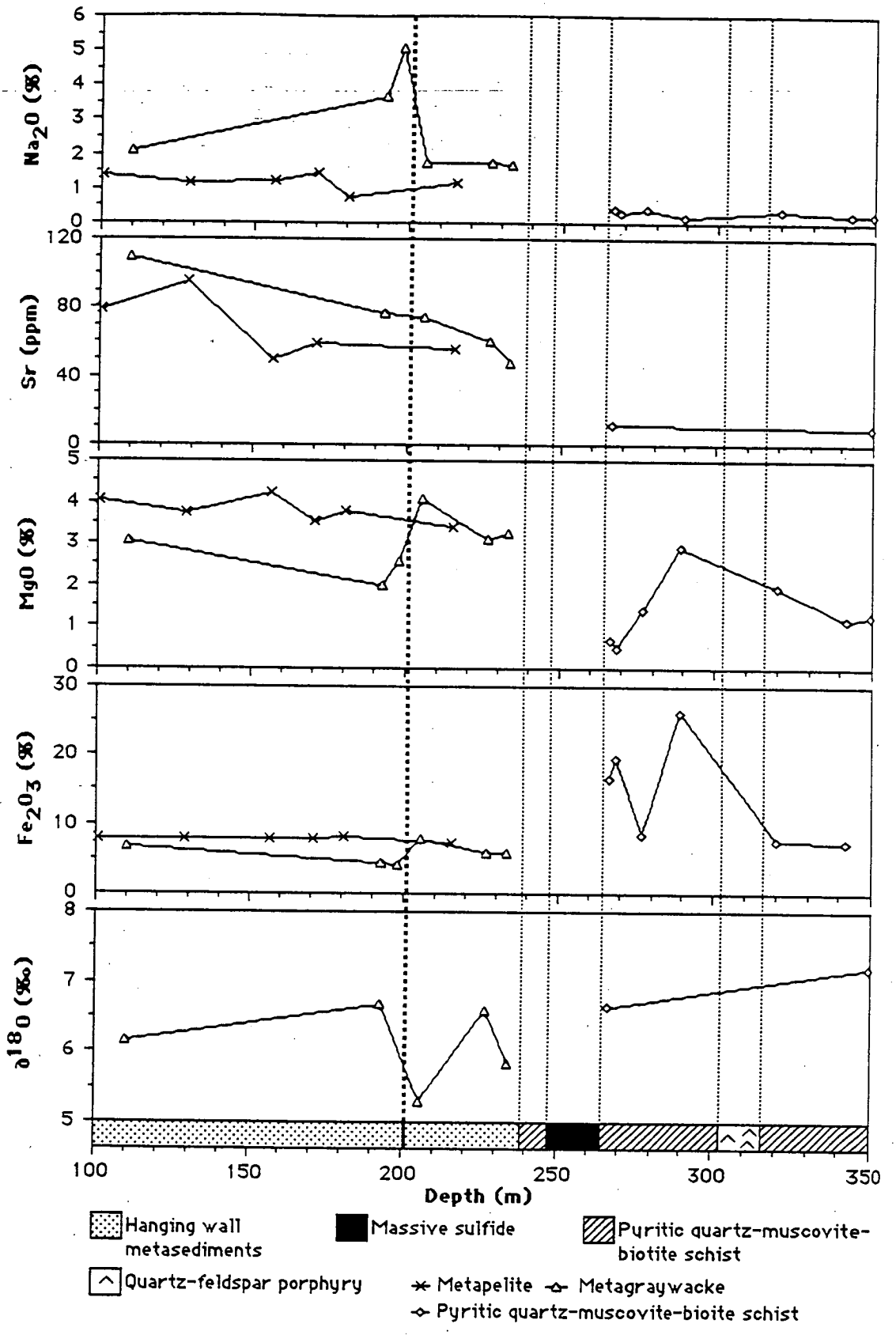

Figure 42. Down hole variation in Na_2O, Sr, MgO, Fe_2O_3 and $\delta^{18}O$ in DRS22, Dry River South prospect.

However, the composition of metapelitic rocks does not appear to change down hole. In fact, the elements of interest from some samples of metagraywacke below a depth of 200 m have values close to the values of the metapelites. An alternative interpretation, therefore, is that the anomalous samples of metagraywacks have a large pelitic content.

Although overlap exists, most metagraywackes have different contents of SiO_2 and Al_2O_3 and different Zr/TiO_2 ratios than the metapelites. Most metagraywackes contain more than 65% SiO_2 and less than 17% Al_2O_3, yet all metapelites contain less than 65% $SiO_2$and more than 17% Al_2O_3. Metagraywackes tend to have Zr/TiO_2 ratios of greater than 0.02, but only three samples of metapelite contain Zr/TiO_2 ratios of greater than 0.02 (Fig. 29). Using these criteria, only sample DRS22-205.6 has a significant pelitic component. Therefore the changes in composition may not be attributed solely to a high pelitic content in the metagraywacke.

The changes in composition may also be caused by internal variations within the metagraywacke as the values are not strongly anomalous. This possibility is lessened because all three samples below a depth of 200 m have consistently different values from the majority of the rest of the samples of metagraywacke. Therefore the apparent decrease in Na_2O and strontium and the apparent increase in Fe_2O_3 and MgO below 200 m depth to the massive sulfide horizon in DRS22 is most likely due to hanging wall alteration associated with massive sulfide deposition. It is recognized, however, that this is a preliminery interpretation and warrants additional study.

The interpretation that hanging wall alteration exists between the 200 m depth and the massive sulfide lens also supports the inferred presence of a major thrust fault at a depth of 200 m in DRS22 (Chapter 3). It is also inconsistent with the interpretation of major fault immediately above the massive sulfide horizon ((Fabray et al., (1986); discussed as option 2 in Chapter 3). The faulting present around the massive sulfide horizon that has locally thrust footwall pyritic quartz-muscovite-biotite schist above the massive sulfide is interpreted as subsidiary to a major thrust tens of meters above the massive sulfide horizon.

The effects of alteration on oxygen isotope systematics

In a further effort to gain an understanding of the systematics of alteration at Balcooma and Dry River South, nineteen samples were analyzed for whole rock oxygen isotope ratios (Table 6). Samples were prepared and analyzed using techniques of Clayton and Mayeda (1963) by M. Power, Jr. at the University of Tasmania.

Numerous studies of the variation in $\delta^{18}O$ about volcanogenic massive sulfide deposits have been undertaken and have been summarized in Franklin et al. (1981). With the single exception of Kidd Creek, sericite-chlorite alteration in the footwall of all deposits resulted in a decrease in whole rock $\delta^{18}O$ of between 2 permil and 13 permil. Altered zones typically have whole rock $\delta^{18}O$ values of between 3 permil and 7 permil (Fig. 43; Franklin et al., 1981).

Recently a more detailed study of the rocks around the Fukazawa deposit in Japan by Green et al. (1983) has documented $\delta^{18}O$ halos in both the footwall and in the hanging wall of this deposit. Green et al. (1983) documented that rocks with a primary $\delta^{18}O$ value of between 6 and 8 permil were altered such that $\delta^{18}O$ increased to 16.9 ± 2.7 permil in the zeolite zone which is the outermost alteration zone in the district. The montmorillonite zone, which nests within the zeolite zone, had lower values of 11.1 ± 2.5 permil, whereas the sericite-chlorite zone, which occurs immediately around the deposit, had $\delta^{18}O$ values of 6.7 ± 1.3 permil. This zone of low $\delta^{18}O$ values, which was associated with the hottest fluids, extended up to 1.5 km away from the deposit in the footwall, and at least 400 m into the hanging wall (Fig. 44; Green et al., 1983).

With the exception of alteration from strong chloritic alteration, all data from the Balcooma and Dry River South prospects falls in the restricted range of 4.0 to 7.5 permil which, based on other deposits described in the literature, would be the range of sericite-chlorite alteration. This interpretation is consistent with interpretations based on whole rock geochemistry. The halo of alteration documented by $\delta^{18}O$ variation appears to be larger than that documented by whole rock geochemistry as volcaniclastic rocks at Balcooma (23-217.7 and Q860-360.1) have low $\delta^{18}O$ values but do not

Table 6. Results of whole rock oxygen isotope analyses.

Sample	Rock type	$\delta^{18}O$ (permil)
Balcooma		
12-42.8	Quartz-muscovite schist with biotite and staurolite porphyroblasts (spotted schist).	5.1
44-91.8	As above.	5.7
12-45.0	As above, weakly chloritized (weak chloritic alteration).	5.6
39-151.5	As above.	5.2
39-143.6	Quartz-chlorite schist (moderate chloritic alteration).	5.6
44-97.6	As above.	5.1
44-124.8	As above.	4.4
16A-141.2	Chlorite schist	2.8
Q860-360.1	Quartz-muscovite-feldspar-biotite schist (ash tuff).	6.0
23-217.7	Felsic lapilli fragmental.	5.8
Dry River South		
DRS22-110.2	Metagraywacke.	6.2
DRS22-192.5	As above.	6.7
DRS22-205.2	As above.	5.3
DRS22-226.6	As above.	6.6
DRS22-233.8	As above.	5.8
DRS22-266.5	Pyritic quartz-muscovite-biotite schist (footwall alteration).	6.6
DRS22-349.1	As above.	7.3
DRS39-171.0	As above, with relic fragmental textures.	7.1

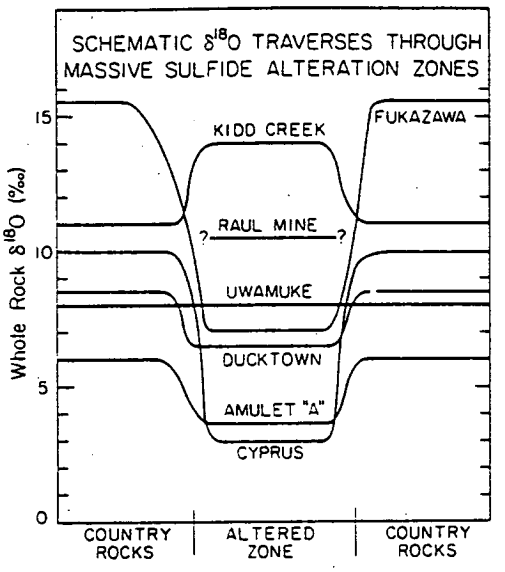

Figure 43. Variation in $\delta^{18}O$ values in rocks surrounding volcanogenic massive sulfide deposits (after Franklin et al., 1981).

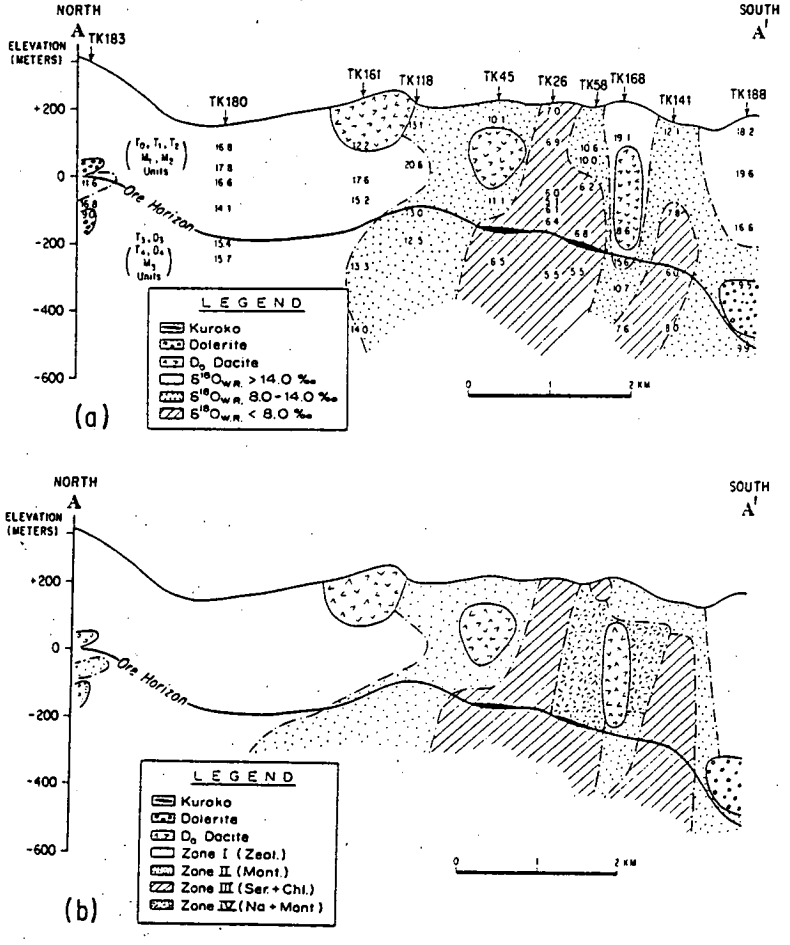

Figure 44. Cross section at the Fukazawa deposit showing (a) zonation in $\delta^{18}O$, and (b) alteration zonation (after Green et al., 1983).

have anomalous geochemistry. The $\delta^{18}O$ halo at Dry River South must also be quite broad as the low $\delta^{18}O$ values extend above the inferred fault in the hanging wall (Fig. 42). As $\delta^{18}O$ have a negative correlation with MgO (Fig. 42), chloritization during primary alteration of the hanging wall seems to have caused a decrease in $\delta^{18}O$, which is similar to the pattern noted by Green et al. (1983) at Fukazawa.

Unfortunately, fresh samples well away from mineralization were not available as the study and drilling were restricted to the area around mineralization. Due to this, no data on the $\delta^{18}O$ values of pristine, unaltered volcaniclastic rocks and graywackes from the region were available. However, estimates may be made by analogy with other similar rock units elsewhere in the world. Taylor and Sheppard (1986) generalized that shales and mudstones typically have $\delta^{18}O$ values between 13 and 20 permil, whereas graywackes and sandstones have more restricted values of between 13 and 14 permil. Wickham and Taylor (1985) found that high grade metamorphism (i.e. above the andalusite isograd) tends to homogenize and slightly lower the primary values, but does not change the values significantly. Data summarized in Taylor and Sheppard (1986) indicate that typical felsic volcanics have values between 6 and 9 permil. As values from both Balcooma and Dry River South generally fall below these values, the low $\delta^{18}O$ of the rocks around the prospects may best be attributed to variable sericite-chlorite alteration in both the footwall and the hanging wall to mineralization. The lateral extents of $\delta^{18}O$ were not determined in this study due to a lack of unweathered samples from non-mineralized areas.

Summary and conclusions

Results from this study indicate that the Balcooma and Dry River South propects were deposited in a sequence of mixed metagraywackes, volcaniclastic and volcanic rocks. The metasediments appear to have a continental island arc provenance, and the volcanics have rhyolitic composition. At both deposits the volcanic rocks occur in the footwall to the mineralized horizon, but at Balcooma metasediments predominate over the volcanics in the footwall.

Primary alteration differs markedly in both extent and composition between Balcooma and Dry River South. Table 7 and Figure 45 summarize the characteristics of alteration at both deposits. The most important characteristics of the Balcooma deposit are as follows:

(1) The deposit is surrounded by a large halo of weak alteration (the spotted schist) that may extend into the hanging wall (the upper metagraywacke). This alteration involves the depletion of Na_2O, CaO and strontium, and the enrichment of sulfur and Fe_2O_3. Mineralogically, plagioclase has been destroyed and pyrite has been added.

(2) Pyritic quartz-muscovite-biotite schist alteration accompanies zinc-lead mineralization. This alteration involves silicification and variable sulfidation accompanied by plagioclase destruction. SiO_2, base metals and sulfur have been added whereas Na_2O, CaO and strontium have been removed.

(3) Quartz-chlorite schist occurs in the alteration pipe to the copper shoots. This alteration involved silicification, sulfidation and chloritization with attendant gains in SiO_2, Fe_2O_3, MgO, copper, zinc and sulfur, and losses in Na_2O, CaO, K_2O, strontium and rubidium. Chlorite schist, which has involved a loss in silica in addition to the other changes occurs in relatively small amounts in the alteration pipe.

(4) Alteration at Balcooma involved the initial destruction of feldspar, followed by strong silicification, then by continued silicification, chloritization and mica destruction, and finally by desilicification and intense chloritization. Sulfide minerals were added throughout the development of alteration.

Dry River South alteration has the following important characteristics:

(1) Footwall alteration is largely restricted to the formation of pyritic quartz-muscovite-biotite schist. This alteration has involved sulfidation, silicification, sericitization and possibly weak chloritization. SiO_2,

Table 7. Characteristics of alteration at Balcooma and Dry River South.

Deposit	Alteration type	Rock type	Distribution	Changes in mineralogy	Elements gained	Elements lost
Balcooma	Weak pyritization/ feldspar destruction	Spotted schist and upper metagraywacke	Broad halo surrounding mineralization and intense alteration. Extends into the hanging wall.	Pyrite addition and feldspar destruction	Fe, S, Cu and Zn	Na, Ca, Sr and Pb
	Quartz-sericite-pyrite	Pyritic quartz-muscovite-biotite schist	Largely in the footwall to zinc-lead-rich mineralization.	Sulfide addition, feldspar destruction and silicification	Si, Cu, Pb, Zn and S	Na, Ca, Sr, Mg and Rb
	Quartz-chlorite	Quartz-chlorite schist	Forms a pipe underneath the copper-rich lens.	Sulfide addition, feldspar destruction, silicification, chlorite addition and muscovite destruction	Si, Fe, Mg, Zn, Cu and S	Na, Ca, Sr, K, Rb and Pb
	Chloritization of spotted schist	Weak chloritic alteration	Occurs as 1-10 m transition zones between moderate chloritic alteration and spotted schist.	Chloritization of biotite and staurolite, silicification and muscovite destruction	Si, Fe and Mg	Cu, Pb and Zn
	Chlorite	Strong chloritic alteration	Occurs as veins and lenses within most other lithologies.	Chloritization, quartz and sulfide removal, and mica destruction	Mg	Si, S and K
Dry River South	Quartz-sericite-pyrite	Pyritic quartz-muscovite-biotite schist	Occurs as a large, laterally extensive zone below the massive sulfide lens.	Sulfide addition, feldspar destruction, silicification, muscovite addition and chloritization	Si, Fe, Zn, Cu, Pb, S, K, Rb and Mg	Na, Ca and Sr
	Quartz-chlorite	Quartz-chlorite-biotite schist	Occurs in the footwall to massive sulfide, particularly on the eastern edge.	Sulfide additon and chloritization	No data	No data
	Hanging wall (?)	Metagraywacke	Occurs in the hanging wall to the massive sulfide lens.	Unknown, possibly feldspar destruction.	Fe and Mg	Na and Sr

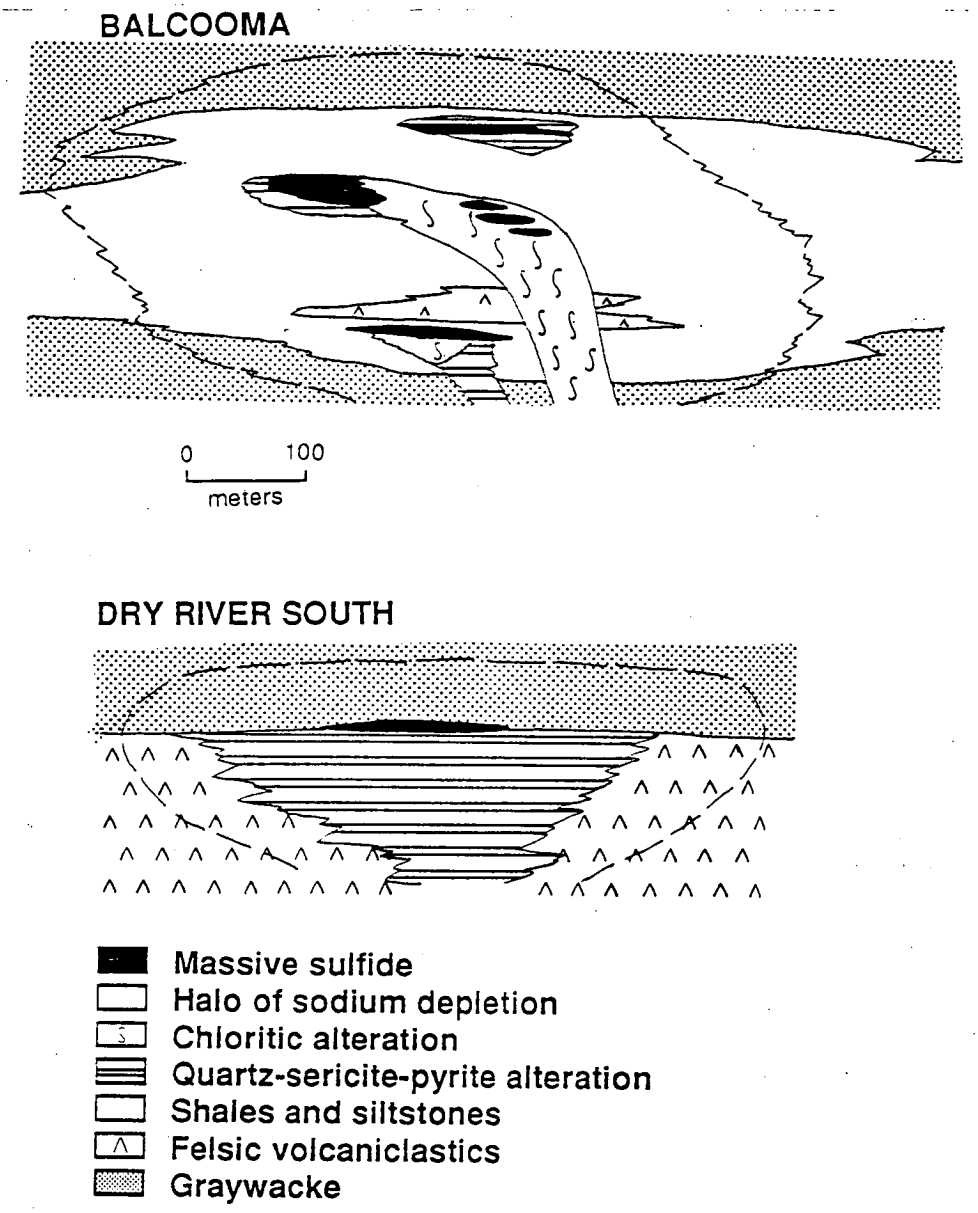

Figure 45. Schematic diagram showing alteration zoning along undeformed east-west cross sections across the Balcooma and Dry River South deposits.

sulfur, base metals, K_2O, rubidium and MgO have been added whereas Na_2O, CaO and strontium have been lost.

(2) Hanging wall alteration involving slight additions of MgO and Fe_2O_3 accompanied by slight depletions of Na_2O and strontium which may occur up to 50 m above the massive sulfide horizon. Due to the subtleties of these changes, this interpretation is preliminary and requires additional sampling for confirmation.

The alteration zone at Dry River South forms a rather large zone that extends beyond the lateral extent of the massive sulfide lens, whereas at Balcooma chloritic alteration occurs in a restricted pipe stratigraphically below the major copper-rich massive sulfide lens. The presence of a large portion of fragmental rocks in the Dry River South prospect probably allowed unfocussed flow of the hydrothermal fluids to form the wide alteration zone, but hydrothermal flow at Balcooma was restricted to a narrow pipe due to the predominance of relatively impermeable pelites and fine grained psammites in the footwall.

The other major difference between the two deposits is the predominance of quartz-chlorite schist as alteration at Balcooma as compared to the predominance of pyritic quartz-muscovite-biotite schist at Dry River South. This difference appears to relate to the dominance of copper-rich mineralization at Balcooma relative to the zinc-lead-rich nature of the Dry River South prospect (Chapter 8).

Chapter 5
Metal zonation and relationships between metals at Balcooma and Dry River South

Introduction

The general metal zonation of the major base metals in volcanogenic massive sulfide deposits has been relatively well understood and described for the past several decades (e.g. Stanton, 1970; Sangster, 1972; and Large, 1977). Recent papers that summarize these studies include Franklin et al. (1981) and Ohmoto et al. (1983). Typically, the deposits are enriched in copper at the base and lead and zinc towards the top. Deposits of Proterozoic and Phanerozoic age also have barite capping the deposit in many cases. The existance of a large set of computerized assay data from the footwall alteration zones and massive sulfide lenses at Balcooma and Dry River South for copper, lead, zinc, silver and gold has enabled a detailed study of metal zonation and metal associations. Relationships between zinc and lead are discussed in Part 3, Chapter 1, wheras the relationships between base metals, silver and gold are addressed herein.

Balcooma

Geologic data involving the extent of oxidation, rock type, mineralization style and mineralogy from core logs by the author and company geologists was merged with an analytical data base on the University of Tasmania Prime 9955 computer. Using this geologic data base, the samples were subdivided into five groups according to rock and mineralization type: (1) quartz-chlorite and chlorite schist with disseminated and stringer sulfide (moderate and strong chloritic alteration; 1285 samples), (2) pyritic quartz-muscovite-biotite schist (462 samples), (3) massive magnetite (99 samples), (4) massive pyrite-chalcopyrite (547 samples), and (5) massive pyrite-sphalerite-galena (133 samples). Analyses of percussion rock chips, oxidized core and other rock types were not considered this analysis of data.

As metal relationships in both chloritic schist and massive magnetite are similar to those in massive pyrite-chalcopyrite, and

metal relationships in pyritic quartz-muscovite-biotite schist are similar to the those observed in massive pyrite-sphalerite-galena (Huston, 1987), for brevity's sake, only the relationships in massive mineralization will be discussed.

Figures 46 and 47 illustrate the relationships between gold, silver, copper, lead and zinc for massive pyrite-chalcopyrite and massive sphalerite-galena-pyrite, respectively. Gold correlates better with copper than zinc in both types of mineralization, but the correlation between copper and gold in massive pyrite-chalcopyrite is better than that in massive pyrite-sphalerite.

Figures 48b and 48c support this observation in the massive pyrite-chalcopyrite lens on section 8900 mN. High concentrations of gold and copper occur together within the lens; outside the massive lens both copper and gold grades decrease dramatically which indicates that very little gold has been remobilized and deposited adjacent the massive sulfide. Most of the higher (to 2000 ppm) lead (and by inference, zinc) values also occur in the massive sulfide lens (Fig. 51d). This accounts for the lower, but still significant, correlation between gold and zinc in massive pyrite-chalcopyrite (the statistical significance of correlation coefficients derived in this study is determined from tables in Dixon and Massey (1957) at a 99% level of confidence). In addition to the strong correlation with copper, gold also displays a strong correlation to bismuth in copper-rich mineralization (Fig. 49). Copper also has a strong correlation to bismuth. The inter-correlation between gold, copper and bismuth is born out by the mineralogical association of bismuth minerals and electrum with chalcopyrite (Chapter 7).

Gold and copper also have a weak, but statistically significant, correlation in massive pyrite-sphalerite-galena mineralization. In contrast, gold does not have a statistically significant correlation with either zinc or silver (Fig. 47). This association differs markedly from observations made at Rosebery (Part 2, Chapter 2) and Que River (Large et al., 1988) where zinc and gold are strongly correlated in zinc-rich ore. Rather, the characteristic distribution of gold in both zinc-lead-rich and copper-rich mineralization at Balcooma is more similar to the copper-gold association present at the Paleozoic Mt. Chalmers and Mt. Lyell deposits, and the Archean Scuddles deposit (Part 3, Chapters 2 and 4; and Ruxton (1987)).

Silver has quite contrasting associations between the two types of massive sulfide. In massive pyrite-chalcopyrite zones silver has

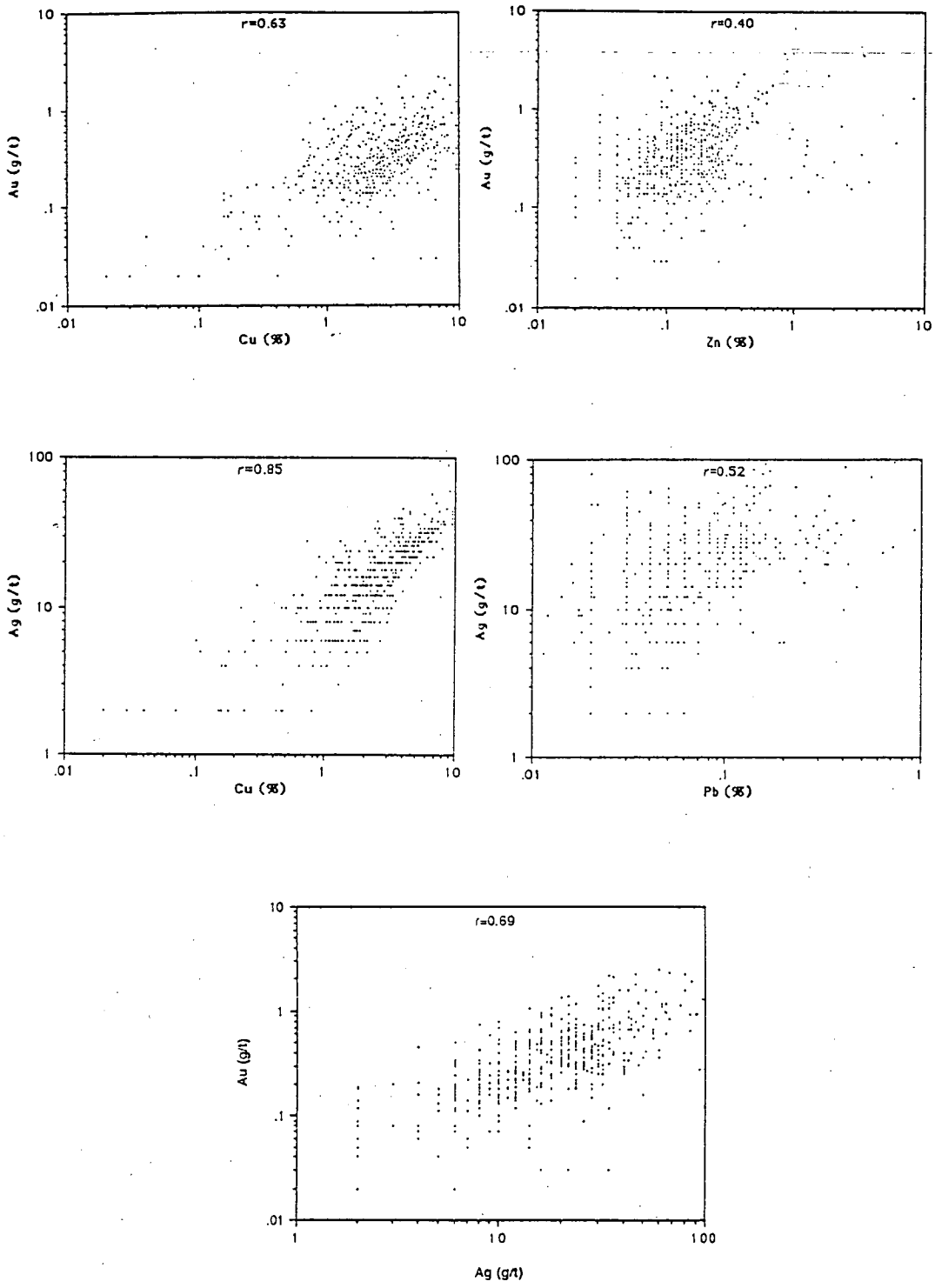

Figure 46. Scattergrams showing the relationships between base metals, gold and silver in massive pyrite-chalcopyrite mineralization, Balcooma prospect.

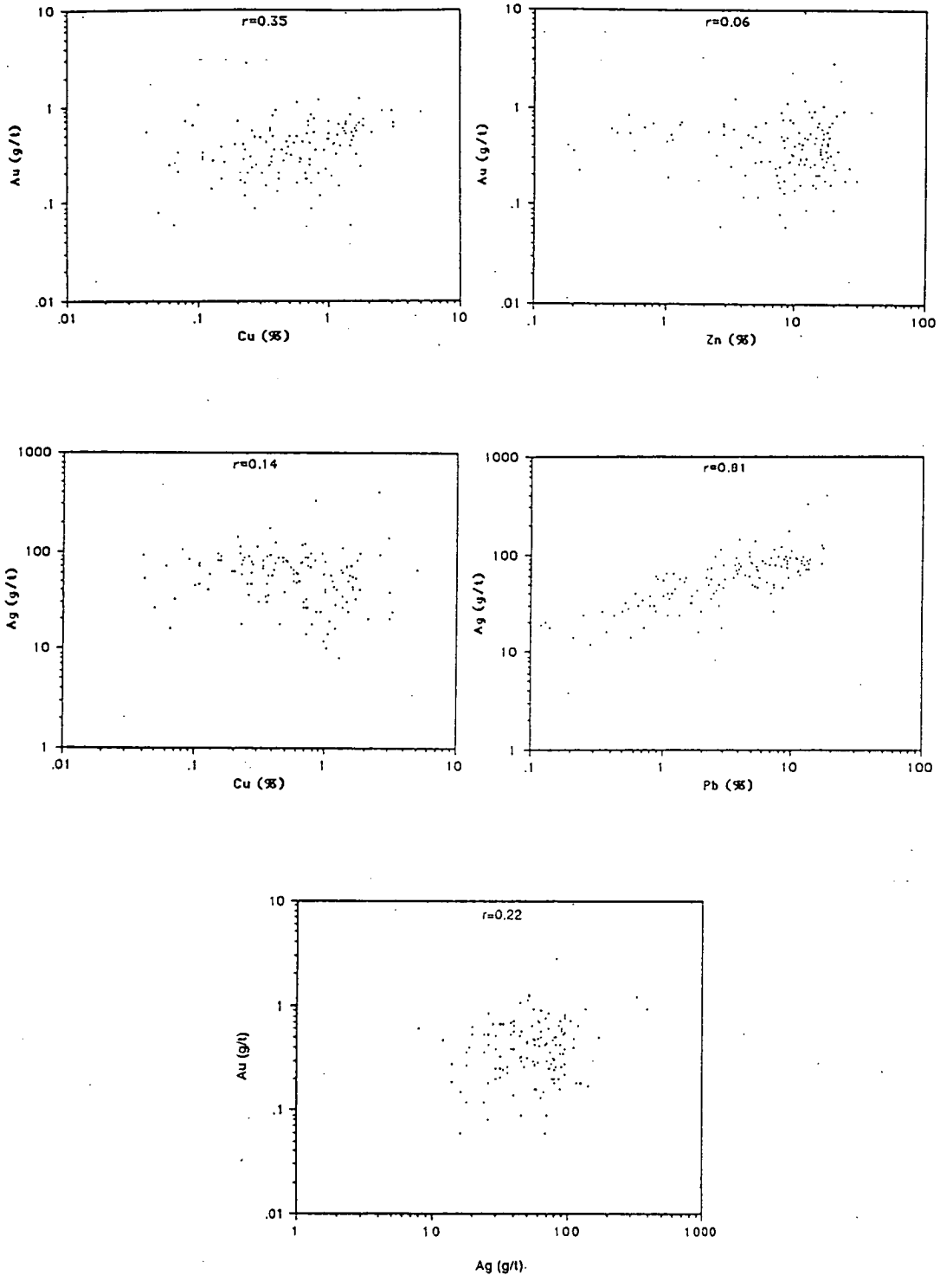

Figure 47. Scattergrams showing the relationships between base metals, gold and silver in massive pyrite-sphalerite-galena mineralization, Balcooma prospect.

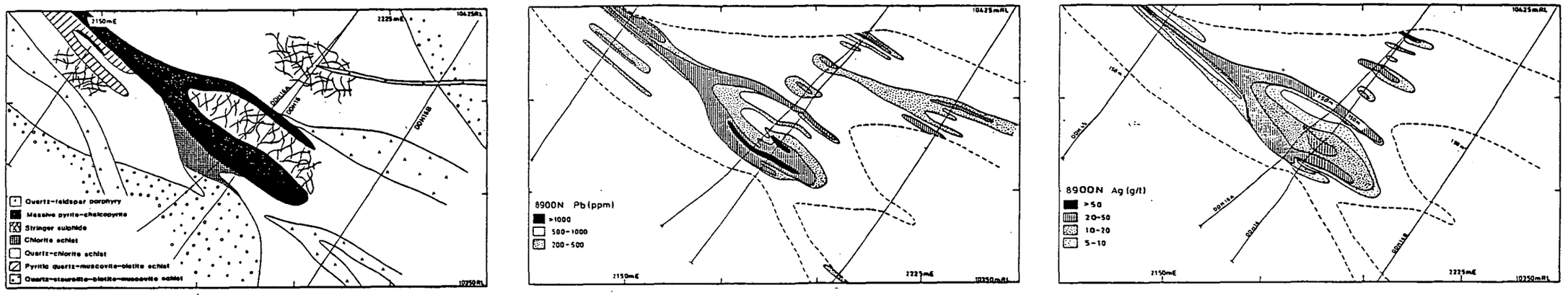

Figure 48. Geology and the distribution of gold, copper, silver and lead from section 8900 mN.

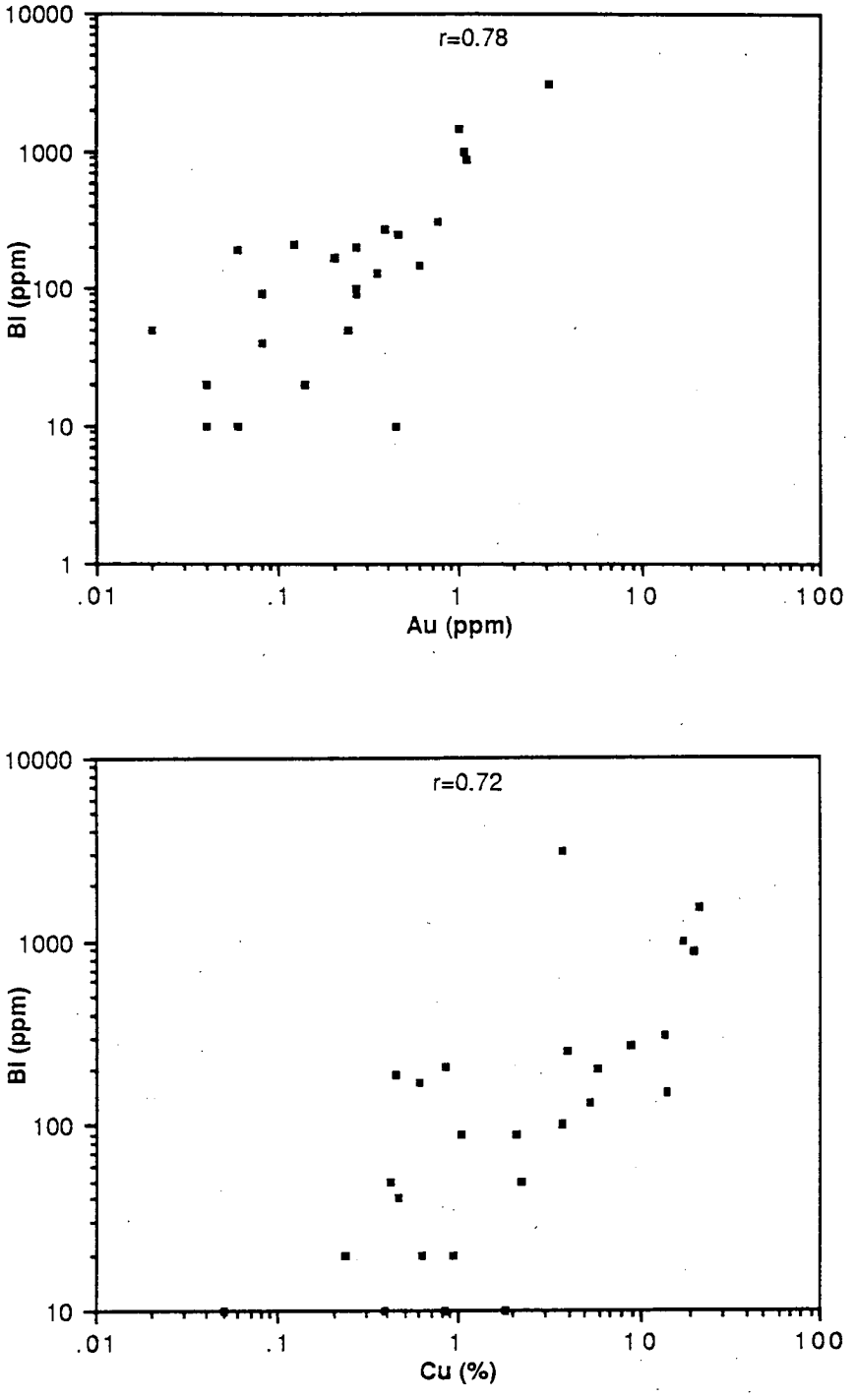

Figure 49. Scattergrams showing the relationship between bismuth, copper and gold at the Balcooma prospect.

a strong correlation to copper, whereas in massive pyrite-sphalerite-galena silver has a strong correlation to lead (Figs. 46 and 47). The silver-lead association is typical of most massive sulfide deposits (Amcoff, 1984; see also Part 2, Chapter 2 and Part 3, Chapter 3), but the silver-copper association is much less common (e.g. Millenbach; Knuckey et al., 1982). The distribution of silver on section 8900 mN (Fig. 51d) corresponds to copper, and is restricted to the massive pyrite-chalcopyrite lens. These data indicate that the hosts to silver at Balcooma are chalcopyrite (140 ppm Ag) in copper-rich mineralization and galena (1200 ppm) in lead-zinc mineralization if all or most of the silver is assumed to be contained in the respective mineral. The strong correlation between silver and gold in massive pyrite-chalcopyrite (Fig. 46) is probably due to the association between silver-bearing chalcopyrite and electrum.

Dry River South

As at Balcooma, geologic data, which was collected by the author, was encoded and merged with assay data on the computer, and this data file was then used to separate assays into three groups: (1) pyritic quartz-muscovite-biotite schist (487 samples), (2) massive pyrite-chalcopyrite (69 samples), and (3) massive pyrite-sphalerite-galena (88 samples).

In all types of mineralization silver has the best correlation with gold (Figs. 50 through 52). As at Balcooma, gold has a much stronger correlation with copper than zinc in massive lenses (Figs. 51 and 52), but in the footwall alteration zone the correlations of gold with copper and gold with zinc are similar (Fig. 53). In massive sphalerite-galena gold does not have a statistially significant correlation with zinc (Fig. 52). These correlations are not born out in the mineralogy as electrum has a wide variety of associations at Dry River South (Chapter 7).

Lead correlates best with silver in all types of mineralization although a weak correlation between silver and copper exists in the footwall alteration zone and massive pyrite-chalcopyrite. These data indicate that galena is the major host of most silver at Dry River South as tetrahedrite and other silver-rich minerals are rare in the massive sulfide (Chapter 7). In massive pyrite-chalcopyrite,

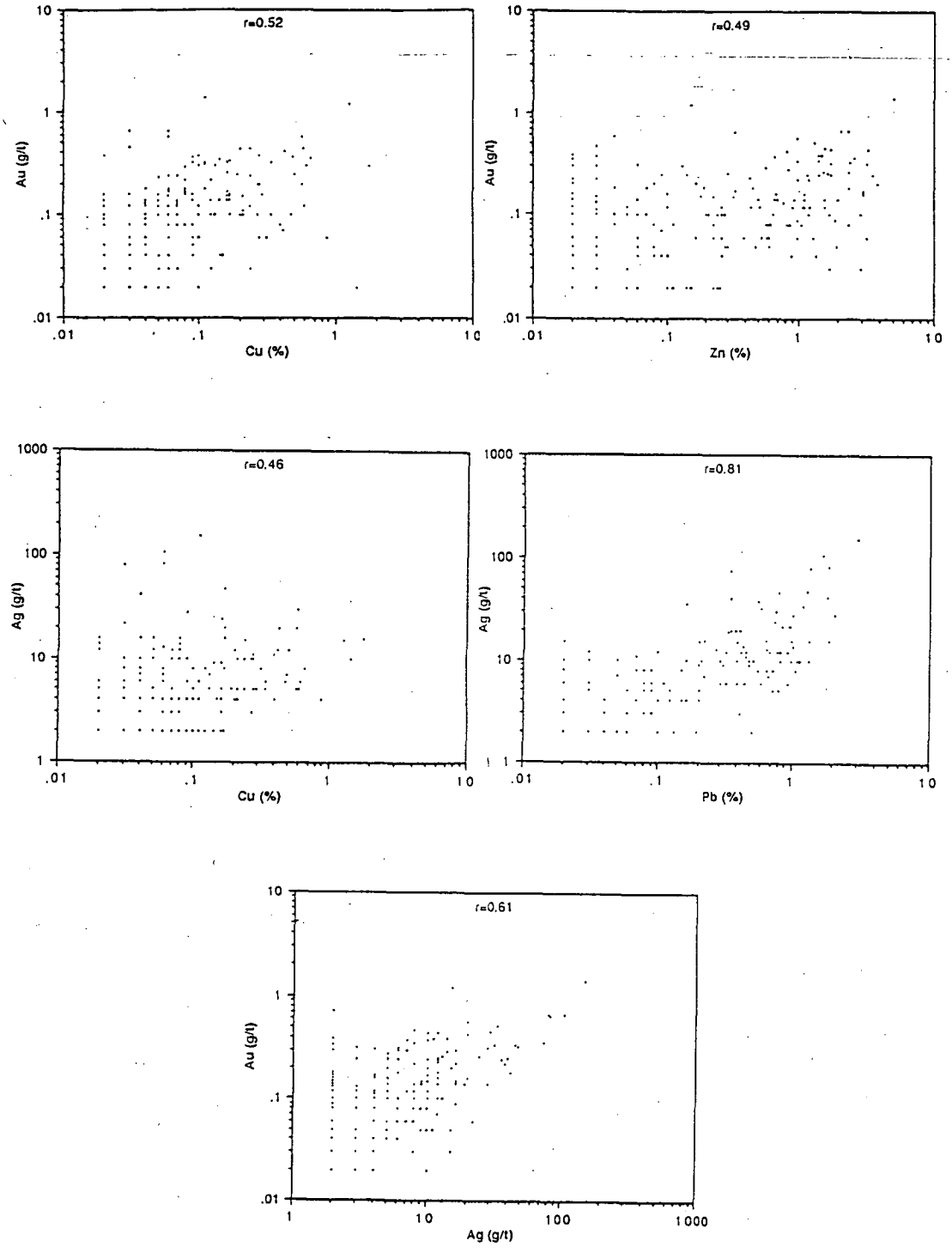

Figure 50. Scattergrams showing the relationships between base metals, gold and silver in the footwall alteration zone, Dry River South.

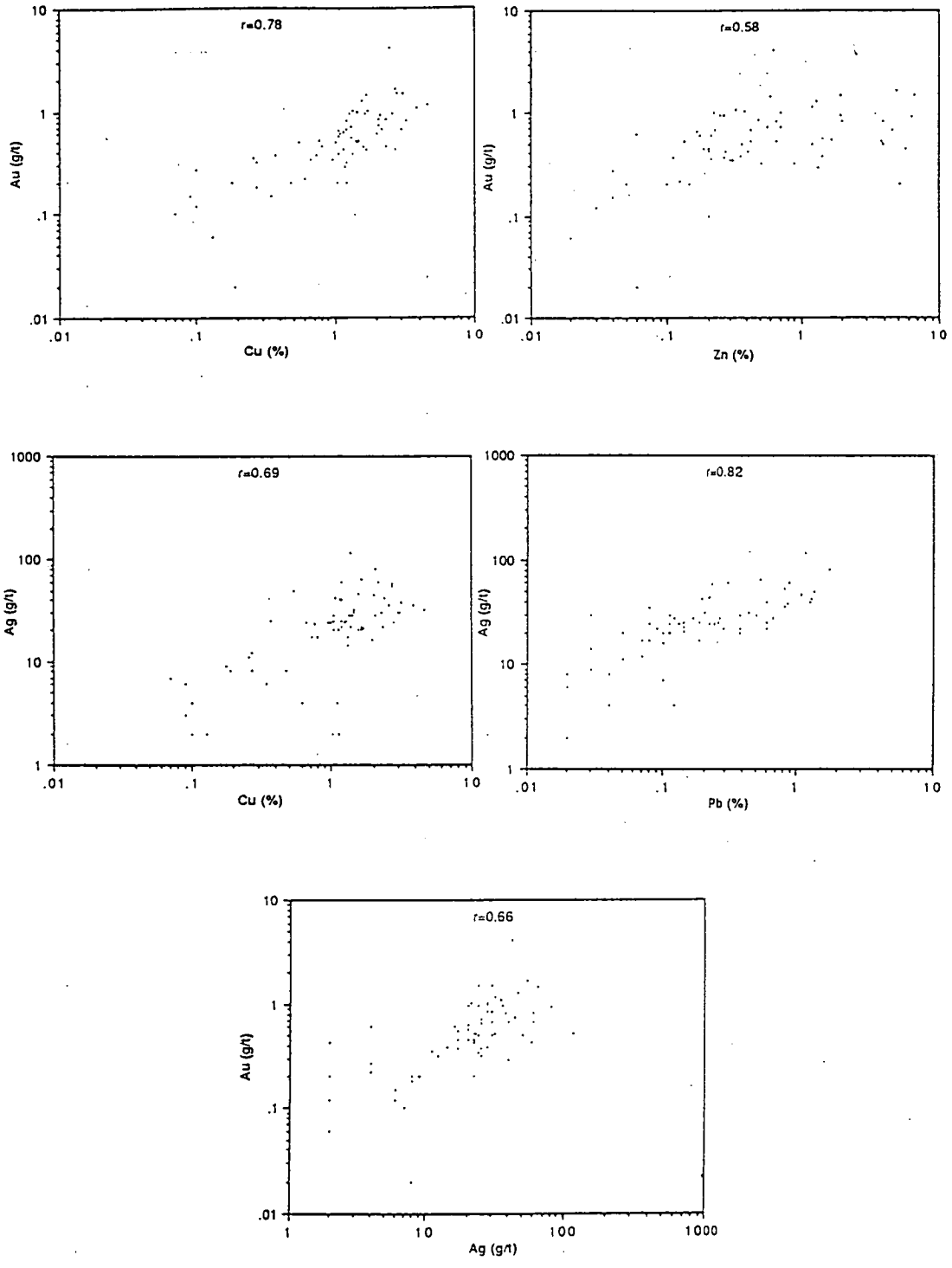

Figure 51. Scattergrams showing the relationships between base metals, gold and silver in massive pyrite-chalcopyrite, Dry River South.

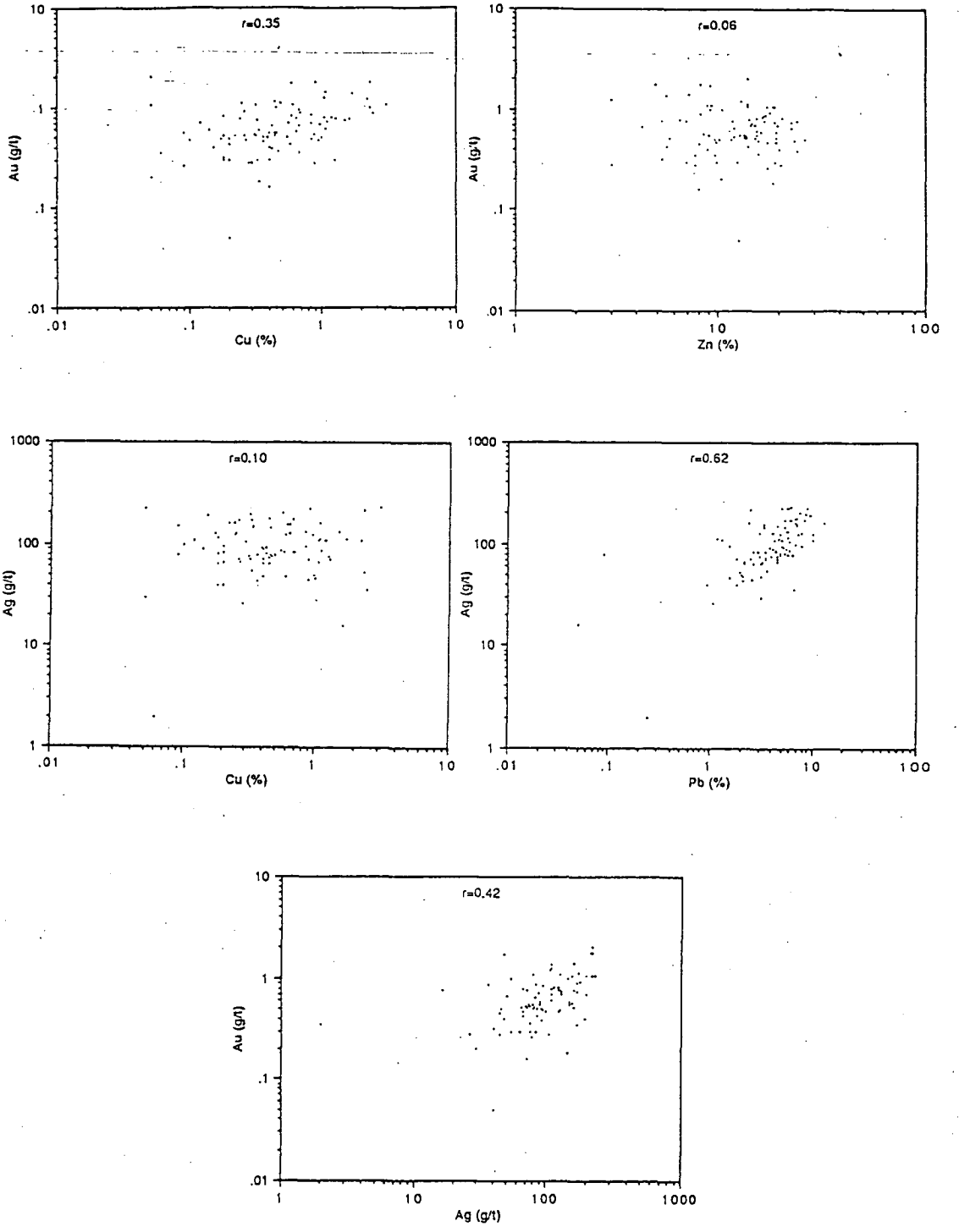

Figure 52. Scattergrams showing the relationships between base metals, gold and silver in massive pyrite-sphalerite-galena, Dry River South.

chalcopyrite may also be a subordinate silver-bearing phase to galena due to the previously noted weak correlation.

The correlations between metals in the footwall alteration zone are illustrated on Figure 53 which shows the variation in copper, lead, silver and gold along section 5700 mN. Silver and lead have very similar, possibly strataform distribution patterns in the alteration zone (due to the lack of closely spaced drilling, the distribution patterns are somewhat interpretive, so the results are equivocal). Copper also has a similar pattern, but the highs are slighly offset from the lead/silver highs. Gold has a more complicated distribution pattern; gold highs occur both with copper and lead (and consequently zinc) highs. This accounts for the nearly equal correlation coefficients of gold with copper and zinc (Fig. 50).

Two aspects of metal distribution in the Dry River South alteration zone are anomalous: (1) the apparent strataform nature of base metal mineralization, and (2) the offset of base metal-rich footwall mineralization to the west of the massive sulfide lens. These anomalies may be explained by the presence of a reverse east-west shear on the mineralization; the alteration pipe would be strung out into a pseudo-strataform distribution to the west of the massive sulfide lens. This interpretation is unacceptable however as the inferred shear at the prospect and the regional shear has an east-west thrust sense (Chapters 1 and 3). An east-west thrust would produce a strung out alteration pipe to the east of the deposit, not to the west.

Options other than shearing with an east-west reverse sense that explain the distribution of base metals include: (1) base metal mineralization along stratiform permeable zones below the massive sulfie lens, or (2) the previous existance of a massive sulfide lens along the western edge of the prospect that has either been displaced by the upper quartz-feldspar porphyry or has been faulted out. The latter option may not be proven one way or the other with the present data. The former option also cannot be proven, but is supported by the presence of fragmental textures within many of the base metal-rich zones in the footwall alteration zone (c.f. Fig. 17c). Fluids flowing along aquifers laterally from the main fluid flow may have mixed with inflowing seawater to precipitate metals. Due to lack of drilling, however, the cause of base metal-rich alteration to the west of the massive sulfide lens at Dry River South remains engmatic.

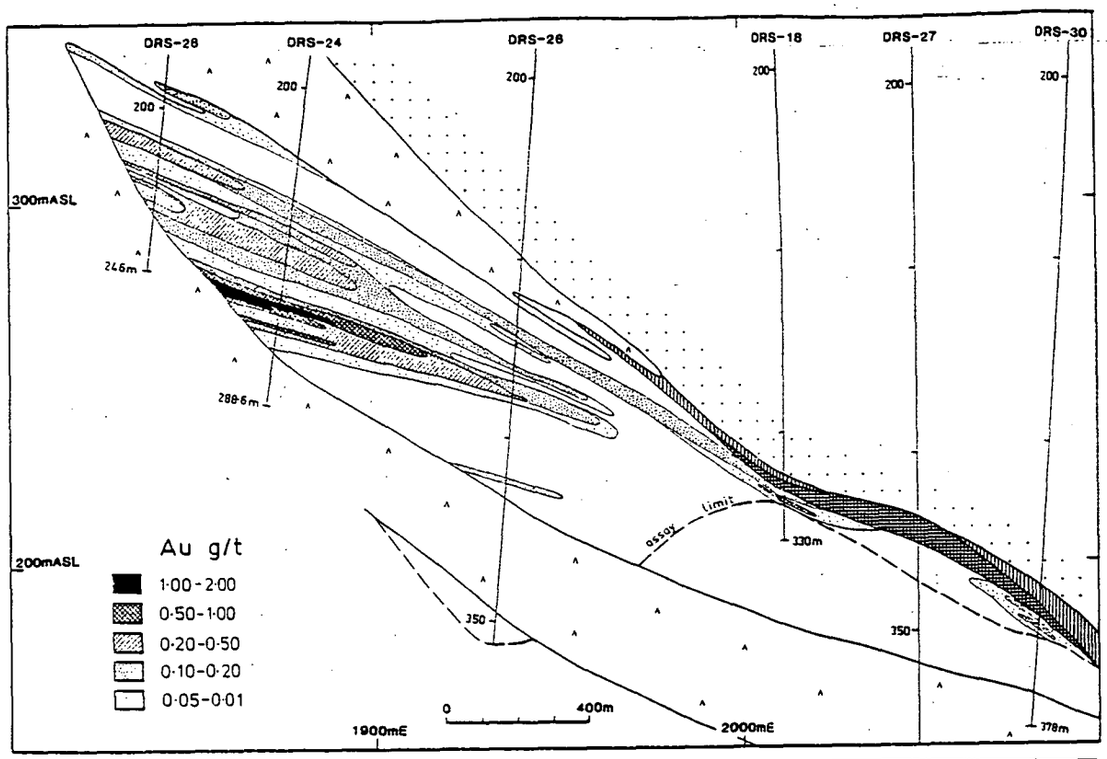

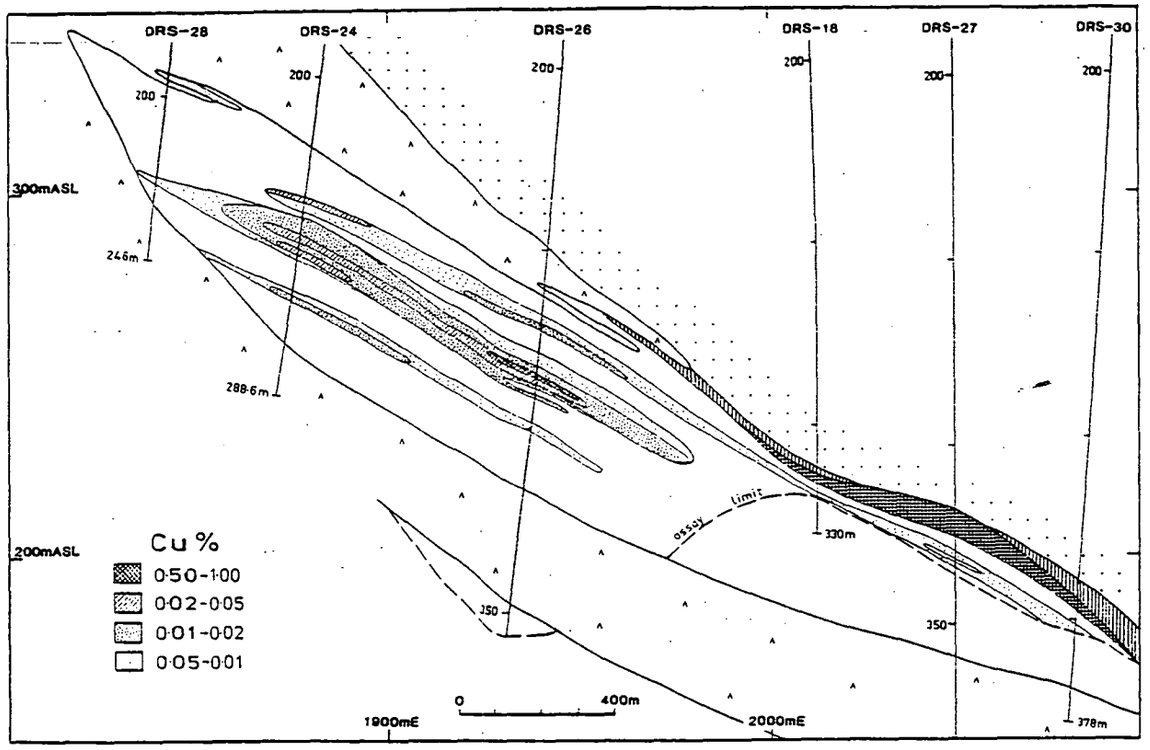

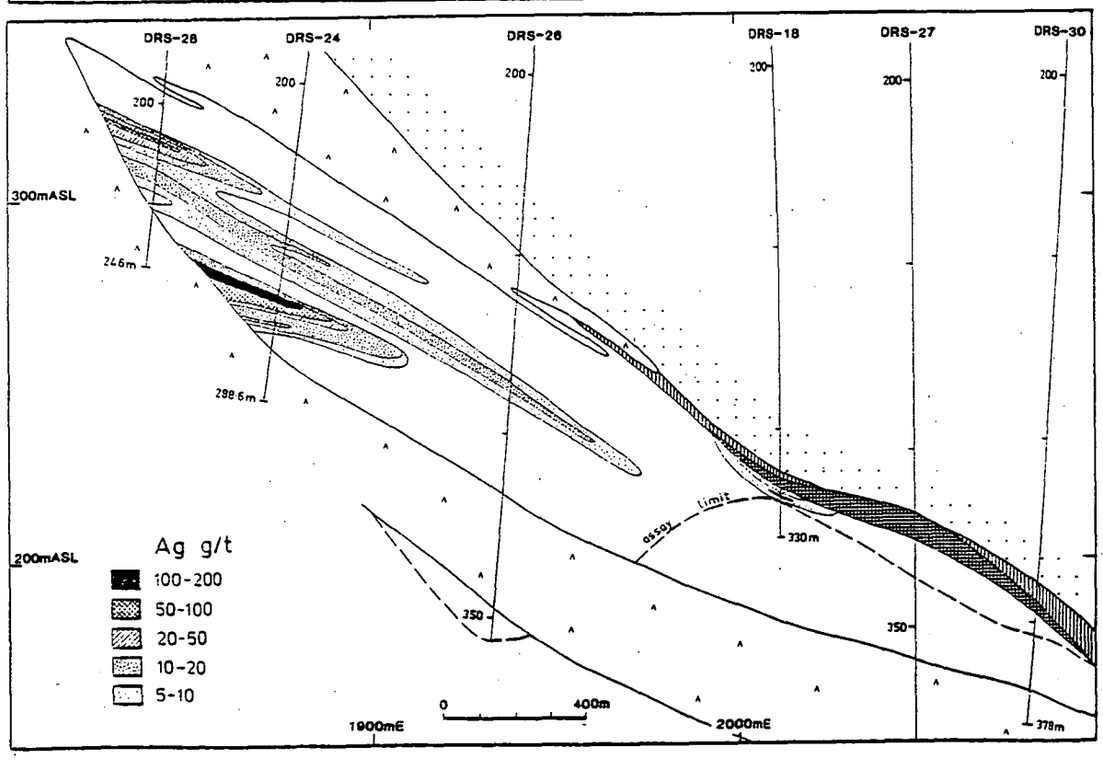

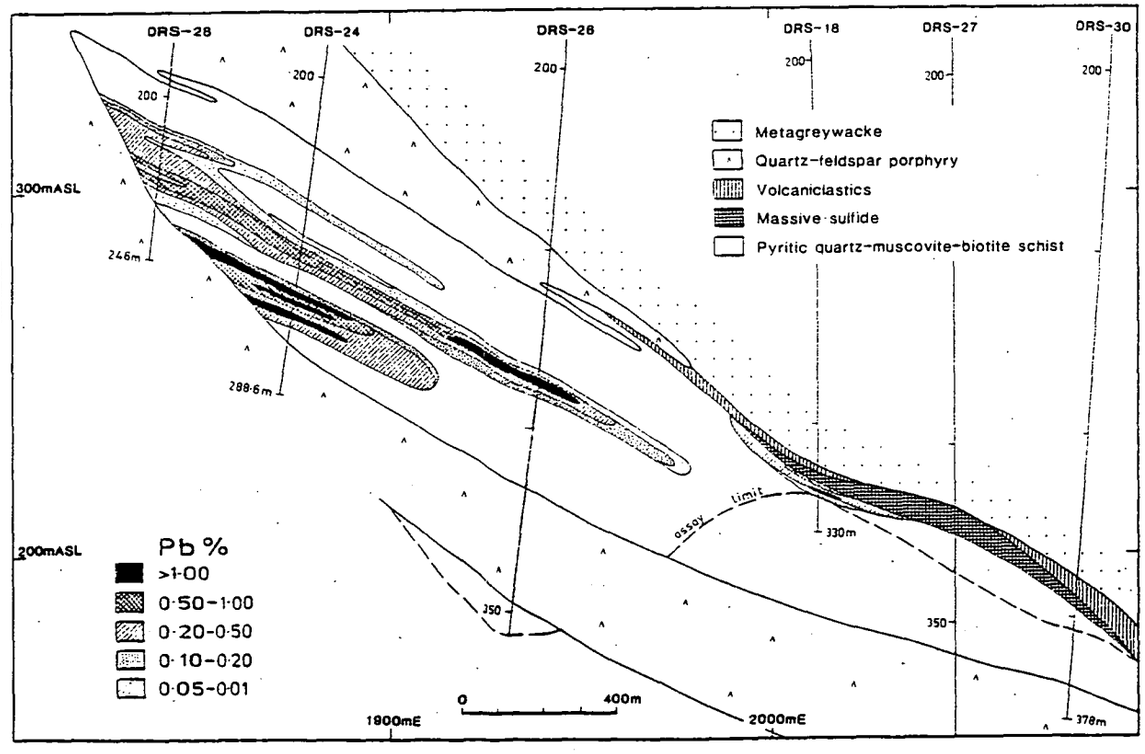

Figure 53. Distribution of gold, copper, silver and lead from section 5700 mN, Dry River South prospect.

Trace metals

Twenty composite samples of massive sulfide (eight of massive pyrite-chalcopyrite and twelve of massive pyrite-sphalerite-galena) were analyzed for Carpentaria Exploration Company by Australian Laboratory Services using inductive coupled plasma analysis. The results are tabulated in Appendix 2 and selected scattergrams are presented in Figure 54. In Figure 54 open squares signify samples of massive pyrite-sphalerite-galena whereas solid squares signify samples of massive pyrite-chalcopyrite.

The distribution of trace elements at Dry River South differs in many ways from that at Balcooma and Rosebery (Part 2, Chapter 2). In particular the metal associations of bismuth and antimony differ. Whereas bismuth has a strong correlation with both copper and gold at Balcooma, this correlation does not exist at Dry River South. Moreover, the concentration of bismuth does not differ significantly between massive pyrite-sphalerite-galena and massive pyrite-chalcopyrite. This differs from observations made at Rosebery (Part 2, Chapter 2) and the Stekkenjokk deposit in Sweden (Zachrisson, 1982) where bismuth is concentrated in copper-rich ores. Bismuth at Dry River South does, however, have a strong positive correlation with silver in massive pyrite-sphalerite-galena. This contrasts to the strong association between silver and antimony at Rosebery (Part 2, Chapter 2). In fact, silver does not correlate with antimony at Dry River South. The relatively low antimony content (less than 100 ppm) of the Dry River South massive sulfide accounts for the rarity of antimony bearing phases (Chapter 7).

The association of cadmium and gallium with zinc is best interpreted as the result of small amounts of cadmium and gallium in sphalerite. Patterson (1986b) noted the presence of tin minerals in galena and the association of cassiterite with sphalerite, which explains the association of tin with zinc. Tin has been noted at several deposits in the Canadian shield, with the best example being Kidd Creek (Walker et al., 1975) where the ores contain up to 3% tin.

The Dry River South and Balcooma deposits are anomalous for polymetallic Phanerozoic massive sulfide deposits in that both lack barite. Barium analyses at Dry River South are always less than 700 ppm. The barium present has no significant correlation to other elements.

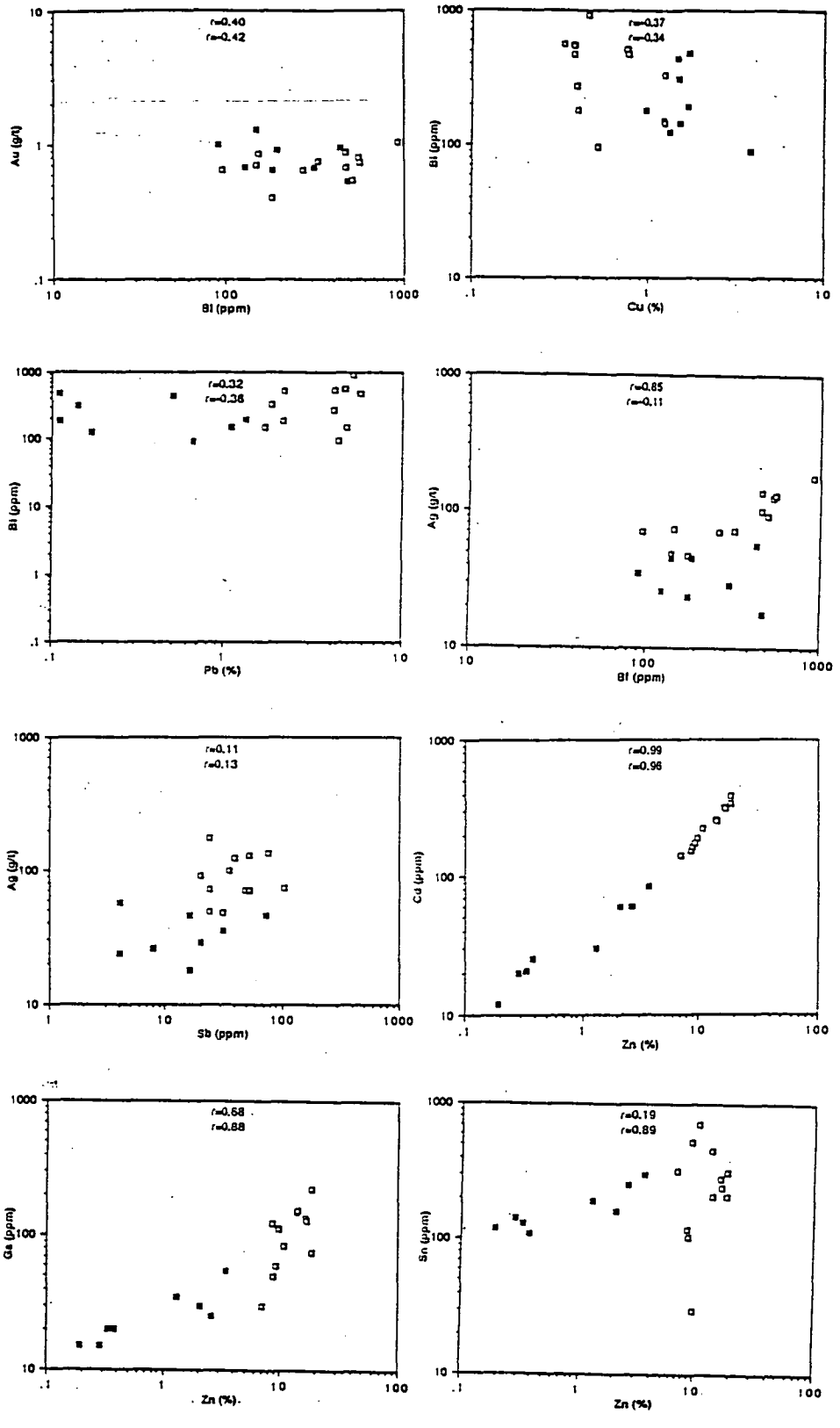

Figure 54. Scattergrams showing the relationships between selected elements in Dry River South massive sulfide. Open squares and upper correlation coefficients are from massive pyrite-sphalerite-galena. Solid squares and lower correlation coefficients are from massive pyrite-chalcopyrite.

Chapter 6
Metamorphism in the Balcooma massive sulfide district

Introduction

The Balcooma metamorpic belt have undergone at least four cleavage forming deformation events. Metamorphic mineral growth has accompanied at least two of these events, and the common presence of staurolite, andalusite and cordierite in the rocks indicates at least lower amphibolite conditions during peak metamorphism.

In order to understand the effect of metamorphism on sulfide mineralization at Balcooma and Dry River South and to determine the timing of mineralization, the metamorphic history of the country rocks must be determined. This chapter describes the metamorphic history of the region based on silicate petrography and metamorphic petrogenesis. The effects of metamorphism on alteration and the usefulness of the zinc content of staurolite as an exploration tool are also discussed. Chapter 7 describes the effect of metamorphism on sulfide minerals, and attempts to set limits on the timing of mineralization.

Growth of metamorphic minerals

The pelitic schists at Balcooma and Dry River South provide information about the metamorphic history due to the variety of metamorphic minerals developed. Conversely, metagraywackes and metavolcaniclastic rocks in the region provide little information of the metamorphic history due to their lack of characteristic mineral assemblages.

F. Van der Hor (1986) undertook microstructural studies to determine the sequence of metamorphic crystallization in metapelites from the Balcooma prospect as part of his Ph.D. studies. The small amount of microstructural study undertaken by the author confirms the general results of Van der Hor (1986) with slight modifications (Fig. 55).

Muscovite can be demonstrated to have been stable since the development of S_2 when it crystallized to form the dominant S_2

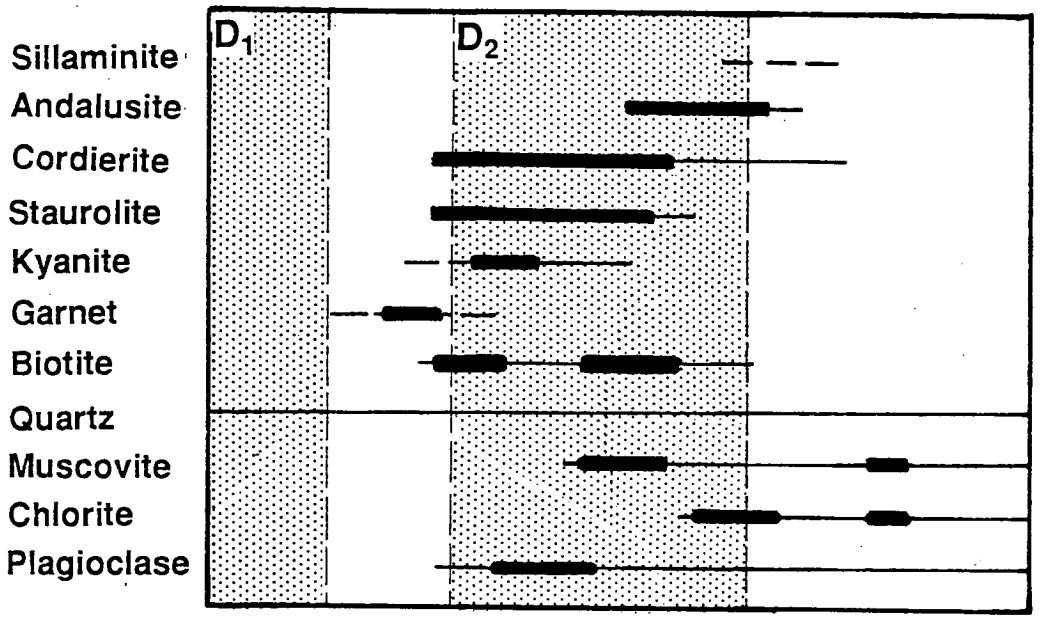

Figure 55. Mineral growth in pelitic schists from the Balcooma and Dry River South prospects. Thin lines indicate periods of demonstrable mineral stability and thick bars indicate periods of mineral growth or crystallization. Revised after Van der Hor (1986) based on observations in the present study.

cleavage with biotite (Figs. 56a and 56b). In the presence of biotite porphyroblasts, muscovite forms a discontinuous S_2 cleavage that wraps around both biotite and staurolite porphyroblasts (Figs. 56b). Minor sericite growth also occurred late in the metamorphic history as staurolite porphyroblasts may be replaced extensively by a mixture of sericite and chlorite with an anomalous birefringence.

Garnet is the earliest formed porphyroblastic phase and commmonly includes relic S_1 cleavage. Garnets are pre- to syn-kinematic with respect to D_2 as S_2 always wraps around them. They are the first formed porphyroblast as they are often included in porphyroblasts of biotite, cordierite and staurolite (Fig. 56c).

Biotite, staurolite and cordierite porphyroblasts formed early during D_2 as the S_2 foliation party wraps around them (Figs. 56a, 56b and 56d). Porphyroblastic biotite often is replaced and pseudomorphed by staurolite (Fig. 56d), but this texture is interpreted as an equilibrium texture where the higher crystalloblastic strength of staurolite has enabled it to overgrow contemporaneous biotite.

In the Balcooma snowball schist, cordierite porphyroblasts grew early during D_2 as discussed previously (Fig. 56a). Van der Hor (1986) did not recognize this early growth of cordierite. Rather, he interpreted syn- or late-kinematic growth of cordierite based on textures where cordierite and chlorite appear to replace biotite and staurolite. The same textures have been recognized in this study, but have been interpreted as an equilibrium texture. This growth is thought to be a syn- or late-kinematic late D_2 texture (Fig. 55).

Andalusite is also a syn- to late-kinematic D_2 mineral. Often it grows in equilibrium with staurolite, but it overgrows biotite porphyroblasts in a similar manner to staurolite. This is also interpreted to be a equilibrium texture brought about by the high crystalloblastic strength of andalusite relative to biotite. In some sections, andalusite overgrows the S_2fabric, which indicates that locally it is a post-kinematic phase (Fig. 56e). Sections that contain andalusite are often poor or lacking in muscovite, which indicates that andalusite may have grown at the expense of muscovite. Some late retrogressive alteration of andalusite may occur locally as

Figure 56. Photomicrographs of textures in pelitic schist from Balcooma and Dry River South: (a) syn-kinematice D_2 cordierite (cd) porphyroblast with quartz inclusions defining S_1 (23-148.1; crossed nichols), (b) kinked, syn-kinematic D_2 biotite (bi) porphyroblast wrapped by S_2 foliation defined by muscovite (3-138.5), (c) staurolite (st) porphyroblast with an included garnet porphyroblast (3-128.8), (d) Poikoloblastic staurolite porphyroblast with solid areas where biotite has been overgrown (DRS27-255.9), (e) andalusite (and) overgrowing S_2 foliation (DRS25-129.0), (f) chlorite (chl) replacing biotite and overgrowing S_2 (23-174.5), and (g) cordierite rimming and replacing a solid staurolite porphyroblast from quartz-chlorite schist (12-160.0; crossed nichols).

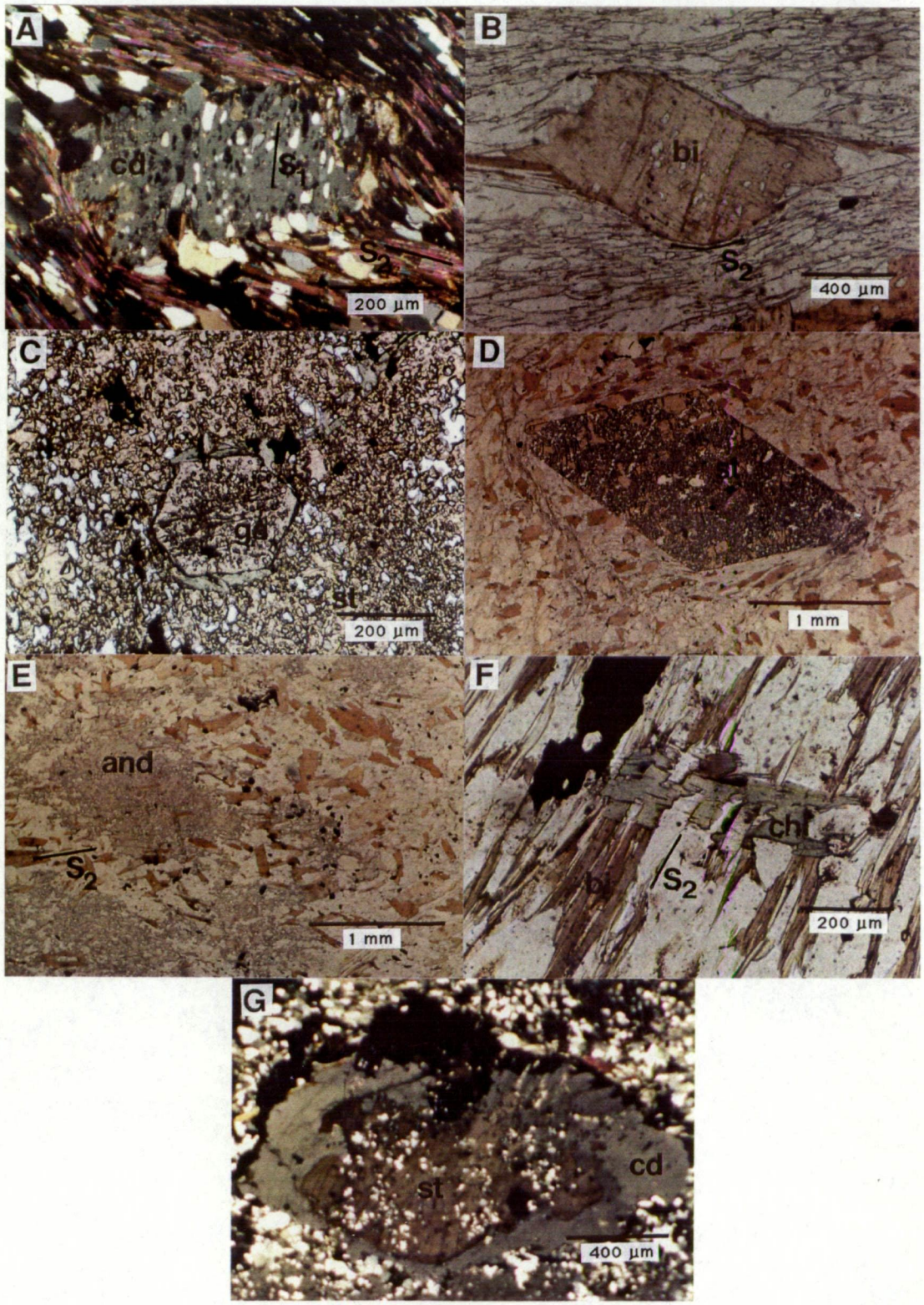
A
cd
S_1
S_2
200 µm
B
bi
S_2
400 µm
C
gt
st
200 µm
D
1 mm
E
and
S_2
1 mm
F
chl
S_2
200 µm
G
st
cd
400 µm

in section D860-153.6 a probable andalusite porphyroblast has been entirely sericitized in the vicinity of thin quartz veins.

Plagioclase also occurs as a minor poikiloblastic phase in the Balcooma spotted schists. It includes grains of porphyroblastic biotite, which indicates that it formed either at the same time as or shortly after biotite, staurolite and cordierite. Van der Hor (1986) reported that locally plagioclase may comprise up to 30% of the rock, but this of very limited extent as plagioclase is rare in section and pelitic rocks from Balcooma contain very little Na_2O and CaO (Chapter 4).

Sillimanite developed late during or after D_2 as it typically replaces either muscovite or biotite. This is consistent with the timing inferred by Van der Hor (1986).

Chlorite is a common, retrogressive, minor phase that developed late- or post-kinematic to D_2. Typically, chlorite replaces both porphyroblastic and groundmass biotite (Fig. 56f). In pelitic schists, chlorite may either grow parallel to S_2, or it may overgrow this cleavage with minor kinking related to weak, late S_2 or S_3 cleavage development (Fig. 56f). Growth of chlorite preceeded the onset of the D_3 crenulation event.

Van der Hor (1986) also reported the occurrence of porphyroblastic kyanite (Fig. 55). The occurrence of kyanite was not observed in this study. This may be due to the fact that kyanite has a very restricted geographic occurrence (F. Van der Hor, pers. com.).

Pressure-temperature conditions of metamorphism

Pelitic schists react readily under metamorpic conditions to form a variety of metamorphic minerals which can be used to constrain the pressure and temperature of peak meamorphism. The coexistence of staurolite, cordierite and andalusite during the latter part of D_2 indicates that peak metamorphism occurred at a minimum pressure of between 2.0 and 2.5 kilobars at a temperature of between 550°C and 600°C (Fig. 57). As the mineral compositions used to construct Figure 57 are in the FASH system (i.e. Mg absent), any significant magnesium content of the minerals will cause an underestimation of the true pressure (Turner, 1981). As the staurolites from Dry River

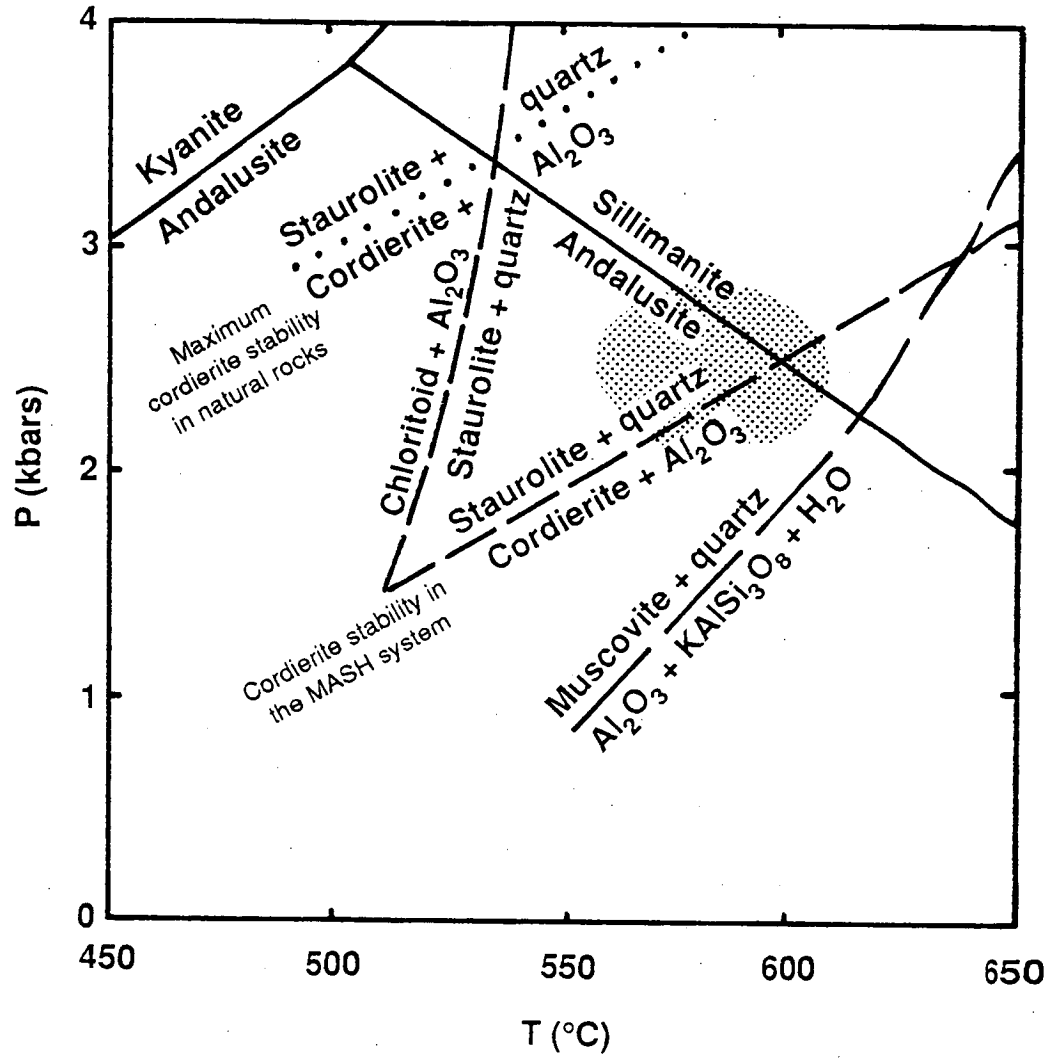

Figure 57. Mineral assemblages in the K-Al-Fe-Si-O-H system showing the conditions of peak temperature metamorphism in the northern part of the Balcooma metamorphic belt (modified after Turner, 1981).

South are relatively iron-rich (Mg number between 21 and 38 for staurolite from the hanging wall metasediments), the underestimation of pressure should be minimal. Van Der Hor (1986) inferred a peak metamorphic temperature of 600°C and a pressure of 2.0 to 2.5 kilobars, but indicates that the presence of early kyanite may indicate a pressure of 3 to 4 kilobars prior to peak temperature metamorphic conditions.

Effect of metamorphism on alteration

The two general types of footwall alteration associated with massive sulfide mineralization have behaved quite differently during metamorphism. Mineralogical changes in quartz-sericite-pyrite alteration zones appear to have been minimal, with the only changes being reaction of chlorite to biotite. Metamorphic minerals such as staurolite and andalusite are rare in pyritic quartz-muscovite-biotite schist, which is the metamorphosed equivalent of quartz-sericite-pyrite alteration. The most significant effect of metamorphism on this alteration type is recrystallization and the development of a cleavage.

The effect of metamorphism on chloritic alteration at Balcooma, however, has resulted in the crystallization of metamorphic minerals and the development of metamorphic fabrics. The most common porphyroblastic phases are garnet, staurolite and cordierite. Garnet typically occurs in sulfide-poor samples whereas staurolite can also occur in sulfide-rich samples. In quartz-chlorite schists (weak and moderate chloritic alteration), staurolite can be either sieved or solid (Fig. 56g), but in chlorite schists staurolite porphyroblasts tend to be solid. Staurolite has been observed to replace gahnite in several samples (e.g. 12-146.8; see also Fig. 56g). Cordierite occurs almost exclusively as rims that corrode staurolite porphyroblasts, and it is replaced by a yellowish brown chlorite-like or serpentine-like mineral (Fig. 56g).

Biotite occurs both as porphyroblasts in strong chloritic alteration and as fine grained, foliated grains in weak or moderate chloritic alteration. Biotite is commonly retrogressed to chlorite, but biotite and chlorite often show equilibrium intergrowths. These two minerals often form the predominant S_2 foliation in these rocks. This contrasts to unaltered or weakly altered rock types where

chlorite is strictly a retrogressive mineral that formed late during or after D_2.

Chlorite

The occurrence of equilibrium D_2 chlorite in zones of chloritic alteration may relate to the high magnesium content of these alteration zones (Chapter 4). The magnesium enrichment of the alteration is also reflected in the composition of the chlorites. Microprobe analyses of chlorite from this study and Patterson (1986a) indicate that the Mg number of chlorite from the Balcooma chloritic alteration zones have a restricted range of between 58 and 72. As the stability of magnesium-rich chlorite extends up to 730°C (Jenkins and Chernosky, 1986), chloritite was probably stable through conditions of peak metamorphism although recrystallization has destroyed all textural evidence of early formed chlorite and probably has changed the composition.

Bryndzia and Scott (1987) calibrated a petrogenetic grid based on the activity of daphnite ($FeAl_{0.4}Si_{0.6}O_2(OH)_{1.6}$) in coexistance with quartz, aluminosilicate, magnetite, pyrite and pyrrhotite. With the exception of aluminosilicate, all of these minerals are relatively common in the Balcooma alteration pipe although the whole assemblage is not commonly present in a single thin section. Despite these problems, the conditions estimated using chlorite compositions assuming andalusite stability (2.5 kilobars and 575°C) are remarkably close to the conditions estimated using the metamorphic assemblage in pelitic wall rocks (2.5 to 3.0 kilobars and 550°C to 600°C).

Stable isotope systematics

To provide more information on water-rock interactions in the Balcooma chloritic alteration zone, four chlorite mineral separates and two biotite mineral separates were analyzed for oxygen and hydrogen isotopes (Table 8). Oxygen isotopes were analyzed as before, whereas hydrogen isotopes were analyzed by combustion with Cu_2O and the reduction of the collected water on zinc (Durham et al., 1982) by M. Power, Sr., C. Cook and the author. The results have little variation in both isotopes, and the chlorite separates have

Table 8. Results of oxygen and hydrogen isotope analyses of Balcooma mineral separates. Fractionation data for chlorite from Taylor (1979) and Graham et al. (1987). Fractionation data for biotite from Shieh and Schwarcz (1974), Clayton et al. (1972), and Suzuoki and Epstein (1976) using a biotite composition of $(K_{.78}Na_{.07})(Fe_{.09}Mg_{1.38}Al_{.48})Al(Al_{.22}Ti_{.04}Si_{2.74})O_{10}(OH)_2$, which is the average of three microprobe analyses of biotite from 39-140.4. All values relative to SMOW.

Sample	Coexisting water					
			300 °C		550 °C	
	δD	$\delta^{18}O$	δD	$\delta^{18}O$	δD	$\delta^{18}O$
Chlorite						
16A-141.2	-67	1.9	-32	1.9	-39	4.4
39-140.4	-69	2.3	-34	2.3	-41	4.8
40-311.0	-66	2.9	-31	2.9	-38	5.4
L920-163.2	-69	2.3	-34	2.3	-41	4.8
Biotite						
39-140.4	-66	3.1	---	---	-34	5.9
L920-163.2	-68	2.0	---	---	-36	4.9

similar isotopic compositions to the biotite separates. In order to determine whether the chlorites equibrated with a hydrothermal fluid or a metamorphic fluid, the isotopic composition of coexisting waters were calculated at 300°C (likely hydrothermal temperature) and 550°C (peak metamorphic temperature). The results of these calculations are also tabulated in Table 8 and illustrated in Figure 58.

Pisutha-Arnond and Ohmoto (1983) estimated that the hydrothermal fluid that produced massive sulfide mineralization in the Kuroko district had δD values of between -30 permil and +15 permil and $\delta^{18}O$ values of between -6 permil and +4 permil. If 300°C is accepted as a probable temperature for the formation of hydrothermal chloritic alteration, the Balcooma chlorites were in equilibrium with a fluid with δD values ranging betweem -31 permil and -42 permil, and $\delta^{18}O$ values ranging between 1.9 permil and 2.9 permil. Although the Balcooma $\delta^{18}O$ values are compatible with the Kuroko fluids, Balcooma δD values are significantly lower than those from Kuroko fluids. This implies that a simple Kuroko analogy is not appropriate for fluids in equilibrium with Balcooma chlorites.

Two alternative explanations exist for the deviation of the fluids in equilibration with Balcooma chlorites from Kuroko fluids: (1) volcanogenic fluids during the Cambro-Ordovician had significantly different isotope signatures that the Kuroko fluids; or (2) Balcooma chlorites re-equilibrated with later fluids (e.g. metamorphic fluids). Taylor (1979) estimated that Phanerozoic ocean water may have been up to 10 permil lighter in deuterium than at present owing to glacial melting. If the same sort of evolution that produced Kuroko fluids applied to seawater 10 permil lighter in deuterium, the range in δD values would decrease by 10 permil. Specifically, a Kuroko fluid derived from seawater with a δD of -10 permil would have a δD range between -40 and +5 permil. The fluids in equilibrium with Balcooma chlorite at 300°C straddle the lower boundary of this inferred field. Although it is possible that the fluids in equilibrium with Balcooma chlorites were of volcanogenic origin, a more likely interpretation is that the chlorites re-equilibrated with later fluids.

The most likely fluid for the chlorite to have re-equilibrated with is a metamorphic fluid. To test this, the isotopic composition of a fluid in equilibrium with Balcooma chlorites was calculated at a peak metamorphic temperature of 550°C (Table 8). The calculated

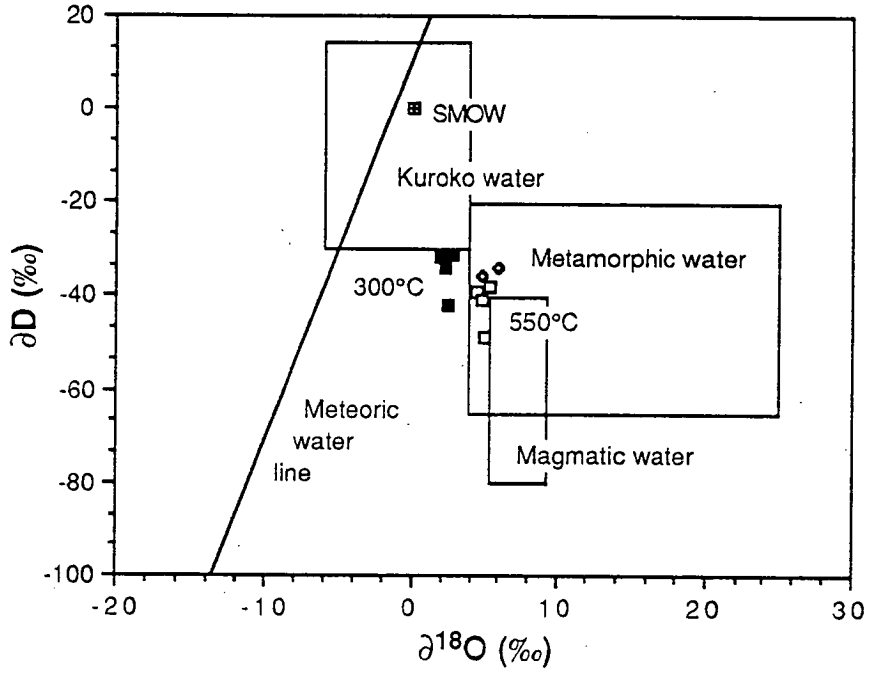

Figure 58. δD-$\delta^{18}O$ diagram illustrating possible fluids in equilibrium with Balcooma chlorite (meteoric water line, magmatic and metamorphic boxes after Taylor (1979) and Kuroko ore fluid box after Pisutha-Arnond and Ohmoto (1983)). Solid squares indicate fluids in equilibrium with chlorite at 300 °C (hydrothermal fluids), and open squares indicate fluids in equilibrium with chlorite at 550 °C (metamorphic fluids). Open diamonds indicate fluids in equilbrium with metamorphic biotite at 550 °C.

isotopic composition falls within the metamorphic box of Taylor (1979) which is consistent with re-equilibration of the Balcooma chlorites with a metamorphic fluid. This interpretation is supported by the similarity of the isotopic composition of fluids in equilibrium with chlorite to those in equilibrium with metamorphic biotite at 550°C (Fig. 58 and Table 8).

The zinc content of staurolite--implications for exploration

Patterson (1986a) noted the presence of zinc-rich staurolites (3.73% to 4.22% Zn) from "random" samples within the Balcooma ore-grade zone. Subsequent analyses of staurolites from schists adjacent to the deposit varied from nil to 0.65%, increasing in general from "unaltered" to "altered" (Patterson, 1986b).

Patterson (1986a) also noted that M. Rubenach (James Cook University) has reported zinc-rich staurolite (up to 4.18% Zn), which formed under physicochemical conditions near the staurolite-in and staurolite-out isograds, from the Robertson River metamorphics. Ashworth (1975) noted that staurolite grains formed under higher grade conditions tend to have high zinc values.

Studies by Spry and Scott (1986) indicated that the zinc content of staurolite grains in pelitic schists varies from nil to 6%, with the vast majority falling below 3%. The zinc content of staurolite grains associated with mineralization varies from 1% to 9%, with the majority falling above 6% (Spry and Scott, 1986).

This information suggests that zinc-rich staurolite grains may be associated with ore grade mineralization or that they may occur in amphibolite grade pelitic scists at particular physicochemical conditions, particularly under upper amphibolite grade conditions. Given this background, 65 staurolite grains from 23 samples collected at 10 m to 15 m intervals along DRS-22, which intersected ore grade mineralization at the Dry River South prospect, were analyzed using a Jeol JX50A microprobe to determine their zinc contents (Appendix 2). The purpose of the exercize was to evaluate the application of the zinc content of staurolite as an exploration tool.

Results and discussion

Figure 59 illustrates the down hole variation of zinc, titanium and the Zn/Ti ratio in staurolite from DRS-22. The following observations are apparent.

Zinc. The distribution of zinc in staurolite (Fig. 62) reflects the distibution of semi-massive to massive sulfide very well. All analyzed staurolite grains between 242.4 m and 266.7 m, which came from samples containing semi-massive to massive pyrite, contained between 2.50% and 6.79% zinc. Only one sample (DRS22-266.7) contained significant chalcopyrite and none contained sphalerite or galena. Staurolite grains from even zinc-poor massive sulfide give good responses, and staurolite grains in coexistance with sphalerite should give better results (Spry and Scott, 1986).

The zinc content of hanging wall staurolite grains, with the exception of those in DRS22-192.7, never exceeds 1.00%, which gives excellent contrast to those associated with massive sulfide mineralization. The zinc content of staurolite varies inversely with the staurolite content of the rock.

Inspection of DRS22-192.7 indicated that the staurolite grains in this sample are related to healed veinlets, and that the sample contains 2% to 3% disseminated opaque minerals--dominantly pyrrhotite with minor chalcopyrite and traces of sphalerite and several unknowns. The anomalous zinc content in staurolite grains from this sample may relate to this minor mineralization.

In the footwall, the zinc contents are similar, but slightly higher (0.43% to 1.25% Zn) than those in the hanging wall. As pyrite is the only sulfide mineral present, there may have not been enough zinc in the mineralization to produce a response in staurolite. Staurolite grains from footwall mineralization with zinc-lead stringers may give a good response, but this was not tested.

The zinc-rich staurolite grains observed in this study tend to be inclusion free, anhedral and veined, whereas staurolite grains that are not zinc-rich tend to be poikoliblastic and subhedral to anhedral in form.

Titanium. An unexpected result of this study is the behavior of titanium (Fig. 59). In the hanging wall, titanium values vary between 0.40% and 0.90% and usually fall between 0.45% and 0.60%. On the other hand, titanium values vary from 0.24% to 0.60% in the footwall and usually lie between 0.30% and 0.50%.

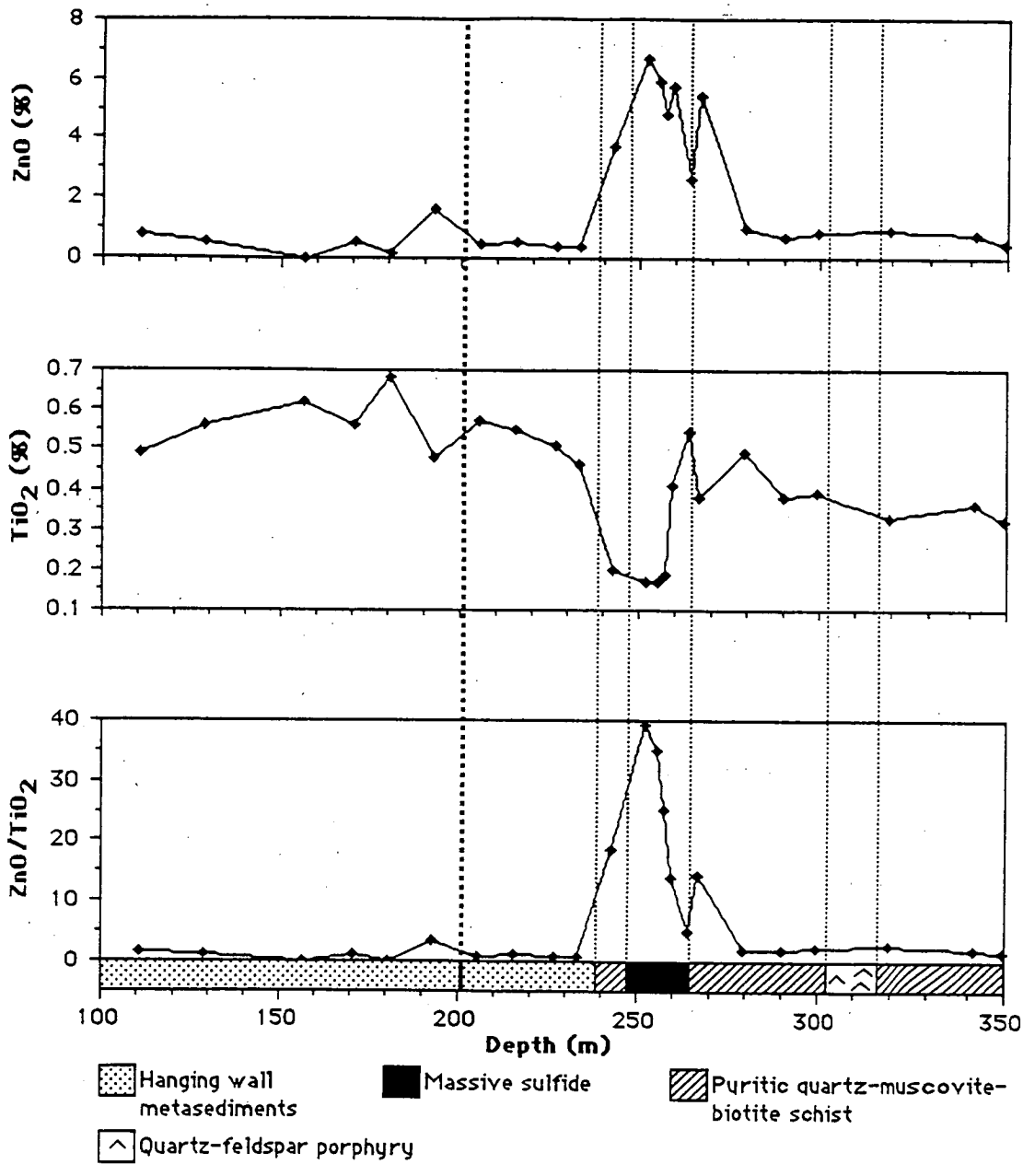

Figure 59. Downhole variation in zinc, titanium and the Zn/Ti ratio in hole in DRS22, Dry River South prospect.

Titanium has an unusual distribution within staurolite grains from semi-massive to massive sulfide. In zinc-rich staurolite grains between DRS22-242.4 and DRS22-257.1, the titanium content of staurolites is anomalously low (0.12% to 0.32%), while zinc-rich staurolite grains between DRS22-259.1 and DRS22-266.7 have titanium values similar to those from the footwall (0.31% to 0.61%).

Hutchinson and Searle (1971) demonstrated that syngenetic, exhalative mineralization contains little titanium, whereas intense, epigenetic stringer mineralization retains the signature of the footwall lithology due to the immobility of titanium. This suggests that zinc-rich, titanium-poor starurolite grains developed from syngenetic mineralization, whereas zinc- and titanium-rich staurolite grains developed from intense epigenetic mineralization. Based on independent drill core logging, the seawater interface at the time of mineralization has been placed at 256.9 m which is consistent with the break in titanium values.

A significant problem in using the zinc content of staurolite as an exploration guide is the possibility that zinc-rich staurolite grains may develop from unmineralized metapelites. Four analyses of zinc-rich staurolite grains from unmineralized metapelite rocks in Deer et al. (1982) have titanium contents ranging from 0.58% to 0.88%, and two analyses of zinc-rich staurolite grains from the Robertson River Metamorphics have titanium contents of 0.38% and 0.55%, respectively (Patterson, 1986a). Based on these limited analyses, the titanium content of zinc-rich staurolite grains associated with exhalative mineralization would be expected to be low, while the titanium content of zinc-rich staurolite grains associated with metapelites or footwall alteration zones would be higher. Thus, the discovery of zinc-rich staurolite grains with low titanium (< 0.30% Ti) would be of more interest than those with high titanium. This hypothesis needs further testing.

To improve the contrast between the hanging wall, the massive sulfide horizon and the footwall, the Zn/Ti ratio was calculated and plotted in Figure 59. Altered footwall rocks have an elevated Zn/Ti compared to the hanging wall metasediments, and samples from semi-massive to massive sulfides have the highest values, with greater contrast than using zinc content alone.

Application to exploration

The zinc content of staurolite readily defines massive sulfide mineralization at the Dry River South prospect. Unmineralized hanging wall metasediments do not produce the zinc-rich staurolites seen in other metapelitic terranes. Technically the zinc content of staurolites is an excellent guide to massive sulfide mineralization in amphibolite grade metamorphic terranes.

The practical value of the method is a different matter. As there is no significant halo above and only a weak halo below massive sulfides, the technique is only useful to characterize massive sulfide mineralization--a rock type which should be picked up by any competent geologist. The lateral distribution along the massive sulfide horizon is as yet untested, so at this time the technique would not yield new information as a down-hole exploration technique.

In a reconnaissance program the technique holds more promise. Staurolite is both a dense and resistate mineral, so staurolite collection via heavy mineral concentrates in the drainage system may be a guide to massive sulfide mineralization.

Chapter 7
Mineragraphy of Balcooma and Dry River South mineralization

Introduction

Due to the intensity of deformation and metamorphism in the Balcooma metamorphic belt, primary sulfide textures from the Balcooma and Dry River South deposits have been destroyed and replaced by textures developed during regional metamorphism. The ore mineralogy of the Balcooma prospect has been described in an internal company report by Patterson (1981), and sulfide minerals from Dry River South have been described in reports by Patterson (1986b), Fehne (1986) and Joyce (1986). Additionally, the author has examined over 100 sections from both deposits in the present study. The ore minerals and textures are more or less typical of strongly deformed and metamorphosed volcanogenic massive sulfide deposits (c.f. Vokes, 1969, 1971; Stanton, 1972; and Gilligan and Marshall (1987)).

Ore minerals and textures

Compared to the well banded, fine grained ores at Rosebery (Brathwaite, 1969) and Woodlawn (McKay and Hazeldene, 1987), the Balcooma and Dry River South ores are more massive. In particular, copper-rich massive sulfide tends to be massive, and in chalcopyrite-rich samples, pyrite prophyroblasts are commonly fractured or brecciated. Zinc-lead-rich massive sulfide can be either massive or banded with 1-5 cm alternating pyrite-rich or sphalerite-rich bands. This banding may be folded by F_3 folds (Fig. 19b). Owing to the intensity of deformation and the lack of exposure, the origin of the banding (i.e. primary or deformational) can not be resolved.

Over twenty separate opaque minerals have been observed at the Balcooma and Dry River South prospects (Patterson, 1981, 1986b; Fehne, 1986; Joyce, 1986; and this study). Of the minerals observed, six (pyrite, magnetite, pyrrhotite, chalcopyrite, sphalerite and galena) occur as major ore minerals, whereas numerous others occur in minor or trace quantities.

Major ore minerals

Pyrite and marcasite. Pyrite by far is the dominant sulfide mineral in the Balcooma and Dry River South prospects. In massive sulfide, pyrite typically comprises between 40% and 90% of both copper-rich and zinc-lead-rich samples. The most common habit for pyrite is as coarse (0.5-10 mm) porphyroblasts that are commonly veined or corroded by other minerals, including magnetite, chalcopyrite, pyrrhotite, spahalerite and galena(Fig. 60a). In pyrite-rich zones, pyrite commonly loses the idioblastic form and occurs as annealed, polycrystalline aggregates. Pyrite commonly contains poikiloblastic inclusions of chalcopyrite and pyrrhotite which indicates the presence of these minerals during porphyroblast growth. Pyrite is commonly fractured, with fractures filled by siderite (Fig. 60b). This texture occurs more commonly at Dry River South where faulting, both during and after metamorphism, appears to be more important (Chapter 4).

Pyrite also has two other habits, both of which developed after porphyroblastic pyrite (Fig. 60c). In the first of these habits, pyrite is intimately intergrown with marcasite in a "birds eye" texture which Ramdohr (1969) interpreted as an alteration product of pyrrhotite. In the second habit, pyrite is delicately intergrown with magnetite in interstices between porphyroblastic pyrite (Fig. 60d). This texture is interpreted as the result of hypogene oxidation of pyrrhotite (Picot and Johan, 1982); locally pyrite-magnetite intergrowths with this texture partially alter pyrrhotite.

Pyrite crystallized during D_2 as idioblastic pyrite occurs parallel to the pervasive S_2 foliation in chloritic schists (Fig. 60e). Other sulfides are also recrystallized into S_2. This implies sulfide (re)crystallization must have occurred during D_2 which is consistent with the interpretation that the Harvey lens at Balcooma was mobilized into the antiform at this time (Chapter 2).

Magnetite. Magnetite is the second most common mineral in the copper shoots at Balcooma. Massive zones of magnetite over 10 m wide have been intersected in core. Outside of these zones, magnetite commonly is a major constituent of massive pyrite-chalcopyrite mineralization, but it is only a minor or trace constituent of massive pyrite-sphalerite-galena mineralization. The Dry River South

Figure 60. Photomicrographs showing sulfide textures: (a) pyrite (py) porphyroblast veined by chalcopyrite (cp) and pyrrhotite (po; 16A-135.9), (b) intensely fractured pyrite with fractures filled by carbonate (car; DRS15-196.3), (c) pyrite and marcasite (py/mar) intergrown in "birds eye texture" after pyrrhotite which originally veined a fractured pyrite porphyroblast (DRS46-405.6), (d) delicate intergrowth of pyrite and magnetite (mt) in the interstices of pyrite porphyroblasts (12-153.5), (e) elongate pyrite porhyroblasts and anhedral chalcopyrite growing parallel to S_2 (42-271.8), (f) magnetite porphyroblast veined by carbonate (16A-135.9), (g) radiating, acicular needles of magnetite surrounding a molybdenite (mo) grain (4-98.9), and (h) intergrowth of chalcopyrite, sphalerite (sl) and galena (gn) that surrounds and corrodes pyrite porphyroblasts (24-131.1).

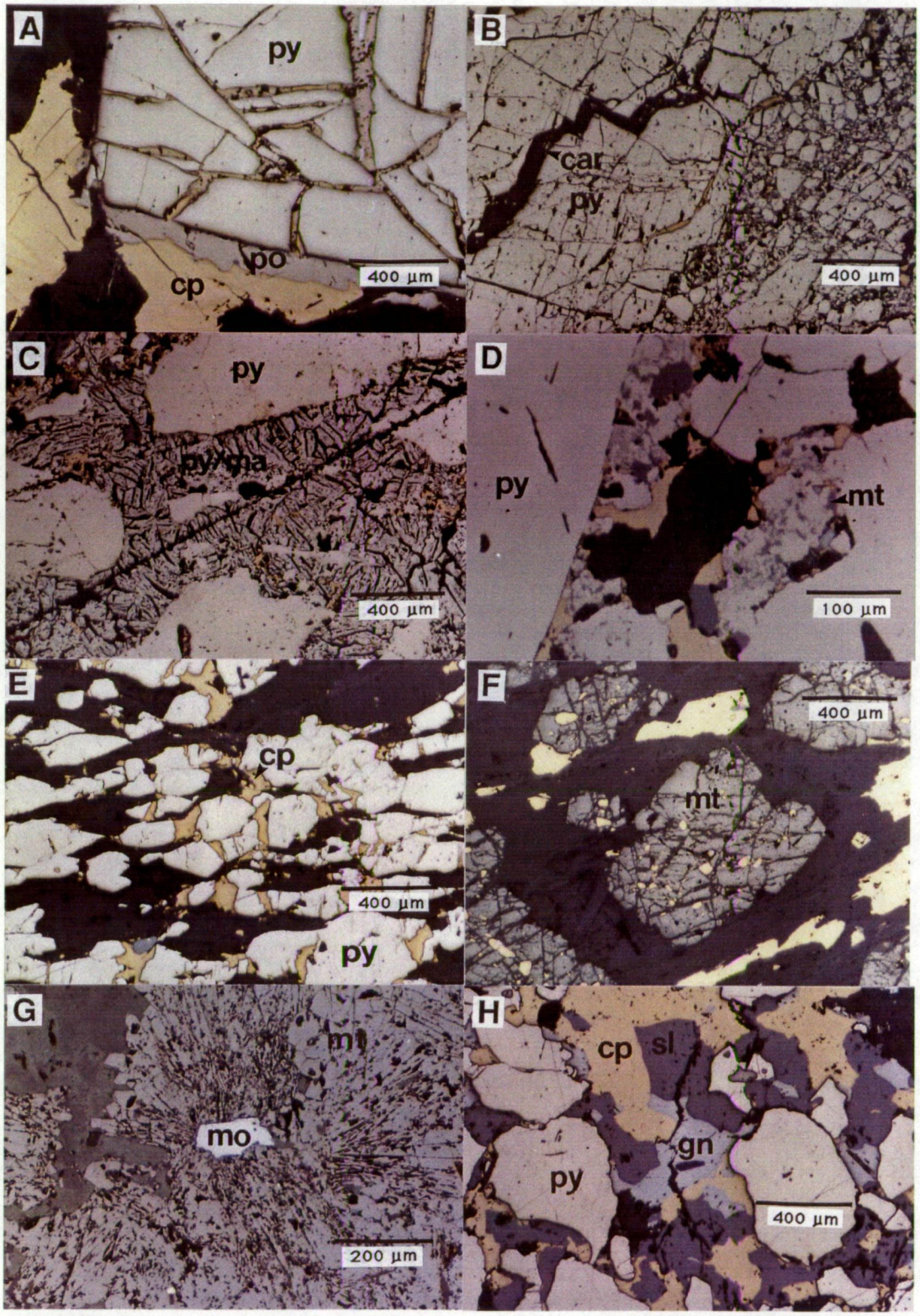
A
py
po
cp
400 µm
B
car
py
400 µm
C
py
py/ma
400 µm
D
py
mt
100 µm
E
cp
400 µm
py
F
400 µm
mt
G
mt
mo
200 µm
H
cp
sl
gn
py
400 µm

prospect contains only minor amounts of magnetite, and zones of massive magnetite are confined to thin intersections on the western side (e.g. DRS39).

Magnetite commonly occurs as anhedral polycrystalline aggregates with minor interstitial chalcopyrite. When isolated grains are present, magnetite occurs as subhedra that are commonly fractured (Fig. 60f). When intergrown with porphyroblastic pyrite, magnetite may occupy interstices between pyrite grains or may occur as inclusions within pyrite; this indicates pyrite and magnetite (re)crystallization at about the same time. Another, more unusual habit present in zones of massive magnetite is radiating, acicular needles (Fig. 60g) which are interpreted as pseudomorphs after hematite. Magnetite with this habit usually corrodes pyrite porphyroblasts. Unreplaced hematite laths are occasionally observed in magnetite-rich zones.

Chalcopyrite and pyrrhotite. Chalcopyrite and pyrrhotite are common minerals in copper-rich zones at both deposits although pyrrhotite is much less common at Dry River South. Both minerals also occur in minor quantities in zinc-lead-rich zones at both deposits. The presence of chalocpyrite in the S_2 foliation (Fig. 60e) indicates that this mineral was (re)crystallized during D_2. As pyrite-marcasite intergrowths with birdseye textures (Fig. 60c) and delicate pyrite-magnetite intergrowths (Fig. 60d) indicates the alteration of pre-existing pyrrhotite, the common occurrence of these textures indicates that pyrrhotite was once a more widespread mineral at Balcooma and Dry River South than at present.

Sphalerite and galena. Sphalerite and galena are common minerals in zinc-lead-rich mineralization, but only minor to trace minerals in copper-rich mineralization. In zinc-lead-rich mineralization, sphalerite and galena occur as intergrown, anhedral and annealed 0.05-0.5 mm grains that may also be locally intergrown with chalcopyrite and corrode pyrite porphyroblasts (Fig. 60g). At Dry River South, galena from zinc-lead-rich massive sulfide commonly contains inclusions of native bismuth (Fig. 61a); this has also been noted at Balcooma, but is much less common. Balcooma galena may also contain minor inclusions of bismuthinite.

In copper-rich mineralization, both sphalerite and galena occur sporadically in association with chalcopyrite and pyrrhotite. Galena has a further association with bismuth minerals and occurs in pools

Figure 61. Photomicrographs showing sulfide textures: (a) inclusions of native bismuth (Bi) and tetrahedrite (td) in galena (DRS15-196.5), (b) stannite (sn) replacing chalcopyrite along a carbonate vein (DRS27-323.7), (c) chalcopyrite, native bismuth, galena, gruenlingite (gr) and electrum (el) pool in silicate gangue (RA8011), (d) electrum grain in a chalcopyrite-pyrrhotite vein with bismuth minerals that cuts a strongly fractured pyrite porphyroblast (16A-135.9), (e) two electrum grains associated with native bismuth in galena (40-67.2), (f) electrum grain partly enclosed by spongy pyrite which was plucked during repolishing (40-67.2), (g) electrum grains in a chalcopyrite-galena microveinlet that cuts pyrite and is truncated by sphalerite (12-132.7), and (h) electrum grains in a quartz (qtz)-sphalerite microveinlet between two pyrite grains (DRS15-193.7).

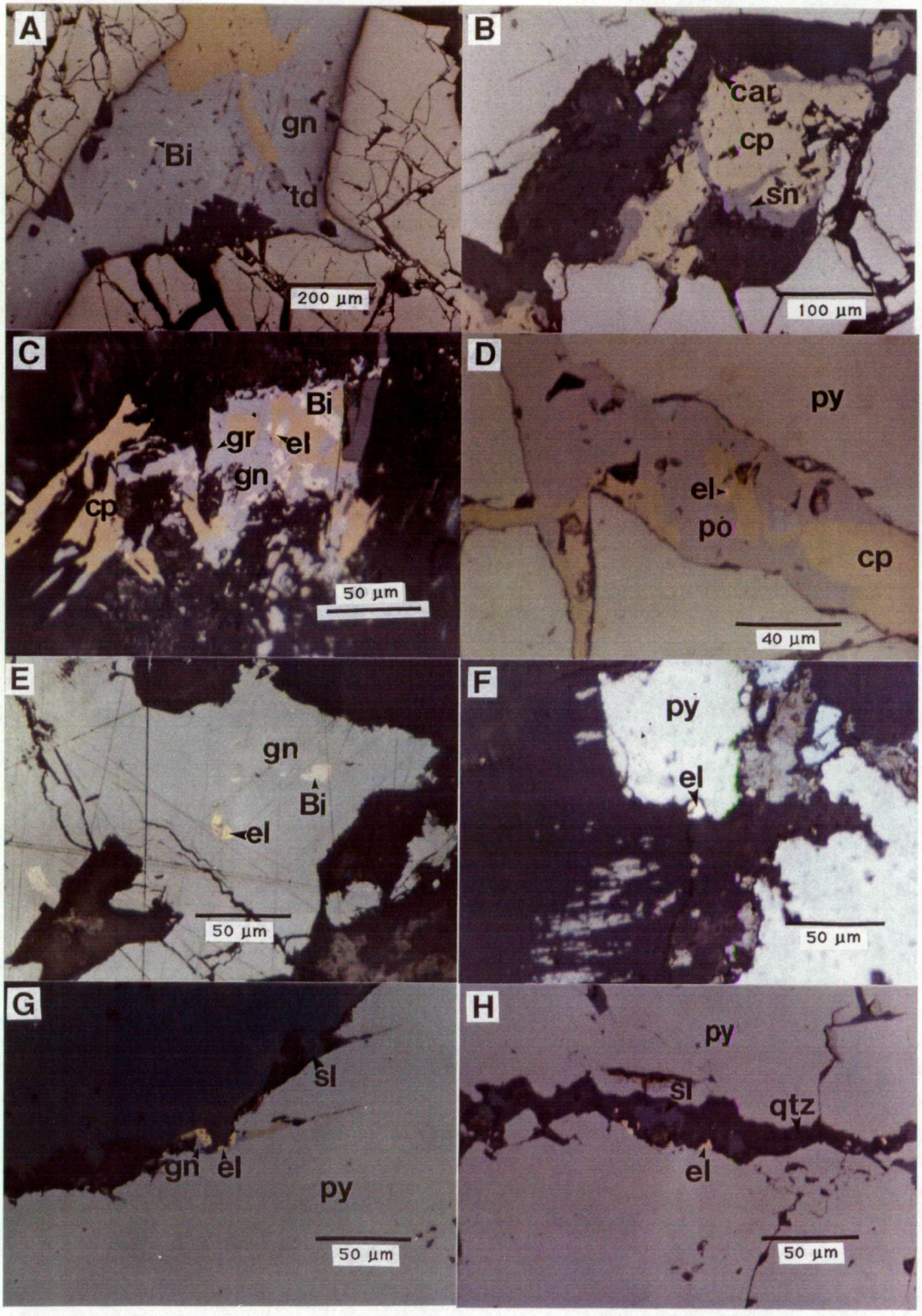
A
gn
Bi
td
200 µm
B
car
cp
sn
100 µm
C
Bi
gr
el
gn
cp
50 µm
D
py
el
po
cp
40 µm
E
gn
Bi
el
50 µm
F
py
el
50 µm
G
sl
gn
el
py
50 µm
H
py
sl
qtz
el
50 µm

with chalcopyrite, naitve bismuth, bismuthinite, bismuth sulfosalts and bismuth tellurides (Fig. 61b). The color of sphalerite in transmitted light is generally deep red to purple in all types of mineralization which may indicate a relatively high iron content although other trace metals (Cd, Mn, etc.) may also cause this effect.

Minor to trace minerals

Hematite, ilmenite and rutile. Hematite occurs as unoriented laths with exsolved ilmenite in chloritic schists in and around massive sulfide lenses at Balcooma. The laths are rare or non-existant in the massive sulfide itself. Patterson (1981) noted that these grains are commonly replaced by bismuth minerals and chalcopyrite in sulfide-rich samples.

Hematite also occurs as rare, needles up to 0.5 mm long in zones of massive magnetite (e.g. sections 24-167.0 and 49-97.0). These grains are interpreted as relic hematite grains preserved after pre-existing hematite was altered to magnetite in these zones (see above).

Rutile occurs as sparse, but ubiquitous, anhedral 0.01-0.05 mm grains included in chalcopyrite and porphyroblastic pyrite from Balcooma massive sulfide. Patterson (1981) notes that it also forms an alteration product of ilmenite.

Molybdenite. Molybdenite is an uncommon accessory mineral at both Balcooma and Dry River South (Patterson, 1981, 1986b). In the present study it was observed largely as thin flakes that commonly parallel the dominant S_2 foliation. The dominant occurrence observed in this study is with massive magnetite, although Patterson (1981, 1986b) noted an association with pyrrhotite, chalcopyrite and/or pyrite.

Arsenopyrite. Arsenopyrite occurs both at Balcooma and Dry River South as trace 0.01-0.2 mm anhedral to euhedral grains in both massive pyrite-chalcopyrite and pyrite-sphalerite-galena mineralization. No particular mineral association was observed.

Tin minerals. Patterson (1986b) noted the presence of several tin minerals at Dry River South; this has since been confirmed in this study. Tin minerals have not been recognized at the Balcooma prospect. Patterson (1986b) reported that euherdral cassiterite and

stannite (Cu_2FeSnS_4) are included in pyrite and sphalerite grains. This study has noted the common occurrence of anhedral, 0.05-0.2 mm grains of cassiterite associated with sphalerite. Stannite has also been observed replacing chalcopyrite along siderite veinlets (Fig. 61b). Patterson (1986b) also noted the presence of a mixture of poorly identified tin minerals (cassiterite or native tin, tin sulfides and stannite) that occur as anhedral patches within galena. The association of tin minerals with sphalerite and galena explains the strong corrrelation between tin and zinc in massive pyrite-sphalerite-galena mineralization at Dry River South (Chapter 6).

Antimony-bearing minerals. Despite the relatively low concentration of antimony at Dry River South (<100 ppm), several trace antimony-bearing minerals have been observed. Patterson (1986b) noted the presence of silver-rich (17-24%), nearly end-member tetrahedrite (24-28% Sb, 0-1% As) as rare anhedral pools in galena. This has since been confirmed by this study (Fig. 61a). Patterson (1986b) inferred, based on these occurrences, that tetrahedrite is the probable major host of silver at Dry River South. This conclusion is considered unlikely for the following reasons: (1) tetrahedrite is a rare mineral and is unlikely to account for the ~90 g/t silver tenor of the mineralization, (2) silver assays do not correlate with antimony analyses (Chapter 6), and (3) antimony values at Dry River South are typically half of the silver assays (Appendix 2). If all antimony is assumed to beld in tetrahedrite and Patterson's (1986b) analyses of tetrahedrite are assumed to be typical, tetrahedrite can only account for roughly 35% of the silver when averaged analyses from Appendix 2 are used. As other antimony minerals (luzonite; Fehne, 1986) are present, the estimate that tetrahedrite accounts for 35% of the silver at Dry River South must be considered a maximum value.

Patterson (1986b) also noted the presence of silver-poor tennantite in association with bismuth minerals and chalcopyrite at Dry River South as well as the occurrence of native antimony in carbonate associated with sphalerite and galena. Fehne (1986) reports the occurrence of antimony-rich luzonite ($Cu_3(As,Sb)S_4$) as vein fillings and inclusions in pyrite, and the possibility of boulangerite ($Pb_3Sb_4S_{11}$) as an inclusion in galena. Patterson (1986b) also reported a Pb-Sb sulfosalt (boulangerite (?)).

The only antimony bearing minerals observed at Balcooma are rare grains of tetrahedrite. As with Dry River South, the probable host mineral to silver is galena in massive pyrite-sphalerite-galena mineralization and chalcopyrite in massive pyrite-chalcopyrite mineralization (Chapter 6).

Bismuth minerals. Patterson (1981) reported the presence of five bismuth phases at Balcooma: native bismuth, bismuthinite, two Pb-Bi-Te-Se-S phases possibly related to galenobismutite ($PbBi_2S_4$) and poubaite ($PbBi_2Se_2(Te,S)_2$), and a bismuth telluride with x-ray pattens indicating a mixture between joseite-A and joseite-B (Bi_3TeS). Semi-quantitative microprobe analysis in this study suggests a composition for the last phase close to that of gruenlingite (Bi_4TeS_3) which has x-ray patterns similar to joseite (Palache et al., 1946). Bismuth minerals generally occur together in pools with chalcopyrite and galena (Fig. 61c). Although bismuth and bismuthinite occur as inclusions in galena in pyrite-sphalerite-galena mineralization at Balcooma in section N875-106.6, bismuth minerals most commonly occur in pyrite-chalcopyrite mineralization.

At Dry River South, native bismuth occurs almost exclusively as inclusions in galena (Fig. 61a). Copper-rich mineralization contains fewer bismuth minerals based on observations in the present study (e.g. DRS15-206.4). These results confirm the generally lower bismuth tenor in massive pyrite-chalcopyrite than massive pyrite-sphalerite-galena at Dry River South (Chapter 6).

Electrum at Balcooma. Patterson (1981) first noted electrum at Balcooma. Additional observations (12 grains in 7 occurrences from 3 sections) by the author indicate that electrum occurs as very fine grained grains (>10 μm) of moderate fineness (670-790 fine) at Balcooma. Electrum grains have a strong association with chalcopyrite, bismuth minerals and galena (Figs. 61c, 61d and 61e). A single electrum grain was noted in association with spongy pyrite (Fig. 61f). Electrum commonly occurs in veinlets and that cut pyrite porphyroblasts. Electrum from zinc-rich mineralization has the same association with chalcopyrite (Fig. 61g) observed in copper-rich mineralization. This mineralogical association with chalcopyrite is consistent with the metal association of copper and gold (Chapter 6).

Electrum at Dry River South. Patterson (1986b) also was the first to notice electrum at Dry River South. He observed an oval

electrum grain with a fineness of 740 and an average dimension of 10 μm in association with chalcopyrite. Although this is very similar to the Balcooma occurrences, subsequent observations by the author (14 grains in 3 occurrences from three polihed thin sections, and numerous grains in a polished block) have indicated very complicated mineral associations and compositions for Dry River South electrum: (1) with chalcopyrite, (2) in a sphalerite-quartz veinlet between pyrite grains (Fig. 61h), (3) in cracks within gahnite grains (Fig. 62a), (4) in a quartz-carbonate vein that fills fractures in strongly fractured massive pyrite (Fig. 62b), and (5) in remobilized chalcopyrite veinlets in the hanging wall metagraywackes (Figs. 62c and 62d). The average grain size varied from 1.5 μm to 60μm and the fineness varied from 490 to 760 fine. Although not verified by microprobe, the electrum in the hanging wall metagraywacke is of high fineness owing to the color in polished block.

This variation in occurrence, grain size and fineness contrasts markedly with the uniform electrum-chalcopyrite-bismuth mineral association, small grain size and uniform fineness present at Balcooma. There has been significant mobilization of electrum during deformation at Dry River South. Evidence for this exists in the presence of electrum in cracks in gahnite, which is a metamorphic mineral, the occurrence of electrum in carbonate veins between strongly fractured pyrite, and the occurrence of electrum in remobilized chalcopyrite veinlets in the hanging wall. Evidence for electrum mobility to this extent does not exist at Balcooma. Electrum mobilization may have been enhanced by the strong shearing that is inferred to have occurred at Dry River South (Chapter 4).

Oxide and supergene minerals

As both zinc-lead-rich and copper-rich lenses crop out up plunge as gossans, secondary weathering is locally a strong factor in enriching the massive sulfide. In some samples from the supergene zones, copper assays may exceed 30%, whereas in the lead gossan, grab samples contain up to 60% lead and 700 g/t silver (Harvey, 1984b).

The gossan over the surface extension of the Harvey shoot is comprised of iron oxides and hydroxides. Harvey (1984b) has inferred that the surface expression of massive sulfide results in iron stained siliceous breccias caused by the dissolution of massive iron oxides produced from the oxidation of massive sulfide by groundwater

Figure 62. Photomicrographs showing sulfide textures: (a) electrum grains associated with chalcopyrite and sphalerite in cracks within a gahnite (gh) porphyroblast (DRS20-197.5), (b) electrum grains in a quartz-carbonate-sphalerite-chalcopyrite veinlet cutting fractured pyrite grains (DRS27-323.7), (c) chalcopyrite-pyrite±sphalerite veins in hanging wall metagraywacke (DRS49-439.6), (d) as before showing electrum grains associated with chalcopyrite veinlets, (e) chalcopyrite replaced by a mixture of chalcocite (cc), covellite (cv) and limonite (li; L920-66.8)), (f) garnet porphyroblast with sygmoidal pressure shadows associated with rotation during D_2 containing inclusions of pyrite and sphalerite in the center (42-271.8), (g) gahnite porphyroblast which is wrapped by S_2 and contains oriented inclusions of pyrite and sphalerite (24-122.2), and (h) alternating pyrite-quartz-rich and muscovite (mus)-rich bands that are overprinted by the pervasive S_2 cleavage (12-122.9).

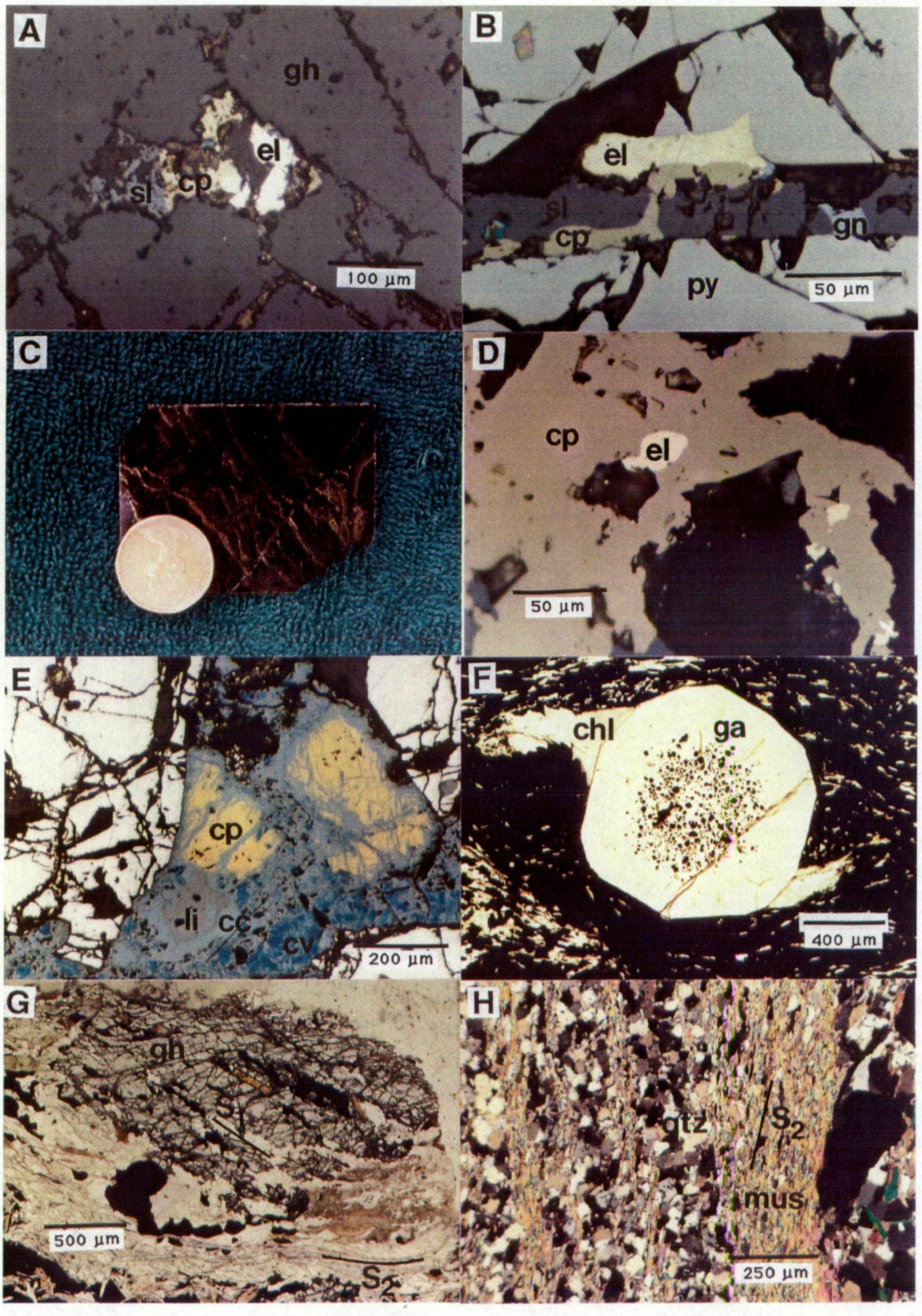
A
gh
el
sl
cp
100 µm
B
el
sl
cp
gn
py
50 µm
C
D
cp
el
50 µm
E
cp
li
cc
cv
200 µm
F
chl
ga
400 µm
G
gh
S1
500 µm
S2
H
qtz
S2
mus
250 µm

at or about the water table to form cavitites. As weathering proceeds, these cavities are filled by the collapse of material from the walls and by insoluble material left over from leaching to form breccias. True gossan only forms over areas of disseminated sulfide. Harvey (1984b) also reported strong silicification and kaolinitization in the country rocks surrounding outcrop of gossan.

Lead gossan consists of a mixture with variable proportions of anglesite, cerussite, and iron oxides and hydroxides. Harvey (1984b) also reported the occurrence of cassiterite in this zone.

Oxidation and supergene mineralization at Balcooma extend to a depth of over 50 meters. Harvey (1984b) noted the presence of malachite, azurite, tenorite and native copper in core and at the surface. Chrysocolla has been observed in section 35-27.8 during this study. Chalcocite, covellite and limonite are common supergene minerals in oxidized zones below the oxide zone in the Harvey shoot around 9200 mN. Chalcopyrite, which occurs in the interstices of pyrite grains, is initially replaced by chalcocite, and the iron in the chalcopyrite is converted to limonite that occurs as islands surrounded by supergene chalcocite (Fig. 62e). Chalcocite is then replaced along grain boundaries by covellite. Pyrite appears to be unaffected by these processes.

Gangue mineralogy

The gangue mineralogy at Balcooma and Dry River South varies significantly with the style of mineralization.

Balcooma

Copper-rich mineralization at Balcooma contains a gangue mineralogy similar to that of the chloritic alteration zones. The most common gangue minerals, chlorite and biotite, occur in the interstices of sulfide minerals as does quartz, which is a less common gangue. Staurolite is the most common prophyroblastic gangue mineral, and it is commonly rimmed and corroded by cordierite (49-137.1). Idioblastic garnet is also an uncommon porphyroblastic gangue. Many of the ferromagnesian minerals, in particular cordierite, are altered to a yellowish or brownish serpentine- or chlorite-like mineral. Albite also occurs infrequently, an amphibole

has been observed in section 42-217.8, and sillimanite occurs as needles surrounded by massive magnetite in section 4-99.8.

In Balcooma massive pyrite-sphalerite-galena mineralization, quartz, muscovite and biotite are the most common gangue minerals. Chlorite is also present, but it commonly replaces biotite. The biotite itself is quite distinct in that it is very light brown in color and weakly pleochroic. Relatively rare gangue minerals include albite (which is usually strongly sericitized), garnet and epidote.

Dry River South

In general, the gangue mineralogy at Dry River South is simpler than that at Balcooma. The most common gangue in Dry River South massive pyrite-chalcopyrite is biotite, followed by chlorite, and then quartz. Staurolite occurs relatively frequently as 2-10 mm non-poikiloblastic porphyroblasts. The unusual serpentine-like alteration of ferromagnesian minerals has also been noted at Dry River South (Patterson, 1986b).

The gangue mineralogy of Dry River South massive pyrite-sphalerite-galena is simply quartz, muscovite and biotite. This assemblage is very similar to the alteration assemblage in the Dry River South footwall schists.

All types of mineralization from both prospects have two other relatively minor gangue minerals: gahnite and carbonate (identified by Patterson (1981, 1986b) as siderite). Gahnite occurs as 1-5 mm anhedral porphyroblasts with sulfide inclusions commonly found in the interstices between sulfide minerals, and appears to be more common at Dry River South than Balcooma. It also occurs more frequently in massive pyrite-sphalerite-galena than massive pyrite-chalcopyrite as it is a zinc-bearing mineral.

Carbonate is an uncommon gangue that typically occurs in interstices between sulfide gains and as cross cutting veinlets, commonly in association with chlorite with an anomalous blue birefringence. At Dry River South carbonate occurs as vein filling within late fractures developed in massive pyrite. Patterson (1981, 1986b) noted that the carbonate (siderite) commomly veins and replaces magnetite.

Timing and style of mineralization

Although mineralization at Balcooma and Dry River South has many of the characteristics of syngenetic mineralization (stratiform character and asymetric alteration) the complexity of deformation in the Balcooma metamorphic belt has destroyed the primary depositional textures of the ores. As a result, the exact timing of mineralization in the two deposits cannot be constrained, however by using microstructural relationships a **minimum** timing relative to deformation events may be determined.

Pervasive evidence of a syn- or pre-D_2 timing to mineralization may be found in both deposits as sulfide minerals (particularly pyrite and chalcopyrite) are commonly aligned in the prevalent S_2 cleavage (Fig. 60e). Evidence establishing an earlier timing is less common, but is present in several sections. In Figure 62f an idioblastic garnet, which has been rotated relative to S_2, contains inclusions of pyrite and sphalerite in the center. This indicates that sulfide minerals were present either before or during the earliest stages of D_2. In Figure 62g a gahnite porphyroblast that is wrapped by S_2 contains oriented inclusions of sphalerite and galena. These inclusions are best interpreted to have been oriented by S_1, and this indicates the presence of sulfide minerals during D_1. In section 12-122.9, finely laminated alternations of quartz-pyrite-rich bands and muscovite-rich bands have been overprinted by the prevasive S_2 foliation (Fig. 62b). Whereas this texture clearly indicates a pre-D_2 timing of mineralization, primary exhalative processes best explain the fine banding in this sample. Evidence from mineral textures demonstrate quite conclusively a pre- or syn-D_1 timing and strongly suggest a syngenetic timing of mineralization.

These results support the interpretation that the Balcooma and Dry River South (and by inferrence, Surveyor) prospects are strongly deformed massive sulfide deposits of the volcanogenic type.

Sulfur isotope studies

To evaluate the source of sulfur in the deposits, a total of 91 mineral separates from 56 Balcooma samples and 35 mineral separates from 25 Dry River South samples were analyzed for sulfur isotopes using the techniques of Robinson and Kusabe (1975) on a VG Micromass 602D spectometer under the direction of M. Power, Sr. in the Central Science Laboratory of the University of Tasmania. The samples were calibrated against standard galenas from Broken Hill ($\delta^{34}S$ = 3.2 permil) and Tullah ($\delta^{34}S$ = 15.3 permil). Reproducibility of the standards was always within 0.2 permil, and the reproducibility of sample replicates was generally better than 0.5 permil. The greater variability in sample replicates is probably due to variations of the sulfur isotope values of a particular mineral in a block. The results are tabulated in Appendix B and summarized in Figure 63.

Results from Balcooma

Sulfur isotope values at Balcooma cluster tightly about a mode at 10 permil with 90% of the data falling between 8.5 permil and 11.5 permil. This distribution has a shoulder of values to the high side of the peak (Fig. 63), which has significance when the data is separated according to massive sulfide lens (Fig. 64 and 65). Mineral separates from the Mulroney lens (Fig. 64) have a slightly higher range in $\delta^{34}S$ values than samples from the Harvey and Morris lenses (Fig. 65). This difference does not appear to be the effect of the predominance of massive pyrite-sphalerite-galena in the Mulroney lens versus massive pyrite-chalcopyrite in the Harvey and Morris lenses as samples of massive pyrite-chalcopyrite from the Mulroney have significantly higher $\delta^{34}S$ values than corresponding samples from the Harvey and Morris lenses. The differences between the lenses are enhanced when only pyrite separates are considered (Fig. 66). Pyrites from the Harvey and Morris lenses average 9.70 permil with a standard deviation of 0.74, whereas pyrites from the Mulroney lens average 10.69 permil with a standard deviation of 0.60 permil. An F-test to test whether the two populations are statistically different indicates that they are at a 99% level of confidence. These results are consistent with the interpretation

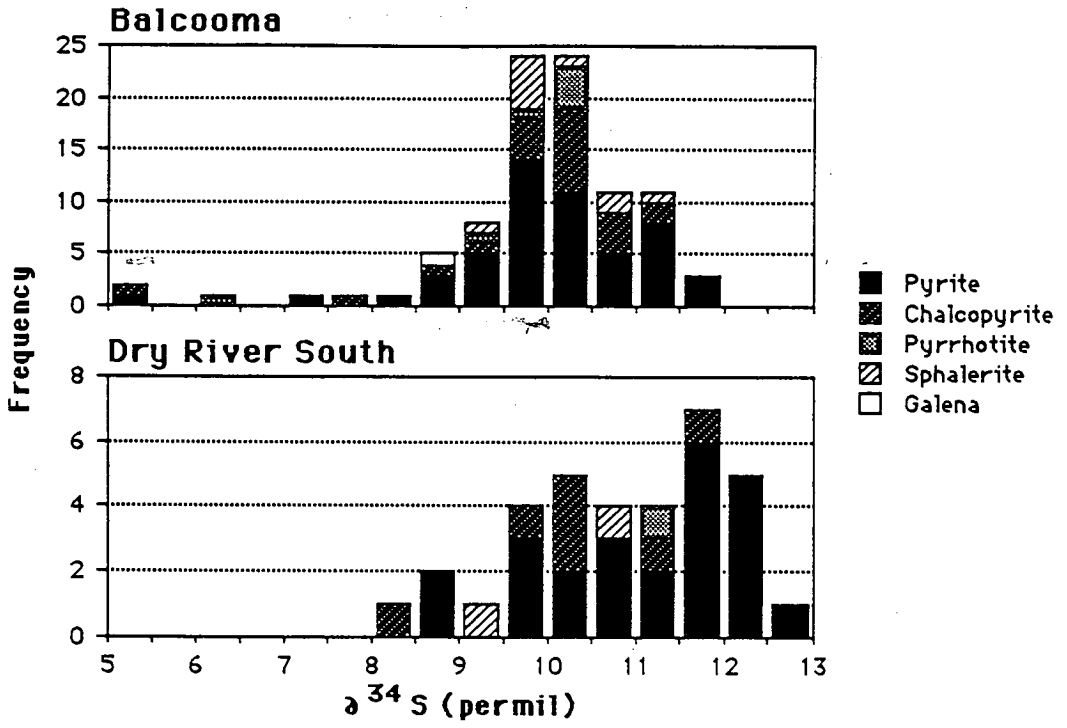

Figure 63. Histograms summarizing the $\delta^{34}S$ values of mineral separates from Balcooma and Dry River South.

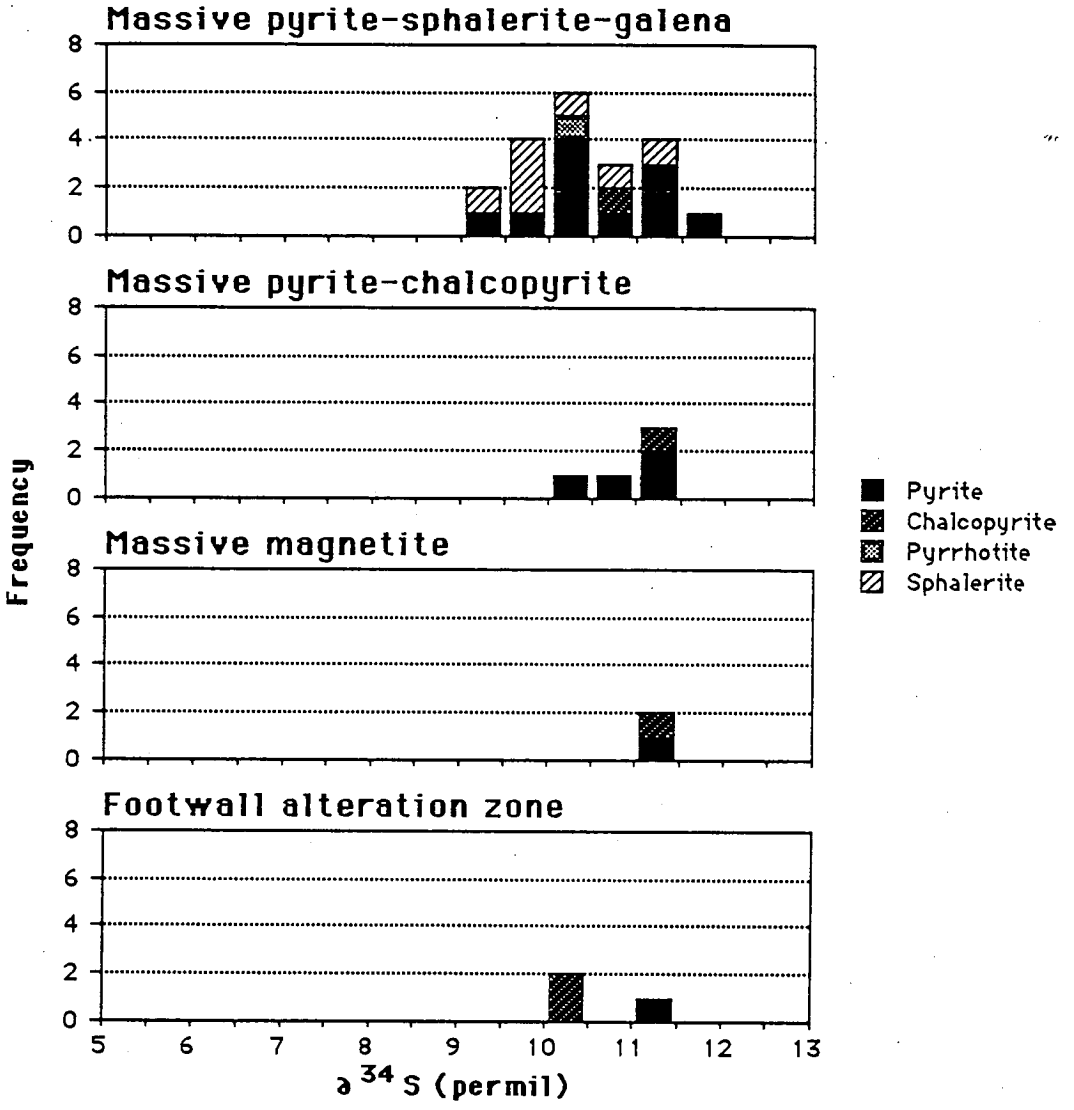

Figure 64. Histograms showing the variation in $\delta^{34}S$ values in mineral separates according to mineralization type in the Mulroney lens, Balcooma.

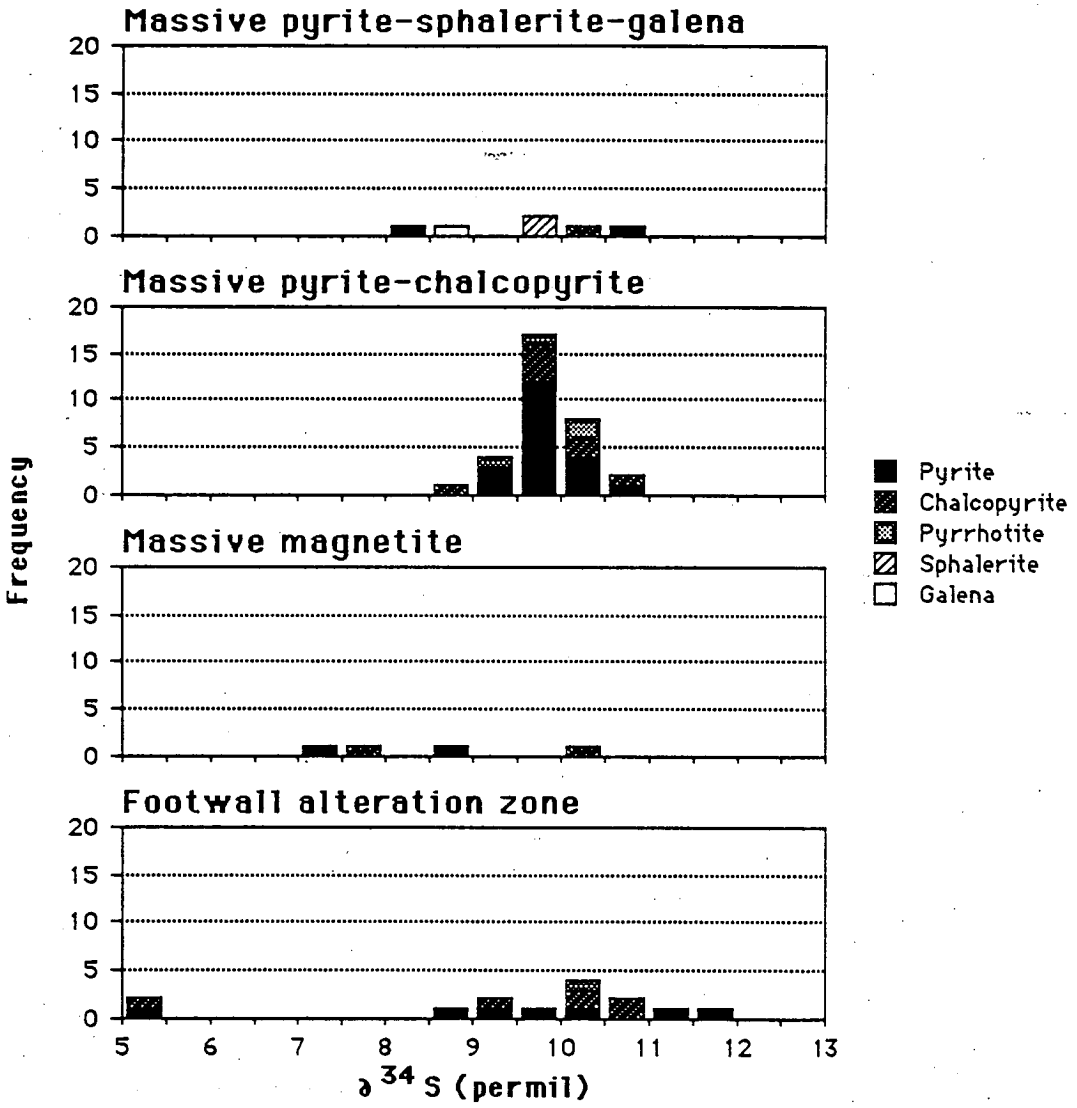

Figure 65. Histograms showing the variation in $\delta^{34}S$ values in mineral separates according to mineralization type in the Harvey and Morris lenses, Balcooma.

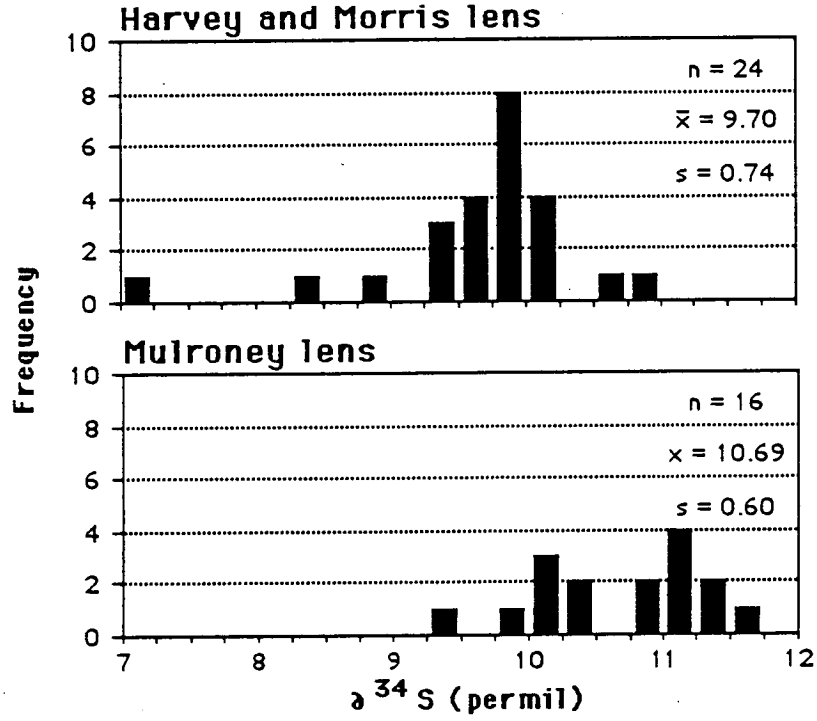

Figure 66. Histograms comparing the variation in $\delta^{34}S$ in pyrite between the Mulroney lens and the Harvey and Morris lenses, Balcooma.

that the Harvey and Morris lenses lie at a separate stratigraphic horizon to the Mulroney lens.

When mineral separates are separated according to types of mineralization (Figs. 64 and 65), no significant difference exists in values from the footwall alteration zone, massive magnetite, massive pyrite-chalcopyrite and massive pyrite-sphalerite-galena. This differs from some deposits where a vertical zonation in sulfur isotope values has been noted (e.g. Rosebery; Green et al., 1981). Temperatures were also calculated for mineral pairs in textural equilibrium (e.g. sphalerite-galena and chalcopyrite-pyrrhotite), but the resulting temperatures were too high to be geologically reasonable (some exceeded 1000°C) even if they were considered metamorphic temperatures. These results are either the results of non-equilibria or contamination of the mineral separtes during drilling. Lack of equilibrium is quite common in sulfur isotopes in volcanogenic massive sulfide deposits (Ohmoto, 1986).

Results from Dry River South

Dry River South mineralization has a slightly higher range in $\delta^{34}S$ values than Balcooma. Whereas Balcooma mineralization is concentrated between 8.5 permil and 11.5 permil with a mode at 10 permil, Dry River South mineralization is concentrated between 9.5 permil and 12.5 permil without a strong mode (Fig. 63). As at Balcooma, different styles of mineralization have very similar $\delta^{34}S$ values (Fig. 67), and a lack of equilibrium is observed in chalcopyrite-pyrrhotite pairs that show evidence of textural equilibrium.

Discussion

The Dry River South and Balcooma deposits have very similar sulfur isotope systematics to volcanogenic massive sulfide deposits of similar age in eastern Australia (Fig. 68). The two deposits are similar to other Phanerozoic deposits (c.f. Sangster, 1968) in that their $\delta^{34}S$ values fall between contemporaneous seawater and 0 permil (Fig. 69). When interpreting the source of sulfur, four possible reservoirs must be considered: (1) evolved seawater sulfur, (2) ambient seawater sulfur, (3) sulfur present in footwall units, and

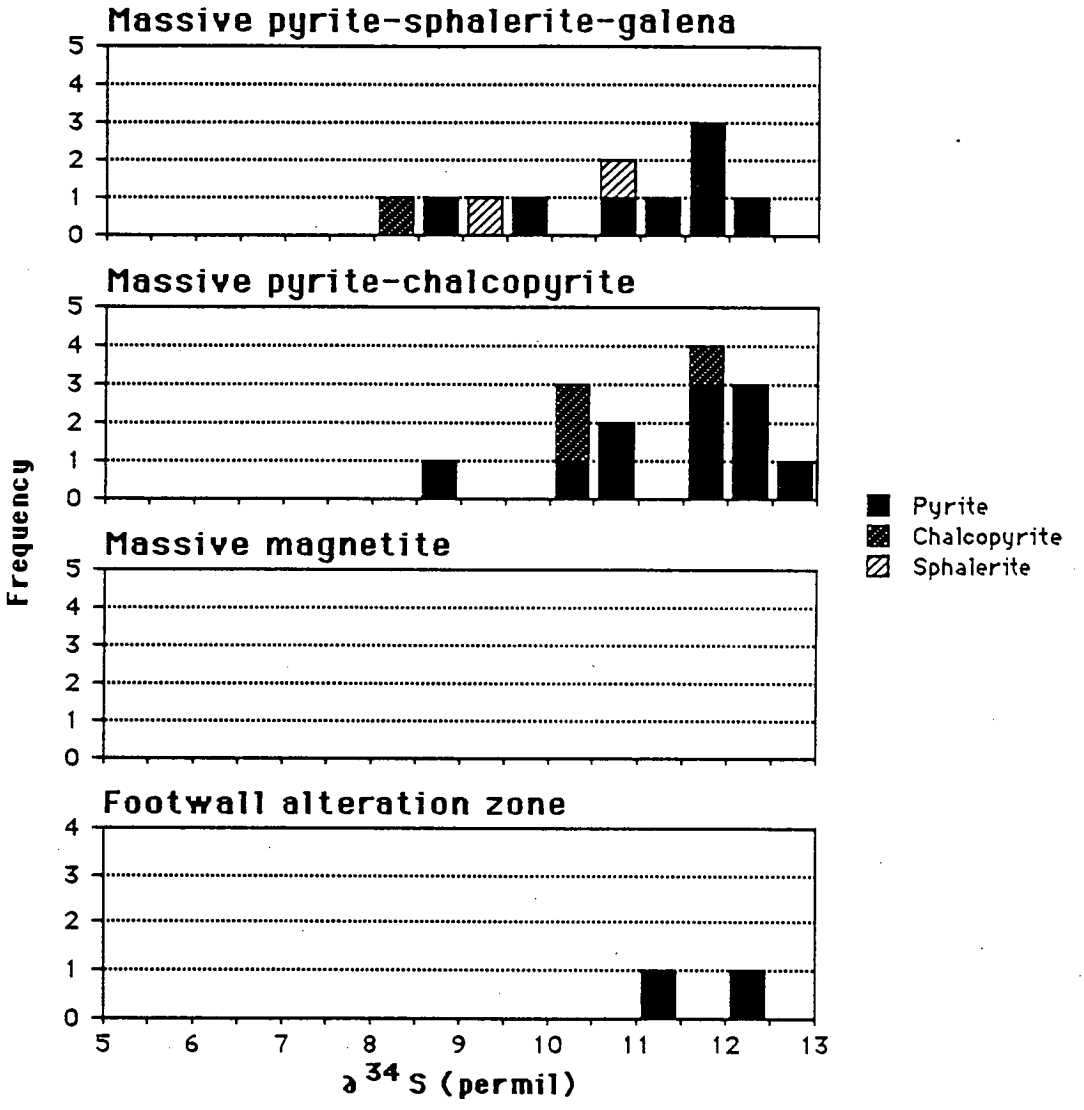

Figure 67. Histograms showing the variation in $\delta^{34}S$ values in mineral separates according to mineralization type, Dry River South.

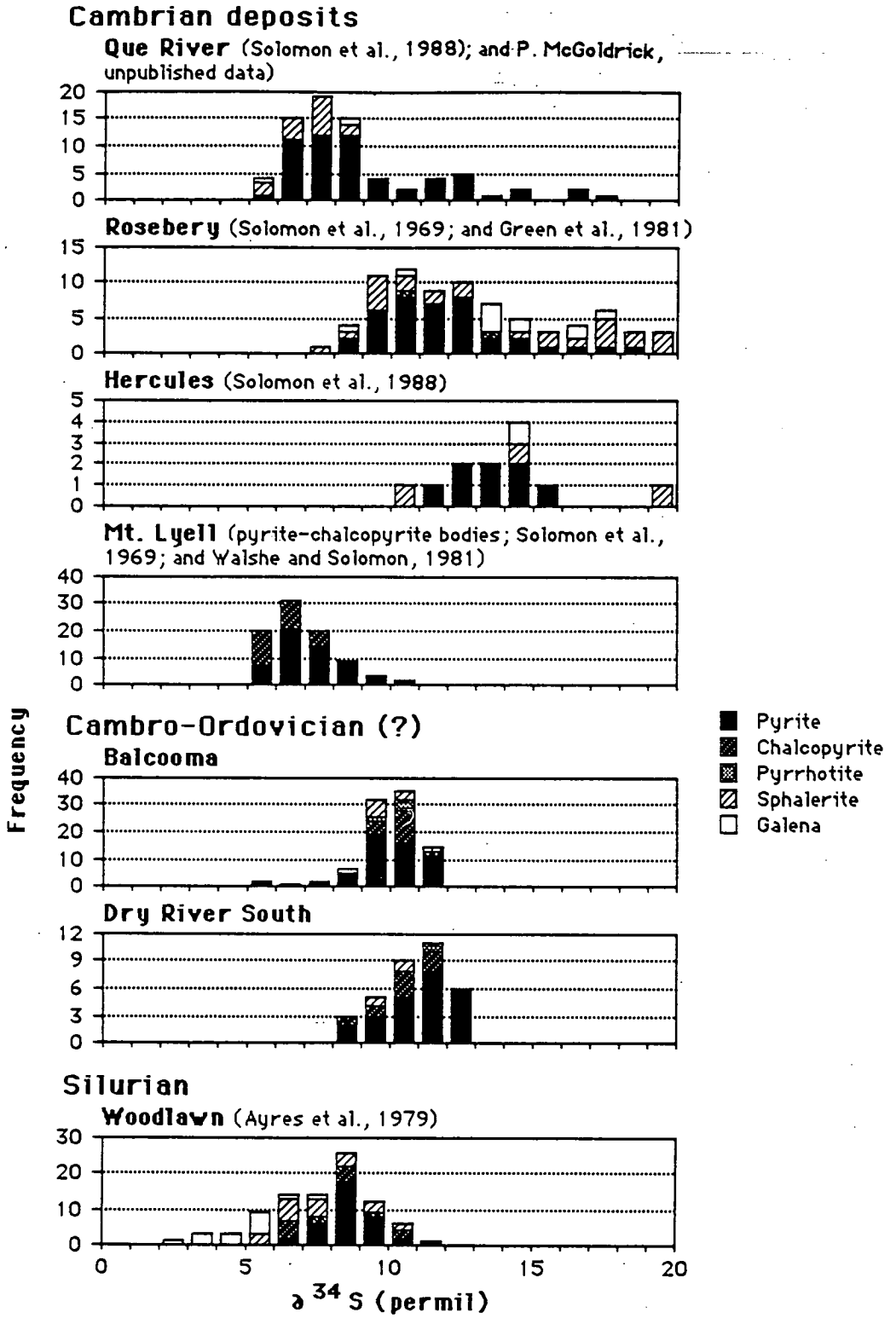

Figure 68. Histograms showing the variation in $\delta^{34}S$ values in eastern Australian Paleozoic massive sulfide deposits (data from Solomon et al., 1969, 1988; Green et al., 1981; Walshe and Solomon, 1981; Ayres et al., 1979; P. McGoldrick, unpub. data; and this study).

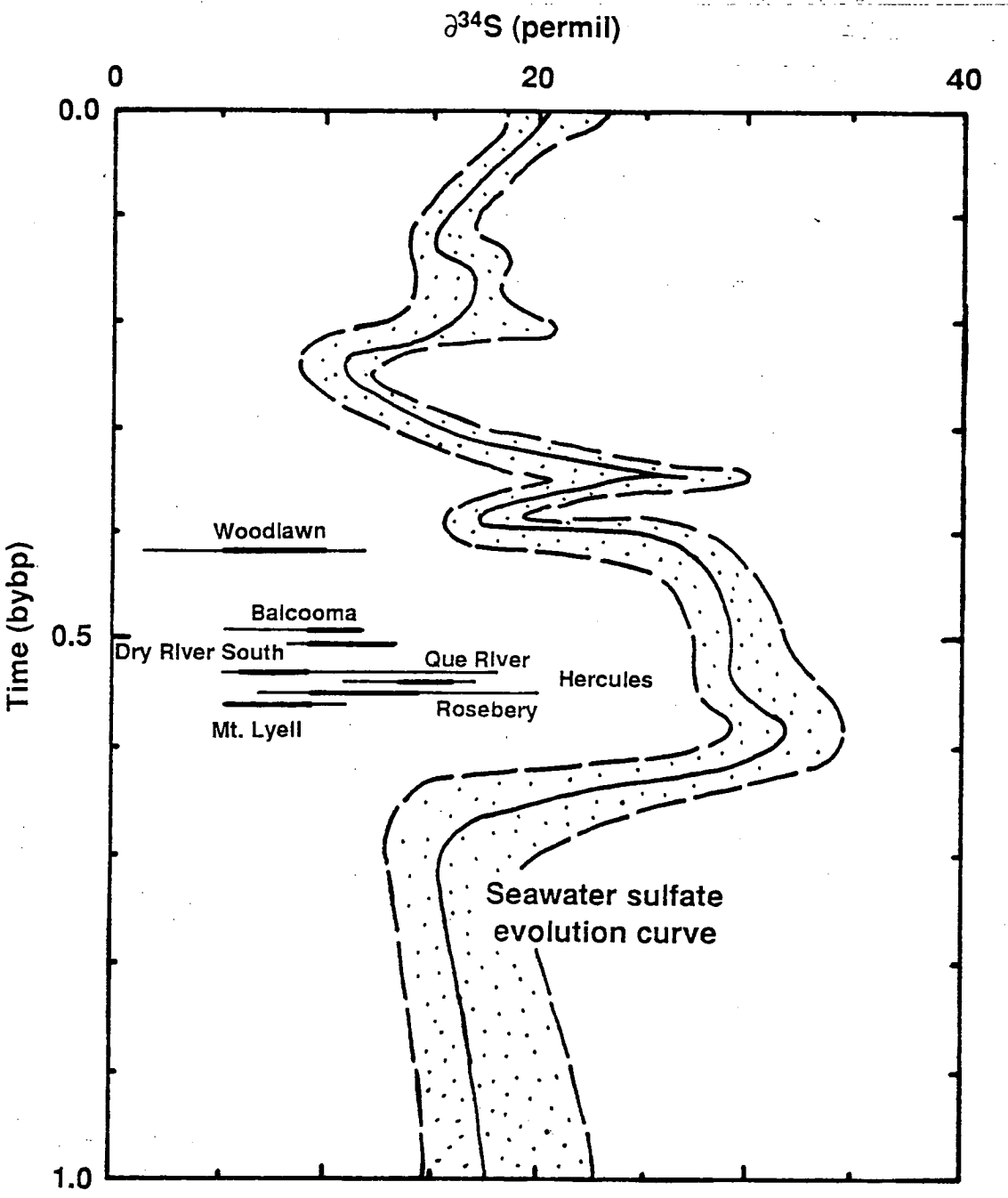

Figure 69. Comparison of eastern Australian volcanogenic massive sulfide deposits to seawater sulfate values of contemporaneous seawater (data as Fig. 68; sulfate evolution curve from Ohmoto, 1986).

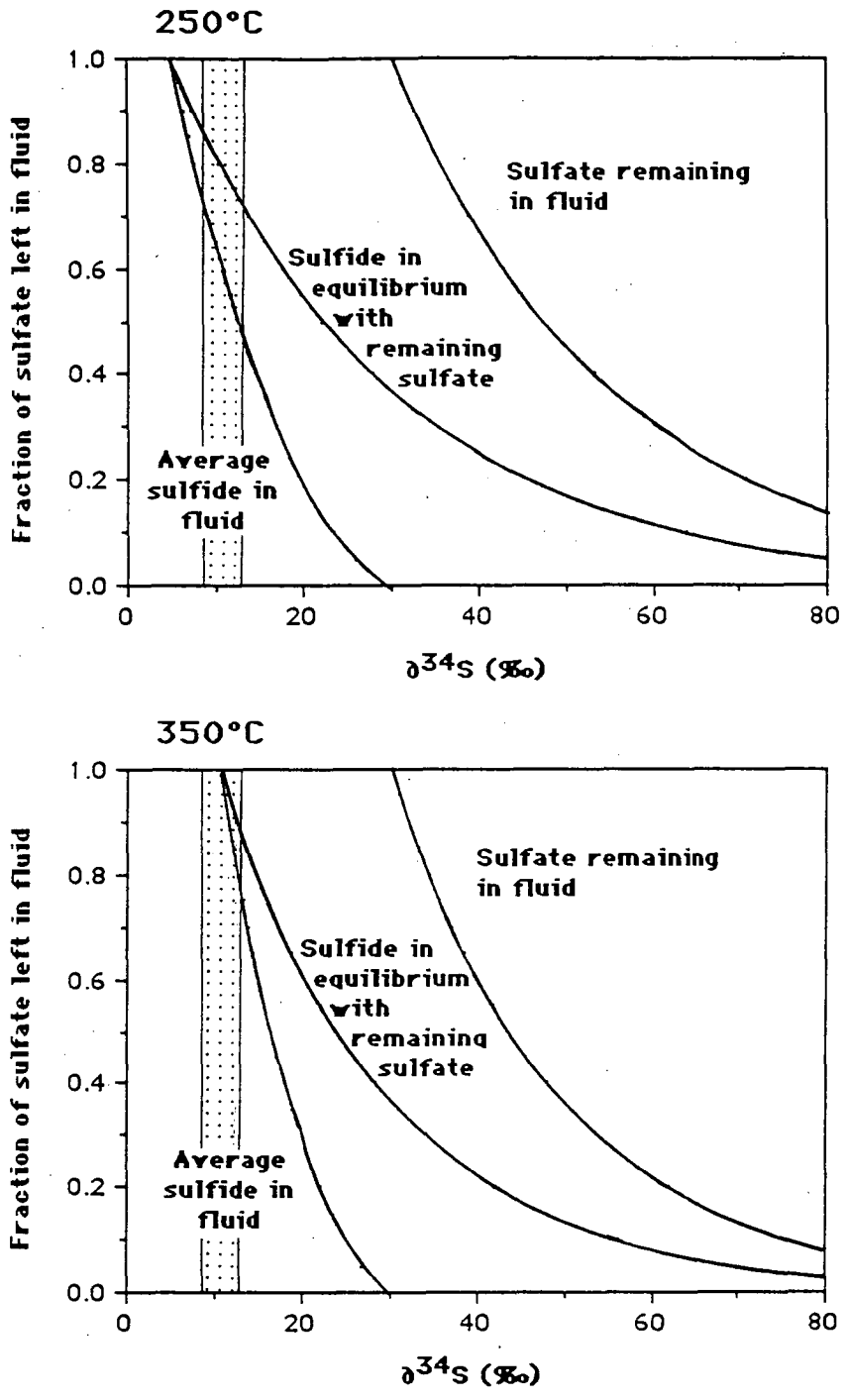

Figure 70. Sulfur isotope evolution of a volcanogenic fluid assuming reduction of contemporaneous seawater as the only sulfur source and Rayleigh distillation. Stippled area indicates the range observed at Balcooma and Dry River South.

(4) magmatic sulfur. Over the years, the interpretation of sulfur isotope systematics in volcanogenic massive sulfides has varied significantly. Sangster (1968) initially proposed that the sulfur in the ores was derived from bacterially reduced seawater sulfate, wheras Ishihara and Sasaki (1978) interpreted that sulfide in the Kuroko district in Japan was derived from magmatic sulfur which has similar values to the ores. The latest interpretaion (e.g. Ohmoto et al., 1983; and Solomon et al., 1988) inferred that the sulfur in the deposits was derived by inorganic reduction of seawater sulfate (that may have involved early anhydrite precipitation) and dissolution of rock sulfur in the leaching zone. Ohmoto (1986) suggested that the variation in $\delta^{34}S$ in the individual deposits is too small to have been produced by either biogenically derived or magmatic sulfur.

To test whether inorganic reduction of Cambro-Ordovician seawater sulfate could have produced the sulfur isotope signatures of the Balcooma and Dry River South deposits, the reduction of sulfate to sulfide was modelled using a Rayleigh distillation model at temperatures of 250°C and 350°C following work by Solomon et al. (1988; Fig. 70). A value of 30 permil was taken to represent the value of Cambro-Ordovician seawater sulfate (Ohmoto, 1986). In the model sulfide produced by the reaction was assumed not to react with the remaining sulfate in the fluid. The model predicts the $\delta^{34}S$ of the sulfate remaining in the fluid according to the fraction of unreacted sulfate left in the seawater. Using these data, the $\delta^{34}S$ value of sulfide in equilibrium with the sulfate may be calculated using sulfate-sulfide fractionation factors, and the average $\delta^{34}S$ value of sulfide produced by the reaction and removed from further reaction may be calculated using mass balance. The precipitation of sulfide minerals from solution sulfide will not affect the solution $\delta^{34}S$ value significantly as $\Delta^{34}S_{i\text{-}H_2S}$ (i is any common sulfide mineral except galena) varies between 0 and 2 permil for temperatures over 200°C. This average value best reflects the eventual $\delta^{34}S$ of the mineralizing fluid. Given this constraint, seawater sulfate reduction produces the observed Balcooma and Dry River South sulfur isotope systematics ($\delta^{34}S$ between 9 permil and 12 permil) when between 1% and 50% of the sulfate has been reduced to sulfide (depending on temperature). If a large amount of sulfate remained in

the hydrothermal fluid (e.g. $SO_4^{2-}/H_2S > 1$), sulfate minerals (e.g. barite) would have precipitated either in the alteration pipe or at the seawater interface. As there is no evidence of barite and the avialible evidence indicates reduced fluids, sulfate was only a minor specimen in solution. Consequently, as the modelling produces the observed values if a large proportion of sulfate remains in solution, a second source of light sulfur is required. One possibility is light rock sulfur, but this can not be modelled owing to a lack of data.

Chapter 8
Summary and conclusions

Tectonic setting and stratigraphic relationships in the Balcooma metamorphic belt

Although intense deformation and metamorphism have destroyed primary textures and have complicated the relationships between units, a fairly simple gross stratigraphic picture may be constructed for the Balcooma metamorphic belt. Metagraywackes of the Clayhole Creek Beds intercalate with the metavolcanics of the Dry River Volcanics to the west (Fig. 71). The quartz-feldspar sills and granitic intrusions at Balcooma and Dry River South are probably comagmatic with the Dry River Volcanics. The package of rocks which contains the West Branch Creek Beds, Lochlea Volcanics, Highway Beds and Golden Creek Volcanics are in faulted contact with the Dry River Volcanics and cannot be correlated.

Chemical analyses of samples from the Clayhole Creek Beds indicate that this unit was derived from an active continental arc. This tectonic setting is very similar to the Seventy Mile Group some 200 km to the south (Henderson, 1986) which contains the Mt. Windsor Volcanics and associated volcanogenic massive sulfide deposits (e.g. Thalanga and Liontown). Figure 71 schematically compares the interpreted relationships in both belts. However, after a brief field visit to the Seventy Mile Group, a direct lithologic correlation between the two sequences is considered tenuous. Although the Dry River Volcanics are similar to the Mt. Windsor Volcanics, the associated sedimentary packages cannot be easily correlated.

Comparison of massive sulfide deposits in the Balcooma metamorphic belt

Table 9 summarizes the characteristics of the Balcooma and Dry River South deposits as outlined previously and the Surveyor and West Boyds Creek deposits as described in the Noranda Australia Prospectus (1985) and Mulroney (1983), respectively. Examination of Table 9

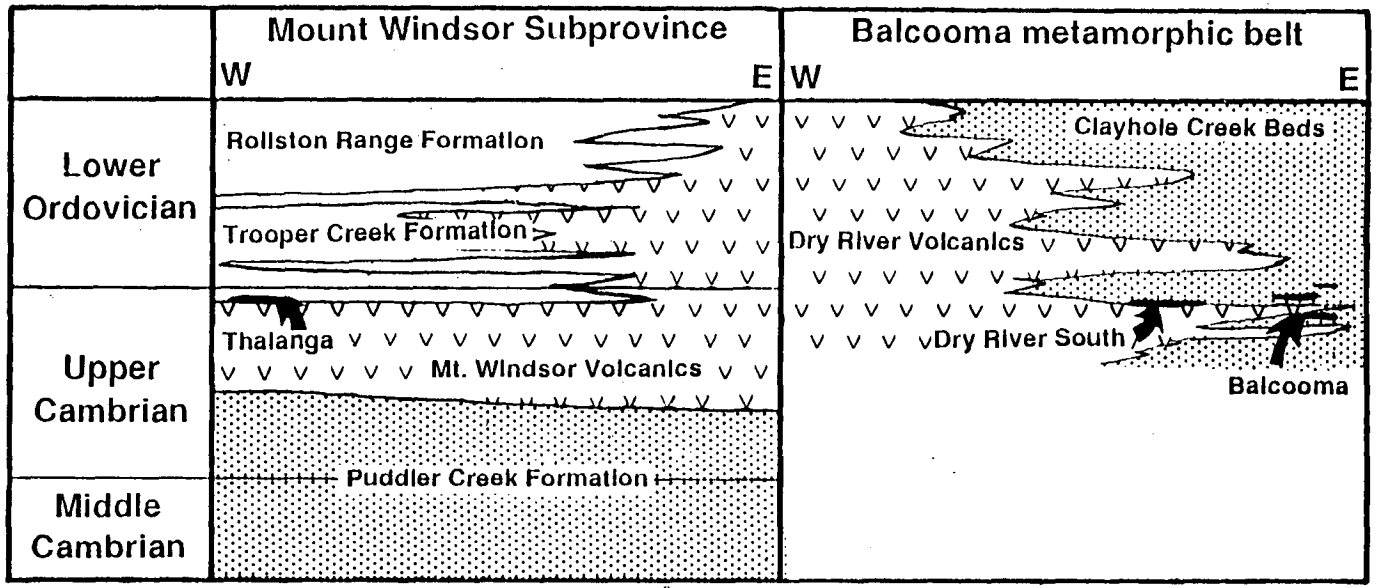

Figure 71. Comparison of the tectonic settings of the Mt. Windsor Supergroup (Henderson, 1986) and the Balcooma metamorphic belt.

indicates that the deposits differ markedly in terms of local stratigraphy, structure, mineralogy and alteration.

Stratigraphy

The local stratigraphy of the Balcooma prospecta differs somewhat from the statigraphy of the Surveyor and Dry River South prospects (Table 9). Balcooma mineralization occurs in a relatively thick lens of metapelite within a monotonous sequence of metagraywacke with minor intebedded metapelite. The most striking difference between the hanging wall sequence and the footwall sequence at Balcooma is the presence of a significant amount of volcaniclastic rocks (~10%) in the footwall metagraywackes. The metapelitic lens also contains volcaniclastic units, but the hanging wall metagraywacke contains only very minor volcaniclastic lenses.

This differs from the Dry River South prospect where the footwall is comprised of altered rhyodacitic to rhyolitic volcanic, and the hanging wall is comprised of metagraywacke with minor metapelite. The hanging walls to the Balcooma and Dry River South prospects are similar, but the footwalls are quite different.

The footwalls and host rocks to the Dry River South and Surveyor prospects are similar packages of felsic volcanics and volcaniclastic rocks, but the hanging wall to the Surveyor deposit is occupied by a quartz-feldspar porphyry which is interpreted in the Noranda Pacific prospectus (1985) as a "quartzo-feldspathic tuff." Due to the similarity of this lithology to the quartz-feldspar porphyry sills at Dry River South and Balcooma, this unit is more likely an intrusion and the original hanging wall lithology of the Surveyor prospect is unknown.

As the Dry River South and Surveyor prospects have similar stratigraphies, they probably lie at the same stratigraphic position at or near the contact between the felsic volcanics of the Dry River Volcanics and the metagraywackes of the Clayhole Creek Beds. As the Balcooma prospect occurs near the point in the stratigraphy where volcaniclastic sedimentation ceased, it is interpreted to occur at the same stratigraphic position as Surveyor and Dry River South, but in a location more removed from the volcanic arc where volcaniclastic beds lens out (Fig. 71).

The West Boyds Creek prospect is located within the West Branch Creek Beds at a different stratigraphic position to the other

Table 9. Summary characteristics of massive sulfide prospects in the Balcooma metamorphic belt

	Balcooma (this study)	Surveyor (Noranda Australia Prospectus, 1985)	Dry River South (this study)	West Boyds Creek (Mulroney, 1983)
Stratigraphy				
Enclosing unit	Clayhole Creek Beds.	Dry River Volcanics/ Clayhole Creek Beds (?).	Clayhole Creek Beds/ Dry River Volcanics.	West Branch Creek Beds.
Hanging wall lithology	Weakly altered metagraywacke.	"Quartzo-feldspathic crystal tuff" (?).	Metagraywacke.	Slate with minor felsic tuff and volcaniclastics.
Host lithology	Metapelite and minor interbedded volcaniclastics.	Altered lapilli tuff and dacitic flows and tuffs.	Minor rhyodacitic volcaniclastics.	Contact between metasediments and metavolcanics.
Footwall lithology	Metagraywacke and 10% interbedded volcaniclastics.	Altered rhyodacitic metavolcanics.	Altered rhyodacitic metavolcanics.	Altered felsic tuffs and volcanoclastics.
Intrusive units	Quartz-feldspar porphyry sills.	Quartz-feldspar porphyry sills.	Quartz-feldspar porphyry sills.	Dolerite sills.
Structure	Tear fault separating a southern structural domain characterized by shallow, east dipping bedding from a northern domain with a D_2 antiform-synform pair and steeply dipping bedding Copper-rich mineralization occurs in the antiform core.	Tight to isoclinal folds with sub-vertical axial planes that are located in the nose of a regional D_3 anticlinorium. Mineralization is located in the core of a syncline.	Gentle east dipping monocline that steepens to the east. Shearing and faulting appear to be important several tens of meters above the massive.	Steeply dipping and west facing. Most primary textures are preserved.
Mineralization	Three stratigraphic horizons with five lens. The central horizon contains the major copper-rich lenses whereas the lower horizon has the major zinc-lead-rich lens. Minerals present include pyrite, magnetite, chalcopyrite, pyrrhotite, sphalerite and galena.	A single lens containing pyrite, sphalerite, galena and chalcopyrite.	A single lens containing pyrite, sphalerite, galena and chalcopyrite with lesser magnetite and pyrrhotite.	Lensoid horizon containing massive barite-carbonate with minor pyrite, sphalerite and galena.
Alteration	Pipe-like zone of pyritic quartz-chlorite schist associated with copper-rich mineralization and extensive stratiform zones of pyritic quartz-mucsovite-biotite schist associated with zinc-lead-rich mineralization.	Pyritic quartz-sericite schist.	Extensive zone of pyritic quartz-muscovite-biotite schist with minor zones of chloritic or biotitic schist	Pyritization and silicification with minor disseminated base metal

deposits in the northern part of the Balcooma metamorphic belt (Mulroney, 1983).

Structure

The style of structural deformation differs between the three deposits. Folding dominates the northern structural domain of the Balcooma prospect (Chapter 2) and the Surveyor deposit (Noranda Pacific, 1985) where mineralization has been mobilized into fold hinges, but the southern structural domain of the Balcooma prospect and the Dry River South prospect are relatively unfolded and dip gently to the east (Chapters 2 and 3). The differences in structural style between the deposits may relate to the relative competency of the wall rocks to alteration zones and mineralization. For instance the marked contrast in competency between the chloritic schists and quartz-feldspar porphyry at Balcooma may have enhanced folding, but the lack of competency contrast between pyritic quartz-muscovite-biotite schists, quartz-feldspar porphyries and metagraywackes at Dry River South may have prevented folding of the type present at Balcooma. Position in particular folds may have also controlled the extent of deformation. For instance, the strongly folded Surveyor deposit occurs at the nose of a major D_3 anticlinorium whereas the Mulroney lens of the Balcooma prospect occurs on a limb of the Balcooma D_2 antiform.

Mineralization

Although the Surveyor deposit is significantly richer in metals than the Dry River South prospect (Table 1), both deposits are very similar in that they are both restricted to a single stratigraphic horizon and are dominated by pyrite, sphalerite, galena and lesser chalcopyrite. Conversely, the Balcooma deposit contains mineralization at three different stratigraphic horizons, and the major copper-rich lens contains predominantly pyrite, magnetite, chalcopyrite and pyrrhotite. These differences probably relate to: (1) the rate of sedimentation at the various deposits, and (2) the temperatures of formation of the deposits.

Whereas the presence of metagraywackes and volcaniclastic units at Dry River South and Surveyor indicates rapid sedimentation,

sedimentation at Balcooma must have been slower to produce the pelitic lens that contains the mineralization. The slower sedimentation at Balcooma allowed the development of multiple periods of mineralization, whereas rapid sedimentation at Surveyor and Dry River South allowed mineralization only on a single horizon.

Chemistry of the ore forming fluids. Due to deformation in the Balcooma metamorphic belt and mineral recrystallization associated with metamorphism, very little data regarding the conditions of mineralization may be deduced directly from mineralogical observations. The most useful observations are the presence of arsenopyrite as a trace mineral and the lack of barite in the mineralization. The lack of barite in Phanerozoic massive sulfide deposits has been used by Lydon (1988) as evidence that the Ordovician Brunswick #12 deposit formed in the presence of locally reduced seawater. The presence of arsenopyrite also indicates reduced conditions as arsenopyrite is only stable under low f_{O_2} conditions in the pyrite stability field (c.f. Heinrich and Eadington, 1986).

The presence of pyrrhotite and magnetite could also indicate reduced conditions of mineralization, however many authors (c.f. Mookherjee, 1976) interpret the occurrence of pyrrhotite as a metamorphic feature. Large (1977) infers that these minerals formed during primary mineralization by changing f_{O_2} conditions in the ore fluids. As primary ore textures have been destroyed, the question as to the origin of magnetite and pyrrhotite is not resolvable, but the presence of large amounts of magnetite in the copper lodes at Balcooma must indicate a primary occurrence of at least some of the magnetite. The question of primary or metamorphic magnetite is complicated by oxidation and reduction of iron minerals during metamorphism as evidenced by the replacement of pyrrhotite by pyrite and magnetite, and by the pseudomorphing of some hematite by magnetite.

Owing to metamorphism of gangue minerals, other physicochemical contitions (e.g. pH, temperature, salinity and a_{H_2S}) may not be constrained although the presence of only minor carbonate gangue and the lack of calc-silicates (i.e. metasomatized carbonate) indicates a moderately acid pH (<5) during sulfide deposition. Due to the intensity of deformation, fluid inclusion studies were not undertaken

as they were considered unlikely to reflect the original conditions of deposition.

Although temperatures of deposition may not be determined directly, they may be inferred based on studies of undeformed volcanogenic massive sulfide deposits. Based on analogies to the Kuroko district of Japan (Eldridge et al., 1983; and Pisutha-Arnond and Ohmoto, 1983) copper-rich mineralization in the Balcooma district was probably deposited from hotter (>300°C) fluids whereas zinc-lead-rich mineralization was deposited from cooler (200-300°C) fluids.

In summary, mineralization at Balcooma and Dry River South probably occurred when reduced, moderately acid volcanogenic fluids mixed with cold, reduced seawater. Copper-rich mineralization fluids precipitated from hotter (<300°C) fluids whereas zinc-lead-rich mineralization precipitated from cooler (<300°C) fluids.

Conversely, the presence of barite and carbonate (Mulroney, 1983) indicates that the West Boyds Creek prospect was deposited under oxidized, near neutral conditions. The presence of barite and carbonate in the deposit is similar to the gold-rich Highway deposit in the Mt. Windsor Volcanics (Kay, 1982) and gold-rich massive sulfide deposits of the zinc-lead-silver-gold association in general (Part 3, Chapter 2).

Implications for exploration

The three major volcanogenic massive sulfide deposits in the Balcooma metamorphic belt all occur at or near the contact between the Dry River Volcanics and the Clayhole Creek Beds. As is common in many volcanogenic massive sulfide districts, mineralization has occurred at a break in sedimentation, in this case the cessation of a cycle of volcanic and volcaniclastic deposition and the onset of graywacke deposition. The most prospective region in the Balcooma metamorphics is within one kilometer of the contact between the Dry River Volcanics and the Clayhole Creek Beds.

A second prospective horizon occurs in the West Branch Creek Beds. The only deposit located at this position is the West Boyds Creek barite deposit, but this occurrence indicates that the chemistry of formation was different from the deposits in the northern part of the Balcooma metamorphic belt and this style of mineralization may have potential for elevated gold values.

Part II

The geology, geochemistry and mineralogy of precious metals in the Rosebery north-end orebody

Chapter 1
Introduction, and regional and mine geology

Introduction

Relatively few detailed studies on the distibution of gold and silver in volcanogenic massive sulfide deposits exist. All four deposits in western Tasmania of this type (Rosebery, Hellyer, Hercules and Que River) are unusually gold- and silver-rich. Total production and reserves at the Rosebery Mine in western Tasmania are 19.40 million tonnes of 5.0 percent lead, 16.2 percent zinc, 0.74 percent copper, 155 g/t silver and 2.9 g/t gold (Large et al., in press). Total precious metal in the Rosebery ores amounts to 3000 tonnes of silver and 56 tonnes of gold. The potential gold and silver resources of the mine may be higher as significant values may exist outside areas considered to contain economic lead-zinc grades.

Part two of this thesis is a description of the spatial distribution, metal associations and mineralogy of gold and silver in the north-end orebody. Various aspects of this subject have been discussed previously by Brathwaite (1969, 1974), Green et al. (1981), Green (1983), and Henley and Steveson (1978).

This part is intended to be largely descriptive. A review of the distribution of gold and silver in volcanogenic massive sulfide deposits may be found in Part 3, Chapters 2 and 3, respectively, which also present geochemical models for the transport and deposition of gold and silver in these deposits.

Geological setting

The Rosebery Mine lies within the Cambrian Mt. Read Volcanics, which are a 10 to 15 km wide belt of dominantly felsic volcanics on the eastern side of the Cambrian Dundas Trough (Corbett, 1981; Fig. 72). The Rosebery deposit occurs at the western margin of the Mt. Read volcanic belt, within a sequence of rhyolitic to dacitic volcaniclastic rocks and lavas termed the Central Volcanic Complex (Fig. 72). Although the Rosebery deposit is Cambrian in age, it has been affected (locally significantly) by later Devonian

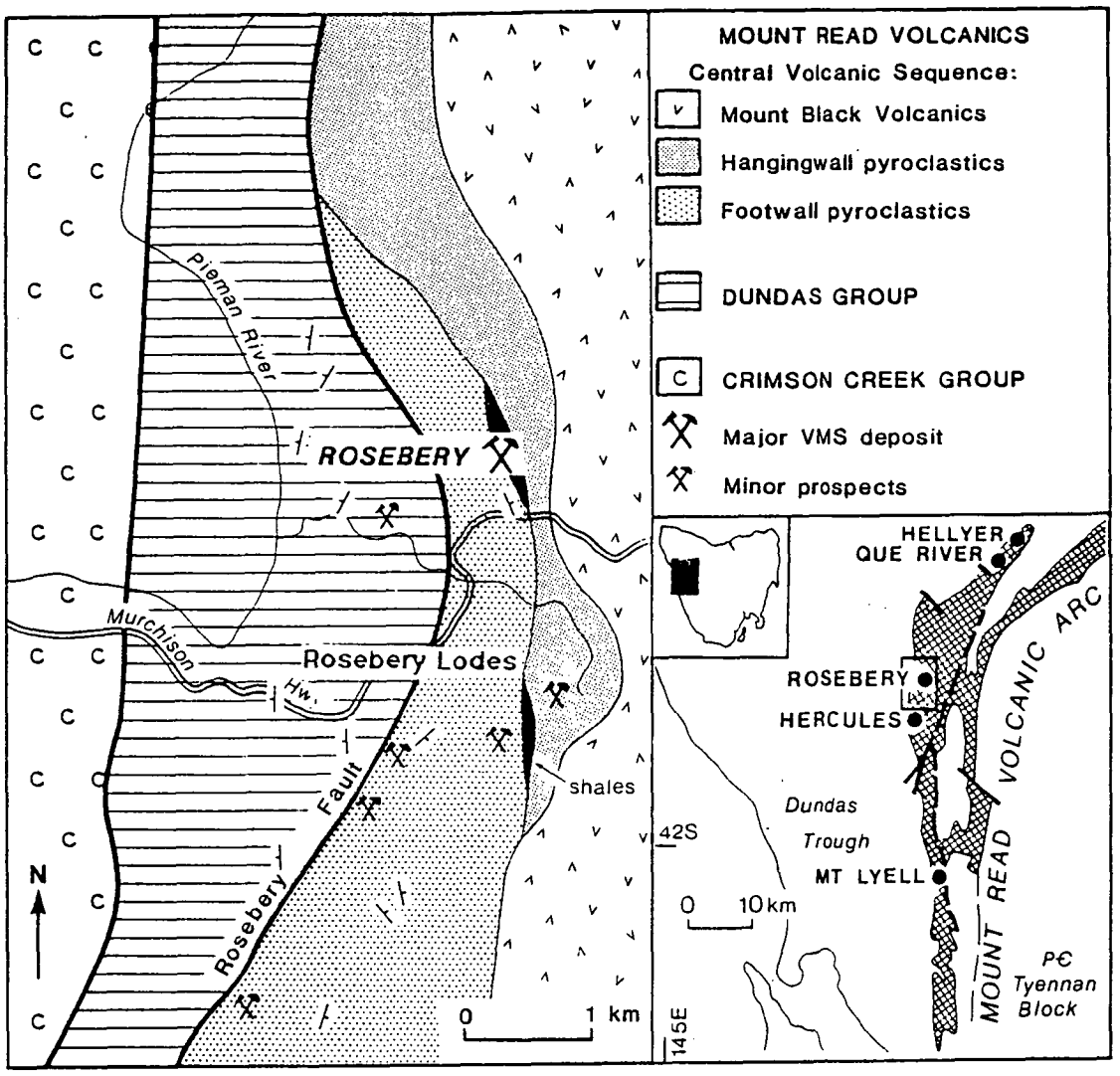

Figure 72. Geology of the Rosebery area (after Corbett and Lees, 1987).

remobilization and mineralization associated with granitoid intrusion (Solomon et al., 1987).

In the Rosebery area, the Central Volcanic Complex has been subdivided into three units: the footwall pyroclastics, the hangingwall tuffs, and the upper lava-rich sequence (Corbett and Lees, 1987). The deposit lies in a lens of sediments at the contact between the footwall pyroclastics and the hangingwall tuffs. More detailed descriptions of the geological setting may be found in Brathwaite (1974) and Green et al. (1981).

The host rocks and ores of the north-end orebody

The north end of the Rosebery deposit was selected for this study due to its relative stratigraphic and structural simplicity. The north end comprises a distinct orebody separated from the southern ore lenses by a zone of barren host rocks (see Green et al., 1981). The mineralization occurs in two distinct blanket-like lenses overlying an extensive zone of footwall alteration.

Footwall alteration zone

The footwall to the mineralization is comprised of an extensive zone of strongly cleaved quartz-sericite-chlorite schists (Eastoe et al., 1987). Green et al. (1981) interpret this unit to be a zone of quartz-sericite alteration associated with the formation of the overlying ores. Laterally the unit grades into weakly cleaved footwall pyroclastics. The footwall alteration zone also contains minor carbonate, tourmaline, pyrite and chalcopyrite (Green et al., 1981).

Stratiform mineralization

Mineralization at Rosebery occurs in two distinct blanket-like zones: (1) stratigraphically lower zinc-lead-copper massive sulfide which is up to 12 m thick, and (2) higher massive barite which occurs to the north of 1100 mN and is up to 12 m thick (Figs. 73 and 74). Two distinct types of massive sulfide ore exist at Rosebery: (1) pyrite-chalcopyrite massive sulfide, and (2) sphalerite-galena-pyrite massive sulfide.

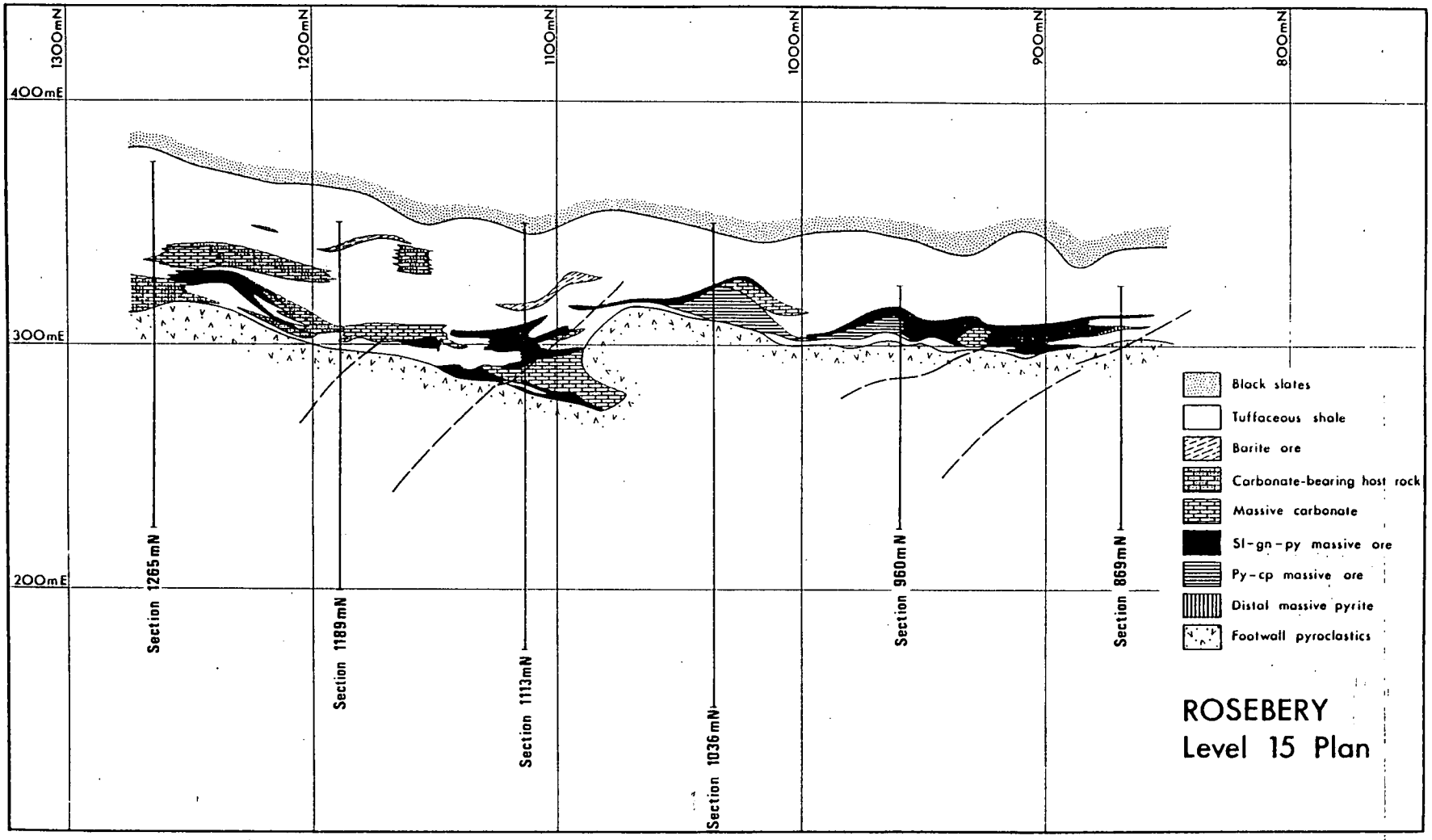

Figure 73. Geology of the Rosebery north-end on 15 level (compiled from company plans).

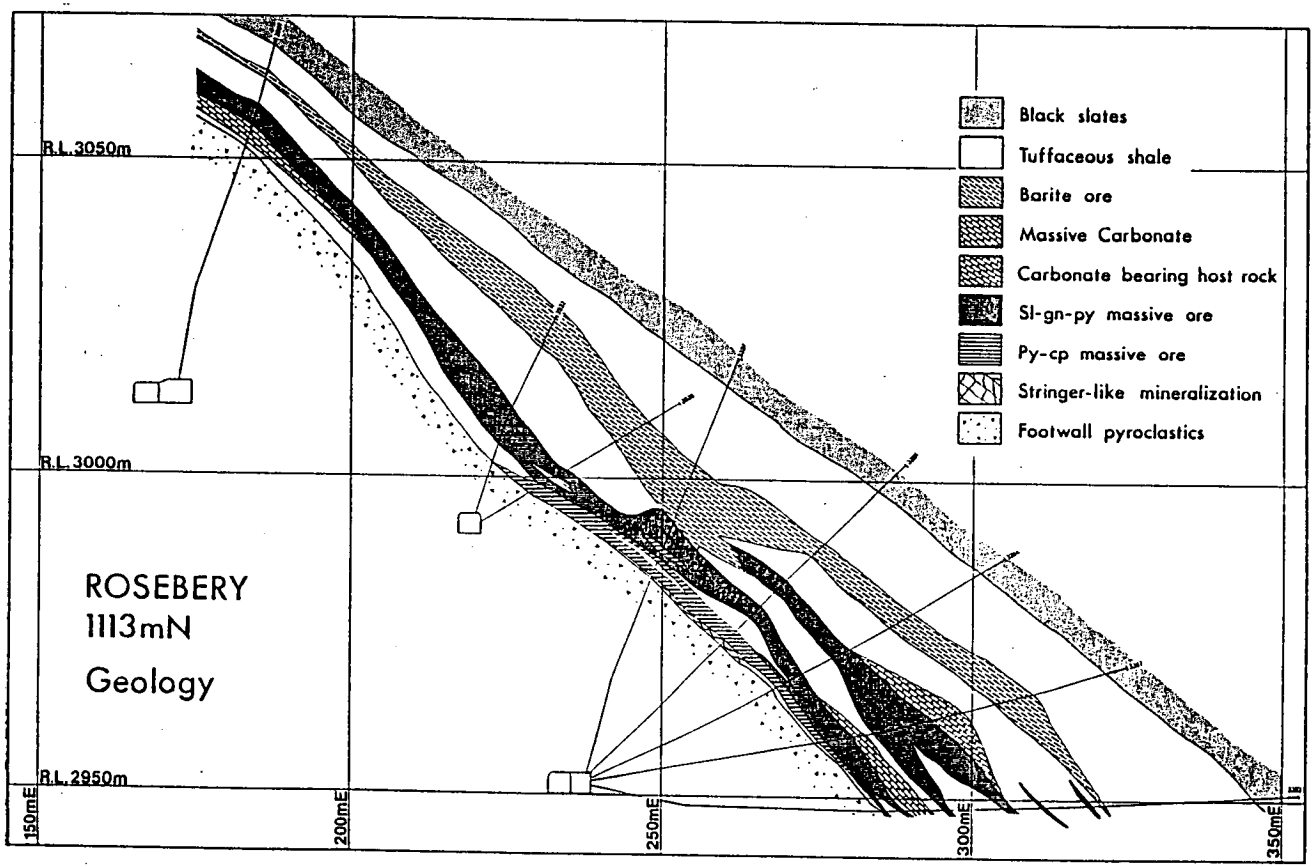

Figure 74. Geology of section 1113 mN, Rosebery deposit.

Pyrite-chalcopyrite massive sulfide. Pyrite-chalcopyrite ore occurs dominantly in discontinuous pods at the base of the zinc-lead-copper zone. Narrow zones of stringer-like copper mineralization and disseminated pyrite in highly chloritized host rocks are occasionally observed below pods of pyrite-chalcopyrite ore.

The mineralogy of the pyrite-chalcopyrite lenses also includes variable amounts of sphalerite and galena, and minor to trace arsenopyrite, tetrahedrite, cosalite, kobellite, and native bismuth (Brathwaite, 1969; Green, 1983; and this study).

Sphalerite-galena-pyrite massive sulfide. The overlying sphalerite-galena-pyrite ore tends to thin laterally from pyrite-chalcopyrite lenses, merging into disseminated low-grade ore at the edges. This ore also contains minor amounts of chalcopyrite, arsenopyrite, tetrahedrite and magnetite (Brathwaite, 1969).

Massive barite mineralization. The barite zone occurs stratigraphically above and usually separated from sphalerite-galena-pyrite ore by intervening host rock. Sulfide minerals present include sphalerite, galena, pyrite, chalcopyrite and tetrahedrite. Compared to sphalerite-galena-pyrite ore, massive barite mineralization is characterized by an enrichment in galena and tetrahedrite, a marked depletion in pyrite and a distinct lack of arsenopyrite (Brathwaite, 1974).

Other types of mineralization

Cambrian massive sulfide mineralization was accompanied by the introduction of large quantities of hydrothermal carbonate and by minor base metal-poor pyritic mineralization. Additionally the massive sulfide has been overprinted by Devonian metamorphism which has produced a body of pyrrhotite-magnetite replacement at the southern end of the mine and minor quartz-carbonate gash veinlets with minor sulfide throughtout the mine.

Carbonate mineralization. The massive sulfide deposits of the Mt. Read Volcanics are unusual in that they contain a high carbonate content. Dixon (1980) interpreted the carbonates to have been deposited from the same fluids that deposited the sulfides but at a lower temperature and a higher pH. Massive carbonate tends to occur below and along strike from sphalerite-galena-pyrite ore (Dixon, 1980). Carbonate also occurs as a ubiquitous gangue in massive sulfide and barite mineralization. Brathwaite (1974) recorded the

mineralogy of the carbonates as rhodochrosite, kutnahorite, dolomite and calcite.

Distal pyrite mineralization. Disseminated to massive pyrite mineralization with minor base metals may occur along strike or above zinc-lead-rich mineralization. Typically this mineralization carries subeconomic base metal values, but it may carry significant gold and silver.

Pyrite-pyrrhotite mineralization. Brathwaite (1969, 1974) ascribed a transgressive body of pyrrhotite with minor chalcopyrite, pyrite and sphalerite that cuts zinc-lead-rich massive sufide at the southern end of the mine to metamorphic remobilization. This body is of interest in that it contains high gold grades (8.0 g/t), but Purvis (1984) inferred that the gold tenor was inherited from pre-existing massive sulfide.

Remobilized mineralization. Blind veins and patches of coarse grained quartz and carbonate (dominantly magnesian kutnahorite) that often carry sulfide and/or sulfosalts occur adjacent to or within fine grained massive sulfides throughout the deposit. Minerals present include galena, chalcopyrite, sphalerite, tetrahedrite, meneghinite, pyrargyrite and jordanite (Brathwaite, 1969). Brathwaite (1969) inferred that this mineralization style was the result of metamorphic remobilization. In addition to the more typical quartz-carbonate-sulfide gash veins, rare remobilized bismuthinite veins have been noted in copper-rich massive sulfide.

Chapter 2
Distribution and association of metals

Distribution of gold and silver in the north-end orebody

This study employs contoured cross sections and scattergrams to determine the distribution and metal associations of silver and gold. Although these results largely agree with previous studies on the distributions of silver at Rosebery (Brathwaite, 1969; Green et al., 1981; Green, 1983; and Naschwitz, 1985), some important new information is provided on the distribution of gold.

Spatial distribution of metals

Figure 75 illustrates the distributions of lead, copper, gold and silver for section 1113 mN. The distribution of base metals reflects the distribution of the major ore types.

Silver. Silver occurs with lead and zinc in sphalerite-galena-pyrite massive sulfide and massive barite mineralization. While all three metals tend to decrease towards the edges of mineralization, elevated silver values can occur at the lateral extensions of the orebodies, often in areas poor in base metals. Silver values tend to increase in the upper parts of both the sphalerite-galena-pyrite massive sulfide and massive barite lenses. Although lead, zinc and silver are usually low in pyrite-chalcopyrite massive sulfide, significant silver values (occasionally exceding 200 g/t) may occur in this ore type. Silver values may also be present to a minor extent in remobilized quartz-carbonate veins.

Gold. Although gold occurs dominantly in lead-zinc ore as noted by Brathwaite (1969), high gold values have six distinct occurrences:

(1) Sphalerite-galena-pyrite ore. This occurrence accounts for most of the gold present at Rosebery. Gold values tend to be fairly homogenous (typically 2 to 7 g/t), with few extreme highs (to 33 g/t) (assays over 1 m to 3 m lengths of split core). The highest gold grades (>5 g/t) have two main occurrences: (a) in the upper half (commonly near the top) of the massive sulfide lens usually above or nearby massive pyrite-chalcopyrite pods, and (b) at the edges of the orebody, particularly at the northern margin.

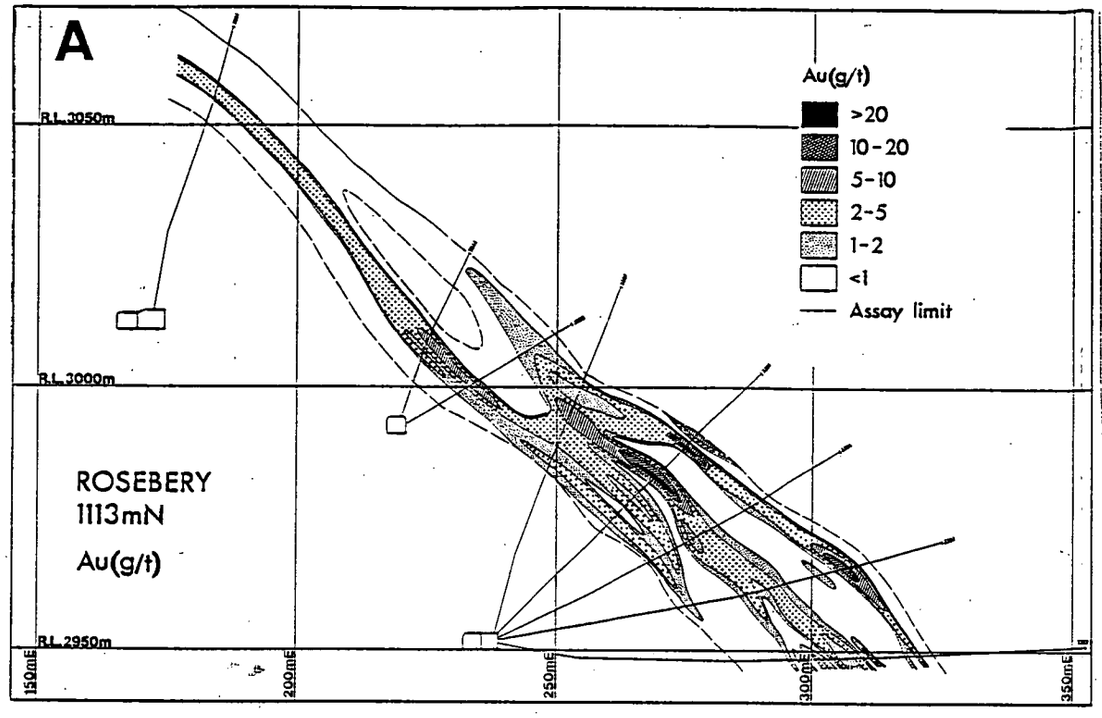

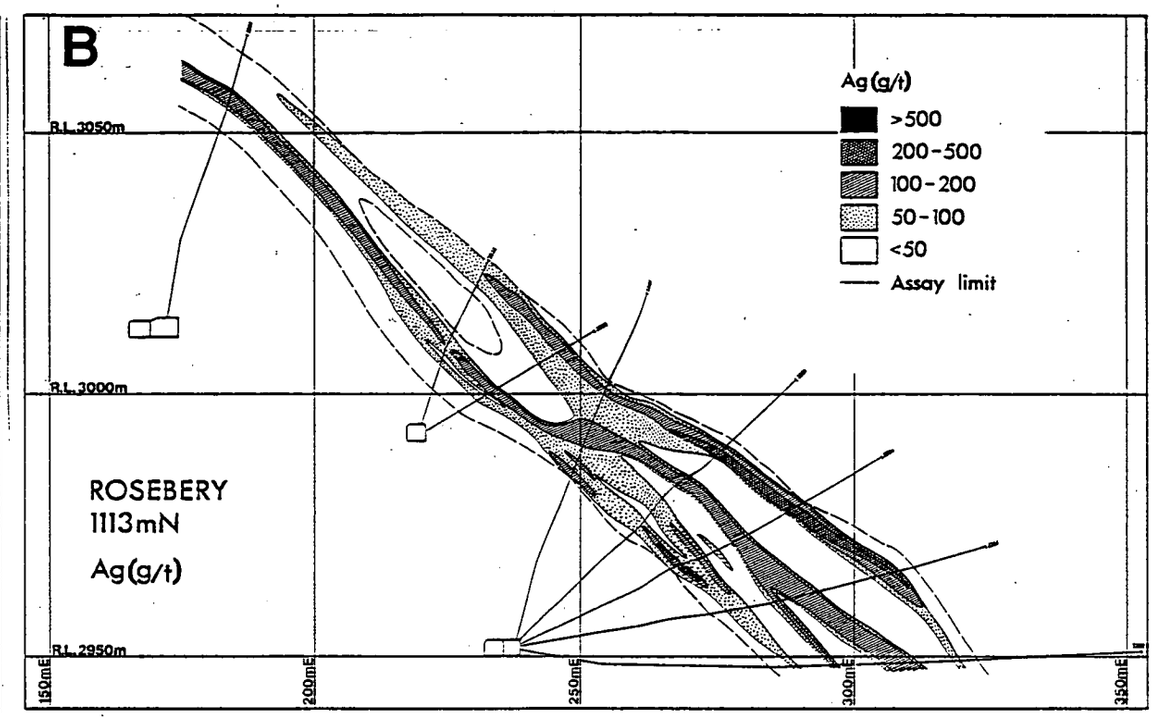

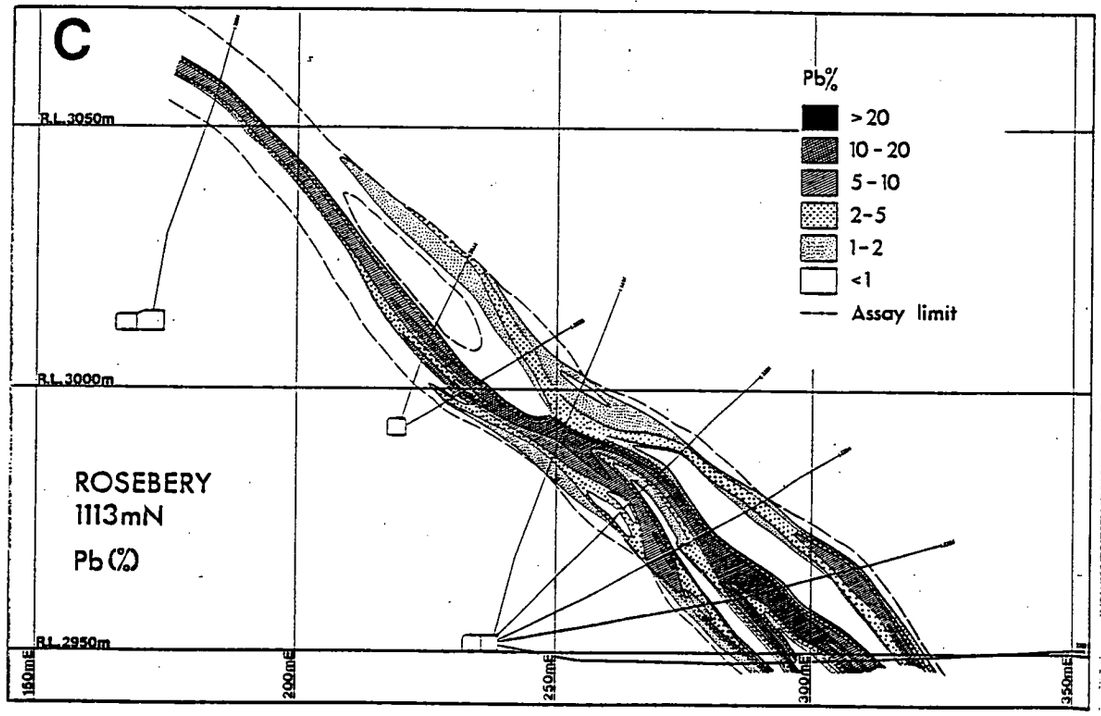

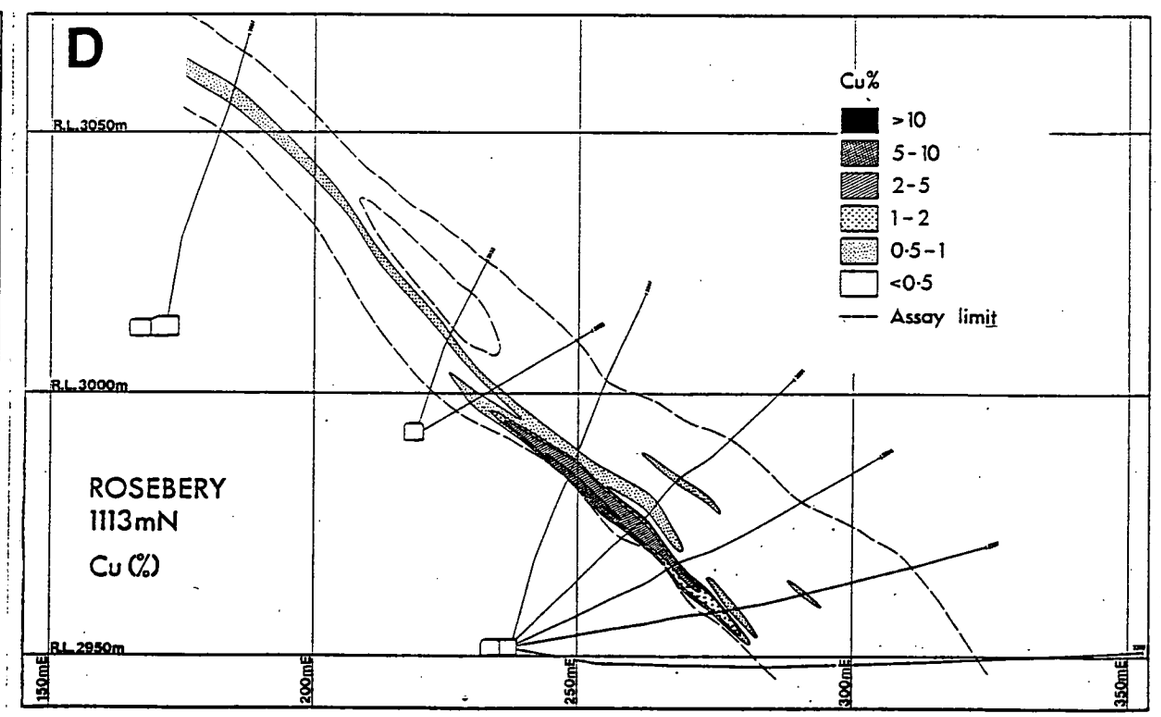

Figure 75. Metal distribution along section 1113 mN, Rosebery deposit: (a) gold, (b) silver, (c) lead and (d) copper.

(2) Massive barite mineralization. Although this mineralization is silver rich, it also contains sporadic high gold grades (to 38 g/t).

(3) Pyrite-chalcopyrite ore. Although this mineralization on average contains low gold values (usually <2 g/t), high gold values (occasionally >10 g/t) may occur near the top of the pods. The lower part of the pyrite-chalcopyrite lens contains low gold values.

(4) Distal pyrite mineralization. The north end of the north-end orebody contains several patches of high gold values (exceeding 20 g/t in one case) associated with disseminated to semi-massive pyrite lateral to the main body of mineralization. This gold mineralization has low base metal and only low to moderate silver values associated with it.

(5) Footwall mineralization. Although poorly understood, anomalous gold values (to 3 g/t) occur within altered footwall pyroclastics. Due to an inadequate number of assays, the exact mineral associations cannot be determined. This style of mineralization may be similar to the "precious metal zones" in the footwall alteration zone at Que River (McGoldrick and Large, 1987).

(6) Remobilized gold. As with silver, gold may be present in quartz-carbonate veins and veinlets. Occasionally gold assays exceed 2 g/t in this mineralization style, and typically these values lie either above or below a massive sulfide lens. Although mineralogically interesting, this mineralization style has little economic value in the north-end orebody.

The conclusion of this study, that gold occurs dominantly with sphalerite-galena-pyrite ore, differs from the copper-gold association suggested by Green et al. (1981). In the latter study, Green et al. (1981) evaluated average assay values taken over the entire width of ore by trend surface analysis. This analysis gave misleading results as high gold grades occur stratigraphically above, but not in, copper-rich ore. Most drill holes pass through all ore types, and when averaged across the width of mineralization show a misleading relationship between copper and gold. G.R. Green (pers. com., 1986) concurs that the copper-gold association is apparent and distorts the true association with silver (and therefore with sphalerite-galena-pyrite ore).

Metal associations as determined from scattergrams

Holes that were collared between late-1978 and late-1984 as part of the 15 level fan drilling program were used in this study. A total of 2039 complete analyses for lead, zinc, copper, iron (atomic absorption), silver and gold (fire assay) were available. Using core logs as a guide, three groups of samples were selected from the total data set as follows: (1) pyrite-dominated massive sulfide (i.e. pyrite-chalcopyrite and pyritic massive sulfide, but may include distal pyrite mineralization; 85 samples), (2) sphalerite-galena-pyrite massive sulfide (379 samples), and (3) massive barite mineralization (94 samples). Figure 76 shows log-normalized scattergrams for each group which relate gold to silver, zinc and copper. While zinc in massive sphalerite-galena-pyrite ore and copper in pyrite-dominated massive sulfide do not show log-normal distributions, all other data do. Therefore, for simplicity and consistency, all data have been log-normalized.

In pyrite-dominated massive sulfide gold has statistically significant positive correlation (at the 99% confidence level; see Dixon and Massey, 1957) with both silver and zinc. In massive sphalerite-galena-pyrite ore, gold has statistically significant correlation with silver, zinc and copper. In both types of mineralization gold correlates best with silver, followed by zinc, and least with copper.

However, in massive barite mineralization, both copper and zinc have better correlation with gold than does silver. An unusual characteristic of massive barite mineralization is the good correlation between gold and copper, which is seen in neither of the other two mineralization types. These data, in combination with mineralogic and fineness data (see below), suggest that gold mineralization in massive barite mineralization has a different character to gold mineralization in the massive sulfide ore.

The use of log-normalized data in scattergrams has the side-effect of obscuring subtle variations in the data. To overcome this problem, zinc has been plotted against gold in a non-transformed scattergram and the resulting distribution has been contoured in Figure 77. Examination of this figure indicates that although most (~90%) of the data plots on a trend of increasing gold with zinc, the highest gold values (>5 g/t) plot above this trend without any correlation to zinc. Although this may be related to the nugget

PYRITE DOMINANT MASSIVE SULFIDE

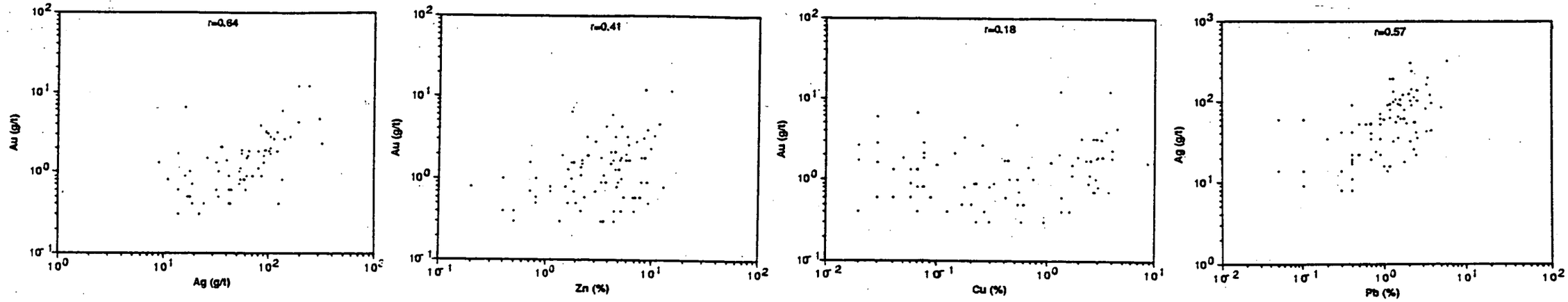

MASSIVE SPHALERITE-GALENA-PYRITE ORE

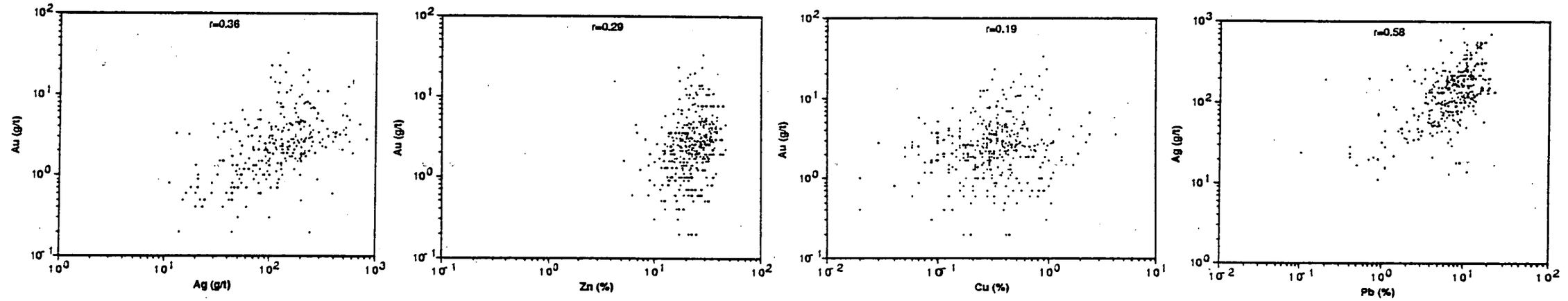

MASSIVE BARITE MINERALIZATION

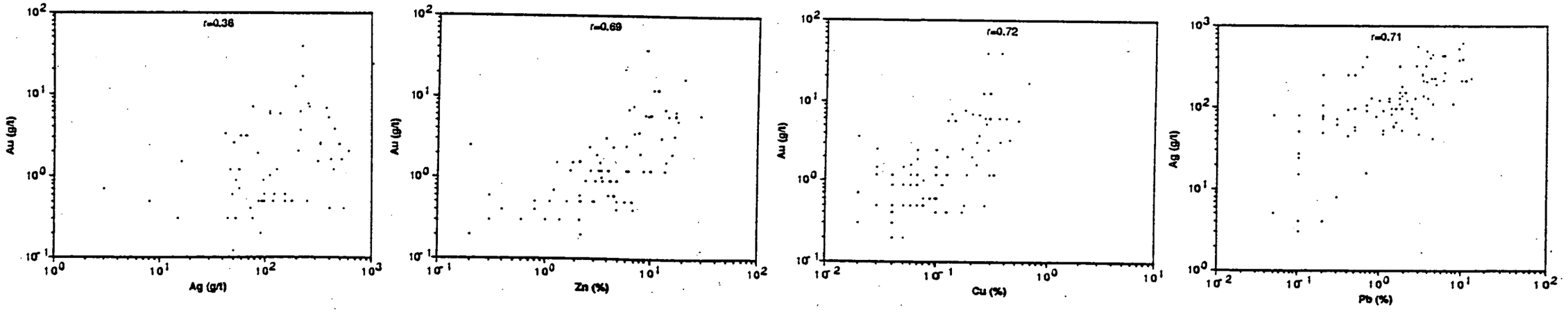

Figure 76. Scattergrams illustrating the relationships between gold, silver, zinc and copper from different types of mineralization, Rosebery deposit.

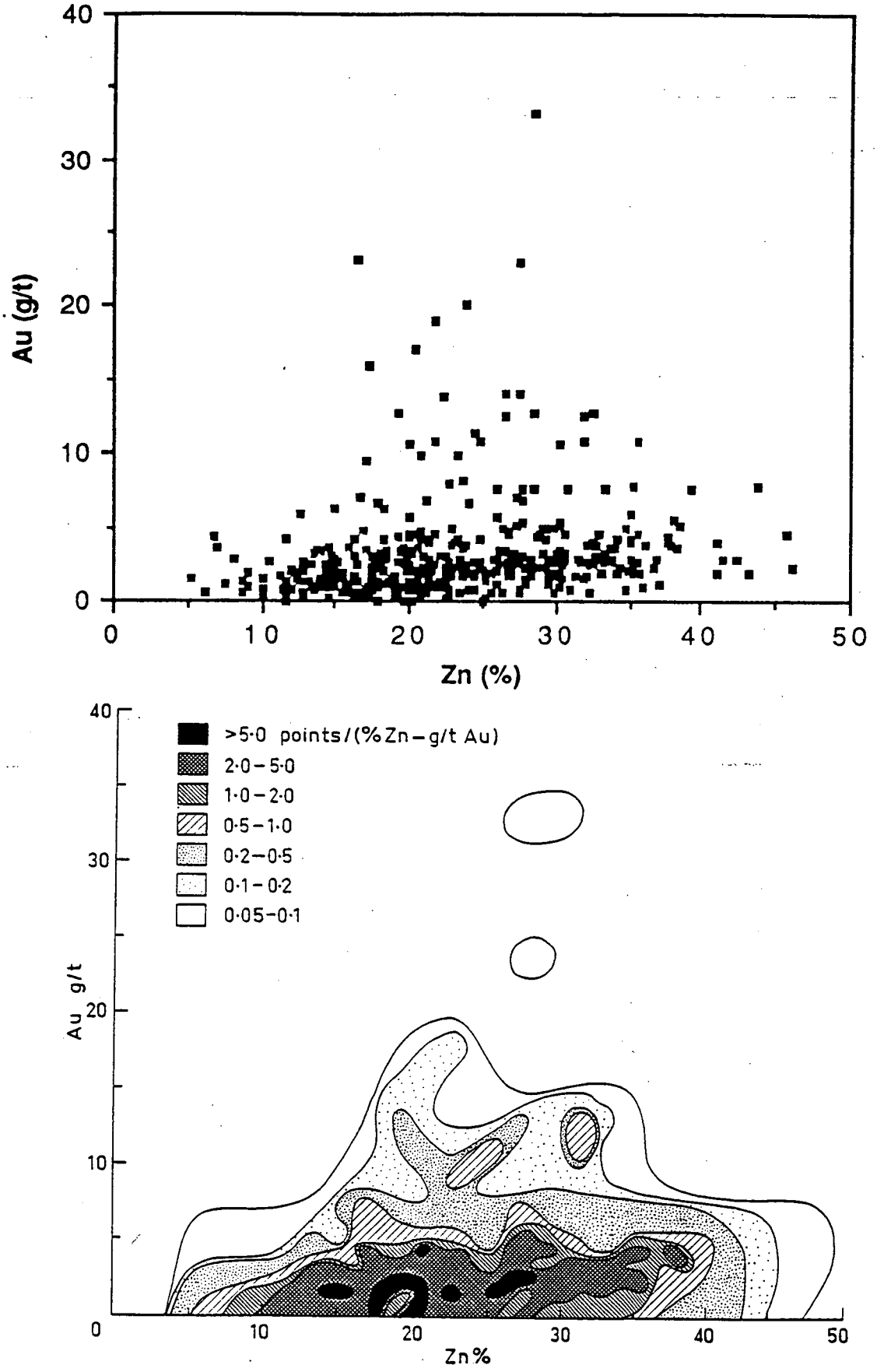

Figure 77. Scattergram and contoured diagram showing the relationship between zinc and gold in massive sphalerite-galena-pyrite ore, Rosebery deposit.

effect, the restriction of the majoritiy of high gold values to the lateral estensions and upper third of the massive sulfide lens (Fig. 78) indicates that the more likely control on these high gold grades may be a process gold refinement towards the top of the lens.

In all types of mineralization, silver has an excellent correlation with lead, which reflects the association observed from metal distributions.

The distribution of selected trace elements in the ores

To quantify trace element variations in the ores, seventy-four mine assay intervals (0.5m to 2 m half core splits) from six recent drill holes from the north-end (R3981, R3988, R4039, R4051, R4055 and R4076) were analyzed using atomic absorption spectrophotometry analysis for Ba (Appendix 1) and x-ray fluorescence analysis for As, Bi, Cd and Sb (Norrish and Chappell, 1977). This information is tabulated with standard mine assays for Pb, Zn, Cu, Fe (atomic absorption spectrophotometry analysis), Ag and Au (fire assay analysis) in Appendix 2 and illustrated in Figure 79 as down hole variation diagrams for three of the drill holes.

Results

Examination of the data indicates that two broad groups of elements are present: (1) those enriched in the copper-rich pods (Cu, Bi, As and Fe), and (2) those enriched in zinc-lead-rich parts of the orebody (Pb, Zn, Ag, Au, Sb, Cd, and Ba).

Of the five major ore metals recovered at Rosebery, four (Pb, Zn, Ag and Au) have similar distribution patterns in the ore (Fig. 79). Additionally, cadmium and antimony show similar patterns. All six elements have high concentrations in Pb-Zn ore and baritic mineralization. Zinc and Cd, and Sb and Ag have particularly good correlations (Figs. 80a and 80b). Cadmium probably occurs in solid solution with sphalerite, and tetrahedrite is the major Ag- and Sb-bearing mineral (Henley and Steveson, 1978).

Conversely, Cu, Bi, As and Fe are enriched in Cu-rich parts of the massive ore. Although these elements show a broadly similar distribution pattern, Bi shows a closer relation to Cu, while As shows a closer relation to Fe (Figs. 80c and 80d). Bismuth bearing minerals such as aikenite (Green et al., 1981), kobellite (Brathwite,

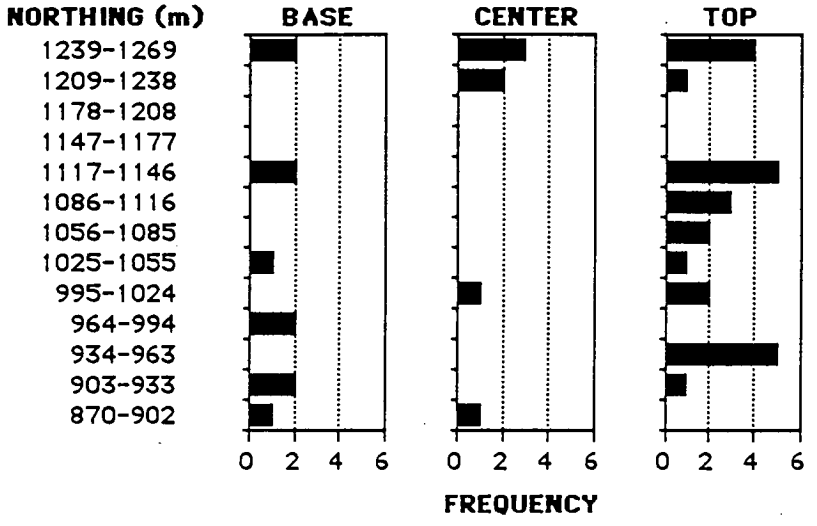

Figure 78. Occurrence of high gold values (>5 g/t) from massive sphalerite-galena-pyrite mineralization indicating stratigraphic and lateral distribution.

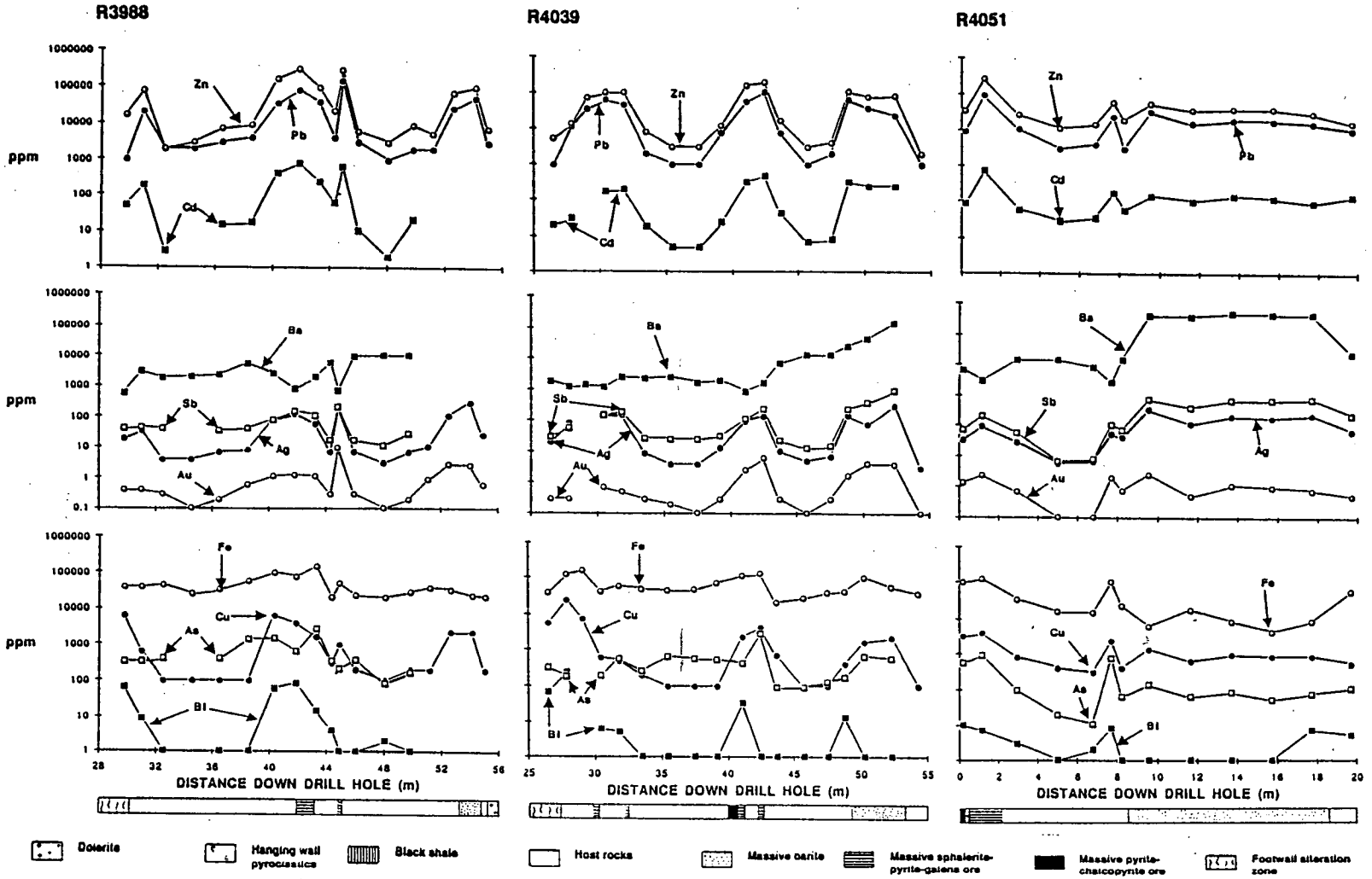

Figure 79. Downhole variations in the concentrations of Pb, Zn, Cd, As, Sb, Ag, Au, Ba, Fe, Cu, As and Bi in drill holes R3988, R4039 and R4051, Rosebery deposit.

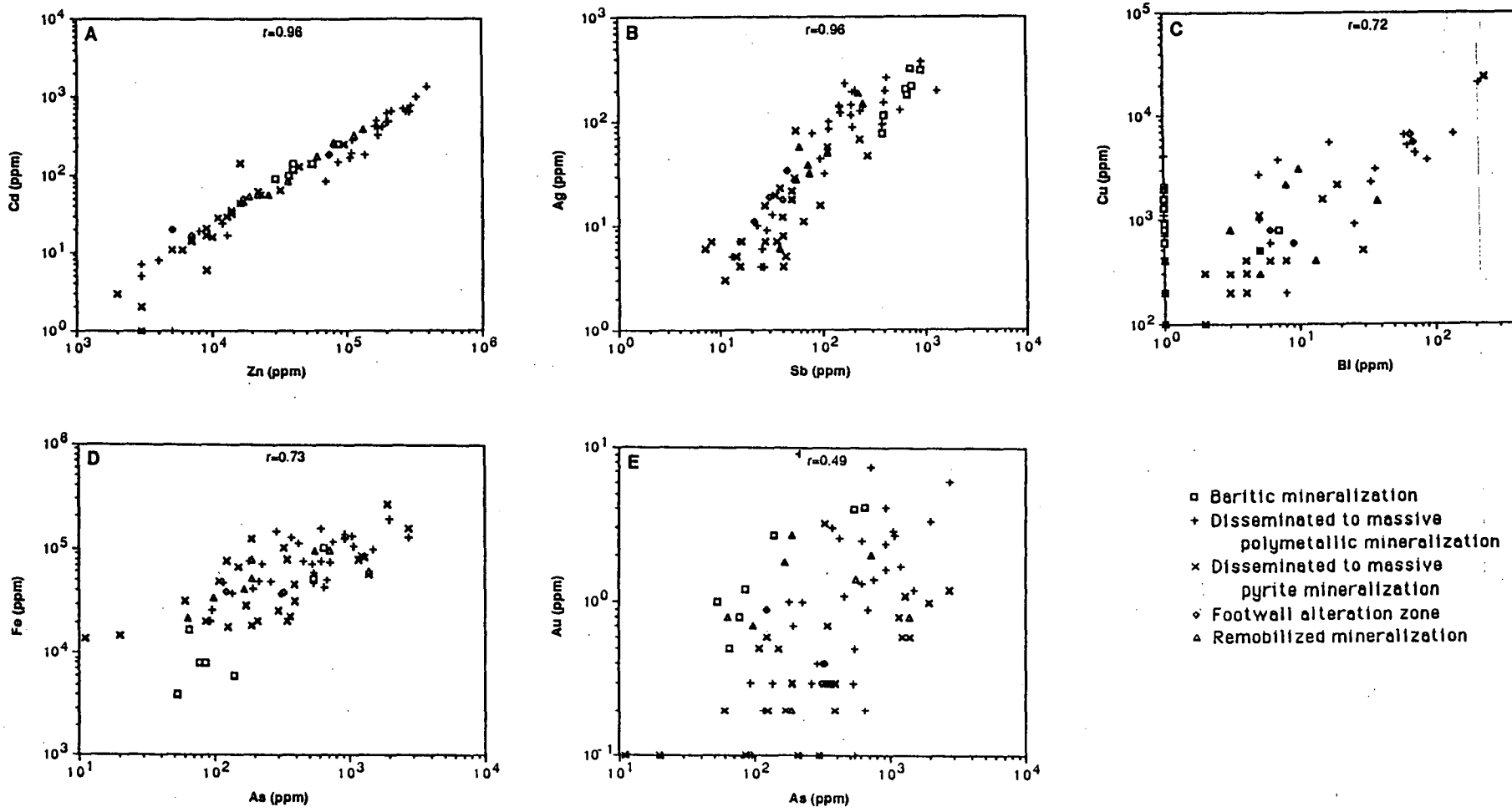

Figure 80. Scattergrams showing relationships between selected elements, Rosebery deposit.

1969), native bismuth and cosalite are restricted to massive pyrite-chalcopyrite lenses and footwall alteration zones. In pyritic mineralization, Au shows a moderate correlation to As (r=0.66; Fig. 79e), which is consistent with the electrum-arsenopyrite association in massive pyrite-chalcopyrite noted in Chapter 3.

Barium is enriched at the top of the sequence in massive barite mineralization. Below this zone, Ba has an antipathetic relationship to Pb, Zn, Ag, Au, Sb and Cd. Within massive barite mineralization, Ag and Sb are both elevated compared to massive sphalerite-galena-pyrite ore. Brathwaite (1969) noted that tetrahedrite is enriched in this mineralization.

Geologic discussion

In volcanogenic massive sulfide deposits in general, basal pyrite-chalcopyrite mineralization was deposited at relatively high temperatures (~300°C) whereas upper sphalerite-galena-pyrite and baritic mineralization was formed at lower temperatures (200-250°C) (Franklin et al., 1981; Eldridge et al., 1983; and Pisutha-Arnond et al., 1983). Estimates by Green et al. (1981) for Rosebery are consistent with these temperatures. Brathwaite (1969) noted an association between Pb, Zn, Ag and Au in the Pb-Zn ores of Rosebery; he also noted that Pb, Zn and Ag have an antipathy for Fe. Naschwitz (1985) observed the same Pb-Zn-Ag-Au association and also recorded a Cu-Fe association. The Pb-Zn-Ag-Au association occurs in the lower temperature sphalerite-galena-pyrite ore whereas the Cu-Fe assocaition occurs in the higher temperature pyrite-chalcopyrite ore (Brathwaite, 1969; and Naschwitz, 1985).

Lead, zinc and cadmium. Lead, zinc and cadmium have the strongest intercorrelations of any elements studied. The zinc-lead association is well known, and in Phanerozoic volcanogenic massive sulfide deposits, the 100Zn/(Zn+Pb) ratio ("Zn ratio") varies consistently between 60 and 85 (Lydon, 1985; and Part 3, Chapter 1).

Zinc and cadmium have a very strong correlation in the ores (r=0.96). As a consequence, the Zn:Cd ratio is very constrained with an average of 420 and a standard deviation of 120. As Cd wholely occurs in sphalerite, the Cd content of sphalerite should average about 0.14%. Microprobe analyses of sphalerite from the north-end (analyses by Khin Zaw and D. Huston) indicate a highly variable Cd content. Although most analyses were below the detection limit of

0.15%, some analyses contained up to 0.44% Cd (Fig. 81). Moreover, the entire variation in Cd content was present in single sphalerite grains.

The chemistry of Zn and Cd is very similar (Barnes, 1979) so these two metals should behave similarly in hydrothermal systems. At 25°C, chlorocomplexes of zinc are much more stable than those of Cd; under hydrothermal conditions, Zn is transported dominantly as a chlorocomplex (Ruaya and Seward, 1986). Therefore Cd was probably transported as a chlorocomplex with much lower stabilities than the corresponding Zn chlorocomplexes.

One explanation for the remarkable correlation between Zn and Cd at Rosebery is the saturation of the ore fluids in both Cd and Zn. Saturation or near saturation of zinc probably existed in the deposit (Part 3, Chapter 1).

A second explanation of the correlation is the presence of a constant amount of Cd in sphalerite. Microprobe analyses clearly demonstrate that this possibility is unlikely as there are large variations in Cd content internal to individual sphalerite grains.

The ratio in the ores may also be controlled by the ratio in the source rocks. Due to a lack of analytical data from the source rocks, this possibility cannot be tested.

Silver and antimony. As demonstrated above, Ag and Sb exhibit excellent correlation. Amcoff (1984) has suggested that paired substitution of Ag with either Sb or Bi in galena (i.e. $AgSbS_2$ or $AgBiS_2$ for Pb_2S_2) controls the distribution of Ag in massive sufide deposits although solvation in chalcopyrite may occur to a lesser extent. The strong correlations between Ag, Sb and Pb noted in this study and others support this contention to an extent, however, argentiferous galena accounts for only 30% of the Ag at Rosebery. Tetrahedrite accounts for 65% of the Ag (Henley and Steveson, 1978). While paired substitution of Ag with Sb (or Bi) may explain the distibution of Ag and Pb/Ag ratios in deposits in which argentiferous galena is the dominant, or only, Ag-bearing phase, this relatively simple model cannot explain the distribution of Ag in deposits in which other phases (i.e. tetrahedrite) are present.

The strong correlation between Ag and Sb is more likely to be due to the increase in Ag content with Sb content in tetrahedrite as noted by Henley and Steveson (1978) and confirmed by the present study (Chapter 3).

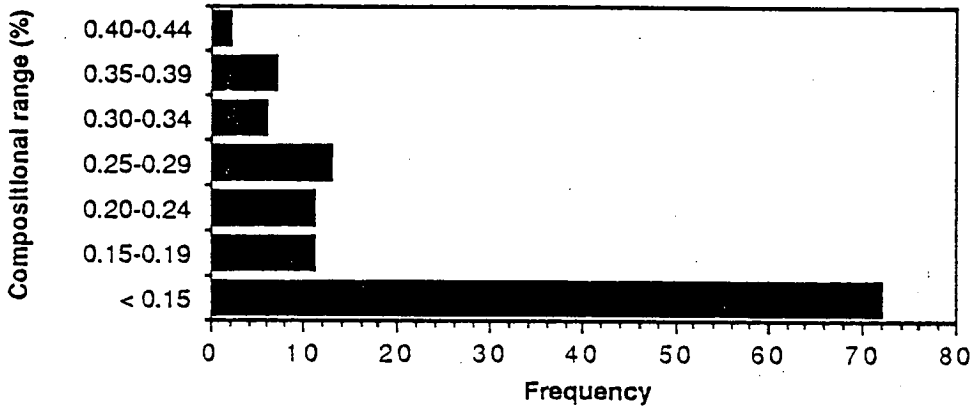

Figure 81. Histogram illustrating the variation in the cadmium content of sphalerite, Rosebery deposit.

Barium. The concentration of barium at Rosebery is controlled by the presence of barite. As barite is a sulfate mineral, it is only stable near or above the boundary between oxidized and reduced sulfur species. As a consequence, barite is only present in the upper part of the ore zone where the hydrothrmal fluids were oxidized by seawater. The notable lack of arsenopyrite in the barite lens (Brathwaite, 1969) is caused by the different redox conditions under which the two minerals are stable. Arsenopyrite is not stable under the oxidizing conditions required to precipitate barite.

Copper and bismuth. The strong association between bismuth and copper and the presence of Bi-bearing minerals only in high temperature pyrite-chalcopyrite mineralization indicates that Bi was deposited at high temperature. A similar Cu-Bi association at the base of the Stekkenjoll deposit in Sweden has been noted by Zachrisson (1982).

Iron and arsenic. Iron and As correlate well both within and outside the ore zone. Outside the ore zone As occurs dominantly within pyrite. Within the ore zone, As occurs dominantly as arsenopyrite, with probable contributions from tetrahedrite and As-bearing pyrite. Massive barite mineralization is notable in that it has lower concentrations of Fe and As and lacks arsenopyrite.

Based on extrapolated thermodynamic data on arsenic-bearing minerals and complexes, Heinrich and Eadington (1986) have modelled the deposition of arsenic. Their results indicate that arsenopyrite is stable in the pyrite field only under reduced conditions near the pyrite-pyrrhotite buffer. As barite is only stable at higher f_{O_2}, baritic mineralization cannot contain arsenopyrite, and any As present must be in other phases. The presence of arsenopyrite in massive sulfide ores indicates that they were formed at low f_{O_2} close to the pyrite-pyrrhotite buffer. At higher f_{O_2}, any arsenic present must occur in either tennantite-tetrahedrite or arsenic-bearing pyrite.

Chapter 3
Mineralogy and mineral associations of gold and silver

Introduction

A second aspect of the distribution of gold and silver at Rosebery is their distribution among different minerals. Several authors (Stillwell, 1934; Williams, 1960; Brathwaite, 1969; Smith, 1975; and Green, 1983) have treated this problem as part of a larger study, while Henley and Steveson (1978) have treated it specifically. In this study, a total of 81 polished blocks or thin sections were cut and examined along with gold bearing samples from previous studies. Of the newly cut sections, 16 were found to have visible electrum.

Silver mineralogy

Stillwell (1934) initially reported the presence of argentiferous tetrahedrite at Rosebery, while Smith (1975) first noted the presence of tennantite. Henley and Steveson (1978) demonstrated that tetrahedrite accounts for the majority of silver at Rosebery (65%).

Eighteen analyses from Smith (1975) along with 79 analyses from this study are shown in Figure 82, which plots silver content against antimony content for the tetrahedrite/tennantite series. The plot has two prominent features: (1) silver content increases with atomic 100Sb/(Sb+As) ratios, and (2) remobilized tetrahedrite is both antimony- and silver rich. Observation (1) is consistent with a similar observation by Henley and Steveson (1978). Figure 82 also suggests that the massive-sphalerite-galena-pyrite mineralization has a distinct trend, while massive barite mineralization has a separate trend which is richer in both silver and antimony.

The other major silver bearing mineral is argentiferous galena (30% of total silver; equivalent to a concentration of 1010 ppm). Minor silver bearing phases include chalcopyrite (180 ppm), sphalerite (30 ppm), and pyrite (2 ppm) (Henley and Steveson, 1978). Other possible silver bearing phases present in trace amounts include enargite, bournonite, boulangerite, electrum, pyrargyrite and

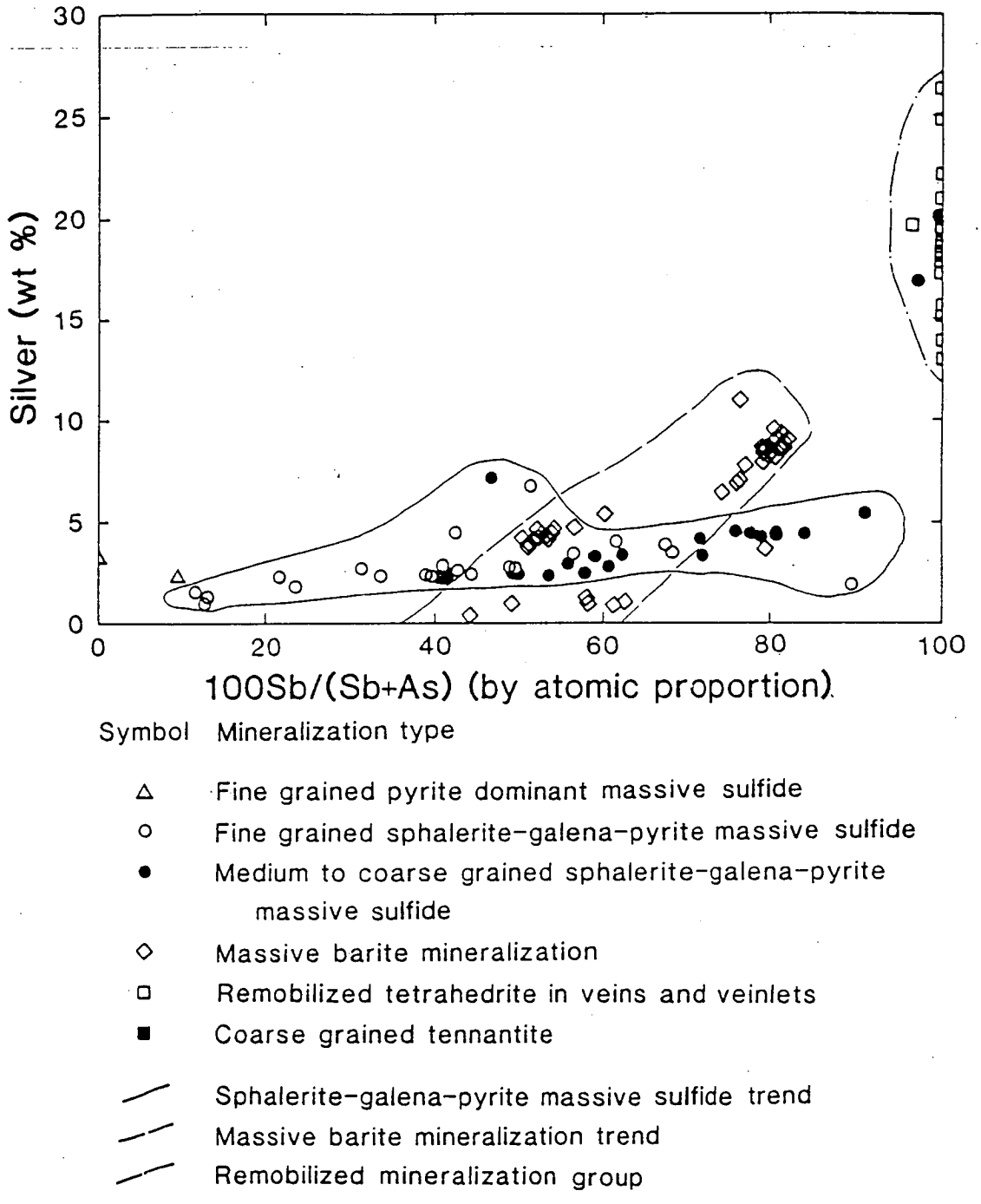

Figure 82. Silver content of tennantite-tetrahedrite series minerals. Data from this study (79 points) and Smith (1975; 18 points).

argentite (Stillwell, 1934; Williams, 1960; Brathwaite, 1969; and this study). Microprobe analyses of two bournonite grains gave 0.25 and 1.26 percent silver, respectively.

Gold mineralogy

Electrum has been observed to have several distinct occurrences in the Rosebery Mine. Stillwell (1934) first reported an association with coarse-grained tetrahedrite, which was later confirmed by Williams (1960), Brathwaite (1969), and Green (1983). Brathwaite (1969) noted that this electrum occurred in patches and as veinlets within tetrahedrite. He also observed electrum in a chalcopyrite-arsenopyrite-tetrahedrite aggregate in sphalerite-galena-pyrite ore. Green (1983) and Brathwaite (1974) noted electrum in pyrite-chalcopyrite ore, but the relationship of gold to other minerals was not described.

In this study, however, the dominant association of electrum was found to be with pyrite. Both sphalerite-galena-pyrite massive sulfide and distal pyrite mineralization show this strong association. However, pyrite-chalcopyrite massive sulfide, massive barite mineralization and remobilized mineralization show other associations.

Pyrite-chalcopyrite ore

Electrum occurred in one sample as inclusions or along cracks within recrystallized arsenopyrite in a crosscutting chalcopyrite vein (Fig. 83a). This occurrence is consistent with the association of electrum with chalcopyrite veins as suggested by G.R. Green (personal communication, 1985). The electrum was possibly remobilized into inclusions or cracks within the arsenopyrite during Devonian recrystallization.

Sphalerite-galena-pyrite ore

Three sections from massive sphalerite-galena-pyrite mineralization were observed to contain seven occurrences (15 individual grains) of electrum in this study. In each case, the electrum has a strong association with pyrite, usually occurring with galena or chalcopyrite in micro-veins within or between grains of

Figure 83. Photomicrographs showing electrum occurrences from the Rosebery north-end: (a) electrum and tetrahedrite inclusions in arsenopyrite (as) in a chalcopyrite vein cutting massive pyrite(py)-chalcopyrite ore (R-8), (b) electrum with sphalerite, galena, and argentite (ag) in a veinlet between recrystallized pyrite grains in massive sphalerite-galena-pyrite ore (R3391-138.25), (c) electrum with galena in a veinlet crosscutting a corroded pyrite grain in massive sphalerite-galena-pyrite ore (R3397-127), (d) electrum in a chalcopyrite pool with barite (ba) gangue in massive barite mineralization (R3391-165.75), (e) electrum among intergrown barite grains with sphalerite, galena and chalcopyrite in massive barite mineralization (R3397-140.5), (f) electrum, tetrahedrite and galena grains between lath-like pyrite grains in a colloform band in distal pyrite mineralization (R3377-220), (g) electrum in a remobilized quartz-sphalerite-chalcopyrite-chlorite-sericite-galena-pyrite-carbonate vein cutting quartz-sericite schist (R3375-114.5; note the delicate replacement of sphalerite by chalcopyrite), and (h) maldonite (mal) pool with myrmekitically intergrown gold (Au) and bismuth along the edges from a remobilized bismuthinite (bi) vein with carbonate gangue (R4021-28.0).

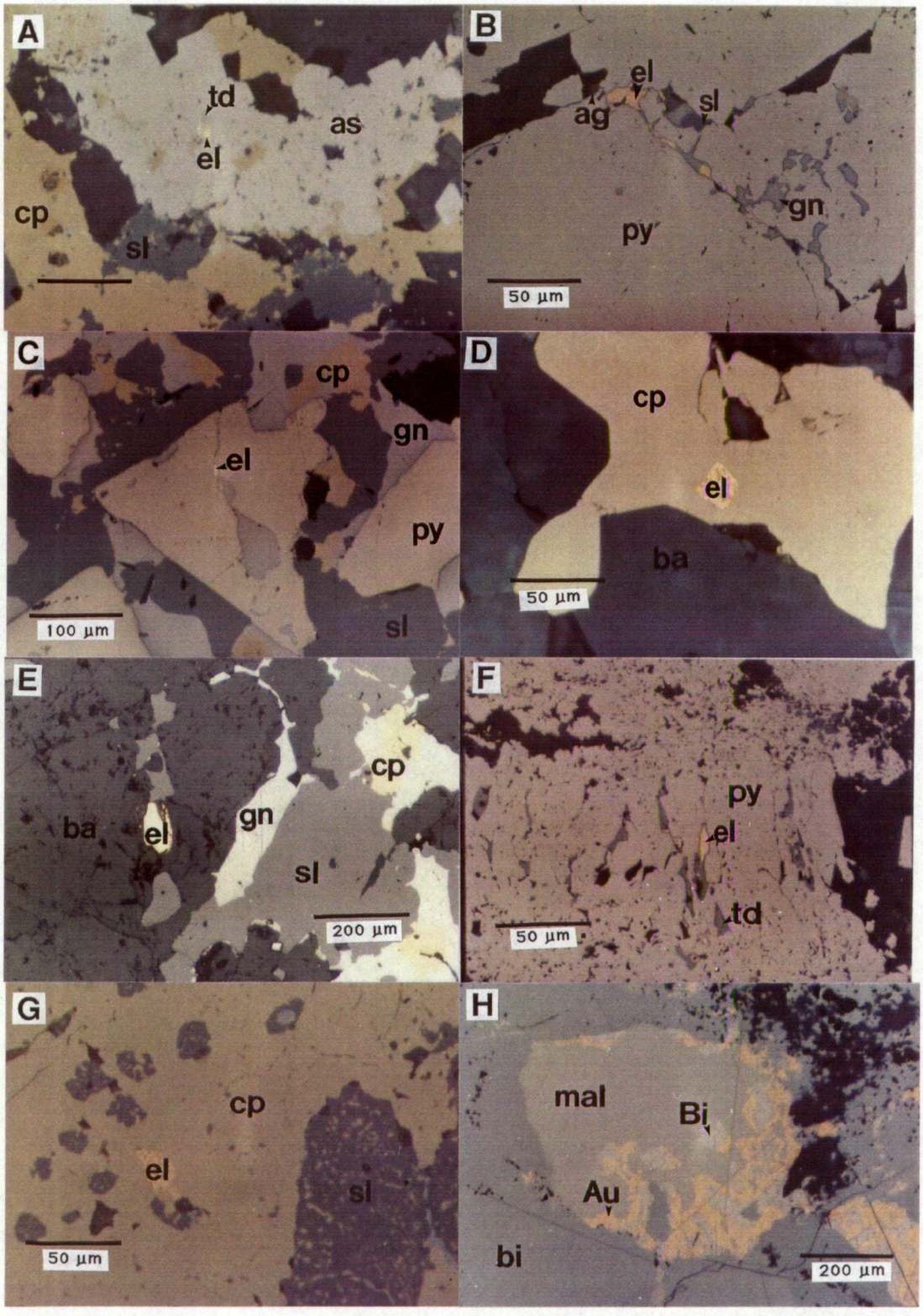
A
td
as
el
cp
sl
B
el
ag
sl
gn
py
50 µm
C
cp
gn
el
py
100 µm
sl
D
cp
el
ba
50 µm
E
cp
ba
el
gn
sl
200 µm
F
py
el
td
50 µm
G
cp
el
sl
50 µm
H
mal
Bi
Au
bi
200 µm

recrystallized pyrite (see Figs. 83b and 83c). The association of electrum with pyrite may be the most significant occurrence as Henley and Steveson (1978) concluded that about half of the gold in the zinc residue was present in pyrite at a level of 2 ppm.

Previous authors (Stillwell, 1934; Williams, 1960; Brathwaite,1969; and Green, 1983) have noted that electrum occurs as patches and veinlets in tetrahedrite and in chalcopyrite-arsenopyrite-tetrahedrite aggregates. Although this association was not observed in the present study, a tetrahedrite-electrum association seems to be a second major occurrence of gold in massive sphalerite-galena-pyrite ore.

Massive barite mineralization

Only three occurrences of electrum in three sections were observed in this study from massive barite mineralization. In each occurrence the electrum had a different association: with chalcopyrite (Fig. 83d), as a discrete grain among intergrown barite grains (Fig. 83e), and as a five micron grain in a galena pool. Additionally, two sections from just below barite mineralization (and similar in many ways to barite mineralization, but lacking visible barite) contained electrum associated with chalcopyrite. Massive barite mineralization lacks the previous association of gold with pyrite, but the actual association is unclear. A possible association is with chalcopyrite, which would be consistent with the metal associations seen in scattergrams.

Distal pyrite mineralization

Four sections from distal pyrite mineralization were observed to contain electrum in this study. In three sections, electrum was observed to occur with pyrite in a similar fashion to electrum in massive sphalerite-galena-pyrite ore.

Although electrum occurs with pyrite in the fourth section (see Fig. 83f), the electrum and pyrite have different habits. The sample came from an unusually cherty interval on the northern edge of the north end that contained masses of colloform pyrite up to 10 cm. In the section, the electrum seems to be restricted to one or more bands of lath-like pyrite near the edges of a colloform mass. The gold occurs with galena and tetrahedrite and galena interstitial to the

lath-like pyrite grains. The lath-like habit of the pyrite grains is unusual and suggests that the habit is a pseudomorphic replacement texture, possibly after anhydrite on morphological grounds. If so, the electrum present may show primary textures of deposition, which suggest that some of the gold in distal pyrite mineralization may have been deposited as free electrum.

Remobilized mineralization

In two sections, electrum occurs with chalcopyrite in crosscutting sulfide-quartz-carbonate veinlets in relatively unmineralized host rock. Two possibilities exist on the timing of the veining: (1) during or closely following massive sulfide deposition, or (2) during Devonian recrystallization. Devonian recrystallization following or during the Tabberabberan orogeny is preferred as in Figure 83g, chalcopyrite shows an intricate replacement of sphalerite which would have been annealed during the Tabberabberan orogeny. Brathwaite (1969) noted that coarse grained remobilized sulfides are likely to be post deformation, which suggests that electrum occurrences with coarse-grained tetrahedrite reported by other authors (Stillwell, 1934; Williams, 1960; Brathwaite, 1969; and Green, 1983) are probably remobilized.

A sample from E lens, in the south-end, contains an unusually gold-rich bismuthinite vein that crosscuts recrystallized massive pyrite-chalcopyrite ore. The mineralization is comprised of a central 2-5 cm vein of nearly massive bismuthinite. Minor amounts of gold and bismuthinite also occur out into the surrounding massive pyrite-chalcopyrite host. The vein also contains remnant sphalerite, chalcopyrite, tetrahedrite and arsenopyrite in minor quantities. Less important minerals associated with the vein include native bismuth, maldonite (Au_2Bi), carbonate (Fig. 83h) and two unknowns (possibly aurobismuthinite ($(Bi,Au,Ag)_5S_6$) and a bismuth sulfosalt). Maldonite occurs as pools within the bismuthinite vein that typically have myrmekitic intergrowths of native bismuth and gold at their edges.

Electrum fineness and grain size

Microprobe analyses of electrum grains observed in this study (30 separate grains) indicate a fineness range of 320 to 970, with

most data falling between 320 and 760. The grain size of the electrum grains has a distinctly log-normal distribution with a mode at 10 μm (see Part 3, Chapter 4 for detailed description). As the mill currently grinds the ore such that 20 percent passes 200 mesh (75 microns), much, if not most, of the gold would remain encased by sulfides. Presumably the gold would then report to the concentrate that the enclosing sulfide would report to; gold encased by pyrite would report to the tails.

Pre-deformation occurrence of gold

The original pre-deformation association of gold at Rosebery is unclear as much of the gold observed has clearly been mobilized into cracks within, or boundaries between, recrystallized pyrite grains. The possibility exists that gold occurred originally within pyrite, either in solid solution or as submicroscopic grains. Boyle (1979) suggested that at high temperatures, gold may occur as solid solution in pyrite or arsenopyrite, but at lower temperatures, the gold migrates to zones of weakness within the sulfides (i.e. cracks or grain boundaries).

Recrystallization of pyrite during deformation might enhance this process. The association of gold with pyrite has already been noted at the Corbet Mine, Canada (Knuckey and Watkins, 1982). Large et al. (in press) noted that the initial gold bearing minerals at the Hellyer and Que River deposits were probably pyrite and arsenopyrite.

Hannington et al. (1986) inferred an association of gold with Pb-As-Sb-Ag sulfosalts for the Axial Seamount and southern Explorer Ridge black smoker deposits. Shimazaki (1974) and Sato (1974) have noted an association with sphalerite, galena and tetrahedrite in black ore of the Kuroko district. The gold-tetrahedrite association #lted by previous workers at Rosebery may be of a similar nature, but is considered by the author to be of lesser importance than the gold-pyrite association.

Chapter 4
Summary and Conclusions

This study and the review of other papers discussed earlier allow the following conclusions with regards to the distribution, mineralogy and geochemistry of precious metals in the north-end orebody at the Rosebery deposit.

Conclusions relative to silver

(1) The highest silver grades occur in the upper parts of the massive sphalerite-galena-pyrite lens and massive barite mineralization.
(2) Silver grades decrease towards the edges of the deposit although high grades can occur at the fringes of the ore lens, in areas with low base metal values.
(3) Silver occurs dominantly in tetrahedrite and, to a lesser extent, in argentiferous galena (Henley and Steveson, 1978).

Conclusions relative to gold

(1) Anomalous or economic gold values occur in six distinct styles of mineralization in the Rosebery north end (in order of significance):
    (a) Sphalerite-galena-pyrite ore (the major occurrence of gold). The highest gold grades tend to occur above copper-rich centers and at the margins of the ore lens. Gold occurs as electrum associated with pyrite or tetrahedrite. The electrum has variable fineness and shows signs of local mobilization during Devonian metamorphism.
    (b) Barite mineralization. This mineralization contains very sporadic gold values which occur as electrum in association with chalcopyrite or galena.
    (c) Pyrite-chalcopyrite ore. Although usually low in gold, this style of mineralization may contain high gold grades near the tops of pyrite-chalcopyrite lenses or in pyrite-

chalcopyrite lenses enclosed within sphalerite-galena-pyrite ore. Electrum was observed in association with arsenopyrite in crosscutting chalcopyrite veins.

(d) Distal pyrite mineralization. High gold grades may also occur in distal disseminated to semi-massive pyrite bodies lateral to or statigraphically above zinc-lead mineralization. The gold occurs as electrum in association with pyrite.

(e) Footwall mineralization. Occasional anomalous gold values were observed in altered footwall pyroclastics, but this mineralization is poorly documented and understood.

(f) Remobilized mineralization. Gold may occur with chalcopyrite in quartz-carbonate veins associated with remobilization during the Devonian Tabberabberan orogeny in the north end, but this does not seem to produce economic grades. Bismuthinite-gold veins are also attributable to Devonian remobilization.

(2) Gold occurs as electrum usually associated with pyrite. Mineragraphic work indicates that much of the gold occurs as grains less than 25 microns in dimension. The small size of the gold grains explains the high gold contents of the mill tails.

Conclusions relative to trace elements

(1) Trace elements in the ores have two distinct associations: (1) Cu-Fe-As-Bi which was produced at higher temperatures (~300 °C), and (2) Zn-Pb-Ag-Au-Cd-Sb-Ba which was produced at lower temperature (~250 °C).

(2) The enrichment of barium at the top and arsenic at the bottom of the sulfide lens may be explained as the result of an increasing f_{O_2} gradient through the massive sulfide during formation.

(3) The strong correlation between zinc and cadmium may be explained by assuming saturation of both metals in the hydrothermal solution.

(4) The strong correlation between silver and antimony is due to the occurrence of most silver in tetrahedrite.

Significance to Exploration

This study suggests that, in addition to the gold contained within the massive ore lenses, significant gold and silver values exist outside massive sphalerite-galena-pyrite and pyrite-chalcopyrite ores. Massive barite mineralization contains some of the highest precious metal values, albeit highly sporadic in the case of gold. These mineralization styles are currently well sampled and understood within the mine. Of possible more significance is the documentation that high gold values can exist in pyritic mineralization lateral to and stratigraphically above the main zinc-lead mineralization, that high silver values can occur at the fringes of the deposit, and that anomalous gold values can occur in the footwall. These mineralization styles occur outside current ore reserves and serve as potential exploration targets in the mine. The descriptions may also serve as exploration models for precious metal targets within volcanogenic massive sulfide systems elsewhere.

Study of trace elements indicates that certain particular parts of the orebody are enriched in trace elements that may cause metallurgical problems. For instance, bismuth and arsenic are concentrated in copper-rich portions of the orebody, whereas cadmium is concentrated in zinc-rich portions of the orebody.

Part III

Geological and geochemical controls on the formation of volcanogenic massive sulfide deposits

Chapter 1
Theoretical and genetic aspects of the zinc ratio (100Zn/[Zn+Pb]) in volcanogenic massive sulfide deposits

Introduction

The ratio 100Zn/(Zn+Pb), hereafter referred to as the zinc ratio, is remarkably consistent in samples from volcanogenic massive sulfide deposits (e.g. Stanton, 1958). In Figure 84a the variation in the bulk zinc ratios for Phanerozoic Zn-Pb-Cu volcanogenic massive sulfide deposits from eastern Australia, the Green Tuff district of Japan, the Iberian pyrite belt, the Buchans, Newfoundland district, and the Bathurst, New Brunswick, district is illustrated as a histogram. The distribution has one mode, with a mean value of 76.3 and a standard deviation of 18.8. Lydon (1985) showed that the Proterozoic lead-poor Cu-Zn massive sulfide deposits of the Canadian Shield have a distinctly higher bulk zinc ratio that the Phanerozoic Zn-Pb-Cu style, with a mode at 95 to 100 (Fig. 84b). Both groups have low standard deviations in comparison to sediment-hosted Pb-Zn deposits (Fig. 84c).

This chapter addresses the genetic controls of the zinc ratio in volcanogenic massive sulfide deposits, and Huston and Large (1987b) described the ratio in other types of Zn-Pb deposits and the exploration uses of the ratio as a discriminator of mineralization style. This study presents data from deposits from the Mt. Read Volcanics in Tasmania and the Balcooma metamorphic belt in Queensland to document variations in the ratio caused by primary mineralization and by later metamorphic recrystallization.

Deposits in the Mt. Read Volcanics, Tasmania

Volcanogenic massive sulfide deposits are by far the most significant base metal resource in the Mt. Read Volcanics. Data for three deposits, Rosebery, Hercules and Hellyer, were available for this study (Fig. 72).

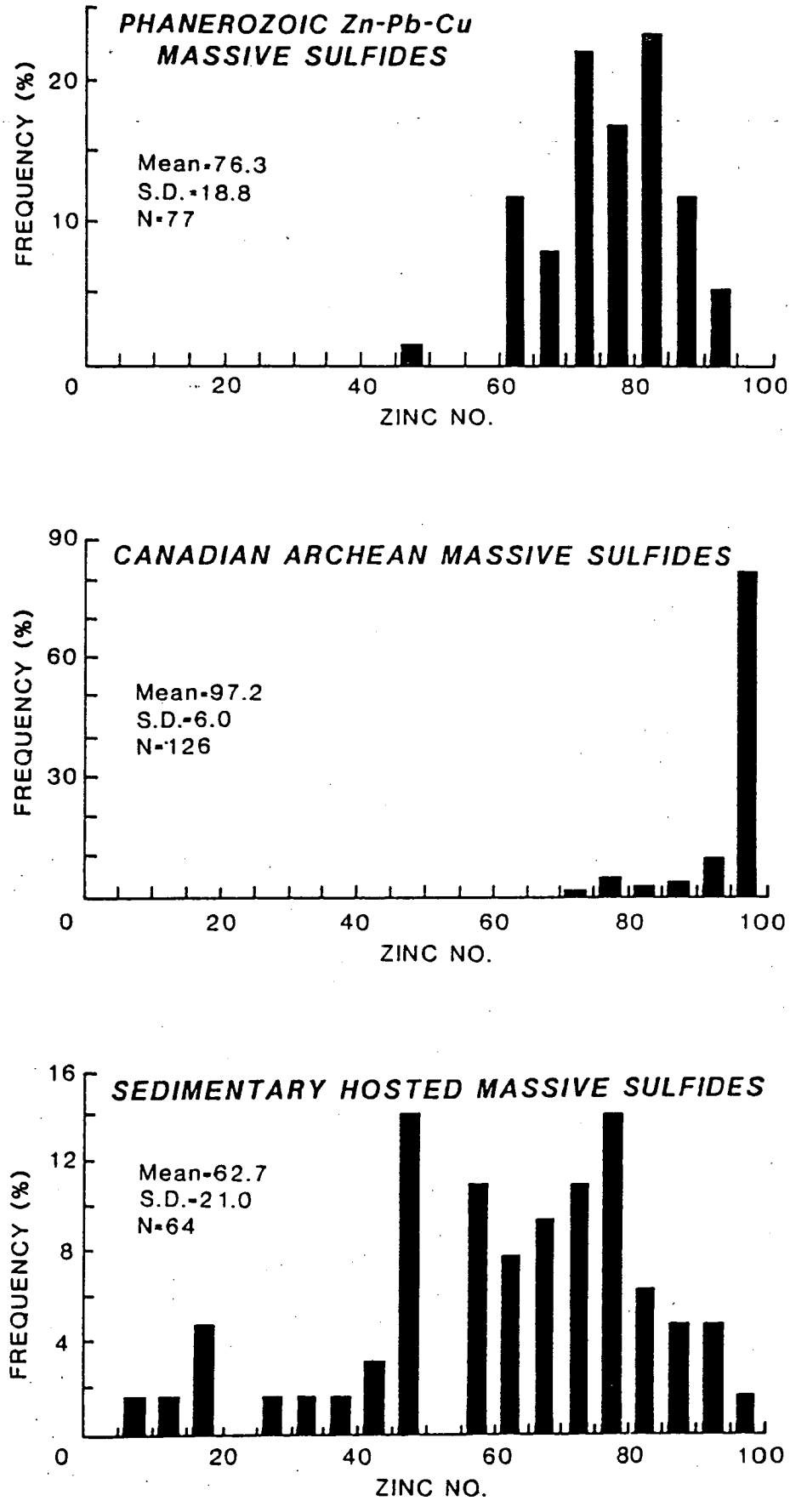

Figure 84. Zinc ratios of (a) Phanerozoic volcanogenic massive sulfide deposits, (b) Canadian shield volcanogenic massive sulfide deposits, and (c) sediment-hosted massive sulfide deposits.

Rosebery

The assay data from 2039 samples from the north-end of the mine were divided into the three groups described in Part 2, Chapter 2 and a fourth group from footwall pyritic sericitic schist (286 samples). The samples are from unweathered core split over lengths of between 0.3 and 2.0 m (usually 1.0-1.5 m).

Figure 85 shows the zinc ratio histograms and plots of lead vs. zinc and zinc vs. zinc ratio for the four data groups. With the exception of the massive barite group, all of the data groups show the following characteristics:

(1) The great majority of points in the lead vs. zinc diagram plot above the line Zn=1.5Pb (i.e. zinc ratio=60.0). This line marks a very sharp cutoff to the low limit of the zinc ratio.

(2) The zinc vs. zinc ratio plots reflect the lead vs. zinc plots in that most data points fall above the line where zinc ratio equals 60. The plots also show that the zinc ratios show a wide scatter below 1 percent zinc; this probably reflects a lower analytical precision at lower concentrations.

(3) The zinc ratio populations for the different data groups have mean values ranging from 71.4 to 74.5 and standard deviations ranging from 9.6 to 14.7. The standard deviations decrease stratigraphically upwards from the footwall through to the top of the orebody. This may reflect a decrease in temperature of the fluids, with higher temperatures having a more variable zinc ratio as predicted from chemical modelling (see discussion below).

The distributions for each group are, for practical purposes, equivalent. The regularity of these parameters through the orebody, even among different ore and mineralization types, are characteristic of volcanogenic massive sulfides of the Mt. Read Volcanics. These parameters are very useful in understanding the chemistry of zinc and lead transport and deposition of these deposits (see below).

The group of samples containing barite gangue differs from the other groups in several respects. First, the data plot along a straight line (Zn=1.9Pb, zinc ratio=65.5) with little dispersion about the line. Second, the zinc ratio shows both a lower mean (68.9) and standard deviation that the other data groups. These

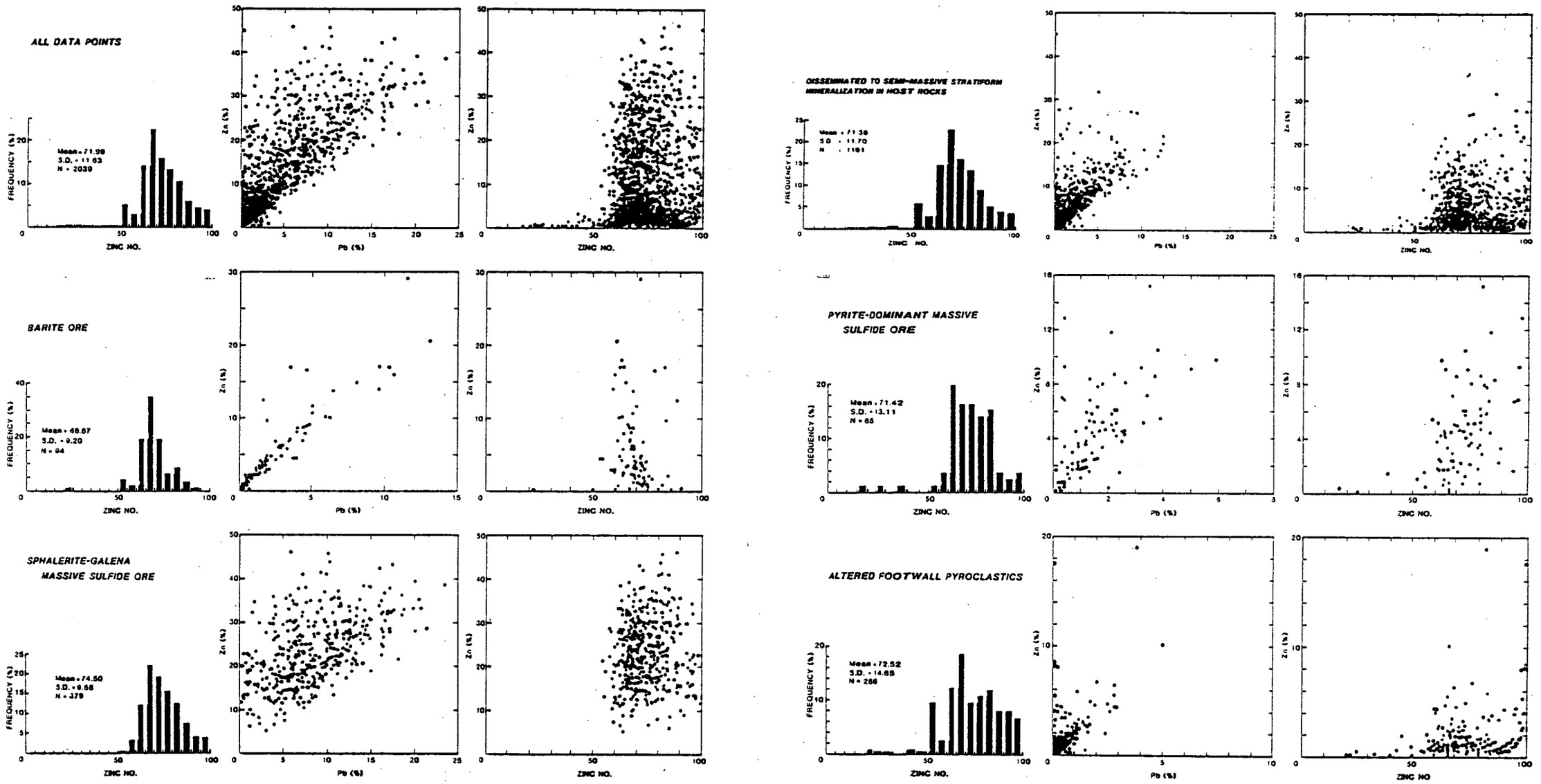

Figure 85. Relationships between lead, zinc and the zinc ratio for various ore types at Rosebery.

differences may be related to different physicochemical conditions for the deposition of massive barite mineralization compared to those for deposition of the massive sulfide ores.

Hercules

The Hercules mine lies seven km south of Rosebery along the same stratigraphic horizon as the Rosebery deposit (Green et al., 1981). The stratigraphy of the mine is similar, but the Hercules ores have been significantly more deformed. Deformation has remobilized sulfides in dilatent areas which include fold hinges and the eastern limbs of drag folds (Burton, 1975). Figure 86 gives the zinc ratio histogram from drill hole assays. The distribution is very similar to that seen at Rosebery although both the mean and the standard deviation at 75.7 and 14.3, respectively, are slightly higher. This implies that remobilization of sulfides has not affected the zinc ratio significantly at relatively low grade (upper greenschist) metamorphic conditions.

Que River and Hellyer

Published ore reserves and grades (Table 10) indicate that both Que River and Hellyer have lower bulk zinc ratios (64.1 and 65.0, respectively) than Rosebery and Hercules. These values do, however, lie within the range defined for Phanerozoic volcanogenic massive sulfides (Fig. 84a) and outside the range of most other mineralization styles in the Mt. Read Volcanics (Huston and Large, 1987b).

The lead vs. zinc plot for the Hellyer deposit (Fig. 87) has the same general characteristics as those of Rosebery, but the lower cutoff line has a shallower slope (Zn=1.2Pb, zinc ratio=54.5). These differences are interpreted to relate to slight differences in chemical conditions as discussed later.

Summary

The zinc ratio histograms plotted from diamond drill hole intersections for individual volcanogenic massive sulfide deposits in the Mt. Read Volcanics exhibit means between 64 and 77, with relatively low standard deviations (less than 15). The distributions

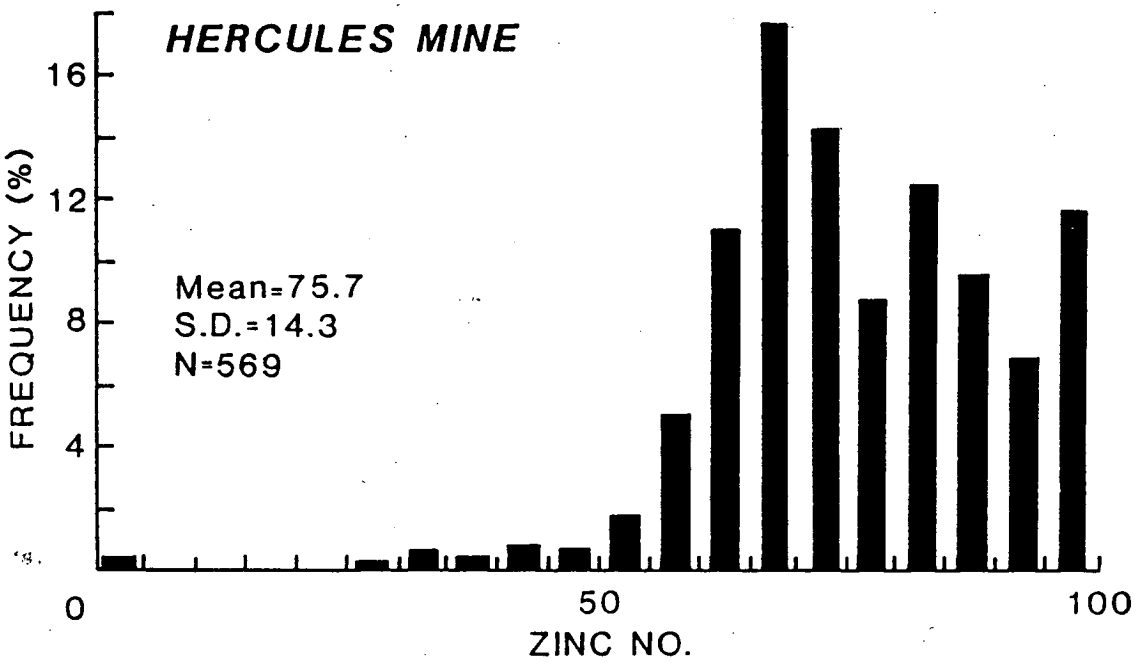

Figure 86. Zinc ratio histogram for the Hercules deposit.

Table 10. Grades, tonnages and mean zinc ratios for volcanogenic massive sulfide deposits in the Mt. Read Volcanics, Tasmania.

Deposit	Tonnage (million tonnes)	Pb (%)	Zn (%)	Cu (%)	Ag (g/t)	Au (g/t)	Zn ratio	Footwall lithology
Rosebery	19.4	5.0	16.2	0.7	155	2.9	76.4	Rhyolite
Hercules	2.6	5.2	16.7	0.4	159	2.7	76.3	Rhyolite
Hellyer	15	7.0	13.0	0.4	160	2.3	65.0	Andesite
Que River	3.5	7.0	12.5	0.4	170	3.3	64.1	Andesite

Data for Rosebery and Hercules from T. Lees (pers. com., 1985); data for Hellyer from Aberfoyle Annual Report (1984) and data for Que River from Read and Meares (1981).

Table 11. Abundances of lead and zinc and expected zinc ratios for selected volcanic rock types (data from Brehler and Wedepohl, 1969; and Sahle et al., 1970).

Rock type	Pb (ppm)	Zn (ppm)	100Zn/(Zn+Pb)
Basalt	4.0	100	96
Andesite	5.8	70	92
Dacite-rhyolite	21.0	100	83

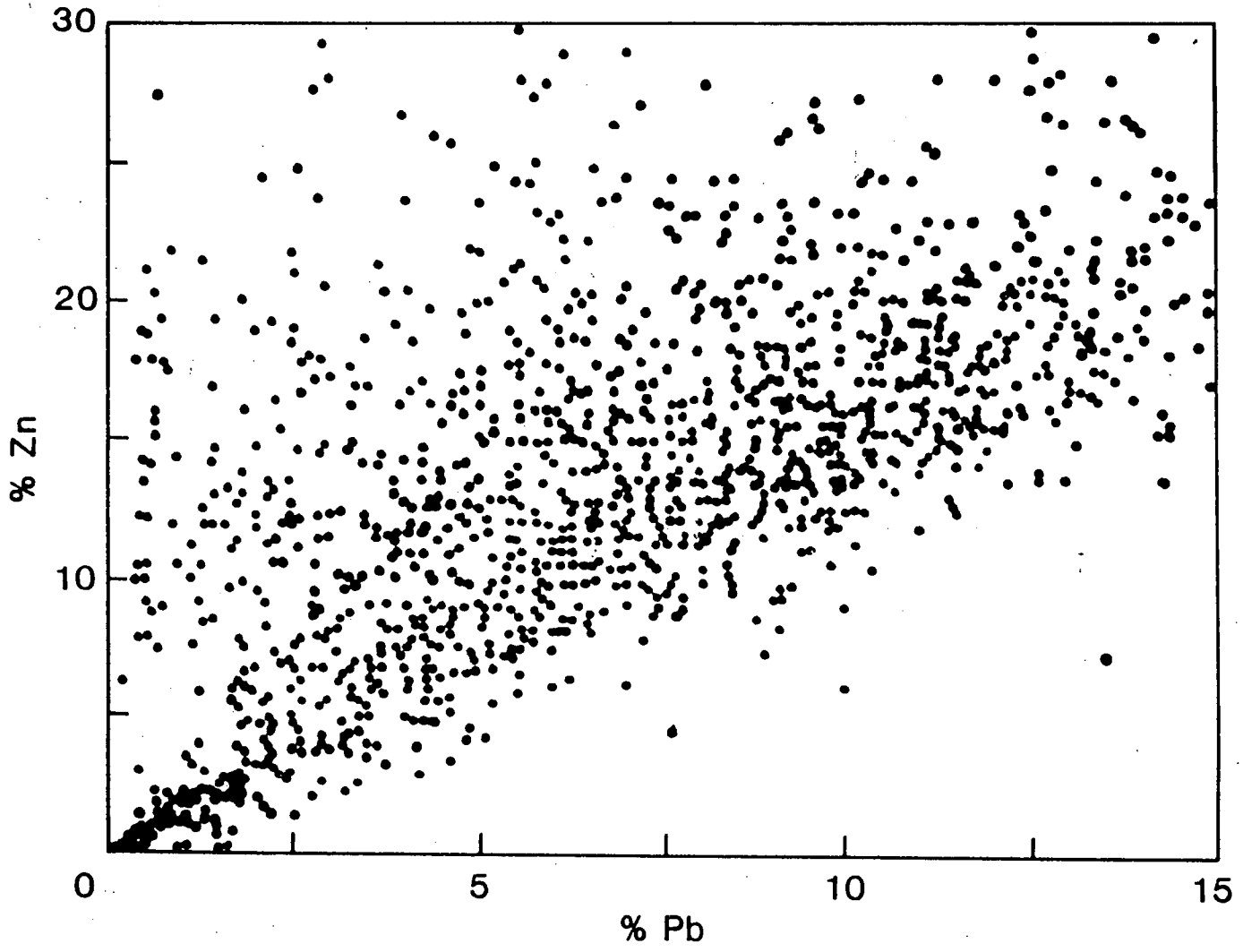

Figure 87. Plot of lead versus zinc for the Hellyer deposit.

are very similar for the Rosebery, Hercules and Hellyer deposits, which suggests that the general chemical conditions controlling lead and zinc deposition in these three deposits were similar. The results also indicate that metamorphic grade up to upper greenschist grade does not significantly affect the zinc ratio.

Deposits in the Balcooma metamorphic belt, Queensland

Deposits of the Balcooma metamorphic belt in northern Queensland differ from those of the Mt. Read Volcanics in both size (Table 1) and metamorphic grade. To extend the data base outside the Mt. Read Volcanics and to evaluate the affect of higher grade metamorphism on the zinc ratio, zinc ratios were calculated from assay data from the Balcooma and Dry River South prospects which have undergone middle amphibolite facies metamorphism.

Balcooma

The assay data was divided into groups as described earlier and zinc ratios were calculated for samples containing greater than 200 ppm lead or zinc (Huston and Large, 1987b). From this data base zinc ratio distributions were calculated and plotted in Figure 88.

The zinc ratio histograms for Balcooma share broadly similar characteristics to the histograms from Rosebery. With the exception of massive magnetite and pyritic quartz-muscovite biotite schist (metamorphosed footwall alteration), the means vary between 70 and 72. Massive magnetite has a slightly higher mean at about 76, whereas pyritic quartz-muscovite-biotite schist has a significantly lower mean at about 60 (Fig. 88). As at Rosebery, the standard deviations decreased from footwall alteration zones into massive sulfide, but in all cases the standard deviations are significantly higher than the equivalent type of mineralization at Rosebery.

Dry River South

As at Balcooma, zinc ratios were calculated for assay data with either zinc or lead values of greater than 200 ppm and have been plotted in Figure 89 according to type of mineralization.

The distribution at Dry River South is broadly similar to the distributions at Rosebery and Balcooma. The means vary between 71

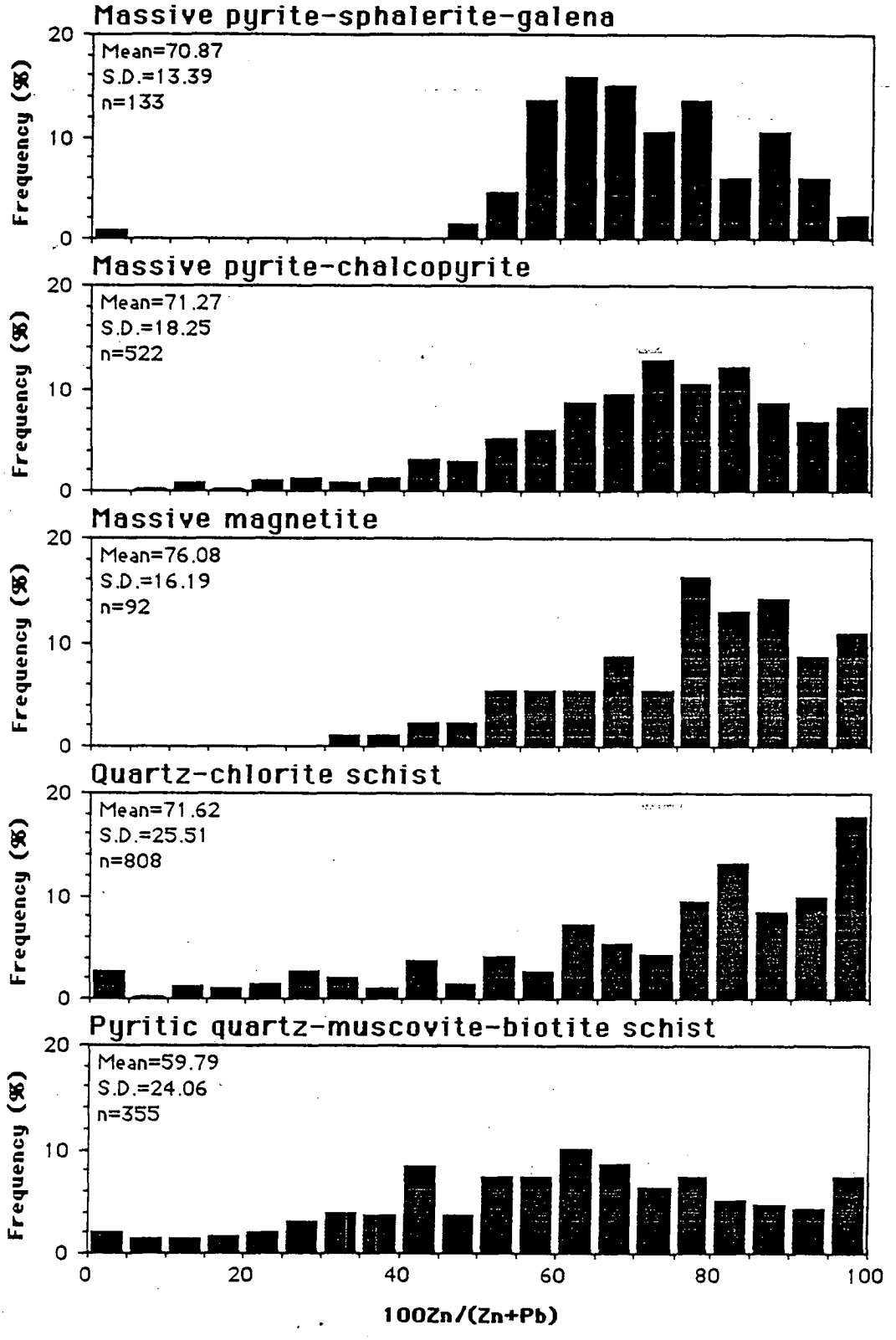

Figure 88. Zinc ratio histograms of various types of mineralization from the Balcooma prospect.

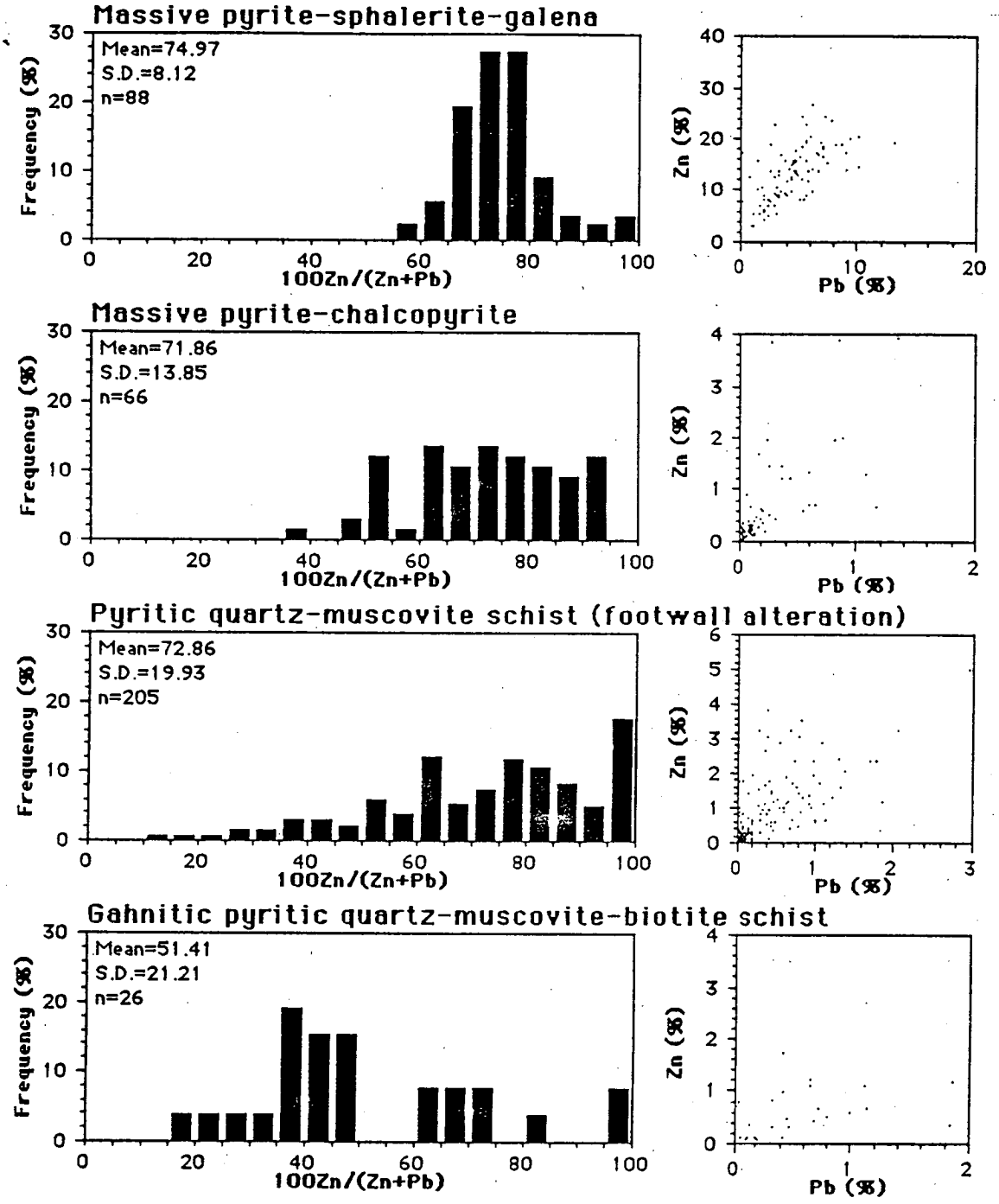

Figure 89. Relationships between lead, zinc and the zinc ratio for various types of mineralization from the Dry River South prospect.

and 75 and the standard deviations increase up stratigraphy from the footwall alteration zone to massive pyrite-chalcopyrite to massive pyrite-sphalerite-galena. The plots of zinc versus lead reflect this distribution and have very sharp lower cutoffs for massive sulfide as at Rosebery. The lead versus zinc plot for the footwall alteration zone differs from the other plots in that it has a diffuse lower cutoff. This diffuse lower cutoff is due to zinc mineralogy. Assay techniques used by Carpentaria Exploration Company to determine zinc concentrations were only partial extractions; zinc held in silicates and spinels was not analyzed. This analytical difficulty is demonstrated when samples from the pyritic quartz-muscovite-bioite schist containing gahnite are considered. The zinc ratio distribution for this data set has a mean of 51.41 and a standard deviation of 21.21 (Fig. 89) which is due to the presence of gahnite in the samples and hence a low zinc assay.

To evaluate this effect, samples from the Dry River South pyritic quartz-muscovite-biotite schist were analyzed for zinc and lead using total extractions (Part 1, Chapter 4). Zinc ratios were calculated for samples from this data base for which previous partial analyses were available and zinc and/or lead assays exceeded 200 ppm. Zinc ratio histograms from both types of extractions are presented in Figure 90. Use of an analytical technique that extracted all zinc improved the zinc ratio distribution significantly. The zinc ratio of gahnitic samples increased into the expected range of zinc ratios. The decrease in some of the zinc ratios from greater than 80 to more typical values is due to the greater analytical precision and the lower detection limits of the analyses undertaken by the author relative to commercial analyses.

Summary

Deposits from the Balcooma and Dry River South prospects, which have undergone amphibolite grade metamorphism have broadly similar zinc ratio distributions to deposits that have undergone lower grade metamorphism. Mean zinc ratios from massive sulfide are similar to Rosebery as are their standard deviations. Zinc ratios from the metamorphosed equivalent of footwall alteration zones differ from the footwall alteration zone at Rosebery in terms of standard deviations. At Balcooma and Dry River South, the standard deviations of the zinc ratio in the footwall alteration zones are significantly higher than

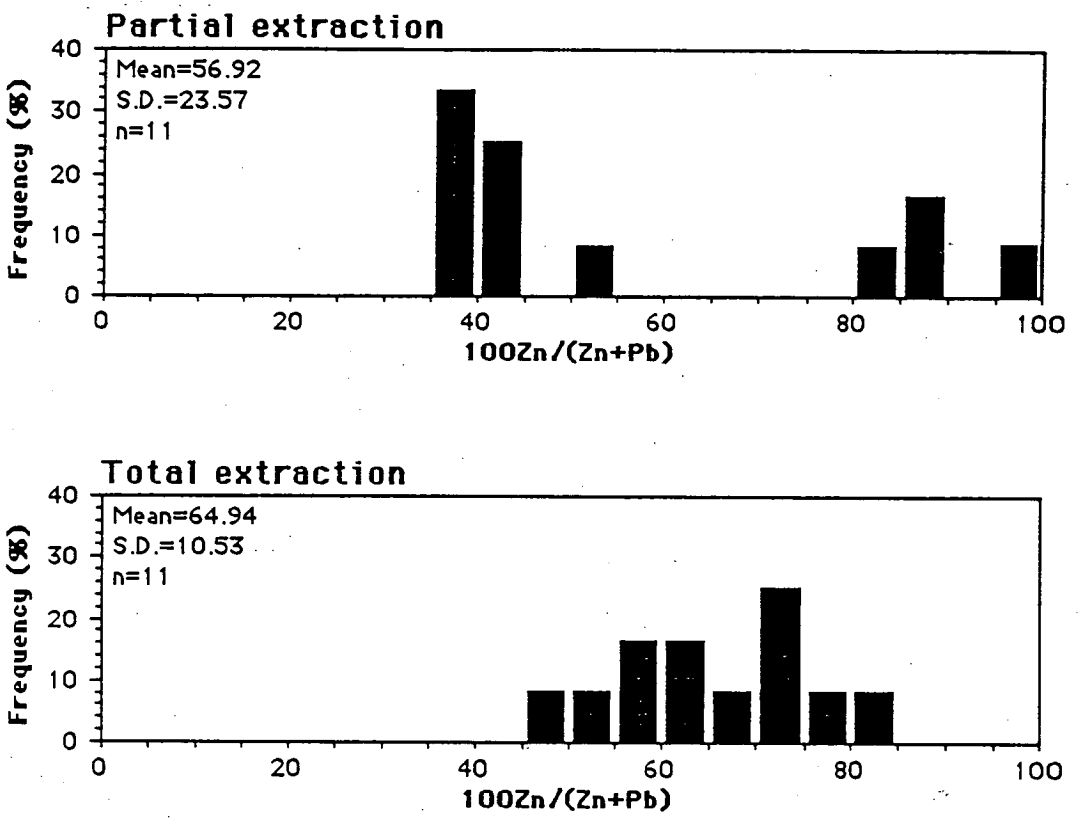

Figure 90. Comparison of the effect of partial versus total extractions on the zinc number using data from the Dry River South pyritic quartz-muscovite-biotite schist.

that of the Rosebery footwall alteration zone. This difference may be due to either the presence of gahnite and zincian staurolite or the low detection limits and lower precision of commercial analytical techniques in weakly mineralized samples. Use of the zinc ratio as an exploration guide in strongly metamorphosed terranes must account for these difficulties.

Theoretical explanations of variations in the zinc ratio

In order to make intelligent use of the zinc ratio as an exploration guide, the specific mechanisms that control the 100Zn/(Zn+Pb) ratio must be understood. In turn, variations in the ratio may yield new information about the source of metals, mechanism of metal transport and conditions of metal deposition for a given mineralizing system. Four possible factors may control the zinc ratio in volcanogenic massive sulfide deposits: (1) the relative concentrations of lead and zinc in the source rocks, (2) the mechanisms of metal solution from the source rocks, (3) the saturation/non-saturation of base metals and the overall chemistry of the metal-bearing solutions, and (4) the efficiency of metal deposition. The explanation must account for both the variations in the shape of the zinc ratio histogram and the nearly constant mean zinc ratio value in volcanogenic massive sulfide deposits.

Lead and zinc concentrations in the source rock

Lydon (1985) suggested that the bimodal nature of the zinc ratio histogram from massive sulfide deposits (Fig. 84) was due to the dominant lithology of the footwall volcanics up to 5 km below the deposits. Cu-Zn-type massive sulfides ($100Zn/(Zn+Pb)>95$) occur with footwalls composed dominantly of mafic volcanics whereas Zn-Pb-Cu-type massive sulfides ($70<100Zn/(Zn+Pb)<80$) occur dominantly with a felsic volcanic footwall. This quantifies and extends earlier observations by Solomon (1976) and Divi et al. (1979). Table 11 lists average values for lead, zinc and zinc ratios for basalts, andesites and dacites-rhyolites. The zinc ratio for basalts is about the same as that of Cu-Zn-type massive sulfides. Similarly, the zinc ratio for felsic volcanics is slightly higher than, but in the same range as, Zn-Pb-Cu-type massive sulfides.

Within the Mt. Read Volcanics, the four major Zn-Pb-Cu massive sulfide deposits fall within or slightly below the expected value for the Zn-Pb-Cu-type calculated in Table 11. Figure 91 illustrates the zinc ratio frequency distribution for a suite of unaltered volcanics from the Mt. Read belt (analyses courtesy of A.J. Crawford, unpub. data) and highlights the trend of and increasing zinc ratio in more mafic volcanics. The mean ratio for felsic volcanics of 80.4 compares well with the mean value of the Rosebery and Hercules deposits. However, the Que River and Hellyer deposits, which have lower mean zinc ratios (64.1 and 65, respectively), overlie a footwall sequence dominated by andesites (Table 10) with higher zinc ratios (mean value 88.4). This observation is contrary to that expected from the empirical association of Lydon (1985). Therefore, other controls besides the source-rock zinc and lead contents appear to have controlled the zinc ratios of massive sulfide deposits in the Mt. Read Volcanics.

Mechanisms of metal solution from the source rocks

A complicating factor relative to a source-rock control involves differing rates of release of the various metals from the source rocks. Graf (1977) proposed such a model based on rare earth element distribution patterns from the ores, iron formations and country rocks of the Brunswick 6 deposit in New Brunswick. He proposed three sequential reactions of hydrothermal solutions with the source rocks which would release elements at different rates. The first reaction involves the alteration of volcanic glass and/or ferromagnesian minerals which would release iron, copper and zinc relative to lead and form the lower parts of massive sulfide deposits. The second reaction alters feldspar with the release of zinc and lead; this correlates with the Zn-Pb-rich portion of the orebody. The final reaction involves less intense alteration with a decrease in available sulfide or an increase in mixing between the hydrothermal solution and seawater (associated with iron-formation deposition).

Given this model, the hydrothermal fluid and ore deposited would be expected to evolve in time with respect to the zinc ratio; early-formed ore would have a high zinc ratio which would decrease with time. Therefore, according to the Graf (1977) model, copper-rich ore would be expected to have a widely different zinc ratio from zinc-lead-rich ore. At Rosebery the zinc ratio does not change

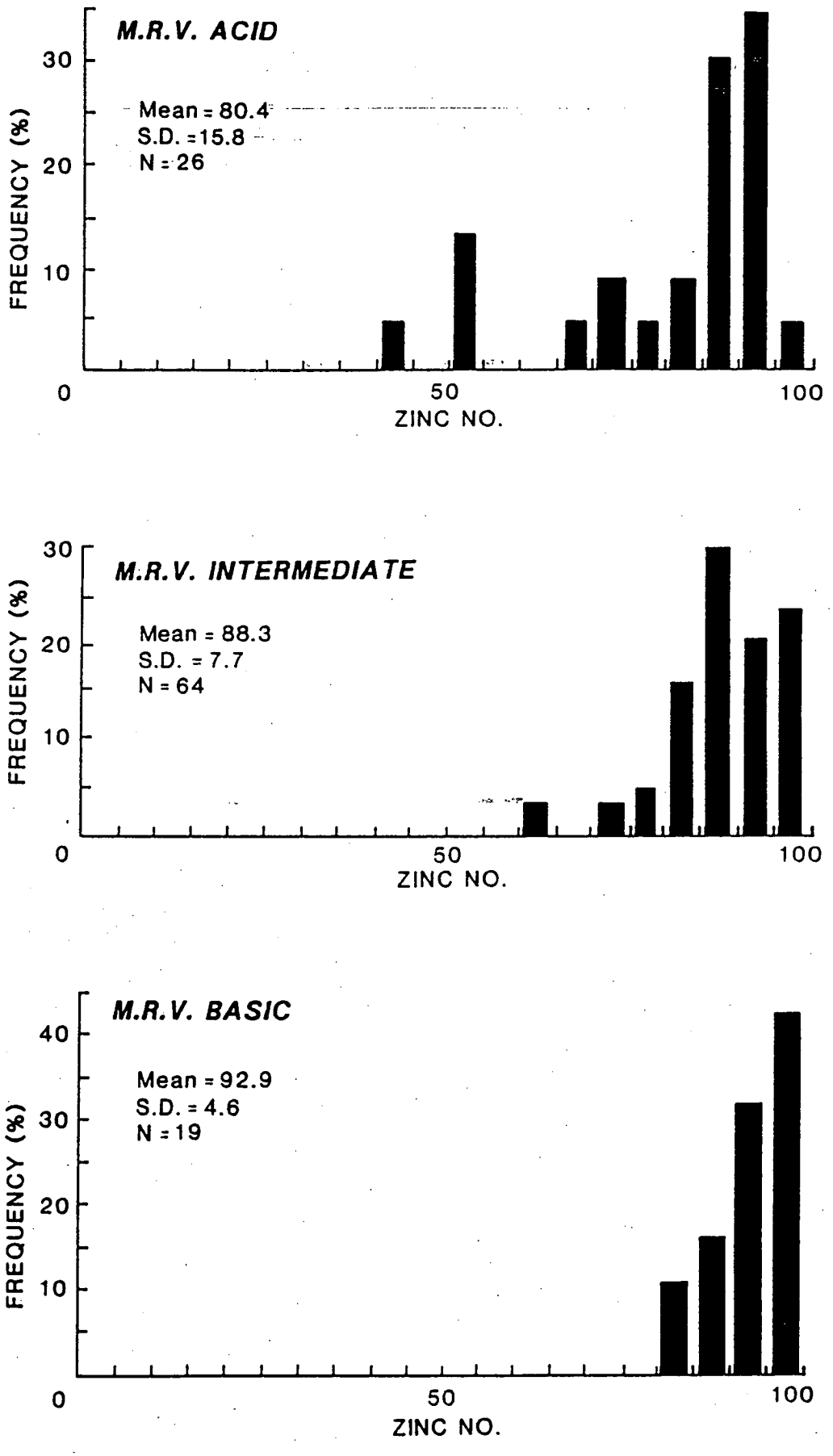

Figure 91. Variation in background zinc ratios for acid, intermediate and basic volcanics from the Mt. Read Volcanics.

significantly from pyrite-chalcopyrite ore (Cu-rich) to sphalerite-galena-pyrite ore (Zn-Pb-rich), which suggests that the Graf (1977) model does not apply at Rosebery. Thus the rate of solution of metals from the source rocks may not affect the zinc ratio of Phanerozoic volcanogenic massive sulfide deposits in general, but it may affect other mineralizing systems.

Chemistry of metal-bearing solutions

A third factor that could explain the observed zinc ratio in volcanogenic massive sulfides is saturation or near-saturation of the solutions with respect to both sphalerite and galena. Under these chemical conditions the zinc ratio of the precipitated sulfides (i.e. the ores) would be constant and equal to the ratio in the hydrothermal fluid. If the hydrothermal solutions were metal deficient relative to total sulfide, the metal ratio in the ore would be the same as that of the fluid, irrespective of saturation, if equilibrium precipitation and near 100 percent deposition is assumed (Ohmoto et al., 1983).

Current ideas on the genesis of volcanogenic massive sulfide deposits require the metals to be transported as chloride complexes and precipitated by the mixing of hydrothermal fluids with cold seawater (Sato, 1972; Large, 1977; and Ohmoto et al., 1983). Several recent studies (Seward, 1984a; Ruaya and Seward, 1986; and Bourcier and Barnes, 1987) have determined association constants for chloride complexes of lead and zinc and have also indicated uncomplexed lead and zinc to be of minor importance at the temperatures and salinities of interest. Both Ruaya and Seward (1986) and Bourcier and Barnes (1987) have studied the stabilities of zinc chlorocomplexes. These two studies produced similar results; the error bars associated with the equilibrium constants overlapped. However, constants determined by Ruaya and Seward (1986) had uncertainties of 0.0X log units, whereas constants determined by Bourcier and Barnes (1987) had uncertainties of 0.X log units. The Ruaya and Seward (1986) data are more precise. Due to the better precision of the Ruaya and Seward (1986) data and the fact that the data came from the same lab from which the lead chlorocomplex data were determined, the data of Ruaya and Seward (1986) were used in subsequent calculations. P. Bethke (U.S.G.S., pers. comm., 1989) and D. Crerrar (Princeton University, pers. comm., 1989) concurred with this choice of data.

To evaluate the possibility that saturation of the hydrothermal solutions with respect to lead and zinc controlled the zinc ratio, the solubilities of lead and zinc, and related zinc ratios, were calculated from 25°C to 300°C and for salinities from 0.25 to 3.0 m NaCl. The association of Na^+ and Cl^- to form $NaCl^0$ was calculated using the dissociation constants from Helgeson et al. (1981). Thermochemical data used in the calculations may be found in Table 12. Activity coefficients for charged species were calculated using the modified Debye-Huckel equation of Helgeson (1969). Activity coefficients for uncharged species were assumed to be unity (Helgeson et al., 1981). The molal ratio of Pb/Zn for a saturated solution may calculated from the following equation:

$$\frac{m_{\Sigma Pb}}{m_{\Sigma Zn}} = \frac{\begin{aligned}&[a^2_{H^+}a_{Cl^-}/(\gamma_{PbCl^+}K_5a_{H_2S}) + a^2_{H^+}a^2_{Cl^-}/(\gamma_{PbCl_2^0}K_6a_{H_2S} +)\\ &a^2_{H^+}a^3_{Cl^-}/(\gamma_{PbCl_3^-}K_7a_{H_2S}) + a^2_{H^+}a^4_{Cl^-}/(\gamma_{PbCl_4^{2-}}K_8a_{H_2S})]\end{aligned}}{\begin{aligned}&[a^2_{H^+}a_{Cl^-}/(\gamma_{ZnCl^+}K_1a_{H_2S}) + a^2_{H^+}a^2_{Cl^-}/(\gamma_{PbCl_2^0}K_2a_{H_2S}) +\\ &a^2_{H^+}a^3_{Cl^-}/(\gamma_{ZnCl_3^-}K_3a_{H_2S}) + a^2_{H^+}a^4_{Cl^-}/(\gamma_{PbCl_4^{2-}}K_4a_{H_2S})]\end{aligned}}, \quad (5)$$

where γ_i is the activity coefficient of species i and K_n is the equilibrium constant of reaction n (Table 12). When terms cancel, the equation reduces to:

$$\frac{m_{\Sigma Pb}}{m_{\Sigma Zn}} = \frac{\begin{aligned}&[1/(\gamma_{PbCl^+}K_5) + a_{Cl^-}/K_6 +\\ &a^2_{Cl^-}/(\gamma_{PbCl_3^-}K_7) + a^3_{Cl^-}/(\gamma_{PbCl_4^{2-}}K_8)]\end{aligned}}{\begin{aligned}&[1/(\gamma_{ZnCl^+}K_1) + a_{Cl^-}/K_2 +\\ &a^2_{Cl^-}/(\gamma_{PbCl_3^-}K_3) + a^3_{Cl^-}/(\gamma_{PbCl_4^{2-}}K_4)]\end{aligned}}. \quad (6)$$

Table 12. Thermodynamic data used in zinc ratio calculations.

Reaction	log K_{eq} 25 °C	50 °C	100 °C	150 °C	200 °C	250 °C	300 °C	Source
(1) $ZnCl^+ + H_2S = ZnS + Cl^- + 2H^+$	3.95	3.28	1.93	0.44	-1.00	-2.47	-3.93	1
(2) $ZnCl_2^0 + H_2S = ZnS + 2Cl^- + 2H^+$	3.75	3.12	1.81	0.37	-0.99	-2.96	-4.90	1
(3) $ZnCl_3^- + H_2S = ZnS + 3Cl^- + 2H^+$	4.03	3.54	2.37	1.31	-0.01			1
(4) $ZnCl_4^{2-} + H_2S = ZnS + 4Cl^- + 2H^+$	4.18	3.13	1.69	0.12	-1.24	-3.51		1
(5) $PbCl^+ + H_2S = PbS + Cl^- + 2H^+$	6.44	5.46	3.78	2.04	0.47	-1.10	-2.60	2
(6) $PbCl_2^0 + H_2S = PbS + 2Cl^- + 2H^+$	5.88	4.76	2.83	0.95	-0.98	-2.90	-4.97	2
(7) $PbCl_3^- + H_2S = PbS + 3Cl^- + 2H^+$	6.19	5.23	3.24	1.29	-0.79	-2.95	-5.47	2
(8) $PbCl_4^{2-} + H_2S = PbS + 4Cl^- + 2H^+$	6.39	5.37	3.52	1.77				2
(9) $Na^+ + Cl^- = NaCl^0$	-0.90	-1.00	-0.95	-0.75	-0.35	0.05	0.65	3

[1]Calculated from Helgeson (1969), Bowers *et al.* (1984), and Ruaya and Seward (1986).
[2]Calculated from Helgeson (1969), Bowers *et al.* (1984), and Seward (1984a).
[3]Helgeson *et al.* (1981).

The 100Zn/(Zn+Pb) weight ratio (zinc ratio) may be calculated as follows:

$$\text{Zinc ratio} = 100Zn/(Zn + Pb) = 100/[1 + (m_{\Sigma Pb}/m_{\Sigma Zn})(\text{at. wt.}_{Pb}/\text{at. wt.}_{Zn}). \quad (7)$$

A close look at the above equations shows that the zinc ratio for a saturated solution is dependent only on the temperature and activity of chloride and is independent of pH, a_{H_2S} and f_{O_2}. Thus a deposit precipitated from a saturated solution where the metals were transported dominantly as chloride complexes would be expected to have a constant zinc ratio at a particular temperature and salinity.

Calculations of the zinc ratio using the thermochemical data in Table 12 yields the results presented in Table 13 and plotted in Figures 92 and 93. These results suggest the following behavior of the zinc ratio in hydrothermal fluids saturated in lead and zinc:

(1) The zinc ratio generally decreases with temperature, but between 200 °C and 250 °C there is an inflection or reversal over all salinities considered.

(2) Below 200 °C salinity has little effect on the zinc ratio, but over 200 °C variations in salinity have as strong an effect as temperature.

(3) Over the temperature and salinity ranges considered typical for lead and zinc deposition in volcanogenic massive sulfide deposits (150 °C-250 °C and 0.5 to 1.5 m NaCl; Large, 1977; Pisutha-Arnond and Ohmoto, 1983), the zinc ratio varies from 58 to 85. This matches the zinc ratios observed in Phanerozoic massive sulfide deposits in general, and Rosebery, Hercules, Hellyer, Balcooma and Dry River South in particular.

(4) Above 250 °C, the zinc ratio decerases rapidly for all salinities considered.

Calculations using the Bourcier and Barnes (1987) data gave the same trends noted above (including the change from zinc-dominated to lead-dominated fluids between 250 °C and 300 °C), but the calculated zinc ratio was consistently higher.

Calculations by Barrett and Anderson (1988) indicated that zinc remains more soluble than lead up to and above 300 °C. This conflicts with the conclusion of this study that between 250 °C and 300 °C lead

Table 13. Zinc ratios of saturated solutions of varying temperatures and salinities as calculated from thermodynamic data. The box indicates the probable characteristics of volcanogenic fluids.

Temperature (°C)	Salinity (equiv. NaCl) 0.25 m	0.50 m	1.00 m	1.50 m	2.00 m	3.00 m
25	99	99	98	98	98	98
50	97	97	97	97	97	98
100	93	91	91	92	93	94
150	86	83	83	85	87	90
200	73	66	62	65	68	73
250	61	58	68	77	83	89
300	34	24	15	11	9	6

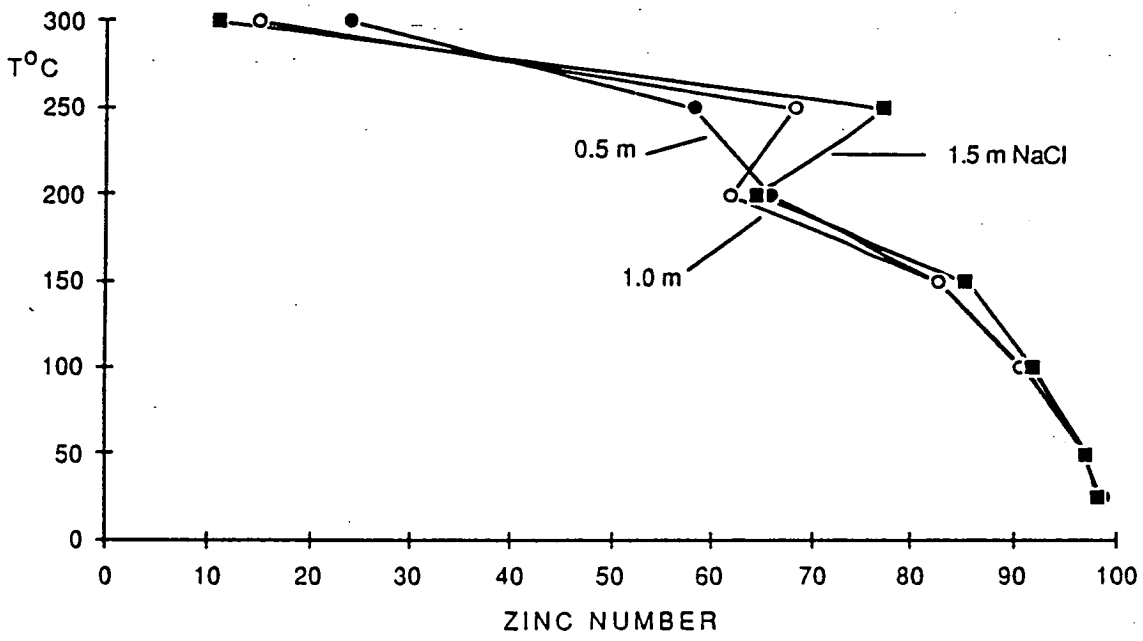

Figure 92. Effect of temperature on the zinc ratio for salinities of 0.5, 1.0 and 1.5 m NaCl.

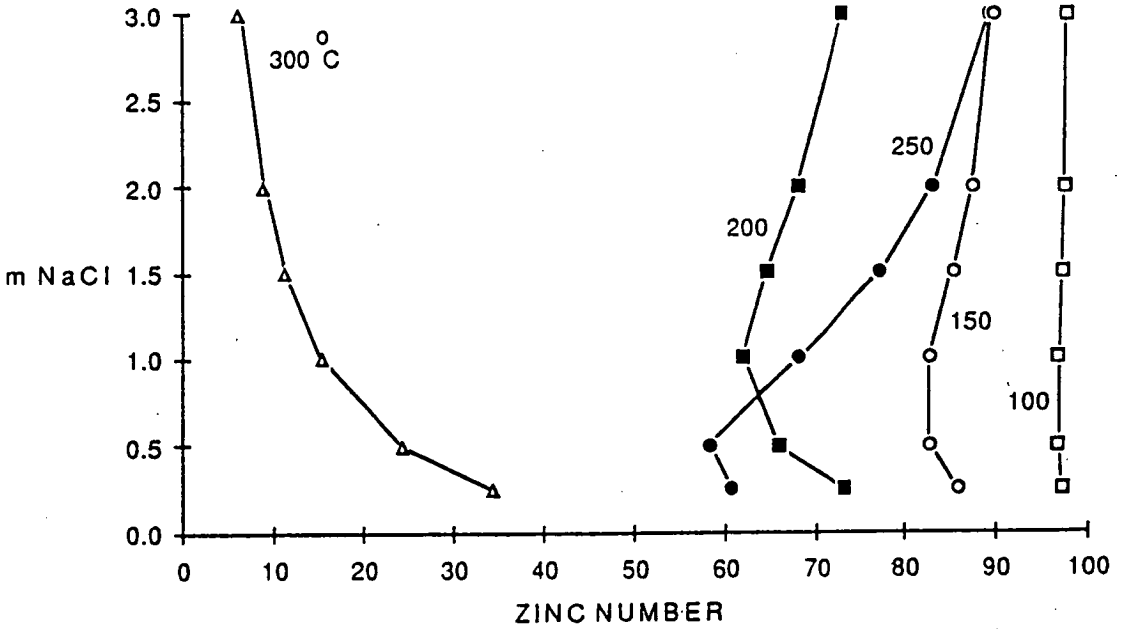

Figure 93. Effect of salinity on the zinc ratio for temperatures from 100 °C to 300 °C.

solubility exceeds zinc solubility. Two significant differences exist between the two studies: (1) different ion size parameters were used, and (2) different K_{sp} values for galena were used. Recalculation of the zinc ratio using the ion size parameters of Barrett and Anderson (1988) made no appreciable difference. However, re-examination of the K_{sp} values for galena (i.e. recalculation of the log K_{sp} values from data in Bowers et al. (1984)) indicate that the values quoted in Barrett and Anderson (1988) are between 0.3 (150°C) and 0.6 (300°C) log units too low. As a result, the values for lead solubility calculated by Barrett and Anderson (1988) are between 0.3 and 0.6 log units too low, and the conclusions of that study relative to lead solubility are considered incorrect.

Figure 94 illustrates the solubilities of zinc and lead for a volcanogenic ore solution with pH=4.5, 1 m NaCl, and log a_{H_2S}=-2.5 (e.g. Large, 1977; Ohmoto et al., 1983). A solution at 250°C is capable of carrying 9 ppm Zn and 4 ppm Pb, which agrees well with suggestions of 3 ppm Zn and Pb for Kuroko fluids (Pisutha-Arnond and Ohmoto, 1983) and 1 to 10 ppm for heavy metals in ore fluids in general (Roedder, 1960). The increase in zinc and lead solubilities with temperature, which suggests that a significant drop in temperature upon mixing with seawater (say 50°C) will precipitate essentially all the metal at a zinc ratio characteristic of the original hydrothermal fluid.

Although the increase in lead and zinc solubilities is partially offset by an increase in a_{H_2S} with temperature (Ohmoto et al., 1983), the net effect is that somewhere between 250°C and 300°C the ore fluids of an evolving volcanogenic massive sulfide system will become undersaturated with respect to zinc and lead and will begin to dissolve previously precipitated sphalerite and galena. This is consistent with the model of Eldridge et al. (1983) in which sphalerite-galena ore is dissolved and replaced by chalcopyrite-pyrite ore at temperatures of around 300°C. One important aspect of this process is that the hotter fluids inherit the zinc ratio of the sphalerite-galena ore they dissolve. Consequently, zinc ratios of volcanogenic massive sulfide deposits will be fixed by the low temperature fluids (<250°C) that deposit early sphalerite-galena ore and these deposits will rarely have zinc ratios below 50.

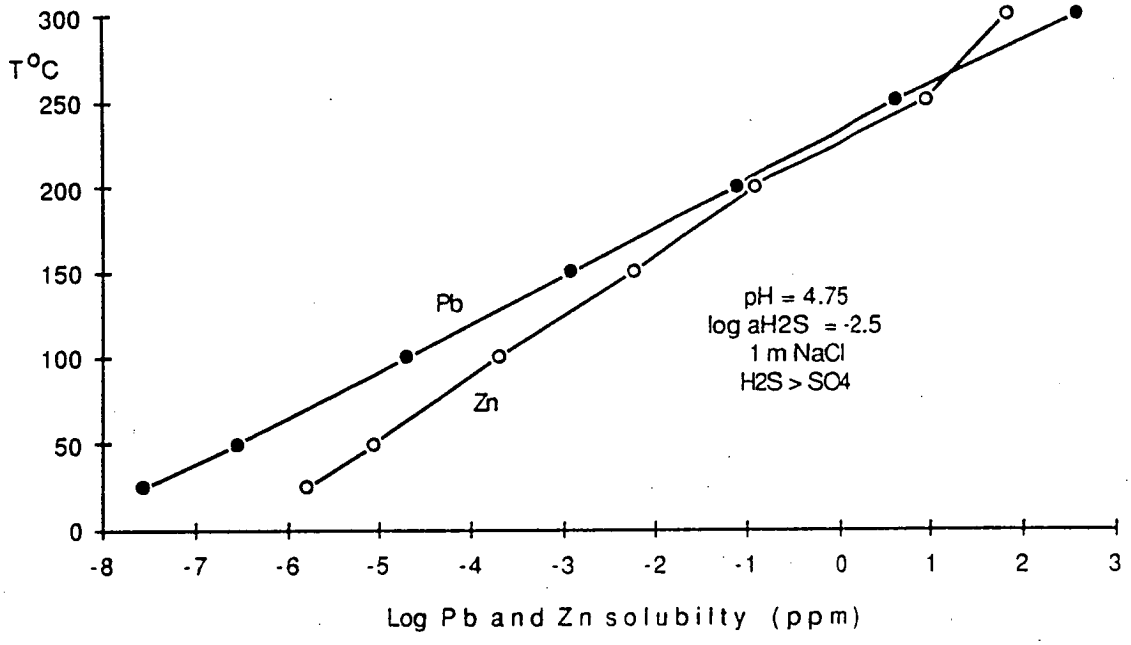

Figure 94. Variations in the solubilities of zinc and lead with temperature at a salinity of 1 m NaCl, pH=4.75 and $a_{H_2S}=10^{-2.5}$ m.

Examination of the lead vs. zinc plots for the north-end of the Rosebery deposit (Fig. 85) indicates that all the data points lie within an area between the zinc axis and a line defined by Zn=1.5Pb (i.e. zinc ratio=60.0). The linearity of the lower limit is significant in that a solution saturated with respect to lead and zinc, with sufficient H_2S, would deposit these two metals giving a unique ratio for a specific temperature. Additionally data from the barite lens plot on a line with Zn=1.9Pb (zinc ratio=65.5) and the plot of the Hellyer deposit has a linear lower limit of Zn=1.2Pb (zinc ratio=54.5; Fig. 87). Zinc-lead-rich mineralization from both Balcooma and Dry River South also shares this characteristic. The linear lower limit in each case suggests saturation. The spread above this line may have several causes: slight undersaturation of lead in the solutions, variations in the temperature or salinity of the hydrothermal fluids, or kinetic effects related to the deposition of sulfides.

The simplest interpretation of the distribution seen in the lead vs. zinc plots is that lead in the hydrothermal system may have varied from being slightly undersaturated, whereas zinc was always saturated. In this case, lead would have been variably depleted relative to zinc, leading to dispersion toward to the zinc-rich portion of the diagam. Additionally, since the barite lens presumably formed under lower temperatures (Green et al., 1981), it is likely that both metals were saturated, which would explain the observed straight-line relationship.

As discussed earlier, the temperature of the hydrothermal fluid, as well as the salinity, would be expected to have an effect of the zinc ratio of the precipitated sulfides. At Rosebery, the barite lens has a higher zinc ratio (65.5) than the cutoff line for other types of mineralization (zinc ratio=60.0). This difference suggests that the barite lens was deposited under slightly different and more constrained chemical conditions than the rest of the deposit. Thermodynamic calculations have indicated that the zinc ratio may vary between 58 and 85 over the expected range of depositional temperatures and salinities (Table 13). Variations in the temperature and salinity during mineralization would produce a fan of lines over the life of the deposit, with the lower cutoff representing a minimum resulting from a particular set of temperature and salinity conditions. Differences between the lower cutoff (and

average) zinc ratio between deposits (e.g. between Rosebery and Hellyer) could be explained by variations in the temperature, and salinity, of the respective ore forming fluids (Fig. 95).

Green et al. (1981) suggested that the ore forming fluids at Rosebery had high salinities of 3.5 m NaCl based on density requirements to form a brine pool. No hard scientific evidence (i.e. fluid inclusion data or the presence of evaporites in the sequence) was offered to support this interpretation. Despite this difficulty the interpretation can not be discarded. Calculations at 3.0 m NaCl (Table 13) produce zinc ratios very consistent with those observed at Rosebery for temperatures between 200°C (calculated zinc ratio = 73) and 250°C (calculated zinc ratio = 89). Even assuming extreme salinities the zinc ratios calculated match those in the deposits.

The third possible cause of the distribution could be a kinetic effect (i.e. sphalerite may precipitate more readily than galena), but adequate studies do not exist for a critical evaluation of the effect. The straight-line distribution observed for the barite lens is inconsistent with this mechanism as reaction kinetics would be expected to be most sluggish at the lower temperatures of the barite lens formation. The kinetics of precipitation may relate to the efficiency of deposition as discussed in the next section.

Of the three mechanisms, the first two are preferred as they provide the best explanations for the observed distribution.

The evidence presented herein suggests that, if the chemistry of the mineralizing fluids controlled the observed zinc ratio in volcanogenic massive sulfide deposits, the metalliferous solutions were saturated or nearly saturated up to temperatures of 250°C with respect to both lead and zinc, and metals were deficient relative to hydrogen sulfide in the solution ($m_{H_2S} > m_{\Sigma metals}$). Ohmoto et al. (1983) suggested that the opposite was true for Kuroko deposits. They proposed that zinc and lead were both undersaturated and hydrogen sulfide was deficient in solution ($m_{\Sigma metals} > m_{H_2S}$). If hydrogen sulfide was deficient, the zinc ratio and Zn/Pb ratio would be expected to be lower (i.e. some data would be expected to plot below the cutoff lines observed in Fig. 85; see Ohmoto et al., 1983, p. 589, for discussion). This is not the case for the massive sulfide deposits in the Mt. Read Volcanics and the Balcooma metamorphic belt.

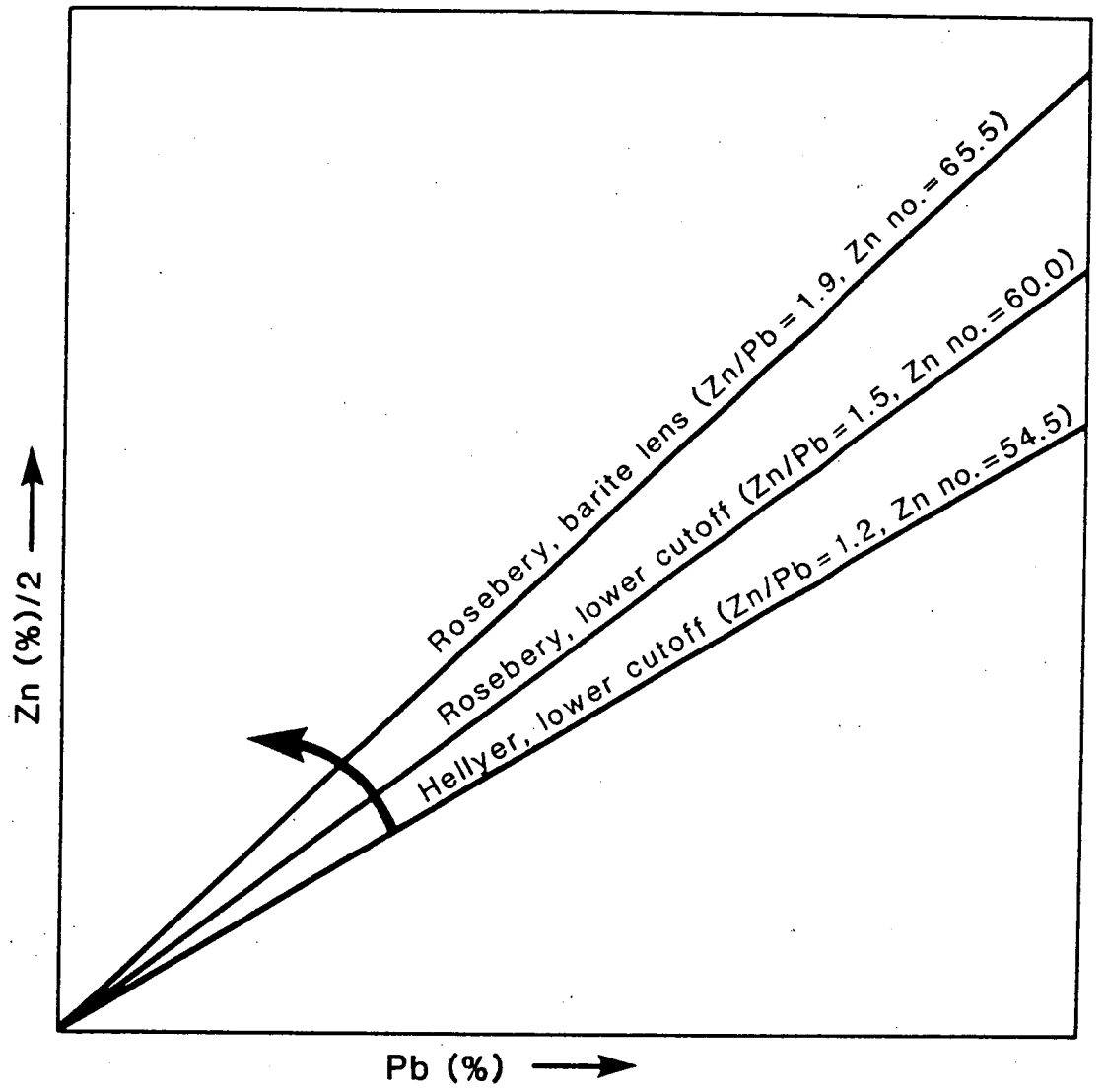

Figure 95. Plot of lead versus zinc illustrating the effect of salinity and temperature on the zinc ratio in Phanerozoic massive sulfide deposits. Lines of equal zinc ratios rotate counterclockwise from the minimum cutoff line in a complex fashion dependant on temperature and salinity (see text).

Efficiency of sulfide deposition

The fourth, most poorly constrained, factor that may affect the zinc ratio is the efficiency at which metal precipitates from the hydrothermal solution and the efficiency at which the precipitates are retained to form a mineral deposit.

The zinc ratio would not be affected by the efficiency of precipitation if nearly all metal precipitated from solution or if the precipitation of zinc and lead were equally efficient. The sudden change in physicochemical conditions upon exhalation of the ore fluids would tend toward total precipitation of lead and zinc, so the zinc ratio would not be affected by differences in precipitation efficiencies.

A more important factor is the physical means of forming the orebody from the precipitates. Sato (1972) addressed this problem initially, followed by Turner and Gustafson (1978), Solomon and Walshe (1979), and Campbell et al. (1984). The predominant control on preservation of the precipitates is the buoyancy of the exhaled hydrothermal fluids relative to seawater. Sato (1972) proposed four behaviors of ascending fluids at the sea floor, to which Turner and Gustafson (1978) and Campbell et al. (1984) each added an additional behavior (5 and 6, respectively): (1) flow downslope of denser brines to a pond and precipitation in the ponded area, (2) mixing of denser brines with seawater to precipitate sulfides, then flow into a pond, (3) initial pluming of less dense brines to mix with seawater and precipitate sulfides followed by flow downslope of the fluid into a pond, (4) pluming of less dense brines to mix with seawater and precipitate sulfides which disperse into the surrounding seawater, (5) "double-diffusive splitting" in which an initially less dense hydrothermal fluid split into two fluids, one denser and one less dense than seawater, and (6) precipitation under an anhydrite cap in a matter consistent with the model proposed by Eldridge et al. (1983). Of these models, all except (4) and (5) would retain all or nearly all of the the precipitated sulfide, so the zinc ratio would remain unaffected. Campbell et al. (1984) considered double-diffusive splitting unlikely and suggested that currents would disperse sulfide from a plume of less dense hydrothermal fluid, which would prevent the formation of significant sulfide accumulation.

Pluming of less dense brines into seawater (option (4)) has been observed in seafloor black smoker deposits as predicted by Solomon

and Walshe (1979). Calculations by Rona (1984) indicated that most (99%) of the metal in the fluids has been lost to the seawater. These deposits have been likened to Cyprus deposits owing to similarities in mineralogy and metal ratios (Oudin and Constantinou, 1984). Preferential loss of metal may affect the zinc ratio in these deposits. However, as large polymetallic massive sulfide deposits are thought to have formed under a sulfate or a sulfide cap (e.g. Campbell et al., 1984) or in a brine pool (e.g. McKay and Hazeldene, 1987), zinc (or lead) loss should not have been a significant problem as most sulfides precipitated would be retained. In summary, it is considered that physical processes of deposition are unlikely to affect the zinc number significantly in polymetallic volcanogenic massive sulfide deposits with the possible exception of Cyprus-type deposits.

Summary

For volcanogenic massive sulfides of the Mt. Read belt and the Balcooma metamorphics, the saturation or near-saturation of the hydrotheraml solutions with respect to zinc and lead controls the zinc ratio. The spread of data above a minimum cutoff in the lead vs. zinc plots for Rosebery, Hellyer, Balcooma and Dry River South is best explained as either the effect of varying salinity and/or temperature or as the result of slight undersaturation with respect to lead.

The distribution of the zinc ratio in Phanerozoic volcanogenic massive sulfides may be explained by this model with slight variations as discussed previously, but the distribution of the Cu-Zn type of Lydon (1985) must have a different control. The simplest mechanism is a lack of lead in the footwall source rocks (Hutchinson, 1973; and Solomon, 1976). The mean value of lead in mafic volcanics (Table 11) may have been too low to allow solutions to become saturated in lead for the Cu-Zn type, to which variations in leaching rates of zinc relative to lead (e.g. Graf, 1977) and the lack of radiogenic lead in the Archean may have also contributed (Hutchinson, 1973). Whichever the case, the zinc ratio for the Cu-Zn type has been profoundly affected by the lack of lead in the source rocks to these deposits.

Summary and conclusions

The zinc ratio has a very narrow range for Phanerozoic volcanogenic massive sulfide deposits throughout the world. Examination of drill core assays from three deposits in the Mt. Read Volcanics (Rosebery, Hercules and Hellyer) and two deposits from the Balcooma metamorphic belt (Balcooma and Dry River South) suggests that this ratio has a characteristic range of means (64-77) coupled with low standard deviations (<15) that in the Rosebery case does not vary significantly according to ore type.

The distributions observed are best explained by assuming that zinc and lead in the hydrothermal solutions are saturated as chloride complexes. The spread of data above a cutoff in the zinc vs. lead plots for Rosebery and Hellyer can be explained by either variations in salinity and/or temperature of the solution, or slight undersaturation of lead. The cutoff line itself may represent a minimum zinc ratio as determined by a combination of temperature and salinity.

A second possible control on the zinc ratio is the zinc and lead concentrations of the footwall source rocks to the massive sulfide. Although the lack of lead in the footwall volcanics of Cu-Zn deposits probably produces high zinc ratios for these deposits, this factor cannot explain the observed variation in the Mt. Read Volcanics. Deposits with more mafic footwall volcanics (Que River and Hellyer) have low zinc ratios (64-65) whereas deposits with felsic footwall volcanics (Rosebery and Hercules) have higher zinc ratios (76-77). This opposes the expected trend if the zinc ratio were controlled by the dominant footwall lithology.

Although low grade metamorphism (greenschist facies and under) does not seem to effect the zinc ratio significantly, higher grade metamorphism appears to have two effects: (1) the concentration of zinc in resistate minerals (e.g. gahnite and zincian staurolite) produces a artificially low zinc ratio if standard analytical techniques are used, and (2) a larger spread about the mean in zones of low grade zinc-lead mineralization (e.g. pyritic massive sulfide or the footwall alteration zone). The latter effect may be due to the lower precision of analytical techniques for low concentrations of lead and zinc.

The distribution of the zinc ratio vertically and horizontally through a volcanogenic massive sulfide orebody may give insight into

the evolution of ore fluids and whether those fluids were saturated in zinc or lead. Analogous ratios (e.g. one involving silver and lead) may also be useful exploration tools and increase our understanding of metal transportation and deposition.

Chapter 2
A geochemical model to explain the distribution of gold in volcanogenic massive sulfide systems

Introduction and overview

Volcanogenic massive sulfide deposits are not only significant sources of the base metals, copper, lead and zinc, but they may also contain significant amounts of the precious metals, silver and gold. The distribution, zonation and geochemistry of transport and deposition of base metals has been understood for several years (e.g. Stanton, 1960; Sangster, 1972; Large, 1977; Franklin et al., 1981; and Ohmoto et al., 1983), but these same parameters for gold are still poorly understood.

Gold grades in volcanogenic massive sulfide deposits vary widely both between and within deposits. Published gold grades typically range between 0.2 and 2 g/t, but some higher grade deposits average between 2 and 20 g/t (e.g. Rosebery at 2.9 g/t and Boliden at 15.7 g/t). Table 14 lists selected deposits for which documentation on gold distribution and/or mineralogy exists. Within individual deposits gold grades may vary even more widely. For instance, gold assays from the Rosebery deposit range from less than 0.1 g/t to 40 g/t.

Gold appears to have two dominant occurrences in volcanogenic massive sulfide deposits: (1) with copper at the base of the massive sulfide and in the stringer zone (e.g. Mt. Chalmers, Millenbach, Mavrouni, Kalavasos, Heath Steele, Mt. Lyell, Mt. Morgan, Balcooma, Dry River South and Nurukawa deposits), or (2) at the top and fringes of the deposit in association with pyrite, sphalerite or galena (e.g. Rosebery, Hellyer, Que River, Corbet, Arizona Proterozoic deposits and Kuroko deposits). In each deposit one type of gold occurrence dominates, usually to the exclusion of the other.

Numerous factors can influence the grade and distribution of gold in volcanogenic massive sulfide deposits. This chapter uses the distribution and mineralogy of gold in six deposits (five in eastern Australia and one in Canada) and previous studies on gold solubility to develop a thermodynamic model which accounts for the distribution and mineralogy of gold in these ores. Other factors that may affect

Table 14. The distribution and mineralogy of gold from selected volcanogenic massive sulfide deposits.

Zinc-gold association

Deposit	Grade and tonnage	Gold mineralogy and distribution	References
Corbett, Quebec, Canada	2.7 m.t. at 2.9% Cu, 2.0% Zn, 20.5 g/t Ag and 0.93 g/t Au.	Gold has a similar distribution to zinc and occurs in the pyritic fringes of the deposit as fine inclusions in pyrite.	Knuckey and Watkins (1982)
Arizona Proterozoic deposits, U.S.A.	Variable.	Gold is enriched in the zinc-rich stratiform ores and chert cappings. It has average grades in copper-rich stratiform ores, and it is depleted in copper-rich stringer ores.	Dewitt (1983)
Garpenberg, Sweden	0.4% Cu, 5.0% Zn, 130 g/t Ag and 0.9 g/t Au.	Gold has a higher concentration in zinc-lead ores than in copper ores.	Vivallo (1985)
Rosebery, Tasmania, Australia	19.4 m.t. at 0.74% Cu, 16.2% Zn, 5.0% Pb, 155 g/t Ag and 2.9 g/t Au.	Gold occurs dominantly as inclusions of native gold and electrum in pyrite and tetrahedrite. Gold concentrates in zinc-lead ore and massive barite mineralization.	Part 2
Hellyer, Tasmania, Australia	19 m.t. at 0.4% Cu, 13% Zn, 7% Pb, 160 g/t Ag and 2.3 g/t Au.	Gold occurs in arsenopyrite and pyrite as either submicroscopic inclusions or in solid solution. Gold is enriched in the upper parts of zinc-rich stratiform ore and in a pyritic chert that caps the stratiform ore.	MacArthur (1986) and Large et al. (in press)
Que River, Tasmania, Australia	2.6 m.t. at 0.42% Cu, 12.9% Zn, 7.4% Pb, 204 g/t Ag and 3.5 g/t Au.	Gold occurs as native gold or electrum associated with galena or as inclusions in pyrite and sphalerite. Arsenopyrite and pyrite also carry gold. Gold concentrates towards the top of zinc-rich stratiform ore and shows an exponential increase with zinc grades.	Large et al. (in press)
Tilt Cove, Newfoundland, Canada	Not available.	Gold occurs as native gold which is more strongly associated with sphalerite than chalcopyrite or pyrite.	Hurley and Crockett (1985)
Kuroko district, Japan	Variable.	Gold occurs as electrum with silver-rich rims. Gold contents of the electrum vary between 52% and 85%. Electrum in the oko (copper-rich) zone has a gold content of 95% to 96% in the Hisaka deposit (Watanabe, 1971; in Shimazaki, 1974). Gold concentrates in the upper part of the kuroko (zinc-lead) ore.	Shimazaki (1974)
Shakanai, Japan	8.73 m.t. at 1.4% Cu, 3.4% Zn, 1.0% Pb, 44 g/t Ag and 0.3 g/t Au.	Gold occurs as electrum generally associated with galena.	Sato (1974) and Tanimura et al. (1983)

Table 14. The distribution and mineralogy of gold from selected volcanogenic massive sulfide deposits (continued).

Deposit	Grade and tonnage	Gold mineralogy and distribution	References
Gold-copper association			
Millenbach, Quebec, Canada	3.0 m.t. at 3.5% Cu, 4.8% Zn, 48 g/t Ag and 0.86 g/t Au.	Gold occurs with copper in the pyrrhotitic core of massive ore. Gold has an antipathetic relationship to zinc.	Knuckey et al. (1982)
Stekkenjokk, Sweden	27.9 m.t. at 1.35% Cu, 2.43% Zn, 0.29% Pb, 46 g/t Ag and 0.27 g/t Au.	Gold is enriched with copper, bismuth, molybdenum and tin at the base of the massive sulfide lens and in the stringer zone.	Zachrisson (1982, 1984)
Mt. Lyell, Tasmania, Australia	98.6 m.t. at 1.17% Cu, 7.15 g/t Ag and 0.39 g/t Au.	Gold occurs as very fine inclusions in or along grain boundaries between chalcopyrite, bornite and pyrite. Coarse grained gold may occur in tension quartz veins. Gold correlates well with copper.	Large et al. (in press)
Balcooma, Queensland, Australia	3.5 m.t. at 3.0% Cu, 20-30 g/t Ag and 0.3-0.4 g/t Au; minor Zn-Pb-Cu-Ag(Au) mineralization is also present.	Gold occurs as fine grained (<10 μm) electrum grains of high fineness (670-790) with a strong association with chalcopyrite, bismuth minerals and pyrrhotite. Gold has a strong correlation with copper and occurs largely in massive sulfide lenses.	Part 1, this study
Dry River South, Queensland, Australia	1.5 m.t. at 1.1% Cu, 3.4% Pb, 9.4% Zn, 97 g/t Ag and 0.7 g/t Au.	Gold occurs as electrum of variable grain size (1-60 μm) and fineness (490-760) without any particular mineral association. Significant mobilization of gold has occurred as syn-deformational chalcopyrite-electrum veins occur in the highwall to the massive sulfide lens and electrum occurs in veinlents in gahnite, a metamorphic mineral. Gold has a strong correlation with copper.	Part 1, this study
Heath Steele B-1 Orebody, New Brunswick, Canada	40.4 m.t. at 1.1% Cu, 4.7% Zn, 1.6% Pb, 64 g/t Ag and 0.9 g/t Au.	Gold occurs as a "discrete mineral phase." It is weakly associated with copper and decreases in grade towards the stratigraphic top of the orebody.	Lusk (1969), Mercer and Crockett (1972) and Mosier et al. (1983)
Mt. Chalmers, Queensland, Australia	4.3 m.t. at 1.6% Cu and 2.3 g/t Au.	Gold occurs as native gold associated with copper in the core of the massive sulfide and the upper part of the stringer zone.	Large and Both (1980)
Mt. Morgan, Queensland, Australia	67 m.t. at 0.70% Cu and 4.87 g/t Au.	Gold occurs as native gold, gold tellurides and in pyrite. All occurrences have an association with pyrite and chalcopyrite.	Frets and Balde (1975), and Fedikow and Govett (1985)

Table 14. The distribution and mineralogy of gold from selected volcanogenic massive sulfide deposits (continued).

Deposit	Grade and tonnage	Gold mineralogy and distribution	References
Cyprus deposits	Variable.	Gold is erratically distributed through the ores. Pyritic ores of the Mathaitis area have higher gold grades than copper-rich bodies at Mavrovouni and Skouriotissa. The highest gold (4.2 g/t) came from the small (0.3 m.t.) copper-rich (2.9% Cu) body at Kinoussa. In the Kilrou area high gold grades occur at the top of stockwork mineralization near the contact with massive sulfide.	Constantinou (1986)
Mavrovouni, Cyprus	17 m.t. at 4.5% Cu, 0.5% Zn, 10 g/t Ag and 0.8 g/t Au.	Gold is associated with chalcopyrite rather than pyrite. Gold occurs in copper-rich ores.	Constantinou (1986) and Hutchinson (1965)
Kalavosos, Cyprus	1.0 m.t. at 0.5-2.5% Cu and 0.7% Zn.	Gold occurs in the copper-rich ores.	Hutchinson (1965)
Nurukawa, Japan	Not available.	Gold occurs in paragenetically early quartz-chalcopyrite veins in siliceous ore and in the footwall stringer zone. Mineralogically gold occurs as electrum with a fineness between 500 and 700. This is a particularly gold-rich (15-100 g/t Au) deposit.	Yamada et al. (1987)

gold grades include the amount of gold in the source rocks, the method of gold release and the trapping efficiency of gold in the ores. Calculations by Stolz and Large (1988) indicate that an enriched source for gold is not necessary to produce gold-rich massive sulfide deposits, and the method of gold release from the source is beyond the scope of the present study. The trapping efficiency of gold in the ores is addressed in Chapter 4.

The distribution of gold in selected volcanogenic massive sulfide deposits

Three deposits from the Paleozoic of Eastern Australia have been selected as examples of precious-metal-rich volcanogenic massive sulfide deposits. The Rosebery and Hellyer deposits lie in the Cambrian Mt. Read Volcanics of western Tasmania, while the Mt. Chalmers deposit occurs in the Permian of east-central Queensland. For comparison, a description of the Archean Millenbach deposit in eastern Canada is also included.

Rosebery

At Rosebery, gold concentrates in the upper parts of sphalerite-galena-pyrite ore and massive barite mineralization rather than pyrite-chalcopyrite ore (Figs. 74 and 75). In detail the distribution of gold is very complex. It has six occurrences, in order of economic importance: (1) in massive sphalerite-galena-pyrite ore, (2) in massive barite mineralization, (3) in the upper parts of pyrite-chalcopyrite pods (in general these pods are gold poor), (4) in distal pyrite mineralization (at the edges of sphalerite-galena-pyrite mineralization and the overlying host rocks), (5) as occasional anomalies in the footwall alteration blanket, and (6) in remobilized quartz-carbonate veins (Part 2, Chapter 2). Brathwaite (1974) noted, and ascribed to the Devonian, gold-bearing, crosscutting pyrrhotite-pyrite bodies in the southern part of the mine. Mineralogically, most gold occurs as electrum (Chapter 4).

Hellyer

The geology and distribution of gold in the Hellyer deposit, which lies 30 km northeast of Rosebery has been described by McArthur (1986) and Large et al. (in press). The deposit consists of a large, lenticular massive sulfide body which overlies a well developed footwall alteration pipe. McArthur (1986) considered the deposit to be a classic example of a relatively undeformed Kuroko-style deposit.

The deposit shows a well developed metal zonation with iron and copper enrichment at the base of the massive sulfide body and zinc, lead, arsenic, silver and gold enrichment at the top. The deposit averages 2.3 g/t in the massive sulfide body but reaches values over 4.0 g/t in the uppermost part of the deposit (Fig. 96). The highest gold grades occur in a pyritic, glassy silica cap that overlies the barite zone at the central part of the deposit (McArthur, 1986). In terms of texture this pyritic cap is similar to some of the distal pyrite gold mineralization at Rosebery (Part 2, Chapter 3).

Mineralogically, arsenopyrite and pyrite are the probable major gold carriers in the deposit as only one electrum grain has been observed despite an intensive search (McArthur, 1986), and gold bearing arsenopyrite has been observed at the nearby Que River deposit (Large et al., in press). Additionally, there is a general trend of increasing gold with increasing arsenic (Large et al., in press).

Mt. Chalmers

The Mt. Chalmers volcanogenic massive sulfide deposit is located 27 km northeast of Rockhampton in eastern Queensland. The deposit lies within a belt of Permian rhyolitic and andesitic volcanics (Large and Both, 1980).

The deposit differs from the Tasmanian gold-rich deposits in that it contains significantly higher copper, lower zinc but comparable gold grades (Table 14). The best gold grades occur in the central part of the stringer zone pyrite-chalcopyrite mineralization and extend up into the overlying copper-rich massive sulfide (Fig. 97). Values of 4 to 10 g/t gold and 3 to 6% copper are common in this zone over sample intervals greater than 5 m. Figure 98 illustrates a linear correlation between copper and gold using drill hole assays. Zinc, lead and silver concentrate in the uppermost

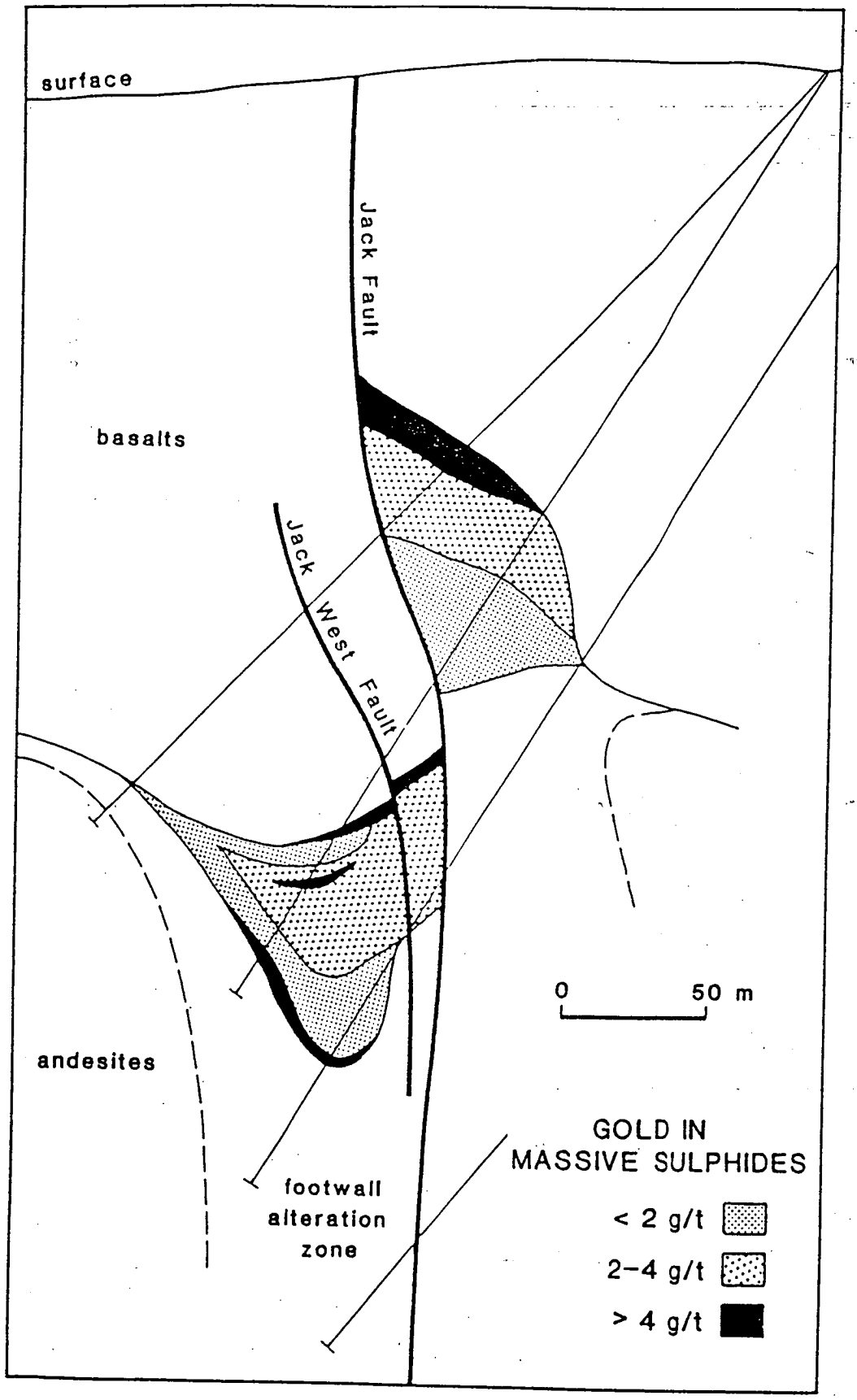

Figure 96. The variation in gold grades in the Hellyer deposit (after Large et al., in press).

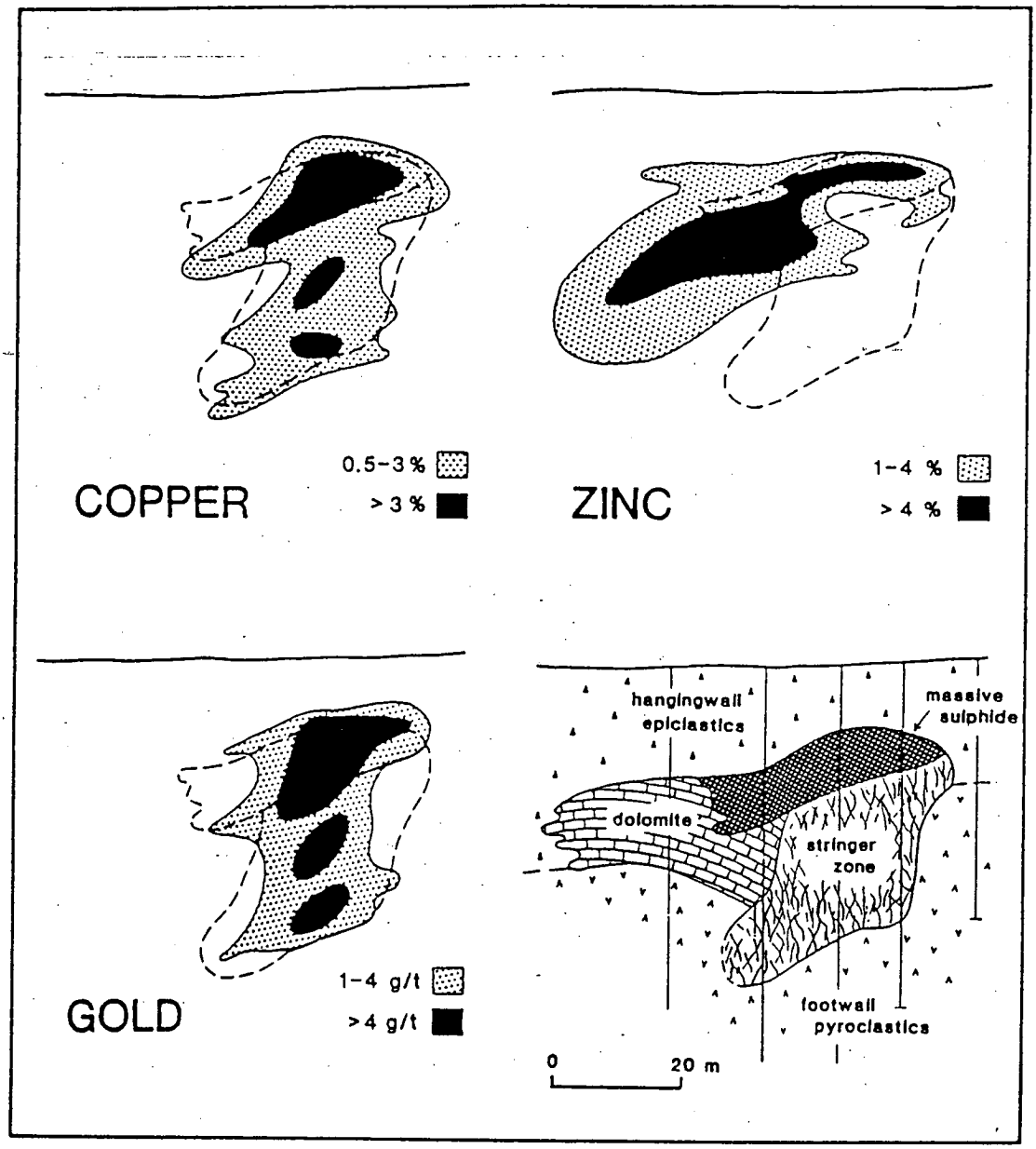

Figure 97. Geology and distribution of gold, zinc and copper along section 4900 mN, Mt. Chalmers deposit.

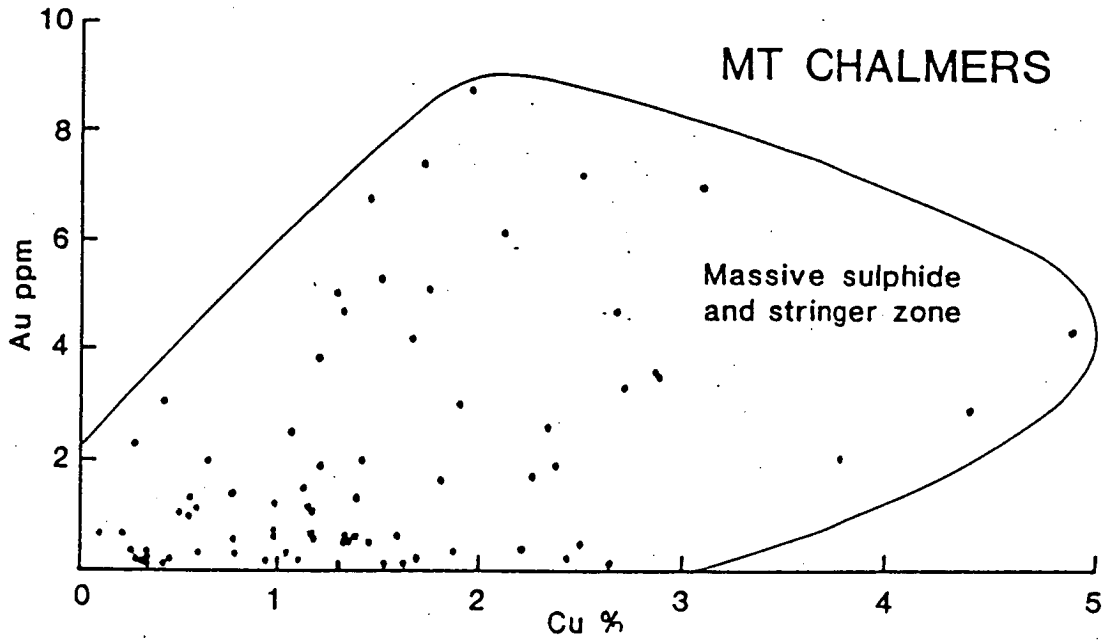

Figure 98. The relation between copper and gold at Mt. Chalmers.

massive sulfide, which lies above the gold-copper zone, and extend laterally down the interpreted sea floor paleoslope (Large and Both, 1980). In the copper-rich ore the gold occurs as free grains and tends to be coarse grained. The Mt. Chalmers copper-gold-rich ore is unusual in that it contains significant kaolinite gangue (McLeod, 1985).

Balcooma and Dry River South

At Balcooma and Dry River South gold has a strong association with copper and lacks a significant association to zinc, even in zinc-rich mineralization. Gold occurs as electrum that has been recrystallized during metamorphism at both deposits and that has been remobilized into the wall rocks in places at Dry River South. Both deposits formed from relatively reduced fluids that exhaled into reduced seawater. Both deposits have relatively low gold grades with Balcooma containing between 0.3 and 0.4 g/t and Dry River South containing 0.7 g/t.

Millenbach

The Millenbach volcanogenic massive sulfide in the Noranda district of eastern Canada is one of the few Archean deposits in which the distribution of gold is described. Studies by Knuckey et al. (1982) indicated that the gold concentrates in the copper-rich core of the deposit which includes the central stringer zone and overlying conical massive sulfide body (Fig. 99). Zinc occurs in the lateral and upper parts of the massive sulfide and is associated with low gold and copper.

Summary

Two distinct gold associations are present in the deposits described above: (1) a gold-zinc-lead-silver association which is commonly found in the upper part of zinc-rich massive sulfide lenses (Rosebery and Hellyer), and (2) a gold-copper association which is commonly developed in the stringer zone and lower portions of copper-rich massive sulfide deposits (Mt. Chalmers, Balcooma, Dry River South and Millenbach). In Table 14 these and other deposits are grouped according to their dominant gold association. Two of the

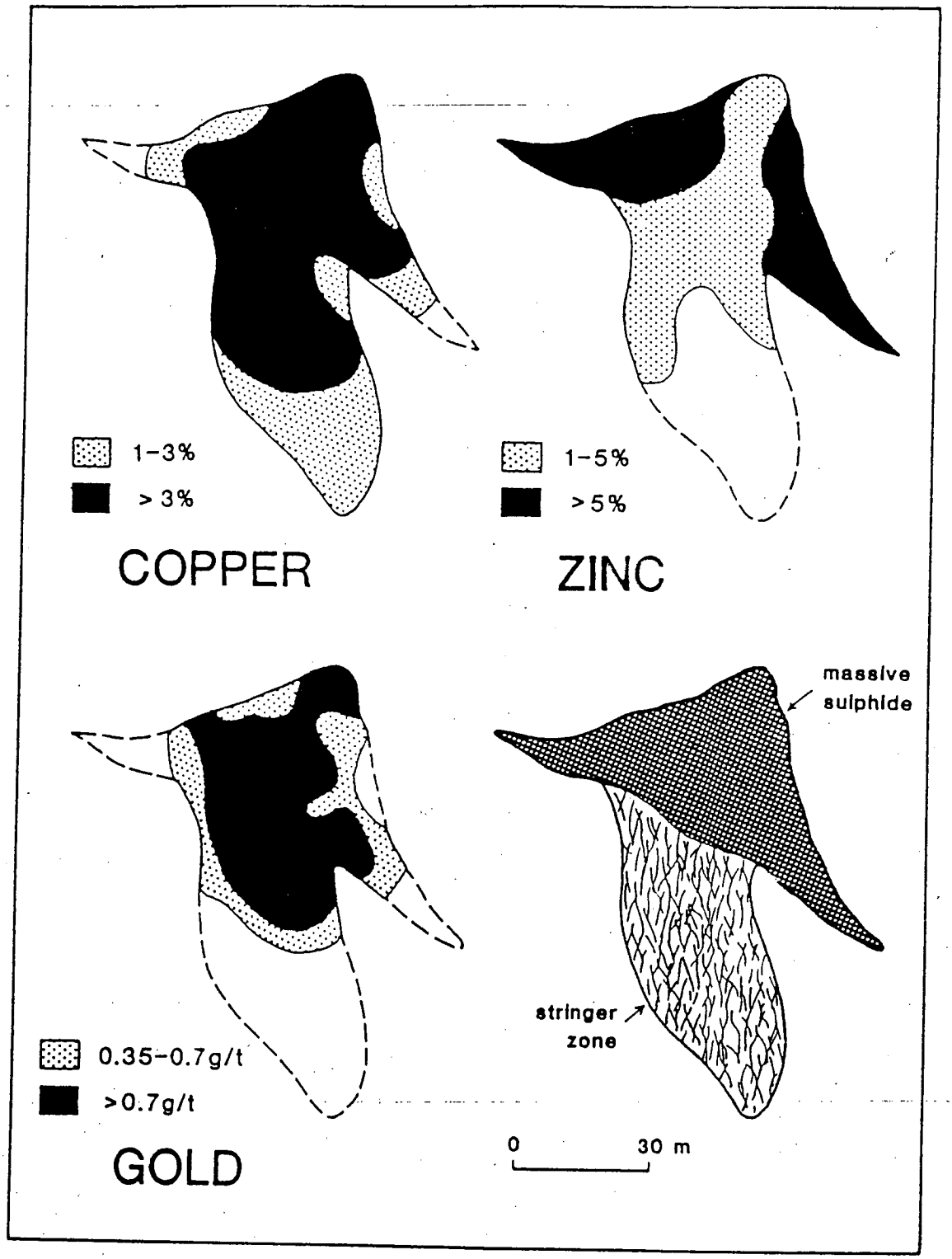

Figure 99. Geology and distribution of gold, zinc and copper from the Millenbach deposit (modified after Knuckey et al., 1982).

deposits in the gold-copper association that have the highest gold grades (Mt. Chalmers and Nurukawa) also contain kaolinite gangue (McLeod, 1985; and Yamada et al., 1987).

Recent studies on gold transport in hydrothermal systems infer that thio-complexes of gold account for nearly all gold transport, and other complexes, in particular chlorocomplexes, have minor or no significance (e.g. Henley and Brown (1985) and Cathles (1986)). The presence of only one mechanism for gold transport cannot explain the two associations of gold in volcanogenic massive sulfide deposits. The purpose of chapter is to evaluate possible gold complexes and then to present a model to account for the distribution and association of gold in volcanogenic massive sulfide deposits.

Although the model and conclusions presented herein apply directly to volcanogenic massive sulfide deposits, most of the processes invoked must occur in other types of deposits.

Mechanisms of gold solubility and deposition

The mechanisms of gold transport and deposition in hydrothermal systems are poorly understood. Presently gold is considered to be transported by thio- or chlorocomplexes although Seward (1984b) considers that ammonia, thioarsenates, thioantimonates, polysulfide ions, sulfite and tellurium species may play some role. Thermodynamic data only exists for the species $Au(HS)_2^-$, $Au_2(HS)_2S^{2-}$ (Seward, 1973) and $AuCl_2^-$ (Helgeson, 1969; and Cole and Drummond, 1986). Cole and Drummond (1986) indicated that the stability of $AuCl_2^-$ may be four of five orders of magnitude greater than predicted by Helgeson (1969). Based on geologic evidence, the estimates by Helgeson are condsidered to be more realistic (Huston and Large, 1989). Figures 100c and 100d illustrate gold solubilities using these data at 250°C and 300°C ($a_{\Sigma S}=10^{-2.5}$ and $a_{Cl^-}=10^0$). Figure 101 illustrates gold solubility as a function of temperature and f_{O_2} at various values of a_S and pH with $a_{Cl^-}=10^0$.

Figure 100. f_{O_2}-pH diagrams at 250°C and 300°C showing: (1) the evolution of the Rosebery (solid arrow) and Mt. Chalmers (open arrow) hydrothermal fluids (a and b), (2) the solubility of gold as $Au(HS)_2^-$ and $AuCl_2^-$, and (3) the solubility of zinc and copper as chlorocomplexes. The diagrams were calculated assuming $a_{\Sigma S}=10^{-2.5}$, $a_{Cl^-}=10^{0.0}$, $a_{Na^+}=10^{0.0}$, $a_{K^+}=10^{-1.0}$, $a_{Mn^{2+}}=10^{-4.0}$, $a_{\Sigma Fe}=10^{-3.0}$ (as $FeCl^+$), $a_{\Sigma C}=10^{-1.0}$ (as H_2CO_3), $a_{\Sigma Ba}=10^{-4.0}$ (as $BaCl^+$) and $a_{H_3AsO_3^0}=10^{-4.0}$ (these parameters are consistent with those estimated for a volcanogenic fluid as estimated by Ohmoto et al. (1983), Pisutha_Arnond and Ohmoto (1983), Reed (1982), Dixon (1980), Green et al. (1981) and Heinrich and Eadington (1986)). Thermodynamic data for this and subsequent diagrams are tabulated in Table 15. The copper solubility was determined from equilibrium constants given by Crerrar and Barnes (1976). These are geologically too high, and John Walshe (pers. comm.) has indicated that the true solubility is two orders of magnitude lower. Consequently, for a more realistic copper solubility the solubilities shown should be divided by 100.

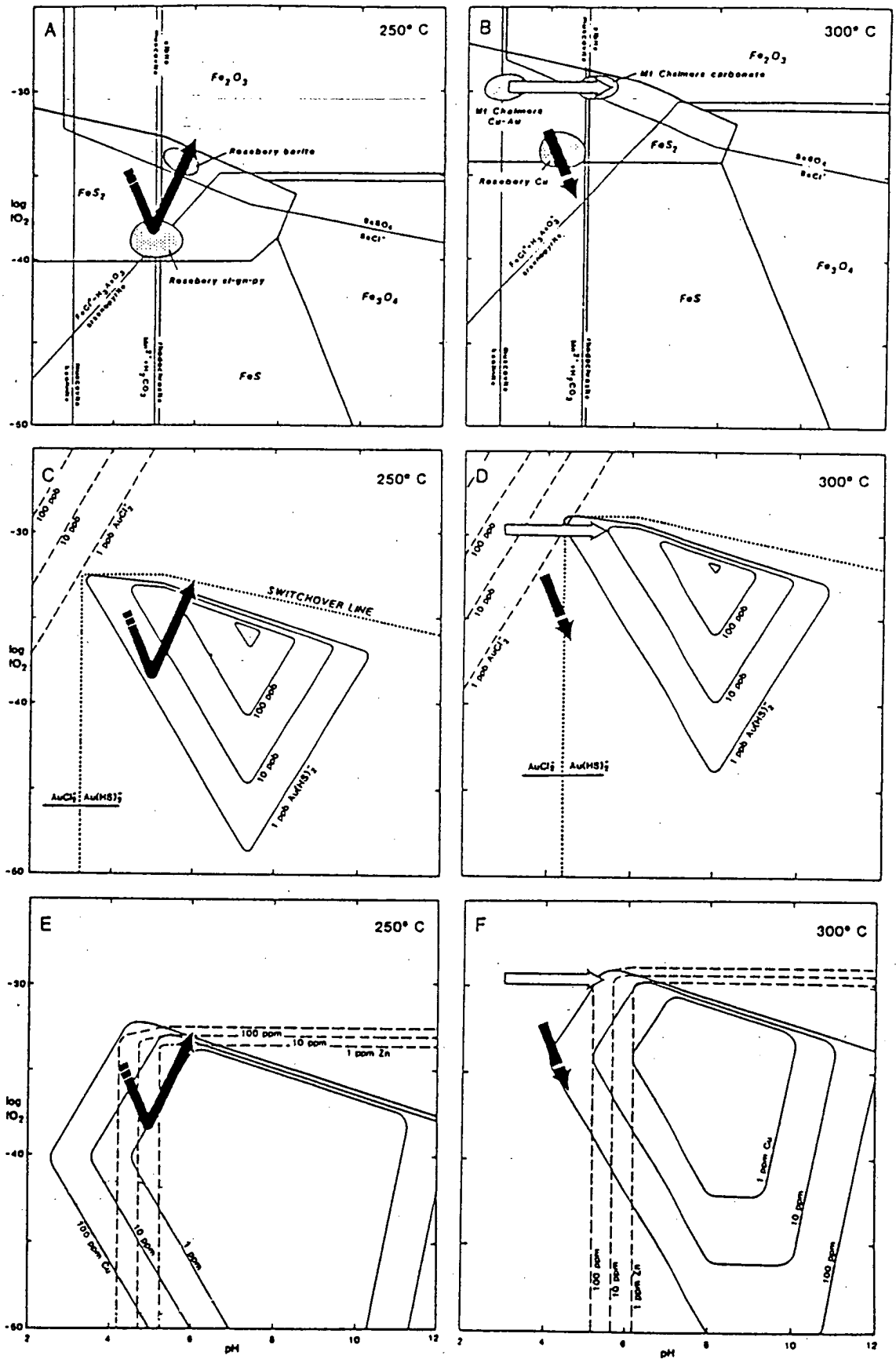
A
250° C
Fe_2O_3
Rosebery barite
FeS_2
$SrSO_4$
$SrCl^+$
Rosebery sl-gn-py
Fe_3O_4
FeS
log fO_2
-30
-40
-50
B
300° C
Fe_2O_3
Mt Chalmers carbonate
Mt Chalmers Cu-Au
FeS_2
Rosebery Cu
$SrSO_4$
$SrCl^+$
Fe_3O_4
FeS
C
250° C
100 ppb
10 ppb
1 ppb $AuCl_2^-$
SWITCHOVER LINE
100 ppb
10 ppb
1 ppb $Au(HS)_2^-$
$AuCl_2^-$ $Au(HS)_2^-$
log fO_2
-30
-40
-50
D
300° C
100 ppb
10 ppb
1 ppb $AuCl_2^-$
100 ppb
10 ppb
1 ppb $Au(HS)_2^-$
$AuCl_2^-$ $Au(HS)_2^-$
E
250° C
100 ppm
10 ppm
1 ppm Zn
100 ppm Cu
10 ppm
1 ppm
log fO_2
-30
-40
-50
2
4
6
8
10
12
pH
F
300° C
1 ppm Cu
10 ppm
100 ppm
100 ppm
10 ppm
1 ppm
2
4
6
8
10
12
pH

Table 15. Thermochemical data used in plotting of diagrams.

Reaction	log K_{eq} 100 °C	150 °C	200 °C	250 °C	300 °C	350 °C	Reference
$HSO_4^- = H^+ + SO_4^{2-}$	-2.99	-3.72	-4.48	-5.27	-6.08	-6.90	1
$H_2S^0 = HS^- + H^+$	-6.63	-6.72	-6.96	-7.35	-8.06	(-8.98)[a]	2
$HS^- + 2O_2 = SO_4^{2-} + H^+$	100.91	85.86	73.82	63.90	55.38	47.28	1
$H_2S^0 + 2O_2 = SO_4^{2-} + 2H^+$	94.28	79.14	66.86	56.55	47.32	(38.30)	3
$H_2S^0 + 2O_2 = HSO_4^- + H^+$	97.27	82.86	71.34	61.82	53.40	(45.20)	3
$2FeS_2 + 2H_2O = 2FeS + 2HS^- + 2H^+ + O_2$	-84.72	-74.11	-66.01	-59.81	-55.25	-52.98	3
$2FeS_2 + 2H_2O = 2FeS + 2H_2S^0 + O_2$	-71.46	-60.67	-52.09	-45.11	-39.13	(-35.02)	3
$6FeS + 6H_2O + O_2 = 2Fe_3O_4 + 6HS^- + 6H^+$	-14.65	-17.19	-20.35	-24.09	-28.97	-37.78	3
$6FeS + 6H_2O + O_2 = 2Fe_3O_4 + 6H_2S^0$	25.14	23.13	21.41	20.01	19.39	(16.10)	3
$3FeS_2 + 6H_2O = Fe_3O_4 + 6HS^- + 6H^+ + O_2$	-134.40	-119.76	-109.19	-101.76	-97.36	-98.36	3
$3FeS_2 + 6H_2O = Fe_3O_4 + 6H_2S^0 + O_2$	-94.62	-79.44	-67.43	-57.66	-49.00	(-44.48)	3
$3FeS_2 + 6H_2O + 11O_2 = Fe_3O_4 + 6SO_4^{2-} + 12H^+$	471.07	395.40	333.73	281.64	234.92	185.32	3
$4Fe_3O_4 + O_2 = 6\ Fe_2O_3$	55.02	46.90	40.50	35.32	31.04	27.44	3
$4FeS_2 + 8H_2O = 2Fe_2O_3 + 8H_2S^0 + O_2$	-107.82	-90.29	-76.41	-65.11	-54.99	(-50.16)	3
$4FeS_2 + 8H_2O + 15O_2 = 2Fe_2O_3 + 8SO_4^{2-} + 16H^+$	646.43	542.83	458.47	387.29	323.57	256.24	3
$4FeS_2 + 8H_2O + 15O_2 = 2Fe_2O_3 + 8HSO_4^- + 8H^+$	670.35	572.59	494.31	429.45	372.21	311.44	3
$4FeAsS + 3O_2 + 4Cl^- + 8H^+ + 6H_2O = 4FeCl^+ + 4H_2S + 4H_3AsO_3^0$	----	----	126.6	117.3	107.0	----	4
$4FeAsS + 11O_2 + 4Cl^- + 4H^+ + 6H_2O = 4FeCl^+ + 4SO_4^{2-} + 4H_3AsO_3^0$	----	----	394.0	343.5	296.3	----	5
$BaCl^+ + HSO_4^- = BaSO_4 + H^+ + Cl^-$	----	----	4.28	3.74	3.57	4.97	6
$BaCl^+ + H_2S^0 + 2O_2 = BaSO_4 + 2H^+ + Cl^-$	----	----	75.62	65.56	56.97	(50.17)	6

Table 15. Thermochemical data used in plotting of diagrams (continued).

Reaction	log K_{eq} 100 °C	150 °C	200 °C	250 °C	300 °C	350 °C	Reference
$BaCl^+ + HS^- + 2O_2 = BaSO_4 + H^+ + Cl^-$	----	----	82.58	72.91	65.03	59.15	6
$MnCO_3 + 2H^+ = Mn^{2+} + H_2CO_3^0$	5.36	5.20	5.14	5.05	4.66	(3.08)	7
$KAl_2(AlSi_3O_{10})(OH)_2 + 6SiO_2 + 3Na^+ = 3NaAlSi_3O_8 + K^+ + 2H^+$	-15.03	-13.39	-12.22	-11.29	-10.53	-9.57	8
$3Al_2Si_2O_5(OH)_4 + 2K^+ = 2KAl_2(AlSi_3O_{10})(OH)_2 + 2H^+ + 3H_2O$	-5.61	-4.99	-4.45	-4.00	-3.60	-3.03	8
$4Au + 8H_2S^0 + O_2 = 4Au(HS)_2^- + 2H_2O + 4H^+$	----	(21.62)	13.40	6.30	(-1.26)	----	9
$4Au + 8HS^- + 4H^+ + O_2 = 4Au(HS)_2^- + 2H_2O$	----	(75.38)	69.08	65.10	(63.22)	----	9
$Au + 8SO_4^{2-} + 12H^+ = 4Au(HS)_2^- + 2H_2O + 15O_2$	----	(-611.50)	-521.48	-446.10	(-379.82)	----	9
$4Au + 8HSO_4^- + 4H^+ = 4Au(HS)_2^- + 2H_2O + 15O_2$	----	(-641.26)	-557.32	-488.26	(-428.46)	----	9
$4Au + 8Cl^- + 4H^+ + O_2 = 4AuCl_2^- + 2H_2O$	7.1	8.8	10.0	11.9	14.1	(15.6)	10
$4Au + 8Cl^- + 4H^+ + O_2 = 4AuCl_2^- + 2H_2O$	(27.1)[b]	29.2	(30.8)[b]	(32.3)[b]	33.3	(34.0)[b]	11
$4CuFeS_2 + 4H^+ + O_2 + 4Cl^- = 4FeS_2 + 2H_2O + 4CuCl^0$	----	----	40.0	38.8	39.2	40.0	12
$4CuFeS_2 + 2H_2O + 4H^+ + 4Cl^- = 4FeS + 4H_2S^0 + 4CuCl^0 + O_2$	----	----	-64.2	-51.4	-39.1	(-30.0)	13
$4CuFeS_2 + 2H_2O + 4Cl^- = 4FeS + 4HS^- + 4CuCl^0 + O_2$	----	----	-92.0	-80.8	-71.3	-66.0	13
$12CuFeS_2 + 18H_2O + 12Cl^- = 4Fe_3O_4 + 24HS^- + 12H^+ + 12CuCl^0 + O_2$	----	----	-316.8	-290.6	-271.8	-273.4	13
$12CuFeS_2 + 18H_2O + 12Cl^- + 47O_2 = 4Fe_3O_4 + 24SO_4^{2-} + 36H^+ + 12CuCl^0$	----	----	1454.9	1243.0	1057.3	861.3	13
$2CuFeS_2 + 3H_2O + 2Cl^- + 8O_2 = Fe_2O_3 + 4SO_4^{2-} + 6H^+ + 2CuCl^0$	----	----	249.2	213.1	181.4	148.1	13
$2CuFeS_2 + 3H_2O + 2Cl^- + 8O_2 = Fe_2O_3 + 4HSO_4^- + 2H^+ + 2CuCl^0$	----	----	267.2	234.1	205.7	175.7	13
$ZnCl^+ + H_2S^0 = ZnS + Cl^- + 2H^+$	1.93	0.44	-1.00	-2.47	-3.93	(-4.37)	14
$ZnCl_2^0 + H_2S^0 = ZnS + 2Cl^- + 2H^+$	1.81	0.37	-0.99	-2.96	-4.90	(-5.91)	14
$ZnCl_3^- + H_2S^0 = ZnS + 3Cl^- + 2H^+$	2.37	1.31	-0.01	----	----	----	14

Table 15. Thermochemical data used in plotting of diagrams (continued).

Reaction	log K_{eq} 100 °C	150 °C	200 °C	250 °C	300 °C	350 °C	Reference
$ZnCl_4^{2-} + H_2S^0 = ZnS + 4Cl^- + 2H^+$	1.69	0.12	-1.24	-3.51	----	----	14
$ZnCl^+ + SO_4^{2-} = ZnS + 2O_2 + Cl^-$	-92.35	-78.70	-67.86	-59.02	-51.25	(-42.67)	15
$ZnCl_2^0 + SO_4^{2-} = ZnS + 2O_2 + 2Cl^-$	-92.47	-78.77	-67.85	-59.51	-52.22	(-44.21)	15
$ZnCl_3^- + SO_4^{2-} = ZnS + 2O_2 + 3Cl^-$	-91.91	-77.83	-66.87	----	----	----	15
$ZnCl_4^{2-} + SO_4^{2-} = ZnS + 2O_2 + 4Cl^-$	-92.59	-79.02	-68.10	-60.06	----	----	15
$ZnCl^+ + HSO_4^- = ZnS + 2O_2 + H^+ + Cl^-$	-95.34	-82.42	-72.34	-64.29	-57.33	(-49.57)	15
$ZnCl_2^0 + HSO_4^- = ZnS + 2O_2 + H^+ + 2Cl^-$	-95.46	-82.49	-72.33	-64.78	-58.30	(-51.11)	15
$ZnCl_3^- + HSO_4^- = ZnS + 2O_2 + H^+ + 3Cl^-$	-94.90	-81.55	-71.35	----	----	----	15
$ZnCl_4^{2-} + HSO_4^- = ZnS + 2O_2 + H^+ + 4Cl^-$	-95.58	-82.74	-72.58	-65.33	----	----	15
$Ag_2S + 2H^+ + 2Cl^- = 2AgCl^0 + H_2S^0$	-15.86	-12.22	(-9.28)	(-6.40)	(-3.52)	(-1.18)	16
$Ag_2S + 2H^+ + 4Cl^- = 2AgCl_2^- + H_2S^0$	-12.70	-9.08	(-5.88)	(-2.86)	(0.42)	(3.46)	16
$Ag_2S + 2H^+ + 6Cl^- = 2AgCl_3^{2-} + H_2S^0$	-13.92	-10.52	(-7.72)	----	----	----	16
$Ag_2S + 2H^+ + 8Cl^- = 2AgCl_4^{3-} + H_2S^0$	-17.74	----	----	----	----	----	16
$Ag_2S + H_2S^0 = Ag_2S(H_2S)^0$	-6.1	-5.9	-5.8	-5.7	----	----	17
$Ag_2S + 2H_2S^0 = Ag_2(H_2S)(HS)^- + H^+$	-10.7	-10.4	-10.7	-11.4	----	----	17
$Ag_2S + 3H_2S^0 = Ag_2S(H_2S)(HS)_2^{2-}$	-3.6	-3.4	-3.3	-3.2	----	----	17
$Ag_2S + 2H_2S^0 = Ag_2S(HS)_2^{2-} + 2H^+$	-18.1	-18.1	-18.9	-19.9	----	----	17
$Au^0 + AgCl_2^- + 2H_2S^0 = Ag^0 + Au(HS)_2^- + 2H^+ + 2Cl^-$	----	(-4.54)	-6.35	(-8.19)	(-10.45)	----	18
$Au^0 + AgCl_2^- = Ag^0 + AuCl_2^-$	-8.7	-7.8	-7.2	(-6.8)	(-6.6)	(-6.9)	19

Table 15. Themodynamic data used in plotting of diagrams (continued).

References

1 Barton (1984).
2 Helgeson (1969).
3 Calculated from Bowers et al. (1984), and Barton (1984).
4 Heinrich and Eadington (1986).
5 Calculated from Bowers et al. (1984), Barton (1984), and Heinrich and Eadington (1986).
6 Calculated from Ohmoto et al. (1983), Bowers et al. (1984), and Barton (1984).
7 Calculated from Bowers et al. (1984), and Henley (1984).
8 Calculated from Bowers et al. (1984).
9 Calculated from Seward (1973), Bowers et al. (1984), and Barton (1984).
10 Calculated from Helgeson (1969), and Bowers et al. (1984).
11 Calculated from Cole and Drummond (1986), and Bowers et al. (1984).
12 Crerrar and Barnes (1976).
13 Calculated from Crerrar and Barnes (1976), Bowers et al. (1984), and Barton (1984).
14 Calculated from Helgeson (1969), Bowers et al. (1984), and Ruaya and Seward (1986).
15 Calculated from Helgeson (1969), Bowers et al. (1984), Ruaya and Seward (1986), and Barton (1984).
16 Calculated from Seward (1976), Bowers et al. (1984), and Helgeson (1969).
17 Calculated from Sugaki et al., Bowers et al. (1984), and Helgeson (1969).
18 Calculated from Seward (1973 and 1976), Barton (1984) and Bowers et al. (1984).
19 Calculated from Seward (1976), Helgeson (1969) and Bowers et al. (1984).

Notes

Values in parentheses are extrapolations or interpolations.

[a]Extrapolated graphically.

[b]Extrapolated and interpolated assuming that log K_{eq} of the reation $Au^{+} + 2Cl^{-} = AuCl_2^{-}$ is a linear function of 1/T.

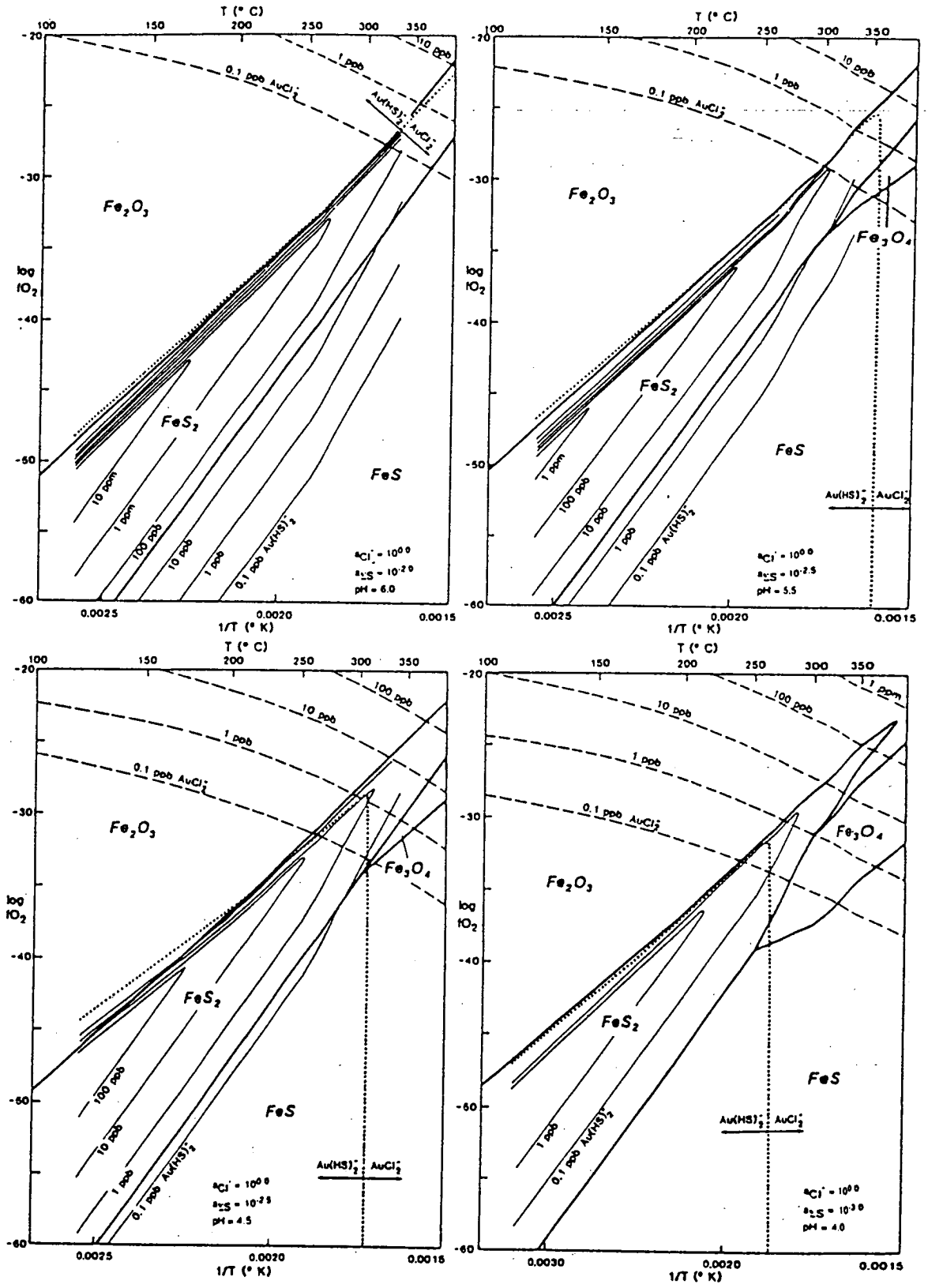

Figure 101. f_{O_2}-pH diagrams at variable pH and $a_{\Sigma S}$ showing the solubility of gold as $Au(HS)_2^-$ and $AuCl_2^-$.

$Au(HS)_2^-$

The reaction relevant to gold precipitation from $Au(HS)_2^-$ is:

$$4Au(HS)_2^- + 2H_2O + 4H^+ = 4Au^0 + 8H_2S + O_2 \quad (8)$$

This reaction indicates that gold precipitation in the H_2S field (most likely conditions of hydrothermal transport) could be caused by a decrease in pH or a_{H_2S}. The effect of pH is illustrated in Figures 100c, 100d and 101, while the effect of temperature and a_{H_2S} is shown in Figure 101. These figures and equation (8) indicate that the solubility of gold will decrease by two orders of magnitude for each order of magnitude decrease in the activity of reduced sulfur. The effect of decreasing pH is much less, only one order of magnitude decrease in solubility for each unit decrease in pH.

At constant pH, the solubility of gold as $Au(HS)_2^-$ actually increases with decreasing temperature, particularly below 200°C, as shown in Figure 101. Gold as $Au(HS)_2^-$ is most soluble in the pyrite field, and the solubility decreases most rapidly at the pyrite-hematite boundary. Gold is relatively insoluble in the pyrrhotite field. This suggests that gold may not be transported as $Au(HS)_2^-$ in very reduced fluids (pyrrhotite stable) or in very oxidized fluids (hematite or magnetite stable) at the common temperatures of hydrothermal transport.

The most effective method of depositing gold is to decrease the activity of reduced sulfur. Seward (1984b) suggested that the activity of reduced sulfur may be decreased by boiling, precipitation of metal sulfides, dilution or oxidation (The decline in a_{H_2S} caused by oxidation and the consequent decrease in gold solubility more than offsets the increase in gold solubility caused by an increase in f_{O_2} (c.f. equation (8)) as shown by Figs. 100c, 100d and 101). With the exception of boiling (see discussion below), all of these factors may

cause gold precipitation when volcanogenic fluids mix with seawater at the ocean floor.

$HAu(HS)_2^0$ and $Au_2(HS)_2S^{2-}$

The equations relevant to the precipitation of gold from $HAu(HS)_2^0$ and $Au_2(HS)_2S^{2-}$ are:

$$4HAu(HS)_2^0 + 2H_2O = 4Au^0 + 8H_2S^0 + O_2 \quad (9)$$

and

$$2Au_2(HS)_2S^{2-} + 2H_2O = 4Au^0 + 6HS^- + 2H^+ + O_2 \quad (10)$$

Conditions of $Au_2(HS)_2S^{2-}$ stability are too alkaline for normal hydrothermal fluids (Fig. 102), no further discussion of this complex will be undertaken.

Conversely, $HAu(HS)_2^0$ may be stable in conditions of likely hydrothermal transport (acid pH). Precipitation of gold from this complex will also be caused by a decrease in the activity of reduced sulfur. As opposed to $Au(HS)_2^-$, Seward (1984b) indicated that solubility of gold as $HAu(HS)_2^0$ would increase with increasing temperature, so a drop in temperature could also bring about gold precipitation; changes in pH will not affect gold precipitation (reaction (9)). Seward (1984b) indicates that the solubility of gold as $HAu(HS)_2^0$ is up to two orders of magnitude less than that of gold as $Au(HS)_2^-$ for temperatures up to 250°C (Fig. 102).

Gold polysulfide complexes

An additional aspect of the oxidation of reduced sulfur that may affect gold transport is the production of polysulfide ions (e.g. S_n^{2-}

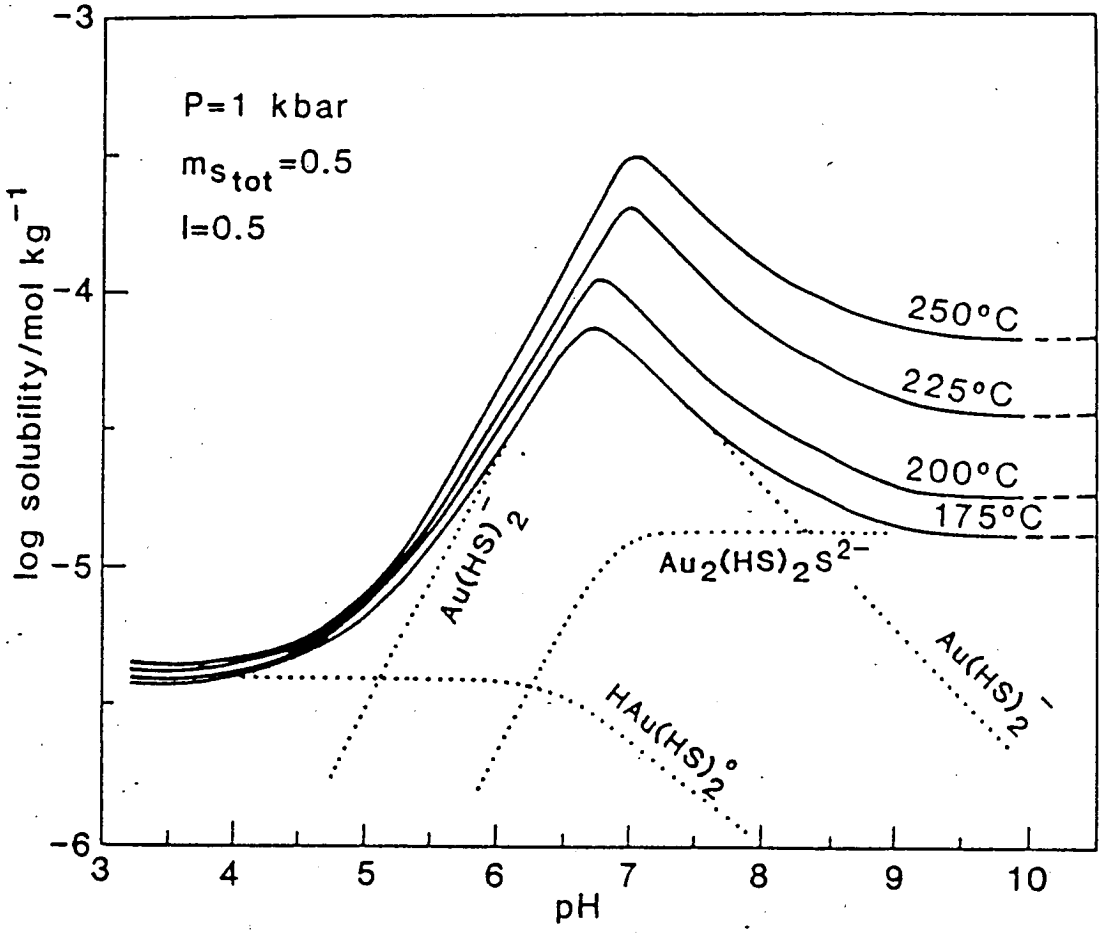

Figure 102. Gold solubility of various thiocomplexes at 250°C (after Seward, 1984).

where n>2) from the partial oxidation of reduced sulfur (Giggenbach, 1974), for instance:

$$4H_2S^0 + O_2 = 2S_2^{2-} + 4H^+ + 2H_2O \quad (11)$$

Giggenbach (1974) indicated that polysulfide ions are stable at neutral pH and temperatures up to 240°C, and metastable at both lower and higher pH and at higher temperatures. Seward (1984b) noted that polysulfide ions may complex with gold (e.g. AuS_2^-), so the formation of polysulfide ions caused by the mixing of seawater and hydrothermal fluid may allow furthur transport of gold along the seafloor in volcanogenic massive sulfide systems.

Deposition of gold from polysulfide complexes will be caused by further oxidation or an increase in pH, as follows:

$$4AuS_2^- + 6H_2O + 13O_2 = 4Au^0 + 8SO_4^{2-} + 12\ H^+ \quad (12)$$

J. Walshe (Australian National University, pers. com., 1986) suggested that one possible kinetic control on the deposition of pyrite may be the formation of polysulfide ions:

$$FeCl^+ + S_2^{2-} = FeS_2 + Cl^- \quad (13)$$

As pyrite precipitates, $a_{S_2^{2-}}$ decreases, causing gold to precipitate:

$$4AuS_2^- + 2H_2O = 4Au^0 + 4S_2^{2-} + 4H^+ + O_2 \quad (14)$$

Either an increase in pH or precipitation of pyrite will cause gold precipitation. The effect of reducing f_{O_2} will be swamped by these other processes.

Webster (1986) demonstrated that $Au(S_2O_3)_2^{3-}$ exists as the major gold complex in neutral to alkaline, oxidized fluids at 25°C. This suggests that other partially reduced sulfur species may complex with gold and play some role in the transport of gold at the seawater interface in volcanogenic massive sulfides, however, the species AuS_2^- is preferred.

$AuCl_2^-$

The reaction relevant to gold precipitation from a chloride complex is (Henley, 1973):

$$4AuCl_2^- + 2H_2O = 4Au^0 + 4H^+ + 8Cl^- + O_2 \quad (15)$$

This reaction indicates that gold precipitation could be caused by an increase in pH or decreases in either a_{Cl^-} or f_{O_2}. Figures 100c, 100d and 101 illustrate the effects of pH and f_{O_2}. Figure 101 also indicates that solubility decreases with temperature. In systems where a_{Cl^-} does not change significantly, gold precipitation will be caused by a decrease in temperature, followed in importance by an increase in pH and a decrease in f_{O_2}.

As indicated in Figures 100 and 101, gold is most likely transported as $AuCl_2^-$ in oxidized, saline and acidic fluids of moderate to high temperature. Large (1975) presented strong evidence for such transport during the formation of the gold-copper-bismuth deposits in the Tennant Creek district of the Northern Terrritory.

Summary

The chemical conditions in which gold chlorocomplexes are favored are significantly different from those under which gold thiocomplexes are favored. Transport of gold as $Au(HS)_2^-$ is favored in solutions of low temperature (<300°C), of high a_{H_2S} or a_{HS^-}, of neutral to alkaline pH, and in equilibrium with pyrite (gold may not be transported in the hematite or magnetite fields, and is unlikely to transported in the pyrrhotite field). Deposition is most effectively produced by decreasing the activity of reduced sulfur, either by oxidation, precipitation of metallic sulfides, dilution (processes typical of volcanogenic massive sulfide deposition) or boiling. Crossing the pyrite-hematite buffer is a particularly good gold precipitator. A decrease in pH on the acid side of neutrality

will also cause deposition. However a decrease in temperature at constant pH will cause an increase in gold solubility as $Au(HS)_2^-$.

On the other hand, transport of gold as $AuCl_2^-$ is favored in solutions of high temperature (>300°C), of high salinity ($a_{Cl^-}>10^0$), and of low pH (<4.5). For systems in which a_{Cl^-} does not change significantly (e.g. volcanogenic massive sulfide systems), deposition is most effectively produced by decreasing temperature or increasing pH. Decreasing f_{O_2} may also produce deposition.

Gold transport by either complex is unlikely in the hematite field at low temperatures (<200°C) and low f_{O_2} ($<10^{-35}$), and in the pyrrhotite field at moderate to high temperatures (>200°C) and low f_{O_2} ($<10^{-40}$).

Other complexes that may play some role under typical hydrothermal conditions are $HAu(HS)_2^0$ and AuS_n^- (n>2). $Au_2(HS)_2S^{2-}$ occurs in conditions that are too alkaline for normal hydrothermal fluids. Due to a lack of thermodynamic data, these complexes may not be modelled quantitatively, however a decrease in the activities of reduced sulfur species (H_2S or S_n^{2-}) by oxidation, boiling or metallic sulfide deposition seems to be the most effective way to precipate gold in each instance.

Gold transport and deposition in volcanogenic massive sulfide systems

In volcanogenic massive sulfide deposits, gold is unique among base and precious metals in that it has a rather complex distribution. Whereas zinc, lead, silver and copper tend to concentrate in particular parts of these deposits, gold can occur in many different ore types throughout the mineralization. As shown earlier, gold can occur in either the zinc-rich, lower temperature tops or the copper-rich, higher temperature bases of the systems. Additionally, gold may be present in more distal parts of the

deposits, such as the barite and distal pyrite mineralization at Rosebery (Part 2, Chapter 2).

Geochemical models of gold transport and deposition in volcanogenic massive sulfide deposits must explain the three distinct occurrences of gold--three occurrences that were deposited under quite different physicochemical conditions. The following model seeks to describe the processes that produce the three different occurrences based on: (1) an understanding of the chemical conditions that existed during gold deposition as deduced from gangue and ore mineralogy, (2) an examination, both quantitative using thermodynamics and qualitative using reaction stoichiometries, of the behavior of possible gold complexes, (3) a comparison of the distribution of gold with that of copper, for which transport and deposition mechanisms are well understood, (4) an examination of the textures and mineral associations of gold to elucidate chemical reactions and conditions that may precipitate gold, and (5) a comparison of gold in volcanogenic massive sulfide deposits with that in other deposits in which the mechanisms of gold transport and deposition are well understood. Owing to a lack of adequate thermodynamic data, especially for gold chlorocomplexes, some aspects of the model are conjectural, and, as such, the model should be regarded as a working model, subject to possible modifications.

Models of massive sulfide formation

A number of chemical fluid models have been developed over the past 15 years to explain the formation and zonation of massive sulfide ores on the sea floor. Detailed reviews are provided by Franklin et al. (1981) and Eldridge et al. (1983). Some of the more important papers that have contributed to the presently accepted model are described below:

(1) Sato (1972) modelled the behaviour of hydrothermal solutions discharging onto the sea floor based on temperature-density- salinity relationships of sodium chloride solutions. Due to their density, high salinity hydrothermal solutions flow down submarine slopes to form stratified brine pools from which sulfides precipitate. Low salinity fluids, however, are less dense than seawater and form plumes which lead to a widely dispersed thin layer of mineralization. Hydrothermal brines with densities

similar to seawater behaved complexly, giving rise to to bimodal deposition around the vent and down the submarine slope.

(2) Sato (1973) developed a thermodynamic model based on metal chloride solubilities to show that during fluid mixing in the plume above the seafloor copper precipitation occurs at higher temperatures, and zinc and lead precipitated at lower temperatures.

(3) Large (1977) studied both ore and gangue mineral zonation in several Canadian Archean deposits and concluded from chemical modelling that stringer ores are precipitated as the hydrothermal fluids mixed with seawater at the top of the volcanic pile. Progressive mixing leads to an increase in solution pH, f_{O_2} and $a_{\Sigma S}$ accompanied by a drop in temperature to give the zonation of pyrite-pyrrhotite-chalcopyrite in the footwall and pyrite-sphalerite-galena in the hanging wall of massive sulfide lenses.

(4) Henley and Thornley (1979) suggested that brecciated feeder zones are developed from high power hydrothermal discharge associated with a vapor plume produced by boiling of the fluids at depth. The upper massive sulfide lens is formed as a fluidized bed which allowed sorting of sulfide minerals to form the metal zonation observed in these deposits.

(5) Based on experimental plume studies and fluid inclusion evidence Solomon and Walshe (1979) suggested that massive sulfide forming solutions are continuously buoyant on entering seawater and form conical plumes from which sulfides precipitate. Copper-bearing sulfides precipitate around the vent, but zinc- and lead-bearing sulfides become entrained in the plume and rain down to form a blanket above the copper-rich mound near the vent. McKay and Hazeldene (1987) have used a similar model to explain the fine banding in the Woodlawn deposit.

(6) Based on systematic studies of ore textures and fluid inclusions from the Kuroko distict of Japan, Eldridge et al. (1983) and Pisutha-Arnond and Ohmoto (1983) concluded that massive sulfide ores develop by a process of progressive upward replacement. Early formed low

temperature precipitates which formed around the hydrothermal vent (colloform pyrite, sphalerite and galena) are replaced by later higher temperature minerals (chalcopyrite and coarse pyrite); this produces a progressively zoned deposit that evolved with time. Goldfarb et al. (1983) and Campbell et al. (1984) reached consistent conclusions based on studies of the zoned copper-zinc-rich chimneys from the East Pacific Rise at 21°N and physical modelling, respectively.

The last model (referred herafter as the Kuroko model) as described by Eldridge et al. (1983) and Pisutha-Arnond and Ohmoto (1983) appears to explain the overall features of volcanogenic massive sulfide deposits and has been accepted as "the state of the art" model. However, most Paleozoic and Archean deposits have suffered some degree of deformation which has resulted in recrystallisation and annealing of minerals and modification of fluid inclusions. Consequently the critical evidence on which the model is based (e.g. chalcopyrite disease and fluid inclusion filling temperature trends) cannot be assessed in older deposits, and the extension of the Kuroko model to all volcanogenic deposits cannot be demonstrated at this time. Despite this limitation it is considered to be the best model available. Options (1; dense hydrothermal brine) and (2; precipitation from a buoyant plume) are discussed later with respect to Rosebery and other similar deposits.

The Kuroko model. The stages of development in the Kuroko model may be summarized as follows (Eldridge et al., 1983; and Pisutha-Arnond and Ohmoto, 1983):

(1) Precipitation of fine grained (<50 μm), often colloform sphalerite, galena, tetrahedrite, barite and minor chalcopyrite caused by the mixing of relatively cool (200°C) hydrothermal fluids with cold seawater.

(2) Recrystallization and coarsening of the fine grained minerals at the base of the growing sulfide mound by hotter (250°C) fluids.

(3) Introduction of hotter (300°C) copper-rich fluids which replace the earlier minerals with chalcopyrite in the lower part of the mound.

(4) Introduction of the hottest (>300°C) copper-undersaturated fluids which dissolve chalcopyrite to form pyrite-rich bases to the deposits.

(5) Precipitation of tetsusekiei (chert-hematite) at the top of the massive ores.

The hydrothermal fluids evolve with time from cool to hot back to cool, and any or all of the described stages may occur at a particular time. Fluids generated during stages (2) through (4) cool as they pass through the sulfide mound and produce stage (4) style mineralization at the top of the massive sulfide body (Eldridge et al., 1983; and Pisutha-Arnond and Ohmoto, 1983).

The question of boiling in volcanogenic massive sulfide systems

Henley and Thornley (1979) and, more recently, Clark (1983) have suggested that the presence of stockwork and other breccias in volcanogenic massive sulfide deposits indicate that boiling or phreatomagmatic explosions occurred during their deposition. On the other hand, Urabe and Sato (1978) and Pisutha-Arnond and Ohmoto (1983) conclude that boiling did not occur in these systems based on fluid inclusion studies.

Boiling is a particularly efficient method of depositing gold in epithermal systems (Buchanan, 1981; Henley, 1984; and Henley and Brown, 1985). R. Henley (Bureau of Mineral Resources, Australia, pers. comm., 1987) suggested that the assemblage of gold-sulfides-feldspar-carbonate, which is observed in the barite lenses at Rosebery, is a common epithermal assemblage.

However, the bulk of the gold at Rosebery occurs in sphalerite-galena-pyrite ore which lacks feldspar and barite (Brathwaite, 1974; Green et al., 1981; Part 2) and therefore is not in a typical epithermal assemblage. Furthermore, Rosebery lacks brecciation in both the ores and the footwall alteration zone. The lack of brecciation in the ores and footwall alteration zone at Rosebery is not consistent with boiling of the hydrothermal fluids.

Similarly, at Mt. Chalmers the lower massive sulfide and footwall volcanics do not show any evidence of hydrothermal brecciation. The uppermost sulfide layers consist of fine brecciated sulfides interlayered with laminated sulfides but with features indicative of sedimentary reworking rather than hydrothermal brecciation (R.R. Large, pers. com., 1986).

The form and grade of volcanogenic massive sulfide deposits also indicates that boiling did not have a major impact on their formation. In epithermal gold-silver deposits, many of which are

acknowledged to be the best examples of boiled systems, mineralization occurs over several hundred meters vertically, with base metals concentrating at the bottom of the interval and precious metals concentrating at the top (Buchanan, 1981). Conversely, in volcanogenic massive sulfide deposits, most metal was deposited within a few meters of the seawater/rock interface, and precious metals occur with base metals. Continual boiling over several hundred meters as seen in epithermal systems clearly cannot produce the accumulation of base and precious metals seen right at the seawater interface in volcanogenic massive sulfide deposits.

In light of these arguments and evidence from fluid inclusion studies in Kuroko deposits (Urabe and Sato, 1978; and Pisutha and Arnond, 1983), boiling does not appear to be an important process in the formation of most volcanogenic massive sulfide deposits. The brecciation observed in the ores and stockworks in these deposits must have been produced by other processes such as intense hydrothermal activity, replacement, slumping and/or faulting.

Evolution of the Rosebery and Mt. Chalmers volcanogenic fluids

Given the constraints of the Kuroko model and gangue and ore mineralogies, the evolution of both the Rosebery and Mt. Chalmers volcanogenic fluids may be modelled.

Rosebery. Figure 100 illustrates the evolution of Rosebery fluids in space and time based on the following mineral assemblages (Brathwaite, 1969, 1974; Dixon, 1980; Green et al., 1981; and Chapter 2): (1) chlorite-sericite with only minor carbonate in the footwall schists, (2) trace arsenopyrite and trace pyrrhotite with only minor carbonate in pyrite-chalcopyrite ore, (3) trace arsenopyrite and significant carbonate in sphalerite-galena-pyrite ore, (4) Major carbonate bodies lateral to sphalerite-galena-pyrite ore, and (5) Barite and albite without arsenopyrite in massive barite mineralization. The evolution of the Rosebery fluids presented in Figure 100 are consistent with those inferred by Green et al. (1981) using an $a_{SO_4^{2-}}/a_{H_2S}$-temperature diagram but discuss changes in pH more quantitatively.

Early formed sphalerite-galena-pyrite ore and massive barite mineralization (stages 1 and 2 of the Kuroko model) were deposited at low to moderate temperatures (200°C to 250°C) from near neutral

fluids (pH=5 to 6) in the pyrite stability field (Fig. 100a). All of the gold-rich polymetallic volcanogenic massive sulfide deposits in Tasmania (Rosebery, Hercules, Hellyer and Que River) are unusual in that they contain high amounts of carbonate which indicates that most zinc-lead ore was deposited at a near neutral pH. During deposition of zinc-lead mineralization, temperature decreased while f_{O_2} and pH increased (Fig. 100a).

Pyrite-chalcopyrite ore (stage 3 of the Kuroko model) replaced sphalerite-galena-pyrite ore under slightly acid conditions (pH=3 to 5) from high temperature fluids in the pyrite stability field near the pyrite-pyrrhotite buffer (Fig. 100b). During replacement temperature and f_{O_2} decreased while pH increased according to equation (16):

$$4CuCl^0 + ZnS + FeS \text{ (in sphalerite)} + 4H^+ + O_2 = 4CuFeS_2 + 4ZnCl^+ + 2H_2O \qquad (16)$$

As these fluids moved up through the sulfide mound they cooled and deposited sphalerite-galena-pyrite ore as described earlier.

Mt. Chalmers. The pyrite-chalcopyrite ores at Mt. Chalmers were deposited during stage 3 of the Kuroko model from high temperature (300°C), oxidized fluids that varied from acidic at the core of the deposit (pH=3 to 4) to neutral at the edges of the deposits (pH=5 to 6) (Fig. 100b). The presence of barite and lack of arsenopyrite in the ores suggests a relatively high f_{O_2} during deposition. The presence of kaolinite in the ore (McLeod, 1985) but the presence of carbonate lateral to ore indicates that the fluid pH increased as it passed from the vent to the peripheries of the deposit. Stages 1 and 2 of the Kuroko model are of minor importance in this deposit.

The gold transport and deposition model

The following model describes the transport and deposition of gold in terms of the evolution of volcanogenic massive sulfide deposits as described by the Kuroko model (Eldridge et al., 1983; and Pisutha-Arnond and Ohmoto, 1983) and the fluid conditions required by

the mineral assemblages described above. Stages 1 through 3 correspond to stages 1 through 3 of the Kuroko model. This model extends earlier modelling by Large and Huston (1985) and Huston and Large (1987a). It is depicted graphically as Figure 103.

(1) In the early, low temperature stages of massive sulfide deposition, gold (as $Au(HS)_2^-$) is transported with silver, lead and zinc (all as chlorocomplexes) to the seawater interface where all metals are deposited. The precipitation of silver, lead and zinc is caused by cooling when hydrothermal fluids mix with seawater. Gold, on the other hand, is precipitated by the oxidation or dilution of the hydrothermal fluids caused by mixing and the precipitation of metallic sulfides (point A; all three processes reduce the activity of reduced sulfur).

(2) As the fluids warm and the sphalerite-galena-pyrite mound grows, gold is mobilized as $Au(HS)_2^-$ from the base (point B) during recrystallization of the deposit (stage 2 of the Kuroko model) and deposited near the top or in barite mineralization (point A), again by a reduction in the activity of reduced sulfur caused by oxidation, dilution or precipitation of metallic sulfides.

Partial oxidation of reduced sulfur caused by mixing with seawater may produce polysulfide ions (or other partially oxidized sulfur species) which then may mobilise gold as AuS_n^- (n>2) (or some similar complex). This gold may then be transported at the seawater-rock interface and deposited in the distal parts of the massive sulfide deposit by continued oxidation of polysulfides or precipitation of pyrite (point C).

As the fluids continue to warm, gold will eventually become less soluble as $Au(HS)_2^-$.

(3) When temperatures reach 300 °C, pyrite-chalcopyrite ore begins to replace sphalerite-galena-pyrite ore (Eldridge et al., 1983). During this time, the higher temperature enables gold transport as a chloride complex. As this replacement occurs, pH increases and temperature and f_{O_2} both decrease (reaction (12)), causing gold precipitation (point D). As the solubility of $AuCl_2^-$ increases with f_{O_2} (see Figs. 100c and 100d), higher gold grades may

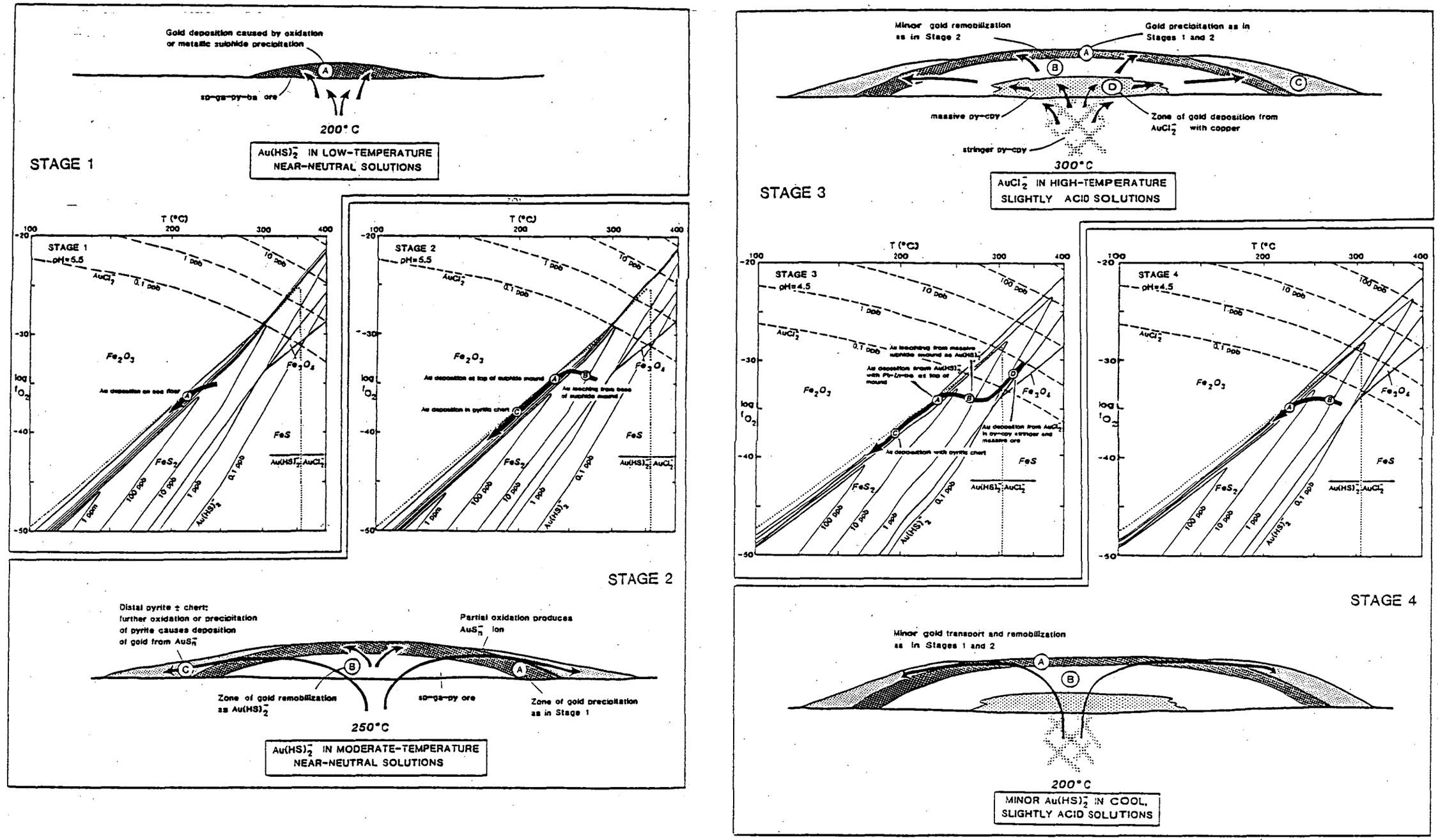

Figure 103. Geochemical model of gold tansport and deposition in volcanogenic massive sulfide deposits.

be associated with pyrite-chalcopyrite ore in which there is evidence of a relatively high f_{O_2} (e.g. barite gangue or the presence of bornite, hematite or magnetite).

When the hydrothermal fluids migrate up through the mound and cool to the point where sphalerite and galena are reprecipitated, gold transport switches over from $AuCl_2^-$ to $Au(HS)_2^-$ and the processes described in stages (1) and (2) apply as pH and f_{O_2} increase.

(4) As the hydrothermal system wanes and fluid temperatures cool, gold transport returns to $Au(HS)_2^-$ and the processes described in stages (1) and (2) apply.

Discussion

The importance of each of the four stages in the evolution of the deposits discussed previously varies significantly. For example, at Rosebery and Hellyer stage 2 was the dominant event while at Mt. Chalmers and Millenbach stage 3 was most important.

Gold deposition in sphalerite-galena-pyrite ore and massive barite mineralization. As the majority of gold at Rosebery is with sphalerite-galena-pyrite and barite mineralization, gold must have been deposited from a near neutral fluid that increased in f_{O_2} and decreased in temperature during deposition (see above). Of the five gold complexes discussed in this chapter, only one, $Au(HS)_2^-$, allows the transport of significant gold at a near neutral pH. An unusual characteristic of this complex is that it becomes more stable at lower temperatures, which is consistent with the lower temperature of deposition for sphalerite-galena-pyrite ore. A second characteristic of this complex is that the solubility of gold increases, and then sharply decreases as f_{O_2} increases across the pyrite field (Figs. 100c, 100d and 101). As seawater mixing causes the f_{O_2} of the hydrothermal fluids to rise, gold will initially be leached from the bottom of the sphalerite-galena-pyrite mound and then precipitated at

the top. An increase in gold grades toward the top of sphalerite-galena-pyrite ore is noted at Rosebery (Part 2), Hellyer and Que River (Large et al., in press).

Gold precipitation from $Au(HS)_2^-$ is best caused by a reduction in a_{H_2S}. In volcanogenic massive sulfide deposits such a reduction may be caused by oxidation and dilution of the hydrothermal fluids by seawater or deposition of metallic sulfides (see below).

Gold deposition in pyrite-chalcopyrite ore. The second major occurrence of gold in volcanogenic massive sulfide ores lies with pyrite-chalcopyrite ore which was deposited under acid conditions and high temperatures. As the stability of $Au(HS)_2^-$ decreases with both increasing temperature and decreasing pH (see Figs. 100c, 100d and 101), this complex is inadequate as a gold transporting mechanism at the conditions of pyrite-chalcopyrite deposition. Additionally, as the fluid pH increases during pyrite-chalcopyrite ore deposition, and the solubility of gold as $Au(HS)_2^-$ increases with pH, this complex will leach, not deposit, gold at conditions in which gold is clearly being deposited. Clearly $Au(HS)_2^-$ is not an adequate complex to explain gold deposition in the gold-copper association.

Gold complexes whose stabilities increase under low pH and high temperature conditions include $AuCl_2^-$ and $HAu(HS)_2^0$. Gold solubility decreases for both complexes with decreasing f_{O_2}. An increase in pH will cause gold precipitation from $AuCl_2^-$ but will not cause precipitation from $HAu(HS)_2^0$, while a decrease in the activity of reduced sulfur will cause gold precipitation from $HAu(HS)_2^0$ (see above).

As the deposition of pyrite-chalcopyrite ore involves the replacement of sphalerite-galena-pyrite ore (hence no significant change in a_{H_2S}; see reaction (12)) and an increase in pH, the logical candidate for gold transport in pyrite-chalcopyrite ore is $AuCl_2^-$.

At Mt. Chalmers and Millenbach, the intimate relationship between copper and gold (Figs. 97 and 99) suggests similar transport

and deposition mechanisms. Examination of the solubility of gold as a chlorocomplex and copper as a chlorocomplex indicates that both metals wil be precipitated by an increase in fluid pH or a drop in temperature at acid pH. In the pyrite stability field, copper and gold will precipitate coherently as their solubility contours are parallel (Figs. 100 and 101). Conversely, if gold was transported as $Au(HS)_2^-$, copper and gold would be precipitated at different times--copper first and gold second given the requisite increase in pH and decrease in temperature during volcanogenic massive sulfide deposition. It is highly unlikely that gold and copper were both transported as thiocomplexes as Crerar and Barnes (1976) report that copper chlorocomplexes are more soluble than copper thiocomplexes above 250°C. The relationship of gold to copper at Mt. Chalmers (Fig. 97) conforms to the expected relationship for gold chlorocomplex transport, while the relationship of gold to copper at Rosebery confirms that $Au(HS)_2^-$ was the dominant complex (Fig. 75).

This argument is strengthened by looking at other high temperature deposits that show the copper-gold association. In particular, gold-rich porphyry copper deposits form in conditions that are too high and too saline to allow thiocomplexing of gold (see below). Sillitoe (1979) argued that gold transport in these deposits must be as chlorocomplexes. As the gold in porphyry copper deposits is strongly related to copper, this strengthens the argument that the gold in volcanogenic massive sulfide deposits showing the gold-copper association can be transported solely as a chlorocomplex. Large (1975) has demonstrated a similar chemistry of transport and metal association in the Tennant Creek gold field of the Northern Territory, Australia.

Gold deposition in distal gold-rich mineralization. When the reduced hydrothermal fluids become oxidized by mixing with seawater, some of the reduced sulfur may be partially oxidized to form polysulfide ions. As gold may form stable polysulfide complexes, gold may then be carried along the seafloor until further oxidation or pyrite precipitation causes its deposition (see above). Distal gold may be found in the Rosebery mine in pyritic bodies at the fringes of sphalerite-galena-pyrite ore or in a siliceous pyritic cap at the top of the Hellyer deposit.

Summary. Based on numerous lines of evidence, gold in sphalerite-galena-pyrite ore in volcanogenic massive sulfide deposits was transported as $Au(HS)_2^-$, gold in distal gold mineralization was transported as a polysulfide complex, and gold in pyrite-chalcopyrite ore was transported as $AuCl_2^-$. Consideration of fluid evolution and reaction stoichiometries preclude $Au(HS)_2^-$ as the transporting complex in pyrite-chalcopyrite ore.

Implications of other genetic models of massive sulfide formation on the gold model

The Rosebery, Dry River South and many other deposits (e.g. Woodlawn; McKay and Hazeldene, 1987) differ from the classical, bulbous Kuroko deposit in having a sheet-like morphology and well banded ores. Solomon (1976) classified these deposits separately as the Rosebery-type of volcanogenic massive sulfide deposit.

Several authors (e.g. Solomon and Walshe, 1979; McKay and Hazeldene, 1987; and Lydon, 1988) suggested that the mechanisms to form this class of deposits differed to those that formed kuroko deposits. The question that needs to be addressed is how great are the differences: can the kuroko model be modified to account for the differences in morphology or is a separate model required?

One model that has been proposed is that the sulfides were deposited in a brine pool (Fig. 104a; e.g. Sato, 1972; Green et al., 1981; and Lydon, 1988). This model has one major deficiency: the highly saline brines (3.5 m NaCl; Green et al., 1981) have not been observed in fluid inclusion studies (e.g. Pisutha-Arnond and Ohmoto (1983); Urabe and Sato, 1978; and Large and Both (1980)). This deficiency may be due to a lack of fluid inclusion studies, but until concrete evidence of highly saline fluids is found, the concept of sheet-like massive sulfides forming from the ponding of dense brines remains speculative.

A second model (Solomon and Walshe, 1979; and McKay and Hazeldene, 1987) involves the precipitation and settling of sulfide minerals from a buoyant plume (Fig. 104b). This has been observed in black smoker deposits, but the sulfide disperses over a wide area to form metalliferous sediment and not accumulations of massive sulfide (Rona, 1984). This difficulty may be overcome by confining the plume

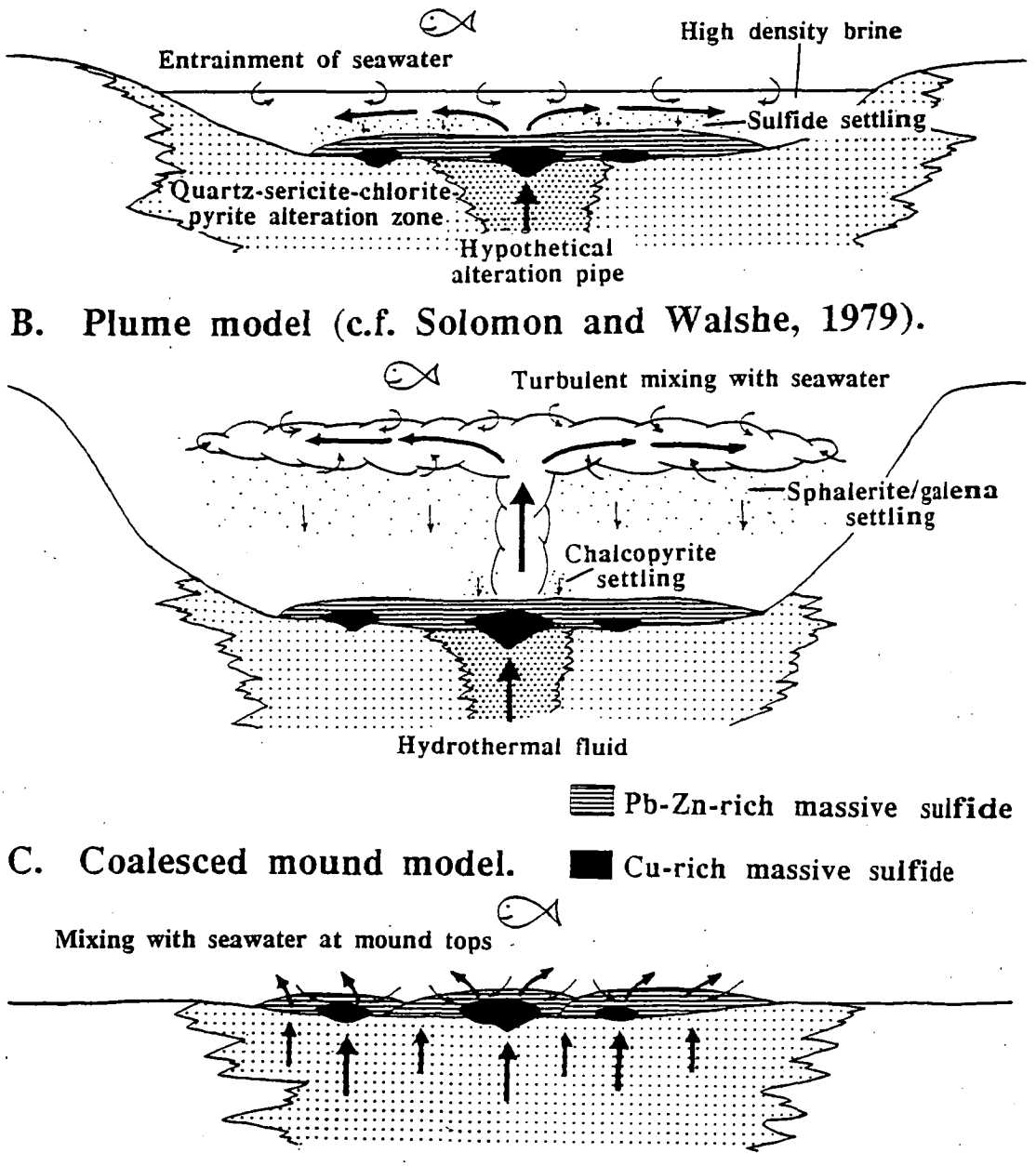

Figure 104. Alternative models for forming "Rosebery-type" volcanogenic massive sulfide deposits.

to the basin containing the massive sulfide accumulation. To explain metal zonation Solomon and Walshe (1979) inferred that chalcopyrite precipitation, occurred at the base of the plume whereas sphalerite and galena precipitation occurred in the upper part of the plume. As a result, chalcopyrite settled first to form a mound that was covered by later settling of sphalerite and galena. However, additional pulses of pluming from the same vent must destroy this zonation, or at least produce transgressive veins (c.f. Green et al., 1981, p. 335). These characteristics have not been noted in the deposits.

McKay and Hazeldene (1987) partially overcome this problem by placing the vent on the side of a submarine hill and accumulating the sulfide in an adjacent depression. In this model, an early copper-rich mound formed from high temperature fluids, followed by the onlapping of sphalerite and galena from lower temperature fluids. However, McKay and Hazeldene (1987; pp. 153 and 159) noted that the kuroko model could explain the characteristics observed at Woodlawn. At Rosebery the problem of zonation disturbance by later bouyant, turbulent fluids can not be dismissed by placing the vent on a hillside adjacent to the accumulation site as copper-rich zones occur as basal pods throughout the deposit (Zaw et al., 1988; and Fig. 73).

One of the critical pieces of evidence used to support precipitation from a brine pool or a buoyant plume is fine banding within the ores. At Rosebery this texture historically has been interpreted as primary bedding (c.f. Brathwaite, 1969; and Green, 1983), however recent studies by Berry (1988; pers. comm., 1989) indicated that this banding is at least in part deformational. He interpreted the fine banding (X mm) as the result of a strong shear that has deformed the ores, but he interpreted the coarser banding (X0 mm) as a primary depositional feature. These conclusions significantly weaken the interpretation that the fine banding at Rosebery was caused by sedimentation of the sulfides from either a brine pool or settling from a rising plume.

Another alternative (preferred) interpretation to explain the morphology of Rosebery-type deposits is that they formed from a coalesced field of overlapping kuroko-type mounds. Many of the Rosebery-type deposits (e.g. Rosebery, Dry River South and Kidd Creek (Walker et al., 1975)) have a laterally extensive alteration zone, which contrasts with the alteration pipe commonly associated with the more bulbous deposits. The large zone of alteration suggests that unfocussed hydrothermal fluids passed under most of the sheet-like

lenses of Rosebery-type deposits. Interaction of seawater with such a widespread hydrothermal system would produce large sheet-like deposits. Local foci caused by fractures would concentrate hot fluids to produce pods of high temperature copper-rich mineralization. As fluid flow would occur over a much larger area, flow velocities would be much slower than comparable kuroko deposits. Such a flow regime might allow more rapid and thorough mixing between seawater and hydrothermal fluid in the sulfide lens, and the fluid exiting the sulfide lens would be much cooler. Such a fluid could form a brine pool at much lower salinities.

All three of these models lack some hard scientific evidence or have physical difficulties. As such, each should be considered as alternative hypotheses. The model for gold concentration in volcanogenic massive sulfide deposits applies directly if Rosebery-type deposits formed from modified kuroko processes. However, even if one of the the other two alternate models are applicable, the processes described in the gold model still apply: in the deposits of the zinc-gold association, gold deposition occurs as the result of the decrease in a_{H_2S} associated with hydrothermal fluid/seawater interaction.

The entrainment or mixing of oxidized seawater into a brine pool (Fig. 104a) both dilutes and oxidizes the fluid already present in the brine pool. Both processes as well as the precipitaion of sulfide minerals reduce a_{H_2S}, which is the primary cause of gold precipitation in this type of deposit. Consequently, the same processes of gold precipitation proposed by the model presented also apply if a brine pool formed. Moreover, as the hydrothermal fluids must pass through the accumulated sulfide, the refining of gold grades to the top of the sulfide lens may also occur.

If, on the other hand, a plume model is assumed, turbulent mixing of seawater into the ascending plume or entrainment of seawater into the stagnant cloud (Fig. 104b) would also decrease a_{H_2S}, and thereby precipitate gold according to the model presented herein. Solomon and Walshe (1979) attribute the metal zonation from copper-rich at the base to zinc-lead-rich at the top of the sulfide lens to be the result of preferential quenching and deposition of chalcopyrite at the base of the ascending plume as opposed to the deposition and settling of sphalerite and galena from the stagnant

cloud. As the amount of seawater entrainment and sulfide precipitation must be least at the base of the mound, a_{H_2S} would be least affected and gold precipitation would be minimal. However, in the stagnant cloud, continued mixing and precipitation would decrease a_{H_2S} and gold precipitation would be at a maximum. This would produce the observed enrichment of gold toward the top of the massive sulfide sheet.

Although a model for gold deposition in volcanogenic massive sulfide deposits based on a modified kuroko model is preferred to explain the characteristics of Rosebery-type deposits, the processes described in this chapter apply equally well if brine pool or plume models are considered more applicable to these deposits.

Comparison with other models

Several other workers have proposed models of gold mineralization, either specifically (Hannington et al., 1986) or as part of a general geochemical model of massive sulfide development (Ohmoto et al., 1983). Cole and Drummond (1986) modelled precious metal transport and deposition in the epithermal environment and some of their conclusions may be applied to volcanogenic massive sulfide deposits.

Hannington et al. (1986) proposed a model in which "gold is preconcentrated to about 200 ppb in high-temperature (>300 °C), Cu-Fe-rich sulfides and subsequently remobilized by late, sustained, low temperature (<250 °C) fluids and concentrated in SiO_2-Ba-Zn-rich precipitates near the surface." The model of Hannington et al. (1986) is similar to this model in that they consider $AuCl_2^-$ and $Au(HS)_2^-$ to be important gold carriers in volcanogenic massive sulfide deposits. $AuCl_2^-$ is called upon as a complex that may be important in the earlier preconcentration of gold, but $Au(HS)_2^-$ remobilises the gold to SiO_2-Ba-Zn-rich precipitates at the surface. For this model they require a "mature" deposit (i.e. one with a developed Cu-rich core) to produce good grades in zinc-rich ore, and they imply that

deposits in which gold is associated with copper are relatively unimportant.

In this model, gold concentrations in zinc-lead-rich (sphalerite-galena-pyrite) ore does not require a pre-existing preconcentration of gold in copper-rich (pyrite-chalcopyrite) ore. Remobilization to the top does occur, but the gold is leached from lower zinc-lead-rich ore by $Au(HS)_2^-$. The same complex was the original carrier of the gold. Therefore, a gold-rich zinc-lead deposit does not require a "mature" deposit with a well developed Cu-rich core. All of the Tasmanian gold-rich polymetallic volcanogenic massive sulfide deposits (Rosebery, Hellyer, Que River and Hercules) have very little copper-rich ore relative to zinc-lead-rich ore (Large et al., in press), consequently the copper-rich ores could not act as preconcentrators owing to simple mass balance constraints.

Additionally, the model presented herein explains the existence of gold- and copper-rich deposits. The Hannington et al. (1986) model can not explain such deposits, examples of which include the Mt. Chalmers and Mt. Morgan deposits in Queensland.

Ohmoto et al. (1983) suggested that gold solubility will decrease with decreasing f_{O_2} based on the equation:

$$4Au + 4H^+ + O_2 = 4Au^+ + 2H_2O \qquad (17)$$

Ohmoto et al. (1983) required gold precipitation to occur in fluids that have cooled and have not mixed with seawater (and thereby increase gold solubility), and suggest that this situation may occur locally in the upper parts of massive zinc-lead-rich ores only after ore has been deposited. However, if gold is deposited from a bisulfide complex (equation (4)) the solubility decrease caused by reducing a_{H_2S} more than offsets the solubility increase caused by increasing f_{O_2} when the mixing occurs (Figs. 100c and 100d). Consequently, it is not necessary for the deposition of gold from $Au(HS)_2^-$ to shield the hydrothermal fluid from oxidation. The deposition of gold from $AuCl_2^-$ requires such shielding, however, and may occur only in areas where seawater mixing does not occur.

Cole and Drummond (1986) predicted that gold transport by $Au(HS)_2^-$ occurs at low temperatures (<250 °C) from low salinity (0.1 m Cl^-) fluids with high a_{H_2S} (>10^{-3} m) and near nuetral pH (>5). On the other hand, gold transport by $AuCl_2^-$ occurs at higher temperatures (>250 °C) from high salinity (1 m Cl^-) fluids with low a $_{H_2S}$ (<10^{-3} m) and acid pH (<5). These conclusions agree broadly with those presented herein. Predictions made by Cole and Drummond (1986) about Ag/Au ratios relative to gold complexes differ from those observed in massive sulfides using this model to predict complexes. This may be due to the fact that silver in massive sulfides occurs dominantly in tetrahedrite and argentiferous galena and not as native silver and argentite, the two minerals used by Cole and Drummond (1986) to model silver deposition.

The final aspect of gold transport and deposition in volcanogenic massive sulfide systems is the possibility of other gold complexes, in particular, thioarsenates, thioantimonates and tellurium species. The geochemical association of gold with arsenic, antimony and tellurium is well established, and gold in the Boliden deposit (Grip and Wirstam, 1970; in Boyle, 1979) and the Hellyer deposit (Large et al., in press) has a strong association with arsenopyrite, whereas some gold occurs as tellurides in the Horne (Price, 1934) and Mt. Morgan (Frets and Balde, 1975) deposits. These associations are difficult to evaluate because of lack of relevant thermochemical data.

Geological controls on gold grades in volcanogenic massive sulfide deposits

Gold grades in volcanogenic massive sulfides vary from low grades at which gold is not worth recovering to very high grades at which the gold tenor alone would warrant exploitation under favorable conditions. An understanding of the geochemical parameters that control gold grades might be useful in predicting the occurrence of gold-rich volcanogenic massive sulfide deposits.

Three factors may be important in determining the gold grade of a particular deposit: (1) the background gold content of the source

rock, (2) the chemistry of the transporting hydrothermal fluid, and (3) the efficiency of deposition in the sulfide lens. Calculations by Stolz and Large (1988) indicated that the gold-rich volcanogenic massive sulfide deposits of the Mt. Read deposits do not require a source rock enriched in gold. Moreover, the sudden change in physicochemical conditions at the seawater interface in Proterozoic and Phanerozoic deposits are a very effective precipitator (see above). Given these parameters, the most important control on gold grades in these deposits is the chemistry of the mineralizing fluid.

An important aspect in understanding the geochemistry of gold in volcanogenic massive sulfide deposits is the concept of switchover from one complex to another. This is controlled by the following reaction:

$$AuCl_2^- + 2H_2S = Au(HS)_2^- + 2Cl^- + 2H^+ \quad (18)$$

The switchover occurs at conditions when $a_{AuCl_2^-} = a_{Au(HS)_2^-}$, and is dependant on a_{H_2S}, a_{Cl^-}, temperature and pH. As a_{Cl^-} and a_{H_2S} are relatively fixed in the ascending fluids that form volcanogenic massive sulfide deposits, the gold switchover is largely dependant on temperature and pH. High pH and low temperature favor thiocomplexes and the zinc-lead-silver-gold association, while low pH and high temperature favor chlorocomplexes and the copper-gold association. Extremes in pH allow high gold solubility whereas a pH near the gold switchover allows only low gold solubility.

Chemical conditions that promote low gold grades

Most worldwide volcanogenic massive sulfide deposits contain much less than 1 g/t gold; deposits exceeding this grade are much less common and, consequently, represent an anomaly. A further characteristic of most volcanogenic massive sulfide deposits is that the fluids that deposited metals were in equilibrium with either sericite or chlorite. Feldspar or kaolinite minerals are rarely present in the stockwork zones of these deposits, although they often occur in alteration external to the central stockwork zone (c.f. Shirozo (1974) and Iijima (1974)). The presence of sericite or

chlorite and lack of feldspar or kaolinite indicates that most volcanogenic massive sulfide deposits formed between a pH of 3.5 and a pH of 5. As the gold switchover occurs within this range the hydrothermal fluids cannot transport significant gold, and the resulting deposit is gold-poor (<1 g/t). Deposits containing only muscovite-chlorite gangue should have lower gold grades that deposits with more complicated gangue mineralogies.

Chemical conditions that promote high gold grades

The gold grades in gold-rich deposits are controlled by pH and temperature. Low pH fluids (3.5-4) at high temperatures (>300°C) will produce gold-rich deposits of the copper-gold association (e.g. Mt. Chalmers (2.3 g/t Au), Mt. Morgan (4.87 g/t) and Nurukawa (>15 g/t)), while higher pH fluids (5-5.5) at lower temperature (<300°C) will produce gold-rich deposits of the zinc-lead-silver-gold association (e.g. Rosebery (2.9 g/t), Que River (3.5 g/t) and Hellyer (2.3 g/t)).

Mt. Chalmers and Nurukawa both contain kaolinite which is intimately associated with the copper-gold mineralization. At Mt. Chalmers, kaolinite is observed as a gangue in the massive sulfide lens and in the footwall alteration zone where is associated and deposited synchronously with veinlet and disseminated chalcopyrite (McLeod, 1985). In the Nurukawa deposit kaolin minerals are present in gold-rich stockwork mineralization (Yamada et al., 1987). The gangue mineralogy intimately associated with base metal mineralization indicates that the depositional fluids had an unusually low pH of between 3 and 4. These conditions promote high gold solubilities as cholorocomplexes at temperatures of about 300°C.

The Rosebery, Que River and Hellyer deposits are characterized by the presence of large quantities of carbonate gangue. Rosebery also contains albite as a ubiquitous gangue in the barite lens. This suggests that these gold-rich deposits were precipitated from solutions of relatively high pH (>5) at 250°C which allows high gold solubilities as a thiocomplex. The presence of more complicated gangue mineralogies (e.g. muscovite-kaolinite or muscovite-feldspar) should be indicative of higher gold grades.

Geological controls on fluid chemistry

The most probable control on the pH of the fluids is the lithology of the source area for the metals. In this zone of leaching, the mineralogy of the rocks probably controlled the pH of the fluids due to a low water to rock ratio. Reed (1982) calculated that a seawater derived hydrothermal fluid at 300 °C in contact with rhyolite would have a pH of 5.1; this pH would not promote high gold grades in a volcanogenic massive sulfide deposit. However, if some anomalous rock (e.g. quartzite, shale or carbonate) were present in the leaching zone, the pH may be buffered to a value more conducive to the formation of gold-rich deposits of either copper-gold or zinc-lead-silver-gold association. This has not been addressed in the literature and deserves some investigation.

Another factor that may produce a fluid of acid pH (and a gold-rich deposit of the copper-gold association) is the presence of a magmatic component in the hydrothermal fluid. Holland (1972) found that the pH of a quenched experimental fluid in equilibrium with a granite at 800 °C was between 1.4 and 2.2. This indicates that a fluid exsolved from a magma may have a very acid pH. If magmatically derived water was introduced into a volcanogenic circulation cell, the resultant fluid may have a pH suitable for transporting gold as a chlorocomplex. The Mt. Chalmers deposit contains salinities up to 13.7 wt. % NaCl with a mean of 10.3 wt. % (Large and Both, 1980). This is significantly higher than deposits of the Kuroko district (3.6-6 wt. % NaCl; Pisutha-Arnond and Ohmoto, 1983) and seawater (3.5 wt. % NaCl). This is consistent with an introduction of additonal chloride into the system, possibly from a magmatic source. Additonal fluid inclusion and stable isotope studies on this deposit may shed some light on this hypothesis.

The effect of the oxidation state of seawater on gold precipitation

In Proterozoic and Phanerozoic deposits, the majority of gold is expected to precipitate with base metals. More specifically, in deposits of the gold-copper association gold and copper have to precipitate concurrently. If pyrite is stable and both metals are saturated, the ratio should be constant. If pyrrhotite, magnetite or hematite was the stable iron mineral, copper and gold may still precipitate together but with a widely variable ratio.

In the zinc-lead-silver gold association, however, zinc and gold do not have to precipitate together. Because seawater was oxidizing during the Proterozoic and Phanerozoic, cooling and oxidation of the hydrothermal fluids occurred and gold precipitated with zinc. However, during the Archean, seawater may have been more reduced (Holland, 1976), and the oxidation associated with seawater/hydrothermal fluid mixing may not have occurred to the same extent (c.f. Large, 1977). Consequently, in the Archean, zinc would have been precipitated due to cooling, but thiocomplexed gold would not have precipitated as oxidation of the hydrothermal fluids would not have occurred.

Gold exploration targets in volcanogenic systems external to massive sufide lenses

An understanding of the chemistry of gold transport has implications not only for the distribution of gold in massive sulfide bodies, but it also has implications elsewhere in the volcanogenic system. These considerations indicate the possibility of gold mineralization in several other geologic environments within volcanogenic systems. Of the four styles of mineralization presented below, two are known to exist and two have not yet been explored for.

Large (1987) has suggested that in the footwall leaching zone, gold may be precipitated if switchover from chlorocomplexing to thiocomplexing occurs at depth due to decreasing temperature in the upward convecting zone. This is the first conceptual exploration target: epigenetic copper-gold mineralization towards the base of the footwall leaching zone (Fig. 105).

The second target is illustated by the precious metal zone at Que River (McGoldrick, 1987). Gold enrichment in the lateral parts of the footwall alteration zone is expected in deposits of the zinc-lead-silver-gold association. At the edges of the alteration zone, the hydrothermal fluids mix with cool seawater within porous volcanics leading to oxidation and cooling in a manner analogous to the top of the massive sulfide mound, and gold precipitation must occur. Gold enrichment therefore may be common along the edges of alteration pipes or zones feeding deposits of the zinc-lead-silver-gold association.

A third target in these systems may be cherts containing colloform pyrite: distal pyrite mineralization at Rosebery (Part 2)

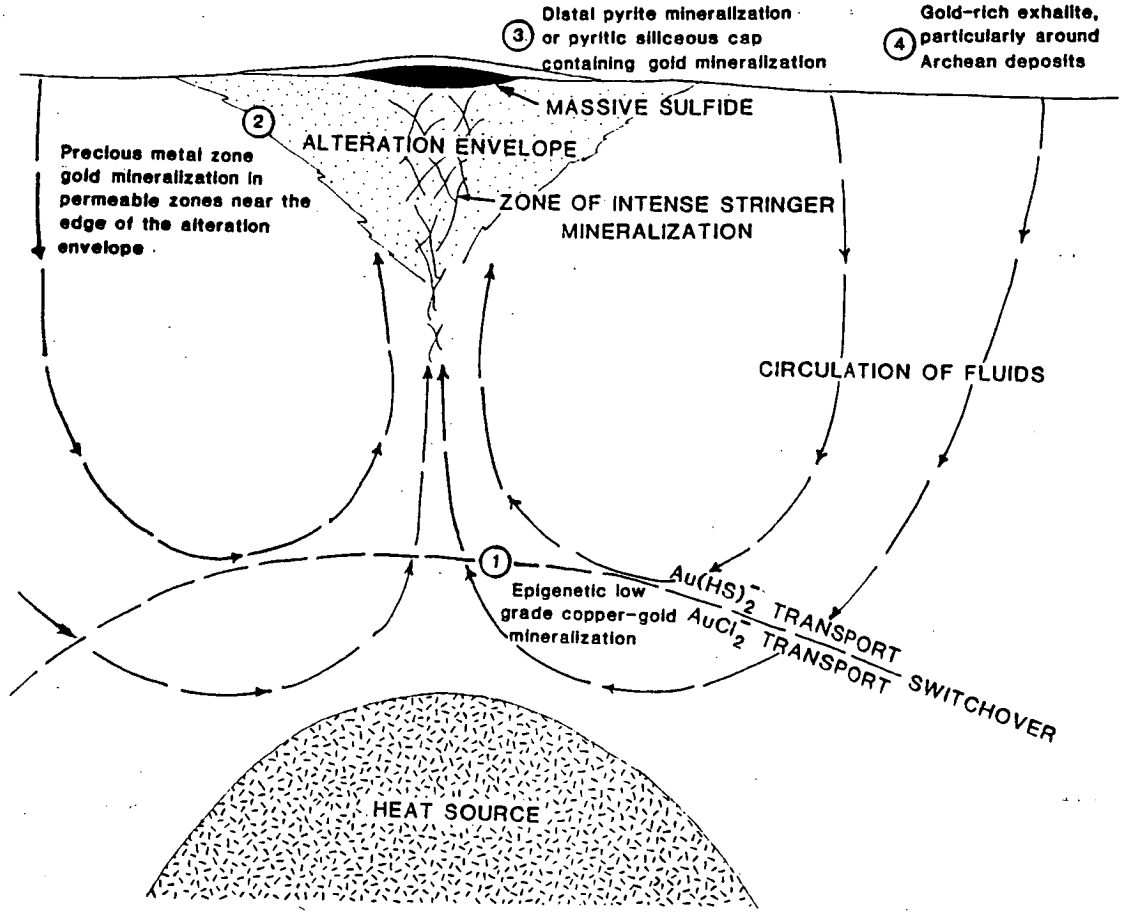

Figure 105. Possible zones of gold deposition external to the massive sulfide lens in volcanogenic systems.

and the glassy chert that caps Hellyer (McArthur, 1986). This process has been ascribed to the formation of gold polysulfide complexes that are later precipitated with pyrite. The formation of polysulfide ions is a kinetic process that may only occur during seawater/hydrothermal fluid mixing. Therefore it will only occur close to deposits of the zinc-lead-silver-gold association.

A fourth gold target are cherts and exhalites associated with Archean deposits. If an Archean deposit was deposited from near neutral solutions, gold may have stayed in solution during zinc deposition and escaped the immediate ore forming environment. The possibility exists that this gold may be deposited later in exhalites removed from the deposit.

Summary and conclusions

A review of the occurrence of gold in volcanogenic massive sulfdie deposits indicates the presence of two associations: (1) copper-gold at the base of the massive sulfide mound, and (2) zinc-lead-silver-gold at the top of the mound. These two associations are rarely found together in the same deposit.

The former association forms at high temperature (>300 °C) from relatively acid fluids (pH<4.5) by cooling and pH increase during replacement of zinc-lead-rich mineralization by copper-rich mineralization. The latter association forms at low temperature (<300 °C) from fluids of higher pH (>4.5) by the interaction of hydrothermal fluids with seawater at the top of the sulfide mound.

The gold model predicts that gold-rich volcanogenic massive sulfide deposits are deposited from high temperature (>300 °C), acid (pH=3.5 to 4) and saline fluids for the copper-gold association and low temperature (<300 °C), near neutral fluids (pH=5 to 5.5) for the zinc-lead-silver-gold association. Gold-poor volcanogenic massive sulfide deposits will be deposited from fluids of intermediate pH (4 to 5).

The lithology of the footwall leaching zone (as opposed to the footwall alteration zone) may control the pH of fluids and, consequently, the gold grades. Unusual rock units (e.g. quartzites, shales or carbonates) may produce a fluid pH that allows significant gold transport. The input of acidic magmatic fluids may allow the transport of gold as a chlorocomplex to form gold-rich volcanogenic massive sulfide deposits of the copper-gold association.

Archean deposits may show the zinc-lead-silver-gold association only under unusual conditions as the seawater may have been too reduced to allow gold precipitation from a thiocomplex.

Gold exploration targets in volcanogenic systems outside the deposit itself include: (1) epigenetic mineralization of the copper-gold association deep in the footwall leaching zone, (2) precious metal zone mineralization (e.g. Que River) which should occur at the lateral edge of all deposits showing the zinc-lead-silver-gold association, (3) distal pyrite mineralization and pyritic cherts around deposits of the zinc-lead-silver-gold association, and (4) exhalative cherts and other exhalites at stratigraphic horizons containing Archean deposits.

Chapter 3

Chemical controls on the distribution and mineralogy of silver in volcanogenic massive sulfide deposits

Introduction and overview

Controls on the distribution of silver in volcanogenic massive sulfide ores are very similar to those controlling lead and zinc. Ohmoto et al. (1983) have indicated that silver precipitation is caused by the rapid mixing of hydrothermal fluids with seawater at the top of the massive sulfide mound. However, studies of the Balcooma, Dry River South and Rosebery deposits, and a review of literature indicates a rather complicated mineralogy for silver, and in some cases, an unexpected distribution.

Examination of Table 16, which is a compilation of the distribution and mineralogy of silver in selected volcanogenic massive sulfides, indicates that in most cases silver is concentrated in the upper part of massive sulfide lenses. However, in two cases (Millenbach and Izok Lake) silver is concentrated with copper in the core of the massive sulfide lens (Knuckey et al., 1982; and Harris et al., 1984). Moreover, in the copper lenses at Balcooma, silver also has a strong association with copper (Part 1, Chapter 5).

In deposits where the highest silver values occur at the top of the massive sulfide mound in association with lead and zinc, silver has two major mineralogical occurrences: tetrahedrite and argentiferous galena. Numerous other silver-bearing minerals have been noted but are of minor importance. In deposits where silver occurs in the core of the deposit in association with copper, the probable host mineral is chalcopyrite. Estimates of the silver content of chalcopyrite range form 140 ppm at Balcooma (Part 1, Chapter 3) to 500 ppm at Izok Lake (Harris et al., 1984). The estimate at Izok Lake has been confirmed by PIXE-probe analysis of chalcopyrite (Harris et al., 1984).

Over the last decade, the understanding of the crystal chemistry of silver-bearing sufosalt minerals has increased markedly, largely due to the investigation of silver-rich epithermal deposits (e.g. Wu and Petersen, 1977; Hackbarth and Petersen, 1984; O'Leary and Sack, 1987; and Gemmell et al., in press). A comparison of the systematics

Table 16. Distribution and mineralogy of silver from selected precious volcanogenic massive sulfide deposits.

Deposit	Grade and tonnage	Gold mineralogy and distribution	References
Copper-zinc deposits			
Millenbach, Quebec, Canada	3.0 m.t. at 3.5% Cu, 4.8% Zn, 48 g/t Ag and 0.86 g/t Au.	Silver occurs with copper in the pyrrhotitic center or massive ore. It has an antipathetic relationship to zinc.	Knuckey et al. (1982)
Izok Lake, Northwest Territory, Canada	12 m.t. at 2.82% Cu, 13.7% Zn, 1.42% Pb and 70.3 g/t Ag.	Silver occurs predominately in silver-rich chalcopyrite (~500 ppm; 76% of total silver) with only minor amounts in argentiferous galena (700-2900 ppm; 9% of total silver).	Harris et al. (1984)
Arizona Proterozoic, U.S.A.	Variable.	Silver is enriched in the zinc-rich stratiform ores and chert cappings. Average grades in copper-rich stratiform ores. Depleted in copper-rich stringer ores.	Dewitt (1983)
Pyhasalmi, Finland	3.1 m.t. at 0.75% Cu, 2.43% Zn, 0.06% Pb, 17 g/t Ag and 0.2 g/t Au.	Silver occurs with sulfosalts and chalcopyrite associated with copper at the margins of orebodies and in areas rich in wall rock inclusions (based on factor analysis).	Helovuori (1979)
Stekkenjokk-Levi, Sweden	27.9 m.t. at 1.35% Cu, 2.79% Zn, 0.29% Pb, 46 g/t Ag and 0.27 g/t Au.	Silver is enriched in zinc-rich massive sulfide ore and depleted in copper-rich string ore. Silver increases laterally with lead to the south as copper decreases.	Zachrisson (1982,1984)
Zinc-lead-copper deposits			
Garpenberg, Sweden	0.4% Cu 5.0% Zn, 4.0% Pb, 130 g/t Ag and 0.9 g/t Au (from production figures).	Silver occurs in tetrahedrite, argentite and native silver. Has higher concentrations in the zinc-lead ores than copper ores.	Vivallo (1985)
Saxberget, Sweden	12.0 m.t.	Silver sustitutes in galena and chalcopyrite, with rare pyrargyrite, argentite, stephanite and native silver. Increases with lead and zinc and decreases with copper.	Amcoff et al. (1985)
Rosebery, Tasmania, Australia	19.4 m.t. at 0.74% Cu, 16.2% Zn, 5.0% Pb, 155 g/t Ag and 2.9 g/t Au.	Silver occurs dominately in tetrahedrite with a smaller contribution from argentiferous galena. It correlates with lead and antimony in zinc-lead ore and massive barite mineralization.	Part 2, and Henley and Steveson (1978)
Cofer, Virginia, U.S.A.	Unvailable.	Silver occurs in tetrahedrite which is more abundant in zinc-lead-rich mineralization than copper-rich mineralization. Tetrahedrite is commonly associated with galena whereas tennantite occurs with chalcopyrite and arsenopyrite.	Miller and Craig (1983)

Table 16. Distribution and mineralogy of silver from selected precious volcanogenic massive sulfide deposits (continued).

Deposit	Grade and tonnage	Gold mineralogy and distribution	References
Balcooma, Queensland, Australia	3.5 m.t. at 3.0% Cu, 20-30 g/t Ag and 0.3-0.4 g/t Au; minor Zn-Pb-Cu-Ag(Au) mineralization is also present.	Silver occurs both in silver-bearing chalcopyrite (140 ppm) from pyrite-chalcopyrite mineralization and in argentiferous galena (1200 ppm) from pyrite-sphalerite-galena mineralization. In the former case it correlates strongly with copper whereas in the latter case it correlates with lead.	Part 1, this study
Dry River South, Queensland, Australia	1.5 m.t. at 1.1% Cu, 3.4% Pb, 9.4% Zn, 97 g/t Ag and 0.7 g/t Au.	Silver occurs predominately in argentiferous galena although minor silver-rich tetrahedrite is present. Silver correlates strongly with lead in all types of mineralization. In massive pyrite-sphalerite-galena mineralization, silver also correlates with bismuth.	Part 1, this study
Heath Steele B-1 Orebody, New Brunswick, Canada	40.4 m.t. at 1.1% Cu, 4.7% Zn, 1.6% Pb, 64 g/t Ag and 0.9 g/t Au.	Silver is enriched with lead and zinc stratigraphically upwards from a copper-rich base. It decreases less quickly laterally than lead or zinc.	Lusk (1969), Mercer and Crockett (1972) and Mosier et al. (1983)
Mt. Chalmers, Queensland, Australia	4.3 m.t. at 1.6% Cu and 2.3 g/t Au.	Silver occurs as silver sulfosalts accociated with zinc and lead in the uppermost parts and flanks of massive ore.	Large and Both (1980)
Kuroko district, Japan (in general)	Variable.	Silver occurs in tetrahedrite with other minor silver-bearing minerals (acanthite, jalpaite, stromeyerite, mckinstryite, sternbergite, polybasite, pearcite, pyrargytie, proustite and native silver). Galena is not considered to be a major silver carrier. Silver concentrates in the upper part of Kuroko (zinc-lead) ore.	Shimazaki (1974)
Shakanai, Japan	8.73 m.t. at 1.4% Cu, 3.4% Zn, 1.0% Pb, 44 g/t Ag and 0.3 g/t Au.	Silver occurs in tetrahedrite and argentiferous galnea with minor jalpaite, argentite and polybasite.	Sato (1974)

of the silver mineralogy in these deposits with volcanogenic massive sulfide deposits in combination with a review and experimental studies in silver sulfosalts (e.g. Sack and Loucks, 1985) and the hydrothermal geochemistry of silver yields new insight into the controls on silver mineralogy in volcanogenic massive sulfide deposits.

Crystal chemistry of silver-bearing minerals

The most common silver-bearing minerals in volcanogenic massive sulfides are of the tetrahedrite-tennnantite series (hereafter referred to as tetrahedrite). The tetrahedrite series is a complex sulfosalt with the following formula:
$(Cu,Ag)_6^{TRG}[(Cu,Ag)_{2/3}(Fe,Zn)_{1/3}]_6^{TET}(Sb, As, Bi)_4^{SM}S_{13}$ where the superscripts TRG, TET and SM refer to the trigonal, tetrahedral and semi-metal coordination sites, respectively. Cadmium, lead, mercury and selenium are relatively minor substitutions in nature (Sack and Loucks, 1985).

Many researchers have noted a strong positive correlation between the atomic ratios Ag/(Ag+Cu) and Sb/(Sb+As), that is silver-rich tetrahedrite also tends to be antimony-rich (Wu and Petersen, 1977; Sandecki and Amcoff, 1981; Miller and Craig, 1983; and Hackbarth and Petersen, 1984). Miller and Craig (1983) concluded that this correlation is "permissive" in that high antimony content permits, but does not require, high silver contents. The presence of large amounts of arsenic in tetrahedrite series minerals effectively precludes the incorporation of significant silver, even if silver is available from the hydrothermal fluids (Miller and Craig, 1983).

Sack and Loucks (1985) demonstrated that for silver-poor tetrahedrite the three principal substitutions in tetrahedrite [$(Ag=Cu)^{TRG}$, $(Fe=Zn)^{TET}$, $(As=Sb)^{SM}$] are ideal reciprocal solutions with standard Gibbs energies of reciprocation independant of temperature. However, for natural silver-rich tetrahedrite, O'Leary and Sack (1987) inferred that the Fe=Zn exchange does not behave ideally and is dependant on the Ag/(Ag+Cu) ratio. Moreover, they found that silver substitution at high silver content occurs both in the trigonal and tetrahedral sites. Consequently, although tetrahedrite may be well behaved energetically (Sack and Loucks,

1985), much work is still required before quantitative predictions of fluid chemistry may be attempted.

The second most common silver-bearing phase in volcanogenic massive sulfide deposits is argentiferous galena. Studies of silver solution in galena indicate that Ag_2S is very insoluble in galena (Van Hook, 1960). However, when the coupled substitution of silver with either antimony or bismuth occurs, the solubility of silver increases significantly. Van Hook (1960) reports a complete solid solution between matildite ($AgBiS_2$) and galena at temperatures over 215°C, and below 200°C galena may contain up to 10 mole percent matildite. Amcoff (1976) investigated the solubility of miargyrite ($AgSbS_2$) in galena and found that it varied from 10 mole percent at 350°C to less than 2 mole percent at 200°C. Coupled substitution of silver and bismuth (or antimony) allows a geologically significant solubility of silver in galena.

Boyle (1968) inferred that silver directly substitutes for copper in the chalcopyrite lattice and reported analyses of up to 3300 ppm silver in chalcopyrite. Sandecki (1983) reported greenish chalcopyrite with up to 1.8% silver in association with native silver and allargentum (Ag_6Sb) from the Garpenberg Norra deposit in Sewden.

Hydrothermal geochemistry of silver in volcanogenic systems

Compared to those of gold, bismuth and other metals pesent in volcanogenic massive sulfide deposits, the hydrothermal geochemistry of silver is well established. Seward (1976) investigated the stability of silver chlorocomplexes in hydrothermal systems up to 350°C and concluded that chlorocomplexes were important under hydrothermal conditions. However Henley and Brown (1985) have suggested that thiocomplexes of silver were important in the Broadlands geothermal system. Sugaki et al. (1987) have investigated the stability of silver thiocomplexes and interpreted that thiocomplexes are important under conditions of very high a_{H_2S}.

Figure 106 illustrates solubility of acanthite/argentite as both thiocomplexes and chlorocomplexes in a volcanogenic fluid with $a_{H_2S}=10^{-2.5}$ amd $m_{NaCl}=10^{0.0}$ (c.f. Large, 1977). Figure 106 was calculated from thermochemical data in Table 15 using the modified

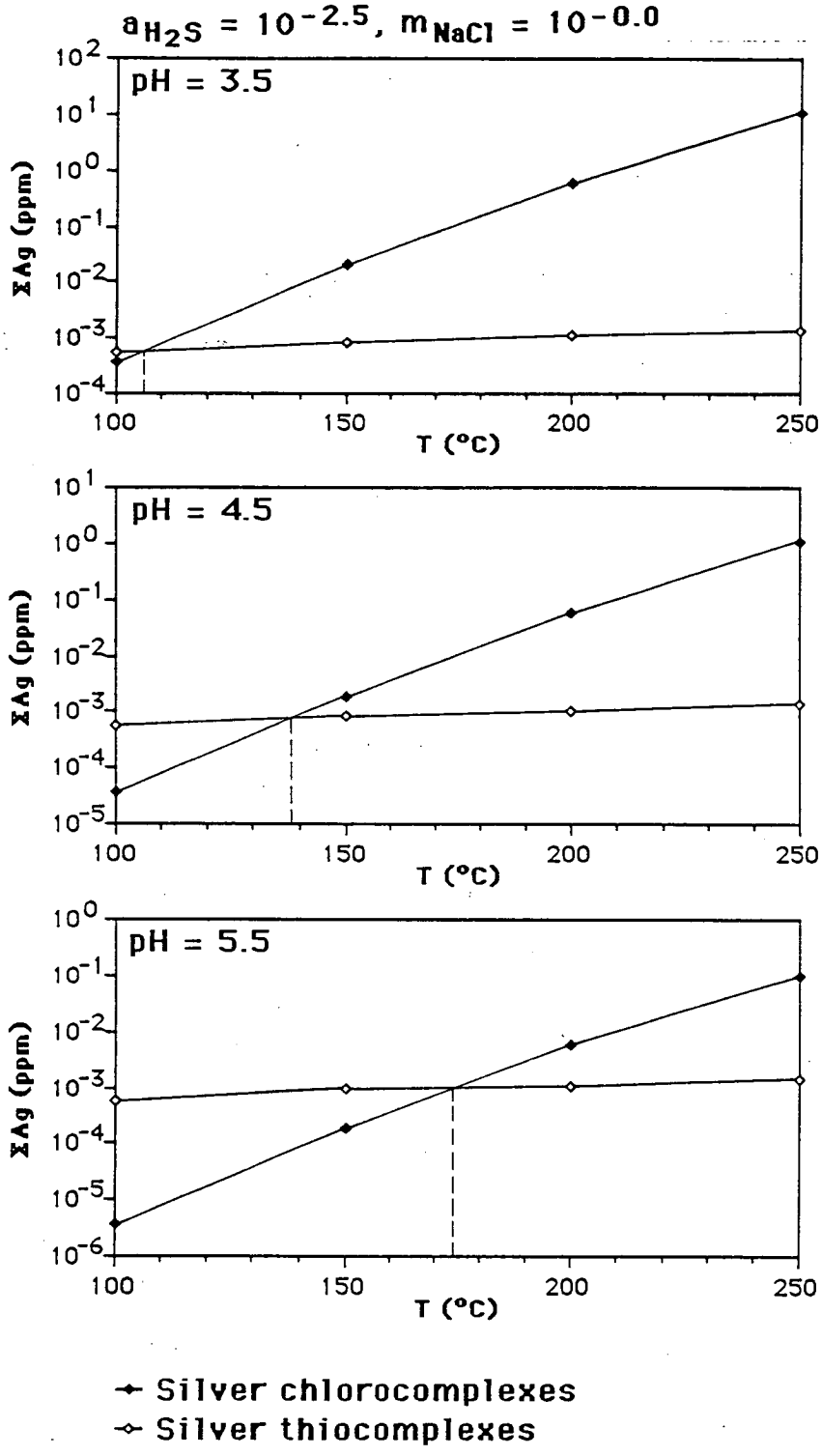

Figure 106.. The solubility of acanthite/argenitite under volcanogenic conditions.

Debye-Huckel equation of Helgeson (1969) and assuming that uncharged species have an activity coefficient of unity. These data indicated that the dominant silver complex in volcanogenic fluids is $AgCl_2^-$. Chlorocomplexes dominate over thiocomplexes above 175°C for a pH of 5.5 and above 105°C for a pH of 3.5. Studies by Seward (1976) indicated that the predominant silver complex under these conditions is $AgCl_2^-$. Hence, the reaction that precipitates silver from hydrothermal fluids may be written:

$$2AgCl_2^- + H_2S^0 = Ag_2S + 4Cl^- + 2H^+ \quad (18)$$

Based on reaction (14) silver may be precipitated due to an increase in pH, a decrease in salinity, an increase in a_{H_2S} or a decrease in temperature. Ohmoto et al. (1983) inferred that silver is deposited due to a drop in temperature associated with seawater mixing. As acanthite is a rare mineral in volcanogenic massive sulfide deposits, equation (14) does not totally describe the mechanisms of silver precipitation. The concentrations of antimony, arsenic and bismuth in solution may have strong effects on the deposition of silver, particularly on the mineralogy of the silver-bearing phase.

Geochemical controls on silver mineralogy in volcanogenic massive sulfide deposits

Of the controls on silver solubiity discussed previously, those most important in volcanogenic systems are temperature and semi-metal ratios in the ore fluids. Changes in salinity and an increase in a_{H_2S} during deposition are unlikely in volcanogenic systems.

Silver in high temperature, copper-rich ores

During the development of high temperature (~300°C) copper-rich ore at the base of the mound, minerals such as sphalerite, galena and tetrahedrite are dissolved to be reprecipitated at the top of the mound (Eldridge et al., 1983). During this process there is a net loss of silver from the base of the mound to the top of the mound.

However, some of the silver appears to be retained in this zone as demonstrated by the presence of silver in copper-rich mineralization at Balcooma, Izok Lake and Millenbach (Table 16). As the silver occurs in chalcopyrite, coprecipitation into the chalcopyrite lattice must be the mechanism by which silver is retained in the copper-rich part of the massive sulfide.

Silver in low temperature, zinc-rich ores

At the surface of the growing sulfide mound, sulfide minerals are precipitated by rapid mixing and cooling at temperatures of ~200°C (Eldridge et al., 1983; and Ohmoto et al., 1983). Within this zone the majority of the silver in volcanogenic massive sulfide deposits is precipitated primarily as silver-bearing tetrahedrite or galena. Based on very limited analytical data (Dry River South and Rosebery), the predominant silver-bearing mineral may be dependant on the relative proportions of semi-metals (As, Sb and Bi) in the hydrothermal fluids.

Amcoff (1984) has suggested controls on silver mineralogy by semi-metals. He interprets that bismuth-silver coupling in galena will form argentiferous galena at the bottom of the mound, whereas antimony-silver coupling in galena occurs near the top of the mound.

Rosebery zinc-lead-rich massive sulfide and massive baritic mineralization is significantly enriched in antimony (100-1000 ppm) whereas it is relatively depleted in bismuth (typically less than 100 ppm with the exception of copper-rich samples). Baritic mineralization is particlularly enriched in antimony (300-1000 ppm) and depleted in bismuth (less than 10 ppm). At Rosebery silver has an extremely strong correlation with antimony but no significant correlation with bismuth (Part 2, Chapter 2; and Appendix 2). Conversely, Dry River South mineralization is depleted in antimony (less than 100 ppm) and enriched in bismuth (100-1000 ppm). Silver correlates with bismuth, but not with antimony, in zinc-lead-rich massive sulfide at Dry River South (Part 1, Chapter 5; and Appendix 2). Calculations by Henley and Steveson (1978) indicated that 65% of Rosebery silver is held by tetrahdrite and 30% is held by galena. In contrast, at most about 35% of Dry River South silver is held by tetrahedrite and up to 65% is held in argentiferous galena (Part 1, Chapter 7).

As depositonal efficiencies in volcanogenic massive sulfide deposits are high (Sato, 1973), the ratios of the metals in the ores probably reflect the ratios in the hydrothermal fluids, particularly at the top of the massive sulfide mound. This implies that bismuth-rich, antimony-poor fluids deposit most of their silver in argentiferous galena due to bismuth-silver coupled substitution in galena (e.g. Dry River South), whereas bismuth-poor, antimony-rich fluids deposit most of their silver in argentinian tetrahedrite (e.g. Rosebery). The availability of galena obviously affects the mineralogy of silver-bearing phases as silver occurs predominantly in argentinian tetrahedrite in lead-poor Archean deposits (Franklin et al., 1981). This model is consistent with experimental studies (Van Hook, 1960; and Amcoff, 1976) that found coupled substitution with bismuth more effectively dissolved silver in galena than coupled substitution with antimony.

Whereas the semi-metal model of Amcoff (1984) is probably broadly correct, the majority of the silver precipitated from bismuth-poor, antimony-rich fluids probably precipitated into argentinian tetrahedrite rather than argentiferous galena. Coupled substitution of silver with antimony into the galena lattice is probably of lesser importance than silver in tetrahedrite.

In deposits at which silver is held in argentian tetrahedrite, the amount of silver held depends on the atomic (Sb/(Sb+As) ratio of tetrahedrite (c.f. Part 2, Chapter 3; and Miller and Craig, 1983). Antimony-poor tetrahedrite also tends to be silver-poor. The covariation of the Ag/(Ag+Cu) and Sb/(Sb+As) ratios can be explained by changes in the temperature of the fluids or fractional crystallization.

Hackbarth and Petersen (1984) have developed a geochemical model in which copper- and arsenic-rich tennantite is deposited from the solution initially, which enriches the hydrothermal fluid in silver and antimony. Silver- and antimony-rich tetrahedrite is precipitated from the residual fluid. This model assumes that the fractionation constants K_1 $(=[dM_{Sb}^{XTL}/dM_{As}^{XTL}]/[M_{Sb}^{LIQ}/M_{As}^{LIQ}])$ and K_2 $(=[dM_{Ag}^{XTL}/dM_{Cu}^{XTL}]/[M_{Ag}^{LIQ}/M_{Cu}^{LIQ}])$ are less than one (M is the number of moles of the element in the growing crystal (XTL) and the hydrothermal fluid (LIQ), respectively). Using this assumption they

modelled the compositional variation of tetrahedrite from Casapalca and Orcopampa, Peru, and Coeur d'Alene, Idaho.

Sack and Loucks (1985) have modelled the variations in tetrahedrite compositions of previous workers more rigorously and concluded that the modelling by Hackbarth and Petersen (1984) was constistent with established thermodynamic parameters of the tetrahedrite-tennantite series. Sack and Loucks (1985) also indicated that the simultaneous precipitation of other specific minerals (e.g. pyrite, sphalerite and chalcopyrite) could affect the compostion trends relative to copper, iron and zinc. Presumably the simultaneous precipitation of other sulfosalts (e.g. enargite, pyrargyrite or polybasite) could affect the trends observed relative to silver, antimony and arsenic.

Gemmell et al. (in press) studied the compositions of co-existing tetrahedrite, pyrargyrite-proustite ($Ag_3(Sb,As)S_3$), polybasite ($(Ag,Cu)_{16}(Sb,As)_2S_{11}$) and stephanite ($(Ag,Cu)_5(Sb,As)S_4$) in the Santo Nino Vein, Fresnillo district, Mexico and concluded that the Sb/(Sb+As) ratio of polybasite and tetrahedrite decreased with temperature. Feiss (1974) has applied a geothermometer using the compositions of enargite-fataminite in co-exixtance with tetrahedrite at Julcani, Peru.

Shimazaki (1974) reported zonation within single grains of tetrahedrite from the Kuroko district although he also noted that not all tetrahedrite grains were zoned. The Rosebery deposit has well developed compositional variations in tetrahedrites. Grains from massive sphalerite-galena-pyrite ores plot along a separate trend with a lower slope relative to grains from massive baritic mineralization (which tend to be enriched in silver and antimony). Moreover remobilized tetrahedrite in Devonian gash veins is very silver-rich and contains nil arsenic (Fig. 82; Part 2, Chapter 2). Miller and Craig (1983) also found systematic variations at the Cofer deposit.

These variations can be either explained by fractional crystallization or by temperature differences. Baritic mineralization, which contains silver- and antimony-rich tetrahedrites, is enriched in silver and antimony and depleted in arsenic, whereas massive sphalerite-galena-pyrite and massive pyrite-chalcopyrite ore is enriched in arsenic and depleted in antimony. Assuming the compositions of the ore types reflects the composition

of the depositing hydrothermal fluids, the silver and semi-metal content of the tetrahedrite grains just reflects the composition of the hydrothermal fluids. Such a mechanism is consistent with the fractional crystallization model of Hackbarth and Petersen (1984).

The enrichment of tetrahedrites from the barite zone in silver and antimony might also be explained by assuming a temperature gradient from the base of the massive sulfide mound to the top (e.g. Eldridge et al., 1983). As baritic mineralization was probably precipitated at lower temperature than massive sphalerite-galena-pyrite and massive pyrite-chalcopyrite ore, the silver-rich and antimony-rich nature of tetrahedrite from this zone may be due to a lower temperature of precipitation (c.f. Gemmell et al. (in press)). Due to the poor constaints on the Rosebery data, the effects of fractional crystallization versus temperature could not be resolved.

The enrichment of remobilized Devonian gash vein tetrahedrite in both silver and antimony suggests that these fluids were enriched in these elements and that these elements were mobilized preferentially to copper and arsenic under low grade metamorphic conditions.

Conclusions

Geochemical modelling of silver transport under volcanogenic conditions indicates that chlorocomplexes predominated. During the formation of copper-rich massive sulfide by the replacement of zinc-lead-rich massive sulfide, most silver was dissolved and reprecipitated at the top of the sulfide mound. Minor silver was retained by coprecipitation in chalcopyrite.

Most silver in volcanogenic massive sulfide deposits is held either in argentiferous galena or argentinian tetrahedrite in zinc-lead-rich massive sulfide near the top of the sulfide mound. The semi-metal content of the precipitating fluids determines the predominant silver phase. If bismuth dominates, most silver occurs in galena due to coupled substitution of silver with bismuth in the galena lattice. If arsenic and antimony dominate, silver occurs in minerals of the tennantite-tetrahedrite series. The As/Sb ratio of the fluids and/or the temperature of deposition probably determines the silver content of the resulting tetrahedrite-tennantite series mineral. A high As/Sb ratio and/or high temperature results in silver-poor, arsenic-rich tennantite, whereas a low As/Sb ratio or low temperature results in a silver-rich, antimony-rich tetrahedrite.

Chapter 4
Controls on the fineness and grain size of electrum in volcanogenic massive sulfide deposits

Introduction

The occurrence of gold and the grain size of electrum in massive sulfide deposits has implications for both the practical aspect of gold recovery and the theoretical aspect of genetic modelling. Grain size and mineral associations of electrum are the primary controls on metallurgical recovery in complex sulfide ores. Coarse grained electrum is more likely to be liberated than fine grained electrum which may remain encased in sulfide minerals during grinding. To date this problem has not been addressed extensively in geological literature related to volcanogenic massive sulfide deposits. Therefore, the first purpose of this chapter is to describe the occurrence and grain size of electrum in eastern Australian volcanogenic massive sulfide deposits and then to discuss geological controls on these characteristics.

Several recent papers (Shikazono and Shimuzu, 1987; and Rose and Morrison, 1988) have used the chemical composition of electrum in a genetic sense as both a classification of gold-bearing deposits and as an indication of the geochemistry of gold transport. Due to a paucity of data on electrum fineness, these exercises have not been undertaken on volcanogenic massive sulfide deposits in a systematic manner. In view of this, the second goal of this chapter is to describe the variation in the fineness of electrum among eastern Australian deposits, and to geochemically model the chemistry of gold transport and electrum deposition in the systems.

Publicly available data on the occurrence, grain size and fineness of electrum exists for the following eastern Australian deposits: Que River and Hellyer (Ramsden and Creelman, 1984; and Whitford et al., 1985), and Rosebery (Huston and Large, 1988; and Part 2, Chapter 3). To this data base, recent studies by the author have added data from the Balcooma prospect, the Dry River South prospect (Part 1, Chapter 7) and the Mt. Chalmers deposit, all of which are located in Queensland. Three deposits are of the zinc-lead-silver-gold association (Hellyer, Que River and Rosebery),

whereas three deposits are of the copper-gold association (Balcooma, Dry River South and Mt. Chalmers; c.f. Chapter 2). Gold grades vary from 0.3-0.4 g/t at Balcooma to 3.5 g/t at Que River (Table 17).

The intensity of deformation among the deposits varies markedly. The Mt. Chalmers and Hellyer deposits are undeformed or weakly deformed and still retain pristine ore textures (Large and Both, 1980; and McArthur, 1986). The Que River deposit has been deformed into a "W"-shaped fold, and although primary textures have been retained locally, the ores may have a mylonitic fabric on the fold limbs (Large et al., 1988). The structure at Rosebery is unresolved although folding (Brathwaite, 1972; and Lees et al., in press) and faulting (R. Berry, pers. comm.) may be present. The copper-rich lens of the Balcooma deposit occurs in the core of an antiformal syncline, whereas the zinc-lead-rich lens lies on the western limb of this fold (Part 1, Chapter 2). Although the Dry River South deposit does not show outward evidence of strong deformation, structures outside of the mineralized zone, and metal zonation and mineral textures within the massive sulfide lens indicates that the deposit has been strongly affected by shearing and faulting.

The degree of metamorphism varies from relatively unmetamorphosed at Mt. Chalmers (Large and Both, 1980) to middle amphibolite at Balcooma and Dry River South (Part 1, Chapter 6). The Hellyer and Que River Deposits have undergone pumpellyite-prehnite facies metamorphism, whereas the Rosebery deposit has undergone lower greenschist facies metamorphism (Green et al., 1981). As a group, these six deposits display a large variation in gold grades, metal associations, deformation intensity and metamorphism which should give insight into the geological processes that control electrum grain size and fineness.

Description of individual deposits

Hellyer and Que River

The Hellyer and Que River ores have been extensively studied by the CSIRO (Whitford et al., 1984; and Ramsden and Creelman, 1984). At Hellyer, which is the least deformed massive sulfide in the Mt. Read Volcanics, only a single grain of electrum has been observed despite a very intensive search (McArthur, 1986). Rather, the gold appears to occur in arsenopyrite at a level of some 500 ppm, and to a

lesser exent in pyrite (Ramsden and Creelman, 1984). Significantly, Ramsden and Creelman (1984) did not analyze arsenopyrite from the barite zone, presumably because none was observbed. This possibility is supported by the sudden drop off in arsenic values from this zone (Ramsden and Creelman, 1984). At Hellyer, which must be considered as the undeformed end-member of the zinc-lead-silver-gold association, gold occurs principally in arsenopyrite and to a lesser extent in pyrite. However, the occurrence of gold in the barite zone was not conclusively resolved by Ramsden and Creelman (1984). The electrum grain observed at Hellyer came from the barite zone in association with galena (G. McArthur, pers. com.).

At Que River, which has been significantly more deformed (Large et al., 1988), Whitford et al. (1984) have recorded the presence of electrum. They noted three general occurrences: (1) coarse grained (10-400 μm; average 100 μm), rounded electrum grains that occur predominantly with galena, (2) fine grained (<10 μm) grains that occur predominately with pyrite, and (3) intermediate sized (>10 μm) grains that occur at the contacts between pyrite grains and other sulfide minerals. The coarsest grained electum occurs in base metal sulfides near pyrite (Whitford et al., 1984). The fineness of electrum grains was found to be highly variable, with a range from 550 to 820 and a mean of 720. Gold was found in pyrite in trace amounts of about 150 ppm (Whitford et al., 1984).

Rosebery

Primary mineralization. The occurrence of electrum from the relatively undeformed north-end orebody at Rosbery has been described in Part 2, Chapter 3. The occurrence varies between ore types. In massive pyrite-chalcopyrite, 1-10 μm electrum grains were observed as inclusions in and along cracks in arsenopyrite grains in a crosscutting chalcopyrite veinlet. As electrum was observed in only one example of this type of mineralization, the occurrence is not considered conclusive.

In massive sphalerite-galena-pyrite ore, electrum is typically very fine grained with a dominant grain size of about 5 μm although grains up to 45 μm were observed (Fig. 107). The grains are always associated with pyrite, and the majority of the grains occur in cracks within or along grain boundaries between pyrite grains. As at Que River, electrum from this style of mineralization has variable

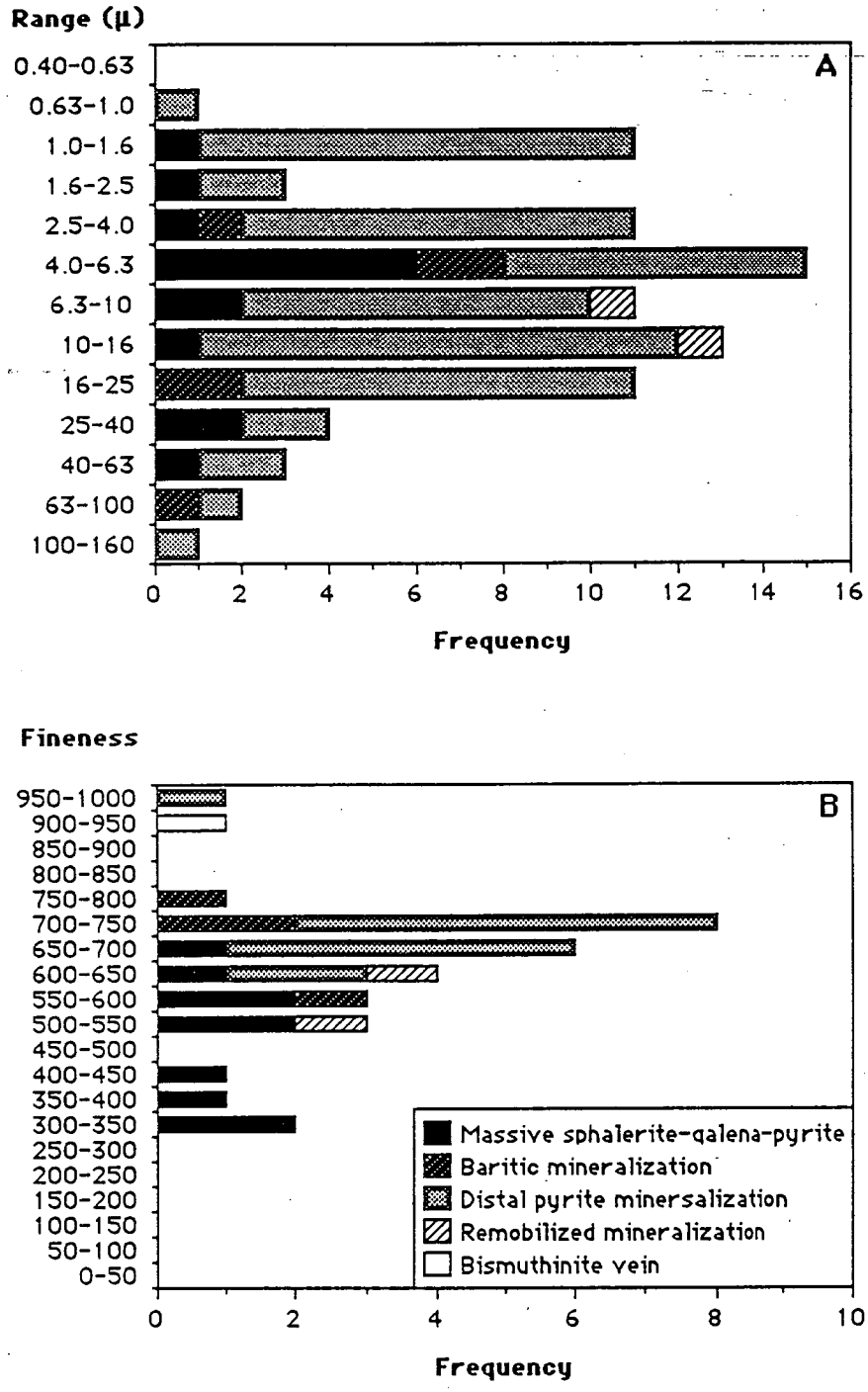

Figure 107. Grain size (a) and fineness (b) of electrum from the Rosebery north-end.

fineness, with a range of between 320 and 700. Fine grained electrum tends to have a lower fineness than coarser grains, and rims of the coarser grains tend to be enriched in silver (Fig. 108). Silver-rich rims have also been noted in electrum from the Kosaka and Shakanai deposits in Japan (Shimizaki, 1974). Brathwaite (1969) noted an occurrence of electrum in a tetrahedrite pool from sphalerite-galena-pyrite ore at Rosebery.

The occurrence and fineness of electrum in Rosebery baritic mineralization differs markedly from that in massive sphalerite-galena-pyrite ore. Electrum occurs in association with chalcopyrite and galena, or without sulfide association; it was not observed in association with pyrite. Limited microprobe analyses indicate that this electrum had a limited range in fineness; three of the four grains analyzed have finesses between 730 and 760, which is higher that the range for massive sphalerite-galena-pyrite ore. In this case, the larger grains did not have silver-rich rims. Grain size was found to be quite variable and between 3 μm and 75 μm.

In distal pyrite mineralization, which is equivalent to the siliceous cap at Hellyer (McArthur, 1986), electrum again occurs with pyrite. In the one sample that contains primary colloform textures in pyrite, the electrum occurs interstitially to pyrite grains in accociation with galena and tetrahedrite. Whereas the variation in grain size is similar to that of massive sphalerite-galena-pyrite ore, the fineness of electrum is higher and has a narrow range (610-730 if one gold-rich sample is excluded).

In general the occurrence of syngenetic electrum varies up stratigraphy at Rosebery. Electrum from massive sphalerite-galena-pyrite has a strong association with pyrite and a low, but variable, finenesss. Electrum from baritic mineralization has a variety of occurrences, but does not occur with pyrite, and has a high fineness. Electrum from distal pyrite mineralization has a strong association with pyrite and a high fineness with a narrow range.

Remobilized mineralization. Due to Devonian metamorphism and metasomatism, the Rosebery deposit has undergone various degrees of recrystallization and remobilization. The intensity is weakest in the north-end and increases towards the south-end where a crosscutting pyrrhotite-pyrite body has replaced syngenetic massive sulfide (Solomon et al., 1987).

All of the original mineragraphic studies of Rosebery ores (Stillwell, 1934; Williams, 1960; Brathwaite, 1969; and Green, 1983)

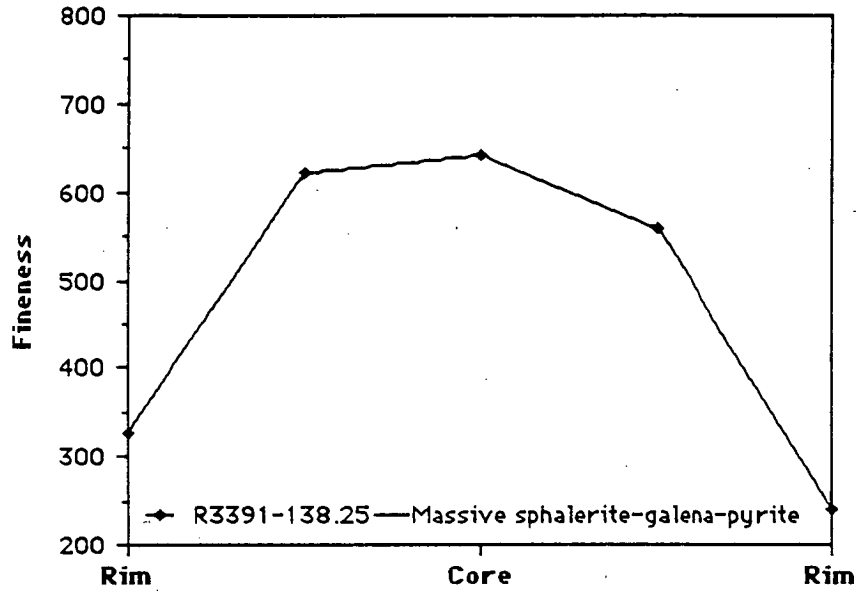

Figure 108. Variation of fineness within an electrum grain from the Rosebery north-end.

noted the occurrence of electrum in recrystallized tetrahderite. Electrum in remobilized quartz-carbonate veins was also noted in association with chalcopyrite (Part 2, Chapter 3). The two grains observed were roughly 10 μm in dimension and had finenesses of 520 and 630, respectively (Fig. 107). Additionally, 930 fine electrum was also observed in a bismuthinite vein in association with maldonite.

Mt. Chalmers

The Mt. Chalmers deposit is an example of an undeformed deposit of the copper-gold association in which primary textures are preserved (Large and Both, 1980; and Part 3, Chapter 2). This study examined the occurrence of electrum form the extensive University of Tasmania reference collection for Mt. Chalmers (collected by R.R. Large). Electrum was observed to have two distinct occurrences: (1) as inclusions in pyrite, and (2) in association with other sulfides. In the latter occurrence, electrum was observed in contact with pyrite, galena and sphalerite although the predominant occurrence was with chalcopyrite. The presence of a Cu-Pb-Bi sulfosalt (probably aikenite ($CuPbBiS_3$)) and native bismuth were also noted in the samples, but not in association with electrum. The grain size of the electrum varied between 1 μm and 60μm, with most grains between 10 μm and 25 μm (Fig. 109).

Based on a limited number of microprobe analyses, the fineness of the electrum varies between narrow limits. Three electrum grains included in pyrite had finenesses between 970 and 990, whereas four grains associated with other sulfides varied between 850 and 870. None of the grains had silver-rich rims.

Balcooma

The Balcooma prospect is an example of a strongly deformed and metamorphosed deposit of the copper-gold association (Part 1). The electrum has a strong association with chalcopyrite and bismuth minerals, and a weaker association with galena. Of the five deposits described herein, Balcooma electrum has the smallest grain size: all observed grains were less than 10 μm (Fig. 110). As at Mt. Chalmers, the fineness is high and has a narrow range (670 to 790).

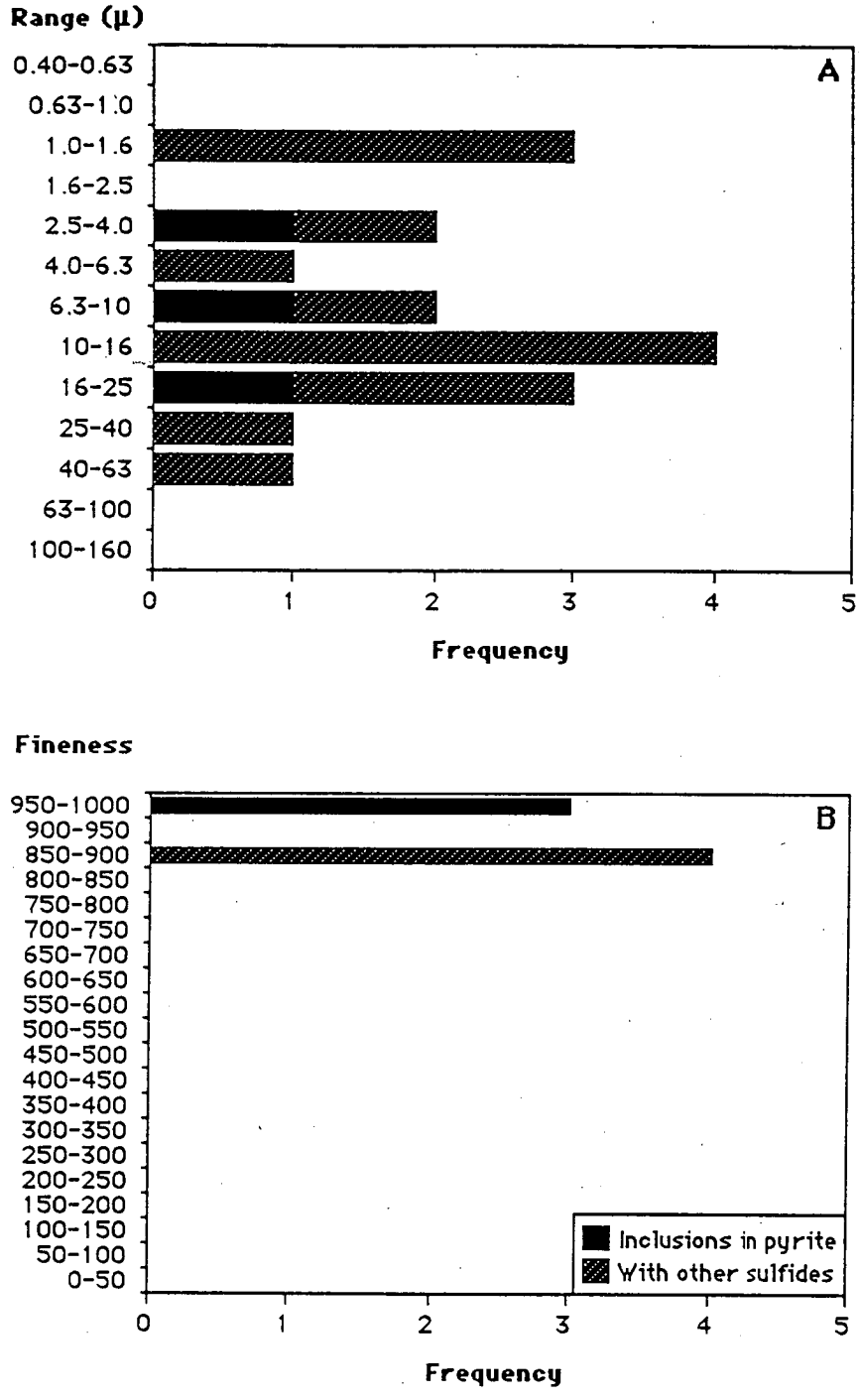

Figure 109. Grain size (a) and fineness (b) of electrum from the Mt. Chalmers deposit.

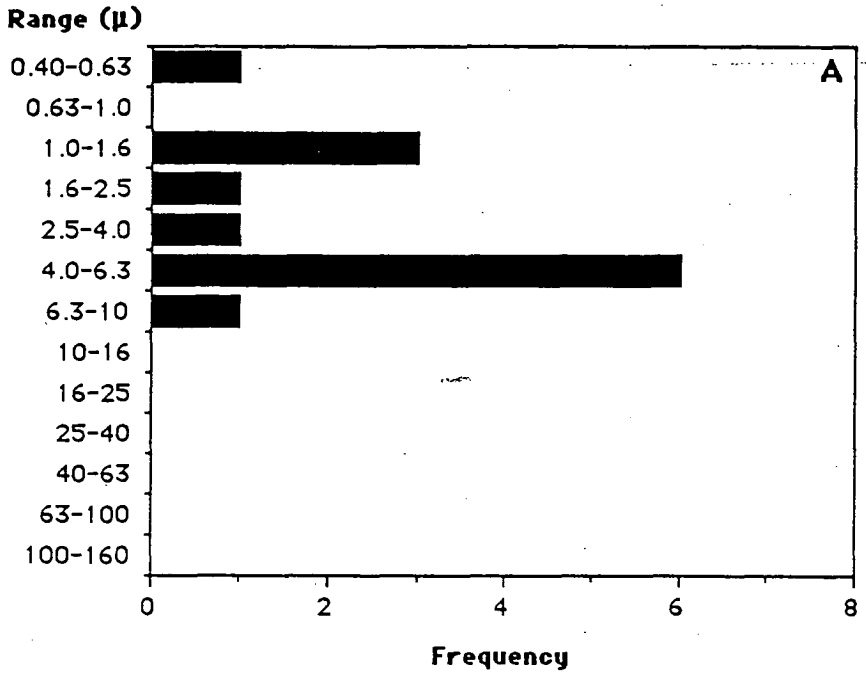

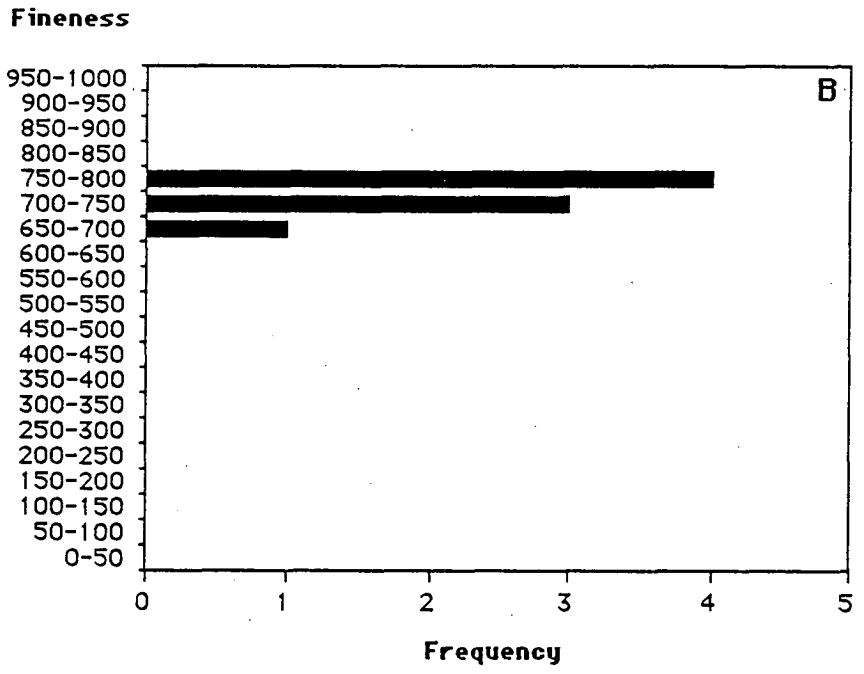

Figure 110. Grain size (a) and fineness (b) of electrum from the Balcooma deposit.

Dry River South

At Dry River South, electrum occurs in association with a variety of minerals including chalcopyrite, sphalerite, quartz, carbonate and galena. The electrum grains all occur in crosscutting veinlets that crosscut recrystallized minerals and even solely metamorphic minerals in the case of gahnite (Part 1, Chapter 7). These textures and the presence of electrum in chalcopyrite veinlets that cut cleavage indicate that much, if not most, of the electrum at Dry River South has been remobilized.

The variation in mineral associations is also reflected in variations in the grain size and fineness of Dry River South electrum (Fig. 111). Grain sizes range from 1.5 μm to 60 μm, and the fineness ranges from 490 to 760. No systematic variations were observed within these distributions.

Other deposits

Outside of these deposits, very little other data exist on electrum in volcanogenic massive sulfide deposits. In the Kuroko deposits electrum occurs in the upper part of kuroko ore in association with galena, sphalerite and tetrahedrite (Shimazaki, 1974). The composition of electrum from kuroko ore in the Kosaka and Shakanai deposits ranges from 520 to 860 fine, but electrum from oko (copper-rich) ore in the Hisaka deposit has a considerably higher fineness of 950-960 (Shimazaki, 1974). In the Nurukawa deposit (Yamada et al., 1987), electrum of tens of microns in diameter was observed in quartz-chalcopyrite veins in keiko and stockwork ores. The electrum was found to vary between 500 and 700 in fineness. At the Mt. Lyell copper-gold deposit in western Tasmania, electrum was found to have a high, and consistent, fineness of about 800 (R. Bottrill, Tasmanian Dept. of Mines, pers. comm.).

The description of electrum from the Hisaka, Nurukawa and Mt. Lyell deposits is very similar to the Mt. Chalmers and Balcooma deposits: electrum of relatively high fineness associated with chalcopyrite and copper-rich mineralization. The occurrence of electrum from the Shakanai and Kosaka deposits differs from the Hellyer deposit where gold occur in arsenopyrite and pyrite, but it is somewhat similar to the occurrence of electrum in the barite zone at Rosebery. Shimazaki (1974) noted that electrum commonly occurs in

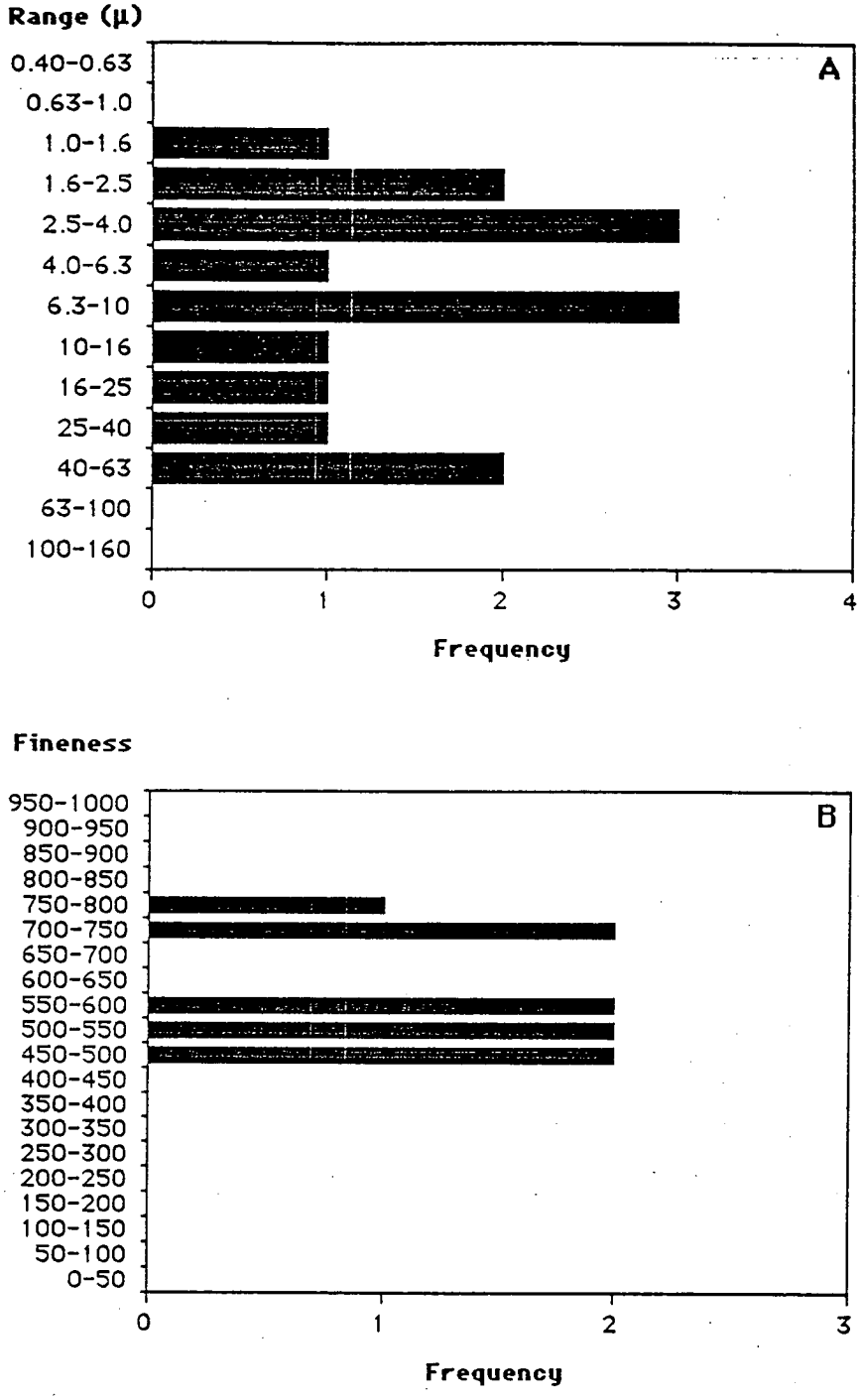

Figure 111. Grain size (a) and fineness (b) of electrum from the Dry River South deposit.

the upper parts of the kuroko ores and that barite is a gangue mineral in these ores.

Summary of characteristics

The distibution of electrum in the zinc-gold association has the following characteristics:

(1) In pristine deposits, gold in massive sphalerite-pyrite-galena ore occurs as trace elements in either pyrite and/or arsenopyrite.

(2) In deformed ores, the gold occurs as electrum that is commonly associated with pyrite and has a very fine grain size. Electrum may also occur as coarser grains in association with other sulfides.

(3) In massive sphalerite-galena-pyrite ore, the recrystallized electrum has a large range in fineness (320 to 820) and coarse grains often have silver-rich rims.

(4) In recrystallized baritic mineralization, electrum occurs with sulfides other than pyrite or without sulfides. The fineness tends to be higher that that of the stratigraphically lower massive sphalerite-galena-pyrite. Evidence from the Japanese deposits indicates that the pristine association is similar; the occurrence of gold in the Hellyer baritic zone was not determined in publicly available CSIRO reports.

(5) In distal pyrite mineralization electrum has a high fineness of between 610 and 730. The electrum has a strong association with pyrite which, in one case, appears to be primary.

Gold distribution in the copper-gold association has the following characteristics:

(1) Primary electrum occurs in association with chalcopyrite, bismuth minerals, galena and pyrite. The electrum is slightly coarser grained and has a higher fineness (>700) with lower variation than recrystallized electrum in the zinc-lead-silver-gold association.

(2) As the grain size of electrum in the strongly deformed and metamorphosed Balcooma prospect is finer than that in the undeformed Mt. Chalmers deposit, recrystallization does not appear to affect electum grain size.

As the grain size and fineness of remobilized electrum at the Dry River South prospect and Rosebery north-end varies significantly, the processes of remobilization appear to increase the variability of the fineness of remobilized electrum.

Geologic controls on the occurrence and grain size of electrum

Three factors may control the occurrence of gold and the grain size of electrum in volcanogenic massive sulfide deposits: (1) primary processes during gold deposition, (2) secondary processes during post-depositional deformation, and (3) the gold tenor of the ores.

Primary controls

Comparison of the six deposits described herein indicates a significantly different primary occurrence of gold between deposits of the zinc-lead-silver-gold and the copper-gold associations. These differences are the result of two different depositional processes: (1) coprecipitation of gold during the crystallization of pyrite and arsenopyrite (e.g. Hellyer), and (2) precipitation of gold independant of any particular sulfide (e.g. Mt. Chalmers and the baritic zones of Rosebery and the Kuroko deposits).

Deposits of the zinc-lead-silver association. In the zinc-lead-silver-gold association the mechanisms of gold precipitation may vary depending on the location in the sulfide mound. Coprecipitation of gold into arsenopyrite is important in massive sphalerite-galena-pyrite ore at Hellyer, but has not been documented in the baritic zone. In the Kuroko district, electrum occurs in the baritic upper parts of kuroko ore in association with galena, sphalerite and tetrahedrite (Shimazaki, 1974). At Rosebery, the barite zone also contains electrum free of pyrite and associated with chalcopyrite and galena.

Baritic zones in volcanogenic massive sulfide deposits are restricted to the top of the mound where oxygenated seawater mixes with upwelling hydrothermal fluid. In this region, precipitation of gold may have been caused by the oxidation of H_2S, and this reaction does not involve sulfide minerals directly. Gold precipitated in this manner would occur as free electrum without any particular

association as has been noted in the baritic zones at Rosebery and the Kuroko deposits.

Further down into the mound, the interaction of the hydrothermal fluids with seawater is not as important as indicated by the lack of barite. In this region the most effective mechanism of gold precipitation is the removal of H_2S from the fluid by sulfide precipitation. Huston and Large (1989) and Romberger (1986) have argued that this mechanism will coprecipitate electrum as submicroscopic inclusions. As minerals that extract more sulfur from solution should coprecipitate more gold by this mechanism, sulfur-rich minerals such as pyrite should contain more gold than sulfur-poor minerals such as sphalerite, galena and arsenopyrite. However, at Hellyer arsenopyrite contains significantly more gold than pyrite (Ramsden and Creelman, 1984).

A summary of the gold content of sulfide minerals by Boyle (1979) indicates that in general arsenopyrite contains more gold than pyrite. Moreover Boyle (1979) infers that the gold in these two minerals is held in the lattice, possibly as a substitution for octahedrally coordinated iron. A more recent study of arsenopyrite by Cathelineau et al. (1988) confirms that gold does not occur as inclusions of native metal but as substitutions into the lattice, and is bonded to arsenic. If the formation of this gold-arsenic bond is an important control on the ability of a mineral to coprecipitate gold, arsenopyrite would concentrate gold in preference to pyrite despite the fact that pyrite contains more sulfur.

Deposits of the copper-gold association. In contrast to gold thiocomplexes, which are important in deposits of the zinc-lead-silver gold association, the deposition of gold from chlorocomplexes, which are important in deposits of the copper-gold association, is not affected by the precipitation of sulfide minerals. As a result, gold from deposits of the copper-gold association does not have an intimate association with sulfides and occurs as relatively coarse grained electrum.

Effects of post depositional processes

Post-depositional deformation and metamorphism also affect the occurrence of gold in volcanogenic massive sulfide deposits. Recrystallization during deformation and metamorphism is controlled

by the following factors: (1) strain rate, (2) temperature of deformation, (3) hydrostatic pressure, and (4) solid state diffusion (Hobbs et al., 1976). At low temperature and/or a high strain rate, recrystallization associated with deformation occurs as grains are flattened and as deformation lamellae and bands form (Hobbs et al., 1976). This type of deformation appears to have occurred at Que River and Rosebery. Whitford et al. (1984) inferred that the coarsest grained electrum occurs in the more deformed parts of the Que River orebody in association with other "soft" minerals (i.e. galena). Hence, the more deformed limbs of the Que River fold should contain coarser electrum than the less deformed core of the fold. The coarsest grains may occur in moderately deformed zones where a spaced cleavage of galena has formed (c.f. Large et al., 1988). By analogy, the coarsest electrum at Rosebery may be found in moderately deformed and recrystallized areas. In less deformed areas such as the core of the Que River fold and the north-end at Rosebery, electrum may not have been liberated from enclosing pyrite.

At high temperature and low strain rates, solid state diffusion becomes important (Hobbs et al., 1976). Clark (1960) found that gold diffuses rapidly through arsenopyrite under anhydrous conditions at temperatures over 600°C. This process may have been important at the Balcooma deposit, which has undergone a high degree of metamorphism and a low strain (i.e. the copper lens occurs in the core of a syncline). However the Balcooma prospect has the finest grained electrum of all deposits studied which belies the premise that more intense metamorphism leads to coarser grained electrum. Some other factor must control the grain size.

Balcooma also contains the lowest gold grade of the deposits at 0.3-0.4 g/t (Table 17). As solid state diffusion can only occur over a limited distance, the amount of gold in the region of diffusion surrounding the growing electrum grain must control the eventual grain size. As Balcooma has much lower grades than the other deposits described, the amount of gold available to the individual grains is less, and therefore the grain size is smaller. A similar effect during primary precipitation may also produce coarser grained electrum from hydrothermal fluids enriched in gold.

Table 17. Gold and silver grades from deposits discussed in this chapter.

Deposit	Ag (g/t)	Au (g/t)	Atomic Ag/Au ratio	Reference
Hellyer	160	2.3	127	Aberfoyle, Ltd. (1984)
Que River				
PQ lens	241	4.4	100	Large et al. (1988)
P-north lens	189	2.9	119	Large et al. (1988)
Rosebery	155	2.9	98	Lees et al. (in press)
Mt. Chalmers				
Main lode	11	1.8	11	Large and Both (1980)
West lode	42	3.0	26	Large and Both (1980)
Balcooma	20-30	0.3-0.4	130	Part 1, Chapter 1
Dry River South	97	0.7	253	Part 1, Chapter 1

Practical implications

As the association and grain size of electrum must control metallurgical recoveries, the previously discussed geologic parameters may have the following effects on gold recoveries:

(1) Deposits of the copper-gold association should have better recoveries than deposits of the zinc-lead-silver-gold association;

(2) In the zinc-lead-silver-gold association, ore from the top of the suiphide mound may have better recoveries than ore from the base of the mound, particularly if barite is present;

(3) Moderate deformation and metamorphism may increase recoveries; and

(4) Deposits of higher grade should have better recoveries than deposits of lower grade.

Geologic controls on electrum fineness

Shikazono and Shimuzu (1987) and Rose and Morrison (1988) have recently used the fineness (or other measures of gold content) of electrum as an aid in classifying gold deposits and as a technique to discern the mechanisms of gold transport. The second purpose of this chapter is to treat electrum from volcanogenic massive sulphide deposits explicitly in these terms.

The two gold associations in volcanogenic massive sulfide deposits have quite different electrum characteristics. Deposits of the zinc-lead-silver-gold association have a relatively low electrum fineness with a rather large variation in the values. On the other hand, electrum from the copper-gold association has a higher fineness, and more importantly, a much narrower variation in values. Gold in deposits of the copper-gold association was probably transported as a chlorocomplex, but gold in deposits of the zinc-lead-silver gold association was transported as a thiocomplex (Chapter 2). In all cases silver was transported as a chlorocomplex (Chapter 3).

In deposits of the zinc-lead-silver-gold association, the fineness of electum is controlled by the reaction (see also Shikazono and Shimuzu, 1987):

$$Au^0 + AgCl_2^- + 2H_2S = Ag^0 + Au(HS)_2^- + 2H^+ + 2Cl^- \quad (20)$$

The ratio a_{Ag^0}/a_{Au^0} (which is related to fineness) may be related to other fluid parameters as follows:

$$\log (a_{Ag^0}/a_{Au^0}) = \log K_{20} + \log (a_{AgCl_2^-}/a_{Au(HS)_2^-}) - 2pH + 2\log a_{Cl^-} + 2\log a_{H_2S} \quad (21)$$

This reaction indicates that a_{Ag^0}/a_{Au^0} (and, hence, fineness) is controlled by $a_{AgCl_2^-}/a_{AuCl_2^-}$, a_{H_2S}, a_{Cl^-}, pH and temperature. Even though a_{H_2S} and a_{Cl^-} might be expected to remain constant in the systems, variations in the other parameters will lead to large variations in the resulting electrum fineness. The most striking characteristic of deposits of the zinc-lead-silver-gold association is the large variation in the fineness of electrum.
Conversely, for gold chlorocomplex transport, the following reaction controls the fineness of electrum (see also Shikazono and Shimuzu, 1987):

$$Au^0 + AgCl_2^- = Ag^0 + AuCl_2^- \quad (22)$$

The ratio a_{Ag^0}/a_{Au^0} is only related to $a_{AgCl_2^-}/a_{AuCl_2^-}$ and temperature as follows:

$$\log (a_{Ag^0}/a_{Au^0}) = \log K_{22} + \log (a_{AgCl_2^-}/a_{AuCl_2^-}) \quad (23)$$

As the temperature of the formation of copper-rich ore is restricted to around 300°C (Pisutha-Arnond and Ohmoto, 1983), the fineness variation in this case should be more restricted.

Using available thermodynamic data (Table 15), the fineness of electrum can be modelled. The activities of gold and silver may be related to their mole fractions in electrum using data from White et

al. (1957). As this data was collected at 800°K (527°C), it is only an approximation to the true activity-composition relationships at the temperatures of interest. Once the mole fraction of gold (X_{Au}) is established, fineness may be determined as follows:

$$\text{Fineness} = 1000X_{Au}AW_{Au}/(AW_{Ag} - X_{Au}(AW_{Ag} - AW_{Au}) \quad (24)$$

where AW_i is the atomic weight of the relevant metal.

Figure 112 illustrates the calculated variation in the fineness of electrum from a volcanogenic fluid assuming log a_{H_2S}= -2.5 and log m_{NaCl}=0. As the dominant silver and gold species in the fluid under these conditions have a -1 charge, the activity coefficients cancel and $a_{AgCl_2^-}/a_{AuCl_2^-}$ is approximately equal to the atomic Ag/Au ratio of the fluid (which is about twice the weight Ag/Au ratio).

In deposits of the zinc-lead-silver-gold association, the efficiency of metal precipitation at the seawater interface indicates that the Ag/Au ratio of the ores approximates that of the hydrothermal fluids. As most volcangenic massive sulfide deposits of the zinc-lead-silver-gold association have an atomic Ag/Au ratio of around 100 Table 17), the modelling, which predicts a variation of between 100 and 900 for temperatures from 200°C to 275°C and pH values between 4.5 and 5.5, matches the observed variation of 320 to 820. The silver-rich rims in electrum noted from several deposits may be caused by a decrease in temperature during deposition.

Thermodynamic modelling assuming gold chlorocomplexes (Fig. 112d) yielded less satisfactory results. Below fluid atomic Ag/Au ratios of 1000, gold fineness was always 1000, and the modelling only matched the observations when the atomic Ag/Au ratio of the fluid varied between 100,000 and 1,000,000 (weight ratios of between 50,000 and 500,000). A high Ag/Au ratio is expected as within the copper zone silver is being leached and gold is being deposited. A weight ratio of 50,000 implies that if 0.1 ppb of gold is carried in solution, 5 ppm of silver is also in solution. Although the silver concentration is high, it may not be unreasonable in high temperature fluids (300°C) which are leaching silver. Another possible reason for the high Ag/Au ratios required to reproduce natural variations is the lack of adequate thermodynamic data for gold chlorocomplexes.

Figure 112. Calculated fineness of electrum predicted from hydrothermal fluids of varying physocochemical conditions and atomic Ag/Au ratios. Diagrams (a) through (c) are calculated at different pH conditions assuming gold thiocomplex and silver chlorocomplex transport, $a_{H_2S} = 10^{-2.5}$ and m_{NaCl} (total) $= 10^{0.0}$. Diagram (d) is calculated assuming gold and silver chlorocomplex transport and is valid under all conditions.

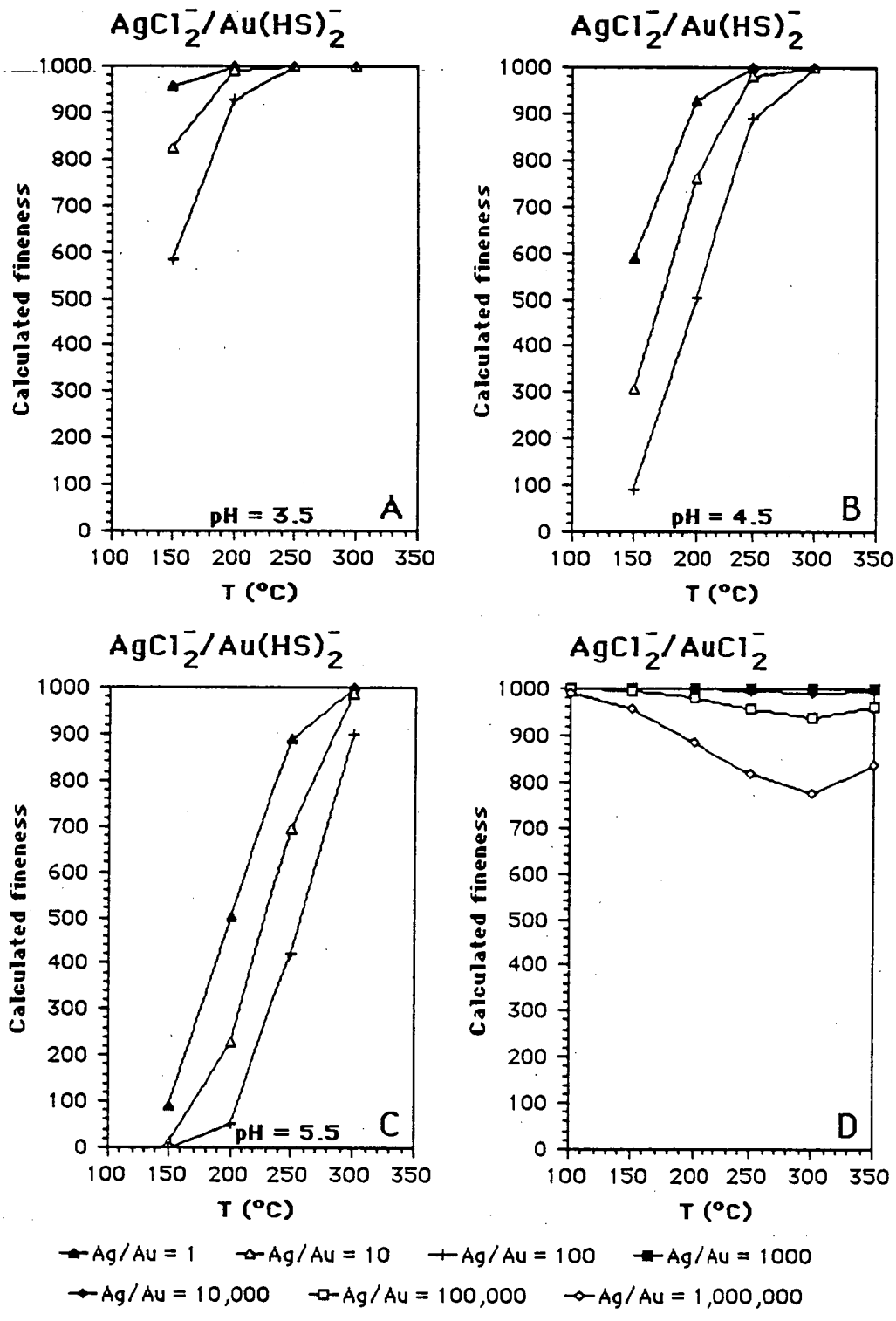
AgCl2-/Au(HS)2-
Calculated fineness
T (°C)
pH = 3.5
A
AgCl2-/Au(HS)2-
pH = 4.5
B
AgCl2-/Au(HS)2-
pH = 5.5
C
AgCl2-/AuCl2-
D
Ag/Au = 1
Ag/Au = 10
Ag/Au = 100
Ag/Au = 1000
Ag/Au = 10,000
Ag/Au = 100,000
Ag/Au = 1,000,000

Helgeson's (1969) data has been theoretically extrapolated from low temperature data and at present no experimental data is available. A decrease in the stability of the $AuCl_2^-$ complex by 1 to 2 orders of magnitude would predict the observed fineness of gold in deposits of the copper-gold association assuming atomic Ag/Au ratios of 100 to 10,000.

Examination of the diagrams in Figure 112 illustrates some important characteristics of electrum deposited from a chlorocomplex relative to electrum deposited from a thiocomplex. Electrum deposited from a gold thiocomplex has an extremely large fineness variation whereas electrum deposited from a gold chlorocomplex has a narrow variation and a high fineness. Moreover, electrum deposited from a gold thiocomplex increases in fineness with increasing temperature, whereas electrum transported as a chlorocomplex decreases in fineness with increasing temperature. Finally, as much overlap exists between the finenesses of electrum deposited from the respective complexes, the average fineness of electrum is not diagnostic in determining the method of gold transport in the system; rather the variability in the fineness values is more useful.

Conclusions

Predictable geologic processes appear to have controlled the occurrence of gold, and the grain size and fineness of electrum in volcanogenic massive sulfide deposits. Depositional processes control the primary occurrence of gold. In deposits of the zinc-lead-silver-gold association, gold may be locked up in untreatable pyrite and arsenopyrite in the core of the deposit, but toward the top of the deposit, the gold may occur as electrum in association with other base metal sulfides. In deposits of the copper-gold association, gold is more likely to occur as electrum in association with chalcopyrite. In undeformed ores, deposits of the copper-gold association should have higher recoveries than deposits of the zinc-lead-silver-gold association.

Deformation and metamorphism will tend to coarsen up electrum so recoveries are higher. This enhancement is probably most effective in areas undergoing moderate strain rates, but the effect of mylonitization is unknown. Deposits that lie in zones of low strain (e.g. closures of folds) may not undergo this upgrading. The grade

of the deposit may also limit the size of the electrum grains. As less gold is available to a growing electrum grain in a lower tenor deposit, this grain will not coarsen to the extent of a grain in a higher tenor deposit.

Deposits of the zinc-lead-silver-gold association have relatively low, but highly variable electrum finenesses. Thermochemical modelling assuming gold transport as a thiocomplex predicts this behaviour. Deposits of the copper-gold association have a higher fineness with a lower variation. Thermodynamic calculatons assuming gold chlorocomplexing predict this behaviour but is less certain due to large uncertainties in the stability of gold chlorocomplexes. The fineness of electrum is not a diagnostic tool of the geochemistry of gold transport as overlap exists in the values produced by deposition from gold thiocomplexes and gold chlorocomplexes.

References

Aberfoyle, Ltd., 1984, Annual report and notice of meeting, 1984: Aberfoyle, Ltd., Melbourne, 25 p.

Amcoff, O., 1976, The solubility of silver and antimony in galena: Neus Jahrb. Mineral. Mh., v. 6, p. 247-261.

Amcoff, O., 1984, Distribution of silver in massive sulphide ores: Mineral. Deposita, v. 19, p.63-69.

Amcoff, O., Jeppsson, M., and Selkman, S., 1985, Distribution and zoning of silver and associated elements in the complex sulfide deposit at Saxberget, central Sweden: Econ. Geol., v. 80, p. 614-626.

Ashworth, J.R., 1975, Staurolites at anomalously high grade: Contr. Mineral. Petrology, v. 53, p. 281-291.

Ayres, D.E., Burns, M.S., and Smith, J.W., 1979, Sulphur-isotopes of the massive sulphide orebody at Woodlawn, New South Wales: Jour. Geol. Soc. Austr., v. 26, p. 197-201.

Barrett, T.J., and Anderson, G.M., 1988, The solubility of sphalerite and galena in 1-5 m NaCl solutions to 300°C: Geochim. Cosmochim. Acta, v. 52, p. 813-820.

Barton, P.B., 1984, Redox reactions in hydrothermal fluids, in Henley, R.W., Truesdell, A.H., and Barton, P.B., eds., Fluid-mineral equilibria in hydrothermal systems: Reviews in Econ. Geol., v. 1, p. 99-114.

Barton, P.B., and Skinner, B.J., 1979, Sulfide mineral stabilities, in Barnes, H.L., ed., Geochemistry of hydrothermal ore deposits, second edition: New York, Wiley, p. 278-403.

Berry, R.F., The structure of the Rosebery mine sequence: Unpub. report, Univ. of Tasmania, 16 p.

Bhatia, M.R., 1983, Plate tectonics and geochemical composition of sandstones: Jour. Geology, v. 91, p. 611-627.

Bhatia, M.R., 1985, Plate tectonics and geochemical composition of sandstones: a reply: Jour. Geology, v. 93, p. 85-87.

Bourcier, W.L., and Barnes, H.L., 1987, Ore solution chemistry--VIII. Stabilities of chloride and bisulfide complexes of zinc to 350°C: Econ. Geol., v. 82, p. 1839-1863.

Bowers, T.S., Jackson, K.J., and Helgeson, H.C., 1984, Equilibrium activity diagrams: Berlin, Springer-Verlag, 397 p.

Boyle, R.W., 1968, The geochemistry of silver and its deposits: Geol. Surv. Can. Bull. 160, 264 p.

Boyle, R.W.,, 1979, The geochemistry of gold and its deposits: Geol. Surv. Can. Bull. 280, 584 p.

Branch, C.D., 1966, Volcanic cauldrons, ring complexes and associated granites of the Georgetown Inlier, Queensland: Bureau of Mineral Resources, Australia, Bulletin 76, 171 p.

Brathwaite, R.L., 1969, The geology of the Rosebery ore deposit: Unpub. Ph.D. thesis, Univ. of Tasmania, 218 p.

Brathwaite, R.L., 1974, The geology and origin of the Rosebery ore deposit: Econ. Geol., v. 69, p. 1086-1101.

Brehler, B., and Wedepohl, K.H., 1970, Zinc, in Wedepohl, K.H., ed., Handbook of geochemistry: Berlin, Springer-Verlag, p. 30-A-1 to 30-O-2.

Bryndzia, L.T., and Scott, S.D., 1987, Application of chlorite-sulfide-oxide equilibria to metamorphosed massive sulfide ores, Snow Lake area, Manitoba: Econ. Geol., v. 82, p. 963-970.

Buchanan, L.J., 1981, Precious metal deposits associated with volcanic environments in the southwest, in Dickinson, W.R., and Payne, W.D., eds., Relations of tectonics to ore deposits in the southern cordillera: Ariz. Geol. Soc. Digest, v. 14, p. 237-262.

Burton, C.C.J., 1975, Hercules and Farrell orebodies, in Knight, C.L., ed., Economic geology of Australia and Papua New Guinea, I. Metals: Aus. Inst. Mining Metal. Mon. 5, p. 619-626.

Campbell, I.H., McDougall, T.J., and Turner, J.S., 1984, A note on fluid dynamic processes which can influence the deposition of massive sulfides: Econ. Geol., v. 79, p. 1905-1913.

Cathelineau, M., Roiron, M.C., Holliger, Ph., and Marion, Ph., 1988, Gold-rich arsenopyrites (abstract): crystal chemistry, gold location and state, physical and chemical conditions of crystallisation: Bicentennial Gold '88, extended abstracts, oral programme, p. 235-240.

Clark, L.A., 1960, The Fe-As-S system: phase relations and applications: Econ. Geol., v. 55, p. 1345-1381 and 1631-1652.

Clark, L.A., 1983, Genetic implications of fragmental ore texture in Japanese kuroko deposits: Can. Inst. Min. Metal. Bull., v. 76, no. 849, p. 105-114.

Clayton, R.N., and Mayeda, T.K., 1963, The use of bromine pentafluoride in the extraction of oxygen from oxides and silicates: Geochim. Cosmochim. Acta, v. 27, p. 43-52.

Clayton, R.N., O'Neill, J.R., and Mayeda, T.K., 1972, Oxygen isotope exchange between quartz and water: J. Geophys. Res., v. 77, p. 3057-3067.

Cole, D.R., and Drummond, S.E., 1986, The effect of transport and boiling on Ag/Au ratios in hydrothermal solutions: a preliminary assessment and implications for the formation of epithermal precious-metal ore deposits: J. Geochem. Explor., v. 25, p. 45-80.

Constantinou, G., 1986, Gold mineralization associated with massive sulphide ores of the Troodos ophiolite, Cyprus: AIME Preprint, 9 p.

Corbett, K.D., 1981, Stratigraphy and mineralization in the Mt. Read Volcanics, western Tasmania: Econ. Geol., v. 76, p. 209-230.

Corbett, K.D., and Lees, T.C., 1987, Revised stratigraphy and tectonics of the Cambrian arc and forearc sequences, and a probable accretionary complex, in the Rosebery-Lyell area, western Tasmania: Aus. Jour. Earth Sci., v. 34, p. 45-67.

Crerrar, D.A., and Barnes, H.L., 1976, Ore solution chemistry V. Solubilities of chalcopyrite and chalcocite assemblages in hydrothermal solutions at 200°C to 350°C: Econ. Geol., v. 71, p. 772-794.

Date, J., Watanabe, Y., and Saeki, Y., 1983, Zonal alteration around the Fukazawa kuroko deposit, in Ohmoto, H., and Skinner, B.J., The kuroko and related volcanogenic massive sulfide deposits: Econ. Geol. Mon. 5, p. 365-386.

Deer, W.A., Howie, R.A., and Zussman, J., 1982, Rock-forming minerals. Volume 1A. Orthosilicates, second edition: Longman, London, 919 p.

Dewitt, E., 1983, Precious metal contents of Proterozoic massive sulfide deposits in Arizona (abstract): Geol. Soc. Am. Abstracts with Programs, v. 15, p. 298.

Divi, S.R., Thorpe, R.I., and Franklin, J.M., 1979, Application of discriminant analysis to evaluate controls on stratiform massive sulfide deposits in Canada: Internat. Assoc. Math. Geology Jour., v. 11, p. 391-406.

Dixon, G.H., 1980, Geological, geochemical and stable isotope studies of the carbonates at Rosebery: Unpub. B.Sc. (Hons.) thesis, Univ. of Tasmania, 173 p.

Dixon, W.J., and Massey, F.J., 1957, Introduction to statistical analysis: McGraw Hill, New York, 488. p.

Durham, J.J., Rouse, J.E., and Moore, G.L., 1982, Reduction of water with zinc for hydrogen isotope analysis: Anal. Chem., v. 54, p. 993-995.

Eldridge, C.S., Barton, P.B., and Ohmoto, H., 1983, Mineral textures and their bearing in the formation of the kuroko orebodies, in Ohmoto, H., and Skinner, B.J., The kuroko and related volcanogenic massive sulfide deposits: Econ. Geol. Mon. 5, p. 241-281.

Fabray, J.F., Hall, R.J., Shalley, M.J., Stainforth, B., and Taylor, T.W., 1986, Second quarterly progress report, Balcooma Joint Venture: Unpub. Carpentaria Exploration Company report.

Fehne, R., 1986, Mineralogical examination of drill core material from the Balcooma Joint Venture, Dry River South area, Queensland, Australia: Unpub. Metallgesellschaft report, 5 p.

Feiss, P.G., 1974, Reconnaissance of the tetrahedrite-tennantite/enargite-famatinite phase relations as a possible geothermometer: Econ. Geol., v. 69, p. 383-390.

Floyd, P.A., and Winchester, J.A., 1978, Identification and discrimination of altered and metamorphosed volcanic rocks using immobile elements: Chem. Geol., v. 21, p. 291-306.

Franklin, J.M., and Thorpe, R.I., 1982, Comparative metallogeny of the Superior, Slave and Churchill Provinces, in Hutchinson, R.W., Spence, C.D., and Franklin, J.M., eds., Precambrian sulphide deposits: Geol. Ass. Can. Special Paper 25, p. 3-90.

Franklin, J.M., Gibb, W., Poulsen, K.H., and Severin, P., 1977, Archean metallogeny and stratigraphy of the south Sturgeon Lake area: Inst. on Lake Superior Geology, 23rd Ann. Mtg., Thunder Bay, Ont., Guidebook, 73 p.

Franklin, J.M., Sangster, D.M., and Lydon, J.W., 1981, Volcanic-associated massive sulfide deposits: Econ. Geol. 75th Anniv. Vol., p. 485-627.

Frets, D.C., and Balde, R., 1975, Mount Morgan copper-gold deposit, in Knight, C.L., ed., Economic geology of Australia and Papua and New Guinea, I. Metals: Aust. Inst. Min. Metall. Mon. 5, p. 779-785.

Gemmell, J.B., Zantop, H., and Birnie, R.W., in press, Silver-sulfosalts of the Santo Nino vein, Fresnillo district, Zacatecas, Mexico: Can. Mineral.

Giggenbach, W.F., 1974, Equilibrium involving polysulfide ions in acqueous solutions up to 240°: Inorganic Chemistry, v. 13, p. 1724-1730.

Gilligan, L.B., and Marshall, B., 1987, Textural evidence for remobilisation in metamorphic environments: Ore Geol. Rev., v. 2, p. 205-230.

Glen, R.A., and Laing, W.P., 1975, The significance of sedimentary structures in the Willyama Complex, New South Wales: Proc. Aust. Inst. Min. Metall., No. 256, p. 15-20.

Goldfarb, M.S., Converse, D.R., Holland, H.D., and Edmond, J.M., 1983, The genesis of hot spring deposits on the East Pacific Rise, 21°N, in Ohmoto, H., and Skinner, B.J., eds., The kuroko and related volcanogenic massive sulphide deposits: Econ. Geol. Mon. 5, p. 184-197.

Graf, J.L., 1977, Rare earth elements as hydrothermal tracers during the formation of massive sulfide deposits in volcanic rocks: Econ. Geol., v. 72, p. 527-548.

Graham, C.M., Viglino, J.A., and Hormon, R.S., 1987, Experimental study of hydrogen-isotope exchange between aluminous chlorite and water and of hydrogen diffusion in chlorite: Amer. Mineral., v. 1987, p. 566-579.

Grant, J.A., 1986, The isocon diagram--a simple solution to Gresen's equations for metasomatic alteration: Econ. Geol., v. 81, p. 1976-1982.

Gresens, R.L., 1967, Composition-volume relationships of metasomatism: Chem. Geol., v. 2, p. 47-65.

Green, G.R., 1983, The geological setting and formation of the Rosebery volcanic-hosted massive sulphide orebody, Tasmania: Unpub. Ph.D. thesis, Univ. of Tasmania, 288 p.

Green, G.R., Solomon, M., and Walshe, J.L., 1981, The formation of the volcanic-hosted massive sulfide ore deposit at Rosebery, Tasmania: Econ. Geol., v. 76, p. 304-338.

Green, G.R., Ohmoto, H., Date, J., and Takahashi, T., 1983, Whole-rock oxygen isotope distribution in the Fukazawa-Kosaka area, Hokuroko District, Japan, and its potential application to mineral exploration, in Ohmoto, H., and Skinner, B.S., eds., The kuroko and related volcanogenic massive sulfide deposits: Econ. Geol. Mon. 5, p. 395-411.

Grip, E., and Wirstam, A., 1970, The Boliden sulphide deposit: Sver. Geol. Unders., Ser. C, no. 651, v. 64, no. 8, 68 p.

Gulson, B.L., and Vaasjoki, M., 1987, Lead isotope data from the Thalanga, Dry River and Mt. Chalmers base metal deposits and their bearing on exploration and ore genesis in eastern Australia: Aust. Jour. Earth Sci., v. 34, p. 159-171.

Hackbarth, C.J., and Petersen, U., 1984, A fractional crystallization model for the deposition of argentininan tetrahedrite: Econ. Geol., v. 79, p. 448-460.

Hall, R.J., Huston, D.L., Shalley, M.J., Stainforth, B., and Taylor, T.W., 1987, Fourth quarterly progress report, Balcooma Joint Venture: Unpub. Carpentaria Exploration Company report.

Hannington, M.D., Peter, J.M., and Scott, S.D., 1986, Gold in seafloor polymetallic sulfide deposits: Econ. Geol., v. 81, p. 1867-1883.

Harris, D.C., Cabri, L.J., and Nobiling, R., 1984, Silver-bearing chalcopyrite, a principal source of silver in the Izok Lake massive-sulfide deposit: confirmation by electron- and proton-microprobe analyses: Can. Mineral., v. 22, p. 493-498.

Harvey, K.J., 1979, Authority to prospect no. 2036M "Balcooma," Charters Towers and Herberton Mining Districts, Report for 6 months ended April 26, 1979: Unpub. Carpentaria Exploration Company, Pty., Ltd. Technical Report 760.

Harvey, K.J., 1984a, The discovery of the Balcooma massive sulfide deposit (abstract): Proceedings of the Seventh Australian Geological Congress, Geol. Soc. Austr. Abstracts, v. 12, p. 218-219.

Harvey, K.J., 1984b, The geology of the Balcooma massive sulfide deposit, north-east Queensland: Unpub. M.Sc. thesis, James Cook Univ., 92 p.

Heinrich, C.A., and Eadington, P.J., 1986, Thermodynamic predictions of the hydrothermal chemistry of arsenic, and their significance for the paragenetic sequence of some cassiterite-arsenopyrite-base metal sulfide deposits: Econ. Geol., v. 81, p. 511-529.

Helgeson, H.C., 1969, Thermodynamics of hydrothermal systems at elevated temperatures and pressures: Am. Jour. Sci., v. 267, p. 729-804.

Helgeson, H.C., Kirkham, D.M., and Flowers, G.C., 1981, Theoretical prediction of the thermodynamic behavior of acqueous electrolytes at high pressures and temperatures: IV. Calculation of activity coefficients, osmotic coefficients and apparent molal and standard and relative partial molal properties to 600°C and 5 kb: Am. Jour. Sci., v. 281, p. 1249-1516.

Helovouri, O., 1979, Geology of the Pyhasalmi ore deposit, Finland: Econ. Geol., v. 74, p. 1084-1101.

Henderson, R.A., 1986, Geology of the Mt. Windsor Subprovince--a Lower Palaeozoic volcano-sedimentary terrane in the northern Tasman Orogenic Zone: Aust. J. Earth Sci., v. 33, p. 343-364.

Henley, K.J., and Steveson, B.G., 1978, The nature and location of precious metals in Rosebery ore (abstract), in Green, D. C., and Williams, P. E., eds., Geology and mineralization of north-west Tasmania: Geol. Soc. Aus., Tasmanian Division, p. 14-15.

Henley, R.W., 1973, The solubility of gold in hydrothermal chloride solutions: Chem. Geol., v. 11, p. 622-635.

Henley, R.W., 1984, Chemical structure of geothermal systems, in Henley, R.W., Truesdell, A.H., and Barton, P.B., eds., Fluid-mineral equilibria in hydrothermal systems: Reviews in Econ. Geol., v. 1, p. 9-27.

Henley, R.W., 1984, pH calculations for hydrothermal fluids, in Henley, R.W., Truesdell, A.H., and Barton, P.B., eds., Fluid-mineral equilibria in hydrothermal systems: Reviews in Econ. Geol., v. 1, p. 83-98.

Henley, R.W., and Brown, K.L., 1985, A practical guide to the thermodynamics of geothermal fluids and hydrothermal ore deposits, in Berger, B.R., and Bethke, P.M., eds., Geology and geochemistry of epithermal systems: Reviews in Econ. Geol., v. 2, p. 25-42.

Henley, R.W., and Thornley, P., 1979, Some geothermal aspects of polymetallic massive sulfide formation: Econ. Geol., v. 74, p. 1600-1612.

Hobbs, B.E., Means, W.D., and Williams, P.F., 1976, An outline of structural geology: Wiley, New York, 571 p.

Holland, H.D., 1972, Granites, solutions, and base metal deposits: Econ. Geol., v. 67, p. 281-301.

Holland, H.D., 1976, The evolution of seawater, in Windley, B.F., ed., The early history of the earth: London, Wiley, p. 559-567.

Hurley, T.D., and Crocket, J.H., 1985, A gold-sphalerite association in a volcanogenic base-metal-sulphide deposit near Tilt Cove, Newfoundland: Can. Min., v. 23, p. 423-430.

Huston, D.L., 1987, The Balcooma prospect, northern Queensland, in Controls on gold and silver grades in volcanogenic sulphide deposits (84/P210), August 1987 progress report: Unpub. AMIRA report, Univ. of Tasmania, p. 150-168.

Huston, D.L., and Large, R.R., 1987a, Precious metals in the Rosebery north-end orebody, Tasmania, Australia: Proc. Pacific Rim Congress 87, p. 199-203.

Huston, D.L., and Large, R.R., 1987b, Genetic and exploration significance of the zinc ratio [100Zn/(Zn+Pb)] in massive sulfide systems, Econ.Geol., v. 82, p. 1521-1539.

Huston, D.L., and Large, R.R., 1988, The distibution, mineralogy and geochemistry of gold and silver in the north-end orebody, Rosebery mine, Tasmania: Econ. Geol., v. 83, p. 1181-1192.

Huston, D.L., and Large, R.R., 1989, A chemical model for the concentration of gold in volcanogenic massive sulphide deposits: Ore Geol. Rev., v. 4, p. 171-200.

Huston, D.L., and Taylar, T.W., in press, The Dry River lead-zinc deposits, in Hughes, F.E., ed., Geology of the mineral deposits of Australia and Papua and New Guinea: Aust. Inst. Min. Metal., Melbourne.

Hutchinson, R.W., 1965, Genesis of Canadian massive sulphides reconsidered by comparison to Cyprus deposits: Can. Inst. Min. Metal. Bull., v. 68, p. 286-300.

Hutchinson, R.W., 1973, Volcanogenic sulfide deposits and their metallogenic significance: Econ. Geol., v. 68, p. 1223-1246..

Hutchinson, R.W., and Searle, D.L., 1971, Stratabound pyrite deposits in Cyprus and relation to other sulphide ores, in Takeuchi, Y., ed., Proceedings of the IMA-IAGOD meetings '70: Mining Geol. Special Issue 3, p. 198-205.

Iijima, A., 1974, Clay and zeolitic alteration zones surrounding kuroko deposits in the Hokuroko district, Northern Akita, as submarine hydrothermal-diagenetic alteration products, in Ishihara, S., ed., Geology of kuroko deposits: Mining Geol. Special Issue 6, p. 267-290.

Ishihara, S., and Sasaki, A., 1978, Sulfur of kuroko deposits--a deep seated origin?: Mining Geol., v. 28, p. 361-367.

Jenkins, D.M., and Chernosky, J.V., 1986, Phase equilibria and crystallochemical properties of Mg-chlorite: Am. Mineral., v. 71, p. 924-936.

Joyce, A.S., 1986, Report on five polished thin sections prepared for Carpentaria Exploration Company, Pty., Ltd.: Unpub. report to the Carpentaria Exploration Company, 8 p.

Kay, J.R., 1982, Notes on the geology of the Highway gold mine, Charters Towers, in Withnall, I.W., ed., Handbook for the 1982 field conference, Charters Towers-Greenvale area: Geol. Soc. Aust., Queensland Division, Brisbane, p. 109-127.

Knuckey, M.J., Comba, C.D.A., and Rivrin, G., 1982, Structure, metal zoning and alteration at the Millenbach deposit, Noranda, Quebec, in Hutchinson, R.W., Spence, C.D., and Franklin, J.M., eds., Precambrian sulphide deposits: Geol. Ass. Can. Special Paper 25, p. 296-317.

Knuckey, M.J., and Watkins, J.J., 1982, The geology of the Corbet massive sulphide deposit, Noranda district, Quebec, Canada, in Hutchinson, R.W., Spence, C. D., and Franklin, J. M., eds., Precambrian sulphide deposits: Geol. Ass. Can. Special Paper 25, p. 296-317.

Large, R.R., 1975, Zonation of hydrothermal minerals at the Juno mine, Tennant Creek goldfield, central Australia: Econ. Geol., v. 70, p. 1387-1413.

Large, R.R., 1977, Chemical zonation and zonation of massive sulfide deposits in volcanic terrains: Econ. Geol., v. 72, p. 549-572.

Large, R.R., 1987, Source and movement of gold in submarine volcanic environments--as discussion paper, in Controls on gold and silver grades in volcanogenic massive sulphide deposis (84/P810): Unpub. AMIRA report, Univ. of Tasmania, p. 169-181.

Large, R.R., and Both, R.A., 1980, The volcanogenic sulfide ores at Mount Chalmers, Eastern Queensland: Econ. Geol., v. 75, p. 992-1009.

Large, R.R., and Huston, D.L., 1985, The relationship of gold to base metals in some volcanogenic ore systems (abstract), in Research trends in gold exploration: Bur. Min. Res. Aus. Record 1985/34, p. 31-36.

Large, R.R., McGoldrick, P.J., Berry, R.F., and Young, C.H., 1988, A tightly folded, gold-rich, massive sulfide deposit: Que River mine, Tasmania: Econ. Geol., v. 83, p. 681-693.

Large, R.R., Carswell, J., Creelman, R., Huston, D.L., McArthur, G., McGoldrick, P.J., Purvis, G., Ramsden, A., and Wallace, D., in press, Gold in western Tasmania, in Mineral resources of Australia: Aus. Inst. Min. Metall., Melbourne.

Laubscher, H.P., 1972, Some overall aspects of Jura dynamics: Am. J. Sci., p. 293-304.

Lees, T., Khin Zaw, Large, R.R., and Huston, D.L., in press, Economic geology of the Rosebery-Hercules area, in Hughes, F.E., ed., Geology of the mineral deposits of Australia and Papua New Guinea: Aust. Inst. Min. Metal., Melbourne.

Lusk, J., 1969, Base metal zoning in the Heath Steele B-1 orebody, New Brunswick, Canada: Econ. Geol., v. 64, p. 509-518.

Lydon, J.W., 1983, Chemical parameters controlling the origin and deposition of sediment-hosted stratiform lead-zind deposits: Mineral. Assoc. Can. Short Course Handbook, v. 8, p. 175-250.

Lydon, J.W., 1985, Ore deposit models--8. Volcanogenic massive sulfide deposits part 1: A descriptive model: Geosci. Canada, v. 11, p. 195-202.

Lydon, J.W., 1988, Ore deposit models #14. Volcanogenic massive sulfide deposits part 2: genetic models: Geosci. Canada, v. 15, p. 43-65.

McArthur, G.J., 1986, The Hellyer massive sulphide deposit (abstract), in Large, R.R., ed., The Mt. Read Volcanics and associated ore deposits: Geol. Soc. Aus., Tasmanian Division, p. 11-20.

McGoldrick, P., and Large, R.R., 1987, Final report on the footwall precious metal zone, Que River, in Controls on gold and silver grades in volcanogenic massive sulphide deposits (84/P810): Unpub. AMIRA report, Univ. of Tasmania, p. 9-41.

McKay, W.J., and Hazeldene, R.K., 1987, Woodlawn Pb-Zn-Cu sulfide deposit, New South Wales: an interpretation of ore formation from field observations and metal zoning: Econ. Geol., v. 82, p. 141-164.

McKinnon, A., 1988, Triako gets half of the Conjuboy project: Metals Gazette, v.1, no. 1, p. 10.

McLeod, R.L., 1985, Preliminary observations of kaolinite in a volcanogenic massive sulphide deposit of Permian age: Tschermaks Miner. Petrogr. Mitt., v. 34, p261-269.

Mercer, W., and Crocket, J., 1972, Gold in host rocks and ores from the Heath Steele B-1 deposit, New Brunswick: 24th Int. Geol. Cong., Sec. 10, p 180-185.

Miller, J.W., and Craig, J.R., 1983, Tetrahedrite-tennantite series compositional variations in the Cofer deposit, Mineral district, Virginia: Am. Mineral., v. 68, p. 227-234.

Mookherjee, A., 1976, Ores and metamorphism: temporal and genetic relationsships, in Wolf, K.H., ed., Handbook of strata-bound and stratiform ore deposits, Vol. 4. Tectonics and metamorphism: Elsevier, Amsterdam, p. 203-260.

Mosier, D.L., Singer, D.A., and Salem, B.B., 1983, Geologic and grade-tonnage information on volcanic-hosted copper-zinc-lead massive sulfide deposits: U. S. Geol. Surv. Open File Report 83-89, 78 p.

Mulroney, M.G., 1982, Authority to prospect no. 2036M "Balcooma," Charters Towers and Herberton Mining Districts, report for 6 months ended October 6, 1982: Unpub. Carpentaria Exploration Company, Pty., Ltd. Technical Report 1165.

Mulroney, M.G., 1983, Authority to prospect no. 2036M "Balcooma," Charters Towers and Heberton Mining Districts, report for 6 months ended April 26, 1983: Unpub. Carpentaria Exploration Company, Pty., Ltd. Technical Report 1184.

Naschwitz, W., 1985, Geochemistry of the Rosebery ore deposit: Unpub. Ph.D. thesis, Univ. of Tasmania, 276 p.

Noranda Pacific, Ltd., 1985, Prospectus for an issue of 40,000,000 ordinary shares: Melbourne, Noranda Pacific, Ltd.

Norrish, K., and Chapell, B.W., 1977, X-ray fluorescence spectrography, in Zussman, J., ed., Physical methods in determinative mineralogy: New York, Academic Press, p. 161-214.

Norrish, K., and Hutton, J.T., 1969, An accurate X-ray spectrographic method for analysis of a wide range of geologic samples: Geochim. Cosmochim. Acta, v. 33, p. 431-454.

Ohmoto, H., 1986, Stable isotope geochemistry of ore deposits, in Valley, J.W., Taylor, H.P., and O'Neill, J.R., eds., Stable isotopes in high temperature geological processes: Rev. in Mineralogy, v. 16, p. 491-560.

Ohmoto, H., Mizukami, M., Drummond, S.E., Eldridge, C.S., Pisutha-Arnond, V., and Lenaugh, T.C., 1983, Chemical processes of kuroko formation, in Ohmoto, H., and Skinner, B.J., eds., The kuroko and related volcanogenic massive sulfide deposits: Econ. Geol. Mon. 5, p. 570-604.

O'Leary, M.J., and Sack, R.O., 1987, Fe-Zn exchange reactions between tetrahedrite and sphalerite in natural environments: Contrib. Mineral. Petrol., v. 96, p. 415-425.

Oudin, E., and Constantinou, G., 1984, Black smoker chimney fragments in Cyprus sulfide deposits: Nature, v. 308, p. 349-353.

Osterberg, S.A., Morton, R.L., and Franklin, J.M., 1987, Hydrothermal alteration and physical volcanology of Archean rocks in the vicinity of the Headway-Coulee massive sulfide occurrence, Onaman area, northwestern Ontario: Econ. Geol., v. 82, p. 1505-1520.

Palache, C. Berman, H., and Frondel, C., 1946, The system of mineralogy: Wiley, New York, v. 1, 834 p.

Patterson, D.A., 1981, Mineralogical reconnaissance of diamond drill core, Balcooma DDH16, QH15432-15489 (RA8003-8060): Unpub. Mt. Isa Mines Mineral Services Report 4440, 4 p.

Patterson, D.A., 1986a, Zincian staurolites from the Balcooma area: Unpub. Mt. Isa Mines Mineral Services Report 5132, 16 p.

Patterson, D.A., 1986b, Petrology of samples from Dry River South, QH26524-28: Unpub. Mt. Isa Mines Mineral Services Report 5112, 7 p.

Pemberton, J., 1987, World data base, part 2--the Canadian Precambrian deposits (with emphasis on precious metal distribution): Unpub. AMIRA report, Univ. of Tasmania, 58 p.

Picot, P., and Johan, Z., 1982, Atlas of ore minerals: Elsevier, Amsterdam, 458 p.

Pisutha-Arnond, V., and Ohmoto, H., 1983, Thermal histroy, and chemical and isotopic compositions of the ore forming fluids responsible for the kuroko massive sulfide deposits in the Hokuroko district of Japan, in Ohmoto, H., and Skinner, B.J., eds., The kuroko and related volcanogenic massive sulfide deposits: Econ. Geol. Mon. 5, p. 523-558.

Price, P., 1934, The geology and ore deposits of the Horne Mine, Noranda, Quebec: Can. Inst. Min. Metal. Trans., v. 37, p. 108-140.

Ramdohr, P., 1969, The ore minerals and their intergrowths: Pergamon, London, 1174 p.

Ramsden, A.R., and Creelman, R.A., 1984, Precious metal mineralogy of Hellyer and Que River ores: CSIRO Restricted Investigation Report 1561R, 27 p.

Reed, M., 1982, Calculation of multicomponent chemical equilibria and reaction processes in systems involving minerals, gases and an aqueous phase: Geochim. Cosmochim. Acta, v. 46, p. 513-528.

Reid, K.O., and Meares, R.M.D., 1981, Exploration for volcanic-hosted sulfide deposits in western Tasmania: Econ. Geol., v. 76, p. 350-364.

Robinson, B.W., and Kusabe, M., 1975, Quantitative preparation of SO_2 for $^{34}S/^{32}S$ analysis, from sulphides by combustion with cuprous oxide: Analytical Chem., v. 47, p. 1179-1181.

Roedder, E., 1960, Fluid inclusions as samples of ore-forming fluids: Internat. Geol. Cong., 21st, Copenhagen, Proc., pt. 16, p. 218-229.

Rona, P.A., 1984, Hydrothermal mineralization at seafloor spreading centres: Earth-Science Reviews, v. 20, p. 1-104.

Rose, W.J., and Morrison, G.W., 1988, Classification of gold deposits using the silver content (fineness) of gold (abstract): Bicentennial Gold '88, extended abstracts, v. 2, p. 464-468.

Ruaya, J.R., and Seward, T.M., 1986, the stability of chlorozinc (II) complexes in hydrothermal solutions up to 350°C: Geochim. Cosmochim. Acta, v. 50, p. 651-661.

Rubenach, M.J., 1978, Northernmost section of the Tasman Orogenic Zone, in Rubenach, M.J., ed., Excursion handbook, Third Australian Geological Convention: Geol. Soc. Austr., Queensland Divison, Brisbane, p.43-67.

Ruxton, P., 1986, World data base, part 1--the kuroko deposits: Unpub. AMIRA report, Univ. of Tasmania, 27 p.

Ruxton, P., 1987, Gold-base metal relationships at Scuddles, Western Australia, in Controls on gold and silver grades in volcanogenic sulphide deposits (84/P810), August 1987 progress report: Unpub. AMIRA report, Univ. of Tasmania, p. 131-149.

Sack, R.O., and Loucks, R.R., 1985, Thermodynamic properties of tetrahedrite-tennantites: constraints on the interdependance of the Ag=Cu, Fe=Zn, Cu=Fe, and As=Sb exchange reactions: Am. Mineral., v. 70, p. 1270-1289.

Sahl, K., Doe, B.R., and Wedepohl, K.D., 1970, Lead, in Wedepohl, K.H., ed., Handbook of geochemistry: Berlin, Springer-Verlag, V. II-5, p. 82-A-1 to 82-O-1.

Sandecki, J., 1983, Silver-rich minerals at Garpenberg Norra, central Sweden: Neus Jahrb. Mineral. Mh., v. 8, p. 365-374.

Sandecki, J., and Amcoff, O., 1981, On the occurrence of silver-rich tetrahedrite at Garpenberg Norra, central Sweden: Neus Jahrb. Mineral. Abh., v. 141, p. 324-340.

Sangster, D.F., 1968, Relative sulphur isotope abundances of ancient seas and stratabound sulphide deposits: Geol. Assoc. Canada, Proc., v. 19, p. 79-91.

Sangster, D.F., 1972, Precambrian volcanogenic massive sulphide deposits in Canada: a review: Geol. Surv. Canada Paper 72-22, 44 p.

Sato, J., 1974, Ores and ore minerals from the Shakanai Mine, Akita Prefecture, Japan, in Ishihara, S., Geology of kuroko deposits: Min. Geol. Spec. Issue No. 6, p. 323-336.

Sato, T., 1972, Behaviors of ore-forming solutions in seawater: Min. Geol., v. 22, p. 31-42.

Sato, T., 1973, A chloride complex model for kuroko mineralisation: Geochem. Jour., v. 7, p. 245-270.

Seward, T.M., 1973, Thio complexes of gold in hydrothermal ore solutions: Geochim. Cosmochim. Acta, v. 37, p. 379-399.

Seward, T.M., 1976, The stability of chloride complexes of silver in hydrothermal solutions up to 350°C: Geochim. Cosmochim. Acta, v. 48, p. 1329-1341.

Seward, T.M., 1984a, The formation of lead (II) chloride complexes to 300°C: A spectroscopic study: Geochim. Cosmochim. Acta, v. 48, p. 121-134.

Seward, T.M., 1984b, The transport and deposition of gold in hydrothermal systems, in Foster, R. P., Gold '82: The geology, geochemistry and genesis of gold deposits: Geol. Soc. of Zimbabwe Spec. Pub. 1, p. 165-181.

Shalley, M.J., TEM in exploration for massive sulphides--a new discovery (abstract): Exploration Geophysics, v. 18, p. 199-201.

Shieh, Y.N., and Schwarcz, H.R., 1974, Oxygen isotope studies of granite and migmatite, Grenville province of Ontario: Geochim. Cosmochim. Acta, v. 38, p. 21-45.

Shikazono, N., and Shimuzu, M., 1987, The Ag/Au ratio of native gold and electrum and the geochemical environment of gold vein deposits in Japan: Mineral. Deposita, v. 22, p. 309-314.

Shimazaki, Y., 1974, Ores of kuroko-type deposits, in Ishihara, S., ed., Geology of kuroko deposits: Min. Geol. Spec. Issue No. 6, p. 311-322.

Shirozu, H., 1974, Clay minerals in altered wall rocks of the kuroko-type deposits, in Ishihara, S., ed., Geology of the kuroko deposits: Mining Geol. Special Issue 6, p. 303-310.

Shrock, R.R., 1948, Sequence in layered rocks: McGraw Hill, New York, 507 p.

Sillitoe, R.H., 1979, Some thoughts on gold-rich porphyry copper deposits: Mineral. Deposita, v. 14, p. 161-174.

Smith, R.N., 1975, Precious and volatile metal distributions in the ores and host rocks of the Rosebery sulphide deposit: Unpub. M.Sc. thesis, Univ. of Melbourne, 171 p.

Solomon, M., 1976, "Volcanic" massive sulfide deposits and their host rocks--a review and an explanation, in Wolf, K.A., ed., Handbook of strata-bound and stratiform ore deposits: Elsevier, Amsterdam, v. 6, p. 21-50.

Solomon, M., and Walshe, J.L., 1979, The formation of massive sulfide deposits on the sea floor: Econ. Geol., v. 74, p. 797-813.

Solomon, M., Rafter, T.A., and Jensen, M.L., 1969, Isotope studies on the Rosebery, Mount Farrell and Mount Lyell ores, Tasmania: Mineral. Deposita, v. 4, p. 172-199.

Solomon, M., Vokes, F.M., and Walshe, J.L., 1987, Chemical remobilization of volcanic-hosted sulfide deposits at Rosebery and Mt. Lyell, Tasmania: Ore Geol. Rev., v. 1, p. 173-190.

Solomon, M., Eastoe, C.J., Walshe, J.L., and Green, G.R., 1988, Mineral deposits and sulfur isotope abundances in the Mt. Read Volcanics between Que River and Mt. Darwin, Tasmania: Econ. Geol., v. 83, p. 1307-1328.

Spry, P.G., and Scott, S.D., 1986, Zincian spinel and staurolite as guides to ore in the Appalachians and Scandanavian Caledonides: Can. Mineral., v. 24, p. 147-163.

Stanton, R.L., 1959, Abundances of copper, zinc and lead in some sulfide deposits: Jour. Geol., v. 66, p. 484-502.

Stanton, R.L., 1960, General features of conformable pyritic orebodies: Can. Inst. Min. Metall. Bull., v. 63, p. 22-36.

Stanton, R.L., 1972, Ore petrology: McGraw Hill, New York, 713 p.

Stillwell, F.L., 1934, Observations on the zinc-lead lode at Rosebery, Tasmania: Proc. Aust. Inst. Min. Metal., no. 94, p. 43-67.

Stolz, A.J., and Large, R.R., 1988, The source of gold in the western Tasmanian volcanogenic massive sulphide deposits, in Controls on gold and silver grades in volcanogenic sulphide deposits: Unpub. AMIRA report, Univ. of Tasmania, p. 71-136.

Sugaki, A., Scott, S.D., Hayashi, K., and Kitakaze, A., 1987, Ag_2S solubility in sulfide solutions up to 250°C: Geochem. Jour., v. 21, p. 291-305.

Suzuoki, T., and Epstein, S., 1976, Hydrogen isotpoe fractionation between OH-bearing minerals and water: Geochim. Cosmochim. Acta, v. 40, p. 1229-1240.

Tanimura, S., Date, J., Takahashi, T. and Ohmoto, H., 1983, Geologic setting of the kuroko deposits, Japan, in Ohmoto, H., and Skinner, B. J., eds., The kuroko and related volcanogenic massive sulphide deposits: Econ. Geol. Mon. 5, p. 24-38.

Taylor, H.P., 1979, Oxygen and hydrogen isotope relationships in hydrothermal mineral deposits, in Barnes, H.L., ed., Geochemistry of hydrothermal ore deposits, second edition: Wiley, New York, p. 236-277.

Taylor, H.P., and Sheppard, S.M.F., 1986, Igneous rocks: I. Processes of isotopic factionaltion and isotope systematics, in Valley, J.W., Taylor, H.P., and O'Neill, J.R., eds., Stable isotopes in high temperature geological processes: Rev. in Mineralogy, v. 16, p. 227-272.

Thom, R., 1984, Summary of my contribution to the Balcooma project: Unpub. Chevron Exploration internal report, 7 p.

Turner, F.J., 1981, Metamorphic petrology, second edition: Wiley, New York, 524 p.

Turner, J.S., and Gustafson, L.B., 1978, The flow of hot saline solutions from vents on the sea floor: Some implications for exhalative massive sulfides and other ore deposits: Econ. Geol., v. 73, p. 1082-1100.

Urabe, T., and Sato, T, 1978, Kuroko deposits of the Kosaka Mine, Northeast Honshu, Japan: products of submarine hot springs on Miocene sea floor: Econ. Geol., v. 73, p. 161-179.

Van der Hor, F., 1984, 1983 annual report: Unpub. report to Carpentaria Exploration Company, Pty., Ltd., 25 p.

Van der Hor, F., 1986, Metamorphic hydrothermal alteration at the Balcooma massive sulfide deposit: Unpub. report to Carpentaria Exploration Company, Pty., Ltd., 46 p.

Van Hook, H.J., 1960, The ternary system Ag_2S-Bi_2S_3-PbS: Econ. Geol., v. 55, p. 759-788.

Vivallo, W., 1985, The geology and genesis of the Proterozoic massive sulfide deposit at Garpenberg, central Sweden: Econ. Geol., v. 80, p. 17-32.

Vokes, F.M., 1969, A review of the metamorphism of sulphide deposits: Earth-Sci. Rev., v. 5, p. 99-143.

Vokes, F.M., 1971, Some aspects of the regional metamorphic remobilisation of pre-existing sulphide deposits: Mineral. Deposita, v. 6, p. 122-129.

Walker, R.R., Matulich, A., Amos, A.C., Watkins, J.J., and Mannard, G.W., 1975, The geology of the Kidd Creek mine: Econ. Geol., v. 70, p. 80-89.

Walshe, J.L., and Solomon, M., 1981, An investigation into the environment of formation of the volcanic-hosted Mt. Lyell copper deposits using geology, mineralogy, stable isotopes and a six-component chlorite solid solution model: Econ. Geol., v. 76, p. 246-284.

Watanabe, N., 1971, Green tuff iron formations and associated ore deposits in the inner basins of Northeast Japan: Unpub. Ph.D. thesis, Waseda Univ. (in Japanese).

Whickham, S.M., and Taylor, H.P., 1985, Stable isotope evidence for large scale seawater infiltration in a regional metamorphic terrane; the Trois Seigneurs massif, Pyrenees, France: Contrib. Mineral. Petrol., v. 91, p. 122-137.

White, D.A., 1962, Einasleigh 1:250,000 Geological series sheet E/55-9: Bureau Mineral Resources, Australia, Explanatory Notes.

White, D.A., 1965, The geology of the Georgetown/Clarke River area: Bureau of Mineral Resources, Australia, Bulletin 71, 171 p.

White, J.L., Ore, R.L., and Hultgren, R., 1957, The thermodynamic properties of silver-gold alloys: Acta Metal., v. 5, p. 747-760.

Whitford, D.J., Creelman, R.A., and Ramsden, A.R., 1984, Petrological, geochemical and mineragraphic studies at Que River and Hellyer: CSIRO Restricted Investigation Report 1544R, 36 p.

Williams, K.L., 1960, Some less common minerals in the Rosebery and Hercules zinc-lead ores: Proc. Aust. Inst. Min. Metal., no. 196, p. 51-60.

Winchester, J.A., and Floyd, P.A., 1977, Geochemical discrimination of different magma series and their differentiation products using immobile elements: Chem. Geology, v. 20, p. 325-343.

Withnall, I.W., 1982, The geology of the Greenvale-Balcooma area, in Withnall, I.W., ed., Handbook for the 1982 field conference, Charters Towers-Greenvale area: Geol. Soc. Austr., Queensland Branch, Brisbane, p. 31-47.

Withnall, I.W., 1988, Preliminary compilation of the Conjubuoy 1:100,000 Sheet (7860): Geological Survey of Queensland, 1 sheet.

Withnall, I.W., Bain, J.H.C., and Rubenach, M.J., 1980, The Precambrian geology of northeastern Queensland, in, Henderson, R.A., and Stephenson, P.J., eds., The geology and geophysics of northeastern Australia: Geol. Soc. Aust., Queensland Division, Brisbane, p. 109-127.

Wood, S.A., Crerrar, D.A., and Borcsik, M.P., 1987, Solubility of the assemblage pyrite-pyrrhotite-magnetite-sphalerite-galena-gold-stibnite-bismuthinite-argentite-molybdenite in H_2O-NaCl-CO_2 solutions from 200°C to 350°C: Econ. Geol., v. 82, p. 1864-1887.

Wu, I., and Petersen, U., 1977, Geochemistry of tetraherite and mineral zoning at Casapalca, Peru: Econ. Geol., v. 72, p. 993-1016.

Yamada, R., Suyama, T., and Ogushi, O., 1987, Gold-bearing siliceous ore of the Nurukawa kuroko deposit, Akita prefecture, Japan: Mining Geol., v. 37, p. 109-118 (in Japanese).

Zachrisson, E., 1982, Spillitisation, mineralisation and vertical zonation at the Stekkenjokk stratabound sulphide deposit, Scandanavian Caledonides: Trans. Inst. Min. Metall., v. 91, p. B192-B199.

Zachrisson, E., 1984, Lateral metal zonation and stringer zone development, reflecting fissure-controlled exhalations at the Stekkenjokk-Levi stratabound sulfide deposit, central Scandanavian Caledonides: Econ. Geol., v.79, p. 1643-1659.

Zaw, K., Huston, D.L., and Large, R.R., 1988, Ore metal distribution, zonation and structural relationships at Rosebery, western Tasmania: Unpub. report, Univ. Tasmania, 20 p.

Appendix 1

Analytical techniques

Low level Na_2O determinations

Preparation of radiation buffer solution

(1) Dissolve 11.5 g $CaCl_2.2H_2O$ and 60.4 g $Sr(NO_3)_2$ in approximately 200 ml of distilled water.
(2) Dissolve 3.125 g Fe filings and 6.25 g Al powder in 50 ml concentrated hydrochloric acid. Heat slowly to complete dissolution.
(3) Filter both solutions into a 500 ml volumetric flask and dilute to volume.

Preparation of standard solutions

(1) Make up 1000 ppm Na stock solution by dissulving 1.271 g dry NaCl in distilled water and dilute to 500 ml.
(2) Dilute a 10 ml aliquot of stock solution to 1000 ml to make a 10 ppm Na solution.
(3) To each of four 100 ml volumetric flasks add 4 ml radiation buffer solution and 0, 2, 5 and 10 ml of the 10 ppm solution to make standards of 0, .2, .5 and 1.0 ppm Na.

Preparation of sample solutions

(1) To a teflon crucible add 200 mg of powdered sample, 10 ml nitric acid and 5 ml hydrofluoric acid. Heat and decompose. Rinse walls and evaporate dry.
(2) Add 5 ml nitric acid, rinse walls and evaporate dry.
(3) Add 2 ml perchloric acid, rinse walls, evaporate to white fumes, rinse walls and evaporate to no fumes.
(4) Add 20 ml of 1% hydrochloric acid and heat. Filter and dilute to 200 ml in volumetric flask.
(5) To a 100 ml volumetric flask transfer 4 ml radiation buffer solution and 10 ml sample solution. Dilute to volume with distilled water (overall dilution now 10000 X). Store in polythene bottles. Analyze as soon as possible.
(6) Repeat steps 1 through 5 with no sample twice to give two reagent blanks.

Analysis and data reduction

(1) Set atomic absorption spectrophotometer as follows: wavelength = 589.0 nm; slit = 0.33 nm; and air/C_2H_2 slightly oxidized flame with crossed burner.
(2) The sample blanks must be averaged and subtracted from samples to remove reagent contamination.
(3) The sample solution Na concentration in ppm is equal to the sample Na content in percent. The Na_2O content of the sample (in percent) may be calculated by multiplying the solution Na concentration (in ppm) by 1.35.

High level Cu, Pb and Zn analysis

Preparation of standard solutions

(1) Dissolve 0.500 g Zn metal in 50 ml 1:1 hydrochloric acid, 0.500 g Cu metal in 20 ml 1:1 nitric acid and 0.7993 g $Pb(NO_3)_2$ in 50 ml distilled water. Combine all solutions in a 500 ml volumetric flask and dilute to volume to produce a stock solution of 1000 ppm Zn, Cu and Pb.
(2) Dilute a 50 ml aliquot of the stock solution to 500 ml in a volumetric flask to produce a 100 ppm standard solution.
(3) To each of five 100 ml volumetric flasks add 1 g of Na_2O_2 and 10 ml 6 M hydrochloric acid. Add 0, 5, 10, 15 and 20 ml of 100 ppm standard solution to the flasks and dilute to volume. This produces standards containing 0, 5, 10, 15 and 20 ppm of Zn, Cu and Pb.

Preparation of sample solutions

(1) Add 1.0 g Na_2O_2 and 0.100 g of pulverized sample to a zirconium crucible and mix thouroughly.
(2) Heat, swirling gently, over a flame for three minutes. The mixture should melt and have a dull-red color only (higher temperatures damage the crucible).
(3) Cool and carefully add distilled water one drop at a time. A reaction will ensue.
(4) When the reaction has ceased, wash into a 150 ml beaker using distilled water until the volume is approximately 40 ml.
(5) Wash the crucible with 5 ml 6 M hydrochloric acid and heat for a few minutes.
(6) Add acid washings and an additional 5 ml of 6 M hydrochloric acid to the beaker and stir.
(7) Heat for 10 minutes; a clear solution should result.
(8) Cool and dilute to 100 ml in a volumetric flask using distilled water (1000 X dilution).

Analysis and data reduction

(1) The atomic absorption spectrophotometer should be set up as follows: air/C_2H_2 flame for all elements; 324.7 nm wavelength and 0.2 nm slit for copper; 217.0 nm wavelength and 1.0 nm slit for lead; and 213.9 nm wavelength and 0.2 nm slit with crossed burner for zinc.
(2) The concentrations in the sample can be calculated by multiplying the concentrations in the solution by 1000.

Sulfur analysis

Preparation of reagents

(1) Dissolve 4.44 g of KIO_3 and dilute to 1 liter with distilled water (KIO_3 solution).

(2) Dilute 15 ml of concentrated hydrochloric acid to 1 liter with distilled water (hydrochloric acid solution).

(3) Suspend 2 g Arrowroot starch in 50 ml of distilled water. Add suspension to 150 ml boiling distilled water slowly and stir. Boil for one minute, cool and add 6 g KI to the solution (starch solution). The solution must be clear; if not it may be filtered. It will keep for one week and should be discarded when it takes on a reddish tinge during titration. This solution is appropriate for samples containing between 0 and 40% sulfur and has a detection limit of 0.1%.

Sample analysis

(1) To a disposable porcelain crucible add 0.3 g sample and about 3 g copper filings. For high sulfur samples use 0.1 to 0.2 g sample and 1 to 2 g copper filings.

(2) Insert the porcelain crucible into the induction furnace on a Leco 632-000 automatic titration aparatus and close. Half fill the glass reaction vessel on the titrator with hydrochloric acid solution and add 5 ml of starch solution to produce a deep blue color. Top up the titrator with KIO_3 solution.

(3) Bubble oxygen through the furnace and solution in the titrator reaction vessel. Begin combustion by starting the induction furnace at the medium setting. The reaction will begin slowly, but after several minutes the grid reading should begin to climb. If not, turn the induction furnace up to the high setting. For complete combustion of sulfur the grid reading should exceed 500, but if it exceeds 500 for too long, the copper filings might melt through the crucible and damage the apparatus. When the reading reaches 500, turn the induction furnace setting to low. Let combustion proceed for six minutes. If SO_2 is still forming at the end of this period, continue combustion until it ceases. Read the amount of KIO_3 solution titrated on the titration tube.

(4) Analyze one standard for every ten samples.

Data reduction

(1) Conversion factors (F) may be calculated from the known standards using the following equation:

$$F = (\text{known concentration})(\text{weight})/(\text{titration reading})$$

The calculated conversions should then be averaged to produce the accepted conversion factor.

(2) The sample concentration may be calculated by multiplying the conversion factor by the titaration reading for the sample and the sample weight.

Barium analysis

Preparation of standard solutions

(1) Dissolve 1.4369 g $BaCO_3$ in weak hydrochloric acid containing 0.2% K (3.8 g/l KCl) to produce a 1000 ppm stock solution.
(2) Dilute a 50 ml aliquot of stock solution to 500 ml in a volumetric flask using 0.2% K solution to produce a 100 ppm stock solution.
(3) To each of four 100 ml volumetric flasks add 0 ml, 10 ml, 20 ml and 50 ml of 100 ppm stock solution and dilute to volume. This produces standard solutions containing 0, 10, 20 and 50 ppm of Ba.

Preparation of sample solutions

(1) Add 2.0 g Na_2O_2 and 0.200 g sample to a zirconium crucible and mix thoroughly.
(2) Heat, swirling gently, over a flame for three minutes. The mixture should melt and have a dull red color only (higher temperatures may damage the crucible).
(3) Cool and carefully add distilled water one drop at a time. A reaction will ensue.
(4) When the reaction has ceased wash precipitate with distilled water, centrifuge and decant. Repeat. Dissolve precipitate with HCl and wash into and dilute to volume in a 50 ml volumetric flask (250x dilution) using 0.2% K solution.

Analysis and data reduction

(1) The atomic absorption spectrophotometer should be set up as follows: NO_2/C_2H_2 flame with a lamp current of 20 mA, a wavelength of 553.6 nm and a 0.2 nm slit.
(2) The concentrations in the sample can be calculated by multiplying the concentrations in the solution by 250.

* Dilute using 0.2% K solution unless otherwise indicated.

Appendix 2

Analytical results

Table A2-1. Whole rock analyses from Balcooma.

Sample	SiO2 (%)	TiO2 (%)	Al2O3 (%)	Fe2O3 (%)	MnO (%)	MgO (%)	CaO (%)	Na2O (%)	K2O (%)	P2O5 (%)	LOSS (%)	TOTAL (%)	S (%)	Pb (ppm)	Zn (ppm)	Cu (ppm)	Nb (ppm)	Zr (ppm)	Y (ppm)	Sr (ppm)	Rb (ppm)
Microgranite																					
6-205.0	68.57	0.54	14.55	4.62	0.03	1.57	1.58	7.13	0.35	0.16	0.87	99.97	0.0	3	22	11	18	359	40	152	15
6-111.8	78.17	0.16	11.99	1.51	0.01	0.33	0.95	5.64	0.90	0.01	0.71	100.38	0.0	3	6	6	17	156	43	95	19
Quartz-feldspar porphyry																					
39A-109.7	77.83	0.08	11.97	1.40	0.01	0.20	0.27	6.04	0.52	0.00	0.98	99.32	0.1	31	110	57	14	104	36	61	11
6-419.6	73.23	0.24	13.95	1.49	0.02	0.46	1.45	6.04	1.49	0.04	1.08	99.50	0.0	9	3	9	13	165	26	145	29
Felsite																					
54-236.5	78.50	0.13	11.95	0.90	0.01	0.33	0.32	6.09	0.48	0.00	0.67	99.38	0.0	16	2	1	18	205	52	87	15
Quartz-muscovite schist with biotite and staurolite porphyroblasts (spotted schist)																					
4-117.8	77.03	0.40	8.17	5.96	0.06	2.44	0.17	0.24	2.18	0.12	2.33	99.09	1.3	44	24	42	9	227	21	13	87
12-42.8	63.21	0.77	15.59	10.30	0.12	3.39	0.27	0.27	2.83	0.15	2.68	99.58	1.0	20	141	202	17	197	34	15	133
12A-71.3	72.06	0.57	10.47	7.64	0.07	2.25	0.25	0.21	2.77	0.12	3.44	99.84	1.6	71	20	596	12	218	27	16	96
44-91.8	66.15	0.72	15.75	9.14	0.09	3.02	0.27	0.41	2.81	0.14	1.83	100.35	0.7	92	477	130	18	166	29	31	109
F896-172.5	56.71	0.83	18.29	11.64	0.12	4.36	0.22	0.29	4.21	0.15	2.89	99.70	1.4	30	116	691	21	159	37	18	176
Quartz-biotite-muscovite schist with staurolite porphyroblasts (snowball schist)																					
23-233.6	66.28	0.71	16.37	6.39	0.09	3.04	0.84	1.79	2.67	0.13	2.05	100.37	0.0	21	93	14	17	208	37	70	94
23A-162.7	63.35	0.77	16.80	7.58	0.14	3.60	0.68	0.75	3.94	0.14	2.03	99.78	0.0	55	136	41	18	167	35	58	136
D860-193.8	63.73	0.80	17.16	6.94	0.10	3.20	0.45	0.82	4.05	0.16	2.19	99.60	0.1	23	74	20	20	192	35	39	180
Quartz-muscovite-biotite±albite schist (upper metagraywacke)																					
6-299.3	73.49	0.65	12.69	4.01	0.04	1.98	0.99	2.23	2.46	0.18	1.50	100.22	0.0	17	31	4	17	304	37	75	82
49-166.4	72.51	0.55	11.08	8.30	0.14	2.74	0.25	0.12	2.19	0.14	1.08	99.10	0.0	12	207	14	13	195	27	11	103
D860-57.9	80.48	0.42	8.44	4.12	0.08	1.96	0.42	0.13	2.47	0.12	1.35	99.99	0.3	14	16	34	10	208	25	40	95
Quartz-biotite-albite schist (lower metagraywacke)																					
23-170.0	78.13	0.46	9.79	3.06	0.05	2.07	1.23	1.55	2.03	0.16	0.90	99.43	0.0	46	57	3	11	344	26	87	68
23A-149.7	79.92	0.38	8.24	4.56	0.05	1.93	0.43	0.28	2.57	0.16	1.84	100.36	0.2	20	42	60	11	300	19	20	71
D860-117.5	74.86	0.55	11.44	4.66	0.05	2.14	0.60	2.01	2.36	0.15	1.30	100.11	0.1	7	27	13	13	226	27	63	95
Quartz-muscovite-biotite-feldspar schist and felsic fragmentals (metatuff)																					
23-217.7	74.38	0.25	13.14	3.07	0.04	1.65	0.58	3.80	1.74	0.02	1.37	100.04	0.3	23	63	6	19	202	40	69	84
Q860-360.1	73.82	0.20	13.24	3.99	0.05	1.75	0.10	0.37	3.91	0.01	2.27	99.72	0.3	8	96	39	15	215	33	19	151
J900-136.0	74.57	0.24	13.54	2.92	0.03	1.18	0.42	0.59	3.44	0.02	2.61	99.56	0.5	36	90	6	15	278	38	35	122

Table A2-1. Whole rock analyses from Balcooma (continued).

Sample	SiO2 (%)	TiO2 (%)	Al2O3 (%)	Fe2O3 (%)	MnO (%)	MgO (%)	CaO (%)	Na2O (%)	K2O (%)	P2O5 (%)	LOSS (%)	TOTAL (%)	S (%)	Pb (ppm)	Zn (ppm)	Cu (ppm)	Nb (ppm)	Zr (ppm)	Y (ppm)	Sr (ppm)	Rb (ppm)
Weakly chloritized quartz-muscovite-biotite-staurolite schist (weak chloritic alteration)																					
12-45.5	74.44	0.49	9.03	7.51	0.06	1.93	0.61	0.21	1.88	0.16	3.52	99.84	1.8	8	63	283	13	437	31	15	70
12-45.0	77.99	0.39	8.41	6.82	0.07	2.51	0.19	0.41	1.43	0.12	1.30	99.64	0.6	5	93	67	10	268	25	5	62
39-154.7	77.55	0.44	9.44	6.71	0.04	2.47	0.26	0.42	2.04	0.14	0.83	100.35	0.0	11	5	8	13	212	23	36	76
39-151.5	69.20	0.56	11.23	11.97	0.14	3.68	0.32	0.10	1.17	0.15	1.30	99.82	0.0	5	80	16	14	233	32	10	53
55-338.1	74.09	0.68	11.71	4.60	0.06	2.47	0.63	2.51	1.64	0.24	0.96	99.60	0.0	11	69	2	15	398	35	44	84
L920-164.5	63.62	0.66	12.34	11.33	0.18	4.41	0.30	0.10	2.47	0.14	3.90	99.46	1.4	69	577	1290	17	174	25	15	134
Quartz-chlorite schist (moderate chloritic alteration)																					
4-82.0	56.45	0.56	12.33	16.12	0.22	7.03	0.24	0.00	0.55	0.13	5.38	99.01	0.2	6	258	145	12	159	27	5	32
4-109.8	59.92	0.33	5.72	18.60	0.13	4.68	0.26	0.15	0.26	0.20	8.95	99.20	7.9	26	257	1470	9	327	25	4	11
39-143.6	73.23	0.37	6.78	11.91	0.10	3.25	0.20	0.00	0.02	0.09	3.27	99.22	0.0	0	134	134	9	150	24	15	2
41-141.4	67.37	0.15	9.74	15.29	0.16	4.47	0.10	0.00	0.00	0.02	2.58	99.88	0.4	0	87	422	9	133	48	0	0
44-94.5	72.69	0.37	7.02	12.71	0.10	3.85	0.10	0.02	0.03	0.07	2.07	99.02	0.2	2	470	154	9	74	13	4	0
44-97.6	57.36	0.43	10.66	16.61	0.13	5.45	0.95	1.29	1.17	0.10	5.70	99.85	3.3	78	470	4150	14	171	33	41	51
44-124.8	64.48	0.16	2.98	27.62	0.12	2.64	0.12	0.00	0.22	0.01	1.26	99.61	1.3	23	306	1110	2	30	4	4	10
49-127.9	68.41	0.46	8.94	14.94	0.19	4.85	0.18	0.09	0.01	0.11	2.07	100.24	0.2	2	254	147	11	97	17	0	0
Chlorite schist (strong chloritic alteration)																					
3-228.5	32.31	1.00	20.83	13.04	0.35	18.55	0.93	0.09	2.77	0.30	9.40	99.57	0.4	32	839	5	23	540	52	7	146
12A-85.3	29.36	0.30	22.92	29.10	1.48	7.50	0.46	0.00	1.76	0.02	7.52	100.42	3.0	62	771	1410	12	364	74	9	76
12A-92.1	19.07	0.29	12.53	39.87	0.26	6.42	0.20	0.00	1.46	0.02	18.75	98.87	16.6	154	894	4790	22	252	28	3	76
16A-141.2	34.32	0.44	16.65	30.96	0.18	10.99	0.26	0.00	0.00	0.14	6.21	100.15	0.3	2	376	259	15	158	13	0	0
39-140.4	27.84	0.33	20.04	31.30	0.08	10.19	0.13	0.12	3.51	0.04	5.96	99.54	0.7	34	520	622	16	397	67	6	133
40-311.0	27.03	0.91	19.47	15.05	0.47	21.01	0.37	0.00	1.26	0.30	12.79	98.65	4.4	6960	3130	347	69	362	39	0	70
L920-160.0	28.49	0.94	21.10	13.19	0.36	22.94	0.18	0.00	0.01	0.15	12.04	99.40	0.0	5	2040	12	21	148	35	0	0
L920-163.2	24.30	0.89	20.55	23.84	0.39	16.58	0.31	0.00	0.78	0.22	10.56	98.42	3.6	217	3040	4670	26	299	44	4	41
Pyritic quartz-muscovite-biotite schist (Quartz-sericite-pyrite alteration)																					
3-138.5	68.88	0.72	15.07	5.89	0.02	1.04	0.17	0.37	4.04	0.12	3.86	100.18	2.5	87	137	354	17	154	29	20	152
4-103.7	74.30	0.50	10.08	6.02	0.05	0.59	0.70	0.32	2.09	0.11	4.70	99.47	2.1	58	54	48	14.2	136	20	28	66
12A-87.0	89.21	0.18	3.49	3.53	0.03	0.89	0.01	0.00	0.72	0.00	1.28	99.34	0.6	58	108	606	8	48	7	9	32
24-123.4	46.73	0.57	28.98	6.18	0.03	1.82	0.44	0.99	6.96	0.03	6.56	99.29	2.9	575	2060	2	58	547	67	51	256
44-92.9	58.39	0.56	11.09	16.81	0.17	6.35	0.21	0.00	0.06	0.13	4.54	98.32	0.9	0	1520	350	16	134	21	4	8
J920-71.7	78.60	0.17	10.27	3.55	0.03	1.44	0.05	0.11	2.75	0.02	2.45	99.45	1.6	99	4060	284	14	218	35	15	117
12-114.1	71.57	0.61	13.29	3.90	0.04	2.11	0.12	0.25	4.08	0.09	3.14	99.20	1.5	112	2190	353	21	195	32	25	192

Table A2-1. Whole rock analyses from Balcooma (continued).

Sample	SiO2 (%)	TiO2 (%)	Al2O3 (%)	Fe2O3 (%)	MnO (%)	MgO (%)	CaO (%)	Na2O (%)	K2O (%)	P2O5 (%)	LOSS (%)	TOTAL (%)	S (%)	Pb (ppm)	Zn (ppm)	Cu (ppm)	Nb (ppm)	Zr (ppm)	Y (ppm)	Sr (ppm)	Rb (ppm)
Replicates																					
D860-193.8(REP)	64.15	0.84	17.21	6.80	0.11	3.00	0.45	0.92	4.41	0.19	2.18	100.26	0.1	23	75	20	19	197	34	40	180
D860-57.9(REP)	80.61	0.41	8.38	4.09	0.07	1.97	0.42	0.29	2.36	0.14	0.88	99.62	0.2	11	15	33	10	216	24	41	97
44-97.6(REP)	58.69	0.46	10.67	15.72	0.13	5.23	0.95	1.14	1.20	0.10	5.83	100.12	3.2	84	459	4133	14	181	36	39	51
39A-109.7(REP)	79.00	0.08	12.20	1.37	0.01	0.02	0.27	6.04	0.52	0.00	0.61	100.14	0.2	31	112	55	15	109	39	65	12
44-124.8(REP)	66.11	0.17	3.05	25.22	0.13	2.71	0.14	0.08	0.23	0.00	1.24	99.09	1.2	22	294	1078	3	32	3	0	10

Table A2-2. Whole rock analyses from Dry River South.

Sample	SiO2 (%)	TiO2 (%)	Al2O3 (%)	Fe2O3 (%)	MnO (%)	MgO (%)	CaO (%)	Na2O (%)	K2O (%)	P2O5 (%)	LOSS (%)	TOTAL (%)	S (%)	Pb (ppm)	Zn (ppm)	Cu (ppm)	Nb (ppm)	Zr (ppm)	Y (ppm)	Sr (ppm)	Rb (ppm)
Intrusive felsite																					
DRS38-298.8	76.59	0.17	12.32	2.64	0.02	0.86	0.63	4.66	1.50	0.00	0.76	100.15	0.0	8	24	6	34	292	79	68	69
Quartz-feldspar-porphyry																					
DRS20-241.9	71.70	0.33	13.38	3.87	0.07	1.78	1.91	4.47	1.33	0.06	0.68	99.58	0.0	35	44	6	12	156	31	215	70
DRS21-131.6	71.50	0.25	13.80	3.36	0.05	1.24	1.38	6.15	0.97	0.06	0.86	99.62	0.0	13	62	7	13	171	29	89	43
DRS16-288.3 (QH37315)	67.60	0.31	13.10	3.59	0.05	1.36	1.65	4.65	2.80	0.07	0.66	95.84									
Altered quartz-feldspar porphyry																					
DRS46W-408.7	63.15	0.28	13.95	9.82	0.06	2.34	0.05	0.41	4.19	0.05	5.27	99.57	4.9	200	661	9	22	249	141	18	174
Quartz-muscovite-biotite schist																					
QH26573	70.00	0.17	11.30	4.88	0.03	1.07	0.27	2.04	2.41	0.03	2.15	94.35									
Quartz-biotite-muscovite schist with staurolite porphyroblasts (metapelite); within massive sulfide																					
DRS15-199.1	62.69	0.61	15.53	7.62	0.11	4.53	0.51	1.00	4.58	0.12	2.15	99.45	0.3	254	676	47	29	154	42	43	213
Muscovite-biotite-quartz phyllite (metapelite)																					
DRS22-100.9	55.42	0.84	21.52	7.78	0.10	4.03	0.43	1.39	5.49	0.14	3.01	100.15	0.0	8	120	43	22	137	35	79	206
Quartz-muscovite-biotite schist with staurolite porphyroblasts (metapelite)																					
DRS19-169.6	56.29	0.78	21.16	8.02	0.11	4.05	0.36	0.99	4.73	0.16	2.99	99.64	0.2	12	255	65	20	130	39	49	183
DRS22-128.4	49.12	1.04	23.99	7.83	0.19	3.73	1.01	1.14	5.06	0.18	5.89	99.18	0.0	7	181	1	23	265	57	95	220
DRS22-156.8	59.78	0.82	19.82	7.92	0.09	4.22	0.67	1.21	3.78	0.14	1.83	100.28	0.0	10	145	51	19	136	33	50	163
DRS22-170.6	60.13	0.78	19.26	7.95	0.12	3.56	0.68	1.43	4.33	0.13	2.00	100.37	0.1	107	348	54	19	135	32	59	185
DRS22-180.8 (QH37310)	60.30	0.78	18.50	8.29	0.12	3.80	0.29	0.73	5.91	0.17	2.11	101.00									
DRS22-215.6	57.28	0.83	20.61	7.21	0.08	3.40	0.25	1.19	4.85	0.12	3.88	99.70	0.1	10	121	40	19	128	34	56	170
DRS25-83.2	58.81	0.71	18.90	8.89	0.08	3.71	0.28	0.89	4.37	0.14	3.53	100.31	0.5	7	86	169	18	128	33	41	170
DRS25-313.1	60.62	0.78	17.93	7.45	0.10	3.98	0.94	1.55	3.79	0.18	1.99	99.31	0.0	8	140	9	19	156	35	56	172
DRS27-255.9	58.09	0.79	19.70	8.41	0.08	4.38	0.44	1.55	4.44	0.15	2.34	100.37	0.0	10	141	49	20	132	35	39	184
DRS32-132.5	64.44	0.51	11.64	6.83	0.38	3.94	7.42	2.08	0.72	0.09	1.19	99.24	0.0	8	161	14	13	184	39	157	31
DRS32-259.4	62.59	0.76	17.58	7.16	0.10	3.57	0.62	1.01	3.64	0.17	2.56	99.76	0.1	49	138	22	19	161	36	37	144

Table A2-2. Whole rock analyses from Dry River South (continued).

Sample	SiO2 (%)	TiO2 (%)	Al2O3 (%)	Fe2O3 (%)	MnO (%)	MgO (%)	CaO (%)	Na2O (%)	K2O (%)	P2O5 (%)	LOSS (%)	TOTAL (%)	S (%)	Pb (ppm)	Zn (ppm)	Cu (ppm)	Nb (ppm)	Zr (ppm)	Y (ppm)	Sr (ppm)	Rb (ppm)
Quartz-biotite-albite schist (metagraywacke)																					
DRS15-132.7	69.90	0.67	13.27	4.59	0.08	2.80	1.25	4.23	1.18	0.21	1.38	99.56	0.0	5	95	4	17	298	38	111	49
DRS19-159.4	74.00	0.59	12.39	4.33	0.07	2.15	0.94	2.31	2.15	0.18	1.27	100.38	0.0	6	82	4	15	295	36	92	92
DRS22-110.2	63.48	0.75	16.71	6.56	0.07	3.04	1.12	2.08	3.77	0.15	1.90	99.63	0.0	9	74	4	17	179	36	110	137
DRS22-192.7	72.76	0.59	12.54	4.44	0.09	1.97	0.86	3.67	1.38	0.16	1.11	99.57	0.4	442	322	62	15	318	36	77	65
DRS22-197.8 (QH37311)	66.50	0.68	11.20	3.94	0.04	2.56	0.61	5.04	0.19	0.20	1.63	92.59									
DRS22-205.6	55.95	0.89	21.45	7.73	0.09	4.08	0.26	1.74	4.37	0.18	3.12	99.86	0.1	9	116	91	22	149	38	75	154
DRS22-226.7	67.16	0.72	15.47	5.76	0.07	3.11	0.71	1.74	2.95	0.16	1.88	99.73	0.0	10	92	6	17	233	32	60	124
DRS22-233.5	70.69	0.63	13.32	5.80	0.06	3.23	0.65	1.71	2.41	0.16	1.81	100.47	0.0	11	125	8	16	236	29	48	102
DRS25-129.0	60.16	0.85	19.66	6.76	0.09	3.53	0.54	1.86	4.12	0.15	2.69	100.41	0.0	11	41	10	21	165	34	96	148
DRS25-197.1	68.86	0.61	13.57	5.81	0.06	3.10	0.63	2.74	2.01	0.13	1.73	99.25	0.0	8	30	4	15	162	28	114	97
DRS25-302.4	73.23	0.60	11.92	4.01	0.06	2.63	0.75	4.40	0.56	0.17	1.51	99.84	0.0	3	70	4	14	332	34	74	22
DRS32-245.4	71.91	0.57	11.79	4.82	0.06	3.04	0.79	2.91	1.65	0.11	1.59	99.24	0.0	7	149	5	15	288	34	78	82
Felsic fragmental; probable volcanoclastic																					
DRS15-197.5	62.52	0.36	19.47	3.81	0.05	2.32	1.36	2.53	4.17	0.04	2.90	99.53	0.0	348	241	2	19	388	75	125	166
Felsite (extrusive?)																					
DRS17-263.0	70.03	0.34	15.50	3.00	0.05	1.36	1.73	6.07	1.04	0.08	1.28	100.48	0.0	68	107	5	14	268	46	100	42
Fragmental pyritic quartz-muscovite-biotite schist in hanging wall																					
DRS36-395.2 (QH45169)	60.75	0.15	12.81	14.20	0.08	1.97	0.28	0.55	3.87	0.01	5.08	99.75	5.4	132	203	1490	30	280	70	28	135
Pyrite quartz-chlorite schist (chloritic alteration)																					
DRS22-289.3 (QH37312)	43.80	0.12	10.40	26.20	0.10	2.93	0.08	0.20	2.50	0.02	12.00	98.35									
Pyritic quartz-muscovite-biotite schist (quartz-sericite-pyrite alteration)																					
DRS16-225.6 (QH37033)	24.37	0.12	10.51	31.67	0.06	4.13	0.03	0.28	3.52	0.03	23.71	98.43	23.2	257	1180	35	35	280	53	11	222
DRS18-318.7 (QH37113)	69.19	0.11	10.05	10.16	0.04	1.55	0.04	0.13	2.52	0.03	6.07	99.89	5.4	627	719	393	26	227	43	15	90
DRS22-266.5 (QH26681)	53.09	0.16	13.21	16.71	0.02	0.67	0.03	0.39	3.59	0.02	12.14	100.03	11.5	193	347	3760	37	296	82	12	125
DRS22-268.5 (QH37316)	57.80	0.12	9.60	19.60	0.01	0.50	0.03	0.29	2.70	0.03	9.41	100.09									
DRS22-276.5 (QH37317)	70.30	0.14	12.80	8.57	0.04	1.40	0.03	0.38	3.82	0.03	2.76	100.27									
DRS22-319.8 (QH37313)	65.20	0.14	12.50	7.67	0.04	1.95	0.06	0.36	4.20	0.03	4.09	96.24									
DRS22-341.8 (QH37314)	67.00	0.13	10.70	7.37	0.03	1.16	0.05	0.21	4.02	0.01	4.14	94.82									
DRS22-349.3	72.87	0.12	10.50	7.04	0.03	1.24	0.03	0.21	3.06	0.00	4.17	99.27	3.5	43	90	15	27	228	55	9	147
DRS24-235.5	56.89	0.19	17.72	8.82	0.03	0.92	0.04	0.69	3.99	0.03	6.27	95.59	5.9	12900	21100	1190	78	458	66	17	194
DRS25-351.3	70.83	0.15	12.72	7.84	0.08	1.38	0.03	0.27	2.98	0.01	2.96	99.25	1.5	14	45	247	17	275	45	10	120
DRS27-338.3	67.40	0.13	11.22	10.77	0.37	2.25	0.06	0.21	2.47	0.01	4.10	98.99	3.0	60	289	1960	29	245	78	10	101
DRS27-349.9	76.62	0.14	12.23	3.83	0.06	1.41	0.01	0.24	3.52	0.01	2.23	100.30	0.6	42	3420	100	32	273	80	12	144
DRS32-276.5 (QH37412)	69.82	0.15	12.27	7.79	0.04	1.74	0.27	0.22	3.19	0.01	4.26	99.76	2.4	472	1430	603	32	296	73	21	120

Table A2-2. Whole rock analyses from Dry River South (continued).

Sample	SiO2 (%)	TiO2 (%)	Al2O3 (%)	Fe2O3 (%)	MnO (%)	MgO (%)	CaO (%)	Na2O (%)	K2O (%)	P2O5 (%)	LOSS (%)	TOTAL (%)	S (%)	Pb (ppm)	Zn (ppm)	Cu (ppm)	Nb (ppm)	Zr (ppm)	Y (ppm)	Sr (ppm)	Rb (ppm)
Pyritic quartz-muscovite-biotite schist (continued)																					
DRS32-277.5 (QH37413)	70.90	0.13	11.34	7.10	0.03	0.88	0.86	0.24	2.93	0.02	5.00	99.43	3.4	225	488	208	31	264	64	26	102
DRS38-275.5 (QH45130)	67.70	0.14	13.61	6.84	0.02	0.68	0.02	0.36	3.53	0.00	3.59	96.49	3.4	7860	10100	527	49	344	58	16	150
DRS38-276.5 (QH45131)	65.29	0.17	16.10	5.94	0.02	1.03	0.02	0.41	4.33	0.00	3.84	97.15	2.9	12500	10700	1130	69	429	72	19	192
Fragmental pyritic-quartz-muscovite-biotite schist (Quartz-sericite-pyrite alteration of a volcaniclastic)																					
DRS39-168.9 (QH45180)	55.73	0.29	15.14	10.85	0.07	3.67	0.52	1.85	3.16	0.13	6.26	97.67	6.4	11000	13800	1060	50	350	60	73	179
DRS39-170.0 (QH45199)	66.26	0.27	15.53	4.89	0.06	2.75	0.38	2.20	3.37	0.02	2.93	98.66	1.5	1590	4020	196	25	301	51	53	146
DRS39-171.0 (QH45200)	62.58	0.24	14.62	7.47	0.06	2.51	0.43	1.87	2.98	0.02	4.38	97.16	3.9	5100	12400	973	38	338	71	57	134
DRS39-172.0 (QH45201)	55.18	0.36	13.07	13.93	0.08	3.18	0.45	0.63	3.44	0.05	8.27	98.64	8.9	1108	3040	312	31	257	47	44	175
Replicates																					
DRS25-83.2 (REP)	58.66	0.73	18.90	8.86	0.08	3.76	0.29	0.86	4.55	0.14	3.52	100.35	0.5	7	82	166	18	129	34	43	172
DRS16-225.6 (REP)	24.35	0.12	10.51	31.84	0.06	4.02	0.02	0.22	3.38	0.03	23.74	98.29	22.9	268	1170	36	36	272	55	12	229
DRS27-338.3(REP)	68.61	0.15	11.44	10.40	0.37	2.06	0.05	0.23	2.57	0.00	4.06	99.94	3.0	61	289	1880	29	248	78	10	102
DRS22-170.4(REP)	60.62	0.82	19.09	7.65	0.10	3.36	0.69	1.47	4.36	0.15	2.08	100.39	0.1	109	328	52	18	138	32	61	188

Table A2-3. Trace element analyses of bulked splits from Dry River South massive sulfide (analyses by Australian Laboratory Services for Carpentaria Exploration Company by induction coupled plasma).

Drill hole	From (m)	To (m)	Cu (%)	Pb (%)	Zn (%)	Ag (ppm)	Au (ppm)	As (ppm)	Ba (ppm)	Bi (ppm)	Ga (ppm)	Ge (ppm)	Hg (ppm)	Se (ppm)	Sb (ppm)	Sn (ppm)	Tl (ppm)	Cd (ppm)	Co (ppm)
Massive pyrite-chalcopyrite																			
DRS19	209.9	210.7	1.56	1.08	1.30	46	1.30	330	140	145	35	<20	<4	<2	72	190	20	30	130
DRS22	247.6	249.2	1.77	0.11	0.19	18	0.53	145	240	480	15	<20	<4	8	16	120	<10	12	150
DRS22	251.5	254.2	1.37	0.17	0.33	26	0.67	280	20	125	20	<20	<4	2	8	130	10	21	40
DRS27W	317.2	319.0	1.73	1.30	3.43	46	0.91	290	150	190	55	<20	<4	<2	16	300	30	85	45
DRS27W	320.9	322.7	3.91	0.65	2.55	35	0.99	400	40	90	25	<20	<4	2	32	250	<10	60	50
DRS32W	265.5	268.5	1.54	0.14	0.38	29	0.68	440	70	310	20	<20	<4	6	20	110	<10	25	150
DRS33	280.2	282.2	0.96	0.11	0.29	24	0.65	95	210	180	15	<20	<4	10	4	140	<10	20	75
DRS35	347.4	349.5	1.50	0.50	2.06	57	0.96	145	160	440	30	<20	<4	16	4	160	<10	60	145
Massive pyrite-sphalerite-galena																			
DRS17	266.3	269.4	0.38	4.19	10.73	125	0.80	220	70	550	85	<20	<4	<2	40	710	10	220	160
DRS19	205.2	207.6	1.25	4.88	16.86	73	0.86	940	180	150	130	<20	<4	<2	104	240	10	310	15
DRS19	207.6	209.9	0.38	5.74	14.03	135	0.88	320	640	470	155	<20	<4	<2	76	210	20	250	20
DRS19	210.7	212.3	0.33	4.77	8.55	131	0.73	70	510	560	125	<20	<4	<2	52	120	20	155	55
DRS21	177.6	181.4	0.52	4.40	9.76	70	0.65	<5	680	95	115	<20	<4	<2	52	30	<10	190	10
DRS22	249.2	251.5	0.77	5.85	16.51	100	0.67	220	40	470	135	<20	<4	<2	36	280	10	320	25
DRS27W	319.0	320.9	1.27	1.68	9.27	49	0.71	310	40	145	60	<20	<4	<2	24	520	<10	175	35
DRS27W	322.7	324.3	0.46	7.91	18.70	177	1.05	15	40	920	220	<20	<4	<2	24	310	10	340	20
DRS31	320.6	321.5	0.40	2.12	8.84	48	0.40	165	50	180	50	<20	<4	<2	32	105	10	165	35
DRS32W	262.3	265.5	0.39	4.08	13.61	71	0.65	150	90	270	150	<20	<4	<2	48	450	20	260	25
DRS32W	268.5	271.6	0.76	2.15	18.74	91	0.55	55	70	410	75	<20	<4	<2	20	210	10	390	20
DRS34	373.9	375.0	1.28	1.81	6.92	72	0.75	260	30	330	30	<20	<4	<2	24	320	20	140	70

Table A2-4. Microprobe analyses of staurolites from DRS-22, Dry River South Prospect, Northern Queensland.

Sample	Grain	MgO (%)	Al_2O_3 (%)	SiO_2 (%)	TiO_2 (%)	Fe_2O_3 (%)	ZnO (%)	Total (%)	ZnO/TiO_2
DRS22-110.5	1	1.63	53.63	26.13	0.48	13.76	0.57	96.20	1.19
DRS22-110.5	2	1.98	54.57	26.70	0.51	13.81	0.76	98.33	1.49
DRS22-110.5	3	2.04	54.05	27.04	0.47	13.57	1.00	98.17	2.13
DRS22-128.4	1	3.38	53.49	25.99	0.47	13.01	0.75	97.10	1.60
DRS22-128.4	2	3.42	53.56	26.54	0.60	13.23	0.43	97.78	0.72
DRS22-128.4	3	3.19	53.42	25.83	0.60	13.00	0.55	96.59	0.92
DRS22-156.8	1	2.48	54.36	25.49	0.55	13.84	0.00	96.71	0.00
DRS22-156.8	2	2.42	54.48	25.06	0.53	13.65	0.00	96.13	0.00
DRS22-156.8	3	2.81	53.96	26.20	0.78	13.73	0.00	97.47	0.00
DRS22-170.6	1	2.30	53.88	26.67	0.48	13.60	0.56	97.49	1.17
DRS22-170.6	2	2.23	54.41	26.90	0.52	14.03	0.61	98.70	1.17
DRS22-170.6	3	1.94	53.91	26.94	0.69	14.22	0.54	98.24	0.78
DRS22-180.5	1	3.47	53.34	27.27	0.49	13.18	0.00	97.76	0.00
DRS22-180.5	2	3.50	53.64	27.44	0.97	13.42	0.00	98.96	0.00
DRS22-180.5	3	3.23	54.55	26.99	0.57	13.66	0.38	99.37	0.67
DRS22-192.7	1	3.35	53.39	26.51	0.50	12.31	1.66	97.71	3.32
DRS22-192.7	2	3.35	53.57	27.00	0.38	12.35	1.54	98.20	4.05
DRS22-192.7	3	3.37	53.65	26.55	0.49	11.93	1.72	97.71	3.51
DRS22-192.7	4	3.23	53.44	27.61	0.55	11.94	1.69	98.46	3.07
DRS22-205.6	1	2.30	53.89	26.24	0.54	14.26	0.42	97.69	0.78
DRS22-205.6	2	2.19	54.46	26.28	0.63	14.09	0.54	98.20	0.86
DRS22-205.6	3	2.41	54.48	26.69	0.55	13.75	0.53	98.42	0.96
DRS22-215.6	1	2.34	55.55	26.21	0.47	13.66	0.65	98.88	1.38
DRS22-215.6	2	2.22	56.19	25.84	0.40	13.91	0.61	99.16	0.53
DRS22-215.6	3	2.44	54.27	26.33	0.79	14.27	0.44	98.51	0.56
DRS22-226.7	1	3.19	53.56	26.17	0.61	13.66	0.47	97.66	0.77
DRS22-226.7	2	3.31	54.13	26.23	0.41	13.37	0.45	97.89	1.10
DRS22-226.7	3	3.59	53.98	27.26	0.52	13.23	0.28	98.86	0.54
DRS22-233.5	1	2.99	54.31	27.02	0.41	13.49	0.48	98.69	1.17
DRS22-233.5	2	3.06	53.58	26.21	0.45	13.76	0.43	97.50	0.96
DRS22-233.5	3	3.22	52.69	27.15	0.51	13.41	0.25	97.24	0.49
DRS22-242.4	1	3.95	52.48	26.52	0.32	11.76	3.79	98.81	11.84
DRS22-242.4	2	3.59	52.23	26.17	0.17	11.35	3.62	97.13	21.29
DRS22-242.4	3	4.00	53.84	26.76	0.21	11.25	3.84	99.89	18.14
DRS22-252.2	1	2.04	53.37	26.30	0.21	8.29	6.79	97.01	32.33
DRS22-252.2	2	2.62	53.08	27.05	0.13	9.83	6.52	98.21	50.15
DRS22-255.2	1	3.19	54.05	27.08	0.20	8.98	5.85	99.35	29.25
DRS22-255.2	2	2.76	53.34	27.00	0.12	8.97	5.81	98.02	48.42
DRS22-255.2	3	2.51	53.24	26.32	0.19	9.19	6.08	97.53	32.00
DRS22-257.1	1	3.75	53.39	26.32	0.15	9.68	4.66	97.94	31.07
DRS22-257.1	2	4.26	53.08	26.46	0.16	9.62	4.98	98.58	31.13
DRS22-257.1	3	3.89	52.30	26.65	0.26	9.29	4.72	97.10	18.15
DRS22-259.1	1	3.48	52.29	25.91	0.44	9.10	5.63	96.86	12.80
DRS22-259.1	2	3.86	52.81	25.97	0.33	9.10	5.83	97.91	17.67
DRS22-259.1	3	3.86	54.42	25.83	0.45	9.44	5.77	99.74	12.82

Sample	Grain	MgO (%)	Al_2O_3 (%)	SiO_2 (%)	TiO_2 (%)	Fe_2O_3 (%)	ZnO (%)	Total (%)	ZnO/TiO_2
DRS22-263.7	1	3.50	52.43	26.53	0.46	10.74	2.82	96.46	6.13
DRS22-263.7	2	3.70	52.77	26.16	0.61	11.03	2.52	96.93	4.13
DRS22-266.7	1	3.44	52.72	25.70	0.45	9.17	5.39	96.87	11.98
DRS22-266.7	2	4.16	53.86	26.52	0.30	9.04	5.50	99.38	18.33
DRS22-279.1	1	3.47	52.61	26.53	0.60	12.21	1.25	96.67	2.08
DRS22-279.1	2	3.47	53.14	27.00	0.48	12.67	1.07	97.84	2.23
DRS22-279.1	3	3.47	53.74	26.96	0.39	13.05	0.74	98.36	1.90
DRS22-290.3	1	3.81	53.13	26.93	0.41	13.58	0.65	98.53	1.59
DRS22-290.3	2	3.61	52.05	26.94	0.48	13.44	0.77	97.29	1.60
DRS22-290.3	3	3.20	53.43	26.63	0.24	13.68	0.78	97.94	3.25
DRS22-299.1	1	3.71	52.51	26.47	0.40	13.44	0.87	97.41	2.18
DRS22-299.1	2	3.52	52.90	27.12	0.44	13.59	0.89	98.46	2.02
DRS22-299.1	3	3.72	52.87	26.43	0.32	13.71	0.86	97.89	2.69
DRS22-319.6	1	3.33	53.93	26.43	0.33	12.71	0.90	97.61	2.73
DRS22-341.6	1	3.02	52.75	28.23	0.33	12.45	1.03	97.81	3.12
DRS22-341.6	2	3.83	52.53	27.14	0.43	13.16	0.39	97.48	0.91
DRS22-341.6	3	3.66	53.15	27.48	0.33	12.73	0.84	98.21	2.55
DRS22-349.3	1	3.44	53.79	26.74	0.25	12.83	0.44	97.48	1.76
DRS22-349.3	2	3.64	53.53	26.85	0.24	13.45	0.56	98.26	2.33
DRS22-349.3	3	3.78	53.95	27.35	0.47	13.30	0.43	99.29	0.91

Table A2-5. Sulfur isotope analyses from Balcooma ($\delta^{34}S$ in permil relative to Canyon Diablo troilite).

Sample	Early pyrite	Late pyrite	Chalco-pyrite	Pyrrho-tite	Sphal-erite	Galena
			Southern Messenger lens			
Massive pyrite-chalcopyrite						
T860-182.4	10.23	-----	-----	-----	-----	-----
Massive pyrite-sphalerite-galena						
N875-106.6	8.98	-----	-----	-----	-----	-----
T860-181.7	11.79	-----	-----	-----	10.93	-----
			Harvey and Morris lenses			
Pyritic chloritic schists						
16A-135.3	11.16	-----	10.55	10.48 (10.41)	-----	-----
40-63.7	10.01	-----	10.23	-----	-----	-----
40-86.5	-----	-----	10.56 (11.05)	-----	-----	-----
41-158.9	8.60	-----	-----	-----	-----	-----
42-102.4	11.51	-----	10.49 (10.60)	-----	-----	-----
52-91.9	9.44 (9.96)	-----	-----	-----	-----	-----
54-253.3	5.41	-----	-----	5.12	-----	-----
Pyritic quartz-muscovite-biotite schist						
12A-87.0	9.77 (10.24)	-----	-----	-----	-----	-----
Massive magnetite						
4-98.9	7.15	-----	7.85	-----	-----	-----
39-100.2	-----	-----	10.31 (10.34)	-----	-----	-----
39A-116.9	8.99	-----	-----	-----	-----	-----
Massive pyrite-chalcopyrite						
2B-98.2	9.49 (9.13)	-----	9.62	9.49	-----	-----
4-98.9	9.49	-----	-----	-----	-----	-----
4-99.8	9.69	10.18	8.68	-----	-----	-----
4-101.0	10.11	-----	-----	-----	-----	-----
9A-171.2	9.93	-----	10.17 (10.05)	10.04	-----	-----
12A-93.3	9.79 (9.86)	-----	-----	-----	-----	-----
16A-167.4	10.97	-----	-----	-----	-----	-----
39-92.8	10.20	-----	-----	-----	-----	-----

Sample	Early pyrite	Late pyrite	Chalco-pyrite	Pyrrho-tite	Sphal-erite	Galena
			Harvey and Morris lenses (continued)			
Massive pyrite-chalcopyrite (continued)						
39-98.8	9.97	9.54 (9.62)	9.64 (10.06)	-----	-----	-----
39-106.3	9.40	-----	-----	-----	-----	-----
39-116.9	9.70 (9.61)	-----	-----	-----	-----	-----
39-124.0	9.95	-----	9.69	-----	-----	-----
39A-100.0	9.59 (10.37)	-----	-----	-----	-----	-----
39A-120.0	9.86	-----	-----	-----	-----	-----
44-118.4	10.12 (11.12)	-----	-----	-----	-----	-----
44-132.6	-----	-----	10.12	10.04	-----	-----
49-104.0	9.77	9.75	-----	-----	-----	-----
49-137.1	9.99	-----	9.72	9.65	-----	-----
Massive pyrite-sphalerite-galena						
N850-249.6	-----	-----	-----	-----	9.71 (9.73)	-----
N860-219.3	-----	-----	10.24	-----	9.58	8.92
N875-200.5	8.41	-----	-----	-----	-----	-----
P860-245.1	10.65	-----	-----	-----	-----	-----
			Mulroney lens			
Pyritic chloritic schists						
10-362.7	-----	-----	10.46	-----	-----	-----
11-336.1	11.41	-----	-----	-----	-----	-----
12-135.4	-----	-----	10.19	-----	-----	-----
Massive magnetite						
24-167.0	11.18	-----	11.43	-----	-----	-----
Massive pyrite-chalcopyrite						
12-143.2	10.16	-----	-----	-----	-----	-----
12-153.5	10.90 (11.22)	-----	-----	-----	-----	-----
39-350.1	11.43	-----	11.03	-----	-----	-----
42-271.8	11.29	-----	-----	-----	-----	-----
Massive pyrite-sphalerite-galena						
3-183.5	9.43	-----	-----	-----	-----	-----
10-357.2	11.12	-----	-----	-----	10.66	-----
10-361.7	11.00	-----	10.67	-----	11.22	-----
12-132.7	11.05	-----	-----	-----	10.47	-----
24-131.1	10.00	-----	-----	-----	9.75	-----
24-135.8	10.46	-----	-----	-----	9.66	-----
24-136.0	10.36	-----	-----	-----	9.57	-----

Sample	Early pyrite	Late pyrite	Chalco-pyrite	Pyrrho-tite	Sphal-erite	Galena
			Mulroney lens (continued)			
Massive pyrite-sphalerite-galena (continued)						
24-148.3	9.90 (9.83)	-----	-----	-----	9.19	-----
42-270.7	11.52	-----	-----	-----	-----	-----
49-356.8	10.44	-----	-----	10.38	-----	-----
			Late pyrrhotite vein			
11-279.6	-----	-----	-----	6.19 (6.33)	-----	-----

Table A2-6. Sulfur isotope analyses from Dry River South ($\delta^{34}S$ in permil relative to Canyon Diablo troilite).

Sample	Early pyrite	Late pyrite	Chalco-pyrite	Pyrrho-tite	Sphal-erite
Pyritic chloritic schists					
DRS16-225.7	12.22	-----	-----	-----	-----
Pyritic quartz-muscovite-biotite schist					
DRS16-244.6	11.39	-----	-----	-----	-----
Sulfide stringers and veins					
DRS16-220.2	10.49	9.70	-----	-----	-----
DRS32-269.8	11.92	-----	11.41	11.09	-----
DRS46-406.5	9.64	-----	10.38	-----	-----
DRS46W-405.4	-----	-----	9.78	-----	-----
Massive pyrite-chalcopyrite					
DRS15-196.5	8.55	-----	-----	-----	-----
DRS15-203.7	12.68	-----	-----	-----	-----
DRS15-206.4	10.70	-----	10.46	-----	-----
DRS19-210.4	12.09	-----	-----	-----	-----
DRS20-196.5	10.13	-----	10.49 (10.57)	-----	-----
DRS22-251.8	11.68	-----	-----	-----	-----
DRS22-252.2	11.82	-----	-----	-----	-----
DRS22-255.2	12.16 (12.31)	-----	-----	-----	-----
DRS27-319.1	11.50	-----	11.61	-----	-----
DRS27-323.7	12.13	-----	-----	-----	-----
DRS39-165.7	10.54	-----	-----	-----	-----
Massive pyrite-sphalerite-galena					
DRS15-191.9	8.57	-----	8.42	-----	-----
DRS15-193.7	9.87	-----	9.43	-----	9.43
DRS16-222.0	11.84	-----	-----	-----	-----
DRS19-209.0	10.89	-----	-----	-----	-----
DRS21-178.2	11.61	-----	-----	-----	10.71
DRS22-249.3	11.57	-----	-----	-----	-----
DRS27-324.3	11.29	-----	-----	-----	-----
DRS32-264.2	12.31	-----	-----	-----	-----

Table A2-7. Trace element analyses from selected drill holes from the north end, Rosebery deposit (Pb, Zn, Cu, Ba and Fe in percent; Ag, Au, Bi, As, Sb and Cd in ppm).

Sample	Pb	Zn	Cu	Ag	Au	Fe	Ba	Bi	As	Sb	Cd
R3981-34.3	0.3	1.6	0.05	16	0.7	7.9	0.40	29	344	27	44
R3981-35.15	11.9	18.2	0.11	195	1.0	7.1	0.36	0	222	207	425
R3981-36.15	1.9	3.2	0.04	29	0.6	8.6	0.32	4	1231	53	65
R3981-38.0	0.7	1.4	0.04	22	1.1	8.3	0.47	6	1276	50	33
R3981-40.0	0.3	0.5	0.02	12	0.8	7.8	0.37	4	1154	40	11
R3981-41.15	9.1	13.2	0.20	187	2.7	5.1	0.46	0	190	224	391
R3981-42.15	0.6	1.7	0.04	20	0.5	6.6	0.62	8	151	34	45
R3981-43.35	1.3	4.4	0.11	23	3.2	10.2	0.57	5	330	38	129
R3981-43.9	6.4	21.5	2.10	233	3.0	13.0	0.35	214	372	165	635
R3981-45.35	1.6	5.4	0.22	48	1.0	26.5	0.22	19	1917	270	144
R3981-46.1	3.3	39.0	0.09	86	1.0	7.7	0.17	25	180	114	1380
R3981-47.1	8.9	28.2	0.07	265	1.7	8.4	0.28	0	1186	420	707
R3981-47.85	0.5	1.3	0.09	32	0.9	5.0	0.94	0	689	105	17
R3981-48.2	2.9	7.0	0.02	44	0.4	14.4	----	8	287	92	84
R3981-48.55	0.2	0.5	0.01	6	0.2	4.6	2.41	0	115	25	0
R3981-48.9	5.6	13.5	0.31	200	2.5	15.4	0.35	37	624	1329	183
R3981-49.75	0.6	0.9	0.02	16	0.2	3.2	2.40	3	60	94	6
R3988-29.75	0.1	1.7	0.65	18	0.4	3.9	0.06	67	325	40	50
R3988-30.0	2.0	7.4	0.06	34	0.4	3.8	0.29	9	319	45	183
R3398-32.5	0.2	0.2	0.00	4	0.3	4.5	0.18	0	391	40	3
R3398-34.5	0.2	0.3	0.00	4	0.1	2.5	0.20	--	--	--	--
R3988-36.5	0.3	0.7	0.01	7	0.2	3.2	0.23	0	393	35	15
R3988-38.5	0.4	0.9	0.01	8	0.6	5.6	0.53	0	1392	41	17
R3988-40.3	3.5	16.3	0.65	77	1.2	10.0	0.24	61	1487	80	415
R3988-41.85	8.2	29.5	0.38	122	1.3	7.7	0.08	88	621	150	777
R3988-43.25	3.8	9.5	0.16	58	1.2	15.6	0.19	15	2741	111	249
R3988-44.35	0.4	2.2	0.03	7	0.3	2.1	0.56	4	343	16	62
R3988-44.9	14.2	27.8	0.10	189	9.2	4.9	0.07	0	214	197	645
R3988-46.0	0.3	0.6	0.02	7	0.3	2.3	0.91	0	367	16	11
R3988-48.0	0.1	0.3	0.00	3	0.0	2.1	0.96	2	85	11	2
R3988-49.75	0.2	0.9	0.02	7	0.2	2.9	0.98	0	168	27	21
R3988-51.15	0.2	0.5	0.02	10	0.9	3.9	----	--	--	--	--
R3988-52.55	2.6	7.2	0.02	108	2.8	3.4	----	--	--	--	--
R3988-54.05	5.0	10.1	0.22	287	2.6	2.4	----	--	--	--	--
R3988-54.95	0.3	0.7	0.22	24	0.6	2.2	----	--	--	--	--
R4039-26.55	0.1	0.5	0.55	19	0.3	3.7	0.18	70	311	30	20
R4039-27.9	1.1	1.3	2.40	83	0.3	12.3	0.12	237	186	54	30
R4039-29.05	3.5	7.5	0.73	--	---	16.0	0.14	--	--	--	--
R4039-30.45	6.4	10.6	0.06	140	0.7	4.1	0.12	6	192	144	171
R4039-31.8	4.8	10.8	0.05	145	0.5	5.9	0.25	5	548	189	193
R4039-33.5	0.2	0.8	0.02	9	0.3	4.8	0.23	0	263	28	19
R4039-35.5	0.1	0.3	0.01	4	0.2	4.3	0.25	0	643	26	5
R4039-37.5	0.1	0.3	0.01	4	0.1	4.6	0.17	0	539	24	5
R4039-39.2	0.7	1.2	0.01	13	0.3	7.2	0.20	0	530	32	24
R4039-41.1	5.7	16.8	0.23	101	2.6	11.3	0.09	34	422	115	330

Sample	Pb	Zn	Cu	Ag	Au	Fe	Ba	Bi	As	Sb	Cd
R4039-42.5	10.8	20.2	0.41	140	6.1	12.9	0.17	0	2744	247	485
R4039-43.7	0.7	1.6	0.07	10	0.3	2.1	0.69	0	92	23	43
R4039-45.7	0.1	0.3	0.01	5	0.1	2.6	1.32	0	95	13	7
R4039-47.5	0.2	0.4	0.01	7	0.3	3.7	1.39	0	134	15	8
R4039-48.8	6.4	11.4	0.04	146	1.8	4.1	2.67	13	167	245	318
R4039-50.3	3.8	8.1	0.16	76	4.1	10.2	4.72	0	653	384	244
R4039-52.3	2.3	8.7	0.21	313	4.0	5.2	15.76	0	550	913	250*
R4039-54.3	0.1	0.2	0.01	3	0.0	3.6	----	--	---	--	--
R4051-0.2	0.9	3.6	0.31	32	1.4	9.7	0.67	10	557	73	84
R4051-1.15	9.2	26.0	0.38	88	2.4	12.3	0.30	7	924	197	711
R4051-2.95	1.0	2.6	0.08	28	0.7	3.4	1.47	3	98	55	57
R4051-5.0	0.3	1.1	0.04	6	0.0	1.5	1.47	0	20	7	28
R4051-6.75	0.4	1.4	0.03	7	0.1	1.4	0.85	2	11	8	36
R4051-7.7	2.3	6.1	0.22	51	2.0	9.7	0.27	8	719	111	173
R4051-8.2	0.3	1.9	0.04	39	0.8	2.2	1.53	0	64	72	55
R4051-9.55	3.3	5.6	0.13	324	2.7	0.6	43.70	0	139	720	140*
R4051-11.65	1.5	3.7	0.06	114	0.5	1.7	41.30	0	65	400	100*
R4051-13.7	1.9	4.0	0.09	201	1.2	0.8	50.00	0	86	660	140*
R4051-15.7	1.8	4.0	0.08	177	1.0	0.4	46.80	0	53	670	120*
R4051-17.7	1.5	3.0	0.08	221	0.8	0.8	45.80	7	77	750	90*
R4051-19.7	1.0	1.6	0.05	68	0.5	4.9	2.33	5	108	229	141
R4055-7.4	1.1	2.3	0.05	18	0.6	7.7	2.37	5	122	50	57
R4055-8.75	5.4	11.2	0.27	94	1.1	7.6	0.90	5	456	383	284
R4055-9.75	4.9	19.8	0.44	115	2.9	13.2	0.42	72	1045	190	480
R4055-10.25	3.5	8.7	0.10	130	1.4	11.8	0.35	5	753	580	147
R4055-11.0	0.1	0.3	0.01	4	0.3	1.9	1.22	0	190	15	0
R4055-12.2	0.2	0.3	0.01	5	0.1	2.1	1.42	0	206	14	0
R4055-12.9	13.4	29.0	0.08	373	4.1	13.8	0.17	0	921	923	653
R4055-14.0	0.4	1.0	0.03	11	0.1	2.6	0.97	3	296	65	16
R4076-5.7	0.2	0.7	0.08	11	0.9	3.8	0.39	6	123	21	17
R4076-6.9	1.8	2.2	0.03	6	0.2	7.8	0.66	5	190	38	56
R4076-7.65	5.6	17.2	0.55	142	7.6	7.4	0.29	17	721	143	401
R4076-8.4	1.4	8.0	0.15	57	0.8	6.1	0.48	38	1393	59	259
R4076-9.55	4.4	16.4	0.67	151	3.4	18.7	0.33	139	1972	394	490
R4076-11.2	6.4	33.2	0.67	195	2.7	10.7	0.14	68	1074	417	985
R4076-12.6	4.3	20.0	0.52	125	1.6	12.7	0.45	64	919	235	617
R4076-14.3	0.3	0.7	0.02	5	0.2	1.8	0.51	0	125	43	14

-- Not analyzed.
* Semi-quantitative result for cadmium due to barium interference.

Table A2-8. Microprobe analyses of tetrahedrite-tennantite series minerals from the Rosebery deposit (data from this study and Smith (1975); analyses in percent).

Sample	S	Fe	Cu	Zn	As	Ag	Sb	Total	Style
R3391-164	24.09	2.23	31.62	5.21	4.25	11.03	22.40	100.83	Bar
R3391-164	24.41	2.40	33.54	4.97	4.20	7.06	22.03	98.62	Bar
R3391-164	24.70	2.53	33.62	4.68	4.28	6.97	22.22	99.00	Bar
R3391-164	24.72	2.21	35.22	5.12	4.63	6.48	21.72	100.11	Bar
R3391-166	24.43	2.85	32.82	4.52	3.73	8.52	23.14	100.00	Bar
R3391-166	24.45	3.09	32.35	4.45	3.24	8.88	23.66	100.14	Bar
R3391-166	24.43	3.21	32.54	4.43	3.30	8.67	23.83	100.40	Bar
R3391-166	24.44	3.10	32.16	4.80	3.35	9.30	23.97	101.14	Bar
R3391-166	24.19	3.04	33.21	4.42	3.68	8.59	23.38	100.52	Bar
R3391-166	24.11	2.98	32.73	4.41	3.20	9.04	24.01	100.50	Bar
R3391-166	24.43	3.08	33.32	4.07	3.66	8.00	22.71	99.27	Bar
R3391-166	24.39	3.00	32.69	4.39	3.85	8.74	23.54	100.58	Bar
R3391-166	24.50	3.12	32.67	4.10	3.42	9.12	23.71	100.63	Bar
R3391-166	24.62	3.10	32.53	4.09	3.50	8.26	23.87	99.96	Bar
R3391-166	24.50	2.98	33.32	4.59	4.13	7.79	22.54	99.86	Bar
R3391-166	24.72	3.13	33.05	4.31	3.59	8.50	23.14	100.44	Bar
R3391-166	24.69	2.81	33.00	4.77	3.55	8.65	23.51	100.98	Bar
R3391-166	24.25	2.90	32.35	4.42	3.52	8.63	24.00	100.07	Bar
R3391-166	24.40	3.05	33.12	4.37	3.65	8.39	23.71	100.70	Bar
R3391-166	24.52	3.04	32.75	4.07	3.67	8.69	23.10	99.84	Bar
R3391-166	24.07	3.03	32.15	4.03	3.53	9.57	23.84	100.23	Bar
R3382-270.25	26.05	3.88	39.42	3.90	6.89	1.07	18.81	100.04	Bar
R3382-270.25	25.98	4.06	39.81	3.94	7.67	1.26	17.30	100.05	Bar
R3382-270.25	26.31	4.16	39.36	3.57	7.75	0.99	17.62	99.75	Bar
R3382-270.25	26.05	4.23	39.49	3.55	7.78	1.28	17.60	99.99	Bar
R3382-270.25	26.29	4.27	39.71	3.39	7.31	0.89	18.82	100.68	Bar
R3382-270.25	26.58	4.19	40.75	3.43	9.63	1.01	15.15	100.74	Bar
R3382-270.25	26.61	4.14	40.76	3.83	10.66	0.41	13.70	100.21	Bar
R3394-181	25.82	3.44	37.44	4.45	8.79	4.38	15.89	100.21	Bar
R3394-181	25.89	3.59	36.11	6.46	8.56	4.63	16.51	101.75	Bar
R3394-181	26.20	2.97	37.87	4.92	9.00	3.81	15.27	100.03	Bar
R3394-181	25.99	2.81	38.45	5.08	9.09	3.99	15.51	101.31	Bar
R3394-181	26.03	3.23	37.79	4.69	8.96	4.37	16.14	101.22	Bar
R3394-181	25.89	3.13	37.38	4.87	8.89	4.24	15.46	99.86	Bar
R3394-181	26.21	2.99	38.27	5.06	9.25	4.21	15.28	101.26	Bar
R3394-181	25.57	2.87	36.02	5.00	7.27	5.39	17.98	100.09	Bar
R3394-181	25.43	2.67	36.98	4.83	8.16	4.82	17.33	100.22	Bar
R3394-181	26.20	2.86	37.54	4.74	8.40	4.22	15.80	99.76	Bar
R3394-181	25.77	3.16	37.25	4.64	8.45	4.30	15.78	99.33	Bar
R3394-181	25.74	3.03	37.29	4.75	8.70	4.64	15.41	99.56	Bar
R3394-181	25.60	2.81	37.24	4.87	8.32	4.45	16.00	99.28	Bar
R4055-32.5	22.45	5.49	24.38	1.27	0.00	17.78	28.81	99.55	Rem
R4055-32.5	22.68	5.24	22.96	0.78	0.00	17.79	26.58	96.02	Rem
R4055-32.5	22.38	5.59	23.62	0.98	0.00	18.42	27.72	98.70	Rem
R4055-32.5	22.29	5.11	23.51	1.22	0.00	18.11	28.12	98.36	Rem

Sample	S	Fe	Cu	Zn	As	Ag	Sb	Total	Style
R4055-32.5	22.62	5.44	24.55	1.13	0.00	17.24	27.96	98.94	Rem
R3456-298.5	22.58	4.10	25.73	2.40	0.00	15.67	28.15	98.61	Rem
R3456-298.5	23.51	4.17	25.99	2.48	0.00	15.14	28.62	99.92	Rem
R3456-298.5	23.12	4.23	26.96	2.49	0.00	13.91	28.72	99.43	Rem
R3456-298.5	23.27	4.87	28.41	1.77	0.00	13.04	29.11	100.46	Rem
R3374-104.5	22.71	5.09	24.26	1.38	0.00	18.43	28.09	99.95	Rem
R3374-104.5	23.32	4.92	26.94	1.98	0.00	15.71	28.55	101.42	Rem
R3374-104.5	21.43	5.24	20.28	0.80	0.00	22.13	27.96	97.84	Rem
R3374-104.5	23.35	6.78	23.25	1.51	0.00	19.49	26.57	100.94	Rem
R3374-104.5	23.03	5.79	24.82	1.09	0.00	18.27	28.57	102.07	Rem
R3374-104.5	21.65	5.68	20.47	1.02	0.00	24.82	28.07	101.70	Rem
R3374-104.5	22.95	5.91	23.42	2.44	0.00	18.75	27.59	101.03	Rem
R3374-104.5	22.69	5.35	24.10	1.07	0.00	19.41	28.14	100.78	Rem
R3374-104.5	22.66	5.66	24.01	1.00	0.00	19.75	28.56	101.64	Rem
R3374-104.5	21.63	5.92	19.19	0.52	0.00	26.32	27.66	101.24	Rem
R3374-104.5	23.37	6.23	25.47	0.80	0.00	18.11	28.66	102.63	Rem
R1163-149*	23.10	2.50	22.30	3.70	0.60	19.60	27.00	98.80	Rem
R3391-138.25	22.96	5.23	25.33	1.80	0.00	17.98	27.98	101.29	Rem?
R3391-138.25	22.64	4.68	25.39	1.51	0.00	18.20	28.26	100.67	Rem?
R3391-138.25	22.41	5.09	24.07	1.59	0.00	19.41	28.10	100.66	Rem?
R3391-138.25	21.79	5.26	22.53	1.70	0.00	19.98	27.26	98.51	Rem?
R3391-138.25	22.08	5.28	23.29	1.68	0.00	18.66	27.30	98.28	Rem?
R3391-138.25	22.36	5.09	22.79	1.94	0.00	20.97	28.30	101.44	Rem?
R3391-142.5	24.99	3.80	35.51	4.53	5.16	4.14	21.01	99.13	Rms
R3391-142.5	24.99	3.40	36.33	4.69	4.32	4.54	22.23	100.49	Rms
R3391-142.5	24.62	2.68	36.06	4.47	3.51	4.46	23.93	99.73	Rms
R3391-142.5	25.28	3.71	37.20	4.36	6.97	2.79	17.52	97.91	Rms
R3391-142.5	25.70	3.87	38.47	4.25	6.94	3.35	18.64	101.22	Rms
R3391-142.5	26.10	3.42	38.32	4.99	5.26	3.32	21.78	103.19	Rms
R3391-142.5	26.96	4.12	40.06	4.02	10.82	2.40	14.03	102.42	Rms
R3391-142.5	23.91	2.85	35.67	4.40	4.06	4.44	23.09	98.42	Rms
R3391-142.5	23.92	3.01	36.14	5.06	3.78	4.28	23.08	100.13	Rms
R3391-142.5	26.50	3.86	38.73	4.07	9.53	2.43	15.41	100.52	Rms
R3391-142.5	24.68	3.23	35.56	4.73	3.50	4.33	23.88	99.91	Rms
R3391-142.5	24.35	2.35	34.51	5.10	1.55	5.43	26.07	100.31	Rms
R3391-142.5	25.97	4.85	34.29	4.71	2.85	4.42	24.32	101.42	Rms
R3391-142.5	26.11	3.45	38.79	4.26	8.44	2.35	15.92	99.31	Rms
R3391-142.5	25.44	3.79	38.69	4.55	8.06	2.92	16.68	100.13	Rms
R3391-142.5	25.61	3.57	38.46	4.71	7.77	2.49	17.41	100.03	Rms
R3391-142.5	26.36	3.76	38.97	4.31	9.42	2.58	14.82	100.22	Rms
R3391-142.5	26.14	3.48	37.90	4.12	7.56	3.29	17.77	100.25	Rms
R1163-134*	26.90	3.40	35.00	3.20	10.20	7.20	14.60	100.50	Rms
R1205-371.3*	22.20	3.20	23.20	5.70	0.50	16.90	27.50	99.20	Rms
ROC*#	23.60	5.30	22.50	1.30	0.10	20.10	27.40	100.30	Rms
CGT*##	26.80	3.00	39.30	3.70	11.60	2.30	13.10	99.80	Cgt

Sample	S	Fe	Cu	Zn	As	Ag	Sb	Total	Style
CGT*##	27.40	2.90	39.60	4.10	11.40	2.40	13.10	100.90	Cgt
R1163-131*	26.10	2.60	37.50	3.70	8.10	3.40	17.30	98.70	Sms
R1163-154*	29.00	4.30	39.90	3.20	14.70	1.80	7.40	100.30	Sms
R1163-238*	28.40	4.90	41.50	1.80	18.00	1.00	4.30	99.70	Sms
R1205-492*	25.80	4.30	36.00	3.30	2.00	1.90	27.90	100.20	Sms
R49*	29.50	9.00	31.30	2.30	17.60	2.30	8.00	100.00	Sms
R50*	26.10	2.90	36.10	3.90	6.30	3.90	21.20	100.40	Sms
R50*	26.60	2.70	37.30	4.20	6.00	3.50	21.00	101.30	Sms
R50*	26.60	4.00	38.30	2.80	9.60	2.70	15.40	99.40	Sms
62R/1015*	26.20	4.00	34.40	2.90	9.60	6.80	16.60	99.50	Sms
62R/1020*	26.60	3.80	37.80	2.90	10.90	4.50	13.10	99.60	Sms
R3394-147.5	26.21	4.55	38.55	4.23	11.26	2.40	11.73	98.93	Sms
R3394-147.5	27.75	5.07	42.90	3.24	16.97	1.54	3.68	101.14	Sms
R3394-147.5	27.10	4.13	40.80	4.03	11.66	2.34	12.45	102.50	Sms
R3394-147.5	25.72	3.89	37.28	4.43	7.08	4.04	18.42	100.86	Sms
R3394-147.5	26.85	4.30	40.24	3.73	12.86	2.70	9.69	100.38	Sms
R3394-147.5	26.20	4.28	39.00	4.44	10.77	2.62	13.07	100.39	Sms
R3394-147.5	28.18	8.40	35.23	3.77	8.75	2.77	13.63	100.74	Sms
R3394-147.5	26.76	5.34	38.93	4.29	13.07	2.33	10.80	101.52	Sms
R3394-147.5	26.31	4.38	39.02	4.32	11.22	2.87	12.63	100.74	Sms
R3394-147.5	27.55	5.02	41.23	3.36	16.62	1.34	4.08	99.20	Sms
R1205-282*	29.50	4.50	39.20	3.20	18.30	2.30	3.10	100.10	Pms
R1205-488.5*	25.90	5.50	35.50	2.40	3.90	3.30	23.30	99.60	Pms

Key
Bar=massive barite mineralization.
Rem=remobilized sulfides in veins or veinlets.
Rms=medium or coarse grained recrystallized massive sulfide.
Cgt=coarse grained tetrahedrite.
Sms=fine grained sphalerite-galena-pyrite massive sulfide.
Pms=fine grained pyrite dominant massive sulfide.
* Samples from Smith (1975).
# Sample from Rosebery open cut.
Coarse grained tetrahedrite from G lens, 15 level.
Samples R49 and R50 are from G lens, 15 level, 152 mN, 314 mN. For all other samples the sample number indicates the drill hole and the number of feet from the collar.

Appendix 3

Catalogue of samples

Table A3-1. Samples from the Balcooma deposit.

Catalogue number	Field number (Drill hole-depth in meters)	Description
108000	2B-98.2	Medium grained massive chalcopyrite-pyrite-pyrrhotite (PTS).
108001	3-103.9	Fine grained quartz-chlorite schist with garnet-rich bands (TS).
108002	3-108.4	Fine grained quartz schist with biotite and staurolite porphyroblasts (TS).
108003	3-126.8	Medium grained quartz-biotite-cordierite schist with disseminated magnetite and pyrite (PTS).
108004	3-128.6	Fine grained quartz-chlorite schist with biotite and staurolite porphyroblasts (TS).
108005	3-131.3	Fine grained quartz-chlorite schist (TS).
108006	3-134.5	Fine grained quartz-muscovite schist with biotite and staurolite porphyroblasts (TS).
108007	3-138.5	Fine grained quartz-muscovite schist with biotite porphyroblasts (TS).
108008	3-183.5	Medium grained massive pyrite-sphalerite-galena (PTS).
108009	3-227.8	Fine grained quartz schist with with biotite, andalusite, staurolite and cordierite porphyroblasts (TS).
108010	3-228.5	Medium grained chlorite-biotite schist with disseminated pyrite (PTS).
108011	4-31.2	Hematitic and kaolinitic quartz-amphibole schist (PTS).
108012	4-33.8	Hematitic, fine grained quartz-muscovite schist (PTS).
108013	4-37.1	Hematitic, fine grained muscovite quartzite (PTS).
108014	4-49.2	Hematitic, fine grained quartz-chlorite schist (TS).
108015	4-53.4	Hematitic, fine grained biotite-chlorite schist (TS).
108016	4-69.6	Contact (bedding) between fined grained quartz-biotite-chlorite schist and fine grained quartz-biotite-chlorite schist with staurolite porphyroblasts (TS).
108017	4-72.0	Contact between fine to medium grained biotite-quartz-chlorite schist and fine grained quartz-chlorite schist with garnet porhyroblasts (TS).
108018	4-76.2	Contact (bedding) between fine to medium grained quartz-biotite-albite schist and fine grained quartz schist with biotite, staurolite and andalusite porphyroblasts (PTS).
108019	4-78.8	Fine to medium grained quartz-biotite-chlorite schist with disseminated pyrite which is cut by a staurolite-magnetite vein (PTS).
108020	4-82.0	Fine to medium grained chlorite-quartz schist with staurolite porphyroblasts and disseminated magnetite and pyrite (PTS).
108021	4-86.8	Schistose quartz-albite porphyry (TS).
108022	4-98.8	Fine grained massive magnetite with lesser pyrite and chalcopyrite (PTS).
108023	4-98.9	Fine grained, banded massive magnetite-pyrite (PTS).
108024	4-99.8	Fine grained, banded massive magnetite-pyrite-chalcopyrite with pyrite porphyroblasts (PTS).
108025	4-101.0	Fine grained massive pyrite (PTS).
108026	4-103.1	Fine grained pyritic quartz-muscovite schist (TS).
108027	4-109.8	Fine grained pyritic quartz-chlorite schist (PTS).
108028	4-111.8	Fine grained quartz schist with biotite and staurolite porphyroblasts (PTS).
108029	4-117.8	Fine grained quartz-muscovite schist with biotite porphyroblasts (TS).
108030	6-102.0	Fine grained hornblende-biotite-albite-quartz schist (TS).
108031	6-111.8	Porphyritic microgranite (TS).
108032	6-205.0	Microgranite (TS).
108033	6-271.7	Foliated biotite microgranite (TS).
108034	6-275.5	Fine grained, strongly foliated muscovite-quartz-biotite-feldspar schist with staurolite porphyroblasts (TS).
108035	6-299.3	Fine grained quartz-biotite-muscovite-albite schist (TS).
108036	6-417.9	Fine grained feldspar-quartz-biotite schist with hornblende porhyroblasts and relic, anhedral quartz phenocrysts (?) (TS).
108037	6-419.6	Schistose biotite quartz-feldspar porphyry (TS).
108038	6-420.1	Fine grained feldspar-epidote-biotite-hornblende schist (TS).
108039	6-437.6	Fine grained quartz-feldspar-muscovite-biotite schist with relic quartz and feldspar porphyroblasts and with a relic fragmental texture (TS).
108040	9A-172.1	Medium grained massive chalcopyrite-pyrite-pyrrhotite (PTS).

Table A3-1. Samples from the Balcooma deposit (continued).

Catalogue number	Field number (Drill hole-depth in meters)	Description
108041	10-130.8	Contact between fine grained quartz-chlorite schist and medium grained chlorite-biotite schist with garnet porphyroblasts (PTS).
108042	10-327.2	Fine grained quartz-muscovite-biotite schsit with cordierite porphyroblasts (TS).
108043	10-357.0	Fine to medium grained pyritic biotite-chlorite schist with garnet porphyroblasts and chalcopyrite (PTS).
108044	10-357.2	Contact between medium grained massive sphalerite-pyrite-galena and medium grained biotite-chlorite schist with gahnite and albite (?) porphyroblasts (PTS).
108045	10-361.7	Medium grained massive chalcopyrite-sphalerite-pyrrhotite-pyrite-galena (PTS).
108046	10-362.7	Quartz-chalcopyrite-pyrrhotite vein cutting medium grained chlorite-biotite schist (PTS).
108047	10-364.2	Medium grained massive pyrite-sphalerite-galena (PTS).
108048	10-367.2	Fine grained quartz-biotite schist with gahnite porphyroblasts and disseminated pyrite, sphalerite and galena (PTS).
108049	10-367.4	Fine grained quartz-biotite-feldspar schist with gahnite porphyroblasts (PTS).
108050	10-374.5	Fine grained quartz-biotite-chlorite schist with cordierite porphyroblasts (TS).
108051	11-279.6	Pyrrhotite-chlorite-quartz vein (PTS).
108052	11-307.7	Fine grained quartz-muscovite schist with a 10 mm band of quartz-biotite schist (PTS).
108053	11-334.7	Fine grained pyritic quartz-muscovite schist (PTS).
108054	11-336.1	Medium grained pyritic quartz-biotite-chlorite schsit with garnet porphyroblasts (PTS).
108055	12-42.8	Fine grained quartz-muscovite schist with biotite and staurolite porphyroblasts (TS).
108056	12-45.0	Fine grained quartz-chlorite schist with biotite and staurolite porphyroblasts (PTS).
108057	12-45.5	Fine grained quartz-muscovite-chlorite schist with chloritized biotite and sericitized staurolite porphyroblasts (TS).
108058	12-89.9	Banded sample with three bands: medium grained biotite-quartz schist, fine grained quartz schist with biotite porphyroblasts, and quartz-schist with biotite and gahnite porphyroblasts (TS).
108059	12-96.8	Medium grained, pyritic and sericitized quartz-feldspar-biotite schist which is cut by carbonate veinlets (PTS).
108060	12-97.7	Fine to medium grained quartz-biotite schist separated by a 1-5 mm zeolitic and mylonitic shear from a fine grained quartz-muscovite-biotite schist (PTS).
108061	12-106.4	Fine to medium grained hornblende feldspar schist (TS).
108062	12-114.1	Fine to medium grained pyritic quartz-muscovite-biotite shcist (TS).
108063	12-120.8	Medium grained semi-massive sphalerite-galena-pyrite with crenulated, schistose quartz-muscovite-biotite gangue (PTS).
108064	12-122.9	Banded, fine grained, pyritic quartz-muscovite schist (PTS).
108065	12-132.7	Medium grained massive sphalerite-galena-pyrite (PTS)
108066	12-135.4	Chalcopyrite-pyrite stringer or vein cutting medium grained biotite-chlorite schist (PTS).
108067	12-140.5	Contact between fine grained pyritic quartz-biotite schist and medium grained pyritic biotite-chlorite schist with staurolite porphyroblasts (PTS).
108068	12-143.2	Fine grained massive pyrite-chalcopyrite (PTS).
108069	12-146.8	Medium grained pyritic chlorite-biotite schist with staurolite porphyroblasts (PTS).
108070	12-152.8	Fine grained semi-massive chalcopyrite-pyrite with chlorite gangue (PTS).
108071	12-153.5	Fine to medium grained massive pyrite-chalcopyrite with chlorite and biotite gangue (PTS).
108072	12-160.0	Fine grained quartz-chlorite schist with biotite porphyroblasts and staurolite porphyroblasts that are rimmed by cordierite (PTS).
108073	12-206.5	Fine grained, sericitized, biotite-feldspar-quartz-biotite-hornblende schist with disseminated magnetite (TS).
108074	12A-48.5	Fine grained biotite-feldspar-quartz schist with disseminated magnetite (TS).
108075	12A-50.8	Fine grained quartz-albite-biotite schist with relic anhedral quartz and albite phenocrysts and disseminated magnetite (TS).
108076	12A-58.0	Fine grained quartz schist with biotite, andalusite and staurolite porphyroblasts (TS).
108077	12A-71.3	Fine grained quartz-muscovite schist with biotite porphyroblasts (TS).

Table A3-1. Samples from the Balcooma deposit (continued).

Catalogue number	Field number (Drill hole-depth in meters)	Description
108078	12A-82.2	Fine grained quartz schist with andalusite, staurolite and biotite porphyroblasts (TS).
108079	12A-84.1	Fine grained pyritic quartz schsit with biotite and staurolite porphyroblasts (TS).
108080	12A-85.3	Contact between fine grained pyritic quartz-chlorite-biotite schist and medium grained pyritic biotite-chlorite schist with staurolite porphyroblasts (TS).
108081	12A-87.0	Pyrite vein cutting fine grained quartz-biotite schist (PTS).
108082	12A-89.8	Fine to medium grained quartz-biotite schist with andalusite porphyroblasts (TS).
108083	12A-92.1	Medium grained pyritic biotite-chlorite schist with staurolite porphyroblasts (TS).
108084	12A-93.3	Fine to medium grained massive pyrite-chalcopyrite (PTS).
108085	12A-95.8	Fine to medium grained quartz-chlorite schist (TS).
108086	12A-98.1	Fine to medium grained quartz-biotite-chlorite schist with disseminated magnetite.
108087	12A-114.0	Medium grained chlorite-quartz schist (PTS).
108088	16A-135.9	Medium grained semi-massive chalcopyrite-pyrrhotite with pyrite and magnetite porphyroblasts and chlorite gangue (PTS).
108089	16A-141.2	Contact between fine grained quartz-chlorite schist with garnet porphyroblasts and fine grained chlorite schist with garnet porphyroblasts (PTS).
108090	16A-167.4	Medium grained semi-massive pyrite-chalcopyrite with chlorite-biotite gangue and staurolite porphyroblasts which are overgrown by cordierite (PTS).
108091	23-41.5	Fine grained quartz-biotite-muscovite schsit (TS).
108092	23-68.5	Fine grained quartz-biotite-muscovite schist with staurolite porphyroblasts (PTS).
108093	23-136.7	Fine grained quartz-muscovite schist with biotite and staurolite porphyroblasts (PTS).
108094	23-148.1	Fine grained quartz-biotite-muscovite schist with cordierite porphyroblasts (TS).
108095	23-170.0	Fine grained quartz-biotite-muscovite-albite schist (TS).
108096	23-174.5	Fine grained quartz-biotite-muscovite schist with staurolite porphyroblasts (TS).
108097	23-201.9	Fine grained quartz-albite-muscovite-biotite schist (TS).
108098	23-217.7	Contact (bedding) between fine grained quartz-muscovite-biotite schist and metavolcaniclastics with 5-20 mm angular blocks of albite porphyry in a fine grained schistose quartz-muscovite-biotite matrix (TS).
108099	23-233.6	Fine grained quartz-biotite-muscovite schist with staurolite and andalusite porphyroblasts (TS).
108100	23A-149.6	Fine grained quartz-biotite-albite-muscovite schist (TS).
108101	23A-162.7	Fine grained quartz-biotite-muscovite schist with staurolite porphyroblasts (PTS).
108102	23A-205.2	Fine grained quartz-muscovite-biotite schist with staurolite porphyroblasts (TS).
108103	23A-222.0	Metavolcanoiclastic with flattened felsite fragments in a schistose quartz-muscovite-biotite matrix (TS).
108104	23A-227.5	Contact (bedding betweeen fine grained quartz-muscovite-biotite-albite schist and metavolcaniclastics with angular and flattened 3-20 mm blocks of albite porphyry in a fine grained schistose quartz-muscovite-biotite matrix (PTS).
108105	23A-246.4	Fine grained quartz-feldspar-biotite-chlorite schist with unoriented hornblende porphyroblasts. The sample is cut by numerous carbonate-feldspar veins (PTS).
108106	23A-259.3	Fine grained muscovite-biotite-quartz schist with staurolite porphyroblasts (TS).
108107	24-121.7	Strongly sericitized medium grained hornblende-biotite-quartz-feldspar schist (TS).
108108	24-122.2	Contact between medium grained massive pyrite-sphalerite-galena and fine grained pyritic quartz-sillimanite-muscovite-biotite schist with gahnite porphyroblasts (PTS).
108109	24-123.4	Fine grained muscovite-quartz-biotite schist (TS).
108110	24-127.9	Fine grained muscovite-biotite schist with staurolite porphyroblasts (TS).
108111	24-131.1	Medium grained massive sphalerite-galena-pyrite (PTS).
108112	24-135.8	Medium grained massive sphalerite-galena-pyrite with quartz-biotite gangue (PTS).
108113	24-136.0	Medium grained massive sphalerite-galena-pyrite (PTS).
108114	24-136.1	Contact between medium grained semi-massive chalcopyrite-pyrite with quartz-biotite gangue and fine grained muscovite-quartz-biotite schist with gahnite porphyroblasts (PTS).
108115	24-146.1	Contact between medium grained massive pyrite chalcopyrite and fine to medium grained quartz-biotite schist with staurolite porphyroblasts (PTS).

Table A3-1. Samples from the Balcooma deposit (continued).

Catalogue number	Field number (Drill hole-depth in meters)	Description
108116	24-148.3	Medium grained massive pyrite-sphalerite-galena (PTS).
108117	24-167.0	Fractured and brecciated semi-massive magnetite-pyrite with chlorite-quartz gangue (PTS).
108118	24-196.0	Fine grained quartz schist with chloritized biotite and sericitized staurolite porphyroblasts (PTS).
108119	31-230.2	Fine grained quartz schist with chloritized biotite and sericitized staurolite porphyroblasts (PTS).
108120	31-427.6	Fine grained pyritic quartz-muscovite schist (PTS).
108121	35-27.8	Chrysocolla-limonite pod within very fine grained clay (PTS).
108122	36-71.3	Medium grained massive pyrite-chalcopyraite with crosscutting clay veins and alteration of chalcopyrite to chalcocite and covellite (PTS).
108123	39-92.8	Fine to medium grained massive pyrite-chalcopyrite (PTS).
108124	39-98.8	Medium grained massive chalcopyrite-pyrite with chlorite gangue (PTS).
108125	39-100.2	Fine grained massive magnetite with chlorite gangue cut by chalcopyrite veins (PTS).
108126	39-106.3	Medium grained massive pyrite-chalcopyrite (PTS).
108127	39-108.2	Schistose quartz-feldspar porphyry (TS).
108128	39-116.9	Brecciated fine to medium grained massive pyrite with 1-10 mm angular clasts in a carbonate-chalcopyrite matrix (PTS).
108129	39-124.0	Medium grained massive chalcopyrite-pyrite with pyrite prophyroblasts (PTS).
108130	39-125.1	Medium grained biotite-chlorite schist with disseminated pyrite, chalcopyrite and magnetite (PTS).
108131	39-125.4	Brecciated and limonitic quartz-feldspar porphyry (TS).
108132	39-140.4	Medium grained pyritic chlorite-biotite schist (PTS).
108133	39-142.3	Medium grained biotite-chlorite-quartz schsit with garnet porphyroblasts (PTS).
108134	39-143.6	Banded, fine grained quartz-chlorite schist with garnet and staurolite porphyroblasts and disseminated magnetite (PTS).
108135	39-151.5	Fine grained quartz-chlorite-biotite schist with garnet and staurolite porphyroblasts and disseminated magnetite (PTS).
108136	39-154.7	Fine grained quartz-muscovite schist with biotite, staurolite and albite prophyroblasts (PTS).
108137	39-179.6	Fine grained sericite (after feldspar)-quartz-chlorite schist with unoriented hornblende porphyroblasts (?) (TS).
108138	39-207.8	Fine grained quartz-biotite-feldspar schist with minor andalusite and sillimanite (TS).
108139	39-293.2	Fine grained quartz-biotite-muscovite schist with andalusite porphyroblasts and disseminated pyrite (TS).
108140	39-350.1	Fine to medium grained massive pyrite-chalcopyrite with biotite and staurolite gangue (PTS).
108141	39A-95.1	Medium grained massive chalcopyrite-pyrite with chlorite gangue (PTS).
108142	39A-100.0	Brecciated semi-massive pyrite with 1-10 mm angular blocks of fine grained massive pyrite in a biotite-chlorite-quartz matrix (PTS).
108143	39A-109.7	Quartz-feldspar porphyry (TS).
108144	39A-116.9	Fine to medium grained, banded massive pyrite-magnetite-chalcopyrite (PTS).
108145	39A-120.0	Fine grained massive pyrite-chalcopyrite (PTS).
108146	39A-131.8	Schistose quartz-feldspar porphyry (TS).
108147	39B-96.9	Fine grained quartz-chlorite schist with garnet porphyroblasts (TS).
108148	39B-105.0	Fine grained quartz-chlorite schist with disseminated magnetite (TS).
108149	39B-116.6	Fine grained quartz-chlorite schist with scattered biotite and staurolite porphyroblasts cut by pyrite-birdseye pyrite/marcasite veins and pods (PTS).
108150	40-60.9	Fine grained chlorite schist with disseminated magnetite (TS).
108151	40-62.7	Contact between fine grained quartz-chlorite-biotite schist with disseminated chalcopyrite and pyrite and medium grained massive chalcopyrite-pyrite with quartz-chlorite gangue (PTS).
108152	40-63.7	Medium grained chlorite-biotite schist with 20% foliated medium grained pyrite and chalcopyrite (PTS).
108153	40-70.8	Fine grained quartz-chlorite schist with bands of garnet porphyroblasts (TS).
108154	40-86.2	Fine grained banded massive magnetite-chalcopyrite with chlorite and biotite gangue (PTS).
108155	40-90.4	Medium grained massive chalcopyrite-pyrrhotite with corroded coarse grained pyrite porphyroblasts (PB).
108156	40-111.4	Schistose quartz-feldspar porphyry (TS).

Table A3-1. Samples from the Balcooma deposit (continued).

Catalogue number	Field number (Drill hole-depth in meters)	Description
108157	40-116.2	Fine grained quartz-biotite-epidote-amphibole-feldspar schsit (TS).
108158	40-311.0	Fine grained chlorite schist with disseminated pyrite (TS).
108159	40-312.1	Fine to medium grained quartz-biotite-garnet schist with scattered strongly sieved staurolite porphyroblasts and disseminated pyrite (TS).
108160	40-322.8	Medium grained massive sphalerite-pyrite-galena with several 10-30 mm rounded blocks of fine to medium grained quartz-biotite schist (PTS).
108161	40-323.5	Fine grained quartz-muscovite-biotite schist with gahnite porphyroblasts and disseminated pyrite, sphalerite and galena (PTS).
108162	41-124.2	Fine grained quartz-muscovite schist with biotite, cordierite and andalusite porphyroblasts (TS).
108163	41-126.1	Fine grained quartz-muscovite schist with biotite, andalusite and staurolite porphyroblasts and disseminated magnetite (PTS).
108164	41-126.9	Fine to medium grained quartz-biotite-chlorite schist with cordierite and staurolite porphyroblasts and 20% disseminated and blebby pyrite (PTS).
108165	41-128.2	Fine grained quartz-muscovite schist with biotite, staurolite and andalusite porphyroblasts and disseminated pyrite (PTS).
108166	41-132.6	Fine grained quartz-feldspar-biotite-andalusite-staurolite schist with disseminated chalcopyrite (PTS).
108167	41-135.5	Augen textured fine grained quartz-biotite-feldspar schist with disseminated magnetite and pyrite with a 10 mm band of semi-massive magnetite, and with relic anhedral quartz phenocrysts (PTS).
108168	41-141.4	Fine grained quartz-chlorite shcist with staurolite porphyroblasts, relic anhedral quartz eyes and disseminated magnetite and pyrrhotite (PTS).
108169	41-158.9	Medium grained biotite-quartz-carbonate schist with 30-40% medium grained pyrite (PTS).
108170	42-88.9	Medium to coarse grained massive pyrite-chalcopyrite-magnetite (PTS).
108171	42-102.4	Fine to medium grained chlorite schist with staurolite porphyroblasts rimmed by cordierite which is altered to serpentine (?), and with disseminated and blebby pyrite and chalcopyrite (PTS).
108172	42-152.8	Contact (bedding) between fine grained quartz-biotite schist and fine grained quartz-muscovite schist with andalusite and biotite porphyroblasts (TS).
108173	42-158.6	Fine grained quartz-chlorite-biotite schsit (TS).
108174	42-270.7	Medium grained massive pyrite-sphalerite-galena (PTS).
108175	42-271.8	Fine grained massive pyrite-chalcopyrite with chlorite gangue (PTS).
108176	44-91.8	Fine grained quartz-muscovite schist with biotite and staurolite porphyroblasts (TS).
108177	44-92.9	Fine grained quartz-chlorite schist with cordierite porphyroblasts and disseminated magnetite (TS).
108178	44-94.5	Fine to medium grained quartz-biotite-chlorite schist (TS).
108179	44-97.6	Fine to medium grained quartz-biotite-chlorite schist (TS).
108180	44-118.4	Fine to medium grained massive pyrite-magnetite-chalcopyrite (PTS).
108181	44-124.8	Fine grained quartz-chlorite schist with disseminated and stringer magnetite (PTS).
108182	44-132.6	Medium grained massive pyrrhotite-pyrite-chalcopyrite with a 10 mm band of massive magnetite (PTS).
108183	49-97.0	10-30 mm, rounded blocks of fine grained massive magnetite and fine to medium grained quartz-biotite schist set in a matrix of medium grained chalcopyrite-pyrrhotite-pyrite (PTS).
108184	49-104.0	Fine grained massive pyrite-chalcopyrite with chlorite gangue (PTS).
108185	49-109.2	Medium grained massive chalcopyrite with 5-10% 1-5 mm pyrite porphyroblasts (PB).
108186	49-120.8	Fine grained quartz-chlorite schist with cordierite and garnet porphyroblasts (TS).
108187	49-127.9	Fine grained quartz-chlorite schist with garnet porphyroblasts (TS).
108188	49-137.1	Medium grained semi-massive chalcopyrite-pyrrhotite with cordierite and chlorite gangue (PTS).
108189	49-166.4	Contact (bedding) between fine grained quartz-muscovite-biotite schist and fine to medium grained quartz-biotite-muscovite schist with staurolite porphyroblasts (TS).
108190	49-179.2	Schistose quartz-feldspar porphyry (TS).
108191	49-234.4	Fine grained quartz-albite-biotite-muscovite schist with relic albite phenocrysts and garnet porphyroblasts (TS).
108192	49-257.1	Fine grained quartz-muscovite schist with biotite and staurolite porphyroblasts (TS).

Table A3-1. Samples from the Balcooma deposit (continued).

Catalogue number	Field number (Drill hole-depth in meters)	Description
108193	49-271.9	Fine grained quartz-muscovite schist with chloritized biotite and completely sericitized staurolite porphyroblasts (TS).
108194	49-356.8	Contact between fine grained quartz-biotite schist with disseminated pyrrhotite and pyrite and medium grained massive pyrrhotite-pyrite with biotite-cordierite-epidote-hornblende gangue (PTS).
108195	49-364.6	Contact between medium grained massive sphalerite-pyrite-galena and medium grained biotite-chlorite-serpentine (?) schist with disseminated pyrite (PTS).
108196	49-369.6	Fine grained quartz-biotite-muscovite schist (TS).
108197	49-385.6	Fine grained quartz-biotite-muscovite schist (TS).
108198	52-91.9	Medium grained massive pyrite-chalcopyrite (PTS).
108199	52-93.9	Medium grained massive pyrite-chalcopyrite (PTS).
108200	54-235.6	Albite porphyry with disseminated pyrite (PTS).
108201	54-253.4	Medium grained biotite shcist with disseminated and blebby pyrite and chalcopyrite (PTS).
108202	55-338.1	Fine grained quartz-biotite-albite schist with sillimanite clots and staurolite porphyroblasts (TS).
108203	N850-249.6	Medium grained massive sphalerite-galena-pyrite with quartz-muscovite gangue (PTS).
108204	D860-57.9	Fine grained quartz-biotite-muscovite schist (TS).
108205	D860-71.8	Fine grained quartz-biotite schist with cordierite porphyroblasts (TS).
108206	D860-117.5	Contact (bedding) between fine grained quartz-biotite-albite-muscovite schist and fine grained quartz-biotite schist with andalusite and staurolite porphyroblasts (TS).
108207	D860-153.8	Fine grained quartz-albite-biotite schist with sericitized andalusite (?) porphyroblasts cut by a quartz vein (TS).
108208	D860-193.9	Fine grained quartz-biotite-muscovite schist with staurolite porphyroblasts (TS).
108209	D860-236.7	Fine grained quartz-biotite-albite-muscovite schist (TS).
108210	D860-264.5	Crenulated fine grained quartz-muscovite-biotite schist with garnet porphyroblasts (TS).
108211	N860-219.3	Medium grained massive sphalerite-galena-chalcopyrite-pyrite with quartz-biotite-gahnite gangue (PTS).
108212	P860-245.1	Medium grained massive pyrite-sphalerite-pyrite (PTS).
108213	Q860-360.1	Fine grained quartz-muscovite-biotite schist with relic anhedral quartz phenocrysts (TS).
108214	T860-181.7	Medium grained massive sphalerite-pyrite-galena with biotite-quartz-chlorite gangue (PTS).
108215	T860-184.2	Medium grained massive pyrite-chalcopyrite-sphalerite (PTS).
108216	N875-106.6	Fine grained semi-massive sphalerite-pyrite-galena with quartz gangue (PTS).
108217	N875-200.5	Medium grained massive pyrite-sphaleritie-galena with carbonate and chlorite gangue (PTS).
108218	F896-137.2	Fine grained quartz-muscovite schist with biotite and albite porphyroblasts (TS).
108219	F896-172.5	Fine grained quartz-muscovite schist with biotite and staurolite porphyroblasts (TS).
108220	J900-136.0	Fined graine quartz-muscovite-biotite-feldspar augen schist (TS).
108221	J920-45.7	Slightly brecciated, fine to medium grained massive pyrite-sphalerite-galena with quartz gangue cut by clay veins (PTS).
108222	J920-71.7	Fine grained quartz-muscovite schist with biotite and gahnite porphyroblasts (TS).
108223	L920-49.6	Fine grained albite-quartz-magnetite-biotite schist with unoriented hornblende laths (TS).
108224	L920-56.3	Fine grained massive pyrite-chalcopyrite with chlorite gangue and a 30 mm pod of fine grained massive magnetite (PTS).
108225	L920-58.6	Quartz-chalcopyrite-pyrite vein with minor alteration of chalcopyrite to covellite (PTS).
108226	L920-62.5	Medium grained massive pyrite-chalcopyrite (PTS).
108227	L920-66.8	Medium grained massive pyrite-chalcopyrite with chalcopyrite largely altered to limonite, chalcocite and covellite (PTS).
108228	L920-89.8	Fine grained quartz-muscovite schist with biotite, staurolite and cordierite porphyroblasts (PTS).
108229	L920-103.0	Fine grained quartz-sericite schist with biotite, staurolite and cordierite porphyroblasts (PTS).
108230	L920-149.9	Fine grained quartz-biotite schist with andalusite, codierite and staurolite porphyroblasts (TS).
108231	L920-152.2	Fine grained quartz-biotite schist with sericitized cordierite porphyroblasts (TS).
108232	L920-156.9	Fine grained quartz-biotite schist with andalusite porphyroblasts that are rimmed by sericitized cordeirite (TS).

Table A3-1. Samples from the Balcooma deposit (continued).

Catalogue number	Field number (Drill hole-depth in meters)	Description
108233	L920-160.0	Fine grained chlorite schist (TS).
108234	L920-163.2	Fine to medium grained chlorite schist with staurolite and gahnite porphyroblasts along with disseminated pyrite (PTS).
108235	L920-163.7	Medium to coarse grained biotite-chlorite-staurolite schist with disseminated pyrite (TS).
108236	L920-164.5	Fine grained quartz-biotite schist with biotite and cordierite porphyrblasts and disseminated pyrite (TS).
108237	L920-167.9	Fine grained quartz-muscovite schist with biotite, andalusite and staurolite porphyroblasts and disseminated pyrite (TS).
108238	L920-176.5	Quartz-biotite-pyrite-chalcopyrite vein (PTS).

Table A3-2. Samples from the Dry River South deposit.

Catalogue number	Field number (Drill hole-depth in meters)	Description
108239	DRS15-132.7	Fine grained quartz-biotite-albite schist (TS).
108240	DRS15-191.9	Medium grained massive pyrite-chalcopyrite-sphalerite-galena (PTS).
108241	DRS15-193.7	Medium grained massive pyrite-sphalerite-galena (PTS).
108242	DRS15-196.5	Fractured medium grained massive pyrite-sphalerite-chalcopyrite-galena with carbonate veinlets (PTS).
108243	DRS15-197.5	Fine grained quartz-biotite-muscovite schist with 10-30 mm, elengate blocks of fine to medium grained quartz-albite-muscovite-biotite schist with relic anhedral quartz phenocrysts (TS).
108244	DRS15-199.4	Fine grained quartz-muscovite schist with biotite and staurolite porphyroblasts (PTS).
108245	DRS15-203.7	Fine to medium grained massive pyrite-chalcopyrite with biotite-chlorite gangue (PTS).
108246	DRS15-206.4	Fine to medium grained massive pyrite-chalcopyrite with chlorite-biotite gangue (PTS).
108247	DRS15-210.1	Fine grained quartz-muscovite schist with gahnite and staurolite porphyroblasts and disseminated pyrite (PTS).
108248	DRS16-220.2	30 mm pyrite-carbonate-biotite-chalcopyrite vein cutting medium grained biotite-carbonate-zeolite schist (PTS).
108249	DRS16-222.0	Medium grained massive pyrite-sphalerite-galena with minor chlorite gangue (PTS).
108250	DRS16-225.7	Medium grained biotite schist with 30% disseminated and blebby pyrite (PTS).
108251	DRS16-239.5	Fine grained quartz-muscovite schist with biotite and staurolite porphyroblasts and dissemated pyrite (PTS).
108252	DRS16-244.0	Fine grained quartz-muscovite schist with andalusite porphyroblasts and 15-25% disseminated and stringer pyrite (PTS).
108253	DRS17-263.0	Albite-quartz-biotite augen schist (TS).
108254	DRS18-318.4	Fine grained quartz-muscovite-biotite schist with staurolite porphyroblasts and disseminated pyrite (PTS).
108255	DRS19-159.4	Fine grained quartz-biotite-albite schist (TS).
108256	DRS19-169.6	Crenulated fine grained quartz-biotite-muscovite schist with staurolite porphyroblasts (TS).
108257	DRS19-209.0	Medium grained semi-massive pyrite-sphalerite-galena with quartz-biotite gangue that may occur as rounded blocks up to 30 mm.
108258	DRS19-210.4	Medium grained massive pyrite-chalcopyrite with chlorite-biotite-quartz gangue (PTS).
108259	DRS20-196.5	Medium grained massive chalcopyrite-pyrite-sphalerite with chlorite-gahnite gangue (PTS).
108260	DRS20-241.9	Schistose quartz-feldspar porphyry (TS).
108261	DRS21-131.6	Schistose quartz-feldspar porphyry (TS).
108262	DRS22-101.0	Strongly crenulated biotite-quartz-muscovite schist (PTS).
108263	DRS22-110.5	Fine grained quartz-biotite-muscovite schist with staurolite porphyroblasts (PTS).
108264	DRS22-132.5	Lightly sericitized albite-quartz schist with garnet and oriented hornblende porphyroblasts (PTS).
108265	DRS22-156.8	Fine grained quartz-biotite-muscovite schist with staurolite porphyroblasts (PTS).
108266	DRS22-170.6	Fine grained quartz-muscovite schist with biotite and staurolite porphyroblasts (PTS).
108267	DRS22-180.5	Crenulated, fine grained quartz-muscovite schist with biotite and staurolite porphyroblasts (PTS).
108268	DRS22-192.3	Fine grained quartz-biotite-albite schist with minor staurolite porphyrobalsts and disseminated pyrite (PTS).
108269	DRS22-205.6	Fine grained quartz-biotite schist with staurolite porphyroblasts (PTS).
108270	DRS22-215.6	Crenulated, fine grained quartz muscovite schist with biotite, staurolite and andalusite porphyroblasts (PTS).
108271	DRS22-226.7	Fine grained quartz-biotite-muscovite-albite schist with staurolite porphyroblasts (PTS).
108272	DRS22-233.5	Fine grained quartz-biotite-albite schist with staurolite porphyrobalsts (PTS).
108273	DRS22-242.4	Fine to medium grained biotite schist with staurolite and 10-15% pyrite (PTS).
108274	DRS22-249.3	Medium grained massive pyrite-sphalerite-galena with quartz-biotite-gahnite gangue (PTS).
108275	DRS22-251.8	Medium grained massive pyrite with minor interstitial chalcopyrite (PTS).
108276	DRS22-255.2	Medium grained massive pyrite with staurolite porphyroblasts (PTS).
108277	DRS22-257.1	Medium grained biotite schist with staurolite porphyroblasts and 10% blebby pyrite (PTS).

Table A3-2. Samples from the Dry River South deposit.

Catalogue number	Field number (Drill hole-depth in meters)	Description
108278	DRS22-259.1	Crenulated, fine grained muscovite schist with staurolite porphyroblasts and 10% disseminated pyrite (PTS).
108279	DRS22-263.7	Medium grained biotite schist with staurolite porphyroblasts and 5-10% blebby and disseminated pyrite (PTS).
108280	DRS22-266.7	Crenulated, fine grained muscovite-quartz schist with staurolite and biotite porphyroblasts and disseminated and stringer pyrite (PTS).
108281	DRS22-279.1	Fine grained quartz-muscovite-biotite schist with biotite and staurolite porphyrblasts and minor disseminated pyrite (PTS).
108282	DRS22-290.3	Crenulated, fine grained muscovite-quartz schist with biotite and staurolite porphyroblasts and 5-7% disseminated pyrite (PTS).
108283	DRS22-299.1	Fine grained quartz-muscovite-sillimanite schist with staurolite and biotite porphyroblasts and 5-7% disseminated medium grained pyrite (PTS).
108284	DRS22-319.6	Fine grained quartz-muscovite schist with biotite and staurolite porphyroblasts and disseminated pyrite (PTS).
108285	DRS22-341.6	Fine grained quartz-muscovite schist with staurolite, biotite and andalusite porphyroblasts and disseminated pyrite (PTS).
108286	DRS22-349.3	Fine grained quartz-muscovite schist with biotite and staurolite porphyrobalsts and disseminated pyrite (PTS).
108287	DRS24-260.1	Fine grained quartz-muscovite schist with 10-30 mm quartz-muscovite augen wrapped by medium grained pyrite-sphalerite-galena veins and bands to form a relic clastic texture (PB).
108288	DRS25-129.0	Fine grained quartz-muscovite-biotite schist with staurolite porphyroblasts (PTS).
108289	DRS25-313.1	Fine grained quartz-muscovite-biotite schist with staurolite porphyroblasts (PTS).
108290	DRS25-351.3	Fine grained quartz-muscovite schist with biotite and staurolite porphyroblasts and blebby and stringer pyrite (PTS).
108291	DRS27-255.9	Fine grained quartz-muscovite schist with biotite and staruolite porphyroblasts (TS).
108292	DRS27-318.8	10 mm quartz-carbonate-magnetite-chalcopyrite vein cutting feldspar-carbonate-chlorite shcist with disseminated chalcopyrite and magnetite (PTS).
108293	DRS27-323.7	Fractured medium grained massive pyrite-chalcopyrite with carbonate-chlorite gangue (PTS).
108294	DRS27-338.3	Medium grained quartz-muscovite schist with biotite and staurolite porphyroblasts and blebby and stringer pyrite (PTS).
108295	DRS27-349.9	Fine grained quartz-muscovite schist with biotite and staurolite porphyroblats and minor disseminated pyrite (PTS).
108296	DRS32-245.4	Fine grained quartz-biotite-albite schist (TS).
108297	DRS32-259.4	Fine grained quartz-biotie-muscovite-albite schist with staurolite porphyroblasts (TS).
108298	DRS32-264.2	Fine to medium grained massive pyrite-chalcopyrite with quartz-biotite-gahnite gangue (PTS).
108299	DRS32-269.8	Medium grained massive chalcopyrite with pyrite porphyroblasts and quartz-biotie-gahnite gangue from a massive stringer (PTS).
108300	DRS32-276.5	Crenulated, fine grained quartz-muscovite schist with biotite and staurolite porphyroblasts and disseminated pyrite (PTS).
108301	DRS32-277.0	Fine grained quartz-muscovite-biotite augen schist with disseminated pyrite (PTS).
108302	DRS39-165.7	Contact between fine grained massive magnetite with chlorite gangue and medium grained semi-massive pyrite with quartz-chlorite-staurolite gangue (PTS).
108303	DRS46-405.6	Fine to medium grained biotite-feldspar chlorite-hornblende schist with blebs of pyrite-chalcopyrite (PTS).
108304	DRS46W-405.4	1-10 mm chalcopyrite-magnetite-sphalerite veins cutting feldspar-quartz-biotite schist with disseminated pyrite and chalcopyrite (PB).
108305	DRS49-439.6	0.5-2 mm chalcopyrite-pyrite veins cutting fine grained quartz-biotite-albite schist (PB).
108306	DRS52-339.0	Intensely carbonated non-foliated dolerite (TS).

Table A3-3. Samples from the Rosebery deposit.

Catalogue number	Field number	Description
106767	R-1	Hanging wall pyroclastics (TS).
106768	R-2	Strongly cleaved sericite-chlorite schist cut by chlorite-pyrite veinlets (PTS).
106769	R-3	Coarsely banded, medium grained massive pyrite-chalcopyrite with minor sphalerite (PB).
106770	R-4	Very fine grained quartz-sericite schist with disseminated medium grained pyrite (TS).
106771	R-5	Sphalerite- and galena-rich massive barite (PS).
106772	R-6	Moderately banded massive sphalerite-galena-pyrite (PB).
106773	R-7	Well banded massive sphalerite-galena-pyrite with quartz and sericite gangue (PTS).
106774	R-8	Very fine grained massive pyrite-chalcopyrite (PB).
106775	R-9	Fine to medium grained, well banded, massive sphalerite-galena-pyrite (PB).
106776	R-10	Medium grained massive hematite (PB).
106777	R-11	Chert with disseminated pyrite (TS).
106778	R-12	Well banded massive barite with bands of sphalerite and galena (PB).
106779	R-13	Fine to medium grained massive sphalerite-galena-pyrite (PB).
106780	R-15	Medium to coarse grained massive pyrite with quartz gangue (PB).
106781	R-16	Very fine grained quartz-sericite schist.
	(Drill hole-depth in feet)	
108307	R3282-117	Fine grained semi-massive pyrite with quartz-chlorite gangue (PTS).
108308	R3346-104.5	Fine grained semi-massive pyrite with chlorite-carbonate gangue (PTS).
108309	R3346-106	Fine grained chlorite-sericite-carbonate-quartz schist with disseminated sphalerite, galena and pyrite (PTS).
108310	R3374-104.5	Fine grained massive carbonate with minor sericite and chlorite cut by a carbonate-sphalerite-galena-chalcopyrite vein (PTS).
108311	R3374-111.5	Massive "oolitic" carbonate cut by 0.02-5 mm pyrite-chalcopyrite-carbonate-sphalerite-galena veinlets (PTS).
108312	R3374-114.5	Massive "oolitic" carbonate with veinlet sulfide (TS).
108313	R3374-129.5	Fine grained semi-massive pyrite with quartz-carbonate-chlorite gangue (PTS).
108314	R3375-114.5	Fine grained sericite-chlorite-quartz schist with disseminate pyrite cut by a 7 mm quartz-chlorite-sphalerite-sericite-chalcopyrite vein (PTS).
108315	R3375-121	Fine grained chlorite-sericite schist with lenses of carbonate and disseminated pyrite (PTS).
108316	R3377-220	Semi-massive colloform pyrite with cherty quartz gangue (PTS).
108317	R3382-185	Contact between fine grained semi-massive pyrite-sphalerite-galena with chlorite-carbonate-sericite gangue and chlorite-sericite schist containing blebby pyrite-sphalerite and stringer-like chalcopyrite (PTS).
108318	R3382-192	Fine grained sericite-quartz schist with elongate, fine to medium grained blebs of sphalerite, pyrite and galena (PTS).
108319	R3382-218	Sphalerite blebs in quartz-sericite schist which grades upwards into semi-massive sphalerite-galena-pyrite with sericite-quartz gangue (PTS).
108320	R3382-221	Semi-massive, fine grained massive pyrite-sphalerite-galena with sericite gangue (PTS).
108321	R3382-241	Medium grained block of massive carbonate with minor chlorite and quartz in fine grained massive pyrite-sphalerite-galena-pyrite (PTS).
108322	R3382-265	Weakly banded, fine grained massive pyrite-sphalerite-galena with albite gangue (PTS).
108323	R3382-268.5	Weakly banded to irregular blebs of honey sphalerite with lesser galena an minor chlacopyrite in a fine grained sericite-carbonate-albite-quartz schist (PTS).
108324	R3382-270.25	Massive fine to medium grained barite and honey sphalerite with lesser galena and minor chalcopyrtie (PTS).
108325	R3391-98.5	Fine grained chlorite-sericite-carbonate schist with chalcopyrite-pyrite stringers (PTS).
108326	R3391-100.5	Fine grained massive pyrite-chalcopyrite with quartz-chlorite gangue (PTS).

Table A3-3. Samples from the Rosebery deposit.

Catalogue number	Field number (Drill hole-depth in feet)	Description
108327	R3391-122	Fine grained semi-massive pyrite-sphalerite-galena with sericite-carbonate-quartz schist (PTS).
108328	R3391-133.75	Fine grained semi-massive pyrite-sphalerite-galena with quartz-sericite-carbonate gangue (PTS).
108329	R3391-138.25	Fine grained semi-massive pyrite-sphalerite-galena with chlorite-sericite-quartz gangue (PTS).
108330	R3391-140	Fine grained semi-massive pyrite-sphalerite-galena with sericite-quartz gangue (PTS).
108331	R3391-142.5	Fine grained massive sphalerite-galena-pyrite cut by a vein (?) of fine to medium grained massive pyrite-sphalerite-chalcopyrite-galena (PTS).
108332	R3391-145.75	Breccia, with fine grained quartz-sericite-carbonate schist blocks veined by an albite-quartz vein, carbonate-quartz-sphalerite-galena-chalcopyrite veins and a quartz-carbonate-tetrahedrite-galena-chalcopyrite vein (PTS).
108333	R3391-164	Fine grained massive barite with weakly banded, disseminated sphalerite, galena, pyrite and tetrahedrite (PTS).
108334	R3391-165.75	Fine grained massive barite with disseminated pyrite, chalcopyrite, sphalerite and galena (PTS).
108335	R3391-166	Fine grained massive sphalerite-galena-pyrite-chalcopyrite with barite gangue surrounding 1-15 mm blocks of medium grained massive barite with disseminiated pyrite, chalcopyrite, sphalerite and galena (PTS).
108336	R3391-169	Fine grained massive barite-carbonate with minor disseminated and blebby chalcopyrite, sphalerite, pyrite and galena which is cut by coarser grained barite and carbonate veins (PTS).
108337	R3391-170.5	Fine grained massive barite-quartz-carbonate with disseminated sphalerite and galena (PTS).
108338	R3391-171.75	Chert with fragments and bands of fine grained quartz and carbonate, and with minor disseminated and blebby pyrite (PTS).
108339	R3391-173.75	Fine grained sericite-quartz-feldspar-carbonate schist with disseminated pyrite (PTS).
108340	R3394-108.25	Fine grained chlorite schist with disseminated fine to medium grained pyrite (PTS).
108341	R3394-112	Fine to medium grained massive sphalerite-galena-pyrite with sericite-quartz gangue (PTS).
108342	R3394-113	Banded, fine grained massive sphalerite-galena-pyrite-chalcopyrite with carbonate-sericite gangue (PTS).
108343	R3394-115.75	Fine grained massive sphalerite-pyrite-chalcopyrite with carbonate-chlorite-sericite gangue (PTS).
108344	R3394-132	Fine grained chlorite schist containing bands of disseminated to massive fine grained pyrite-sphalerite-galena (PTS).
108345	R3394-133.5	Fine grained sericite schist containing fine to medium grained pyrite (in bands) with lesser sphalerite and minor galena (PTS).
108346	R3394-147.5	Banded, fine gained massive sphalerite-galena-pyrite (PTS).
108347	R3394-153	Contact between fine grained semi-massive sphalerite-chalcopyrite-galena-pyrite with sericite-quartz gangue and fine grained sericite-quartz schist with disseminated pyrite which is cut by a fine grained vein of massive chalcopyrite-galena-sphalerite (PTS).
108348	R3394-155	Fine grained sericite-quartz schist with carbonate "oolites" cut by a 10 mm quartz-carboante-sphalerite vein (PTS).
108349	R3394-175.25	Fine to medium grained massive carbonate containing blocks of barite and surrounded by fine grained massive honey sphalerite-galena with barite gangue (PTS).
108350	R3394-181	Fine to medium grained massive barite with honey sphalerite, galena and albite (PTS).
108351	R3394-190	Banded, fine grained massive barite with minor carbonate and very minor disseminated pyrite and sphalerite (PTS).
108352	R3397-50	Fine grained quartz-sericite-chlorite augen schist with disseminated pyrite (altered footwall pyroclastics) cut by a 15 mm quartz-carbonate vein (TS).
108353	R3397-108.5	Fine grained chlorite-sericite-carbonate schist containing stringer-like chalcopyrite and bands of disseminated medium grained pyrite (PTS).
108354	R3397-109.5	Contact between sericite-chlorite schist and fine to medium grained, banded, semi-massive pyrite-chalcopyrite with chlorite-sericite gangue (PTS).
108355	R3397-111.5	Fine grained semi-massive pyrite-chalcopyrite-sphalerite with chlorite-sericite gangue (PTS).
108356	R3397-117	Fine grained massive pyrite-chalcopyrite with sericite gangue and discrete sphalerite blebs up to 20 mm (PTS).
108357	R3397-118	Fine grained massive pyrite-chalcopyrite with sericite gangue (PTS).

Table A3-3. Samples from the Rosebery deposit.

Catalogue number	Field number (Drill hole-depth in feet)	Description
108358	R3397-120	Fine grained massive sphalerite-galena-pyrite with sericite gangue (PTS).
108359	R3397-124.5	Fine to medium grained massive pyrite-sphalerite-galena with sericite gangue (PTS).
108360	R3397-129	Fine to medium grained, weakly banded, semi-massive sphalerite-galena-pyrite with sericite gangue (PTS).
108361	R3397-140.5	Breccia, with blocks of fine grained massive barite and coarse grained carbonate in a matrix of fine to medium grained honey sphalerite and galena (PTS).
108362	R3397-141	Massive fine grained barite with minor carbonate and sphalerite cut by a network of irregular chalcopyrite veins (PTS).
108363	R3397-147	Massive, weakly banded, fine to medium grained barite with minor honey sphalerite and galena (PTS).
108364	R3397-165.75	Massive, fine to medium grained barite with carbonate and minor disseminated pyrite, sphalerite and galena (PTS).
108365	R3421-116.5	Fine grained massive carbonate with disseminated pyrite (TS).
108366	R3456-296.5	Breccia with 0.5-15 mm blocks of fine grained massive carbonate with disseminated pyrite set in a matric of sericite-chlorite schist with disseminated pyrite and minor sphalerite (PTS).
108367	R3456-298.5	Breccia, with blocks of carbonate and quartz in a darker matrix of semi-massive pyrite with carbonate-chlorite gangue (PTS).
108368	R3456-302	Fine to medium grained semi-massive to massive pyrite with sericite-quartz-carbonate gangue (PTS).
108369	R3456-303	Weakly banded, fine to medium grained, massive pyrite with sericite gangue and two fine grained sericite blocks (PTS).
108370	R4021-28.0*	Medium grained bismuthinite vein (PB).
108371	R4055-9.9*	Fine grained massive sphalerite-galena-pyrite with carbonate gangue (PTS).

*Depth in meters.

Table A3-4. Collar locations of drill cores sampled.

Hole	Coordinates in meters North	East	RL	Hole	Coordinates in meters North	East	RL
Balcooma							
2B	9070.6	2198.7	10543.6	39B	9044.2	2231.3	10534.3
3	8956.5	2188.6	10537.9	40	9159.0	2187.2	10540.9
4	9020.0	2160.6	10543.1	41	9198.5	2207.2	10532.3
6	8990.8	2495.5	10531.9	42	9200.3	2167.5	10536.9
9A	8799.3	2279.1	10527.4	44	8949.6	2220.3	10533.7
10	8991.6	2273.1	10528.1	49	8949.2	2256.1	10529.8
11	9196.1	2257.7	10526.4	52	8988.1	2186.9	10533.0
12	9038.8	2015.9	10538.6	54	8916.5	2347.5	10527.8
12A	9038.7	2016.5	10538.5	55	9170.0	2396.0	10523.5
16A	8890.6	2269.7	10524.8	N850	8499.7	2147.5	10528.3
23	9046.0	1939.3	10527.7	D860	8594.0	1982.0	10520.0
23A	9040.0	1922.0	10526.7	Q860	8599.6	2220.5	10534.4
24	8966.6	2014.6	10537.6	T860	8596.8	2296.6	10544.8
31	9097.2	2266.5	10528.5	N875	8755.5	2159.4	10532.7
35	9079.9	2139.2	10557.3	F896	8967.0	2019.1	10538.0
36	8840.0	2165.0	10536.5	J900	9000.0	2074.6	10548.4
39	9047.8	2228.1	10534.3	J920	9202.2	2082.0	10535.6
39A	9042.8	2224.6	10534.3	L920	9212.7	2132.8	10538.9
Dry River South							
DRS15	6000.1	2050.4	527.6	DRS25	5890.0	2251.5	524.9
DRS16	5901.5	2049.5	527.7	DRS27	5689.0	2050.0	532.3
DRS17	5799.7	2003.4	532.2	DRS32	5792.0	2050.0	532.0
DRS18	5699.5	1998.7	533.0	DRS39	5994.0	1950.0	523.5
DRS19	5899.0	1999.0	527.9	DRS46	5386.0	1996.0	533.2
DRS20	5899.5	1949.5	528.4	DRS46W	5386.0	1996.0	533.2
DRS21	5897.0	1900.5	527.7	DRS49	5260.3	1999.8	530.5
DRS22	5901.1	2101.5	529.6	DRS52	5260.6	2050.7	527.6
DRS24	5700.6	1894.7	531.0				
Rosebery (coordinates in feet)							
R3282	2850	783	9683	R3394	3650	783	9686
R3346	3350	783	9687	R3397	3650	781	9689
R3374	3600	783	9687	R3421	3750	777	9690
R3375	3150	786	9685	R3456	4150	771	9686
R3382	3650	783	9682	R4021			
R3391	3650	783	9689	R4055	944.9	225.2	2944.4

Coordinates to R4055 are in meters.